FIBER FRACTURE

EDITED BY

M. Elices & J. Llorca

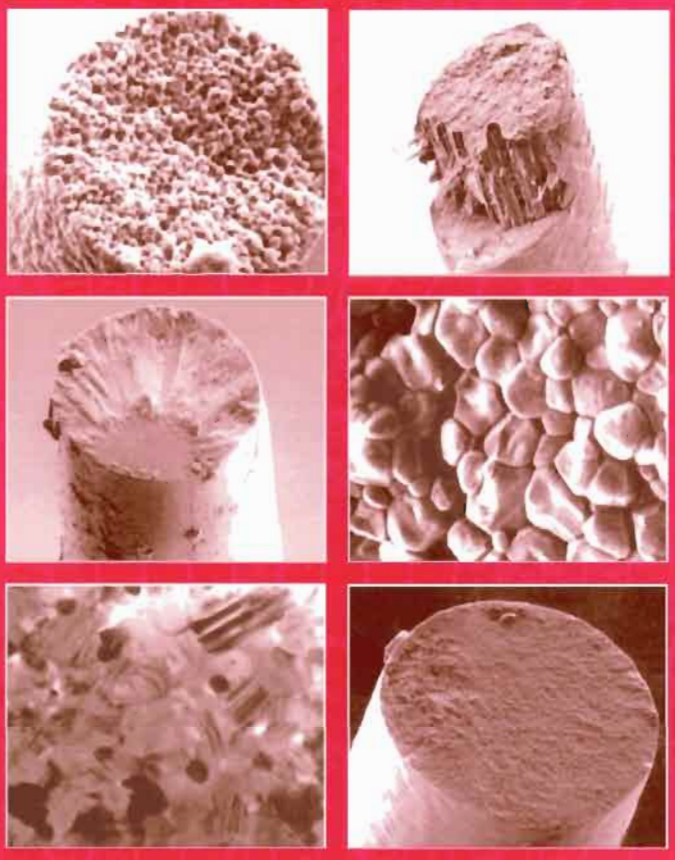

ELSEVIER

FIBER FRACTURE

Elsevier Science Internet Homepage - http://www.elsevier.com

Consult the Elsevier homepage for full catalogue information on all books, journals and electronic products and services.

Elsevier Titles of Related Interest

CARPINTERI
Minimum Reinforcement in Concrete Members.
ISBN: 0-08-043022-8

FUENTES *ET AL.*
Fracture Mechanics: Applications and Challenges.
ISBN: 0-08-043699-4

JONES
Failure Analysis Case Studies II.
ISBN: 0-08-043959-4

MACHA *ET AL.*
Multiaxial Fatigue and Fracture.
ISBN: 0-08-043336-7

MARQUIS & SOLIN
Fatigue Design of Components.
ISBN: 0-08-043318-9

MARQUIS & SOLIN
Fatigue Design and Reliability.
ISBN: 0-08-043329-4

MOORE *ET AL.*
Fracture Mechanics Testing Methods for Polymers, Adhesives and Composites.
ISBN: 0-08-043689-7

MURAKAMI
Metal Fatique Effects of Small Defects and Nonmetallic Inclusions
ISBN: 0-08-044064-9

RAVICHANDRAN *ET AL.*
Small Fatigue Cracks:
Mechanics, Mechanisms & Applications.
ISBN: 0-08-043011-2

RÉMY & PETIT
Temperature-Fatigue Interaction.
ISBN: 0-08-043982-9

TANAKA & DULIKRAVICH
Inverse Problems in Engineering Mechanics II.
ISBN: 0-08-043693-5

UOMOTO
Non-Destructive Testing in Civil Engineering.
ISBN: 0-08-043717-6

VOYIADJIS *ET AL.*
Damage Mechanics in Engineering Materials.
ISBN: 0-08-043322-7

VOYIADJIS & KATTAN
Advances in Damage Mechanics: Metals and Metal Matrix Composites.
ISBN: 0-08-043601-3

WILLIAMS & PAVAN
Fracture of Polymers, Composites and Adhesives.
ISBN: 0-08-043710-9

Related Journals

Free specimen copy gladly sent on request. Elsevier Science Ltd., The Boulevard, Langford Lane, Kidlington, Oxford, OX5 1GB, UK

Acta Metallurgica et Materialia
Cement and Concrete Research
Composite Structures
Computers and Structures
Corrosion Science
Engineering Failure Analysis
Engineering Fracture Mechanics
European Journal of Mechanics A & B
International Journal of Fatigue
International Journal of Impact Engineering
International Journal of Mechanical Sciences
International Journal of Non-Linear Mechanics
International Journal of Plasticity
International Journal of Pressure Vessels and Piping
International Journal of Solids and Structures
Journal of Applied Mathematics and Mechanics
Journal of Construction Steel Research
Journal of the Mechanics and Physics of Solids
Materials Research Bulletin
Mechanics of Materials
Mechanics Research Communications
NDT & E International
Scripta Metallurgica et Materialia
Theoretical and Applied Fracture Mechanics
Tribology International
Wear

To Contact the Publisher

Elsevier Science welcomes enquiries concerning publishing proposals: books, journal special issues, conference proceedings, etc. All formats and media can be considered. Should you have a publishing proposal you wish to discuss, please contact, without obligation, the publisher responsible for Elsevier's mechanics and structural integrity publishing programme:

Dean Eastbury
Senior Publishing Editor, Materials Science & Engineering
Elsevier Science Ltd.
The Boulevard, Langford Lane
Kidlington, Oxford
OX5 1GB, UK

Phone: +44 1865 843580
Fax: +44 1865 843920
E-mail: d.eastbury@elsevier.com

General enquiries, including placing orders, should be directed to Elsevier's Regional Sales Offices – please access the Elsevier homepage for full contact details (homepage details at the top of this page).

FIBER FRACTURE

Editors

M. Elices and J. Llorca

Departamento de Ciencia de Materiales,
Universidad Politecnica de Madrid, Spain

2002
ELSEVIER

AMSTERDAM – BOSTON – LONDON – NEW YORK – OXFORD – PARIS
SAN DIEGO – SAN FRANCISCO – SINGAPORE – SYDNEY – TOKYO

ELSEVIER SCIENCE Ltd.
The Boulevard, Langford Lane
Kidlington, Oxford OX5 1GB, UK

First edition 2002

Library of Congress Cataloging in Publication Data

EURESCO Conference on High Performance Fibers: Euroconference on Fiber Fracture
(2000 : Mallorca, Spain)
Fiber fracture / editors, M. Elices and J. Llorca.
p.cm.
EURESCO Conference on High Performance Fibers: Euroconference on Fiber Fracture held in Cala Viñas (Mallorca, Spain) during the fall of 2000.
Includes bibliographical references and index.
ISBN 0-08-044104-1 (hbk. : alk. paper)
1. Fibers–Congresses. 2. Fracture mechanics–Congresses. I. Elices, Manuel. II. Llorca, J. (Javier) III. Title.

TA418.9F5 E87 2002
620.1'126--dc21

2002029479

British Library Cataloguing in Publication Data
A catalogue record from the British Library has been applied for.

ISBN: 0-08-044104-1

♾ The paper used in this publication meets the requirements of ANSI/NISO Z39.48-1992 (Permanence of Paper).

Printed in The Netherlands.

ACKNOWLEDGEMENTS

This book was conceived during the EURESCO Conference on High Performance Fibers: Euroconference on Fiber Fracture held in Cala Viñas (Mallorca, Spain) during the fall of 2000 under the sponsorship of the European Science Foundation and of the European Union, (through contract HPCF-CT-1999-00126) as well as of the Spanish Ministry of Science and Technology (through grant MAT-1999-1822-E). The Editors would like to acknowledge the support and encouragement of these institutions as well as of others that made possible the Conference and the publication of this book. Particularly we wish to acknowledge the financial support provided by the United States Air Force Office for Scientific Research, NASA Glenn Research Center, and Dupont de Nemours Inc. In addition, the Polytechnic University of Madrid and the University of the Balear Islands contributed actively to the organisation of the Conference and helped with grants for young Spanish researchers.

This book could not have published without the generous co-operation of the distinguished scientists who, besides imparting their keynote lectures at the Conference, agreed to write and polish the manuscripts. The untiring help of Rosa Morera and José Miguel Martínez in the edition of the book is also gratefully acknowledged. Our heart felt thanks to all of them.

MANUEL ELICES and JAVIER LLORCA

Madrid, October 2001

PREFACE

Fibers stand among the stiffest and strongest materials either present in nature or manufactured by man. They are used in structural components, embedded in a matrix which maintains the fibers oriented in the optimum direction, distributes the concentrated loads, protects the fibers against wear and chemical attack from the environment, and provides the transverse stiffness to avoid buckling in compression. These new composite materials are rapidly taking over from the traditional structural materials (metallic alloys and polymers) in many industrial components, and accordingly, a new industry devoted to the manufacture of high performance fibers has emerged. The world wide production of high performance fibers was in excess of 2 millions tons in the year 2000, and it's growing rapidly as new potential uses are envisaged every day.

These novel applications often require further improvements in fiber properties and research in this field is very active. As a result, numerous books and conference proceedings are available on different aspects of fiber processing, properties, or applications but none is focused on the *fracture* behaviour of fibers. Man-made high performance fibers derive their outstanding properties from the strong ionic, covalent or metallic bonds which sustain the load. As the ductility of these links is very limited, fibers are brittle, their ultimate strength being controlled by their fracture behaviour, and further improvements in fiber properties can be obtained through a deeper knowledge of the physical mechanisms involved in fiber fracture. In addition, it has long been known that the excellent combination of strength and ductility exhibited by many natural fibers comes from damage tolerance imparted by their hierarchical structure. However, contact among the researchers working on the mechanical behaviour of natural and synthetic fibers has been very limited so far, and this book also tries to cover this gap by presenting the mechanisms and models of fiber fracture currently available for both kinds of fibers. It is expected that this effort will lead to cross fertilization between the two fields, opening new frontiers to academic research and more competitive products for industry

Finally, a note on the text. Differences in spelling are commonplace in English books written by scholars from different countries, and they normally pass unnoticed. This is not the case, however, in this book where they appear in the very title. Fiber (the american way) and fibre (the traditional British form) are both used freely throughout the book and, although aesthetic considerations would recommend the choice of one or the other, we have decided to keep the original spelling used by each author.

CONTENTS OUTLOOK

The contributions are grouped into seven blocks:

Three introductory chapters are the subject of the first section; *K.K. Chawla* presents an overview of fiber failure. *M. Elices and J. Llorca* review available models of fiber fracture and *J.W.S. Hearle* surveys the diverse forms of fiber fracture exhibited in SEM studies.

The second block is devoted to ceramic fibers, relevant to high temperature metal and ceramic composites. *A.R. Bunsell* deals with SiC fibers. Several generations of these fibers have been produced and the changes in the fracture morphologies between the generations reveal the modifications have been made to improve their behaviour at high temperature. *M.H. Berger* reviews fracture processes in oxide ceramic fibers, stressing the role of microstructure and contaminants in creep failure at high temperatures. The main objective of *A. Sayir and S.C. Farmer* chapter is to examine the fracture characteristics of a new family of single crystal eutectic oxide fibers manufactured by directional solidification which offer greater potential for very high temperature applications owing to their eutectic structure and oxidation resistance.

Glass fibers deserve their own block. They are a major component of the glass industry, which in the last two decades has seen an explosive growth due to the use of silica glass fibers as optical waveguides. Such applications require high tensile strengths over long periods of time, as much as 20 years. *P.K. Gupta* reviews our present understanding of the strength of bare glass fibers.

The combination of stiffness, strength, density and cost makes carbon fibers the best choice for advanced composite materials, and they are dominant in aerospace, automobile, sports goods and other applications. Their fracture properties, together with critical steps in their manufacture, are reviewed by *J.G. Lavin*.

The fifth block is devoted to metallic fibers and thin wires, relevant in the tyre industry, in electrical and electronic applications as well as in civil engineering. *H.U. Künzi* deals with the influence of fabrication processes and microstructure on the strength and fracture of metallic filaments, and *K. Yoshida* analyzes the influence of internal defects during the drawing of these metallic wires.

Polymeric fibers are the subject of the sixth section. Polymeric fibers are, perhaps, commercially the most important of all on account of the magnitude of the textile industry. They may be classified in two broad categories: natural and synthetic. High-modulus and high-tenacity synthetic polymer fibers are reviewed by *J.W.S. Hearle*, stressing the relation between type of loading and fracture mode. *Y. Termonia* summarizes Monte-Carlo lattice models for the study of the factors controlling the mechanical strength and mode of failure of flexible polymer fibers. Natural polymeric fibers are dealt with by *C. Viney*. Their hierarchical structures are recognised as providing enhanced toughness compared to just a fine structure. Factors relevant to fiber assembly and therefore to fracture processes are considered. This block ends with a chapter devoted to fracture of common textile fibers, by *J.W.S. Hearle*. The aim of this chapter is to outline the microstructural changes that occur throughout deformation and lead to ultimate failure, and to remark that defects are not as strong as controlling feature of breakage in these extensible textile fibers, as in many other materials.

The last section is devoted to fracture of nanotubes. Carbon nanotubes have been theoretically predicted to be among the strongest fibers. Their strength, which has already been verified experimentally, may enable unique applications in many critical areas of technology. *J. Bernholc* and collaborators review the mechanical behaviour of carbon nanotubes and the role of bending in changing the electrical properties.

DEFECTS AND MICROSTRUCTURE

Two topics appear in most of the chapters of this book: The role of *defects* in fiber fracture and the *large difference of length scales* in fiber-microstructure. Both features are interwoven and deserve some comments.

Fracture is defect sensitive — contrary to elastic modulus or density — and models of fiber fracture should take into account — and model — such imperfections. Most of our understanding of fiber failure that appears in the chapters is borrowed from bulk concepts — such as the models based on solid state physics — and when Fracture Mechanics is used only idealized defects are considered. Information of the type and shape of actual fiber defects is essential for understanding and modelling fiber fracture, and such information is still scarce.

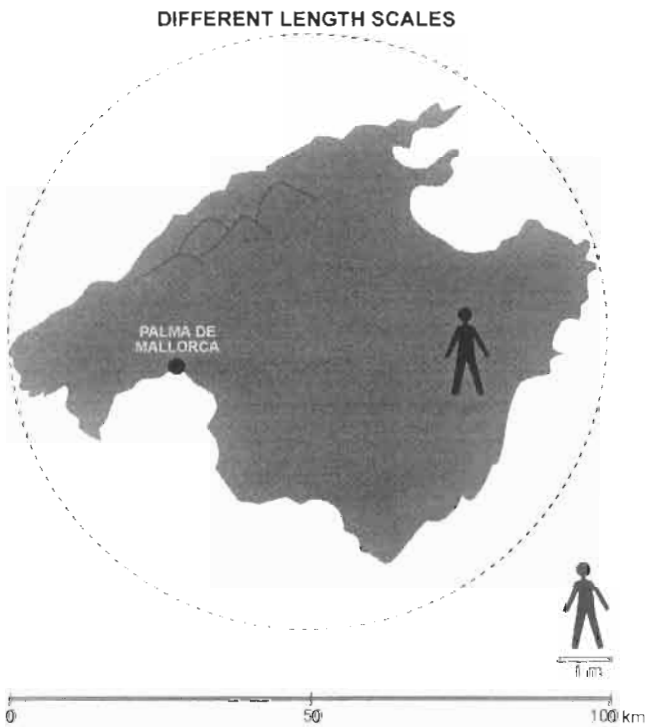

Fiber microstructures span structural details that differ by several orders of magnitude. This makes it difficult to sort out the main structures responsible for the mechanical response one is looking for and this task is more involved when dealing with imperfections. In fibers — and in particular in biological fibers exhibiting highly hierarchical structures — we can find differences in length scales up to five orders of magnitude; from the macromolecular level (1 nm) up to macroscopic level (0.1 mm). This is the same relative difference between the size of a person and the "diameter" of the island of Mallorca, where this Workshop took place (see figure). Looking at the beautiful mountains, landscapes and beaches, it is hard to imagine that fracture may be triggered by defects of human size.

CONTENTS

Acknowledgements v

Preface vii

Introduction

Fiber Fracture: An Overview 3
K.K. Chawla

Models of Fibre Fracture 27
M. Elices and J. Llorca

Forms of Fibre Fracture 57
J.W.S. Hearle

Ceramic Fibers

Fracture Processes in Fine Silicon Carbide Fibres 75
A.R. Bunsell

Fracture Processes in Oxide Ceramic Fibres 89
M.-H. Berger

Fracture Characteristics of Single Crystal and Eutectic Fibers 107
A. Sayir and S.C. Farmer

Glass Fibers

Strength of Glass Fibers 127
P.K. Gupta

Carbon Fibers

Fracture of Carbon Fibers 157
J.G. Lavin

Metallic Fibers

Strength and Fracture of Metallic Filaments 183
H.U. Künzi

Fracture of Superfine Metallic Wires 241
K. Yoshida

Polymeric Fibers

Fracture of Highly Oriented, Chain-Extended Polymer Fibres 265
J.W.S. Hearle

Fracture of Synthetic Polymer Fibers 287
Y. Termonia

Fracture of Natural Polymeric Fibres 303
C. Viney

Fracture of Common Textile Fibres 329
J.W.S. Hearle

Nanofibers

Atomic Transformations, Strength, Plasticity, and Electron Transport in Strained Carbon Nanotubes 357
J. Bernholc, M. Buongiorno Nardelli, D. Orlikowski, C. Roland and Q. Zhao

Author Index 377

Subject Index 389

INTRODUCTION

Fiber Fracture
M. Elices and J. Llorca (Editors)

FIBER FRACTURE: AN OVERVIEW

K.K. Chawla

Department of Materials and Mechanical Engineering, University of Alabama at Birmingham, BEC 254, 1530 3rd Avenue S., Birmingham, AL 35294-4461, USA

Introduction 5
Polymeric Fibers 5
Environmental Effects on Polymeric Fibers 8
Carbon Fibers 9
Metallic Fibers 13
Glass and Ceramic Fibers 17
Conclusions 24
References 24

Abstract

Fracture of fibers during processing or in service is generally an undesirable feature. Fracture in fibers, as in bulk materials, initiates at some flaw(s), internal or on the surface. In general, because of the high surface to volume ratio of fibers, the incidence of a surface flaw leading to fracture is greater in fibers than in bulk materials. Very frequently, a near-surface flaw such as a microvoid or an inclusion is responsible for the initiation of fracture of fiber. In polymeric fibers, the fundamental processes leading to failure are chain scission and/or chain sliding or a combination thereof. Service environment can be a major determining factor in the failure process of fibers. A striking example of this was in the failure of aramid fiber used in the tether rope in space. Metallic fibers represent a relatively mature technology. The surface condition and segregation of inclusions are the two factors that limit the strength of metallic filaments. Ceramic and silica-based fibers (including optical glass fiber) also have the same crack-initiating flaws as in polymeric and metallic fibers. One major problem in glass fibers is that of failure due to static fatigue. In this paper, examples of fracture in different types of fibers are provided. Some of the possible ways to prevent catastrophic

failure in different fibers are pointed out. A considerable amount of progress has been made in the last quarter of the twentieth century.

Keywords

Alumina; Aramid; Carbon; Ceramic; Fibers; Metal; Polyethylene; Polymer; Optical; Steel; Tungsten

INTRODUCTION

Fracture of a fiber is generally an undesirable occurrence. For example, during processing of continuous fibers, frequent breakage of filaments is highly undesirable from a productivity point of view. When this happens in the case of spinning of a polymer, ceramic or a glass fiber, the processing unit must be stopped, the mess of the solution or melt must be cleaned and the process restarted. In the case of a metallic filament, a break means that the starting wire must be pointed again, rethreaded, and the process restarted. In service, of course, one would like the individual fibers whether in a fabric or in a composite to last a reasonable time.

Fracture in fibers, as in bulk materials, initiates at some flaw(s), internal or on the surface. In general, because of the high surface to volume ratio of fibers, the incidence of a surface flaw leading to fracture is greater in fibers than in bulk materials. Fractography, the study of the fracture surface, of fibers can be a useful technique for obtaining fracture parameters and for identifying the sources of failure. In general, the mean strength of a fiber decreases as its length of diameter increases. This size effect is commonly analyzed by applying Weibull statistics to the strength data. As the fiber length or diameter increases, the average strength of the fiber decreases. It is easy to understand this because the probability of finding a critical defect responsible for fracture increases with size. This behavior is shown by organic fibers such as cotton, aramid, as well as inorganic fibers such as tungsten, silicon carbide, glass, or alumina.

In this paper, the salient features of the fracture process in different types of fibers, polymeric, metallic, and ceramic are described. Points of commonality and difference are highlighted.

POLYMERIC FIBERS

A very important characteristic of any polymeric fiber is the degree of molecular chain orientation along the fiber axis. In order to get high strength and stiffness in organic fibers, one must obtain *oriented molecular chains with full extension.* An important result of this chain alignment along the fiber axis is the marked anisotropy in the characteristics of a polymeric fiber.

Rigid-rod polymeric fibers such as aramid fibers show very high strength under axial tension. The failure in tension brings into play the covalent bonding along the axis, which ultimately leads to chain scission and/or chain sliding or a combination thereof. However, they have poor properties under axial compression, torsion, and in the transverse direction. Fig. 1 shows this in a schematic manner. The compressive strength of ceramic fibers, on the other hand, is greater than their tensile strength. The compressive strength of carbon fiber is intermediate to that of polymeric and ceramic fibers. This discrepancy between the tensile and compressive properties has been the subject of investigation by a number of researchers (see Chawla, 1998 for details).

An example of kinking under compression in a high-performance polymeric fiber derived from rigid-rod liquid crystal is shown in Fig. 2 (Kozey and Kumar, 1994). Note that this is a single fiber with preexisting striations on the surface. High-strength

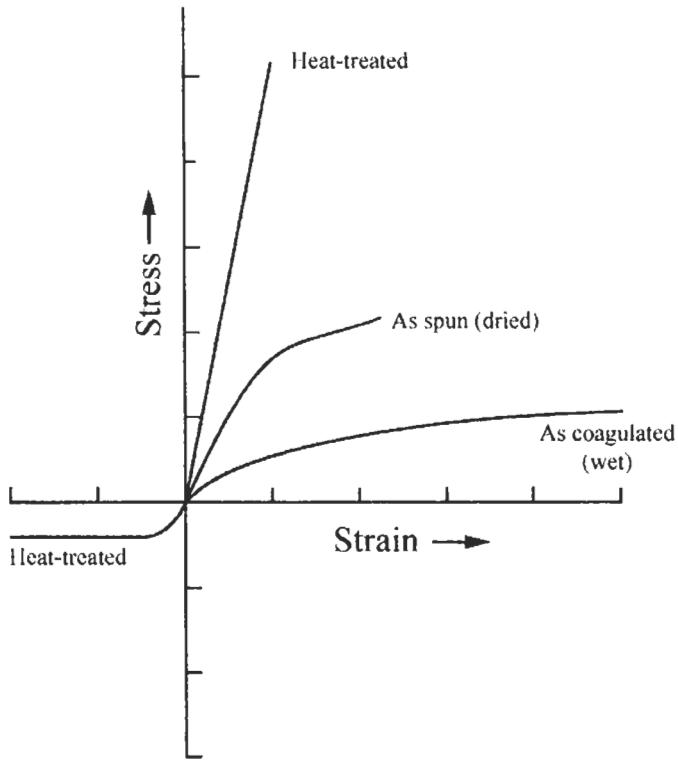

Fig. 1. Schematic stress–strain curves of rigid-rod polymeric fibers in tension and compression. Such fibers show very high strength under axial tension but have poor properties under axial compression, torsion, and in the transverse direction.

organic fibers fail in compression at strains $<1\%$. Microbuckling or shear banding is responsible for easy failure in compression. The spider dragline silk fiber seems to be an exception to this. In general, highly oriented fibers such as aramid fail in a fibrillar fashion. The term fibrillar fracture here signifies that the fracture surface is not transverse to the axis but runs along a number of planes of weakness parallel to the fiber axis. As the orientation of chains in a fiber becomes more parallel to its axis, its axial tensile modules (E) increases but the shear modulus (G) decreases, i.e. the ratio E/G increases tremendously. During failure involving compressive stresses, fibrillation occurs, which results in a large degree of new surface area. This fibrillation process results in high-energy absorption during the process of failure, which makes these fibers useful for resistance against ballistic penetration.

Various models have been proposed to explain this behavior of high-performance fibers. Fig. 3 shows two compressive failure models: (a) elastic *microbuckling* of polymeric chains; and (b) *misorientation*. The microbuckling model involves cooperative in-phase buckling of closely spaced chains in a small region of fiber. The misorientation model takes into account structural imperfections or misorientations that are invariably present in a fiber. In the composites literature it has been reported that regions of

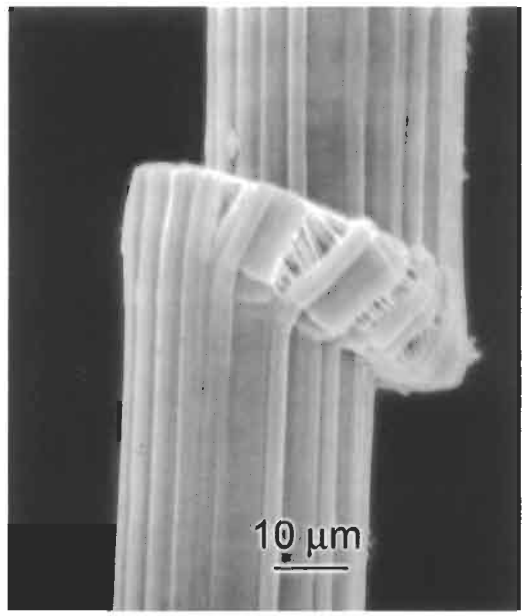

Fig. 2. An example of kinking under compression in a high-performance polymeric fiber derived from rigid-rod liquid crystal (courtesy of Kozey and Kumar). High-strength organic fibers fail in compression at strains <1%. Microbuckling or shear banding is responsible for easy failure in compression.

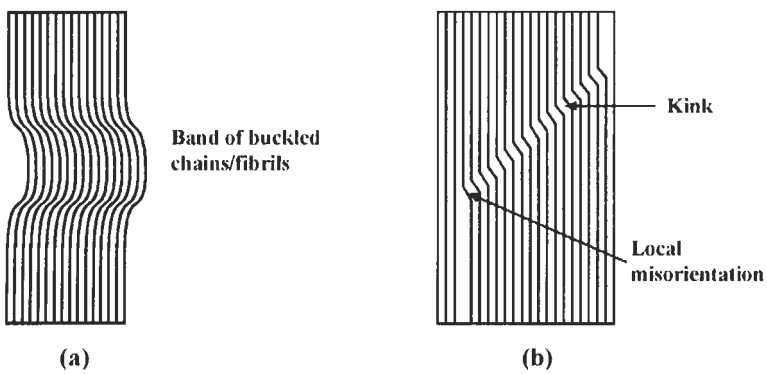

Fig. 3. Two compressive failure models: (a) elastic *microbuckling* of polymeric chains; this model involves cooperative in-phase buckling of closely spaced chains in a small region of fiber; (b) *misorientation*; this model is based on structural imperfections or misorientations that are invariably present in a fiber.

misorientation in a unidirectional composite lead to kink formation under compressive loading (Argon, 1972). The model shown in Fig. 3b is based upon the presence of such a local misorientation in the fiber leading to kink formation under compression. Failure in compression is commonly associated with the formation and propagation of kinks. These kink bands generally start near the fiber surface and then grow to the center of the fiber. It has also been attributed to the ease of microbuckling in such

fibers as well as to the presence of microvoids and the skin–core structure of these fibers. It should be pointed out that poor properties in shear and compression are, however, also observed in other highly oriented polymeric fibers such as polyethylene and poly(*p*-phenylene benzobisoxazole) or PBO fibers, which are not based on rigid-rod polymers. A correlation between good compressive characteristics and a high glass transition temperature (or melting point) has been suggested (Northolt, 1981; Kozey and Kumar, 1994).

Thus, with the glass transition temperature of organic fibers being lower than that of inorganic fibers, the former would be expected to show poorer properties in compression. For aramid and similar fibers, compression results in the formation of kink bands leading to eventual ductile failure. Yielding is observed at about 0.5% strain. This is thought to correspond to a molecular rotation of the amide carbon–nitrogen bond from the normal extended *trans* configuration to a kinked configuration Tanner et al., 1986). This causes a 45° bend in the chain, which propagates across the unit cell, the microfibrils, and a kink band results in the fiber.

Efforts to improve the compressive properties of rigid-rod polymer fibers have involved introduction of cross-linking in the transverse direction. There is a significant effect of intermolecular interaction or intermolecular cross-linking on compressive strength. A polymeric fiber (PIPD) with a compressive strength of 1.6 GPa has been reported (Jenkins et al., 2001). This high compressive strength is ascribed to bi-directional, intermolecular hydrogen bonding. A high degree of intermolecular covalent cross-linking should result in higher compressive strength, as compared to systems in which only hydrogen bonding is present (Jenkins et al., 2001). However, cross-linking may also result in lower tensile strength and increased brittleness of the fiber. Cross-linking by thermal treatment may result in the development of internal stresses. Other cross-linking methods (e.g. via radiation) should be explored in greater detail. One would expect radiation to result in a different cross-linked structure than that obtained by thermal treatment. Here it is instructive to compare the behavior of some carbon fibers. Highly graphitic, mesophase pitch-based fibers show a fibrillar fracture and poor compressive properties. PAN-based carbon fibers, which have some linking of the graphitic planes in the transverse direction, show better properties in compression and not a very fibrillar fracture. Of course metallic and ceramic fibers show little fibrillation during a tensile or compressive failure.

Environmental Effects on Polymeric Fibers

Environmental factors such as humidity, temperature, pH, ultraviolet radiation, and micro-organisms can affect the strength and the fracture process in polymeric fibers. Natural polymeric fibers are more susceptible to environmental degradation than synthetic polymeric fibers. Cellulose is attacked by a variety of bacteria, fungi, and algae. Micro-organisms use cellulose as a food source. Natural fibers based on protein such as wool, hair, silk, etc., can also be a food source for micro-organisms, but such fibers are more prone to degradation due to humidity and temperature. Polymeric fibers, natural or synthetic, undergo photo degradation when exposed to light (both visible and ultraviolet). Physically this results in discoloration, but is also accompanied by a

worsening of mechanical characteristics. A striking example of environmental leading to failure of aramid fiber was the failure of the tether rope for a satellite in space. The rope made of aramid fiber failed because of friction leading to excessive static charge accumulation, which led to premature failure of the tether rope and the loss of an expensive satellite.

In a multifilament yarn or in a braided fabric, frictional force in the radial direction holds the fibers together. Such interfiber friction is desirable if we wish to have strong yarns and fabrics. However, there are situations where we would like to have a smooth fiber surface. For example, for a yarn passing round a guide, a smooth fiber surface will be desirable. If the yarn surface is rough, then a high tension will be required, which, in turn, can lead to fiber breakage. In general, in textile applications, frictional characteristics can affect the handle, feel, wear-resistance, etc. In fibrous composites, the frictional characteristics of fiber can affect the interface strength and toughness characteristics.

CARBON FIBERS

Carbon fibers are, in some ways, similar to polymeric fibers while in other ways they are similar to ceramic fibers. A characteristic feature of the structure of all carbon fibers is the high degree of alignment of the basal planes of graphite along the fiber axis. The degree of alignment of these graphitic planes can vary depending on the precursor used and the processing, especially the heat treatment temperature used. Transmission electron microscopic studies of carbon fiber show the heterogeneous microstructure of carbon fibers. In particular, there occurs a pronounced irregularity in the packing of graphitic lamellae as one goes from the fiber surface inward to the core or fiber axis. The graphitic basal planes are much better aligned in the near-surface region of the fiber, called the *sheath*. The material inside the sheath can have a radial structure or an irregular layer structure, sometimes termed the *onion skin* structure. The radial core and well aligned sheath structure is more commonly observed in mesophase-pitch-based carbon fibers. A variety of arrangement of graphitic layers can be seen in different fibers. In very general terms, the graphitic ribbons are oriented more or less parallel to the fiber axis with random interlinking of layers, longitudinally and laterally (Jain and Abhiraman, 1987; Johnson, 1987; Deurbergue and Oberlin, 1991). Fig. 4 shows a two-dimensional representation of this lamellar structure called *turbostratic* structure. Note the distorted carbon layers and the rather irregular space filling. The degree of alignment of the basal planes increases with the final heat treatment temperature. Examination of lattice images of the cross-section of carbon fiber shows essentially parallel basal planes in the skin region, but extensive folding of layer planes can be seen in the core region. It is thought that this extensive interlinking of lattice planes in the longitudinal direction is responsible for better compressive properties of carbon fiber than aramid fibers. In spite of the better alignment of basal planes in the skin region, the surface of carbon fibers can show extremely fine scale roughness. A scanning electron micrograph of pitch-based carbon fibers is shown in Fig. 5. Note the surface striations and the roughness at a microscopic scale

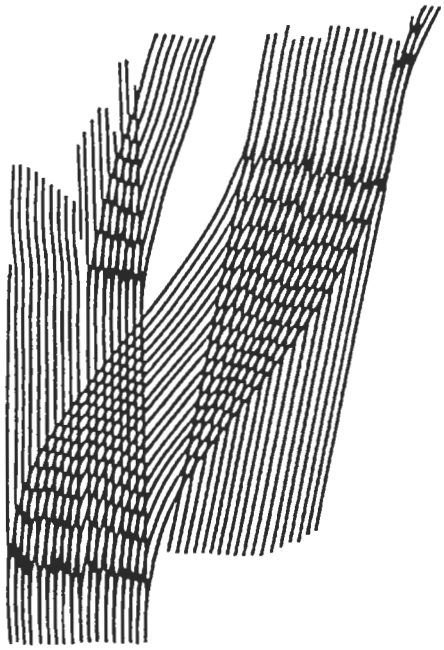

Fig. 4. A two-dimensional representation of the lamellar structure (or *turbostratic* structure) of a carbon fiber. The cross-section of carbon fiber has essentially parallel basal planes in the skin region, but extensive folding of layer planes can be seen in the core region. It is thought that this extensive interlinking of lattice planes in the longitudinal direction is responsible for better compressive properties of carbon fiber than aramid fibers.

A carbon fiber with a perfectly graphitic structure will have the theoretical Young modulus of slightly over 1000 GPa. In practice, however, the Young modulus is about 50% of the theoretical value in the case of PAN-based carbon fiber and may reach as much as 80% of the theoretical value for the mesophase-pitch-based carbon fiber. The strength of carbon fiber falls way short of the theoretical value of 180 GPa (Reynolds, 1981). The practical strength values of carbon fiber may range from 3 to 20 GPa. The main reason for this is that while the modulus is determined mainly by the graphitic crystal structure, the strength is a very sensitive function of any defects that might be present, for example, voids, impurities, inclusions, etc. The strength of carbon fiber thus depends on the gage length, decreasing with increasing gage length. This is because the probability of finding a defect in the carbon fiber increases with its gage length. Understandably, it also depends on the purity of the precursor polymer and the spinning conditions. A filtered polymer dope and a clean spinning atmosphere will result in a higher strength carbon fiber for a given gage length.

Following Hüttinger (1990), we can correlate the modulus and strength of carbon fiber to its diameter. One can use Weibull statistics to analyze the strength distribution in brittle materials such as carbon fiber. As mentioned above, such brittle materials show a *size effect*, viz., the experimental strength decreases with increasing sample size. This is demonstrated in Fig. 6, which shows a log–log plot of Young's modulus as a function

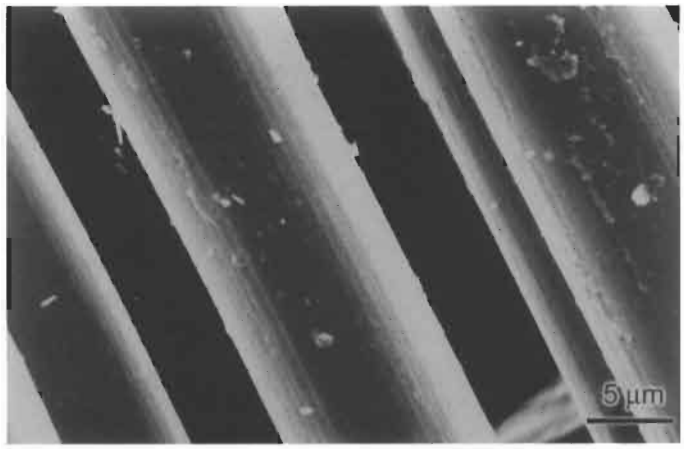

Fig. 5. A scanning electron micrograph of pitch-based carbon fibers. Note the surface striations and the roughness at a microscopic scale.

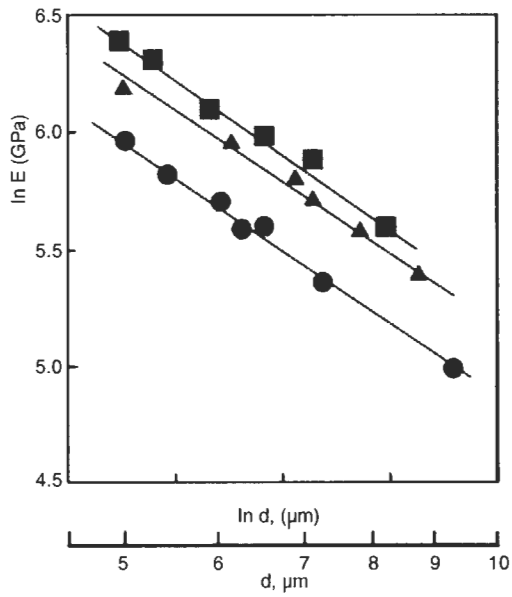

Fig. 6. A log–log plot of Young's modulus as a function of carbon fiber diameter for three different carbon fibers (after Hüttinger, 1990). The curves follow the expression $(E/E_0) = (d_0/d)^n$ where E is Young's modulus of the commercial carbon fiber of diameter d while E_0 is the theoretical Young modulus and d_0 is the fiber diameter corresponding to E_0. The exponent, n obtained from the slope of the straight lines in this figure is about 1.5, and is independent of the fiber type.

of carbon fiber diameter for three different commercially available carbon fibers. The curves in this figure are based on the following expression:

$$(E/E_0) = (d_0/d)^n \tag{1}$$

where E is Young's modulus of the commercial carbon fiber of diameter d while E_0 is the theoretical Young modulus and d_0 is the fiber diameter corresponding to E_0. The exponent, n obtained from the slope of the straight lines in Fig. 6 is about 1.5, and is independent of the fiber type. It would appear that these fibers would attain their theoretical value of modulus at a diameter of about 3 μm.

If we perform a similar analysis with respect to the tensile strength of carbon fibers, we can write:

$$(\sigma/\sigma_0) = (d_0/d)^n \tag{2}$$

where σ is the strength of a fiber with a diameter d, while σ_0 is the higher strength of a fiber with a smaller diameter, d_0.

Now the theoretical strength of a crystalline solid, σ_0 is expected to be about 0.1 E_0 (Meyers and Chawla, 1999), i.e. in this case $\sigma_0 = 100$ GPa. For this value of σ_0, the exponent n in Eq. 2 is between 1.65 and 2 (Meyers and Chawla, 1999). This means that in order to obtain a strength of 100 GPa, the diameter of the carbon fiber must be reduced from d to $d_0 < 1$ μm. Note that this d_0 value corresponding to theoretical strength is less than the d_0 value corresponding to the theoretical modulus. The strength corresponding to a 3 μm diameter carbon fiber from Eq. 3 will be between 12 and 18 GPa, an extremely high value. This can be understood in terms of the heterogeneous structure of carbon fiber. Recall from our discussion above that the near-surface region of a carbon fiber has more oriented basal planes than in the core. As we make the fiber diameter smaller, essentially we are reducing the proportion of the core to the near-surface region.

The fracture in carbon fibers is attributed to the presence of discrete flaws on the fiber surface and within it. Most of the volumetric defects in carbon fibers originate from the following sources:

(1) inorganic inclusions
(2) organic inclusions
(3) irregular voids from rapid coagulation
(4) cylindrical voids precipitated by dissolved gases

These defects get transformed during the high-temperature treatment into diverse imperfections. Basal-plane cracks called *Mrozowski* cracks represent the most important type of flaw that limit the tensile strength of carbon fibers. These occur as a result of anisotropic thermal contractions within the ribbon structure on cooling down from high-temperature treatment (>1500°C). These cracks are generally aligned along the fiber axis. Their presence lowers the tensile strength of the fiber by providing easy crack nucleation sites. The fiber elastic modulus, however, is unaffected because the elastic strains involved in the modulus measurement are too small. Surface flaws can also limit the tensile strength of the carbonized fibers. Oxidation treatments tend to remove the surface defects and thus increase the strength levels of the fiber.

It should be mentioned that compressive strength of carbon fiber is low compared to its tensile strength. The ratio of compressive strength to tensile strength for carbon fibers may vary anywhere between 0.2 and 1 (Kumar, 1989). High-modulus PAN-based carbon fibers buckle on compression, forming kink bands at thinner surface of the fiber. A crack initiates on the tensile side and propagates across the fiber (Johnson,

1990). In contrast, high-modulus mesophase pitch-based carbon fibers deform by a shear mechanism leading to kink bands at 45° to the fiber axis.

METALLIC FIBERS

Metallic filaments represent a fairly mature technology. Steel and other metals are used routinely in the form filaments for reinforcement of tires, surgical purposes, bridge cables, overhead transmission cables, etc. The tire cord is a major application of steel filaments, called cord. The driving force behind the research for high-strength steel wire for tire reinforcement is to make a fuel-efficient car. Increasing the strength of steel reinforcement wire allows a thinner wire to be used for the same strengthening effect. Cabled steel filaments (i.e. twisted bundles) are used in tires as well as in other applications. The reversed loading of a tire occurs at ground contact during rotation. Thus, the behavior of steel filaments in torsion and fatigue becomes an important item. Also, the twist given to the bundles coupled with the state of residual stress in the steel filaments can induce longitudinal splitting in the filaments (Paris, 1996).

Strength levels of up to 5 GPa can be obtained in steel filaments. Conventional galvanized steel wire for bridge cable has a tensile strength of 1.6 GPa. Nippon Steel researchers raised this strength to 1.8 and 2.0 GPa for steel filaments used in the world's longest bridge, the Akashi Strait Bridge (Tarui et al., 1996). Such filaments must withstand static and dynamic loads under a variety of loading conditions. The strand wire rope has a complex geometry. Even when a strand wire rope is loaded in simple tension, it can put individual fibers in tension, torsion, and bending. In particular, bending and torsion can lead to splitting delamination (Brownrigg et al., 1984). Tungsten filaments are used for incandescent lamps. Aluminum and copper are used as electrical conductors, but their ability to withstand static (creep) and dynamic loadings is also important.

Control of inclusion content is of critical importance in metallic filaments. In particular, in steel, microsegregation and interstitial content are also important. C, Mn, and Si are required for strength in steel filaments but their microsegregation must be controlled. P and S must be eliminated. Very large drawing strains are involved in the processing of metallic filaments. The inclusions typically consist of carbides as well as oxides such as alumina, mullite, spinel, and calcium hexaluminate. If the inclusions remain undeformed during the drawing process, decohesion of the matrix/inclusion interface occurs and void(s) are produced. If the inclusion fractures, void(s) form. It is important to avoid the formation of hard microconstituents such as martensite and bainite. Inclusions such as C, Mn, P, etc., tend to segregate to the center of the wire. An important processing-related point in regard to the manufacture of steel cord is the number of breaks per ton of production in the drawing process (Takahashi et al., 1992). Of course, the smaller such breaks the better. Not unexpectedly, the frequency of breaks is a function of the size of nonmetallic inclusions in the wire. The filament break frequency tends to zero for inclusions of a diameter of 5 μm or less (Takahashi et al., 1992). This serves to emphasize a general principle about the importance of inclusion in control.

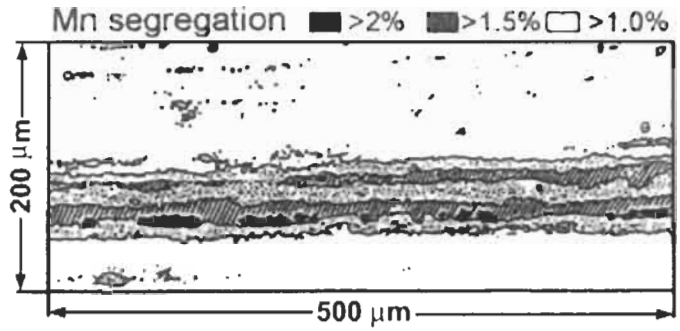

Fig. 7. The segregation of manganese in the center of a rolled steel rod (after Takahashi et al., 1992). Any untransformed austenite in the central zone will transform to martensite (a hard, brittle phase) because of the presence of manganese there.

Steel wires can vary in composition enormously, from simple C–Mn steel to alloy steels containing more than ten alloy additions. Control of impurities (mostly nonmetallic inclusions), chemical segregation, surface imperfections, and chemical segregation, coupled with uniformity in grain size can result in a very high-quality product. The carbon content of steel wire may range from low to high, with the latter generally having carbon content between 0.5 and 0.9 wt%. Eutectoid steel has carbon between 0.8 and 0.9 wt% and consists of a 100% pearlitic microstructure. Steel in the form of wire can be very strong compared to the bulk steel although its modulus does not change very much. The strength of steel wire can span the range of 0.8 to 5 GPa. Wires can range in diameter from coarse ($\geq$1.5 mm) to very fine ($\leq$0.1 mm).

The strength of the steel wire is controlled by delaminations that appear along the wire axis when it is twisted during the cable strand formation. The genesis of nonmetallic inclusions in steel wire lies in the process of steel making. During solidification of steel, because of solute redistribution, elements such as C, Mn and P segregate between the dendrites. This inclusion containing molten steel ends up in the shrinkage cavities at the center of the bar, solidifies there and results in the centerline segregation. Fig. 7 shows the segregation of manganese in the center of a rolled rod (Takahashi et al., 1992). Any untransformed austenite in the central zone will transform to martensite (a hard, brittle phase) because of the presence of manganese there. Segregation of carbon can lead to cementite film formation at austenitic grain boundaries. Such segregation can severely limit the drawability of steel wire. Fig. 8 shows the drawing limit strain as a function of the center segregation in the starting billet (Takahashi et al., 1992). A reduction in segregation size improves drawability. This tendency for centerline segregation can be minimized by finely dispersing the solute-enriched molten steel and pressure welding the shrinkage cavities where this enriched steel accumulates. This can be accomplished by lowering the pouring temperature of molten steel and electromagnetically stirring the molten steel (Takahashi et al., 1992).

The tungsten filament operates in vacuum or surrounded by inert gases at about 2600°C. The high melting point of tungsten (3400°C) allows it to be operated at such a high temperature. At these high operating temperatures, the tungsten filament creeps

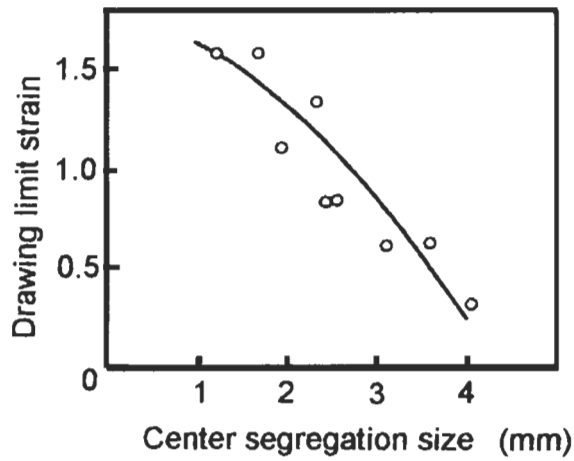

Fig. 8. The drawing limit strain as a function of the center segregation in the starting steel billet. A reduction in segregation size improves drawability. (After Takahashi et al., 1992.)

under its own weight and most of this creep occurs by grain boundary sliding. In order to minimize this creep problem, an elongated, bamboo-type grain boundary structure as produced by wire drawing is desirable. In such a bamboo-type grain structure, we have a small number of grain boundaries perpendicular to the filament axis. The interstitial content, mainly oxygen and to a lesser extent nitrogen and carbon, can affect the ductility of tungsten wire. Very small amounts of oxygen, as little as fifty parts per million, are enough to embrittle tungsten. Tungsten containing minor quantities of aluminum (Al), potassium (K) and silicon (Si), known as the AKS tungsten filament or *non-sag* tungsten filament (Wittenauer et al., 1992) has a controlled microstructure to resist creep deformation, which occurs by grain boundary sliding. Such deformation makes the filament sag under its own weight and form a neck where it eventually breaks. In order to reduce such deformation by creep, a bamboo-type grain structure is desirable. A transmission electron micrograph, Fig. 9, shows this structure. Note the longitudinally aligned boundaries with very few grain boundaries aligned transverse to the filament axis. Under the service conditions for the tungsten filament, such boundaries will undergo sliding and lead to failure of the filament. The addition of potassium to tungsten results in an interlocking grain structure, which results in a reduced rate of grain boundary sliding and longer life for the filament than that of the undoped filament. After sintering the doped tungsten ingot has pores that contain elemental potassium. With wire drawing, these pores assume an elongated, tubular structure. When this material is annealed at a high temperature, these tubular structures containing potassium vapor become unstable as per Rayleigh waves on the surface of a cylindrical fluid. It is important that the deformation during drawing should be large enough to produce potassium cylinders with an aspect ratio > 10, otherwise they will spheroidize to a form a single bubble (Briant, 1989; Vukcevich, 1990). Fig. 10 shows an example of such bubbles in a transmission electron micrograph of a tungsten filament.

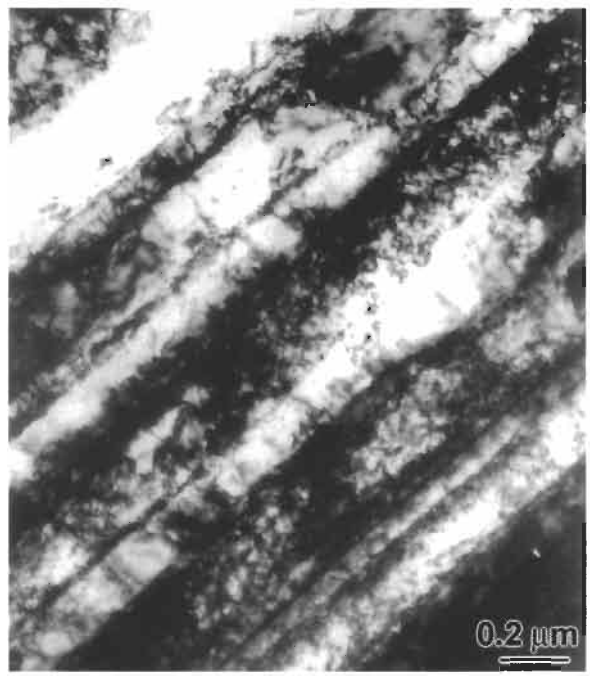

Fig. 9. Bamboo-like grain structure of an AKS tungsten filament. TEM.

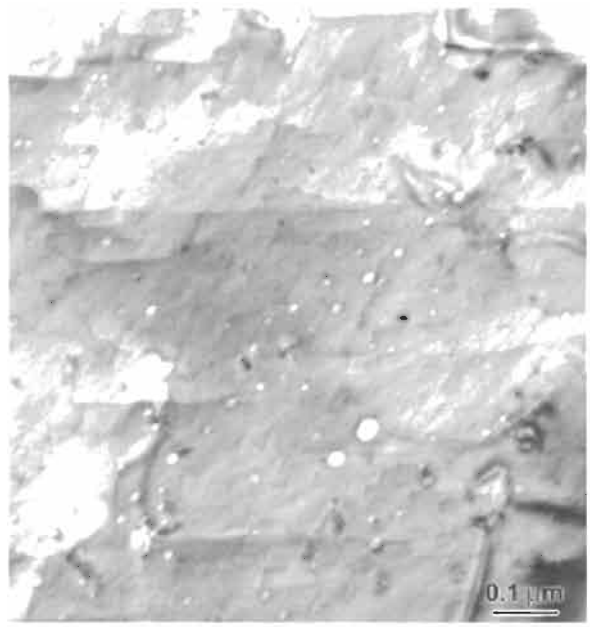

Fig. 10. Bubbles in a tungsten filament. TEM (courtesy of B. Bewlay). The objective is to have a high density of such tiny bubbles so that they pin the grain boundaries effectively against sliding, thus resulting in a microstructure that is stable at the operating temperature.

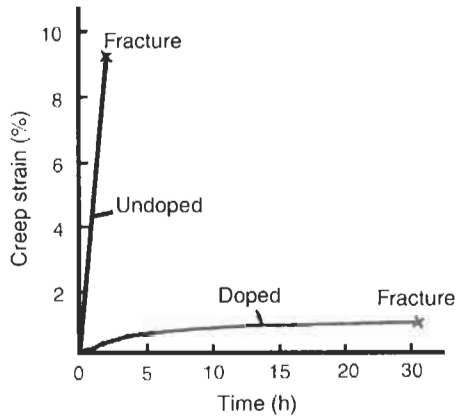

Fig. 11. The superior creep resistance of the doped tungsten filament compared to that of an undoped one (after Horascek, 1989).

The objective is to have a high density of such tiny bubbles so that they pin the grain boundaries effectively against sliding, thus resulting in a microstructure that is stable at the operating temperature. These gas bubbles retard the recrystallization of the wire and give it a very superior creep resistance at the high temperatures prevailing in a glowing lamp and thus a longer life than that of the undoped filament. Fig. 11 shows the superior creep resistance of the doped tungsten filament compared to that of an undoped one (Horascek, 1989).

GLASS AND CERAMIC FIBERS

Ceramic fibers have been researched extensively in the last quarter of the twentieth century past decade. One of the important applications has been the use of ceramic fibers (10–125 μm in diameter) as reinforcement of ceramic matrices to make ceramic matrix composites for high-temperature applications. Improvements in fracture resistance, strength, and creep resistance have been shown due to the incorporation of ceramic fibers into ceramic matrix composites. Another important application has been in the area of optical glass fibers. Specifically, in the nineteen nineties the demand for optical glass fibers increased dramatically due to the advances in telecommunications industry and the availability of the Internet. Optical glass fiber cables are complex structural products. They may contain metal and composite parts for strengthening, water sealants, plastic jackets, etc. When such cables are used in water, corrosion of the metal parts results in the production of hydrogen. If this hydrogen is trapped inside the cable, it can result in an increase in the attenuation of the optical signal via the optical glass fiber. Stresses may also result in the optical glass fiber because of installation. In the case of the optical fibers, the flaws can form during the processing when dust particles and other particles adhere to the surface of the doped silica fiber. Furthermore, there is an increasing demand for optical glass fiber with a large bandwidth and one that can

withstand static fatigue. Slow strength degradation can occur due to static fatigue and eventually causing the optical glass fiber to fracture. With increasing usage of optical glass fiber (some applications are very demanding, e.g. fiber optic cables buried in the top layer of the ocean floor), the issue of reliability has become very important.

Many brittle, amorphous materials such as thermosetting polymers and silica-based inorganic glasses show some telltale markings on their fracture surfaces (Mecholsky et al., 1977, 1979; Chandan et al., 1994). Typically, the fracture surface of a glass fiber shows four distinct regions. These regions are: a smooth *mirror* region, a *misty* region of small radial ridges, a *hackle* region consisting of large ridges, and finally a region of extensive *crack branching*. It turns out that the product of strength, σ, and the square root of the distance of each of these regions from the origin of fracture, is a constant. One can write:

$$\sigma R_i^{0.5} = A_i$$

where A_i is a constant, R_i the radius of the mirror–mist, mist–hackle, or crack branching boundaries. These radii can be related to the initial flaw-depth, a, or the half-width, b, through the fracture mechanics analysis:

$$c/R_i = K_{Ic} Y^2 / 2A_i^2$$

where $c = (ab)^{0.5}$, Y is a geometrical constant and K_{Ic} is the critical stress intensity factor or fracture toughness. The relationship between the mirror radius and the fracture stress of the fiber can be used to generate a plot of σ_f vs. $1/R_i^{1/2}$ as shown in Fig. 12. One can calculate the mirror constant A_i from the slope of the lines. The mirror radius in the case of glass fibers was shown to be much greater than the mirror radius for the polymer-

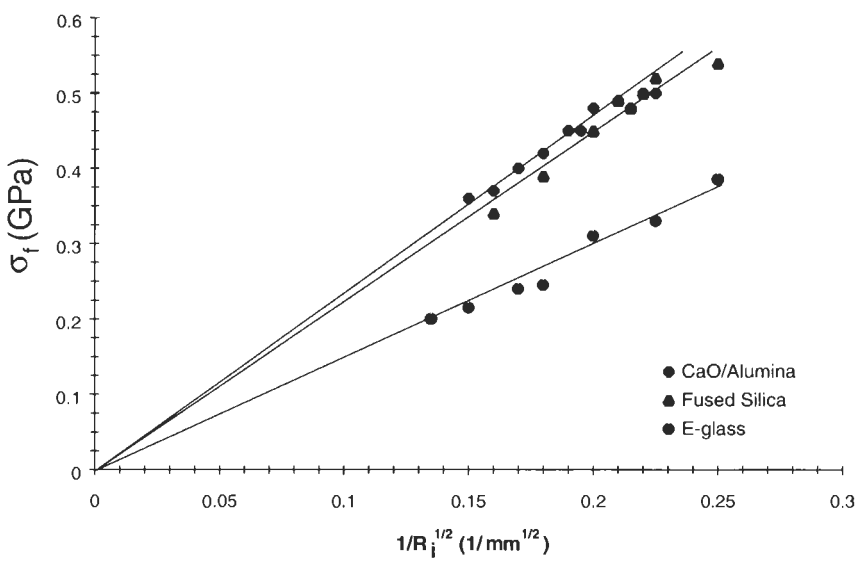

Fig. 12. Plot of fracture stress (σ_f) vs. reciprocal of the mirror radius square root ($1/R_i^{1/2}$) showing the validity of the relationship between the fracture stress and the mirror radius of ceramic and glass fibers.

derived ceramic fibers. The following mirror constants were obtained from the slope of their respective lines in Fig. 12: 1.6 MPa $m^{-1/2}$ for E-glass fiber and 2.2 MPa $m^{-1/2}$ for optical glass and CA fibers. The mirror constant for the fused-silica optical fiber is in good agreement with the A_i value of 2.22 MPa $m^{-1/2}$ and 2.1 MPa $m^{-1/2}$ that was obtained for fused-silica fiber from Chandan et al. (1994) and Mecholsky et al. (1977), respectively. The mirror constants for E-glass and CaO/Al_2O_3 fibers are also in good agreement with previously determined A_i values (Gupta, 1994; Sung and Sung, 1996).

Fractographic work has been done by a number of researchers on polymer-derived SiC fibers (Sawyer et al., 1987; Soraru et al., 1993; Taylor et al., 1998), eutectic oxide–oxide fiber (Yang et al., 1996), and glass fibers (Mecholsky et al., 1977; Chandan et al., 1994; Gupta, 1994; Mecholsky, 1994; Sung and Sung, 1996). Polymer-derived SiC fibers have been tested in several studies and data containing the mirror radius measurements and flaw size measurements were obtained. Fracture surface examination showed two types of flaws to be responsible for the fracture of most of the ceramic fibers: internal and surface flaws or defects. Internal flaws can consist of pores (Taylor et al., 1998), granular defects (Sawyer et al., 1987), and voids. Pores can agglomerate at a certain region and form clusters, and these pore clusters behave similar to a single flaw. Granular defects (e.g. a region of high carbon concentration in a Nicalon fiber) are aggregates of small (0.1 to 2 μm) granular particles.

Surface flaws are common in optical fiber because of the processing technique used for the fabrication of fused-silica fibers. They are also very common in other ceramic fibers such as alumina-based or silicon carbide-based fibers. Airborne particles as well as other elements tend to attach to the surface of the fiber during process or handling.

Alumina-based continuous fibers are available commercially from a number of sources. For example, Nextel series of alumina-based fibers from 3M Co. Nextel 312, 440, 480 (discontinued) have a mullite composition with varying amounts of boria to restrict grain growth. Nextel 720 consists of 85 wt% alumina + 15 wt% silica. Almax fiber from Mitsui Mining Co. fiber while Saphikon is a continuous monocrystalline alumina fiber (diameter between 75 and 225 μm) grown from melt by a process known as edge-defined film-fed growth process. Sometimes Saphikon fibers show undulations on the fiber surface, see Fig. 13. Typically fracture surface of such single crystal fibers show cleavage planes, see Fig. 14. These fibers typically have microvoids formed during fiber growth from the melt. One important feature of ceramic fibers is the surface texture. Their surface roughness scales with grain size. Fig. 15a shows the rough surface of an alumina fiber while Fig. 15b shows the grain structure of an alumina fiber. The rough surface of such brittle fibers makes them break at very low strains and it makes very difficult to handle them in practice. The grain boundaries on the surface can act as notches and weaken the fiber. A surface layer of silica or boron nitride on alumina fiber can heal surface flaws and increase fiber strength. A polycrystalline mullite fiber (Nextel 480), 10 μm in diameter, coated with boron nitride, showed an increase in the Weibull mean strength with increasing coating thickness up to 0.2 μm vis à vis the uncoated fiber, see Table 1 (Chawla et al., 1997). This was due to the surface flaw heating effect of the smooth BN coating. However, for a thicker BN coating (1 μm), there was a decrease in strength. This was because the soft BN coating at 1 μm thickness on a 10 μm diameter fiber had a volume fraction of 0.31.

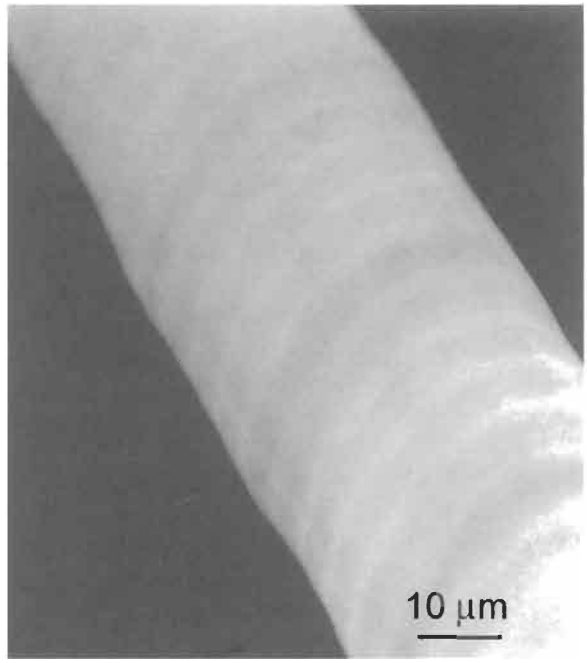

Fig. 13. Processing-induced undulations on the fiber surface of a single crystal alumina fiber, Saphikon fiber.

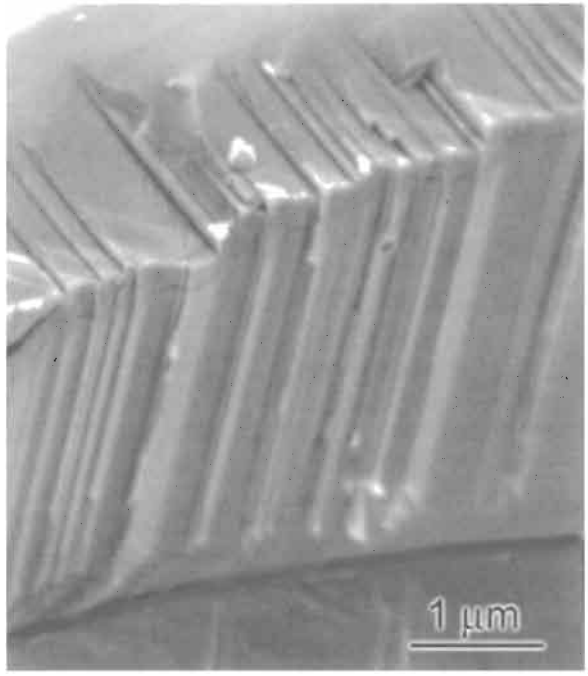

Fig. 14. A typical fracture surface of alumina single crystal fiber showing cleavage planes.

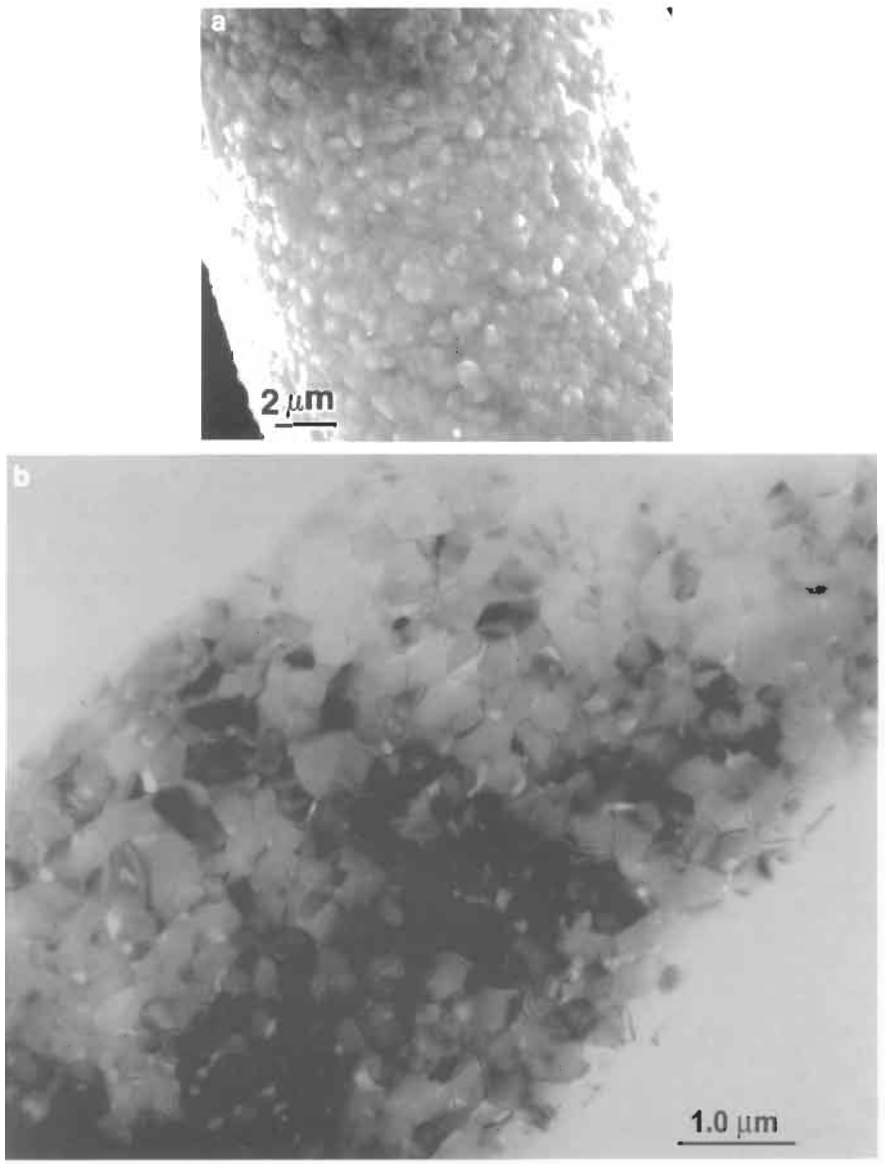

Fig. 15. (a) The rough surface of a polycrystalline alumina fiber. SEM. (b) The grain structure of an alumina fiber. TEM. Rough surface of such brittle fibers makes them break at very low strain and it makes very difficult to handle them in practice.

The room temperature fracture surface of a Nicalon fiber is shown in Fig. 16. Note the initiation of fracture at the fiber surface. The fracture surface shows a crack-initiating site and a planar minor region, a misty region, and finally a hackle region in which crack branching occurs. The initiating flaw may be an impurity, a surface nick due to handling,

Table 1. Effect of BN coating thickness on the mean strength of Nextel 480 fiber (Chawla et al., 1997)

Coating thickness (μm)	Weibull mean strength (GPa)
0	1.63
0.1	2.00
0.2	2.47
0.3	1.82
1.0	1.27

or even a very minor chemical heterogeneity. Thus, it is very important to reduce the number and the size of defects during processing. Similar examples of fracture in E-glass fiber caused by a dust particle or a metallic inclusion in the near-surface region of the fiber, most likely formed during processing, can be found in the literature (Chandan et al., 1994).

In order to meet the increasing demand for bandwidth, dense wavelength division multiplexing (DWDM) system designers must significantly increase the number of channels and decrease channel spacing. This has resulted in ever-stringent demands on the components that make up the telecommunications systems. For example, it is

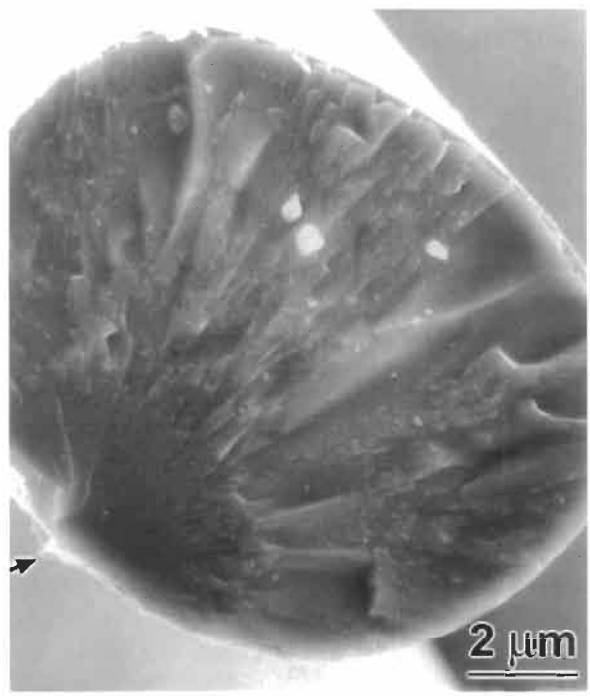

Fig. 16. Fracture surface of a Nicalon fiber tested in tension at room temperature (courtesy of N. Chawla). Arrow indicates the site of initiation of fracture at the fiber surface. The fracture surface shows a planar mirror region, a misty region, and finally a hackle region in which crack branching occurs. The initiating flaw may be an impurity, a surface nick due to handling, or even a very minor chemical heterogeneity.

becoming necessary to write increasingly complex and precise fiber Bragg gratings (FBGs) on short fiber lengths. An FBG involves an optical fiber along whose core there occurs a periodic change in refractive index. Fiber Bragg gratings can be made during fiber drawing by a single laser shot or by using pulsed lasers after fiber drawing. In the single laser shot technique, fiber coating is applied after the grating is made. These FBGs are expected to reliably function for 20 to 40 years in a variety of conditions. Thus their mechanical reliability becomes an important issue. FBGs can be written by an argon-ion laser system operating in continuous wave (CW) mode at 244 nm or by KrF pulsed excimer laser operating at 248 nm. Varelas et al. (1997) studied the effects of laser intensity on the mechanical reliability of FBG. Their main results are summarized in Fig. 17, which shows the Weibull plots of pulse-irradiated fibers and continuous wave

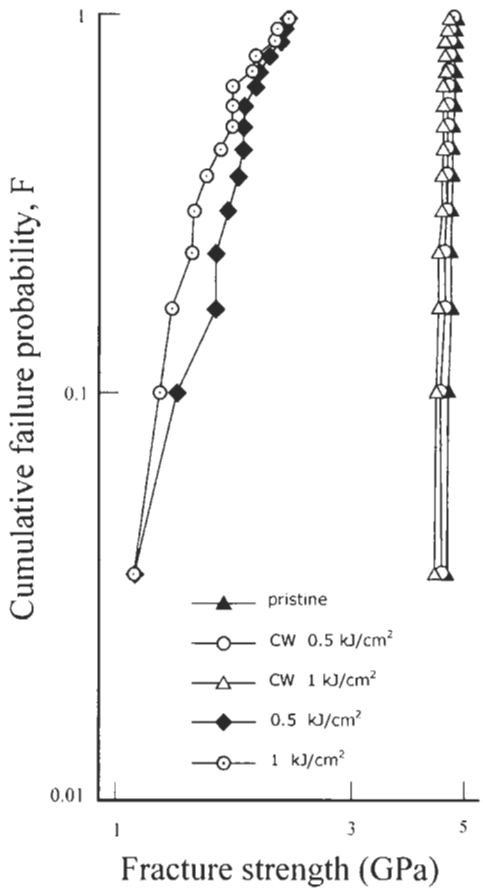

Fig. 17. Weibull plots of optical glass fibers subjected to pulse-irradiation and continuous wave treatments. The use of pulsed excimer radiation lowered the fiber fracture strength by as much as a factor of 4 compared to the fiber that was subjected to a CW argon-ion laser. The lower fracture strength of pulse-irradiated fiber is a result of the formation of microcracks in the material (after Varelas et al., 1997).

fibers. The use of pulsed excimer radiation for FBG production lowered the Weibull modulus as well as the fiber fracture strength by as much as a factor of 4 compared to the fiber that was subjected to a CW argon-ion laser for the FBG production. The lower fracture strength of pulse-irradiated fiber is a result of the formation of microcracks in the material.

CONCLUSIONS

- Typically, fibers have a high surface area/volume ratio, which leads to fiber surface characteristics being very important in the fracture process.
- By far the major cause of fracture in fibers is the presence of flaws either on the surface of the fiber or in the interior. If the size of the flaw can be reduced through processing or safe handling, the strength of the fiber will increase.
- A stringent control of microstructural cleanliness and segregation are very important. This is true for all types of fibers: glass, carbon, metal, polymers, or ceramic.
- Fracture surface analysis of fibers can provide useful information. In particular, for noncrystalline fibers, the following fracture parameters can be obtained from an analysis of features on the fracture surface morphology: the mirror constant, an estimation of fracture toughness K_{Ic}, failure stress, flaw-to-mirror radius ratio, fracture surface energy, and the time to failure.

REFERENCES

Argon, A.S. (1972) In: *Treatise on Materials Science and Technology*, p. 79, Academic Press, New York.
Briant, C.L. (1989) *Met. Trans.*, 20A: 243.
Brownrigg, A., Boelen, A. and Toyama, M. (1984) *Adv. Fract. Mech.*, 2: 350.
Chandan, H.C., Parker, R.D. and Kalish, K. (1994) In: *Fractography of Glass*, R.C. Bradt and R.E. Tressler (Eds.). Plenum Press, New York, NY, p. 143.
Chawla, K.K. (1998) *Fibrous Materials*. Cambridge University Press, Cambridge, p. 206.
Chawla, K.K., Xu, Z.R., Ha, J.-S., Schmücker, M. and Schneider, H. (1997) *Appl. Compos. Mater.*, 4: 263.
Deurbergue, A. and Oberlin, A. (1991) *Carbon*, 29: 621.
Gupta, P.K. (1994) In: *Fractography of Glass*, p. 185, R.C. Bradt and R.E. Tressler (Eds.). Plenum Press, New York, NY.
Horascek, O. (1989) *The Metallurgy of Doped/Non-Sag Tungsten*. Elsevier, London, p. 251.
Hüttinger, K.J. (1990) *Adv. Mater.*, 2: 349.
Jain, M.K. and Abhiraman, A.S. (1987) *J. Mater. Sci.*, 22: 278.
Jenkins, S., Jacob, K.I. and Kumar, S. (2001) In: *Heterophase Polymer Network Materials: Synthesis, Characterization and Properties*, p. 183, B.A. Rozenberg and G.M. Sigalov (Eds.). Gordon and Breach, New York.
Johnson, D.J. (1987) In: *Chemistry and Physics of Carbon*, Vol. 20, p. 1, P.A. Thrower (Ed.). Marcel Dekker, New York.
Johnson, D.J. (1990) In: *Carbon Fibers and Filaments*, p. 119, Kluwer, Boston, MA.
Kozey, V.V. and Kumar, S. (1994) *J. Mater. Res.*, 9: 2717.
Kumar, S. (1989) *SAMPE Q.*, 20: 3.
Mecholsky, J.J. (1994) In: *Fractography of Glass*, p. 37, R.C. Bradt and R.E. Tressler (Eds.). Plenum Press, New York.
Mecholsky, J.J., Freiman, S.W. and Morey, S.M. (1977) *Bull. Am. Ceram. Soc.*, 56: 1016.

Mecholsky, J.J., Freiman, S.W. and Morey, S.M. (1979) In: *Fiber Optics: Advances in Research and Development*, p. 187, B. Bendow and S.S. Mitra (Eds.). Plenum Press, New York.

Meyers, M.A. and Chawla, K.K. (1999) *Mechanical Behavior of Materials*. Prentice-Hall, Upper Saddle River, NJ.

Northolt, M.G. (1981) *J. Mater. Sci.*, 16: 2025.

Paris, H. (1996) In: *Metallurgy, Processing and Applications of Metal Wires*, p. 3, H.G. Paris and D.K. Kim (Eds.). TMS, Warrendale, PA.

Reynolds, W.N. (1981) *Philos. Trans. R. Soc. London*, A29: 451.

Sawyer, L.C., Jamieson, M., Brikowski, D., Haider, M.I. and Chen, R.T. (1987) *J. Am. Ceram. Soc.*, 70: 798.

Soraru, G.D., Mercadini, M. and Maschio, R.D. (1993) *J. Am. Ceram. Soc.*, 76: 2595.

Sung, Y.-M. and Sung, I.-M. (1996) *J. Mater. Sci.*, 31: 4775.

Takahashi, T., Ochiai, I. and Satoh, H. (1992) *Nippon Steel Tech. Rep.* 53, April, p. 102.

Tanner, D., Dhingra, A.K. and Pigliacampi, J.J. (1986) *J. Met.*, 38: 21.

Tarui, T., Takahashi, T., Tashiro, H. and Nishida, S. (1996) In: *Metallurgy, Processing and Applications of Metal Wires*, p. 87, H.G. Paris and D.K. Kim (Eds.). TMS, Warrendale, PA.

Taylor, S.T., Zhu, Y.T., Blumenthal, W.R., Stout, M.G., Butt, D.P. and Lowe, T.C. (1998) *J. Mater. Sci.*, 33: 1465.

Varelas, D., Limberger, H.G. and Salathe, R.P. (1997) *Electr. Lett.*, 33: 704.

Vukcevich, M.R. (1990) In: *Proc. 5th Int. Tungsten Symp.*, p. 157, MPR Publishing, Bellstone.

Wittenauer, J.P., Nieh, T.G. and Wadsworth, J. (1992) *Adv. Mater. Process.*, September, 28.

Yang, J.-M., Jeng, S.M. and Chang, S. (1996) *J. Am. Ceram. Soc.*, 79: 1218.

Fiber Fracture
M. Elices and J. Llorca (Editors)

MODELS OF FIBRE FRACTURE

M. Elices and J. Llorca

Departamento Ciencia de Materiales, Universidad Politécnica de Madrid, E.T.S.I. Caminos, c/ Profesor Aranguren s/n, 28040 Madrid, Spain

Introduction 29
Atomistic Approach 29
Strong Bonds in One Dimension: Polymer Fibres 31
Strong Bonds in Two Dimensions: Carbon Nanotubes 33
Strong Bonds in Three Dimensions: Diamond Whiskers 35
Continuum Approach 37
Homogeneous Fibres 37
Brittle Behaviour 37
Ductile Behaviour 39
Highly Oriented Polymer Fibres 42
Heterogeneous Fibres 46
Composite Fibres 46
Hierarchical Fibres 51
Acknowledgements 54
References 54

Abstract

Fibre fracture is modelled using either an atomistic approach or a continuum approach. In the first case, three different levels were considered; one-dimensional models applied to polymer fibres, two-dimensional models for nanotube fibres, and three-dimensional models for whiskers. Tensile stresses in commercial fibres are, in general, one order of magnitude below theoretical estimates. This discrepancy is due to the presence of defects, and realistic atomistic modelling should take account of these imperfections. Modelling fibre fracture from a continuum point of view deals first with homogeneous fibres and next with the more involved subject of heterogeneous fibres, stressing the relevance of interfaces, where neither strong nor very weak interfaces give optimum fracture results. Quantitative predictions are mostly based on linear elastic

fracture mechanics so they are valid only inside the frame of this theory. The paper ends with some comments on the fracture of biological fibres with a complex hierarchical structure.

Keywords

Crack; Fibre; Fibril; Fracture; Fracture toughness; Interfaces; Linear elastic fracture mechanics (LEFM); Nanotube; Polymer fibre; Stress intensity factor; Tensile stress; Weibull model; Whisker

INTRODUCTION

The aim of this paper is to provide a brief overview of some attempts to model fibre fracture and is intended to complement the next chapter by Hearle devoted to the phenomenology of fibre fracture.

Two different approaches to modelling fibre fracture are presented: the *atomistic* approach, for those who use the tools of quantum mechanics, and the *continuum* approach that relies on continuum mechanics. In the coming years, with the advent of nanotechnology, a hybrid approach will probably be needed to deal with nanofibres and biological fibres.

In every approach one finds a wide range of sophistication. In the continuum approach, the simplest (and most common) models are based on linear elastic fracture mechanics (LEFM), a well developed discipline that requires a linear elastic behaviour and brittle fracture, not always exhibited by fibres. Ductility and the presence of interfaces, not to mention hierarchical structures, make modelling much more involved. The same is true of the atomistic approach; fracture models based on bond breaking of perfect crystals, using well established techniques of solid state physics, allow relatively simple predictions of theoretical tensile stresses, but as soon as real crystals, with defects and impurities, are considered, the problem becomes awkward. Nevertheless solutions provided by these simple models — LEFM or ideal crystals — are valuable upper or lower bounds to fibre tensile strength.

Experimental values of tensile stress of high-performance fibres are about 3 or 5 GPa, one order of magnitude below theoretical predictions. In most cases, such discrepancies are due to the presence of defects not properly accounted for in the models. Apart from the difficulty of modelling such defects, what is felt in the literature is the lack of information on the characteristics of these defects, information that is essential for designing new models. In this respect, fibre fractography in the range of 1 μm to 1 nm should be encouraged.

ATOMISTIC APPROACH

Prediction of the mechanical behaviour of materials beyond the elastic limit using an *atomistic approach*, in particular fracture behaviour, has proved difficult. Problems in predicting the fracture toughness, or the maximum tensile stress, from an atomistic starting point, lie in the large length and time scales that are involved in treating the process zone, associated defects and, in most cases, the plastic zone. At present, calculations using molecular dynamics are still not capable of handling the system sizes corresponding to the process zone around a crack tip (sometimes up to 10^{13} atoms), nor are they capable of treating the required time scales. However, simple predictions of the theoretical tensile strength of *perfect crystals* based on solid state techniques can be made and may be useful as upper limits of the attainable fibre strength.

A perfect crystal, free of defects, is expected to be the strongest form of a fibre; the simplest 'crystal' could be a bundle of perfectly aligned linear chains of carbon atoms covalently bonded. This oversimplified one-dimensional model may represent an

idealised *polymer fibre*. The next step, a two-dimensional model, could be a rolled-up crystalline sheet of atoms; this cylinder can be used as a model for a *nanotube fibre*. Finally, a three-dimensional perfect array of atoms may idealise a *crystal whisker*. In the next sections these three topics are considered more closely.

A crude estimate of the tensile strength of a fibre that has the advantage of being applicable to all fibres, whatever the detailed nature of their interatomic forces, is the model due to Polanyi (1921) and Orowan (1949). This model, summarised in the classical book of Kelly and Macmillan (1986), gives the maximum tensile stress σ_{max} as:

$$\sigma_{max} = (E\gamma/a_0)^{1/2} \tag{1}$$

where E is the Young modulus, γ is the surface energy per unit area, and a_0 the equilibrium separation of atomic planes. In spite of its simplicity, this model gives, in many instances, the correct order of magnitude. More recently, accurate calculations have been made using approximate potential functions describing the interactions between atoms in the crystal lattice, and some results are quoted in subsequent paragraphs.

To check the accuracy of theoretical predictions, or to have an estimate of the strength of perfect fibres, tensile tests have to be performed. To this end, fibres free from flaws and defects must be produced and tested. Whiskers are nearly the ideal samples for *three-dimensional models* and the strongest one should be a whisker of a covalently bonded crystal; to the authors' knowledge, no diamond whiskers have yet been tested, but results obtained for Si and Ge whiskers are of the same order of magnitude as theoretical predictions. Brenner's seminal papers on tensile strength of whiskers, particularly Brenner (1956) on whiskers of iron, copper and silver, are still a good reference. *Two-dimensional models* have been checked by testing carbon nanotubes; experimental results by Yu et al. (2000) agree quite well with atomistic predictions by Bernholc (last chapter in this volume). Simplified *one-dimensional models* for polymer fibres give values one order of magnitude above experimental ones; atomistic failure models for polymer fibres need to be improved by considering the presence of defects, the degree of crystallinity and the role of secondary bonds in cross-linking chains.

Tensile stresses in commercial fibres are, in general, one order of magnitude below theoretical values. As already emphasised, this discrepancy is due to the presence of defects, a fact supported by the increase of the rupture stress as the fibre diameter, or the gauge length, decreases. Extrapolation of these stresses to very small diameters gives, in some cases, values near the theoretical ones. Although high-performance fibres have small diameters, about 10 μm, there is still plenty of room for defects, some of them of nanometer size. Realistic atomistic modelling should consider such defects and the subsequent triggered cracks or plastic deformation. This has been done with success for 'simple' nanotubes (see paper by Bernholc et al. in this volume), but more information is needed — with the help of TEM or AFM — to foster the scientists' ingenuity in modelling fibres in a realistic way. The next section is a brief summary of results of simple computations for perfect fibres, together with some experimental measurements to give a flavour of atomistic modelling.

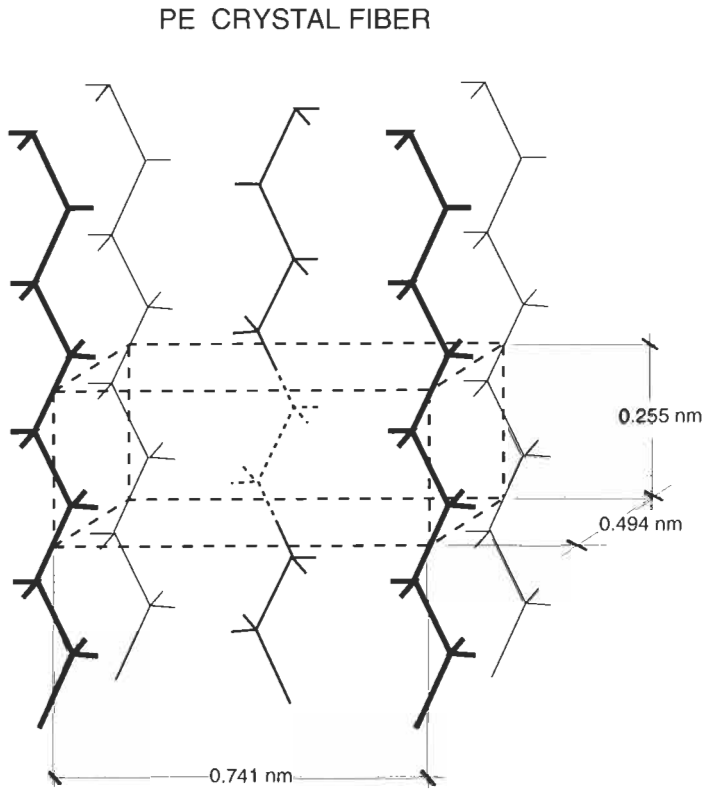

Fig. 1. Unit cell of a perfect crystal fibre of polyethylene (Bunn and Garner, 1947).

Strong Bonds in One Dimension: Polymer Fibres

In organic polymer fibres the intra-chain bonding is always covalent, a strong bond, but the nature of the inter-chain bonding is weaker; in polyolefines the chains are linked by van der Waals bonds, and in polyamides and polyesters inter-chain cohesion is augmented by hydrogen bridging.

A very rough estimate of the theoretical tensile fracture stress of a *fully aligned* polymer can be made quite easily by multiplying the strength of a covalent carbon–carbon bond (about 6×10^{-9} N; see, for example Kelly and Macmillan, 1986) by the number of bonds that can be broken by unit area.

Consider, as an example, polyethylene; if the chains are packed as in the crystal (Fig. 1), there are 5.5×10^{18} per m^2 in the plane perpendicular to their length. Hence the tensile fracture stress would be 33 GPa. Variants of this approach, using simple Morse potentials, provide values ranging from about 19 to 36 GPa. Other calculations using Hartree–Fock self-consistent field methods yield values of 66 GPa at 0 K (Crist et al., 1979). This last value seems a bit high and may be due to inaccuracies of the Hartree–Fock approximation at large atomic separations.

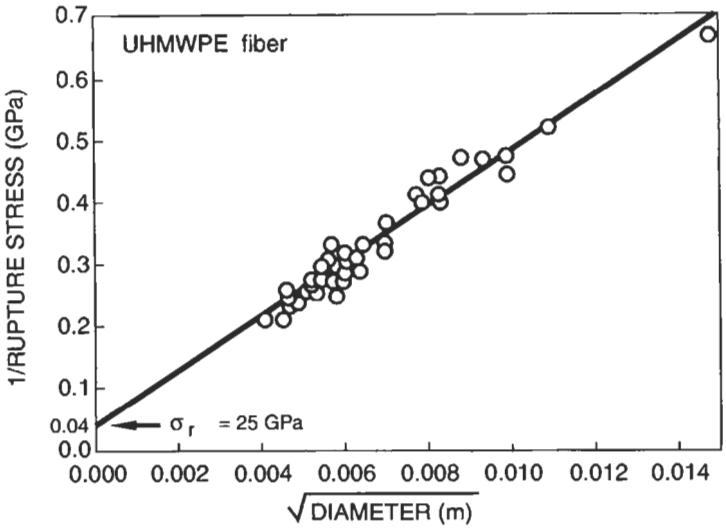

Fig. 2. Linear strength–diameter relationship for fully oriented ultra-high molecular weight polyethylene fibre (Smook et al., 1984).

Based on the kinetic theory of fracture, He (1986) calculated the theoretical strength of polymers, σ_{max}, as:

$$\sigma_{max} = (4EUr/3s^2)^{1/2} \tag{2}$$

where E is the chain Young modulus, U the activation energy of mechanical breakdown, s the cross-section area of the polymer chain and r is the interatomic distance (0.154 nm for a C–C bond). Notice the similarity to the Orowan–Polanyi result (Eq. 1). Both expressions give a rough estimation of σ_{max} of about $0.1E$. For polyethylene, He gives a tensile fracture stress of 32.5 GPa, a figure similar to that obtained by counting bond breaking.

Experimental values of the tensile fracture stress of polyethylene are one order of magnitude less than theoretical ones: Chawla (1998), for example, reports 2.7 GPa for Spectra 900 and 3.0 GPa for Spectra 1000, and Smook et al. (1984) measured 4.6 GPa in fibres of 20 μm diameter and found that the ultimate strength was inversely proportional to the square root of its diameter. Extrapolation to zero diameter yields a strength of 25 GPa (Fig. 2) which equals the theoretical predictions. These authors also found that the fracture process in these fibres involves an activation energy of about 60 to 75 kJ mol^{-1} (well below the activation energy of a –C–C– bond, 368 kJ mol^{-1}), which implies that the strength is mainly determined by the lateral bond strength between chains. Hence, the most probable fracture mechanism would be a step-wise process where a crack grows along the boundary of fibrils, breaking lateral bonds between fibrils, until it meets a defect and cuts through the fibril. Such a mechanism is consistent with the observation as revealed by small-angle X-ray scattering (Smook et al., 1984).

This example suggests some comments to bear in mind when modelling fracture of polymer fibres. Models based on the strength of covalent bonds of the polymer chain

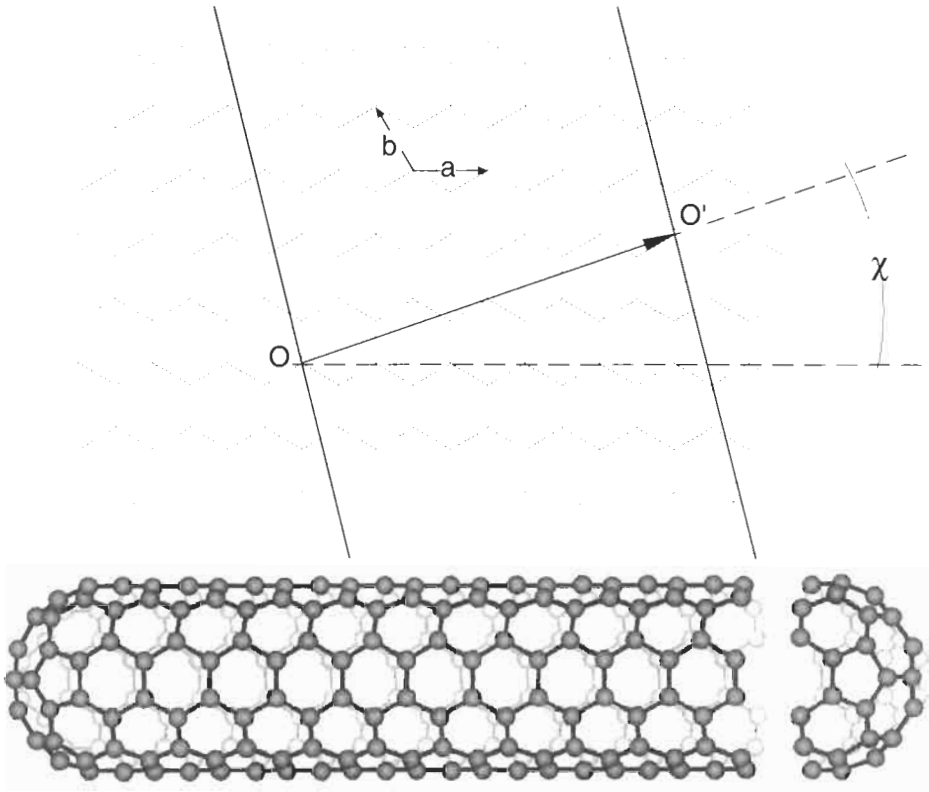

Fig. 3. Schematic model for a single-wall carbon nanotube. Nanotube structures are obtained by rolling a graphene sheet into a cylinder, so that the lattice points O and O' fold onto each other.

will provide an asymptotic value. This theoretical maximum strength will be achieved only for chain molecules of infinite length and fully aligned. Models intended for explaining experimental results should consider the presence of defects (the chain ends act as defects), the disorientation of the chains in relation to the fibre axis, the role of secondary bonds between chains, the non-uniformity of the structure in the cross-section and along the fibre, and the presence of voids and impurities.

Strong Bonds in Two Dimensions: Carbon Nanotubes

Strong bonding (with covalent bonds) in *two dimensions* can be achieved in nanotube fibres. An ideal carbon nanotube can be considered as a hexagonal network of carbon atoms rolled up to make a seamless hollow cylinder (Fig. 3). These fibres can be tens of microns long but with diameters of only about 1 nm and with each end capped with half a fullerene molecule. Carbon nanotubes, formed of seamless cylindrical graphene layers, represent the ideal carbon fibre and should exhibit outstanding mechanical properties.

Single-wall nanotubes, having a shell of only one atom in thickness, are considered

the basic structural unit. They are the building blocks of multi-wall nanotubes, containing several coaxial cylinders of increasing diameter about a common axis, and nanotube ropes, consisting of ordered arrays of single-wall nanotubes.

Carbon nanotubes are dealt with in detail in the final paper of this book. It suffices to underline that experimental measurements of fracture loads agree quite well with theoretical predictions. Large-scale molecular dynamic simulations were used by J. Bernholc and collaborators (Bernholc, 1999, and references in paper by Bernholc et al., this volume) to study the response of carbon nanotubes to a tensile load. Plastic or brittle behaviours can occur depending upon the external conditions and tube symmetry. These simulations uncovered the dominant strain release mechanisms as well as their energetics; beyond a critical value of the tension, the nanotube releases part of its stored energy via formation of defects. Static calculations show that such defects should appear at strains of about 0.05 and act as nucleation centres for the formation of dislocations in the ideal graphite network and can lead to plastic behaviour. Nevertheless, if brittle fracture is triggered, nanotube rupture at this strain may occur at a tensile stress of 62 GPa, a value assuming a linear stress–strain behaviour with a Young modulus of 1250 GPa for single-walled nanotubes (Krishnan et al., 1998).

Recently R.S. Ruoff and collaborators (Yu et al., 2000) measured the mechanical response of 15 single-wall carbon nanotube fibres under tensile load. In 8 of these fibres, strain data were obtained; they broke at strain values of 0.053 or lower. Assuming that the load acting on the nanotube (ranging from 400 to 1300 nN) is carried on the perimeter, tensile stresses ranging from 13 to 52 GPa were obtained. These results add confidence in atomic models of fibre fracture although in this particular example a great part of the success is due to its being simpler to model a perfect nanotube than a bundle of polymer fibres with defects.

Similar results apply to BN nanotubes (Chopra and Zettl, 1998) where Young's modulus has been measured at 1200 GPa, consistent with theoretical estimates. These values suggest maximum tensile stresses of about 60 GPa for single-wall boron nitride nanotubes.

Graphite whiskers can also be considered another example of a two-dimensional strong bonded structure, because they consist of concentric tubes, or rolled-up sheets of graphite layers, extending along the length of the whisker. The degree of alignment of these graphitic layers depends on the precursor used and on the processing technique. The highest stress recorded for a graphite whisker in tension appears to be 20 GPa (Bacon, 1960), whereas tensile stresses for commercial high-performance fibres are about 3 or 4 GPa. Only the polyacrylonitride (PAN)-based fibre, designated T-1000 by Toray, exhibits a tensile stress of 7 GPa (Fitzer and Frohs, 1990). These discrepancies are due to lack of alignment of the graphite layers and the presence of bubbles, holes and other defects that initiate tensile failure. Fig. 4 adds further support to this reasoning, showing a large increase in tensile stress as defects are reduced, when fibre diameters decrease, or gauge length decreases. Carbon fibres are considered in detail in the paper by Lavin in this volume.

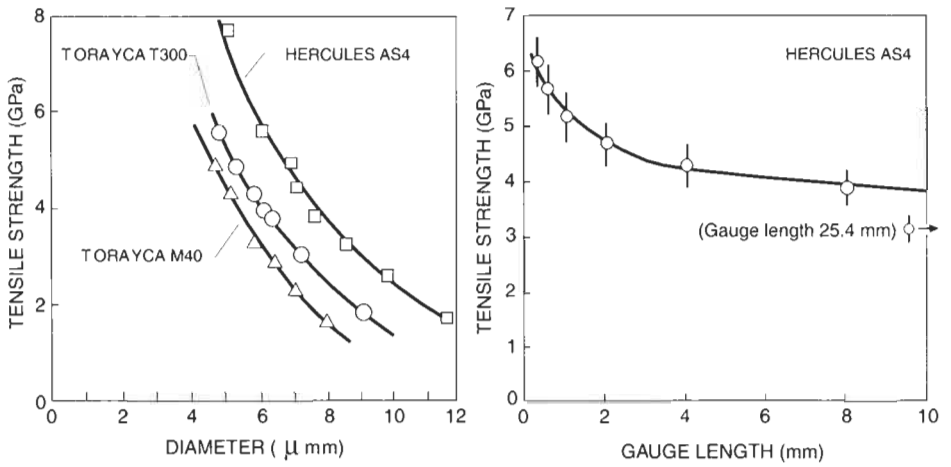

Fig. 4. Tensile strength of carbon fibre as a function of diameter (Fitzer and Künkele, 1990) and gauge length (Waterbury and Drzal, 1991).

Strong Bonds in Three Dimensions: Diamond Whiskers

Diamond is the paradigmatic example of *three-dimensional* covalent bonding and consequently diamond fibres should reach the highest values of tensile stress. The theoretical cleavage stress of diamond can be estimated by following the same reasoning as for polymer fibres, that is, by multiplying the strength of a covalent carbon–carbon bond (6×10^{-9} N) by the number of bonds that can be broken per unit area. For example, the cleavage strength for {111} planes, where there are 1.82×10^{19} bonds per square meter, is 110 GPa. This corresponds to $0.09E$, where E is the measured Young modulus (1250 GPa) and again agrees with the simple Orowan–Polanyi model (Eq. 1). More involved calculations of the strength of diamond are those of Whitlock and Ruoff (1981) which use the third-order elastic coefficients given by Grimsditch et al. (1978). Their results, depending on the direction of stress, are 52 GPa in ⟨111⟩, 53 GPa in ⟨110⟩ and 98 GPa in ⟨100⟩.

The theoretical tensile stress values just quoted are expected in a diamond fibre free of dislocations, cracks and other defects, usually a diamond whisker. Unfortunately there are no experimental data available for whiskers with diamond structure. Compressive strengths of the order of the theoretical tensile strength were observed in diamond anvils used to obtain ultra-high pressures (Wilks and Wilks, 1991), but in other applications diamonds fail at much lower loads due to the above-mentioned defects.

In silicon and germanium, that form bonds that are partly covalent, there are experimental results from whiskers that are of the same order of magnitude as theoretical predictions. In silicon whiskers the highest strength reported was 7.6 GPa (Sandulova et al., 1964). This value ranges from one-half to one-third of the calculated values (Whitlock and Ruoff, 1981): 15.2 GPa in ⟨110⟩, 18.8 GPa in ⟨111⟩ and 22.4 GPa in ⟨100⟩. Similar results were obtained in germanium. The highest stress reported in germanium whiskers is 4.3 GPa (Sandulova et al., 1964) and theoretical predictions by Whitlock and Ruoff

Table 1. Numerical and experimental results for tensile strength of copper ⟨100⟩

Method	σ_{max} (GPa) ⟨100⟩	References
Orowan-Polanyi (Eq. 1)	25	Kelly and Macmillan (1986)
Non-self-consistent KKR	55	Esposito et al. (1980)
Self-consistent ASW_c	32	Esposito et al. (1980)
Non-empirical potential	36	Esposito et al. (1980)
Johnson et al. potential	41	Johnson and Wilson (1972)
Morse-function lattice model	7	Milstein and Farber (1980)
Experimental values (whisker)	1.7	Brenner (1956)
Experimental values (whisker)	1.7	Kobayashi and Hiki (1973)
Flat crystal under shock wave	17	McQueen and Marsh (1962)

(1981) are: 10.4 GPa in ⟨110⟩, 12.6 GPa in ⟨111⟩ and 15.2 GPa in ⟨100⟩. Tensile strengths at 10.9, 22.3 and 15.3 GPa for Al_2O_3 whiskers grown in the ⟨0001⟩, ⟨11$\bar{2}$0⟩, and ⟨1$\bar{1}$00⟩ crystal directions were measured by Soltis (1965) and estimates of 98, 87 and 87 GPa for the ideal uniaxial tensile strength parallel to ⟨0001⟩, ⟨11$\bar{2}$0⟩ and ⟨10$\bar{1}$0⟩, respectively, were computed from the third-order elastic stiffnesses by Gieske (1968). The Orowan–Polanyi equation gives a value of 46 GPa for the ideal ⟨0001⟩ tensile strength.

Metals exhibit the maximum stress only in whisker form because they permit dislocation glide at low stresses, and whiskers are almost free of dislocations. In bcc metals, improved potential models will lead to a better understanding of the ideal strength than has so far been gained from either the Orowan–Polanyi approach or the use of the Morse potential; predictions, for example, of the fracture stress for α-Fe whiskers in the ⟨111⟩ direction using the Orowan–Polanyi equation are 46 GPa, where the maximum tensile stress obtained by Brenner was 13.1 GPa (Brenner, 1956), at an elongation close to 0.05 (see paper by Künzi, this volume).

For fcc metal fibres and whiskers, the Orowan–Polanyi equation and first principle band theory approaches give estimates of the ideal uniaxial tensile stress up to an order of magnitude above the highest stresses measured (see, for example, Table 1). For 'perfect' Cu fibres pulled in tension in the direction ⟨100⟩, for example, predictions of the theoretical tensile stress using the Orowan–Polanyi equation bring 25 GPa. Ab initio calculations (Esposito et al., 1980), based on non-self-consistent KKR using the muffin-tin approximation or using the self-consistent augmented spherical wave (ASW) method, provided values of 55 and 32 GPa, respectively. Other methods, based on a non-empirical pair potential that can be expressed in terms of the cohesive energy and can be evaluated when the energy is a function of the nearest-neighbour distance, give values of 36 GPa (Esposito et al., 1980) and 41 GPa (Johnson and Wilson, 1972). Other computations based upon a simple Morse-function lattice model give values of 7 GPa (Milstein and Farber, 1980). Experimental results on whiskers show values of 1.7 GPa (Brenner, 1956; Kobayashi and Hiki, 1973). Brenner noted that Cu did not cleave but sheared apart, and Kobayashi and Hiki suspected that surface defects were present. McQueen and Marsh (1962) reported a tensile strength of 17 GPa, but Esposito et al. (1980) noticed that this value, based on shock-wave intensity, involves techniques whose validity is difficult to assess.

Silica glass fibres are a further example of simple atomistic computations. An early attempt, following the technique of counting broken bonds, is due to Náray-Szabó and Ladik (1960); using a Morse potential, the breaking force for a Si–O bond was estimated as 2×10^{-9} N and the average member of bonds per m^2 12.5×10^{18}. Hence, the theoretical tensile stress for a perfect fibre should be 25 GPa. The Orowan–Polanyi approximation (Eq. 1) gives 16 GPa. Experimental values of the same order of magnitude, 15 GPa, were measured in silica fibres at 4.2 K, and 10 GPa in argon at room temperature (Proctor et al., 1967). Room temperature values for silica, S-glass and E-glass fibres are not above 5 GPa (see paper by Gupta, this volume). These values are in good agreement with predictions based on molecular dynamics, yielding a stress of 6.7 GPa at 625 K for soda-lime glass (Soules and Busbey, 1983).

CONTINUUM APPROACH

High-performance fibres usually have diameters ranging from 10 μm to 150 μm and are amenable to be modeled using a continuum approach. Unfortunately, fracture strength does not depend only on bulk properties and it is very sensitive to the type and shape of defects. Pertinent information on such microscopic defects is crucial to an understanding and modelling of fracture behaviour at a continuum level.

This section begins with the simplest type of fibres: homogeneous fibres. Among them, those exhibiting a linear elastic and brittle behaviour are the easiest to model, and fracture stresses can be predicted using the well established techniques of linear elastic fracture mechanics (LEFM). Ductile fracture is a more involved problem and some aspects of fibre failure using the techniques of elasto-plastic fracture mechanics (EPFM) are briefly mentioned. Fracture of highly oriented polymer fibres deserves a separate treatment because, although homogeneous, they have a fibrillar microstructure and display characteristic fracture behaviour.

Fracture of heterogeneous fibres is a more complex problem and the few available models are based on linear elastic fracture mechanics concepts and thus restricted to this area. An outstanding aspect of heterogeneous fibre failures is the role of interfaces: neither strong or very weak interfaces give optimum results.

The section ends with some comments on fracture of biological fibres. These fibres are characterised by a hierarchical structural design with length scales ranging from molecular to macroscopic. Clearly, detailed quantitative models for prediction of tensile strength of biological fibres are far from being available. However, some trends in connection with cellulose and keratin fibres are briefly discussed.

Homogeneous Fibres

Brittle Behaviour

Brittle failure of homogeneous fibres can be modelled, at a continuum level, using the tools of linear elastic fracture mechanics (LEFM) because usually the main hypotheses on which LEFM is based are satisfied when the rupture of a fibre is brittle, i.e.: the

stress–strain response is linear elastic, or almost linear, until rupture, and the size of the fracture process zone is negligible in comparison with other relevant lengths.

This behaviour is exhibited in ceramic and glass fibres at room temperature. The physical aspects of fracture of these fibres are described in detail (in this volume) in the papers by Bunsell (silicon carbide fibres), by Berger (oxide ceramic fibres) and by Gupta (glass fibres), and all share features that allow a common treatment based on LEFM. As regards SiC fibres, A. Bunsell remarks that the fracture surfaces of the first generation fibres have an amorphous microstructure, whereas those of the latest generation are clearly granular. With regard to oxide ceramic fibres, M.H. Berger states that fibres with a few percent of amorphous silica exhibit fracture morphologies which resemble those of glass fibres because they enclose transition alumina grains of the order of only 10 nm. Fracture morphologies of pure α-alumina fibres are typical of granular structures made of grains of 0.5 μm. All such fibres, crystalline and amorphous, share similar fracture patterns; they are brittle and linear elastic at room temperature and failure is usually initiated by flaws and surface defects and less by the fibre microstructure.

It is well known that analysis of a failure by LEFM involves the presence of a crack, characterised by its *stress intensity factor* K (a function of the stress state σ, a characteristic length of the crack, usually its depth a, and the geometry of the sample). The failure criterion is usually written as:

$$K(\sigma, a, \text{geometry}) = K_c(T, d\varepsilon/dt, \text{constraint}) \tag{3}$$

where K_c, the *fracture toughness* of the material, is a material property that depends on the temperature T, strain rate $d\varepsilon/dt$, and constraint. The safest assumption is to consider a state of plane strain, where K_c has its lower value.

Stress intensity factors for usual crack geometries are easily available in handbooks (Tada et al., 1985, for example), but this is not the case for cracks in fibres or cylinders. Although there are commercial programs that compute numerically K values for any geometry, these computations are not easy because cracked fibres pose, in general, three-dimensional problems where K changes along the crack border. In practice, cracks in fibres are idcalised by using tractable geometries (elliptical flaws, for example) placed in the most dangerous planes, usually planes perpendicular to the fibre axis.

For fibres with surface cracks, Levan and Royer (1993) made a comprehensive analysis. The authors considered part-circular surface cracks in round bars under tension, bending and twisting. Polynomial expressions are provided, allowing calculation of stress intensity factors at every point on the crack front for a wide range of geometries. Crack shapes satisfying the iso-K criterion are also computed, making it possible to investigate the problem of crack growth behaviour under tensile or bending fatigue loads.

In contrast to the effort devoted to surface cracks in cylindrical specimens, internal cracks have attracted less attention from researchers. The available solutions for the stress intensity factor are of circular cracks centred on the fibre axis (Collins, 1962; Sneddon and Tait, 1963). Only recently, a three-dimensional numerical analysis was made to compute K along the crack front of an eccentric circular internal crack under uniaxial tension (Guinea et al., 2002a).

The size and shape of internal and surface cracks are variable, and this gives rise to variable strength in brittle fibres. Given enough information about the flaw population

it is possible, in principle, to calculate the variability of the fracture strength. Without it, one has to resort to statistical methods. The statistical variation of strength of brittle solids is usually described using a Weibull distribution. Coleman (1958) gave reasons why such a distribution of strength is plausible for fibres whose strength is independent of the rate of loading, and he computed the mean fibre strength as:

$$\sigma_{\text{mean}} = \sigma_0 \left(\frac{L}{L_0} \right)^{1/m} \Gamma(1 + 1/m) \tag{4}$$

where L is the fibre length, m the Weibull modulus, σ_0 is the characteristic strength, defined as the stress at which the failure probability of a fibre of length L_0 is 0.63 and Γ the gamma function.

The Weibull approach, although useful when comparing fibres, does not take account of the failure mechanism. On the other hand, the deterministic theory of LEFM overcomes some of the limitations of the Weibull method but is applicable only when the initial crack geometry is known. There are intermediate cases where the crack geometry is known but not its precise location, as, for example, inner circular cracks located randomly. In these circumstances, LEFM can provide answers to questions such as: what is the maximum rupture stress for a postulated maximum defect size of unknown location?

Some of these questions have been answered in a recent paper (Guinea et al., 2002b) for a very simple family of defects: inner circular cracks and surface circular cracks, both in planes normal to the fibre axis. The main result is plotted in Fig. 5, showing the dependence of minimum rupture stress σ_c on crack radius. This plot may be used to set boundaries for some problems in brittle fibre fracture analysis, i.e.: to evaluate the maximum circular defect size when the rupture stress is known or, conversely, to estimate the rupture stress when defects, of unknown location, can be modelled as circular cracks.

The way of modelling brittle fracture of fibres is paved by LEFM, and good agreement between experimental results has been found. Future refinements will improve the accuracy of the predictions, in particular for anisotropic fibres where cracks propagate in mixed mode. More inputs from fractography and physical aspects of fracture will be helpful in modelling defects able to initiate cracks.

Ductile Behaviour

Modelling fibre ductile fracture is an involved problem, even for homogeneous and macro-defect-free fibres. Under tensile loading, fibres eventually reach an instability point, where strain hardening cannot keep pace with loss in cross-sectional area, and a necked region forms beyond the maximum load. A central crack is nucleated, spreads radially and finally, when approaching the fibre surface, propagates along localised shear planes, at roughly 45° to the axis, to form the 'cone' part of the fracture. This is the typical *cup-and-cone* fracture of a ductile failure after a tensile test.

Exceptions to this form of ductile fracture appear in microstructurally clean high-purity metal fibres, which sometimes neck down to a point. On the contrary, in ductile fibres containing large defects, or deep surface notches, necking is absent and a brittle

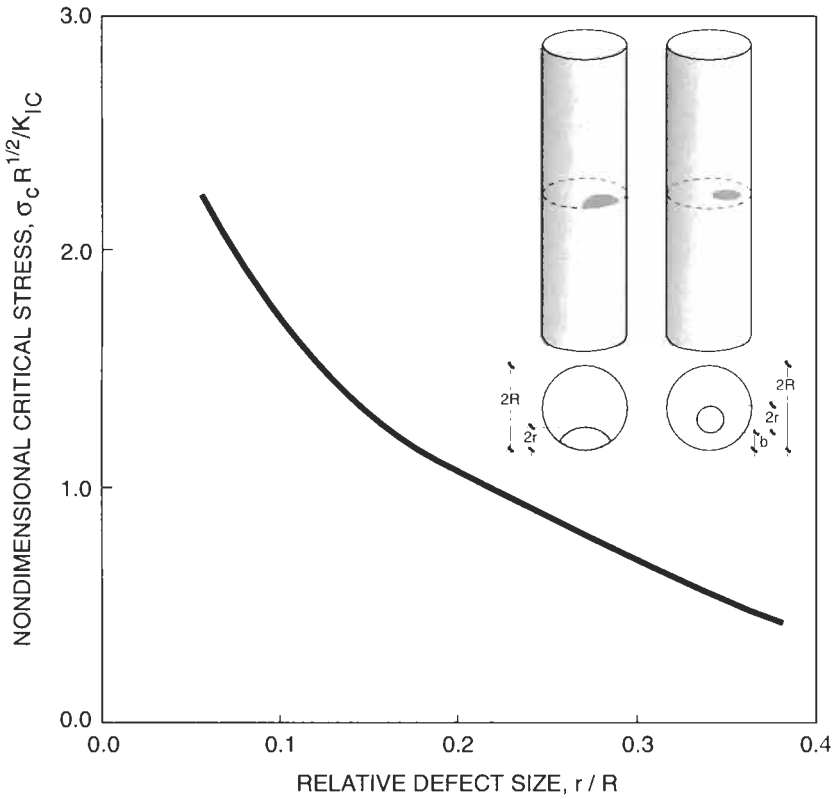

Fig. 5. Dependence of minimum critical fibre stress on fibre defect size (crack radius of circular cracks or crack depth in surface flaws).

fracture occurs. Ruptures under tensile loading and strong transversal forces, as in drawing fibres through dies, are also different (see the paper by Künzi, section 'Drawing Defects, Nonhomogeneous Microstructure and Texture', and the paper by Yoshida, both in this volume). See, for example Elices (1985), for an overview of fracture of steel wires under different loadings.

The physics of ductile fracture exhibit the following stages: formation of a free surface at an inclusion, or second-phase particle, by either interface decohesion or particle cracking, growth of the void around the particle by means of plastic strain and hydrostatic stress, and coalescence of the growing void with adjacent voids, forming a microcrack. When inclusions and second-phase particles are strongly bonded to the matrix, void nucleation is often the critical step and brittle fracture occurs after void formation. When void nucleation is easy, the fracture behaviour is controlled by the growth and coalescence of voids: growing voids reach a critical size, relative to their spacing, and a local plastic instability develops between voids forming a macroscopic flaw, which leads to fracture. These three steps, *nucleation*, *growth* and *coalescence* of voids, occur in highly stressed regions of the fibre: in the necking zone, in smooth

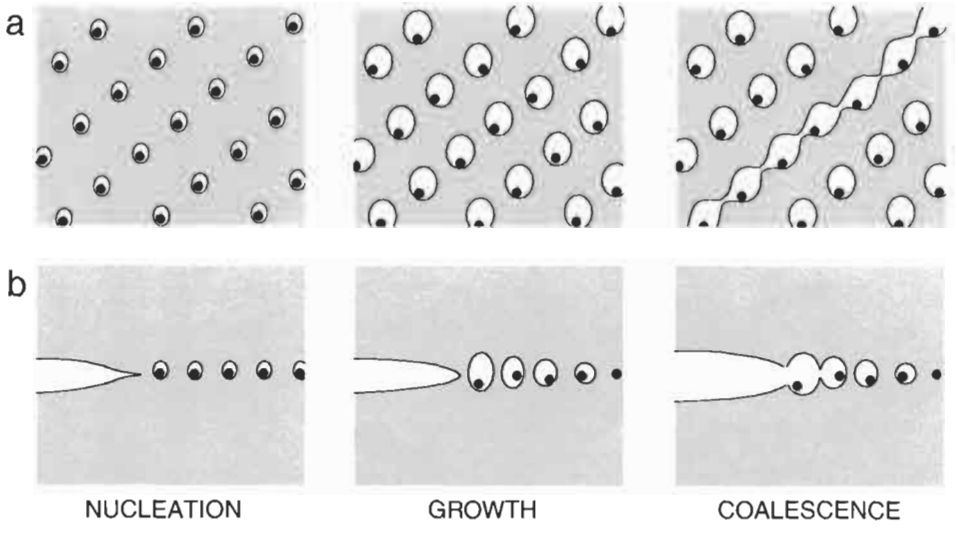

Fig. 6. Nucleation, growth and coalescence of voids: (a) in the necking zone; (b) near cracks and notches.

and perfect fibres, (Fig. 6a) or in stress concentrators, near some cracks or notches (Fig. 6b); the triaxiality ahead of the crack tip provides sufficient stress elevation for void nucleation, so growth and coalescence of microvoids are usually the critical steps in ductile crack growth.

Modelling ductile fibre failure, using the continuum approach, should consider all these facts. A number of models for estimating void nucleation stress have been published; among them, those of Argon et al. (1975) and Beremin (1981) are often used. The most widely referenced models for growth and coalescence of voids were published by Rice and Tracey (1969) and Gurson (1977). Rice and Tracey considered a single void in an infinite solid with a rigid-plastic and a linear strain hardening behaviour. Gurson analysed plastic flow in a porous medium assuming that the material behaves as a continuum and the effect of voids is averaged. The main difference between this model and standard plasticity is that the yield surface in the Gurson model exhibits a weak hydrostatic stress dependence. Ductile fractures are assumed to occur as a result of a plastic instability that produces a band of localised deformation. The Gurson model, and later improvements (Tvergaard and Needleman, 1984 for example), characterise plastic flow quite well in the early stages of the ductile fracture process, but do not provide a good description of the events that lead to final failure, because of not containing discrete voids. These shortcomings are intended to be surmounted by the model of Thomason (1990), where holes are explicitly considered.

Once the crack is nucleated, crack growth can be modelled using the above-mentioned models, or from a more macroscopic point of view by using the techniques of elasto-plastic fracture mechanics (EPFM) (see, for example, Anderson, 1995, and Broberg, 1999). To the authors' knowledge, few results are available of ductile fibre failure based on EPFM, most probably because the small size of fibre diameters invalidates some of the hypotheses on which this theory is based.

Fracture of thin metallic wires during cold drawing is also worth mentioning here. Wire breakage in the industrial practice of wire drawing is often due to the presence of non-metallic inclusions and a severe plastic deformation; the wire is pulled through the dies and highly stressed, withstanding large plastic deformations. Voids, nucleated at the interfaces between inclusions and matrix, generate cracks that eventually lead to fracture. A physical insight into void initiation during wire drawing of pearlitic steels, an important part of commercial metallic fibres, appears, for example, in Nam and Bae (1995). At high strains, globular cementite particles whose size is much larger than the thickness of cementite lamella, provide sites for void formation due to the enhanced stress concentration. These observations may be helpful when modelling fibre fracture at the mesolevel. Numerical predictions of the rupture stress and initiation sites can be obtained using finite element methods (FEM), where elasto-plastic behaviour of elements is complemented by a fracture criterion. In general, these fracture criteria have the following functional form:

$$\int^{\varepsilon_f} F(\text{deformation history})\, d\varepsilon = C \tag{5}$$

where ε is the effective strain, ε_f the effective fracture strain and C is a parameter, usually known as a damage parameter, obtained experimentally. Different forms of the integrand are summarised in Doege et al. (2000). Yoshida, in his paper in this volume, summarises the FE modelling of a superfine wire with a cylindrical inclusion placed on the wire axis.

Highly Oriented Polymer Fibres

Fracture of highly oriented polymer fibres during tensile loading may exhibit different forms: *brittle fracture*, usually due to transverse crack propagation, *ductile fracture*, as a consequence of plastic flow after necking, or *fibrous axial splitting*, where cracking or splitting occurs along planes close to the fibre axis. Modelling the first two types of fracture can be done according to the ideas previously commented, although the strong transverse anisotropy poses additional difficulties. Axial splitting is typical of polymer fibres although it may also happen in severely cold drawn metallic fibres.

Phenomenological aspects of fibre fracture have been discussed elsewhere (see Kausch, 1987 for example). It suffices to remind that the details of the failure process are highly complex and depend upon many factors such as polymer structure, environment, type of loading and time. Molecular fracture does not occur to the same extent in all polymer fibres and the micromechanisms differ in different types of fibres.

The structure of highly oriented polymer fibres is characterised by a fibrillar microstructure; *fibrils* are clusters of partially aligned molecules. Fibril diameters range from 1 to 100 nm. Forces between fibrils are weak, so fibrils can be observed in fibre fractures. *Microfibrils*, the most elementary fibrils, consist of alternating layers or ordered (crystalline) and disordered (amorphous) regions along the fibril length. In poorly oriented fibres the amorphous regions within the microfibrils still contain more than 90% of non-extended chain segments which support most of the load (Kausch, 1987). This is different in ultra-highly oriented fibres where the number of non-extended

chain folds decreases and the structure is more oriented, approaching that of a perfect crystal. For example, in ultra-high molecular weight polyethylene (UHMWPE), with a drawn ratio of 247, the fibre elastic modulus approached a value of 220 GPa (Kanamoto et al., 1983), which is close to the theoretical modulus of a perfect crystal (240–290 GPa).

According to all observations it has to be expected that the ultimate properties of ultra-highly oriented fibres should depend on the properties of the crystalline blocks and on the way these blocks are linked together. Starting from this idea, the *fibril model* has been used to predict the mechanical behaviour; this is one of the oldest models and still enjoys considerable popularity. Many modifications and improvements have been made since then to consider imperfections, degree of crystallinity, molecular weight and so on. All these models give reasonable predictions of Young's modulus, the shape of the stress–strain curve, and to some extent the yield stress. On the contrary, little progress has been made in predicting the ultimate tensile stress, most probably because fracture models rely on imperfections and not enough information is yet available to devise a general enough model.

Peterlin (1981) made interesting comments on the rupture of highly oriented aliphatic fibres and suggested a phenomenological model of rupture, due to crack nucleation and coalescence. The microcracks seem to form primarily at defects of the microfibrilar structure, particularly at the ends of microfibrils (see Fig. 7a). In these places the connection between crystallites by taut tie molecules is poor and these regions favour microcrack nucleation much earlier than the amorphous layers inside the microfibrils. The stress concentration resulting from the opening of these microcracks may rupture also some of the adjacent microfibrils. This nucleation and subsequent lateral growth of the microcrack ruptures the taut tie molecules in its path. Interestingly, the ruptured molecules yield free radicals which can be monitored by electron spin resonance. The failure of the fibre seems to occur when the ratio between the average distance and the diameter of the microcracks reaches a value of about 3. This criterion was checked in nylon, polyethylene and polypropylene.

Morgan et al. (1983) also made very interesting phenomenological comments on the rupture of aromatic fibres, particularly poly(*p*-Phenylene Terephthalamide) (PPTA), the basis of Kevlar®. The deformation and failure processes, together with the structure of the fibre, were commented in the light of fracture topography. The authors conclude that the chain-end concentration and its distribution within the fibre are the primary structural factors affecting the deformation and failure of PPTA fibres, and propose the following model, illustrated in Fig. 7b. The rod-like PPTA macromolecules are assumed to be aligned parallel to the fibre axis. The chain ends are arranged essentially randomly relative to one another but become progressively more clustered in the fibre interior, resulting in periodic transverse weak planes every 200–250 nm, approximately. The chain ends cluster in the vicinity of these weak planes. The fibre core consists of cylindrical crystallites, of about 60 nm in diameter, aligned in the fibre direction. The fibre exterior is assumed to be less crystalline than the interior. The chain-end model, although it does not provide quantitative results for the tensile stress, is consistent with the observed deformation and failure processes of Kevlar fibres. Fig. 7c illustrates the path of a crack that transverses the molecular chain ends of an array of aligned

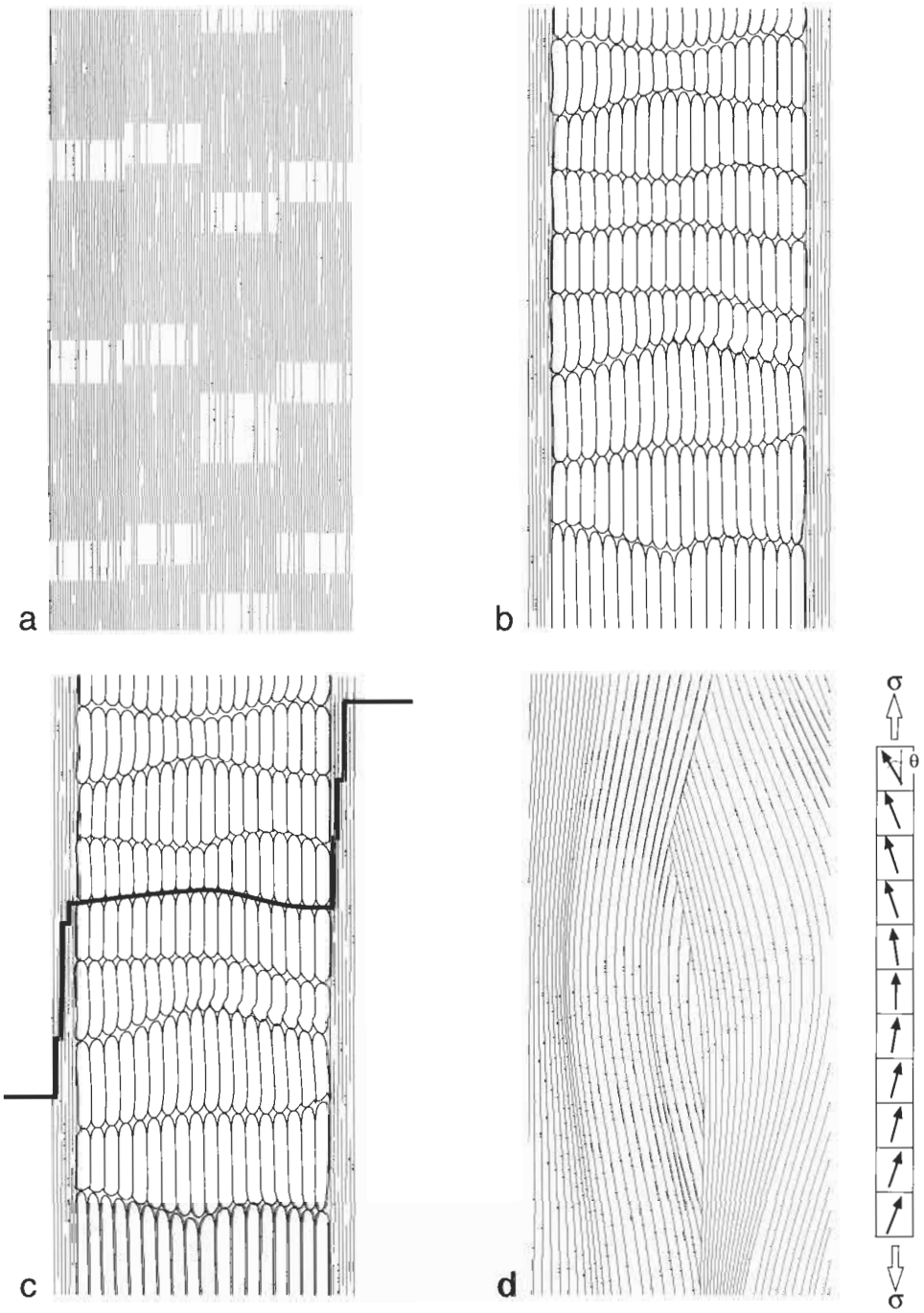

Fig. 7. Models (oversimplified) of highly oriented fibres: (a) Peterlin model; (b) Morgan model; (c) possible crack path (Morgan model); (d) Northolt model.

macromolecules with a skin-core distribution of ends similar to the model; the skin will exhibit a more continuous structural integrity in the fibre direction than the core, and the core will fail more readily by transverse crack propagation. Panar et al. (1983) proposed a similar model. Both emphasise the structural features as observed on etched specimens of PPTA fibres, but do not provide a quantitative interpretation of the tensile properties of these fibres.

Yoon (1990) developed a model for fibre strength similar in reasoning to that of a model for the tensile strength of short fibre-reinforced composites due to Fukuda and Chou (1982). Both the chain length distribution and chain orientation effects of the fibre are included jointly with the molecular weight dependence. The model is based on the consideration that the macroscopic load is transferred along the fibre sample mainly by interchain interaction, and the fibre breakage occurs when the interchain interaction force exceeds a critical value. Then the chains are separated and fibre failure is caused by the rapid accumulation of the interchain voids, resulting in the observed fibrillar fracture. The chain ends act as sites for stress concentration and the molecular weight dependence of the tensile stress is due to the relation between the number of chain ends and the molecular weight. Good agreement with experimental results was obtained for wholly aromatic polyesters.

Another model, along the same line of reasoning, was proposed by Northolt and van der Hout (1985) and Baltussen and Northolt (1996) based on observations by X-ray and electron diffraction. The fibre is considered as being a build-up of a parallel array of identical fibrils. Each fibril consist of a series of crystallites arranged end to end, and the polymer chains run through these crystallites parallel to their symmetry axes, which follow an orientation distribution in relation to the fibre axis (Fig. 7d). The parameters of the model are the chain orientation distribution, the average modulus for shear between the chains, the chain modulus and a simple yield condition based on the critical resolved shear stress. This model provides expressions for the compliance, the elastic tensile curve and the yield stress of the para-aromatic polyamide and other high-modulus fibres. Recently, Picken and Northolt have extended the model to predict fibre fracture stress (Picken and Northolt, 1999), as a function of the degree of orientational order, making use of an expression similar to the Tsai–Hill criterion for the strength of uniaxial composites:

$$\frac{1}{\sigma(\theta)} = \frac{\langle \cos^4\theta \rangle}{\sigma_L} + \frac{\langle \cos^2\theta \operatorname{sen}^2\theta \rangle}{\tau_S} + \frac{\langle \operatorname{sen}^4\theta \rangle}{\sigma_T} \tag{6}$$

where $\sigma(\theta)$ is the rupture stress, θ the angle between the chain segment and the fibre axis, and τ_S, σ_L an σ_T are respectively the shear stress, the longitudinal stress and the transverse stress of the molecular composite. With this model, the authors find that it is possible to explain the effect of molecular orientation in the strength of as-spun fibre and suggest that for *highly oriented aramid* fibres, the transverse term can be ignored and that σ_L is about 6 GPa and τ_S about 0.3 GPa.

An alternative theoretical approach to exploring the limits of the tensile stress of fibres with perfectly oriented and packed polymer molecules was developed by Termonia et al. (1986; Termonia, 2000). The model bypasses details of the deformation on an atomistic scale and focuses instead on a length scale of the order of the distance

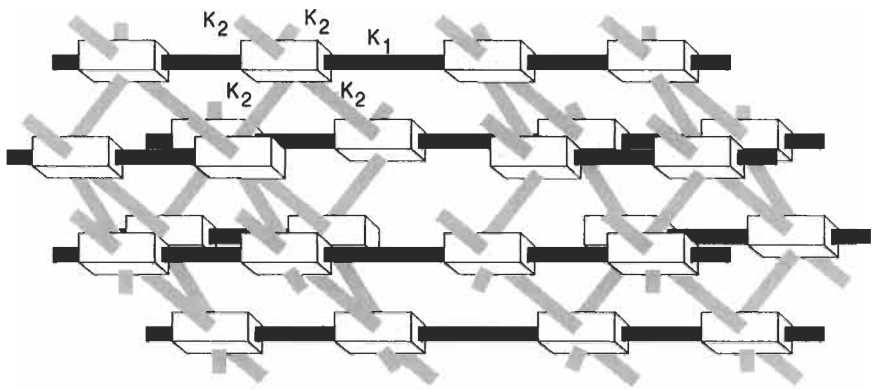

Fig. 8. Termonia model of highly oriented fibre.

between entanglements. No defects are considered other than chain ends resulting from a finite molecular weight. It is based on the kinetic theory of fracture, in which the bond ruptures are simulated by a Monte-Carlo process on a three-dimensional array of nodes, as shown in Fig. 8. The nodes in the figure represent the elementary repetition units of the polymer chains. In the longitudinal direction, the elastic constant K_1 accounts for the primary bonds (i.e. C–C bonds in polyethylene). In the transverse directions, the elastic constant K_2 accounts for the secondary bonds (i.e. hydrogen bonds in nylon or van der Waals forces in polyethylene). Results agree quite well with experimental measures of strength of highly oriented fibres. In polyethylene fibres of low molecular weight, intermolecular slippage involving rupture of secondary bonds occurs in preference to chain fracture, yielding tensile curves that at the end are bell-shaped. At high molecular weights primary as well as secondary bond rupture occurs, yielding tensile curves with brittle fracture. In PPTA fibres, the model predicts that fracture is initiated by the breaking of a small number of primary bonds and not by secondary hydrogen-bond failure; this leads to a brittle fracture of the fibre. This simple model does not predict a fibrillated fracture, as observed in PPTA, PBO and PBT fibres, but this behaviour can be implemented by considering a bundle of fibrils, each one modelled with the simple model, joined by weaker secondary bonds. More details about this model are given in the paper by Termonia (this volume).

Heterogeneous Fibres

Composite Fibres

The simplest composite fibres are the B and SiC monofilaments manufactured by chemical vapour deposition of boron halide or silane gases onto a heated substrate, normally W or C. Their diameter is in the range of 50–150 μm, and they exhibit a concentric microstructure in which four different regions can be distinguished, the composition and thickness of each one depending on the actual fibre characteristics (Fig. 9). A thin (1–2 μm) layer of pyrolytic graphite is deposited onto the C core before the deposition of

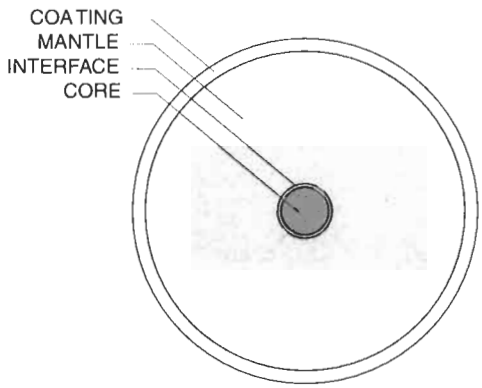

Fig. 9. Cross-section of B and SiC composite monofilaments produced by chemical vapour deposition, showing the concentric core, interface, mantle and coating regions.

SiC or B to accommodate the growth strains that appear during B deposition and the thermal strains generated by the mismatch in the coefficients of thermal expansion. The pyrolytic graphite interface does not react with either B or SiC, and it is weakly bonded to the fibre mantle. On the contrary, SiC and B react with the W core, leading to the formation of an interfacial reaction zone of different thickness and composition. The reaction zone (of about 100 nm in thickness) is a mixture of W_2C, WSi_2, and W_5Si_3 in the SiC/W monofilament, and is strongly bonded to both the W core and the SiC mantle. In the case of B monofilaments, the interfacial reaction zone made up of WB_4 and W_2B_5 completely replaces the original W substrate, and is also well bonded to the B mantle. Various surface coatings (C, C/SiC, TiB_2 for SiC, and SiC, BN for B) are finally applied on the mantle surface. They protect the monofilaments against abrasion during handling and act as diffusion barriers during composite processing at high temperature. In addition, it was observed that some of these coatings significantly increased the strength, and this was attributed to the rearrangement of the residual stresses as well as by the healing effect on the surface flaws. It has been suggested that the amorphous carbon coating seals the SiC grain boundaries at the surface, hence minimising the stress concentration. Moreover, the amorphous C prevents any grain boundaries from extending to the free surface (Wawner, 1988; Chawla, 1998; Cheng et al., 1999).

Fracture characterisation of these composite monofilaments has demonstrated that the strength-limiting flaws were always found at or near the interfacial region between the core and the mantle (Lara-Curzio and Sternstein, 1993; González and Llorca, 2000). In the case of B/W monofilaments, the fracture origins have been associated with voids nucleated along axial die-marks on the W surface (Vega-Boggio and Vingsbo, 1976; Vega-Boggio et al., 1977). This led to the simplest fracture model for these composite fibres, which assumed that the void behaved as an internal elliptical crack, and obtained the fibre strength using the LEFM criteria for homogeneous fibres described above (Vega-Boggio and Vingsbo, 1976). Evidently, this was a first-order approximation which included neither the effect of the residual stresses at the interfacial region nor that of the crack propagation through materials with different properties.

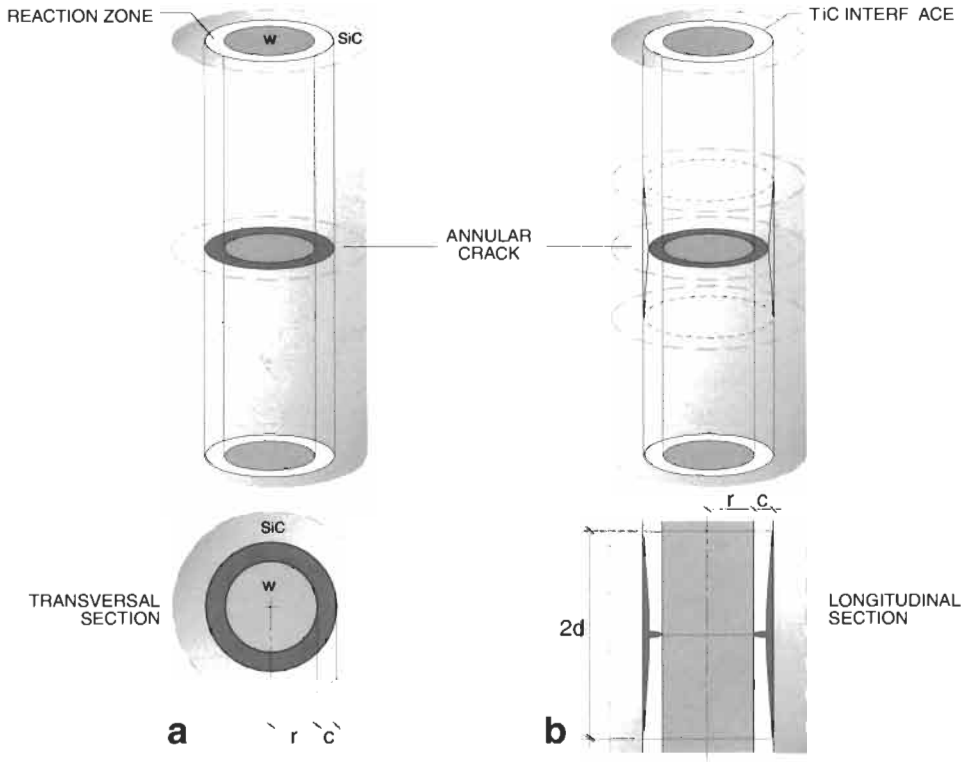

Fig. 10. Fracture model of a composite monofilament by the propagation of an annular crack from the interface reaction zone into the mantle. (a) Strong interface. (b) Weak interface.

A more sophisticated model was developed by Curtin (1991) to account for the dependence of the fibre strength on the thickness of the interfacial reaction zone in SiC monofilaments deposited on W. The thin reaction zone is subjected to very high tensile residual stresses (~2 GPa) in the axial and hoop directions (Faucon et al., 2001) due to the thermal mismatch. Curtin assumed that the residual stresses were relieved by the formation of annular cracks (Fig. 10a) bridged on one side by the W and on the other by the SiC. The critical stress for crack propagation into the brittle SiC mantle was computed assuming that all the interfaces were strongly bonded, and two cases were distinguished depending on whether the W remained elastic or yielded plastically before failure. The resulting values of the monofilament strength were:

$$\sigma = \frac{K_c}{2}\sqrt{\frac{\pi}{2c}} \tag{7}$$

and

$$\sigma = \frac{K_c}{2}\sqrt{\frac{\pi}{r}} + \left\{1 - \sqrt{\frac{2c}{r}}\right\}\sigma_y \tag{8}$$

where K_c ($\approx$2.8 MPa m$^{-1/2}$) is the SiC fracture toughness, σ_y the tungsten yield strength

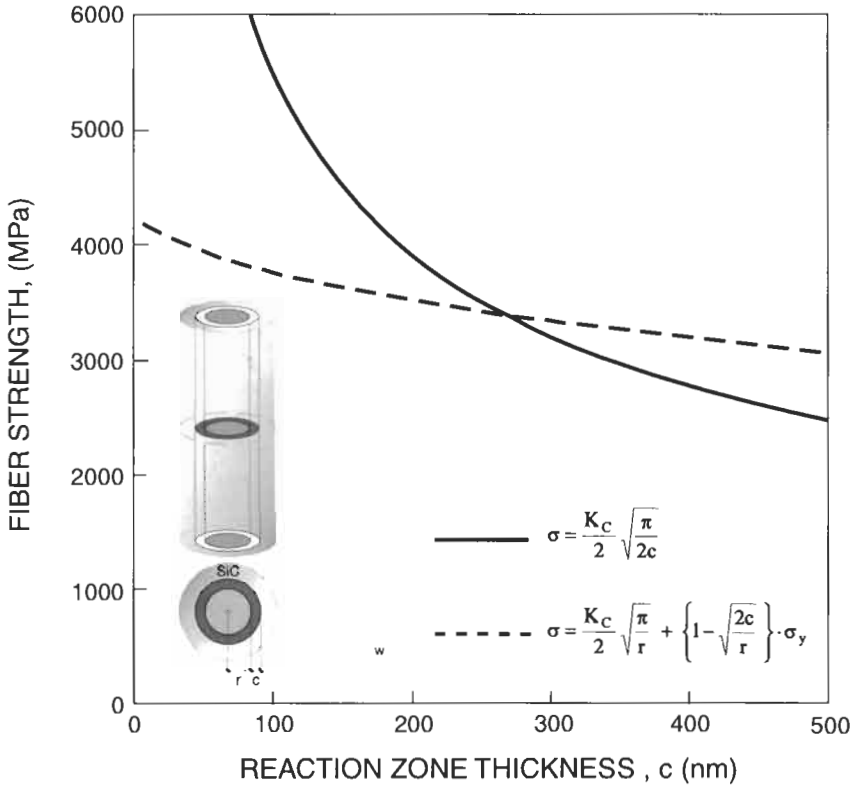

Fig. 11. SiC/W monofilament strength as a function of the reaction zone thickness, c.

(≈3.4 GPa), and r (≈7 μm) and c are given in Fig. 11a. The monofilament strength predicted by both equations is plotted in Fig. 11 as a function of the reaction zone thickness. If c is below 260 nm (as is often the case) failure occurs after the tungsten core has yielded plastically (Eq. 8). The monofilament strength is controlled in this situation by the tungsten yield strength, and the dependence on the reaction zone thickness is weak. On the contrary, the critical condition for brittle fracture provided by Eq. 7 becomes dominant when $c = 260$ nm and the monofilament strength decreases with $c^{-1/2}$.

Further attempts to improve the strength of the SiC/W monofilaments were directed to creating a weak interface between the interface reaction zone and the SiC mantle through the deposition of a thin (250 nm) TiC layer (Faucon et al., 2001). Under such conditions, the annular crack at the interface was deflected along the weak TiC/SiC interface before penetrating into the SiC mantle (Fig. 10b). The interface strength was characterised by the debonding length, d, and the critical condition for crack propagation was computed using an axisymmetric finite element model. The results in terms of the fibre strength are plotted as a function of the d/r ratio in Fig. 12, and they show that the blunting effect of a weak interface was significant when the decohesion length was of

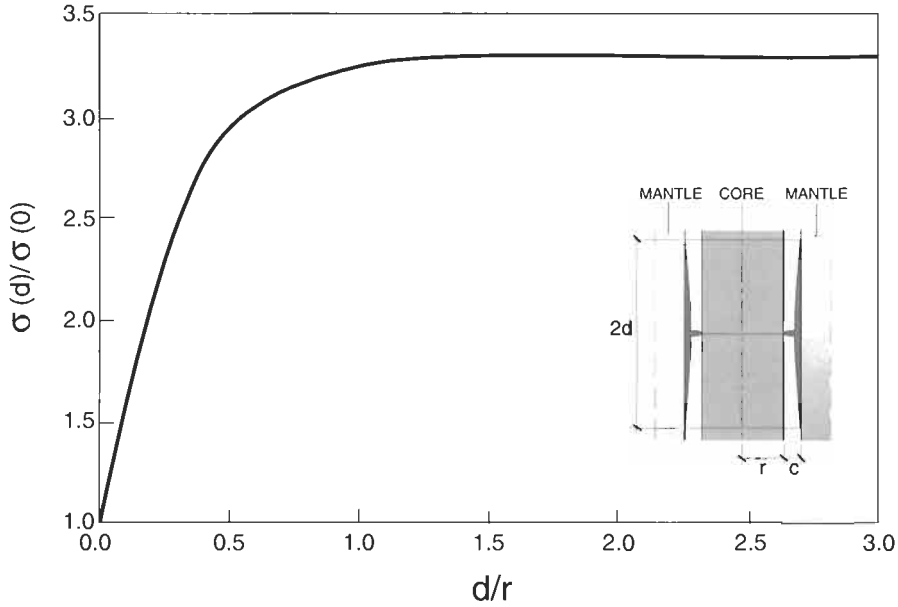

Fig. 12. Relative critical stress for the propagation into the SiC mantle of an annular crack located within the interphase as a function of the debonding length d normalised by the core radius. (The calculations were made assuming the same elastic moduli for all constituents).

the order of the W core radius. The model predictions were in good agreement with the experimental results presented in Faucon et al. (2001).

Another simple architecture of composite fibres is that of a bundle of parallel micro- or nanofibrils oriented along the fibre axis. An example of this microstructure can be found in the silk produced by moths of the Saturniidae family, where the fibres are made up of aligned load-bearing microfibrils of $\sim$1 μm in diameter glued together by a natural adhesive which behaves as a ductile matrix (Poza et al., 2002). A similar structure is seen in multifilamentary superconducting fibres which are composed of hundreds of 4-μm diameter Nb_3Sn microfibrils embedded in a Cu or Cu/Sn matrix (Chawla, 1998). The first approximation to the strength of these fibres can be obtained from the dry fibre bundle theory developed by Coleman (1958), which does not take into account the existence of a continuous matrix among the microfibrils. The microfibrils are assumed to have the same cross-sectional area and stress–strain curve, but differ in the strain (or stress) at failure. The total load taken up by the fibre bundle as the strain increases is the result of two competing phenomena, namely the higher stress in the intact microfibrils and the higher number of broken microfibrils. Assuming that the individual microfibril strength follows the Weibull statistics, the fibre bundle strength, σ_b, can be computed as the maximum load carried by the fibre bundle divided by its initial cross-section, and is given by:

$$\sigma_b = \sigma_0 \left[\frac{L}{L_0} me \right]^{-1/2} \tag{9}$$

where L, m, and σ_0 have the meaning given in Eq. 4 and e is the base of the natural logarithms.

Neglecting the fibre interaction through the matrix is a crude approximation, and the fibre bundle strength can only be considered a lower limit. An improved model is obtained by considering that when one microfibril breaks, the elastic unloading in the microfibril below and above the fracture leads to the development of a shear stress τ at the fibre–matrix interface. This shear stress transmits the load from the matrix back to the fibre, and the stress in the fibre reaches its former value σ at a distance x below and above the fracture section, which is given by:

$$x = \frac{\sigma}{2\tau} r \tag{10}$$

where r is the microfibril radius. Thus, even a soft matrix with low load-bearing capacity changes the mechanical response of the fibre bundle because one microfibril break influences the material only at a distance less than x below and above the fracture section. Each microfibril is then considered to be formed by a chain of links of length $2x$; one section of the fibre is a bundle of such links and the overall fibre is modeled as a series of such bundles. Under such conditions, the fibre strength is given by Eq. 9, where the fibre length L is substituted by $2x$. This leads to a significant increase in the fibre bundle tensile strength, particularly at small values of the Weibull modulus, and the corresponding estimations are plotted in Fig. 13 for arbitrary values of $2x/L = 1$, 0.1 and 0.01.

More sophisticated models for the strength of a multifilamentary fibre were developed in the context of uniaxially reinforced composites (Curtin, 1999). They assume that fibre fracture is initiated randomly, but the stress concentration around the fibre breaks leads to the localisation of damage in the surrounding fibres. Clusters containing broken fibres grow progressively with deformation until they become unstable and the composite fails. The degree of damage localisation (and, thus, the composite strength) depends on the fibre, matrix and interface properties as well as on the fibre volume fraction and spatial arrangement. These models were very successful in predicting the composite strength but they have not been applied to multifilamentary fibres, partially because of the difficulties in measuring the actual properties of the fibre components (microfibrils, matrix and interface).

Hierarchical Fibres

While the composite fibres described in the previous section present a very simple microstructure, many biological fibres exhibit an extremely complex hierarchical structure which is responsible, at least partially, for their excellent combination of strength and damage tolerance (Renuart and Viney, 2000; Viney, 2000). A good example is the cotton fibre (Fig. 14), made up of concentric layers grown over a small cylindrical lumen at the fibre centre. Each layer is composed of parallel cellulose microfibrils laid down in spiral. The helix angle is around 20 to 30°. Cellulose molecules can form highly crystalline structures and, in fact, cotton crystallinity is over 60%. Other vegetal fibres, such as flax, hemp and ramie, present features similar to those of the cotton fibre, although the content of cellulose and the helix angle are lower. The mechanical behaviour of these fibres

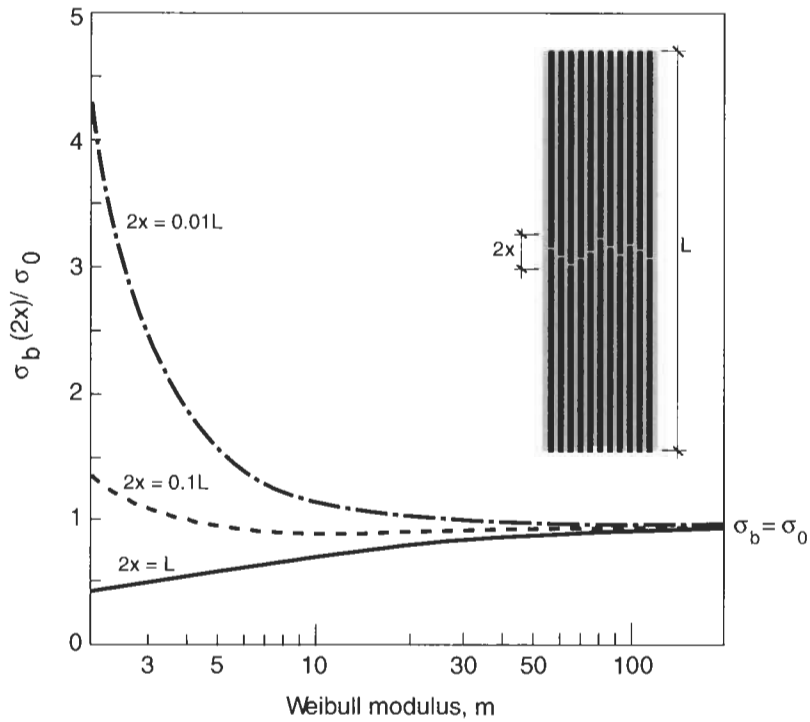

Fig. 13. Influence of the Weibull modulus, m, and of the effective bundle length, $2x$, on the tensile strength of a dry fibre bundle σ_b.

was initially analysed using the principles of twisted-yarn mechanics, which treated the fibre as a solid assembly of molecularly oriented microfibrils arranged in helical paths around a circular cylinder (Hearle, 1967). Later models (Hearle and Sparrow, 1979), which included the effect of deconvolution and of the free untwisting of the helical assembly, yielded stress–strain curves of the same shape as in cotton fibres. Further work is required, however, to include reliable criteria to predict the fibre fracture.

Wool, hair and other animal fibres have a hierarchical microstructure and no reliable model has been developed for prediction of the failure stress of these fibres which encompasses all the relevant length scales. Three models are available to explain the tensile properties of α-keratin fibres; all deal with a system of parallel microfibrils embedded in a proteinaceous matrix at a scale of 10 nm. In 1959, Feughelman laid the foundations of structural interpretation of the stress–strain curve with his two-phase model of microfibrils imbedded in a matrix, a model that was improved in 1994 (Feughelman, 1994). In the same year, Wortmann and Zahn (1994) proposed another version of the microfibril model. The third model, the Chapman and Hearle model (Hearle, 1967; Chapman, 1969) is based on the mechanics of stress transfer in a composite system consisting of microfibrils, which undergo an $\alpha \leftrightarrow \beta$ transition, in parallel with an elastomeric amorphous matrix. The Wortmann and Zahn model does not explicitly mention breakage of fibres, but it is implicit that this must be triggered

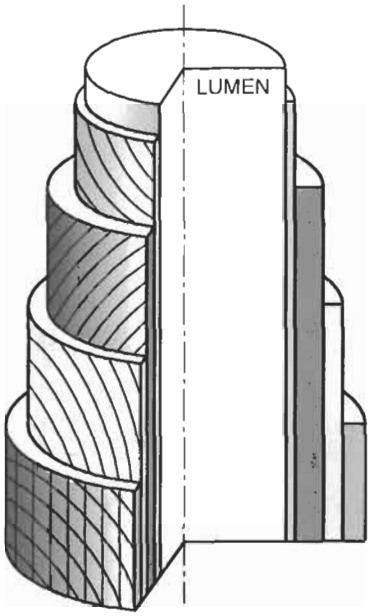

Fig. 14. Schematic structure of cotton fibres.

by rupture of the microfibrils, since the matrix could continue to flow to higher strains. Rupture mechanisms in the Feughelman model are less clear, but seem more likely to be related to the microfibrils. In the Chapman–Hearle model, rupture is postulated as starting in the matrix before the microfibrils have completed the $\alpha \leftrightarrow \beta$ transition. This model fits the observed rupture at around 50% extension. While this approach may reveal some fundamental features of the deformation mechanisms in keratin fibres, it is evident that quantitative predictions of the failure strength need to include the fibre structure at various length scales. A more detailed comparison of the three models is given in Hearle (2000).

Collagen fibres are the building blocks of the biological soft tissues in the skeletal system. Wang et al. (1997) used a different approach, based on viscoelastic models, to simulate and predict the strain rate dependence, the viscoelastic behaviour and the fracture of collagen fibres. They used the Zener model, with two nonlinear springs and one dashpot. The critical values of stress and strain at failure at different strain rates were explored using three different failure criteria: a stress criterion, a strain criterion and the strain energy density criterion. The last one seems to be better than the other two, although further quantitative study is needed to validate this conclusion. According to the authors this approach provides the basis for interpretation of some aspects of the viscoelastic and failure behaviour of hierarchically structured fibres with more economical CPU than full finite element modelling of the whole structure would have required.

Additional information on fracture of fibres hierarchically structured appears in the paper by Viney and in the paper by Hearle ('Fracture of Common Textile Fibres').

ACKNOWLEDGEMENTS

Financial support for this work was provided by the Spanish Ministry of Science and Technology under project MAT2000-1334. The authors thank Gustavo V. Guinea for useful comments and José Miguel Martínez and Rosa María Morera for their help with the illustrations and in typing the manuscript.

REFERENCES

Anderson, T.L. (1995) *Fracture Mechanics*. CRC Press, Boca Raton, FL.

Argon, A.S., Im, J. and Safoglu, R. (1975) Cavity formation from inclusions in ductile fracture. *Metall. Trans.*, 6A: 825–837.

Bacon, R. (1960) Growth, structure, and properties of graphite whiskers. *J. Appl. Phys.*, 31(2): 283–290.

Baltussen, J.J.M. and Northolt, M.G. (1996) A model for the tensile curve with yield of a polymer fibre. *Polym. Bull.*, 36: 125–131.

Beremin, F.M. (1981) Cavity formation from inclusions in ductile fracture of A508 steel. *Metall. Trans.*, 12A: 723–731.

Bernholc, J. (1999) Computational materials science. *Phys. Today* (September), 30–35.

Brenner, S.S. (1956) Tensile strength of whiskers. *J. Appl. Phys.*, 27(12): 1484–1491.

Broberg, K.B. (1999) *Cracks and Fracture*. Academic Press, New York, NY.

Bunn, C.W. and Garner, E.V. (1947) The crystal structures of two polyamides ('nylons'). *Proc. R. Soc. London A*, 189: 39–67.

Chapman, B.M. (1969) A mechanical model for wool and other keratin fibers. *Textile Res. J.*, 39: 1102–1109.

Chawla, K.K. (1998) *Fibrous Materials*. Cambridge University Press, Cambridge.

Cheng, T.T., Jones, I.P., Shatwell, R.A. and Doorbar, P. (1999) The microstructure of sigma 1140^{+} SiC fibres. *Mater. Sci. Eng.*, A260(1-2): 139–145.

Chopra, N.G. and Zettl, A. (1998) Measurement of the elastic modulus of a multi-wall BN nanotube. *Solid State Commun.*, 105: 297–300.

Chung, D.D.L. (1994) *Carbon Fibers Composites*. Butterworth-Heinemann, London.

Coleman, B.D. (1958) On the strength of classical fibers and fiber bundles. *J. Mech. Phys. Solids*, 7: 60–70.

Collins, W.D. (1962) Some axially symmetric stress distributions in elastic solids containing penny-shaped cracks, III. A crack in a circular beam. *Proc. Edinburgh Math. Soc.*, 13(2): 69–78.

Crist, B., Ratner, M.A., Brower, A.L. and Sabin, J.R. (1979) *Ab initio* calculations of the deformation of polyethylene. *J. Appl. Phys.*, 50(10): 6047–6051.

Curtin, W.A. (1991) BP internal report, BP/A-262.

Curtin, W.A. (1999) Stochastic damage evolution and failure in fiber-reinforced composites. *Adv. Appl. Mech.*, 36: 163–253.

Doege, E., Kröff, A. and Rotarescu, M.I. (2000) FEM analysis of wire drawing regarding the material damage. In: *Proceedings TPR*, Cluj-Napoca, pp. 131–136.

Elices, M. (1985) Fracture of steels for reinforcing and prestressing concrete. In: *Fracture Mechanics of Concrete*, pp. 226–271, G.C. Sih and A. DiTommaso (Eds.). Martinus Nijhoff, The Hague.

Esposito, E., Carlsson, A.E., Ling, D.D., Ehrenreich, H. and Gelatt, C.D. (1980) First-principle calculations of the theoretical tensile strength of copper. *Philos. Mag. A*, 41(2): 251–259.

Faucon, A., Lorriot, T., Martin, E., Auvray, S., Lepetitcorps, Y., Dyos, K. and Shatwell, R.A. (2001) Fracture behaviour of model silicon carbide filaments. *Comp. Sci. Technol.*, 61(3): 347–354.

Feughelman, M. (1994) A model for the mechanical properties of the a-keratin cortex. *Text. Res. J.*, 64(4): 236–239.

Fitzer, E. and Frohs, W. (1990) Modern carbon fibres from polyacrylonitrile (PAN)-Polyheteroaromatics with preferred orientation. *Chem. Eng. Technol.*, 13: 41–49.

Fitzer, E. and Künkele, F. (1990) Today's carbon fibres — a new energy-saving and environment-friendly all-round material (a review). *High Temp. High Pressures*, 22: 239–266.

Fukuda, H. and Chou, T.W. (1982) A probabilistic theory of the strength of short-fibre composites with variable fibre length and orientation. *J. Mater. Sci.*, 17: 1003–1011.

Gieske, J.H. (1968) Ph.D. Thesis, The Pennsylvania State University, University Park, PA.

González, C. and Llorca, J. (2000) Mechanical properties of Sigma 1140^{+} SiC fibres prior and after composite processing. *Adv. Comp. Lett.*, 9: 295–302.

Grimsditch, M.H., Anastassakis, E. and Cardona, M. (1978) Effect of uniaxial stress on the zone-center optical phonon of diamond. *Phys. Rev. B*, 18(2): 901–904.

Guinea, G.V., Rojo, F.J. and Elices, M. (2002a) Stress intensity factors for internal circular cracks in fibers under tensile loading. *Eng. Fract. Mech.* (submitted)

Guinea, G.V., Elices, M. and Rosselló, C. (2002b) Assessment of defect size in brittle fibers. *Eng. Fract. Mech.*, 69: 1057–1066.

Gurson, A.L. (1977) Continuum theory of ductile rupture by void nucleation and growth, Part 1. Yield criteria and flow rules for porous ductile media. *J. Eng. Mater. Technol.*, 99: 2–15.

He, T. (1986) An estimate of the strength of polymers. *Polymer*, 27: 253–255.

Hearle, J.W.S. (1967) The structural mechanics of fibers. *J. Polym. Sci., Part C*, 20: 215–251.

Hearle, J.W.S. (2000) A critical review of the structural mechanics of wool and hair fibres. *Int. J. Biol. Macromol.*, 27: 123–128.

Hearle, J.W.S. and Sparrow, J.T. (1979) Mechanics of the extension of cotton fibers, II. Theoretical modeling. *J. Appl. Polym. Sci.*, 24: 1857–1874.

Johnson, R.A. and Wilson, W.D. (1972) In: *Interatomic Potentials and Simulation of Lattice Deffects*, p. 301, P.C. Gehlen, J.R. Beeler and R.I. Jaffe, (Eds.). Plenum, New York.

Kanamoto, T., Tsuruta, A., Tanaka, K., Takeda, M. and Porter, R.S. (1983) *Polym. J.*, 15: 327.

Kausch, H.H. (1987) *Polymer Fracture*. Springer, Berlin.

Kelly, A. and Macmillan, N.H. (1986) *Strong Solids*, 3rd. ed. Clarendon Press, Oxford.

Kobayashi, H. and Hiki, Y. (1973) Anharmonicity in noble metals; nonlinear elasticity in whiskers. *Phys. Rev. B*, 7: 594–601.

Krishnan, A., Dujardin, E., Ebbesen, T.W., Yianilos, P.N. and Treacy, M.M.J. (1998) Young's modulus of single-walled nanotubes. *Phys. Rev. B*, 58: 14014–14019.

Lara-Curzio, E. and Sternstein, S. (1993) Thermoelastic analysis of composite CVD SiC fibers. *Comp. Sci. Technol.*, 46: 265–275.

Levan, A. and Royer, J. (1993) Part-circular surface cracks in round bars under tension, bending and torsion. *Int. J. Fract.*, 61: 71–99.

McQueen, R.G. and Marsh, S.P. (1962) Ultimate yield strength of copper. *J. Appl. Phys.*, 33: 654–665.

Milstein, F. and Farber, B. (1980) On the theoretical strength of copper. *Philos. Mag. A*, 42(1): 19–29.

Morgan, R.J., Pruneda, C.O. and Steele, W.J. (1983) The relationship between the physical structure and the microscopic deformation and failure processes of poly(*p*-phenylene terephthalamide) fibers. *J. Polym. Sci. Polym. Phys. Ed.*, 21: 1757–1783.

Nam, W.J. and Bae, C.M. (1995) Void initiation and microstructural changes during wire drawing of pearlitic steels. *Mater. Sci. Eng.*, 203: 278–285.

Náray-Szabó, I. and Ladik, J. (1960) Strength of silica glass. *Nature*, 188: 226–227.

Northolt, M.G. and van der Hout, R. (1985) Elastic extension of an oriented crystalline fibre. *Polymer*, 26: 310–316.

Orowan, E. (1949) *Rep. Prog. Phys.*, 12: 185.

Panar, M., Avakian, P., Blume, R.C., Gardner, K.H., Gierke, T.D. and Yang, H.H. (1983) Morphology of poly(*p*-Phenylene Terephthalamide) fibers. *J. Polym. Sci. Polym. Phys. Ed.*, 21: 1955–1969.

Perepelkin, K.E. (1972) Comparative estimate of the theoretical, highest attainable strength and rigidity of oriented layer structures. *Sov. Mater. Sci.*, 8(2): 198–202.

Peterlin, A. (1981) Tensile failure of crystalline polymers. *J. Macromol. Sci. Phys. B*, 19: 401–419.

Picken, S.J. and Northolt, M.G. (1999) *A simple model for the strength of high-modulus fibers*. EPS Meeting, Potsdam.

Polanyi, M. (1921) *Z. Phys.*, 7: 323

Poza, P., Pérez-Rigueiro, J., Elices, M. and Llorca, J. (2002) Fractographic analysis of silkworm and spider silk. *Eng. Fract. Mech.*, 69: 1035–1048.

Proctor, B.A., Whitney, I. and Johnson, J.W. (1967) The strength of fused silica. *Proc. R. Soc. A*, 297: 534–557.

Renuart, E. and Viney, C. (2000) Biological fibrous materials. In: *Structural Biological Materials*, pp. 221–267, M. Elices (Ed.). Pergamon Press, Oxford.

Reynolds, W.N. and Moreton, R. (1980) Some factors affecting the strengths of carbon fibres. *Philos. Trans. R. Soc. A*, 294: 451–461.

Rice, J.R. and Tracey, D.M. (1969) On the ductile enlargement of voids in triaxial stress fields. *J. Mech. Phys. Solids*, 17: 201–217.

Sandulova, A.V., Bogoyavlenskii, P.S. and Dronyuk, M.I. (1964) Preparation and some properties of whisker and needle-shaped single crystals of germanium, silicon and their solid solutions. *Sov. Phys. Solid State*, 5(9): 1883–1888.

Smook, J., Hamersma, W. and Pennings, A.J. (1984) The fracture process of ultra-high strength polyethylene fibres. *J. Mater. Sci.*, 19: 1359–1373.

Sneddon, I.N. and Tait, R.J. (1963) The effect of a penny-shaped crack on the distribution of stress in a long circular cylinder. *Int. J. Eng. Sci.*, 1: 391–409.

Soltis, P.J. (1965) Anisotropy in tensile properties of submicron-size sapphire (Al_2O_2) whiskers. *Bull. Am. Phys. Soc.*, 10: 163.

Soules, T.F. and Busbey, R.F. (1983) The rhelogical properties and fracture of a molecular dynamic simulation of sodium silicate glass. *J. Chem. Phys.*, 78: 6307–6316.

Tada, H., Paris, P. and Irwin, G.R. (1985) *The Stress Analysis of Cracks Handbook*. Paris Prod. Inc., St. Louis, MO.

Termonia, Y. (2000) Computer model for the mechanical properties of synthetic and biological polymer fibers. In: *Structural Biological Materials*, pp. 271–291, M. Elices (Ed.). Pergamon Press, Oxford.

Termonia, Y., Meakin, P. and Smith, P. (1985) Theoretical study of the influence of the molecular weight on the maximum tensile strength of polymer fibers. *Macromolecules*, 18: 2246–2252.

Termonia, Y., Meakin, P. and Smith, P. (1986) Theoretical study of the influence of strain rate and temperature on the maximum strength of perfectly ordered and oriented polyethylene. *Macromolecules*, 19: 154–159.

Thomason, P.F. (1990) *Ductile Fracture of Metals*. Pergamon Press, Oxford.

Tvergaard, V. and Needleman, A. (1984) Analysis of the cup-cone fracture in a round tensile bar. *Acta Metall.*, 32: 157–169.

Vega-Boggio, J. and Vingsbo, O. (1976) Application of Griffith criterion to fracture of boron fibers. *J. Mater. Sci.*, 11: 2242–2246.

Vega-Boggio, J., Vingsbo, O. and Carlsson, J.O. (1977) The initial stages of growth and the origin of proximate voids in boron fibres. *J. Mater. Sci.*, 12: 1750–1758.

Viney, C. (2000) Silk fibers: origins, nature and consequences of structure. In: *Structural Biological Materials*, pp. 293–333, M. Elices (Ed.). Pergamon Press, Oxford.

Wang, J.L., Parnianpour, M., Shirazi-Ade, A. and Engin, A.E. (1997) Failure criterion of collagen fiber. *Theor. Appl. Fract. Mech.*, 27: 1–12.

Waterbury, M.C. and Drzal, L.T. (1991) On the determination of fiber strengths by in-situ fiber strength testing. *J. Compos. Technol. Res.*, 13: 22–28.

Wawner, F.E. (1988) Boron and silicon carbide/carbon fibers. In: *Fibre Reinforcements for Composite Materials*, pp. 371–425, A.R. Bunsell (Ed.). Elsevier, Amsterdam.

Whitlock, J. and Ruoff, A.L. (1981) The failure strengths of perfect diamond crystals. *Scr. Metall.*, 15: 525–529.

Wilks, J. and Wilks, E. (1991) *Properties and Applications of Diamond*. Butterworth-Heinemann, London.

Wortmann, F.J. and Zahn, H. (1994) The stress-strain curve of a-keratin fibers and the structure of the intermediate filament. *Textile Res. J.*, 64(12): 737–743.

Yoon, H.N. (1990) Strength of fibers from wholly aromatic polyesters. *Colloid Polym. Sci.*, 268: 230–239.

Yu, M.F., Files, B.S., Arepalli, S. and Ruoff, R.S. (2000) Tensile loading of ropes of single wall carbon nanotubes and their mechanical properties. *Phys. Rev. Lett.*, 84(24): 5552–5555.

Fiber Fracture
M. Elices and J. Llorca (Editors)

FORMS OF FIBRE FRACTURE

J.W.S. Hearle

The Old Vicarage, Mellor, Stockport SK6 5LX, UK

Introduction 59
Tensile Breaks 59
Brittle Fracture 59
Ductile Failure 59
High-Speed Breaks 62
Granular Breaks 62
Fibrillar Breaks 63
Axial Split Breaks 63
Stake-and-Socket 63
Morphological Determinism 64
Other Directions of Deformation 65
Twist Breaks 65
Bending Breaks 65
Lateral Pressure 66
'Fatigue' Breaks 66
Complex Forms of Loading 66
Tensile Fatigue 66
Flex Fatigue 66
Kink-Band Failure 67
Axial Splitting 68
Torsional Fatigue 69
Combined Twisting and Bending 69
Surface Wear 69
Failure in Use 70
Conclusion 70
References 71

Abstract

The diverse forms of fibre fracture are shown in SEM studies. The classification covers the following forms of tensile break: brittle failure in inorganic and elastomeric

fibres; ductile failure in melt-spun synthetics; high-speed breaks in melt-spun synthetics; granular breaks in solution-spun fibres; axial splits in HM-HT polymer fibres; stake-and-socket breaks; and three forms in cotton. There are also breaks due to twisting, bending and lateral pressure. 'Fatigue' breaks occur in tension cycling, repeated bending and twisting, and surface wear. Multiple splitting is the commonest form of failure in use.

Keywords

Fibre; Textile; Fracture; Fatigue; Tensile; Bending; Twisting; Abrasion

INTRODUCTION

There is great diversity in the way in which fibres fracture, depending on the fibre type and the mode of application of stress. The subject can be studied at three levels: the macroscopic applied forces; the microscopic level, which shows the path of fibre breakage; and the response of the molecules. Attempts at theoretical interpretations of the gross experimental observations in terms of molecular effects can be misleading, because abstract statements about the forces involved are related to abstract views of imperfectly understood structures. The intermediate level, for which the scanning electron microscope (SEM) provides concrete evidence, must be taken into account in order to understand the mechanisms of failure.

This paper is intended to set the scene for more detailed discussion by reviewing the pattern of rupture in different fibres under different conditions. Fig. 1 shows a collection of different appearances of fibre ends. The first group are tensile breaks, as found in typical load-elongation tests. The second group are various forms of 'fatigue' failure after repeated loading. The last few include natural ends and other effects, such as melting, which are not relevant to these proceedings.

The review will necessarily be brief. More examples of the forms of break as seen in the SEM or occasionally in optical microscopy are included in our book on fibre fracture (Hearle et al., 1998), which also gives many examples of failure in use.

TENSILE BREAKS

Brittle Fracture

Glass fibres show a classical Griffiths brittle fracture. A smooth crack may run across the whole fibre, Fig. 2a, but usually the mirror region, which progresses from a flaw, turns into multiple cracks, the hackle region, Fig. 2b. Breaks of this type occur in three-dimensionally bonded materials with no yield mechanisms. This group includes ceramic fibres, Fig. 2c,d, and some carbon fibres, Fig. 2e. There can be deviations from the simpler forms of Fig. 1. For example, rupture may occur on the plane of maximum shear stress. All these fibres break at small tensile strains, mostly less than 2%. Surprisingly, the elastomeric fibre, Lycra, Fig. 2f, also shows this type of break at over 500% extension. However, although this starts extension as a low modulus, extensible material, it becomes very stiff near the break point.

Ductile Failure

The melt-spun thermoplastic fibres, nylon, polyester, polypropylene, show a quite different form of breakage. In undrawn fibres, which are unoriented or partially oriented, rupture occurs at the end of a long period of plastic extension at slowly increasing tension. In oriented fibres, which have been drawn, the stress–strain curve terminates in a short yield region, the residual plastic extension, before rupture occurs. Break starts as a crack, usually from a flaw but otherwise self-generated by coalescence of voids, Fig. 3a. The

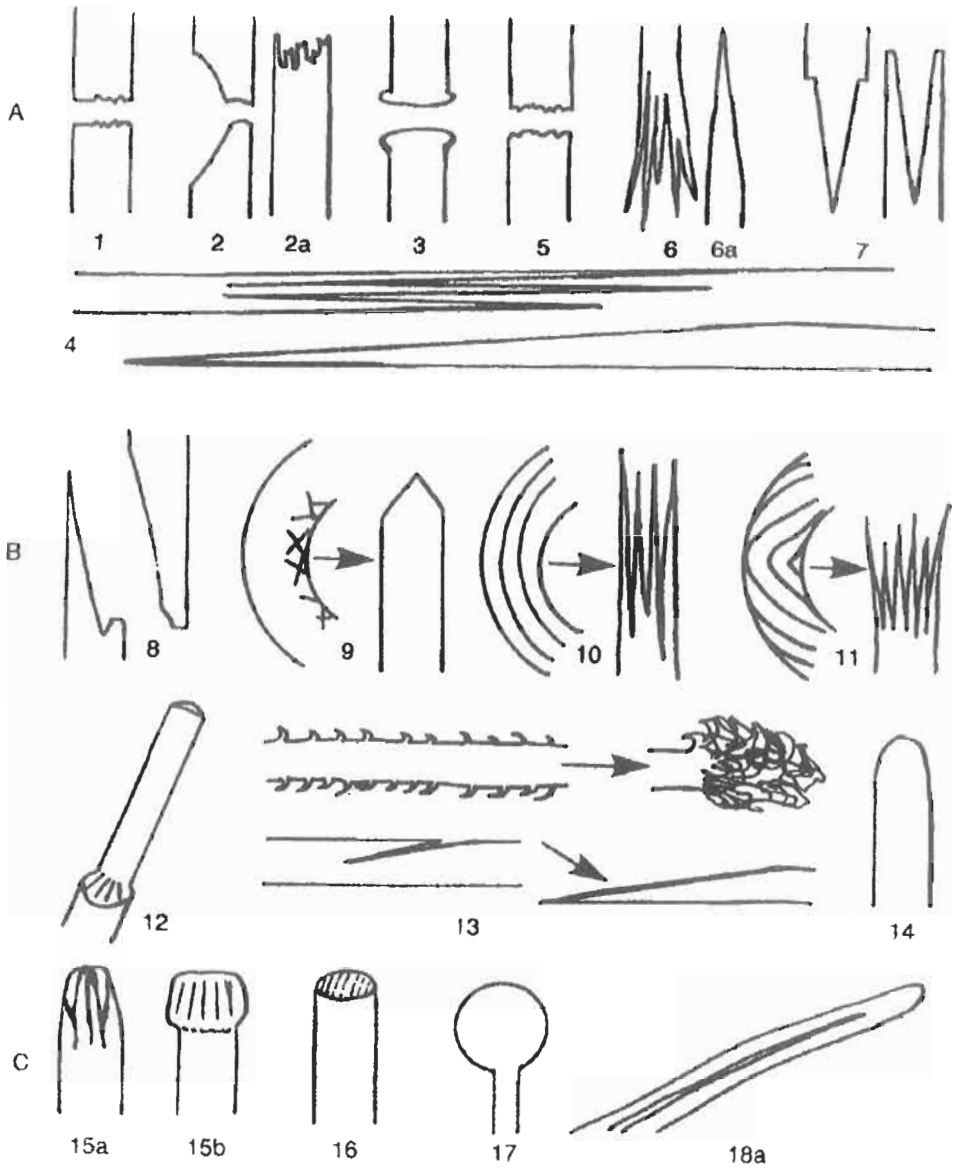

Fig. 1. A collection of fibre ends, based on SEM pictures. (A) Tensile breaks. (1) Brittle fracture. (2) Ductile fracture. (2a) Light-degraded fracture. (3) High-speed mushroom. (4) Axial splits. (5) Granular. (6) Fibrillar. (7) Stake-and-socket. (B) Fatigue. (8) Strip and tail. (9) Kink bands. (10), (11) Splits. (12) Wear. (13) Peeling. (14) Rounding. (C) Others (15) Mangled. (16) Cut. (17) Melted. (18) Natural end of cotton fibre. From Hearle et al. (1998).

NOTE: With the exception of Fig. 3a,b, which is a 1-mm diameter monofil, and Fig. 3d, which is a film, the scales of the SEM pictures can be inferred from the fact that all the fibres are typical textile fibres with diameters in the range of 10 to 20 μm.

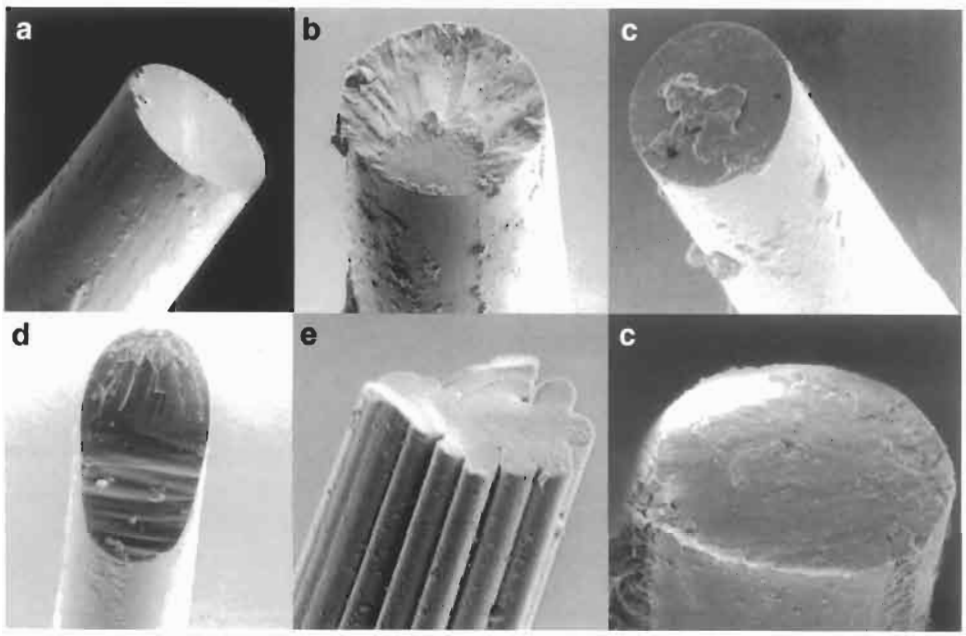

Fig. 2. Brittle fractures. (a,b) Glass fibres. (c,d) Ceramic fibres, Nextel, Nicolon. (e) Carbon fibre from rayon precursor. (f) Elastomeric Lycra. For further explanation, see Fig. 1.

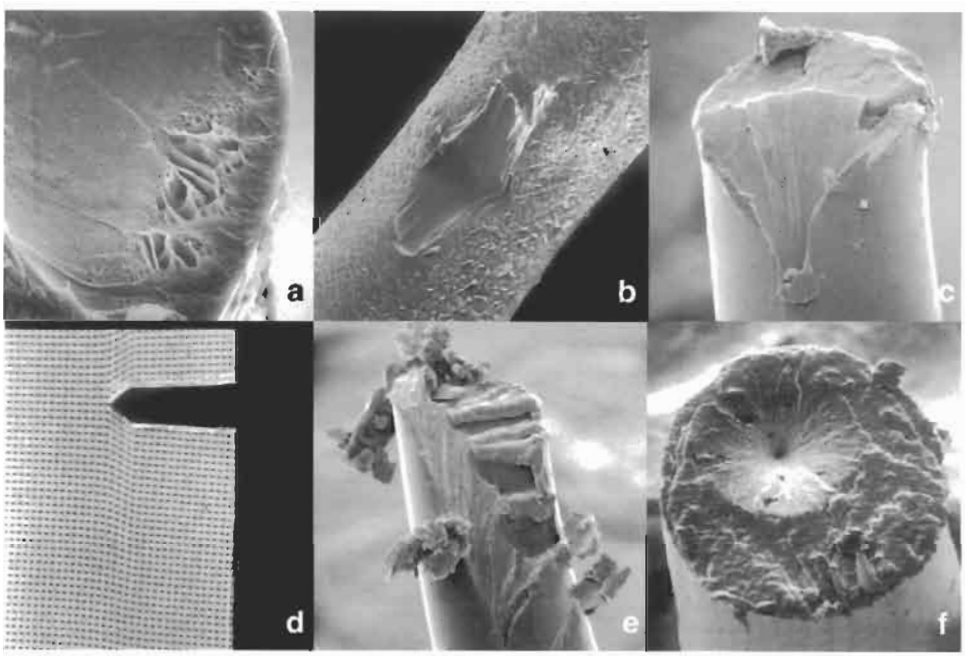

Fig. 3. Ductile fractures. (a,b) Thick undrawn nylon monofilament. (c) Polyester fibre. (d) Polyester film. (e,f) Nylon fibre. For further explanation, see Fig. 1.

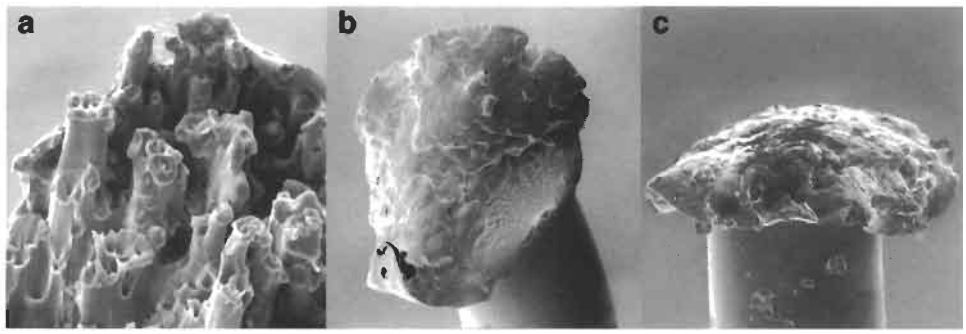

Fig. 4. (a) Light-degraded nylon. (b,c) High-speed break of nylon from pendulum impact. For further explanation, see Fig. 1.

increase in stress on the unbroken side causes additional plastic yielding and the crack opens into a V-notch, Fig. 3b. When this has grown to a critical size, catastrophic failure occurs over the remaining cross-section, Fig. 3c. Tests on polyester film marked with a grid show that the additional elongation represented by the open end of the V-notch is accommodated in the unbroken material by a band of shear, Fig. 3d, which would extend back by many fibre diameters. Plastic deformation over a large volume of the whole circular specimen is a challenge to the theoreticians of fracture mechanics.

There are variant forms. The initial flaw may be a small point, a line perpendicular to the fibre axis, or an angled line, and this changes the detail of the break, Fig. 3e. Occasionally, breaks start from opposite sides of the fibre, giving two V-notch zones and a central catastrophic region. Breaks normally start from the fibre surface, but occasionally from an internal flaw, when the V-notch becomes a double cone, Fig. 3f. A variant on this form occurs in light-degraded nylon. Voids form round the delustrant, titanium dioxide particles, and multiple breaks start from these voids to give a turreted appearance, Fig. 4a.

High-Speed Breaks

As the rate of extension is increased, the V-notch region gets smaller, Fig. 4b, and the catastrophic region gets larger. At ballistic rates, the change is complete and the break appears as a mushroom, Fig. 4c. This is explained as being due to a change from isothermal to adiabatic conditions. Heat generated by the rapid plastic flow causes the material to melt, or at least soften. The elastic energy stored in the fibre remote from the break zone causes snap-back when break occurs. When snap-back stops, the softened material collapses into the mushroom cap.

Granular Breaks

Cellulosic and acrylic fibres, which are spun from solution, show granular breaks, which are similar to lower-magnification views of the structure of a fibre-reinforced composite, Fig. 5a,b. The reasons are similar. The fibres coagulate from solution with

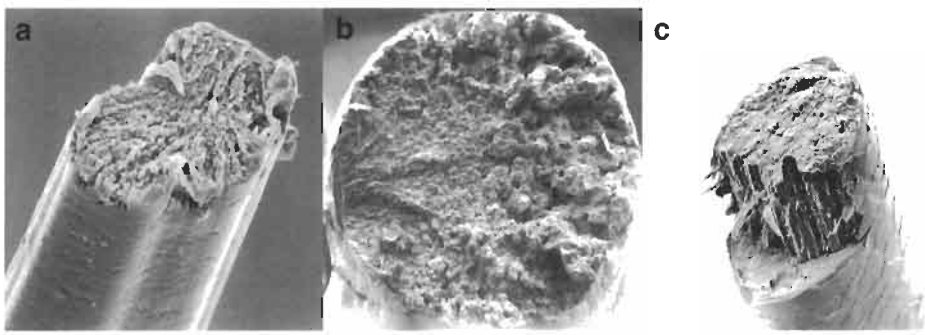

Fig. 5. Granular fractures. (a) Cellulose fibre. (b) Acrylic fibre. (c) Human hair. For further explanation, see Fig. 1.

occluded solvent rather like a sponge. The voids subsequently collapse on drying and are elongated during drawing. However, they remain as weak places in the structure. On extension, individual fibrillar elements start to break, transferring stress to neighbouring elements. Sometimes there is evidence of the break spreading out from a surface flaw, and sometimes the break occurs in separate steps joined by an axial split, Fig. 5c.

In addition to solution-spun textile fibres, granular breaks are also found in some carbon fibres, which reflect their acrylic fibre origin, and in alumina fibres. Granular breaks are also shown in the natural fibres, wool and hair, in cotton at zero moisture content, and in resin-treated, cross-linked cotton at intermediate humidities.

Fibrillar Breaks

In wet cotton the fluidity of the absorbed water between fibrils inhibits stress transfer, so that fibrils break independently, Fig. 6a.

Axial Split Breaks

The characteristic form of tensile rupture in para-aramid, HMPE and other highly oriented, chain-extended fibres consists of long axial splits, often multiple splits on one end, Fig. 6b, and a single split on the other, Fig. 6c,d. This is a result of the axial molecular strength being much greater than the intermolecular strength. Shear stresses cause cracks to propagate and eventually cross the fibre and lead to loss of continuity.

Stake-and-Socket

In some degraded polyester and hair fibres, the breaks have the form of a stake and socket, Fig. 7. An outer ring of degraded material breaks first. Then a circular crack propagates at an off-axis angle to form a positive cone, which finally pulls out of the opposing negative cone. The polyester example from UMIST studies is an overall subject to repeated autoclaving, but this type of break was first reported by Ansell (1983) after boiling PVC-coated polyester fabric, and Holmes (1996) has reported similar breaks after aminolysis of polyester fibres.

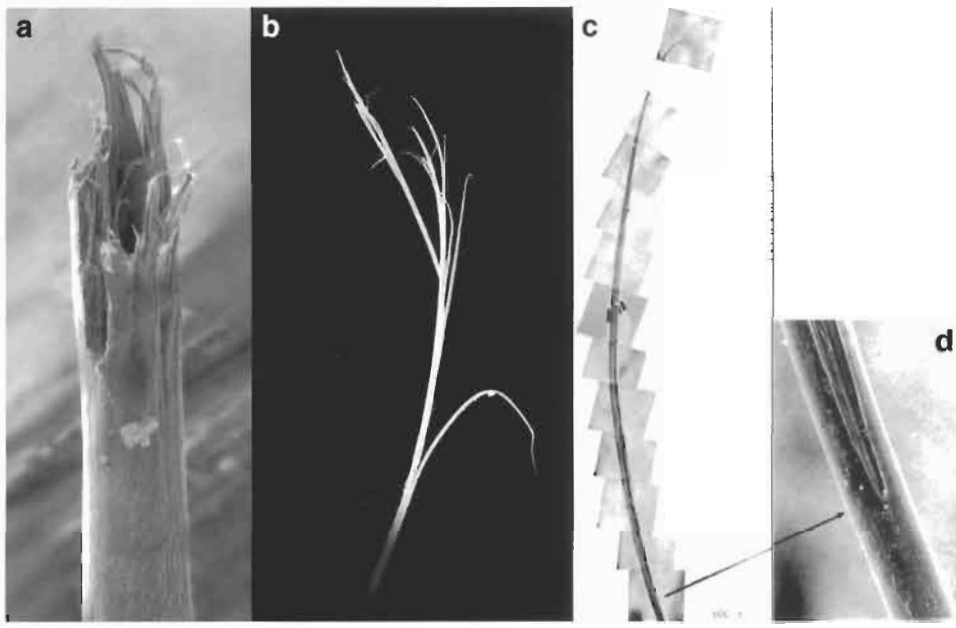

Fig. 6. (a) Fibrillar break in wet cotton. (b) Multiple split break of Kevlar. (c,d) Single split break of Kevlar. For further explanation, see Fig. 1.

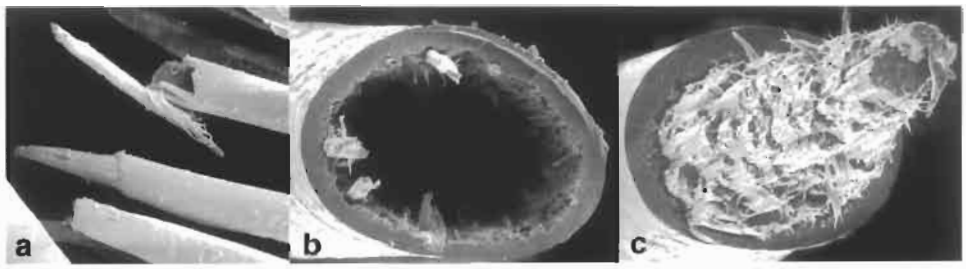

Fig. 7. Stake-and-socket breaks. (a) From frequently autoclaved polyester overall. (b,c) Tensile break of human hair after 700 h of alternating UV radiation and humidification. From Weigmann and Ruetsch, TRI Princeton. For further explanation, see Fig. 1.

Morphological Determinism

As mentioned above, cotton shows a granular break across the fibre in raw cotton at 0% rh, when there is strong hydrogen bonding between fibrils, or in resin-treated cotton with covalent cross-linking at 65% rh, and a fibrillar break when inter-fibrillar bonding is weak in wet cotton. In the intermediate state of raw cotton at medium humidity, or resin-treated cotton when wet, the form of break is dictated by the cotton fibre structure, Fig. 8. Break starts close to a reversal in the sense of the spiral angle at the edge of the zone where material has collapsed into the central void. Tension tends to cause untwisting at the reversal and the resulting shear stresses cause splitting between fibrils

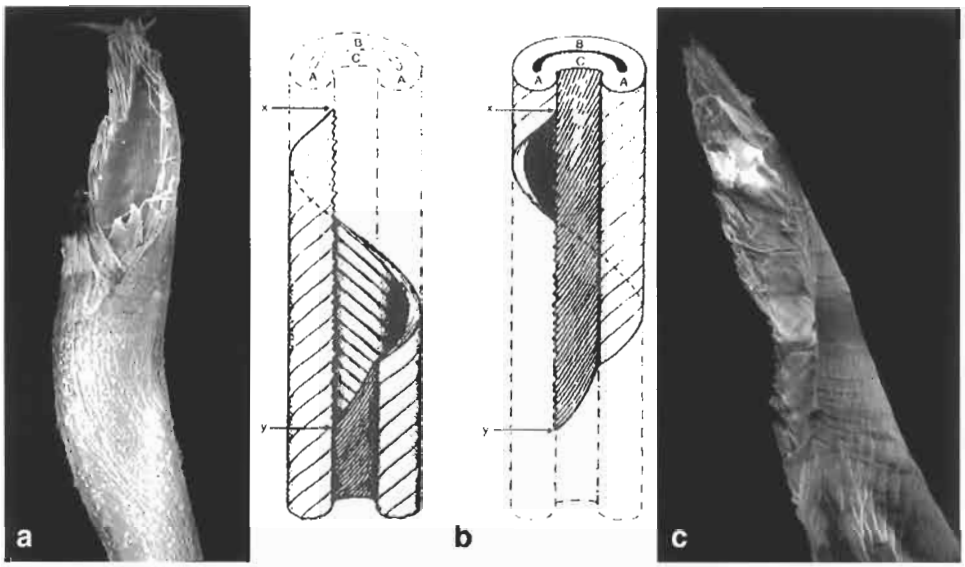

Fig. 8. Cotton breaks. (a) Raw cotton at 65% rh. (b) Schematic view of break. (c) Wet resin-treated cotton. For further explanation, see Fig. 1.

along the line of the helix angle. This continues until the crack reaches the other side of the collapsed zone, when it tears back to the starting point.

OTHER DIRECTIONS OF DEFORMATION

Twist Breaks

Except for glass and other brittle materials, twist angles of 20° to 60° are needed to break fibres. In these conditions, the torsional shear stresses are out-weighed by the tensile stresses due to the increased length on the outside of the fibre. Breaks tend to be geometrically distorted forms of tensile breaks, often with some additional splitting. Although, I do not know of experimental studies, breaks in brittle fibres would be variants of the standard forms.

Bending Breaks

Schoppee and Skelton (1974) showed that break occurred in bending of a glass fibre when the surface strain reached 7.3% and in two carbon fibres at 1.4 and 2.8%. The rupture is a brittle fracture due to tensile extension, but occurs at values slightly greater than the breaking strain in tensile tests because the effective length is much lower. In other high-modulus fibres, such as Kevlar 49, as well as the general textile fibres, the fibres could be bent back on themselves without breaking, which corresponds to a nominal surface strain of 100%. This behaviour is explained by the low compressive

yield stress. Deformation is easier on the compression side than on the tension side. The neutral plane moves out from the central position towards the tension side and maintains the tensile strain below the break extension.

Lateral Pressure

Breaks due to lateral pressure reflect the features of the object employed. Sharp knives give a clean cut; scissors have a characteristic form; and blunt instruments give a squashed appearance. These differences are important in forensic studies, as described by Hearle et al. (1998; chapters 44 to 46).

'FATIGUE' BREAKS

Complex Forms of Loading

The term 'fatigue' is rather loosely used in the fibre literature to cover all circumstances other than those in which break occurs as a result of a monotonically increasing force. 'Static fatigue' or creep rupture, which occurs after a long time under load, gives forms similar to more rapid tensile breaks. Cyclic loading gives rise to a variety of forms.

Tensile Fatigue

Bunsell and Hearle (1971) showed that cyclic loading of nylon commonly gave tensile breaks after the same time as for creep rupture at the peak cyclic load. The exception was when the fibres were cycled from zero load to about 50% of break load. In these circumstances, the break showed a tail on one end, which is typically about five fibre diameters long and had stripped off the other end, Fig. 9a,b. The sequence of failure was first the development of a small transverse crack, which then turned and ran along the fibre at an angle of about 5° to the fibre axis, Fig. 9c. When the crack had crossed half the fibre, the stress on the residual cross-section caused final ductile rupture, Fig. 9d.

A similar loading sequence caused failure in polyester fibres, but on some polyester fibres studied later by Oudet and Bunsell (1987) a low critical minimum load gave the same form of break. An important, and unexplained difference from nylon is that the axial cracks are closely parallel to the fibre axis. Consequently, the tails are extremely long, Fig. 9e,f. In one example, the crack had propagated beyond the final break zone, which was effectively a creep rupture failure from a central flaw, Fig. 9g.

Flex Fatigue

The commonest way of studying flex fatigue in fibres is to pull a fibre backwards and forwards over a pin. Typically the pin diameter is about ten times the fibre diameter, giving a nominal bending strain of 10%, and the tension is about 1/10 of the fibre break load, but the mode of failure depends on the exact conditions. In Kevlar and wool fibres

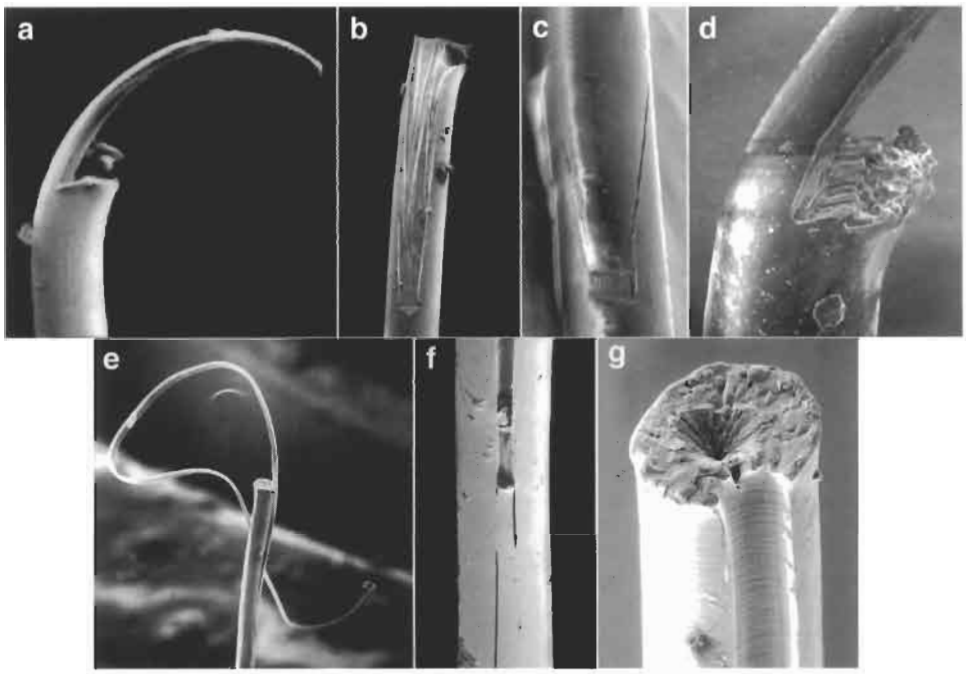

Fig. 9. Tensile fatigue breaks. (a–d) Nylon. (e–g) Polyester. For further explanation, see Fig. 1.

surface wear dominates, so that other methods of flex testing, such as repeated buckling without pin contact, must be used. In nylon and polyester fibres, surface wear dominates at high tensions, but it is easy to find conditions in which the broken fibre shows only minor wear along the line of contact. These are true flex failures, but their form depends on whether the bending forces over the zone of maximum curvature or the shear forces along the zone of variable curvature off the pin cause the breakage.

Kink-Band Failure

Most polymer fibres yield at a much lower stress in compression than in tension. This is due to the formation of kink bands at an angle of about 45° to the fibre axis, which can be seen internally in polarised light microscopy or projecting on the surface in scanning electron microscopy, Fig. 10a,b. Due to the difficulty of applying uniform axial compression, because of whole-fibre buckling, kink bands are usually observed on the inside of bends. After a single bend, the kink bands can be pulled out and there is no appreciable loss of strength. Repeated cycling leads to progressively increased damage at the kink bands, similar to crazing, and eventual rupture across about half the fibre, Fig. 10c,d. Further cycling leads to complete failure. It is common for a central axial split to appear, but it is not known whether this is present before the break, due to the maximum shear stress at the centre of the fibre, or whether it comes later due to the shear stress at the tip of the break.

Kink-band breaks are easily recognised by their sharp angular form, Fig. 10e.

Axial Splitting

The theory of bent beams shows that variable curvature is accommodated by shear stresses, which are a maximum on the central plane. In fibres undergoing flex fatigue these shear stresses can cause failure by axial splitting, Fig. 10f,g.

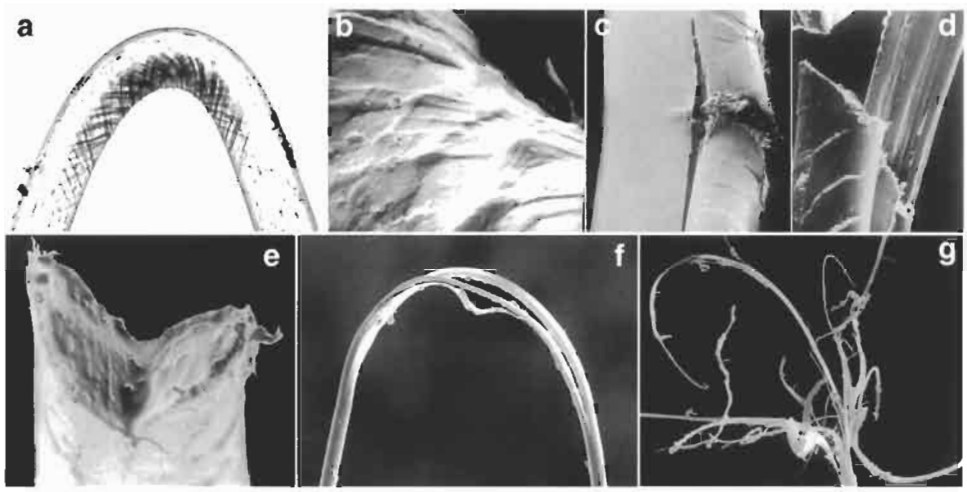

Fig. 10. (a,b) Polyester fibres after a single bend. (c–e) Flex fatigue in polyester: kink-band fracture. (f) Flex fatigue: shear splitting in nylon. (g) Flex fatigue: shear splitting in polyester. For further explanation, see Fig. 1.

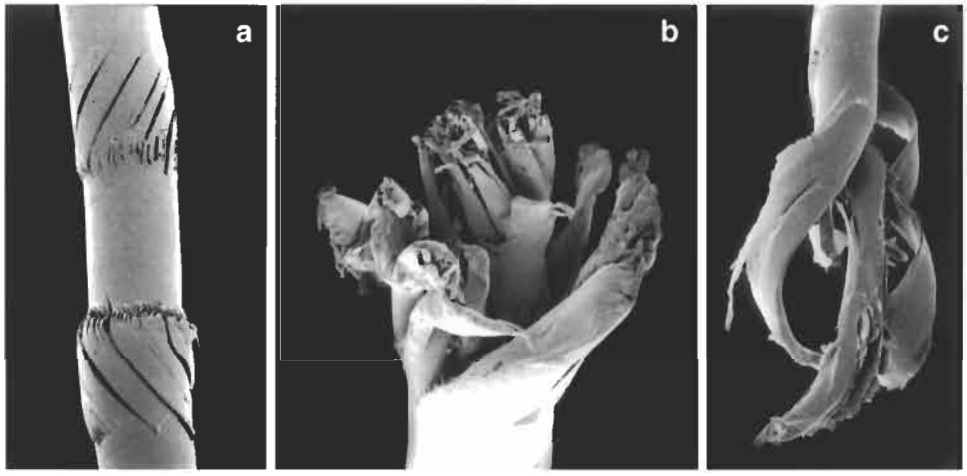

Fig. 11. Biaxial rotation fatigue. (a,b) Thick polyester fibre. (c) Finer polyester fibre. For further explanation, see Fig. 1.

Torsional Fatigue

Cyclic twisting fatigue has been less studied than flex fatigue. Repetitive action at the high twists needed can wear out the tester as well as the fibres. At high twist amplitudes, Goswami et al. (1980) found breaks in polyester fibres at about 500 cycles, which were similar to those in monotonically increasing twist. At lower twist levels, breaks at around 100,000 cycles were due to multiple splitting.

Combined Twisting and Bending

Biaxial rotation is a useful method of laboratory fatigue testing of fibres. For thick monofilaments a short length is bent into an arc of a circle and then rotated from both ends. For fine fibres the bend is concentrated over a pin. Clearly, as the bent fibre rotates, material away from the centre of the fibre alternates between tension and compression, and in the variable curvature off the pin, there will be shear stresses. However, the energy loss in each cycle means that torque must be applied through the rotating grips in order to drive the rotation. This combination of bending and twisting leads to failure by multiple splitting along helical lines, Fig. 11.

Surface Wear

Surface wear can be studied in yarn-on-yarn abrasion by cyclic displacement of a twisted loop or in abrasion against other surfaces by hanging a fibre over a rotating pin. It also occurs in axial cycling over a pin, to a limited extent in nylon and polyester fibres and to a greater extent in Kevlar and wool. Severe wear reduces the fibre cross-section until break occurs under the tensile load, Fig. 12a,b. In Kevlar, the splitting then destroys the worn surface, but in wool both surfaces can be seen. The worn surfaces are usually fairly smooth with some fibrillation visible at the edges.

Studies of nylon and polyester show up more detail, Fig. 12c,d. The local shear stresses caused by surface friction commonly lead to wear by surface peeling. Some of the most interesting results are from inter-fibre abrasion in ropes subject to tension–tension cycling. Wet nylon abrades rapidly with cracks running at an angle across the fibre and converting continuous filaments into short fibres with a consequent loss of rope strength, Fig. 12e–g. Polyester ropes have a much slower loss of strength because, as in tensile fatigue, the cracks run parallel to the fibre axis.

Studies of nylon and polyester show up more detail, Fig. 12c,d. The local shear stresses caused by surface friction commonly lead to wear by surface peeling. Some of the most interesting results are from inter-fibre abrasion in ropes subject to tension–tension cycling. Wet nylon abrades rapidly with cracks running at an angle across the fibre and converting continuous filaments into short fibres with a consequent loss of rope strength, Fig. 12e–g. Polyester ropes have a much slower loss of strength because, as in tensile fatigue, the cracks run parallel to the fibre axis.

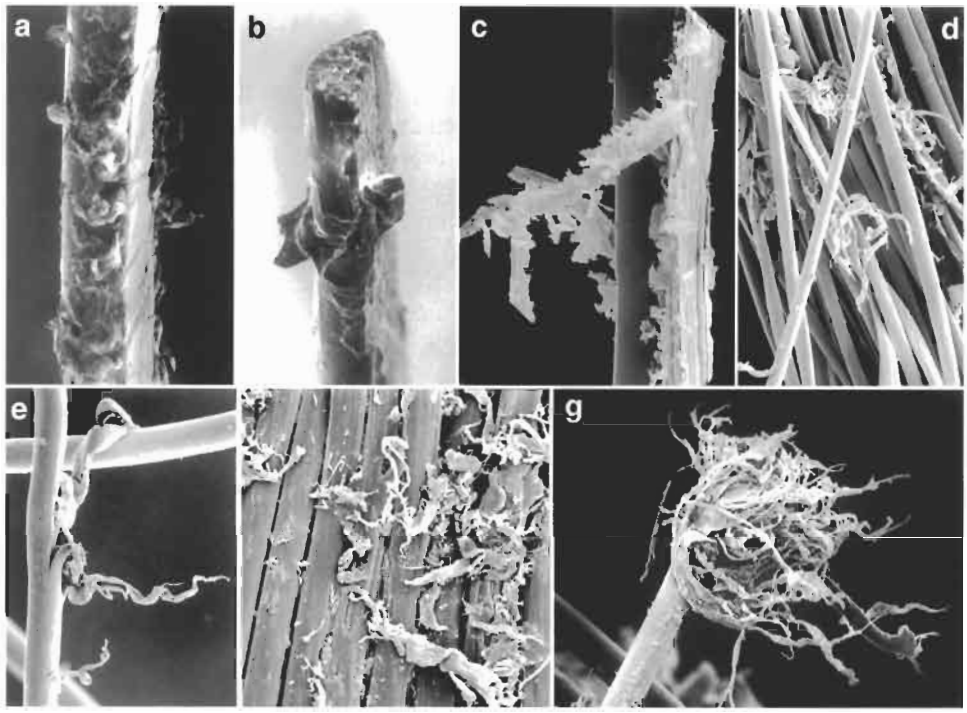

Fig. 12. Surface abrasion. (a) Kevlar pulled to-and-fro over a pin. (b) Wool against a rotating pin. (c) Nylon against a rotating pin. (d) Yarn-on-yarn abrasion of polyester. (e) From wet nylon rope after tension cycling. (f,g) From worn nylon Hovercraft rope. For further explanation, see Fig. 1.

Failure in Use

The most commonly observed form of failure in the ordinary use of textile fabrics is multiple splitting, which may be caused by bending with variable curvature, twisting or a combination of bending and twisting. Another common form is kink-band failure when fibres are forced to buckle into sharp kinks, which may be followed by axial splitting. After breakage, continued wear rubs away material to give a rounded fibre end, Fig. 13a.

CONCLUSION

The aim of this paper has been to illustrate the diversity of form of fibre fracture. Any discussion of the mechanics involved in fibre fracture must be in the context of the pattern of deformation and cracking. Some brief explanations of the mechanisms involved and some examples of the materials and circumstances leading to particular forms of break have been included. Many more examples, both from laboratory testing and failure in use, are given in the Atlas of Fibre Fracture and Damage to Textiles by

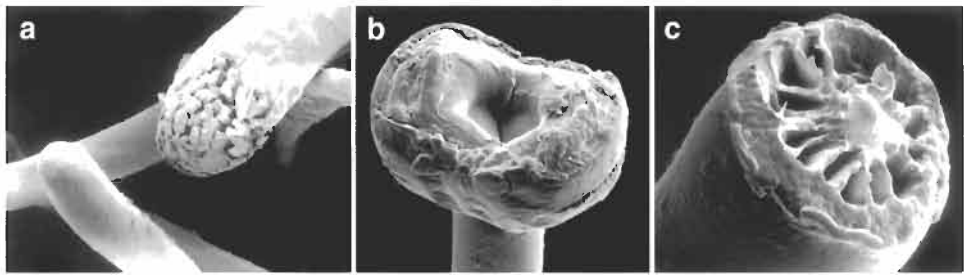

Fig. 13. (a) Final stages of wear: multiple splitting leads to rounded ends. Wool/polyester jacket. (b,c) 'Direct' breaks of nylon after a few cycles of severe biaxial rotation testing. For further explanation, see Fig. 1.

Hearle et al. (1998), which also contains a full list of references. The SEM pictures were reduced from about 40,000 in UMIST files, plus some from other sources, to about 1500 in the Atlas, and to 54 in this paper. More information on stress distributions in twisted and bent fibres is given by Morton and Hearle (1993).

Finally, although it is of more academic than practical interest, the complicated modes of deformation that can occur in fibres are shown by some breaks in the biaxial rotation test with a high angle of wrap round the pins. This generates high torque forces and probably some heating. Bulbous zones of disorientation are formed and 'direct' breaks occur in a few cycles in very curious forms, Fig. 13b,c.

REFERENCES

Ansell, M.P. (1983) The degradation of polyester fibres in a PVC-coated fabric exposed to boiling water. *J. Textile Inst.*, 74: 263–271.

Bunsell, A.R. and Hearle, J.W.S. (1971) A mechanism of fatigue failures in nylon fibres. *J. Mater. Sci.*, 6: 1303–1311.

Goswami, B.C., Duckett, K.E. and Vigo, T.L. (1980) Torsional fatigue and the initiation mechanism of pilling. *Textile Res. J.*, 50: 481–485.

Hearle, J.W.S., Lomas, B. and Cooke, W.D. (1998) *Atlas of Fibre Fracture and Damage to Textiles.* Woodhead Publishing, Cambridge.

Holmes, S.A. (1996) Surface defect geometry/tensile failure relationships of aminolyzed poly(ethylene terephthalate) fibers. *Textile Res. J.*, 66: 214–218.

Morton, W.E. and Hearle, J.W.S. (1993) *Physical Properties of Textile Fibres.* Textile Institute, Manchester.

Oudet, Ch. and Bunsell, A.R. (1987) Effects of structure on the tensile, creep and fatigue of polyester fibres. *J. Mater. Sci.*, 22: 4292–4298.

Schoppee, M.M. and Skelton, J. (1974) Bending limits of some high modulus fibers. *Textile Res. J.*, 44: 968–975.

CERAMIC FIBERS

Fiber Fracture
M. Elices and J. Llorca (Editors)

FRACTURE PROCESSES IN FINE SILICON CARBIDE FIBRES

A.R. Bunsell

Ecole des Mines de Paris, Centre des Matériaux, B.P. 87, Evry Cedex, France

Introduction 76
Spinning of a Polymer Precursor Fibre 76
Cross-Linking of the Precursor Fibre 77
Oxidation Curing 77
Radiation Curing 77
Pyrolysis 78
Near-Stoichiometric SiC Fibres 78
Fracture Morphologies of Successive Generations of SiC Fibres 78
Mechanical Properties and High-Temperature Behaviour 83
Conclusion 87
References 87

Abstract

Small diameter silicon-carbide-based fibres have been available since the beginning of the 1980s and their availability has driven the development of ceramic matrix composites for structural uses at very high temperatures. Several generations of these fibres have been produced and the changes in the fracture morphologies between the generations reveal the modifications which have been made to the fibres so as to improve their behaviour at high temperature. The fracture surfaces of the first generation fibres, as seen in the scanning electron microscope, indicated an amorphous microstructure, whereas those of the latest generation are clearly granular. More detailed analyses by transmission electron microscopy have revealed the increasingly crystalline nature of successive generations of these fibres. These changes have led to the production of fibres which have higher moduli and much improved creep behaviour.

Keywords

Silicon carbide; Fibres; Mechanical properties; Microstructure; Defects

INTRODUCTION

The fabrication of SiC fibres by melt spinning, the crosslinking and the pyrolysis of organosilicon polymers was first described by Yajima et al. (1975). The general principles of fabrication and the main variations existing in the industrialised processes are summarised in Fig. 1.

Spinning of a Polymer Precursor Fibre

The precursor polymer developed by Yajima to produce the first SiC-based fibres was a polycarbosilane (PCS) which can be simplified as $-[SiCH_3H-CH_2]_n-$. The average molecular weight was adjusted to be around 1500 (Yajima et al., 1978) to enable the polymer to be spun from the melt. The industrial application of this polymer for the fabrication of fibres allowed the fabrication in an industrial scale of the first Nicalon fibres in 1983 by Nippon Carbon. These fibres were the Nicalon 100 series which were superseded by the 200 series.

In 1981 Yajima et al., with the collaboration of Iwai and Yamamura from Ube Chemicals, described the synthesis of a polytitanocarbosilane (PTC) and its conversion into

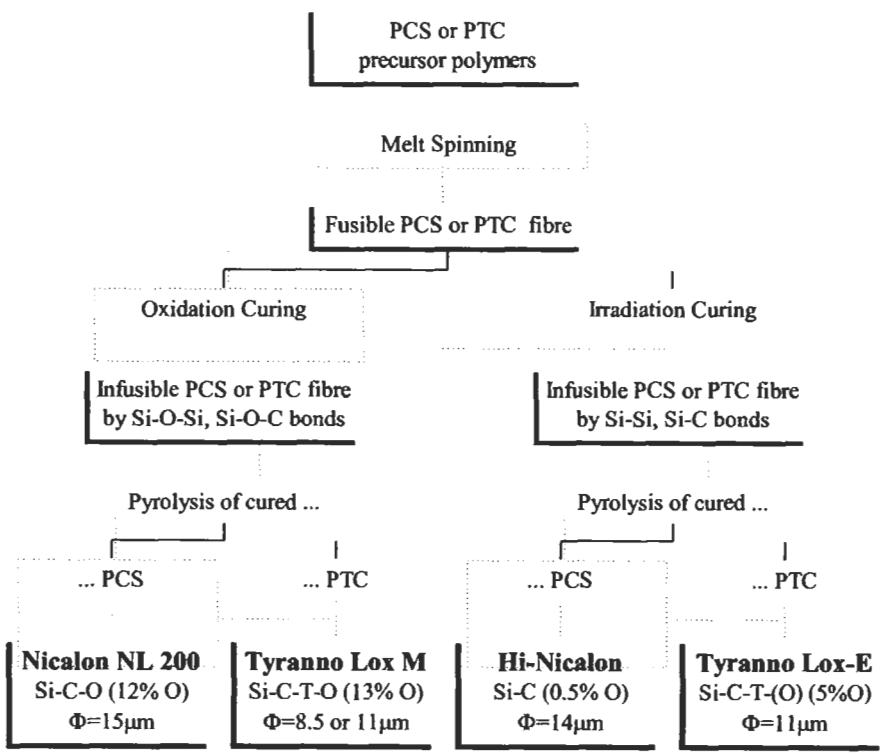

Fig. 1. Routes for producing fine SiC-based fibres from organo-silicon precursors

inorganic SiC based compounds (Yajima et al., 1981). This new precursor was obtained by the grafting of a titanium alkoxide $Ti(OR)_4R{=}C_nH_{2n+1}$ onto the PCS chains. This grafting linked the molecular chains together, increasing the molecular weight of the polymer and hence its spinnability. In 1987 Ube industries announced the development of the Tyranno fibres from this precursor and reported that they had better thermal and chemical stability compared to the then existing Nicalon fibres. The Tyranno fibres could be produced with a diameter half that of the diameters of the Nicalon fibres.

Cross-Linking of the Precursor Fibre

The conversion of PCS or PTC filaments into ceramic fibres is achieved by pyrolysis above 1000°C. Before this step the precursor fibre has to be cured to induce cross-linking between the molecular chains in order to avoid the softening of the fibre during this heating process and to maintain a fibrous form.

Oxidation Curing

The process of cross-linking employed for the first generation of SiC-based fibres was by oxidation in air at around 200°C, in which the Si–H and C–H bonds were oxidised and mainly Si–O–Si but also some Si–O–C bonds were created, linking the molecular chains. This is directly analogous to the manufacture of carbon fibres from polyacrylonitrile precursors which are cross-linked in air (Fitzer and Heine, 1988). The curing process, in both types of fibres, introduces oxygen in their molecular structures. In the case of carbon fibre manufacture, this oxygen is eliminated during pyrolysis. The oxygen in the precursor fibres used for the manufacture of the SiC-based fibres is not, however, totally eliminated during pyrolysis and its presence limits the chemical and mechanical stability of the fibres at high temperature (Simon and Bunsell, 1984). Oxidation curing has been employed for the fabrication of the different grades of the of NL series of Nicalon fibres, as well as the Tyranno A to G and Tyranno S, Tyranno LOX-M fibres and the near-stoichiometric Sylramic fibre produced by Dow Corning.

Radiation Curing

The need to reduce the oxygen content of the fibres led to the modification of the cross-linking process. Cross-linking of polymers can be induced by irradiation by high-energy elementary particles or electromagnetic radiation. The side groupings on the macro-molecules are cut by this technique which permits bonds between the macromolecules to be created without the introduction of oxygen into the polymer. The technique adopted by Nippon Carbon for the fabrication of the Hi-Nicalon in 1992 was the irradiation of PCS, in helium, by an electron beam of 2 MeV with a dose rate of 2–5 kGy/s up to a dose of 15 MGy (1 gray (Gy) = 1 joule/kg) (Takeda et al., 1991). Si–H and C–H bonds are broken and Si–Si or Si–C bonds are formed. The cross-linking step is followed by a heat treatment at 300°C for a short time in order to reduce the number of free radicals which are trapped in the irradiated PCS fibre. Simultaneously Ube Chemicals, using a similar curing technology, produced the Tyranno LOX-E fibre (Yamamura, 1993).

Pyrolysis

The cured PCS or PTC fibres are pyrolysed in a nitrogen or argon atmosphere. The pyrolysis of the Nicalon NL-200 fibres is stopped around 1200°C, the temperature at which their tensile strengths reach a maximum, whereas, for the same reason, the LOX-M is most probably pyrolysed at around 1300°C. It has been reported that the Hi-Nicalon is pyrolysed at 1500°C (Shibuya and Yamamura, 1996) and the LOX-E fibre at 1300°C. Modifications of the microstructures of all the fibres have been detected after post-heat treatments of 1 h at their pyrolysis temperatures. This indicates that the durations of the pyrolysis that the fibres experienced were too short to allow the microstructures to be entirely stabilised.

Near-Stoichiometric SiC Fibres

Nippon Carbon has obtained a near-stoichiometric fibre, the Hi-Nicalon Type S, from a PCS cured, in a hydrogen rich environment, by electron irradiation using a 'modified Hi-Nicalon process'. It is claimed that the excess carbon is reduced from C/Si = 1.39 for the Hi-Nicalon to 1.05 for the Hi-Nicalon Type S.

Dow Corning has produced near-stoichiometric SiC fibres from a PCS containing a small amount of titanium, similar to the route taken for most of the Tyranno fibres. The precursor fibres are cured by oxidation and doped with boron. In this way degradation of the oxicarbide phase at high temperature is controlled and catastrophic grain growth and associated porosity as occurred with the previous oxygen-rich fibres, is avoided. The precursor fibre can then be heated to around 1400°C so that the excess carbon and oxygen are lost as volatile species and then sintered at a higher temperature to yield a polycrystalline, near-stoichiometric, SiC fibre called SYLRAMIC fibre.

Ube Industries has announced the development of a near-stoichiometric fibre made from a polycarbosilane cross-linked by an aluminium compound. The precursor fibre is cured by oxidation, pyrolysed in two steps first to allow the outgassing of CO and then sintered at a temperature up to around 1800°C.

A comprehensive description of SiC fibre manufacture and behaviour is given by Bunsell and Berger (1999).

FRACTURE MORPHOLOGIES OF SUCCESSIVE GENERATIONS OF SIC FIBRES

All the SiC fibres are circular in cross-section with diameters of 15 μm or less. The earliest SiC fibres, the Nicalon 100 series, showed all the fracture characteristics of a glassy structure, although TEM studies showed the presence of very small SiC grains of less than 2 nm as well as even smaller free carbon particles. The Nicalon 200 series became the standard fibre used for most ceramic matrix composites. The fibre has a diameter of 15 μm and also shows a glassy fracture morphology, as Fig. 2 reveals.

This fracture morphology accurately reflects the microstructure of the fibre. Fig. 3 shows a dark field image of the NL 200 fibre.

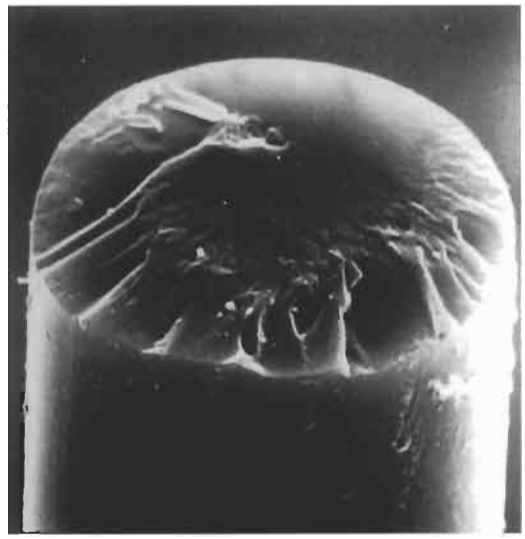

Fig. 2. Nicalon NL 200 room temperature fracture morphology.

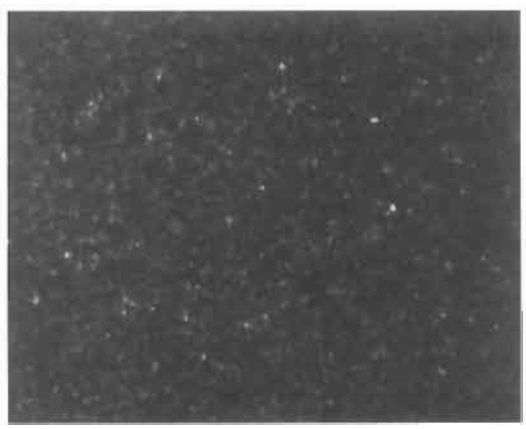

Fig. 3. Dark field image of a Nicalon NL 200 fibre. The white spots indicate SiC grains of approximately 2 nm in size.

The microstructure of the Nicalon NL 200 fibre is composed of 56 wt% β-SiC grains, of around 2 nm, 40% of an intergranular phase which has been calculated to give a mean composition of $SiO_{1.15}C_{0.85}$ and 5% of randomly oriented free carbon aggregates, less than 1 nm in diameter. C_{002} lattice fringes images showed small stacks of two fringes of 0.7 or 0.8 nm suggesting that for the basic structural units (BSUs) a face-to-face association of aromatic ring structures, called dicoronenes, the sizes of which are given as 0.74 nm and in which the hydrogen-to-carbon atomic ratio was 0.5. If a theoretical density is calculated from this composition, the fibre must contain 2% of porosity to fit with the measured density. Some authors consider that the composition of the

intergranular phase must be written as $SiO_xC_{1-x/2}$ instead of SiO_xC_{2-x} (Le Coustumer et al., 1993). This expression permits the composition to vary continuously from SiC to SiO_2 by increasing the percentage of oxygen. The fibre is composed by weight of 56% SiC, 10% C and 34% $SiO_{1.12}C_{0.44}$.

Porosity in the NL 200 as in other polymer-derived fibres has never been imaged in transmission electron microscopy but was theoretically assessed before it was shown experimentally by X-ray scattering techniques. Outgassing of hundreds of volumes of gas formed per volume of fibre has to take place during pyrolysis for the progressive transformation from an organic to a mineral structure to occur. Diffusion through a solid phase would be too slow to allow all this gas to escape during the pyrolysis. Nanochannels must be present at this stage of transformation which then undergo viscous collapse on further heating above the gas evolution temperature. A porosity of 6.2% has been measured by X-ray scattering with the Nicalon NL 100 fibre pyrolysed at 1400°C.

The Tyranno LOX-M fibre has a diameter of 8 μm and contains approximately 13 wt% of oxygen as the use of M, which is the thirteenth letter in the alphabet, indicates. The structure has been described as being composed of β-SiC grains of 2 nm and small aggregates of free carbon of less than 2 nm. Although these fibres are known to contain titanium, no titanium compounds are found in the fibre. It is assumed that the titanium is incorporated into a Si–O–Ti–C amorphous continuum. The density of the fibre is less than that of the Nicalon NL 200 although their compositions and grain sizes are very close indicating a greater amount of porosity.

The Hi-Nicalon represents a departure in the original manufacturing process as cross-linking takes place by electron irradiation. The result is a large reduction in oxygen, to about 0.5 wt%, in the fibre and as a consequence the elimination of the amorphous intergranular phase. Transmission electron microscopy reveals that the fibre contains larger SiC grains of around 5 nm for the majority of the grains but the biggest crystallites can reach 20 nm (Berger et al., 1995). This does not lead to any marked difference in the fracture morphology of the as received Hi-Nicalon fibre as seen in the SEM. Fig. 4 shows that a large fraction of the Si and C atoms is not entirely crystallised in the form of β-SiC and the atoms are present between the β-SiC grains in a less dense arrangement. Free carbon is found with a more organised structure than in the NLM-202 fibre, composed of 4 to 10 distorted layers with an interfringe distance of around 0.36 nm over a length of 2 nm on average with some aggregates measuring up 5 nm.

By analogy with the structure of the NL 200 the small amount of oxygen in the fibre is presumed to be present at the SiC/SiC boundaries. It is supposed that oxygen substitutes for one carbon atom to form SiC_3O tetrahedra.

The structure of the Hi-Nicalon fibre can be represented as being composed of about 59% of β-SiC by weight, 11% of free carbon and the 26% of non-crystallised Si–C combined with the 4% of Si–C–O phase described above, giving 30% of an intergranular phase composed in majority of SiC with some substitution of carbon by oxygen. As with the NL 200 fibre the Hi-Nicalon contains a small amount of nanometric porosity.

The Tyranno LOX-E fibre was produced by Ube Industries by the electron radiation method adopted by Nippon Carbon for the Hi-Nicalon fibre. However, the introduction

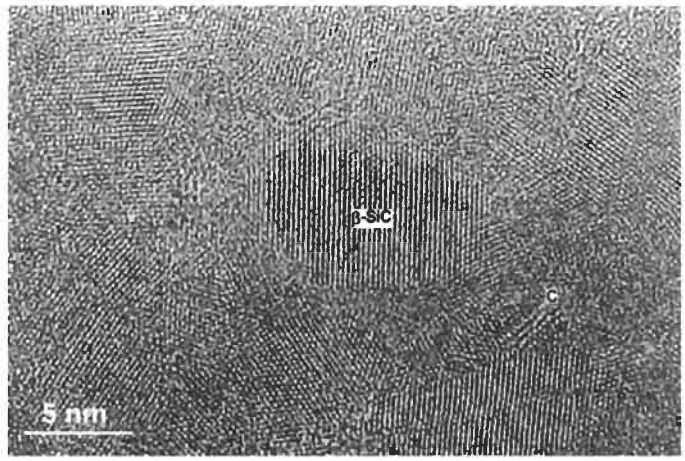

Fig. 4. The micro-structure of the Hi-Nicalon fibre is composed of SiC grains of 5 nm average size and free carbon.

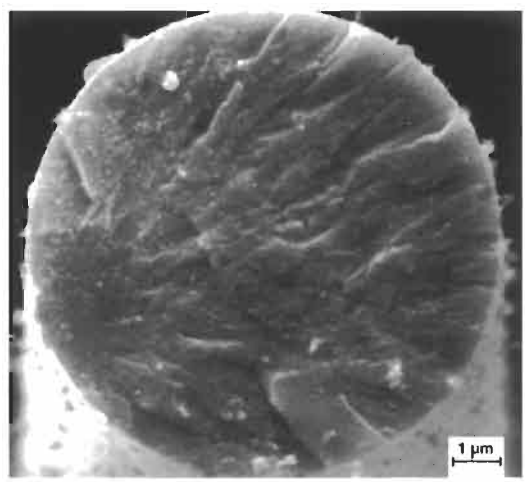

Fig. 5. Room temperature fracture morphology of Tyranno Lox-E.

of titanium in the PTC precursor fibre was made possible by the use of titanium alkoxide which also introduced oxygen into the fibre before the cross-linking process. The microstructure of the Tyranno LOX-E fibre is comparable to that observed with the oxygen cross-linked fibres. The SiC grains have a mean size of around 2 nm, although some larger grains of up to 5 nm have been found. The free carbon aggregates are composed of 2 to 5 turbostratic layers with a length of around 1 to 3 nm. No crystallised Ti compounds are revealed, and the grains must be separated by a Si–C–Ti–O phase. Fig. 5 shows the fracture morphology of a Tyranno LOX-E fibre broken at room temperature.

The latest generation of fibres which are described as being near-stoichiometric shows a marked change in fracture morphology when compared to earlier generations.

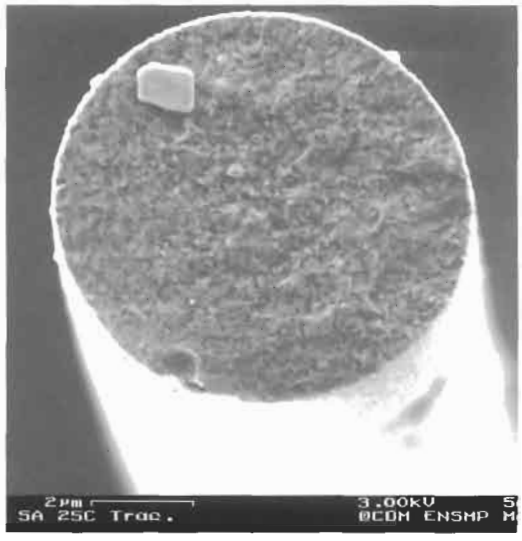

Fig. 6. Fracture morphology of the Tyranno SA fibre broken in tension at room temperature.

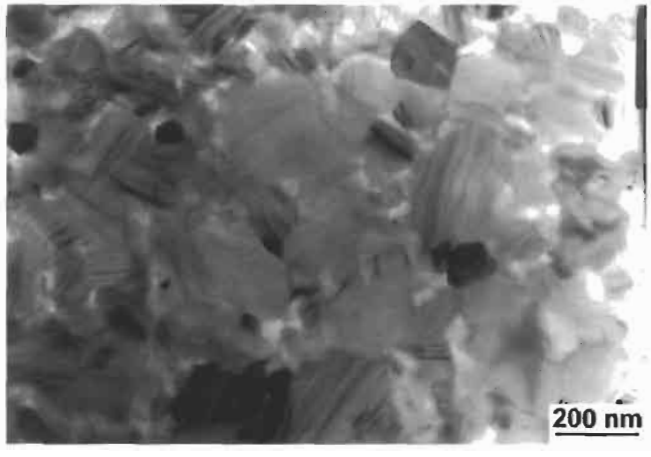

Fig. 7. Microstructure of the Tyranno SA fibre.

Fig. 6 shows the fracture morphology of a Tyranno SA fibre. The fibre has a diameter of 10 μm. The fracture surface can be seen to be markedly granular in sharp contrast to the earlier fibres.

An examination of the microstructure by TEM reveals that the SiC grains in the Tyranno SA fibre are around 200 nm in size, as is shown in Fig. 7. Despite the claim of near-stoichiometry there is considerable free carbon in the fibre and its concentration increases near the centre of the fibre indicating incomplete removal during sintering.

The Sylramic fibre produced by Dow Corning uses a PCT precursor which is doped with boron to aid sintering and to control grain growth during heating to around 1600°C. The fibre has a diameter of 10 μm and SiC grain sizes ranging from 0.1 to 0.5 μm

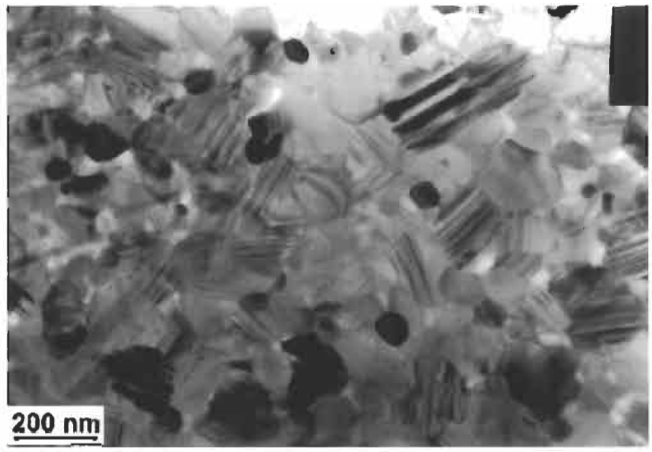

Fig. 8. The microstructure of the as received Sylramic fibre.

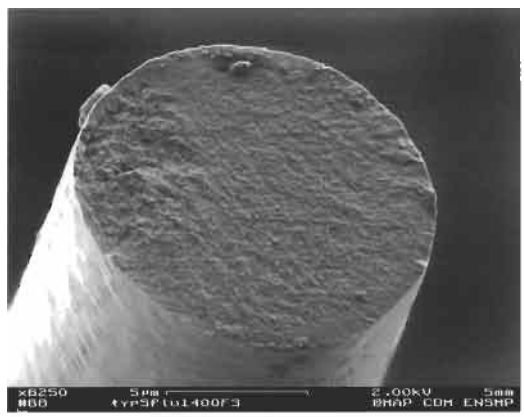

Fig. 9. Fracture morphology of the Hi-Nicalon Type S fibre after a creep test at 1400°C.

with smaller grains of TiB_2 at triple points as seen in Fig. 8. A carbon- and oxygen-rich surface and a BN-like component in the near surface region have been identified.

The Hi-Nicalon Type S, near-stoichiometric fibre from Nippon Carbon shows the greatest stability of the three fibres and Fig. 9 reveals its fracture morphology at 1400°C, which is unchanged in appearance to that obtained at room temperature. The fracture surface is noticeably less granular in appearance than the other two near-stoichiometric fibres, which is due to a smaller average grain size of around 50 nm.

MECHANICAL PROPERTIES AND HIGH-TEMPERATURE BEHAVIOUR

The Young moduli of the Nicalon NL 200 fibre series are 190 GPa and slightly less for the Tyranno LOX-M fibre. These values are increased for the electron irradiated

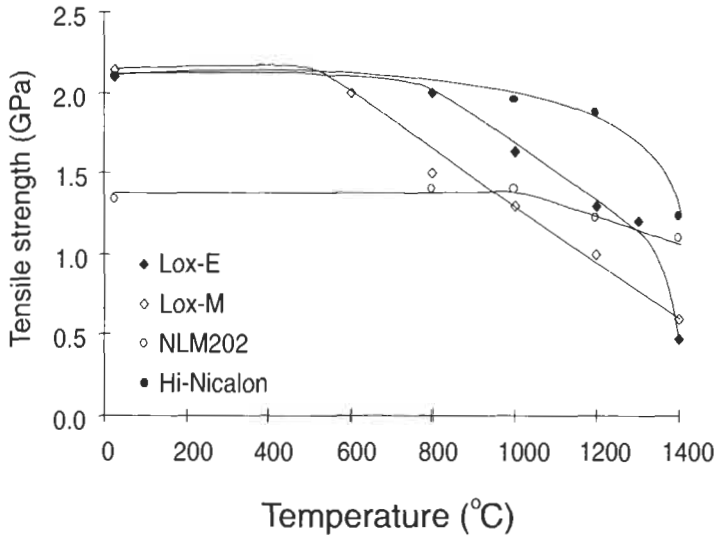

Fig. 10. Strength as a function of temperature in air revealing the greater resistance of the Hi-Nicalon fibre compared to other fibres which contain oxygen-rich intergranular phases.

fibres so that the Tyranno LOX-E fibre has a Young modulus of 199 GPa and the Hi-Nicalon a value of 263 GPa. The strengths of these fibres are shown in Fig. 10 as a function of temperature. It can be seen that the Hi-Nicalon fibres maintained their strengths up to 1200°C in air whilst the other fibres which contained more oxygen and hence a greater amount of intergranular amorphous phase lost strength at lower temperatures (Berger et al., 1997).

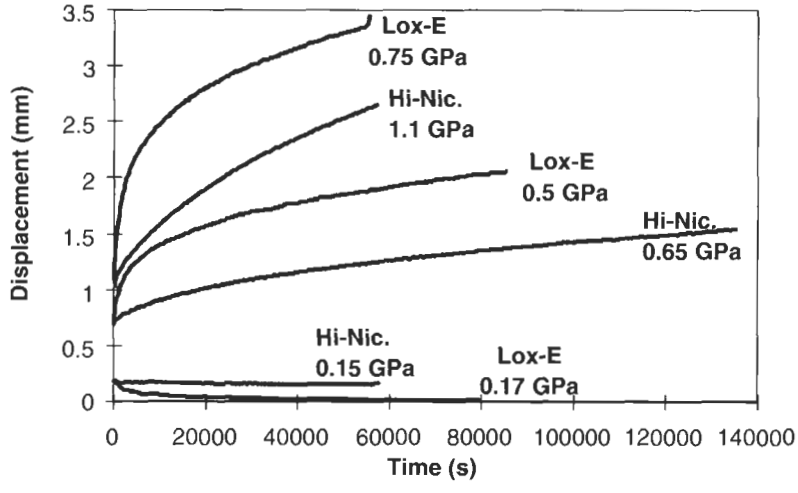

Fig. 11. The Hi-Nicalon fibre shows lower creep rates than does the Tyranno LOX-E fibre because of the absence of an oxygen-rich intergranular phase.

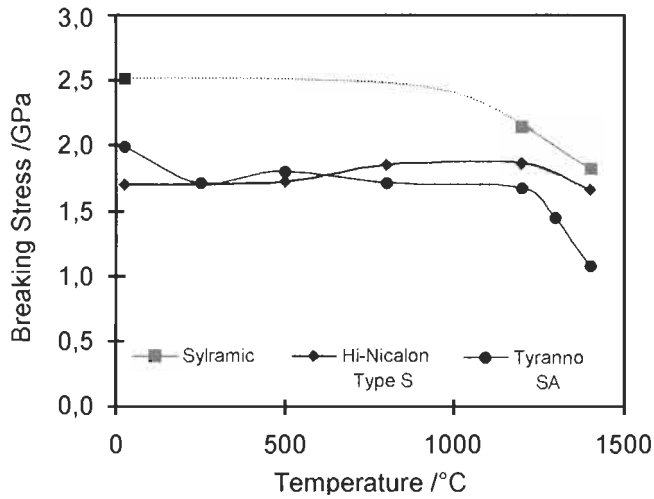

Fig. 12. The strength retention of the near-stoichiometric fibres is superior to that of earlier generations.

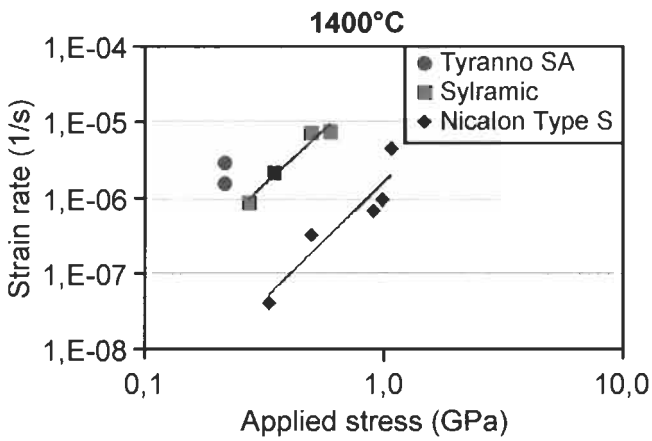

Fig. 13. The creep rates of the Nicalon Type S fibres are lower than the other near-stoichiometric fibres which contain sintering aids.

A comparison of the creep behaviour between the Tyranno LOX-E fibre which contains 5 wt% of oxygen and the Hi-Nicalon fibre which contains 0.5 wt% of oxygen shows the lower creep rates at high temperatures of the latter fibre, as can be seen in Fig. 11.

The Young moduli of the near-stoichiometric fibres are 375 GPa for the Hi-Nicalon Type S, 330 GPa for the Tyranno SA and 390 GPa for the Sylramic fibre. Fig. 12 shows that they retain their strengths to higher temperatures than the earlier generations of fibres. The Hi-Nicalon Type S fibre shows little or no loss of strength even at 1400°C.

As can be seen from Fig. 13 the creep rate of the Hi-Nicalon Type S fibre is one order of magnitude lower than that of the other two near-stoichiometric fibres because of the lack of sintering aids which facilitate creep at high temperatures. Growth of a

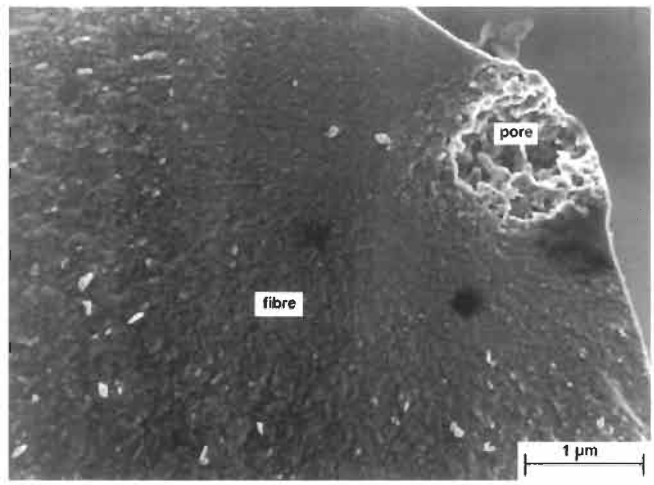

Fig. 14. Local inhomogeneities can lead to degradation at the surface of the fibres when heated above 1200°C in air, as in this Hi-Nicalon fibre.

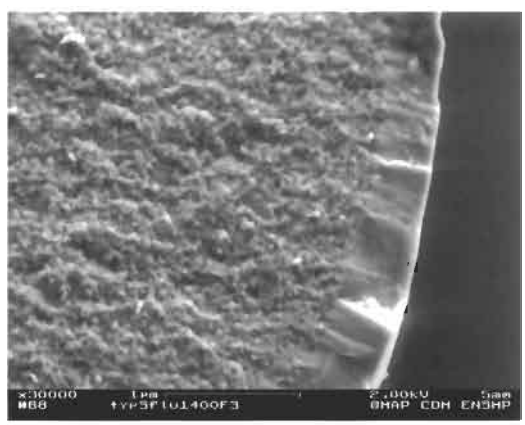

Fig. 15. The surface of a Hi-Nicalon Type S fibre showing the layer of silica which has formed during creep at 1400°C.

silica layer is observed on the surface of the fibres when they are heated from 1200°C in air. This layer can have an irregular thickness along the fibre and pores are formed at the silica/SiC fibres interface in the first generation fibres due to outgassing of oxides of carbon. Pores of several hundreds of nanometres can be formed at 1450°C. Failure surfaces remain brittle in the range of temperatures used, but new types of defects are detected compared to those found at room temperature. Local chemical inhomogeneity at the fibre surface such as carbon-rich zones are preferentially decomposed or oxidised at high temperatures, giving rise to porous weak structures as shown in Fig. 14.

Fig. 15 shows the silica layer formed at the surface of a Hi-Nicalon Type S fibre after creep at 1400°C

CONCLUSION

The fracture morphologies of the fine silicon carbide fibres made from polymer precursors reveal the nature of their microstructures of the fibres. Successive generations of fibres have been created with reduced oxygen contents so producing better controlled microstructures and eliminating the presence of amorphous intergranular phases which limit mechanical behaviour at high temperatures. As a consequence the SiC grains have become larger and the Young moduli have increased. Whereas the earliest SiC fibres had Young moduli of around 200 GPa and showed glassy fracture morphologies because of their nanometric grain structure, the latest, near-stoichiometric fibres have moduli of up to 400 Gpa and fail with a granular fracture morphology reflecting the large SiC grains of their structures.

REFERENCES

Berger, M.H., Hochet, N. and Bunsell, A.R. (1995) *J. Microsc.*, 177: 230–241.
Berger, M.H., Hochet, N. and Bunsell, A.R. (1997) *J. Microsc.*, 185: 243–258.
Bunsell, A.R. and Berger, M.H. (1999) *Fine Ceramic Fibres*. Marcel Dekker, New York, NY.
Fitzer, E. and Heine, M. (1988) In: *Fibre Reinforcements for Composite Materials*, pp. 73–148, A.R. Bunsell (Ed.). Elsevier, Amsterdam.
Le Coustumer, P., Monthioux, M. and Oberlin, A. (1993) *J. Eur. Ceram. Soc.*, 11: 95–103.
Shibuya, M. and Yamamura, T. (1996) *J. Mater. Sci.*, 31: 3231–3235.
Simon, G. and Bunsell, A.R. (1984) *J. Mater. Sci.*, 19: 3658–3670.
Takeda, M., Imai, Y., Ichikawa, H. and Ishikawa, T. (1991) *Ceram. Eng. Sci. Proc.*, 12: 1007–1018.
Yajima, S., Hayashi, J. and Omori, M. (1975) *Chem. Lett.*, 9: 931–934.
Yajima, S., Hasegawa, Y., Hayashi, J. and Iimura, M. (1978) *J. Mater. Sci.*, 13: 2569–2576.
Yajima, S., Iwai, T., Yamamura, T., Okamura, K. and Hasegawa, Y. (1981) *J. Mater. Sci.*, 16: 1349–1355.
Yamamura, T. (1993) In: *Proceedings of the Euro–Japanese Colloquium on Ceramic Fibres, ECCM 6, Bordeaux*, pp. 187–201.

Fiber Fracture
M. Elices and J. Llorca (Editors)

FRACTURE PROCESSES IN OXIDE CERAMIC FIBRES

Marie-Hélène Berger

Ecole des Mines de Paris, Centre des Matériaux, B.P. 87, 91003 Evry Cedex, France

Introduction 91
Fabrication of Alumina Fibres 91
Transitional Alumina Fibres 91
α-Alumina Fibres 94
Single Phase α-Alumina Fibres 94
α-Alumina/Zirconia Fibres 99
α-Alumina/Mullite Fibres 101
Other Oxide Fibres 102
Conclusion 103
References 104

Abstract

Fine oxide ceramic fibres are mainly based on alumina in one of its forms, often combined with silica or other phases such as zirconia or mullite. All such fibres are brittle and linearly elastic at room temperature and failure is most usually initiated by process flaws and surface defects and less by the fibre microstructure. Fibres containing a few percent of amorphous silica exhibit fracture morphologies which resemble those of glass fibres because they enclose transition alumina grains of the order of only 10 nm. Fracture morphologies of pure α-alumina fibres are typical of granular structures made of grains of 0.5 μm. Crack propagation is both inter- and intra-granular at room temperature and evolves toward an intergranular mode above 1000°C. Failure in creep is caused by damage accumulation throughout the fibre. The coalescence of intergranular microcracks leads to a non-planar intergranular fracture. Creep resistance of α-alumina fibres can be improved by the inclusion of a second phase such as zirconia or mullite, the latter giving the lowest creep rates. Failure at high temperatures can however be

dominated by the presence of alkaline contaminants inducing the formation of a low melting point silicate phase and the rapid growth of large alumina grains.

Keywords

Ceramic; Oxide; Alumina; Silica; Zirconia; Mullite; High temperature; Tension; Creep

INTRODUCTION

If high performance fibres are to be exposed to oxidative atmospheres and temperatures above 1200°C, they will have to be made from oxides with high melting points. α-alumina is widely used for its refractory properties. Its complex crystal structure provides large Burgers vectors so that high stresses are necessary to generate plasticity in monocrystals. Monocrystalline α-alumina fibres showing no creep up to 1600°C can be obtained if the fibre axis strictly corresponds to the [0001] axis (Gooch and Groves, 1973). However, no viable processes exist at present to produce fine and flexible continuous monocrystalline fibres. Therefore only polycrystalline fibres can be considered for the reinforcement of ceramics. Various processing routes exist for making such fibres and these lead to a large range of microstructures and fracture behaviours (Berger et al., 1999).

FABRICATION OF ALUMINA FIBRES

Precursors of alumina are viscous aqueous solutions of basic aluminium salts, $AlX_n(OH)_{3-n}$, where X can be an inorganic ligand (Cl^-, NO^{3-}...) or an organic ligand ($HCOOH^-$...) (Taylor, 1999). Spinning of the precursor produces a gel fibre which is then dried and heat-treated. Decomposition of the precursor induces the precipitation of aluminium hydroxides, such as boehmite AlO(OH), and the outgassing of a large volume of residual compounds. The associated volume change and porosity at this step has to be carefully controlled. It is also possible to directly spin aqueous sols based on aluminium hydroxides. Dehydration between 300°C and 400°C yields amorphous aluminas and leaves nanometric pores in its structure. Further heating to around 1100°C induces the sequential development of transitional forms of alumina. These aluminas have spinnel structures containing aluminium vacancies on the octahedral and tetrahedral sites. They only differ by the degree of order in the distribution of these vacancies. At this stage the fibre is composed of alumina grains of a few tens of nanometres, poorly sintered with a finely divided porosity. Above 1100°C stable α-alumina nucleates and a rapid growth of μm-sized grains occurs together with coalescence of pores. Porosity generated during the first steps of the formation of metastable aluminas cannot be eliminated and is increased by the higher density of α-alumina compared to the transitional forms. The fibres become extremely brittle due the presence of large grains. Fracture initiated from large grain boundaries emerging at the fibre surface and crack propagation is mainly intergranular. Alumina fibres cannot be used in this form and the nucleation and growth of α-alumina have to be controlled by adding either silica precursors or seeds for α-alumina formation to the fibre precursors. This has led to two classes of alumina-based fibres with different fracture behaviours which are transitional alumina fibres and α-alumina fibres.

TRANSITIONAL ALUMINA FIBRES

Alumina–silica fibres were the first ceramic fibres produced in the early 1970s, for thermal insulation applications. Small amounts of silica, ≈3 wt% in the Saffil short

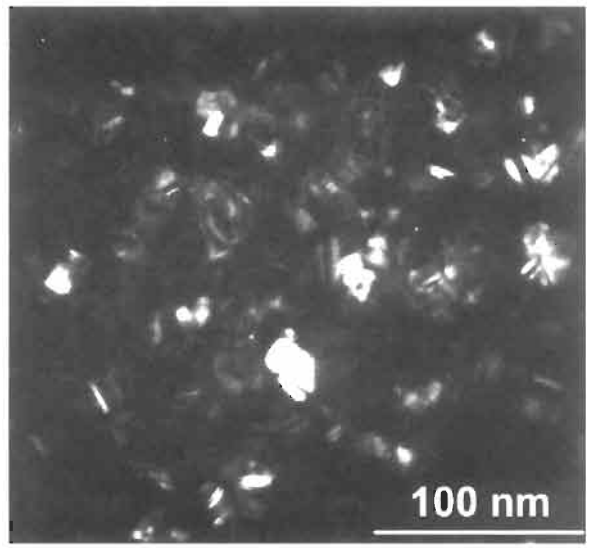

Fig. 1. TEM dark field image of the as received Altex fibre composed of γ-alumina grains of about 20 nm in an amorphous silicate intergranular phase.

fibres from ICI (Birchall, 1983), 15 wt% in the Altex fibre from Sumitomo (Abe et al., 1982) allow the sintering of the transitional forms of alumina of less than 50 nm, as shown in Fig. 1, in a silicate intergranular phase and produce above 1100°C the crystallisation of mullite grains, as illustrated in Fig. 2, with a composition ranging between $2Al_2O_3 \cdot SiO_2$ and $3Al_2O_3 \cdot 2SiO_2$. This delays the nucleation of α-alumina to 1300°C, the growth of which is then restricted by the presence of the mullite intergranular phase.

The α-alumina formation can be totally suppressed if enough silica is added to consume the metastable alumina by mullite formation. 3M produces the Nextel series of fibres having the composition of mullite. Boria addition lowers the temperature of mullite formation, helps sintering and increases the fibre strength. Various degrees of crystallinity can be obtained according to the amount of boria and the pyrolysis temperature. Nextel 312 with 14% B_2O_3 is a quasi amorphous fibre (Johnson, 1981), the high-temperature properties of which are limited by the volatilisation of boron compounds from 1100°C. Nextel 440 contains 2% B_2O_3 and is composed of γ-alumina in amorphous silica. The same fibre composition, heated above the mullitisation temperature yields fully dense crystallised mullite with 50 to 100 nm grain sizes (Johnson et al., 1987). However, the good high-temperature creep resistance which could be expected from the complex mullite structure is not obtained due to the presence of an amorphous boro-silicate intergranular phase.

The effect of silica on the room-temperature properties of alumina fibres is to reduce their overall stiffness ($E_{SiO_2} \approx 70$ GPa, $E_{Al_2O_3} \approx 400$ GPa) as can be seen in Fig. 3, and to increase their room-temperature strength by avoiding the formation of large grains (Fig. 4). This results in flexible fibres which can be used in the form of bricks or woven cloths for thermal insulation. All these fibres have an external appearance similar to that of glass fibres and their fracture is brittle and most often initiated from

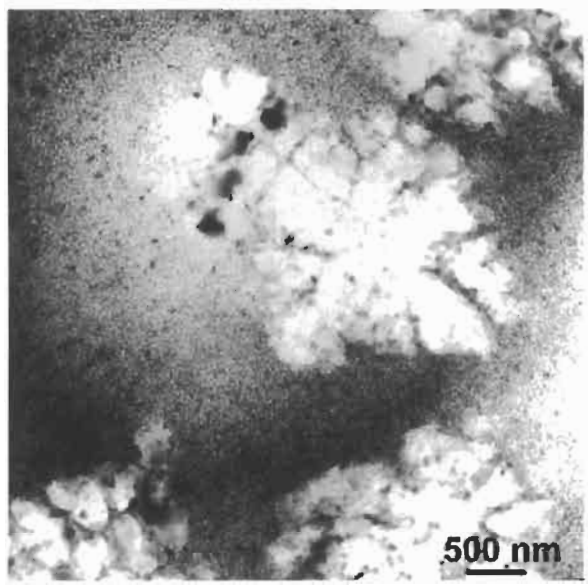

Fig. 2. TEM bright field image of the Altex fibre after a heat treatment at 1130°C. Growth of mullite grains surrounded by smaller grains of transitional forms of alumina.

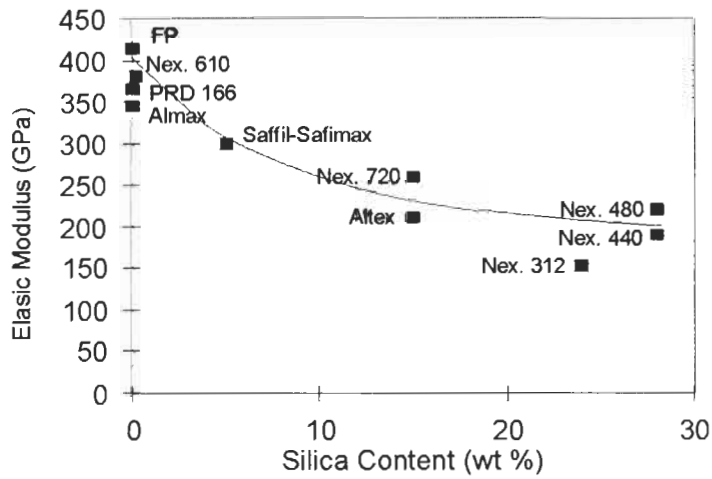

Fig. 3. Evolution of elastic moduli of alumina-based fibres as a function of the silica content.

surface defects, as illustrated by Fig. 5, generated during the fabrication process or fibre handling. Strength loss at high temperature occurs from 1000°C. Above 1200°C the growth of mullite grains and large α-alumina grains renders the fibres extremely weaker. Moreover, the presence of an amorphous silicate intergranular phase enhances creep which begins from 900°C so that these fibres cannot be used for structural applications above this temperature.

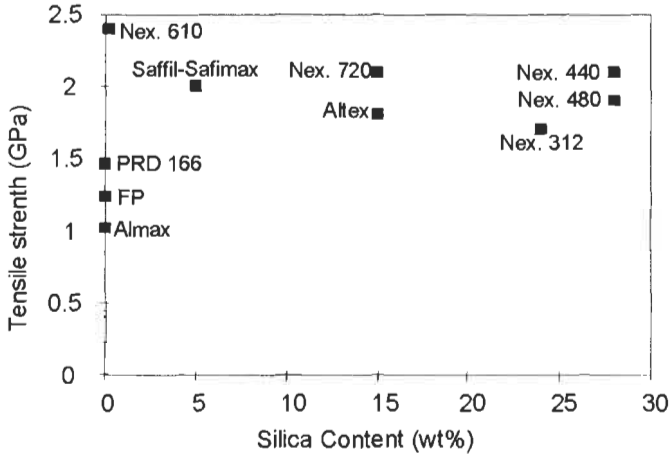

Fig. 4. Evolution of the room temperature tensile strength as a function of the silica content. The lower strengths of pure alumina FP and Almax fibres are induced by their larger grain sizes of 0.5 μm, in contrast to Nextel 610 and silica-containing alumina fibres.

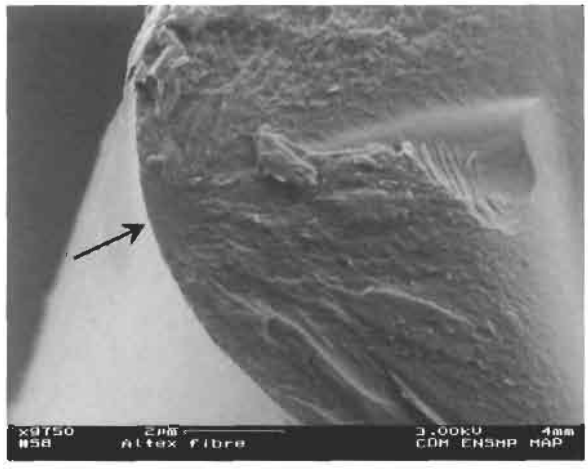

Fig. 5. Typical room temperature fracture morphology of an alumina fibre containing silica addition. Fracture has been initiated from a surface flaw, which can not be identified by SEM, located at the centre of a mirror zone.

α-ALUMINA FIBRES

Single Phase α-Alumina Fibres

To increase the creep resistance alumina fibres, intergranular silicate phases have to be reduced drastically. This imposes processes other than the addition of silica to control α-alumina growth. A pure α-alumina fibre was first produced by Du Pont in 1979 (Dhingra, 1980). 'Fiber FP' was obtained by the addition, to an alumina precursor,

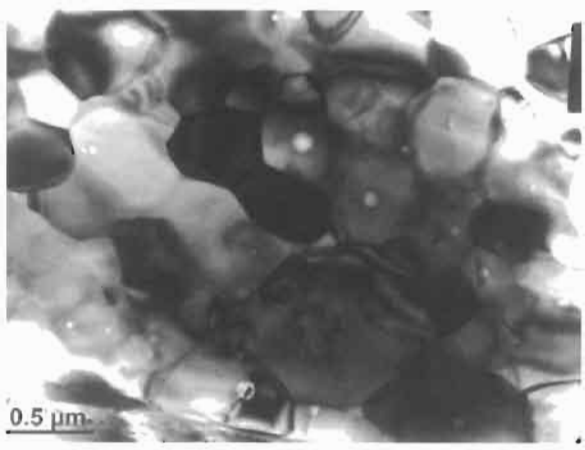

Fig. 6. TEM image of Fiber FP revealing a dense microstructure of α-alumina grains of 0.5 μm.

of more than 40 wt% of α-alumina powder having a grain size of less than 0.5 μm. The use of a lower fraction of precursor reduces the porosity due to its decomposition and to the dehydration of hydrous aluminas.

α-Alumina particles act as seeds for the growth of α-alumina and so remove the problems associated with the delay of nucleation and rapid grain growth. In the case of Fiber FP the grain size of the powder included in the precursor precluded the spinning of fine filaments. The FP fibre had a diameter of 20 μm, this, added to the intrinsic high stiffness of α-alumina ($E_{FP} = 410$ GPa) and low strength (1.5 GPa at 25 mm) due to its large grain size of 0.5 μm as shown in Fig. 6, made the fibre unsuitable for weaving. Flexible α-alumina fibres require diameters of around 10 μm. This was first achieved by Mitsui Mining by reducing the size of the α-alumina powder. In this way the number of seeding sites could be maintained to a sufficient fraction of the volume with a smaller amount of powder. However, this affected the control of porosity and the resulting Almax fibre (Saitow et al., 1992) encloses a significant amount of pores inside alumina grains which are of 0.5 μm in size (Fig. 7) (Lavaste et al., 1995). Later, 3M produced the Nextel 610 fibre (Wilson et al., 1993) which is a fully dense α-alumina fibre of 10 μm in diameter, with a grain size of 0.1 μm as seen in Fig. 8, and possesses the highest strength of the three α-alumina fibres described (2.4 GPa at gauge length of 51 mm). This is achieved by the use of a ferric nitrate solution which produces 0.4 to 0.7 wt% of very fine seeds of α-Fe_2O_3, isomorphous to α-Al_2O_3. The ratio of nuclei sites per volume is notably increased by this route and the addition of 0.2% of SiO_2 helps to produce a dense sintered microstructure at 1300°C.

The observation of the room-temperature fracture morphologies of Fiber FP (Fig. 9) and Almax fibre (Fig. 10) reveals more granular structures compared to the previous alumina–silica fibres. For these pure α-alumina fibres the defect initiating the failure cannot be seen. It is supposed that some larger and weaker grain boundaries reaching the surface are responsible for crack initiation. Crack propagation was mixed inter- and intra-granular for the FP fibre, whereas the presence of intragranular porosity weakened the grains in the Almax fibre leading to a more marked intragranular crack propagation mode.

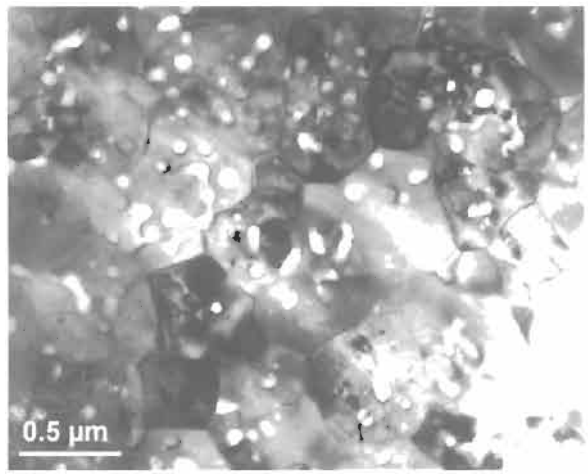

Fig. 7. TEM image of Almax fibre. Numerous intragranular pores can be seen.

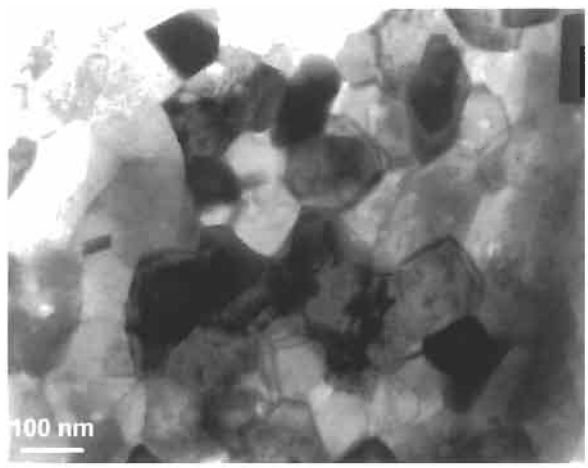

Fig. 8. Nextel 610 fibre is a dense α-alumina fibre with a grain size of 100 nm.

In the Nextel 610 fibre, the grains are smaller than the critical defect size and failure is initiated from extrinsic defects such as pores or surface process flaws. The control of the sizes of such defects leads to higher room-temperature strengths when compared to Fiber FP and Almax fibre and distinct room-temperature fracture morphologies are also obtained. As can be seen from Fig. 11 the failure surface shows two zones. Crack propagation was at first stable and intragranular creating a first mirror zone which fanned out symmetrically from the defect initiating the failure. In this fibre, failure was induced by a pore with sharp edges, located at the near surface. The second zone of the fracture surface corresponds to a mixed failure mode and was created during catastrophic rapid final failure.

The high-temperature behaviours of these three fibres are controlled by their mi-

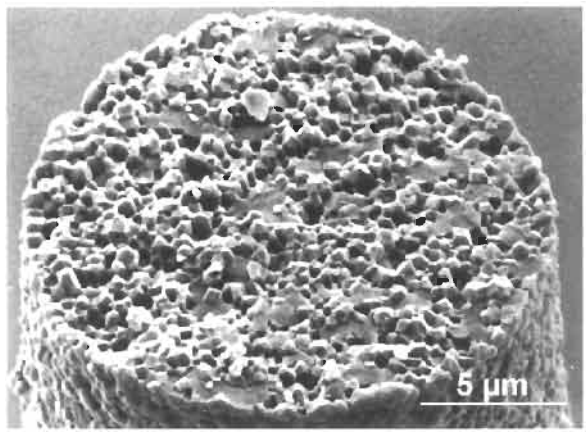

Fig. 9. Fracture morphology of Fiber FP broken in tension at room temperature. The crack propagation is both inter- and intra-granular.

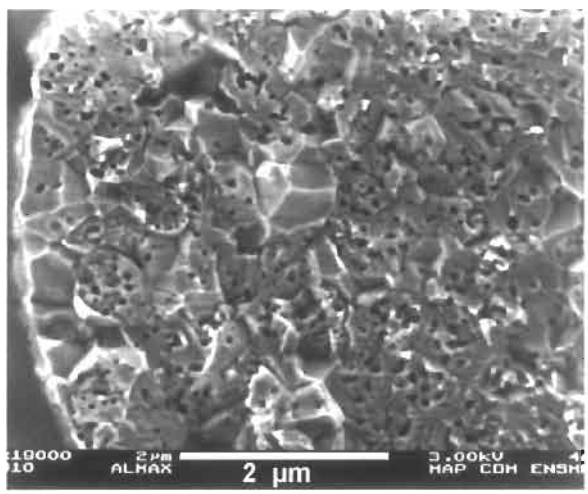

Fig. 10. Detail of a failure surface of Almax fibre broken in tension at room temperature. Pores inside the grains induce an intragranular fracture mode.

crostructures which are made of fine isotropic grains. Plasticity occurs from 1000°C and superplastic behaviour can be obtained at 1300°C with the FP fibre (Pysher and Tressler, 1992; Lavaste et al., 1995). No intragranular plasticity can develop in these fibres as the small distances between two grain boundaries, perpendicularly to the load axis, prevent the formation of dislocation sources and pin dislocation movement. However, the large ratio of boundary surfaces allows deformation by grain boundary sliding. This mechanism involves movement of intergranular dislocations and is accommodated by interfacial controlled diffusion mechanisms. Amongst the three fibres, the lowest deformation rates are obtained with the FP fibre ($\sim 10^{-3}$ s^{-1} at 1300°C). Diffusion and deformation are facilitated by porosity in the Almax and by grain size in the Nextel 610,

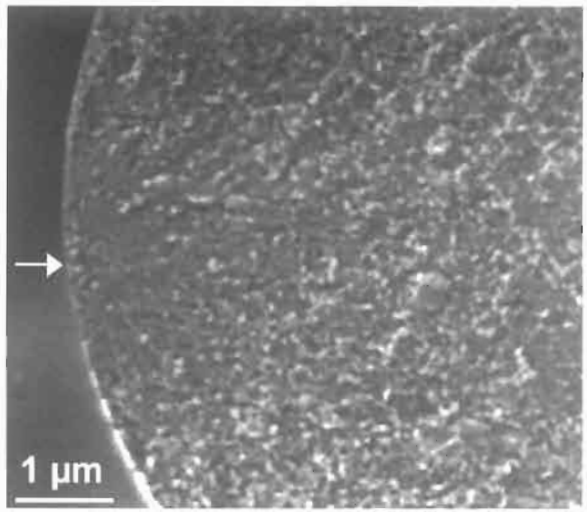

Fig. 11. Detail of a failure surface of Nextel 610 fibre broken in tension at room temperature. The arrow indicates the crack initiation defect surrounded by a mirror zone.

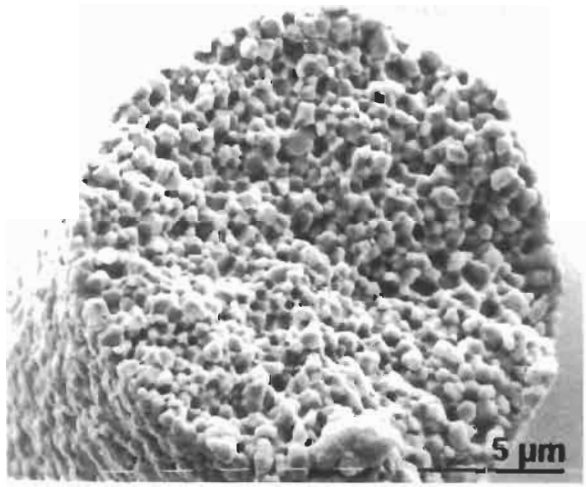

Fig. 12. Typical tensile fracture morphology of a pure alumina fibre at high temperature (Fiber FP at 1300°C). Fracture occurs by the coalescence of microcracks leading to a non-flat fracture surface.

which is five times smaller than in the other two fibres. Damage occurs by the growth of cavities at triple points and the coalescence of intergranular microcracks (Fig. 12) induces a non-flat failure (Fig. 13). The times to failure in creep are considerably reduced in the Almax fibre by the build-up of large intergranular pores.

These three fibres are stiff and chemically stable. They can therefore be used to reinforce matrices, such as light alloys, working in intermediate temperature ranges, or for applications at higher temperatures, but for which no load bearing capacity is

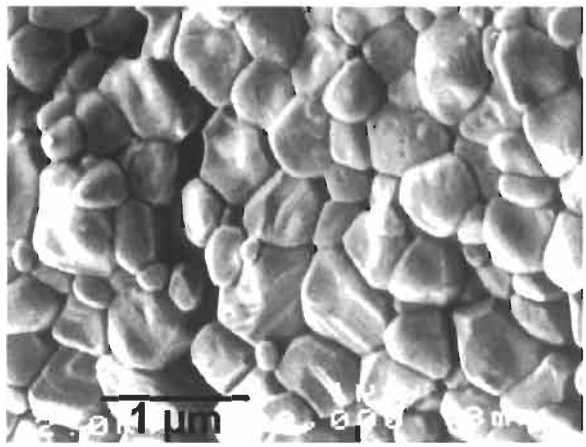

Fig. 13. External surface of the FP fibre broken at 1300°C exhibiting grain boundary decohesions and intergranular microcracks.

required, as in thermal insulation. They were not developed to work in the conditions for which their poor creep resistances have been demonstrated. However, the creep mechanisms which have been revealed have allowed the microstructure which would improve the high-temperature behaviour of α-alumina-based fibres to be better defined. These fibres must have fine grains, as large grains are detrimental for the fibre strength, but grain sliding has to be inhibited. Inclusions of second phases and fine but elongated oriented grains have been considered as possible solutions to achieve these goals.

α-Alumina/Zirconia Fibres

The dispersion of small particles of tetragonal zirconia between α-alumina grains was first employed by Du Pont with the aim of producing a modified FP fibre with improved flexibility. This fibre, called PRD-166 (Romine, 1987), was obtained by the addition of zirconium acetate and yttrium chloride to the blend of the alumina precursor and α-alumina powder. The fibre had a diameter of 20 µm and contained 20 wt% of yttrium-stabilised tetragonal zirconia in the form of grains of 0.1 µm as can be seen in Fig. 14, which restricted the growth of α-alumina grains to 0.3 µm, on average (Lavaste et al., 1995). Young's modulus was lowered to 370 GPa because of the lower stiffness of zirconia ($E_{ZrO_2} \approx 200$ GPa). Tetragonal to monoclinic transformation of zirconia around the crack tip at room temperature (Fig. 15) toughened the fibre and a higher strength was obtained (1.8 GPa at 25 mm). However, this was not sufficient to ensure flexibility and the production did not progress beyond the pilot stage.

The effect of the addition of zirconia on the high-temperature mechanical behaviour is to delay the onset of plasticity to 1100°C and to decrease the strain rates in creep (Pysher and Tressler, 1992; Lavaste et al., 1995). The mechanisms proposed have been the pinning of the grain boundaries by the intergranular zirconia particles and more recently the modification of the Al^{3+} diffusion rates at the alumina/alumina grain boundaries by the presence of Zr^{4+} and Y^{3+} ions. However, these mechanisms are less

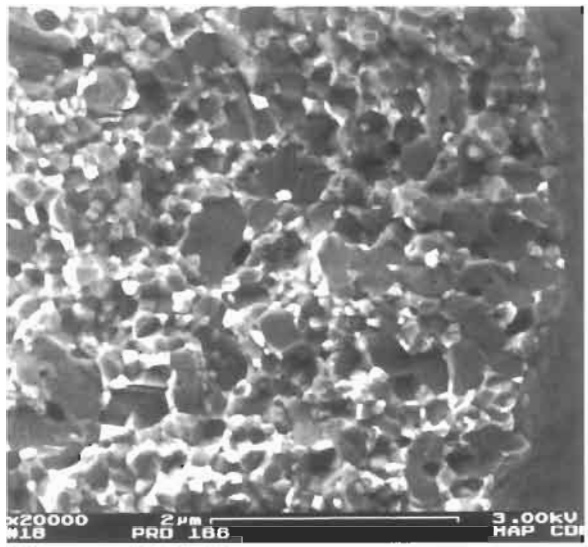

Fig. 14. Detail of a fracture surface of the PRD 166 fibre composed of alumina, in dark and zirconia, in bright.

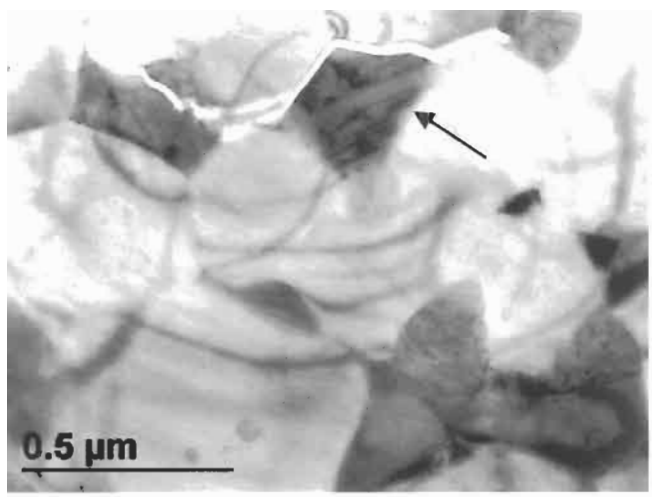

Fig. 15. Crack propagation in a zirconia-reinforced alumina fibre, the PRD 166 fibre, broken at room temperature after creep test at 1000°C. Zirconia darker grains around the crack are twinned.

efficient as the temperature exceeds 1100°C. At 1300°C the creep rates as well as the failure modes of FP and PRD 166 fibres are similar.

A flexible α-alumina–zirconia fibre, Nextel 650 fibre, has been recently developed by 3M, with the aim of increasing the creep resistance with respect to that of the α-alumina Nextel 610 fibre. Its smaller diameter and grain sizes, when compared to PRD 166 fibre, give rise to a flexible fibre and 3M reports high strength (2.5 GPa at 25 mm). As

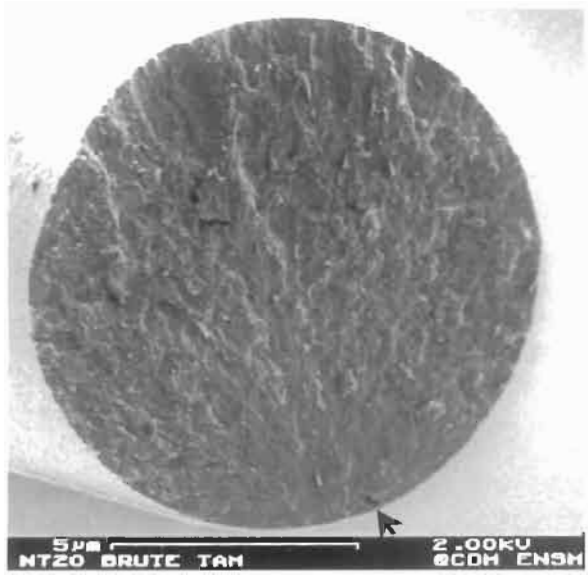

Fig. 16. Fracture morphology of Nextel 720 at room temperature.

creep is controlled by intergranular mechanisms, a smaller grain size increases the grain boundary/bulk ratio which should be detrimental for the creep resistance. Despite this, lower creep rates are measured with Nextel 650 (10^{-7} s^{-1} at 300 MPa) than with PRD 166 fibre ($5 \cdot 10^{-7}$ s^{-1} at 300 MPa) (Wilson and Visser, 2000). Specific additives in the Nextel 650 fibre induce a co-segregation of Y^{3+}, Si^{4+} and Fe^{3+} at the grain boundaries which enhances the formation of oriented elongated α-alumina grains during creep. The diffusion paths are then increased and the creep rates reduced compared to those of an isotropic fine grain microstructure (Poulon-Quintin et al., 2001).

α-Alumina/Mullite Fibres

The complex crystal structure of mullite provides creep resistance materials if a sintered microstructure can be obtained without the help of an excess of silica. 3M produced a dense mullite–α-alumina fibre, called Nextel 720 (Wilson et al., 1995), by using an aqueous sol, composed of intimately mixed silica and alumina precursors, with iron compounds used as the seeds for α-alumina. The fibre shown in Figs. 16 and 17 is composed of a continuum of mullite mosaic grains of about 0.5 µm with wavy contours, with no silicate intergranular phase (Deléglise et al., 2001).

Each mosaic grain consists of several mullite grains which are slightly mutually misoriented and encloses spherical and elongated particles of α-alumina of respectively 50 nm in diameter and 100 nm in length. The elongated particles show some preferential alignment with respect to the fibre axis and their long facets correspond to the basal plane of α-alumina.

After heat treatment, from 1300°C, the microstructure evolves towards facetted mullite ($3Al_2O_3 \cdot 2SiO_2$) grains deprived of intragranular alumina particles together with

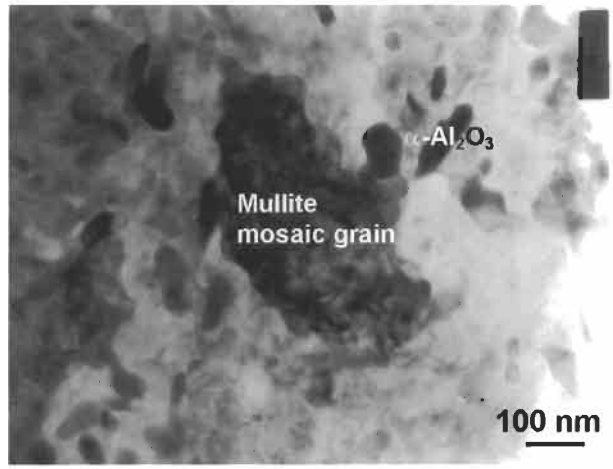

Fig. 17. Microstructure of Nextel 720 composed of a continuum of mosaic mullite grains enclosing α-alumina round or elongated grains.

larger α-alumina particles which become intergranular with a bimodal distribution in size (Hay et al., 1999; Deléglise et al., 2001). Some of the elongated α-alumina grains show exaggerated growth. This evolution of the microstructure is accelerated by the combination of temperature and load. When tested in creep, these fibres show much reduced creep rates when compared to pure α-alumina fibres and creep rates of the order of 10^{-6} s^{-1} have been measured at 1400°C. This remarkable behaviour is attributed to the high creep resistance of mullite and to the presence of the elongated and oriented α-alumina grains (Fig. 18). The fibres are however very sensitive to alkaline-containing environments. Mullite decomposes in the presence of a low concentration of alkalines to form alumino-silicate phases of melting points lower than 1200°C. Under load fast growth of large alumina grains occurs by liquid transportation, which is detrimental for the fibre strength and tensile strength is seen to vary with the loading rate suggesting a slow crack growth process (Deléglise et al., 2002). The failure surface shown in Fig. 19 presents an intergranular zone that fans out symmetrically from platelet grains and an intragranular zone corresponding to a fast propagation preceding failure. This observation could seriously limit the use in real environments at high temperature of fibres based on the Al_2O_3–SiO_2 system.

OTHER OXIDE FIBRES

Polycrystalline-alumina-based fibres can at present not compete with silicon-carbide-based fibres when low creep rates are required. Fibres with higher resistance to creep by dislocation motion could be provided by oxides with high melting point and complex crystal structure, a tendency to order over long distances and the maintenance of this order to high fractions of the melting temperatures (Kelly, 1996). Experimental development of monocrystalline fibres by Czochralski-derived techniques from chrysoberyl

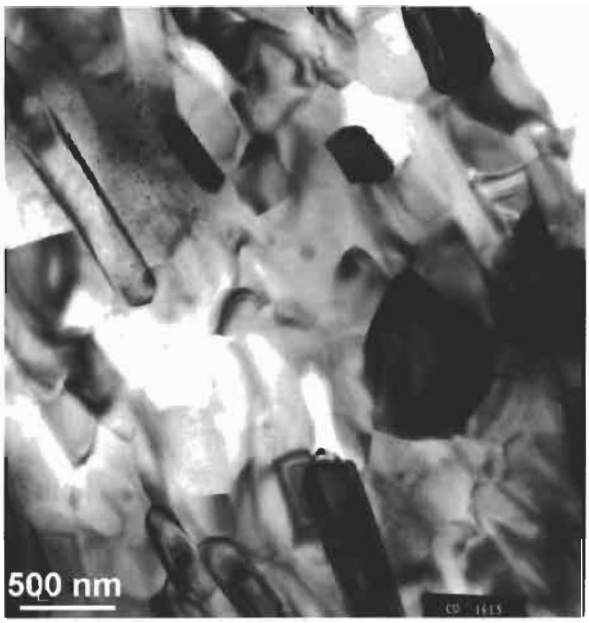

Fig. 18. Evolution of the microstructure after a creep test at 1400°C lasting 14 h.

($BeAl_2O_4$) (Whalen et al., 1991), mullite (Sayir and Farmer, 1995), or of yttrium–aluminium–garnet bulk samples ($Y_3Al_5O_{12}$) (Corman, 1993) have shown the excellent creep resistance of these systems.

However, the fabrication of monocrystalline fibres by solidification from the melt does not permit to produce continuous filaments with the required flexibility, that is with diameters of the order of 10 μm. Fine fibres have been experimentally produced from these systems by sol-gel techniques which then gave rise to polycrystalline structures, (Morscher and Chen, 1994; Lewis et al., 2000). Such single phase fibres exhibited excellent behaviours during bend stress relaxation tests (BSR tests) (Morscher and DiCarlo, 1992), which were an indication of potential good creep resistance. However, the development of large grains during pyrolysis, larger than the critical defect size, was responsible for the low strengths of these fibres and made creep test results in pure tension difficult to obtain. The control of grain size can be achieved by the inclusion of second phases acting as grain growth inhibitors. This has been accomplished in mullite fibres by the inclusion of zirconia particles (Lewis et al., 2000).

CONCLUSION

The requirement to have reinforcing fibres capable of operating at very high temperatures and under corrosive environments demands the development of oxide fibres having high strength and creep resistance.

Their room-temperature fracture behaviour depends on the size of the grains. Those

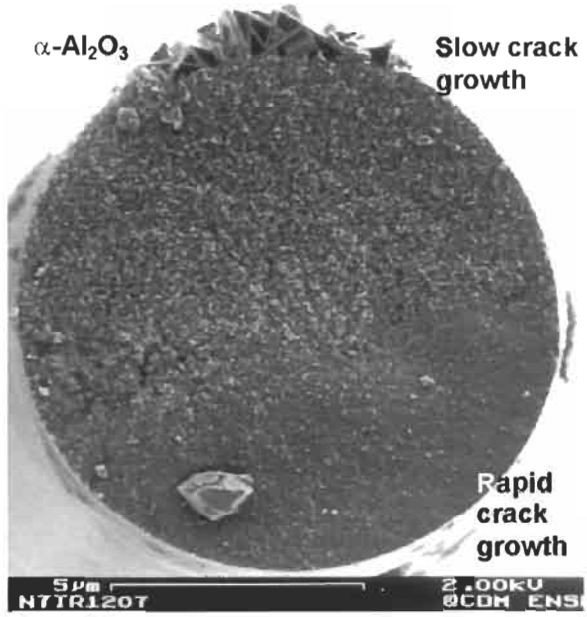

Fig. 19. Fracture morphology of Nextel 720 fibre obtained in tension at 1200°C.

fibres with very fine microstructures with grain sizes less than 100 nm, show a mirror zone around the defect responsible for crack initiation. For fibres with grain sizes of the order of a few tens of nanometres the fracture morphology resembles that of a glass fibre. With a grain size of several hundred nanometres the fibre fracture morphology does not show a mirror zone. Often crack initiating defect can not be identified and is supposed to be a large grain emerging at the surface.

Their high-temperature fracture behaviour depends on the stability of the microstructure. Fibres which are composed of transitional forms of alumina show a phase change at high temperature and the growth of large α-alumina or mullite grains which weaken the fibres. The microstructure of fibres which are composed of α-alumina are stable up to 1300°C. However, fracture at these temperatures is controlled by grain boundary weakening. These fibres can exhibit a superplastic behaviour at 1300°C with the development of microcracks. The addition of second phases, such as zirconia or mullite, can inhibit grain boundary sliding. The development of oxide fibres for very high temperatures is still in its infancy and considerable advances may be expected from the production of fibres based on oxides with complex crystal structures.

REFERENCES

Abe, Y., Horikiri, S., Fujimura, K. and Ichiki, E. (1982) High performance alumina fiber and alumina/aluminum composites. In: *Progress in Science and Engineering of Composites*, pp. 1427–1434, T. Hayashi, K. Kawata and S. Umekawa (Eds.). ICCM–IV Japan Soc. Comp. Mater., Tokyo.

Berger, M.H., Lavaste, V. and Bunsell, A.R. (1999) Small diameter alumina-based fibers. In: *Fine Ceramic*

Fibers, pp. 111–164, A.R. Bunsell and M.H. Berger (Eds.). Marcel Dekker, New York, NY.

Birchall, J.D. (1983) The preparation an properties of polycrystalline aluminium oxide fibres. *Trans. J. Br. Ceram. Soc.*, 82: 143.

Corman, G.S. (1993) Creep of yttrium aluminum garnet single crystals. *J. Mater. Sci.*, 12: 379.

Deléglise, F., Berger, M.H., Jeulin, D. and Bunsell, A.R. (2001) Microstructural stability and room temperature properties of the Nextel 720 fibre. *J. Eur. Ceram. Soc.*, 21: 569.

Deléglise, F., Berger, M.H. and Bunsell, A.R. (2002) Microstructural evolution under load and high temperature deformation mechanisms of a mullite/alumina fibre. *J. Eur. Ceram. Soc.*, 22: 1501.

Dhingra, A.K. (1980) Alumina fiber FP. *Philos. Trans. R. Soc. London A*, 294, 411.

Gooch, D.J. and Groves, G.W. (1973) The creep of sapphire filament with orientations close to the *c*-axis. *J. Mater. Sci.*, 8: 1238.

Hay, R.S., Boakye, E.E., Petry, M.D., Berta, Y., Von Lehmden, K. and Welch, J. (1999) Grain growth and tensile strength of 3M Nextel 720 after thermal exposure. *Ceram. Eng. Sci. Proc.*, 20(3), 153.

Johnson, D.D. (1981) Nextel 312 ceramic fibre from 3M. *J. Coated Fabrics*, 11: 282.

Johnson, D.D., Holtz, A.R. and Grether, M.F. (1987) Properties of Nextel 480 ceramic fibers. *Ceram. Eng. Sci. Proc.*, 8(7-8): 744.

Kelly, A. (1996) The 1995 Bakerian Lecture. Composite material. *Philos. Trans. R. Soc. London*, 354: 1841.

Lavaste, V., Berger, M.H., Bunsell, A.R. and Besson, J. (1995) Microstructure and mechanical characteristics of alpha alumina fibres. *J. Mater. Sci.*, 30: 4215.

Lewis, M.H., York, S., Freeman, C., Alexander, I.C., Al-Dawery, I., Butler, E.G. and Doleman, P.A. (2000) Oxyde CMCs; novel fibres, coatings and fabrication procedures. *Ceram. Eng. Sci. Proc.*, 21(3): 535.

Morscher, G.N. and Chen, K.C. (1994) Creep resistance of developmental polycrystalline yttrium–aluminum garnet fibers. *Ceram. Eng. Sci. Proc.*, 15(4): 755.

Morscher, G.N. and DiCarlo, J.A. (1992) A simple test for thermomechanical evaluation of ceramic fibers. *J. Am. Ceram. Soc.*, 75(1): 136.

Poulon-Quintin, A., Berger, M.H. and Bunsell, A.R. (2001) Mechanical and microstructural characterization of the Nextel 650 alumina–zirconia fibre. In: *Proceedings of the 4th Conference on High Temperature and Ceramic Matrix Composites*, October 1–3, 2001, Munich (in press).

Pysher, D.J. and Tressler, R.E. (1992) Creep rupture studies of two alumina-based ceramic fibres. *J. Mater. Sci.*, 27: 423.

Romine, J.C. (1987) New high-temperature ceramic fiber. *Ceram. Eng. Sci. Proc.*, 8(7-8): 755.

Saitow, Y., Iwanaga, K., Itou, S., Fukumoto, T. and Utsunomiya, T. (1992) Preparation of continuous high purity α-alumina fiber. In: *Proceedings of the 37th International SAMPE Symposium*, March 9–12, pp. 808–819.

Sayir, A. and Farmer, S.C. (1995) Directionally solidified mullite fibers. In: *Ceramic Matrix Composites — Advanced High Temperature Structural Materials, Mater. Res. Soc. Proc.*, 365, pp. 11–21.

Taylor, M.D. (1999) Chemistry of alumina. In: *Fine Ceramic Fibers*, pp. 63–109, A.R., Bunsell and M.H. Berger (Eds.). Marcel Dekker, New York, NY.

Whalen, P.J., Narasimhan, D., Gasdaska, C.G., O'Dell, E.W. and Morris, R.C. (1991) New high-temperature oxide composite reinforcement material: Chrysoberyl. *Ceram. Eng. Sci. Proc.*, 12(9-10): 1774.

Wilson, D.M. and Visser, L.R. (2000) Nexte 650 ceramic oxide fiber: new alumina-based fiber for high temperature composite reinforcement. *Ceram. Eng. Sci. Proc.*, 21(3): 363.

Wilson, D.M., Lueneburg, D.C. and Lieder, S.L. (1993) High temperature properties of Nextel 610 and alumina based nanocomposite fibers. *Ceram. Eng. Sci. Proc.*, 14(7-8): 609.

Wilson, D.M., Lieder, S.L. and Lueneburg, D.C. (1995) Microstructure and high temperature properties of Nextel 720 fibers. *Ceram. Eng. Sci. Proc.*, 16(5): 1005.

Fiber Fracture
M. Elices and J. Llorca (Editors)

FRACTURE CHARACTERISTICS OF SINGLE CRYSTAL AND EUTECTIC FIBERS

Ali Sayir and Serene C. Farmer

NASA Glenn Research Center, Cleveland, OH 44135, USA

Introduction 109
Experimental 109
Results and Discussion 110
Fracture Characteristics of Single-Crystal Y_2O_3, $Y_3Al_5O_{12}$ and Al_2O_3 110
Fracture Strength of ⟨0001⟩ Al_2O_3 Fibers at Elevated Temperatures 114
Directionally Solidified $Al_2O_3/Y_3Al_5O_{12}$ Eutectic Fibers 117
Conclusions 121
References 122

Abstract

Single-crystal fibers are attractive for functional ceramic applications as active devices and are equally important for structural ceramic components as load bearing applications. The fracture characteristics of single-crystal fibers from a variety of crystal systems including the $Al_2O_3/Y_3Al_5O_{12}$ eutectic were examined. The Young moduli of ⟨0001⟩ Al_2O_3, ⟨111⟩ $Y_3Al_5O_{12}$ and ⟨111⟩ Y_2O_3 fibers were 453, 290, and 164 GPa, respectively, and agreed well with the literature. Single crystals of ⟨111⟩ Y_2O_3 were the weakest fibers and their strength did not exceed 700 MPa. The moderate tensile strength of single-crystal ⟨111⟩ $Y_3Al_5O_{12}$ was controlled by the facet forming tendency of the cubic garnet structure and in some cases by the precipitation of cubic perovskite phase $YAlO_3$. High-strength single-crystal ⟨0001⟩ Al_2O_3 fibers did not retain their strength at elevated temperatures. The data suggest that single-crystal ⟨0001⟩ Al_2O_3 failure is dependent on slow crack growth at elevated temperatures. The high-temperature tensile strength of $Al_2O_3/Y_3Al_5O_{12}$ eutectic fibers is superior to sapphire (1.3 GPa at 1100°C)

and demonstrably less prone to slow crack propagation. The $Al_2O_3/Y_3Al_5O_{12}$ eutectic interphase boundary is of a coherent nature with strong bonding.

Keywords

Single-crystal fiber; Garnet fiber; Perovskite; Single-crystal Y_2O_3 (yttria); Directional solidification; Eutectic fiber; Slow crack growth; Creep resistance; Coarsening

INTRODUCTION

The concept of using single-crystal fibers as an active component or load bearing constituent has potential in a variety of applications. In many cases properly processed single-crystal fibers provide high crystalline perfection and sometimes near theoretical strength. The main objective of this paper is to examine the fracture characteristics of single-crystal fibers from a variety of crystal systems and a related directionally solidified eutectic system. Aluminum oxide (α-Al_2O_3), and its single-crystal form as sapphire (trigonal), yttrium sesquioxide Y_2O_3 (bcc-yttria), and yttrium aluminum garnet ($Y_3Al_5O_{12}$; cubic – YAG) will be discussed. The fracture characteristic of single-crystal Y_2O_3 and $Y_3Al_5O_{12}$ will be contrasted with single-crystal Al_2O_3.

The shortcomings of single-crystal fibers Al_2O_3 and $Y_3Al_5O_{12}$, specifically low toughness and slow crack growth, can be overcome by growth of directionally solidified eutectic fibers. In this approach, the eutectic architecture of a continuous reinforcing phase within a higher volume phase or matrix, can be considered as a naturally occurring in-situ composite. This work reports the results of experiments aimed at identifying the sources of high levels of strength retention and creep resistance in a two-phase $Al_2O_3/Y_3Al_5O_{12}$ eutectic system. Examination of the fracture characteristics of the individual end members of the Al_2O_3–$Y_3Al_5O_{12}$ region of the Al_2O_3–Y_2O_3 phase diagram (Viechnicki and Schmid, 1969) provides needed insight for discussion of fracture characteristics of the directionally solidified eutectic fibers.

EXPERIMENTAL

All fibers tested in this study were produced using the laser-heated float zone technique (LHFZ) which has been described in Sayir and Matson (1991) and Farmer et al. (1993). Fibers were grown to ~24 cm in length. For the dynamic studies at different strain rates, cold grips were used with a total fiber gauge length of 23 cm. The fibers were tested in air by placing them in a $MoSi_2$ furnace (CM Inc., Bloomfield, NJ) with a hot zone of 2.5 cm. All fibers fractured within this 2.5 cm length. The strain rates were calculated from the total gauge length and cross-head speed of the test frame (Model 4502, Instron Corp., Canton, MA). This value can be considered a relative strain rate if test conditions remain the same, i.e. temperature and grip method (Sayir, 1993). For static load (stress rupture) studies, the fibers were dead weight loaded in high vacuum ($\sim 10^{-6}$ atm) at 1400°C in a tantalum element furnace with a hot zone of 2 cm.

To accurately measure the micro-strain of the small-diameter single-crystal fibers, a new technique was utilized. This technique was based on original work by Yamaguchi and modified to measure strain on small areas (Barranger, 1990; Lant and Barranger, 1990; Sayir et al., 1994). Yamaguchi's speckle-shift technique requires no specimen surface preparation and allows micro-strain measurements of an extremely small gauge length (on the order of 0.1 mm). It provides a strain resolution of approximately 15 micro-strain. Details about the application of this technique on small-diameter fibers can be taken from previous work (Sayir et al., 1994). This technique requires the reflection of coherent laser light from an optically rough surface that results in a speckle

pattern at a remote sensor plane. The diverse features of speckle patterns could then be replayed in real time or correlated. The correlation was unconstrained as long as the contrast was high. The level of contrast for the speckle pattern was in turn directly related, among other factors, to the surface morphology of the material. A large percent of the argon laser beam is internally reflected down the length of the sapphire, YAG and Y_2O_3 fibers, thereby causing a weak signal return to the camera. The speckle pattern therefore had a relatively low signal-to-noise ratio which, along with multiple returns from the back surface of the fiber, contributed to the scatter in the data. The weak contrast (dim speckles) increased the difficulty of tracking the speckle shift. With each new reference acquired there was a small element of random error introduced into the cumulative speckle shift record (Sayir et al., 1994). This random error further increased scatter in the strain data. In order to reduce the uncertainty and increase the correlation peak in the presence of an erratic pattern, a reference from a new frame was obtained whenever the cumulative speckle displacement within the current reference exceeded the maximum allowable speckle displacement per reference frame. This effort, combined with careful alignment of the fiber, resulted in reduction of the scatter to an acceptable level. Scanning electron microscopy (JOEL 840, UTW Kevex EDS) and X-ray diffractometry (Phillips 3720XRD) were employed to characterize for microstructures and phase identification.

RESULTS AND DISCUSSION

Fracture Characteristics of Single-Crystal Y_2O_3, $Y_3Al_5O_{12}$ and Al_2O_3

The two single-crystal compositions which span the Al_2O_3–$Y_3Al_5O_{12}$ region of the Al_2O_3–Y_2O_3 phase diagram were selected for study. To advance our overall understanding of the fracture characteristics of single-crystal fibers in the Al_2O_3–Y_2O_3 system, single-crystal ⟨111⟩ Y_2O_3 which exhibits different fracture characteristics was also examined. Single crystals of Al_2O_3 and $Y_3Al_5O_{12}$ were grown in ⟨0001⟩ and ⟨111⟩ directions, respectively. The growth directions for these single crystals eliminate the active slip systems (Snow and Heuer, 1973; Corman, 1991). The creep resistance of single-crystal ⟨0001⟩ Al_2O_3 and ⟨111⟩ $Y_3Al_5O_{12}$ are more than adequate for composite applications up to 1500°C (Snow and Heuer, 1973). If single crystals of Al_2O_3 and $Y_3Al_5O_{12}$ are loaded in the growth direction, the creep resistance of the material is sufficiently large that there is no measurable contribution of creep the fracture process. Efforts focused on the measurement of surface strain along one principal fiber axis, determination of Young's modulus, and analysis of the fracture characteristics of these single crystals.

The micro-strain measurements of small-diameter fibers were performed using Yamaguchi's speckle-shift technique (Sayir et al., 1994). The average Young modulus of ⟨0001⟩ Al_2O_3 and ⟨111⟩ $Y_3Al_5O_{12}$ were 453 GPa (±36 GPa) and 290 GPa (±24 GPa), respectively. This average value for ⟨0001⟩ Al_2O_3 (*c*-axis sapphire) is in good agreement with reported data in the literature of 450 GPa (Wachtman, 1960). Yet, the large scatter (8% standard deviation) in Young's modulus of sapphire was the largest

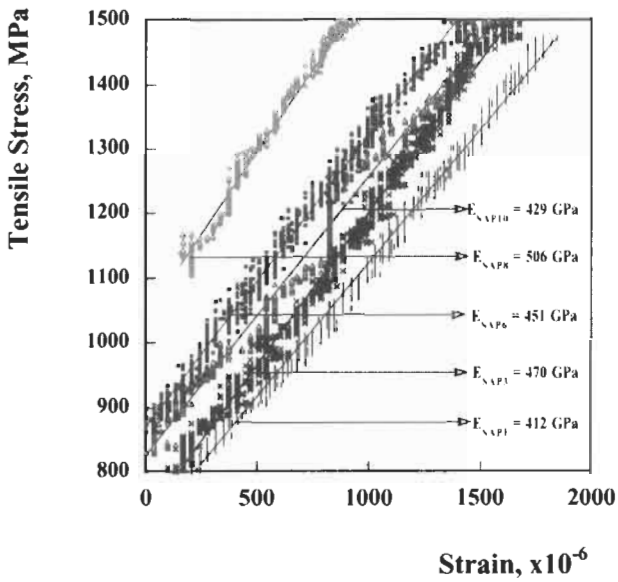

Fig. 1. Stress–strain curves for ⟨0001⟩ Al_2O_3 using Yamaguchi's laser-speckle technique. Data have been shifted an arbitrary amount of pre-load to clearly show the data. Individual points represent the experimental data; the straight lines represent the least-squares fit.

among the observed errors for the laser-speckle strain measurement system and proved to be typical of these sapphire fibers, Fig. 1. The average Young modulus for ⟨111⟩ $Y_3Al_5O_{12}$ was 290 GPa and was in a good agreement with the literature data, but slightly lower than reported values (Corman, 1991; Sayir and Matson, 1991). There was less scatter in the data; ±21 GPa. The change in the scatter of the data for the different crystals indicates that these crystal interact differently with the incoming argon laser, i.e. backreflection characteristics for each crystal type are different. The average Young modulus of ⟨111⟩ Y_2O_3 was 164 GPa along the axis of the fiber. This information could not be independently confirmed by literature values since single-crystal Y_2O_3 has not been grown in bulk form. An independent study was initiated by Palko et al. (2001) to determine bulk and shear moduli of single-crystal Y_2O_3 using Brillouin spectroscopy. This technique was able to measure the elastic constants, which form a fourth rank tensor for Y_2O_3. Young's modulus along the ⟨111⟩ direction of the fiber was 150 GPa. This value is well within the range of data of the present work obtained using Yamaguchi's speckle-shift technique.

The Young moduli of the single-crystal fibers (Table 1) differ strikingly due in part to their crystal structure and the packing density of the oxygen lattice. Y_2O_3 has a simple cubic structure, hence the lowest packing of atoms, and exhibits a very low stiffness value in the range of 164 to 180 GPa. The sapphire hexagonal closely packed structure gives rise to a much higher modulus, 450 GPa. $Y_3Al_5O_{12}$ does not have a closely packed sublattice yielding a moderate value of Young's modulus, 290 GPa.

The single-crystal fibers tested had distinct fracture characteristics and different strengths (Table 1). Single crystals of ⟨111⟩ Y_2O_3 were the weakest fibers and strength

Table 1. Summary of room temperature mechanical properties (mean of 40 tests)

Single crystal	Young' modulus (GPa)	SD (GPa)	Tensile strength (GPa)	SD (GPa)
⟨0001⟩ Al_2O_3	453	±36	6.7	2.2
⟨111⟩ $Y_3Al_5O_{12}$	290	±21	3.4	0.8
⟨111⟩ Y_2O_3	164	±17	0.7	0.1

SD, standard deviation.

did not exceed 700 MPa, with an average strength of 570 MPa (±110 MPa). The tensile strength of single-crystal ⟨0001⟩ Al_2O_3 and ⟨111⟩ $Y_3Al_5O_{12}$ were 6.7 and 3.4 GPa, respectively. The standard deviations were 2.2 GPa for single-crystal ⟨0001⟩ Al_2O_3 and 0.7 GPa for single-crystal ⟨111⟩ $Y_3Al_5O_{12}$ (40 fibers tested for each composition). The underlying reason for the difference in strength can be traced back to the anisotropy of each crystal, but is not necessarily attributable to the intrinsic difference in Young's moduli.

The strength controlling flaws for each fiber were different in nature and originated from the crystal growth conditions. The single-crystal fibers of Y_2O_3 contained growth facets, forming periodic defects along the ⟨111⟩ direction of the fiber. All fibers fractured by octahedral cleavage (Fig. 2), and cleavage was often perpendicular to the fiber axis confirming that the fiber axis coincides with the ⟨111⟩ crystallographic direction as determined from X-ray characterization. X-ray analysis indicated that ⟨111⟩ Y_2O_3 had cubic symmetry and was optically isotropic. The selection of the ⟨111⟩ growth direction and carefully controlled solidification conditions made it possible to eliminate the undesirable phase transformations that may occur in the solid state as expected from the phase diagram (Roth and Schneider, 1960). The tested fibers were all single crystals of the same cubic phase, and the periodic defects were most likely a result of changes in the interface energetic and molecular attachment kinetics during solidification rather than being associated with phase transformations. The layers needed for the growth of the interface are mostly generated in the small curved rim of the liquid–solid interface at the outer edge of the crystal near the meniscus contact line and are located at the different crystallographic positions of the planes. The issue is the 'anisotropy factor' of the interface for the different planes at the liquid–solid interface and the stability of a particular crystal face with respect to facet formation. Although the surface energies of Y_2O_3 are not known, the expected deviation for different planes from the ⟨111⟩ direction would be small and prone to periodic instability during crystal growth. Yet, the degree of anisotropy is large enough to produce step like defects on the surface of the crystal leading to low fiber strength.

For Al_2O_3 fibers the ⟨0001⟩ growth direction was selected to achieve two objectives. First, the mechanical properties of sapphire are closely related to its crystallography, and selection of the ⟨0001⟩ growth direction eliminates the three known slip systems (basal, prismatic, and rhombohedral slip). Second, the selection of the ⟨0001⟩ growth direction provided large enough anisotropy so that the meniscus shape during solidification was constant. The tensile strength of single-crystal ⟨0001⟩ Al_2O_3 fibers was 6.7 GPa (±2.2 GPa), Table 1. A few sapphire fibers with low strength consistently failed

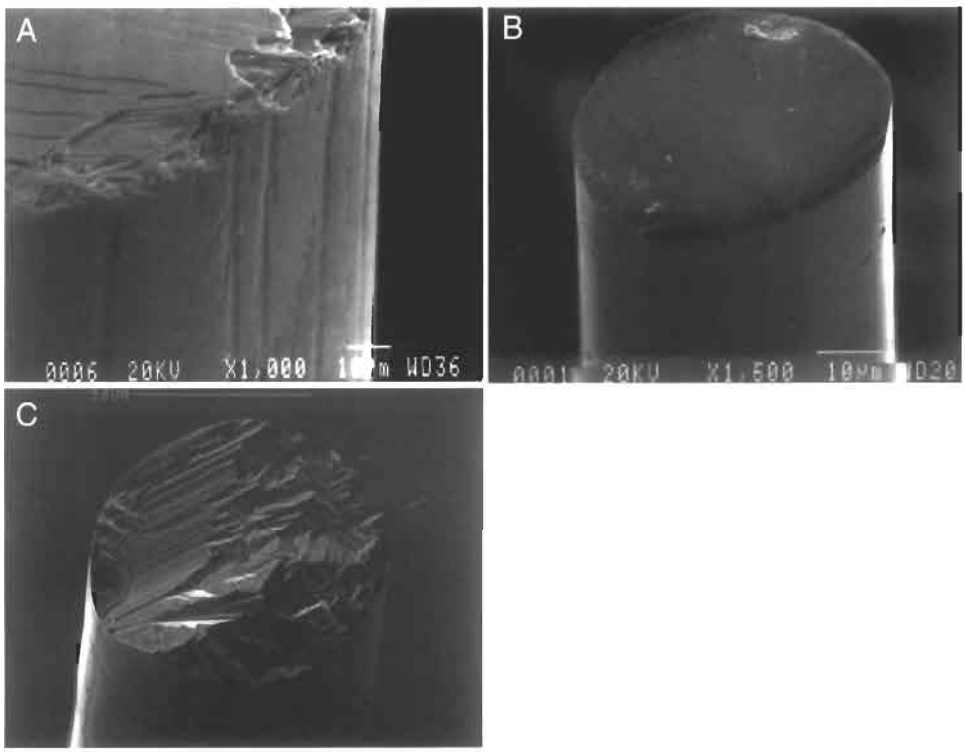

Fig. 2. Representative examples of fracture surfaces of single-crystal ⟨111⟩ Y_2O_3 (A), ⟨111⟩ $Y_3Al_5O_{12}$ (B), and ⟨0001⟩ Al_2O_3 (C). Fracture-originating flaws were consistently easy to find for $Y_3Al_5O_{12}$ and Al_2O_3 but less obvious for Y_2O_3 (due to disintegration). The ⟨111⟩ plane is the highly preferred cleavage plane for Y_2O_3 and is a less common cleavage plane for $Y_3Al_5O_{12}$. ⟨0001⟩ Al_2O_3 fails without preferred cleavage tendency, but shows some degree of preference for fracture near certain planes.

from internal voids. The tensile strengths reported here are among the highest tensile strength values reported in the literature for continuous fibers and a considerable fraction (~20%) of the theoretical strength of sapphire (~45 GPa). This high tensile strength is related to the avoidance of internal voids, and large-scale facets thus leaving only surface-related defects to control fracture of the fibers. The surface flaws (Fig. 2C) are apparently related to three surface features that arise in the molten zone during laser processing and are then frozen into the solid fiber. These are diameter deviations along the fiber length, localized ripples that predominate during non-symmetric heating and periodic striations. The tensile strength of the fibers may be closely related to the shape of the meniscus at the crystal–liquid–vapor interface and the departure of the contact angle from its steady-state value. This difference may also promote small-scale facets. SEM characterization of the fibers grown in the ⟨0001⟩ direction showed no visible facets. The {0001} basal plane in sapphire is one of the low free-energy planes, the other being the $\{0\bar{1}12\}$ *r*-plane (Kitayama, 1999). It was expected that the fiber may have some growth facets relating to these planes at the solid–liquid interface providing an array of re-entrant corners. SEM and optical microscopic characterization of fracture

surfaces failed to show twins. The tensile strength values reported here are very high. Therefore, the expected twin size is beyond the resolution of SEM and may require transmission electron microscopy (TEM) characterization to resolve the question of their occurrence.

The tensile strength of ⟨111⟩ $Y_3Al_5O_{12}$ was moderately high, 3.4 ± 0.8 GPa, but considerably less than Al_2O_3. The fractographic analysis of the fibers revealed that low-strength fibers had a stress concentration associated with [100] planes along the fiber axis, Fig. 2B. The occurrence of these stress concentrations was sensitive to the pull-rate during crystal growth. $Y_3Al_5O_{12}$ has 160 atoms per unit cell (Al_2O_3 has 12) and thus a sluggish crystallization process. Due to the high viscosity and low thermal conductivity of the $Y_3Al_5O_{12}$ melt the changes in tangential temperature gradient along the free surface of the melt did not readily initiate instabilities. The significance of these physical characteristics of the melt was twofold. First, the meniscus angle does not change readily; therefore, smooth exterior surfaces are produced. Fibers have strengths around 3 GPa even though they contain macroscopic facets. This is in strong contrast to single-crystal Y_2O_3, although they both have cubic symmetry. Second, as reported in the literature (Caslavsky and Viechnicki, 1980), the $Y_3Al_5O_{12}$ system can move toward metastable solidification resulting in solidification of perovskite phase with $YAlO_3$ composition. Fibers grown at faster rates failed mostly from internal flaws of precipitated $YAlO_3$ phase as determined by X-ray and Raman spectroscopy analysis. Hence, any attempts to increase pull speed for high volume production are technically not viable.

From the foregoing discussion of the fracture characteristics of single-crystal fibers, it is apparent that single-crystal Al_2O_3 and $Y_3Al_5O_{12}$ are possible candidates for load bearing applications. Yet, $Y_3Al_5O_{12}$ cannot be produced in an economically practical manner due to sluggish crystallization kinetics and hence is not a viable reinforcement for structural composites that require a considerable amount of reinforcement. Hence, Y_2O_3 and $Y_3Al_5O_{12}$ are most attractive for sensors, waveguides, and laser host types of functional applications where the amounts of fiber material required are lower. Accordingly, with the emergence of single-crystal Al_2O_3 fibers as the more promising candidate for reinforcing fibers in structural applications, the strength of Al_2O_3 fibers at elevated temperatures needs to be studied for high-temperature use.

Fracture Strength of ⟨0001⟩ Al_2O_3 Fibers at Elevated Temperatures

Single-crystal ⟨0001⟩ Al_2O_3 fibers with room temperature strengths of 6.7 GPa exhibit strengths at 1400°C of <1 GPa. This reduction in strength may be due to the decrease of the material resistance to crack propagation, that is, the decrease in fracture toughness K_{Ic} with increasing temperature. However, this would require a dramatic decrease of Young's modulus and/or a substantial decrease in the surface energy of sapphire. Young's modulus of single-crystal Al_2O_3 decreased monotonically with a very small slope as a function of temperature. The modulus at 1450°C was only 10 to 14% less than the room temperature value. Since the relative decrease in the elastic modulus, $-(T/E)(dE/dT)$, for Al_2O_3 is not profound, the decrease of other thermodynamic properties with increasing temperature is not expected to be large enough to account for the dramatic decrease of tensile strength at elevated temperatures.

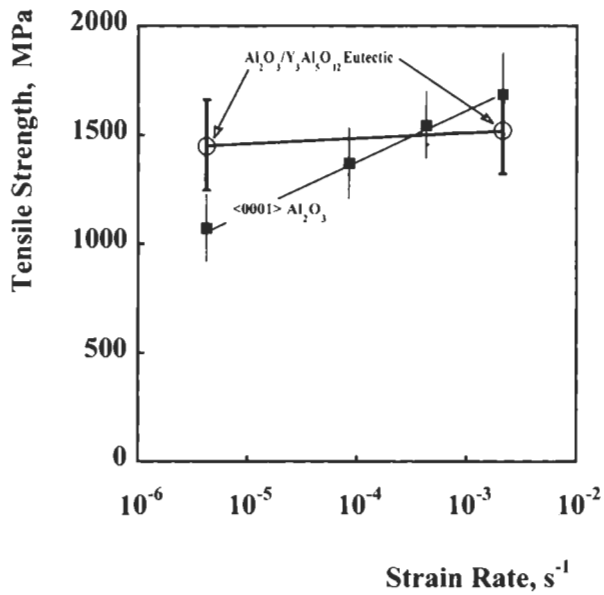

Fig. 3. Tensile strength of single-crystal ⟨0001⟩ Al_2O_3 (squares) and directionally solidified $Al_2O_3/Y_3Al_5O_{12}$ (circles) fibers as a function of strain rate at 1000°C. Each data point represents the mean of 40 tests and error bars represent the standard deviation.

A possible contributor to the loss in strength at high temperatures is static fatigue or delayed failure due to stress-enhanced slow crack growth. This would require that the fiber strength be markedly dependent on loading rate and load application time. Hence, successful structural exploitation of these fibers requires a detailed understanding of fiber strength behavior as a function of stress and time so that accurate failure predictions can be made. The time to failure behavior for uniaxially loaded commercial ⟨0001⟩ Al_2O_3 was tested (Sayir, 1993). This experimental study showed that the failure of ⟨0001⟩ Al_2O_3 fibers was due to slow crack growth at 1000 < 1400°C under static stress and variable stress rate conditions. In the present work fibers grown by the laser-heated float zone technique that had superior room temperature strength were tested. The strong dependence of strength on strain rate for the high strength ⟨0001⟩ Al_2O_3 at 1100°C is shown in Fig. 3 (squares). The dynamic response of high-strength fibers is identical to commercially produced fibers even though their room temperature strength was almost a factor of two higher. The data strongly indicate that single-crystal ⟨0001⟩ Al_2O_3 failure is dependent on the slow crack growth at elevated temperatures and therefore any meaningful improvements to fiber strength at high temperature must consider strength as a function of dynamic loading conditions.

The results of the stress rupture test at 1400°C are shown in Fig. 4. The threshold stress intensity factor below which no crack propagation occurs seems to be around 400 MPa as shown in Fig. 4. To understand slow crack growth in Al_2O_3 fibers and make accurate lifetime predictions, one needs to know the crack velocity as a function of stress intensity factor at high temperatures. It is well established that for a given

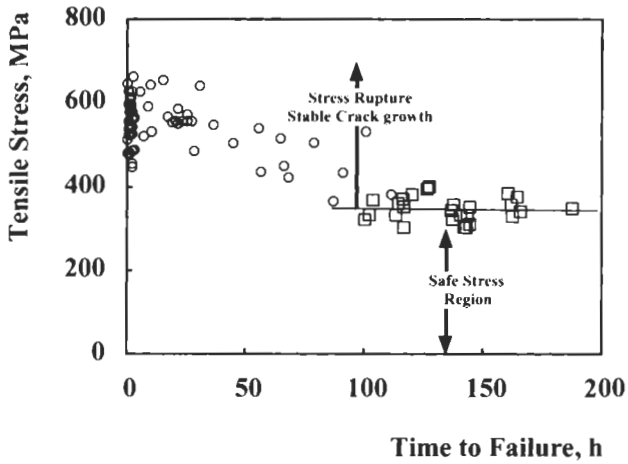

Fig. 4. Stress rupture time of single-crystal ⟨0001⟩ Al_2O_3 as a function of applied stress at 1400°C (vacuum 10^{-6} atm.). Circles represent the time to failure at fracture and squares represent experiments typically interrupted at 100 h or more without fracture.

system (environment, temperature and material), there is a unique relationship between crack growth velocity, v, and crack tip stress intensity factor, K_I. For each condition, it is necessary to derive an empirical relation for these factors. The approach originally developed by Wiederhorn to describe slow crack of ceramics is used here (Wiederhorn, 1968):

$$v = V_0(K_I/K_{I0})^n \tag{1}$$

where K_{I0} is the threshold stress intensity factor below which crack growth is negligible ($V_0 < 10^{-10}$ m/s), n is an empirical constant, and V_0 is the crack velocity at $K_I = K_{I0}$. For lifetime prediction under constant stress conditions, it has been shown that Eq. 1 can be used to predict the time to failure, t_f, by the relation:

$$t_f = 2(K_{Ii}^{2-n} - K_{If}^{2-n})/\left[(n-2)V_0\sigma_a^2 Y^2\right] \tag{2}$$

where K_{Ii} and K_{If} are the initial and final values of the stress intensity factor. Y is a geometric factor that depends on the flaw shape, orientation, location, and on the nature of the applied stress field. The solid line designated as 'dynamic loading' in Fig. 4 was calculated with Eq. 2 using $K_{Ii} = 0.75$ MPa $m^{-1/2}$ and $V_0 = 10^{-10}$ m/s, $n = 10$ for 1400°C which are taken from previous work (Sayir, 1993).

The uncertainty, however, arises if one compares the dynamic failure strength with static loading. The large scatter of lifetimes at constant stress is a direct result of Eq. 1 where slow crack growth rate changes substantially with small changes in K_I. From Eq. 1 to Eq. 2 it was assumed that the factor Y is invariant during flaw growth to simplify the integral. The fact that failure may be initiated by different types of flaws in different fibers should not be ignored. The uncertainty further increased by our limited understanding of the physical phenomena controlling fracture at elevated temperatures. Although single-crystal Al_2O_3 has been well studied, the microscopic mechanisms

which govern high-temperature strength remain to be elucidated. Two proposed possible mechanisms, both thermally activated, are atomistic level crack propagation due to lattice trapping (Hsieh and Thomson, 1973; Lawn, 1975), and/or dislocation assisted crack shielding. The practical conclusions of this study are therefore twofold. First, an understanding of fracture characteristics is needed to improve the high-temperature strength retention of single-crystal Al_2O_3. It should be pointed out that this is not a limitation of the state of the art of crystal growth, but rather a direct result of extensive work that produced fibers with exceptionally high strength, yet were drastically weaker at high temperatures, without any clear explanation. Second, there is a clear need to find a new class of fibers that do not exhibit large strength degradation at high temperatures. This impetus led to the development of directionally solidified $Al_2O_3/Y_3Al_5O_{12}$ eutectic fibers (Sayir and Matson, 1991).

Directionally Solidified $Al_2O_3/Y_3Al_5O_{12}$ Eutectic Fibers

The main driving force for the study of directionally solidified $Al_2O_3/Y_3Al_5O_{12}$ eutectic fibers arose from the shortcomings of single-crystal Al_2O_3 fibers as discussed in the previous section. Accordingly, the major objective in the eutectic work was to examine the time-dependent failure of $Al_2O_3/Y_3Al_5O_{12}$ eutectic fibers at elevated temperatures. First, the tensile strength at 25 and 1100°C of the $Al_2O_3/Y_3Al_5O_{12}$ eutectic fibers were determined. Second, the strain rate-dependent tensile strength of single-crystal Al_2O_3 fibers and directionally solidified $Al_2O_3/Y_3Al_5O_{12}$ eutectic fibers at 1100°C were compared.

The fast-fracture tensile strengths of as-grown fibers tested at 25 and 1100°C are shown as Weibull-probability plots in Fig. 5. A typical primary fracture origin is shown in Fig. 6 as well as corresponding longitudinal fiber surface morphologies. The room temperature tensile strength of $Al_2O_3/Y_3Al_5O_{12}$ eutectic fibers was 2.4 GPa ($\pm$0.336 GPa), considerably lower than the tensile strength of single-crystal ⟨0001⟩ Al_2O_3 fibers. Confocal micro-Raman spectroscopy was performed on a number of $Al_2O_3/Y_3Al_5O_{12}$ eutectic fibers in an attempt to identify $YAlO_3$ precipitates. Raman spectra did not reveal any $YAlO_3$ phase in the $Al_2O_3/Y_3Al_5O_{12}$ eutectic fibers. This is significant because the strength controlling flaws are either pores and/or the facet forming tendencies of the components as determined by SEM characterization, Fig. 6.

The tensile strength of $Al_2O_3/Y_3Al_5O_{12}$ eutectic fibers was 1.3 GPa at 1100°C and was superior to single-crystal ⟨0001⟩ Al_2O_3. To understand why $Al_2O_3/Y_3Al_5O_{12}$ eutectic fibers are stronger than ⟨0001⟩ Al_2O_3 at elevated temperature, it is necessary to compare slow crack growth characteristics of the $Al_2O_3/Y_3Al_5O_{12}$ eutectic with single-crystal ⟨0001⟩ Al_2O_3. The time-dependent failure of $Al_2O_3/Y_3Al_5O_{12}$ eutectic fibers was first evaluated using tensile strength results taken at different strain rates. The strain rate-dependent tensile strengths of directionally solidified eutectic fibers are compared with those of *c*-axis sapphire in Fig. 3. The tensile strength of directionally solidified $Al_2O_3/Y_3Al_5O_{12}$ eutectic fibers did not change with change of strain rate over four orders of magnitude at 1100°C. The tensile strength of the $Al_2O_3/Y_3Al_5O_{12}$ eutectic fibers was 1.39 GPa at 1100°C, a loss of approximately 40% from its room temperature value. At some conditions the tensile strength of ⟨0001⟩ Al_2O_3 showed

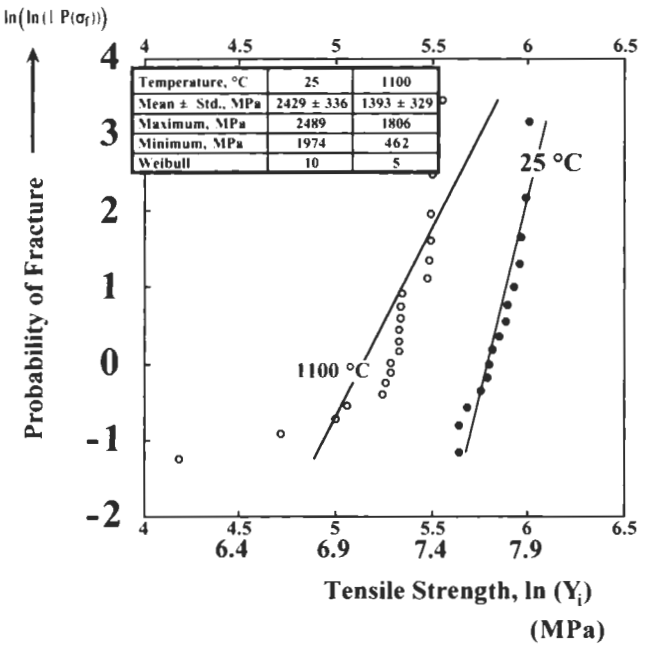

Fig. 5. The fast-fracture tensile strengths (inserted table) and Weibull probability plots of $Al_2O_3/Y_3Al_5O_{12}$ eutectic fibers.

a strong dependence on the strain rate (Fig. 3). This indicates that $Al_2O_3/Y_3Al_5O_{12}$ eutectic fibers show strong resistance to slow crack growth at 1100°C when compared to single-crystal (0001) Al_2O_3.

The resistance and/or susceptibility to slow crack growth can be quantified by determining and comparing the slow crack growth parameter, n from Eq. 1, for each of these fibers. Two test techniques, which have been successfully used for glass and other ceramics (Wiederhorn, 1968; Evans, 1974), were applied for the $Al_2O_3/Y_3Al_5O_{12}$ eutectic fibers to determine n and estimate K_{Ii} in Eq. 2.

The first technique, dynamic loading or dynamic fatigue, can be used to obtain the slow crack growth parameter n as a function of strain rate and temperature. The dynamic loading technique requires a large number of tests for each strain rate. If the strength distributions in two series of specimens are the same, then at equivalent failure probabilities (Evans, 1974):

$$\log \sigma_2 = \log \sigma_1 - \frac{1}{n+1} \log \frac{\dot{\varepsilon}_1}{\dot{\varepsilon}_2} \tag{3}$$

where σ_i is the tensile strength and ε_i is the strain rate used to measure σ_i. The slow crack growth parameter, n, was calculated from the $\log \sigma_i$ versus $\log \varepsilon_i$ re-plots of Fig. 3 at 1100°C (re-plots are not shown). The systematic error due to the uncertainty of absolute strain rate measurement does not introduce large errors in the calculation, because the slow crack growth parameter is being determined from the ratio of at least two different strain rates. The slow crack parameter for $Al_2O_3/Y_3Al_5O_{12}$ eutectic fibers

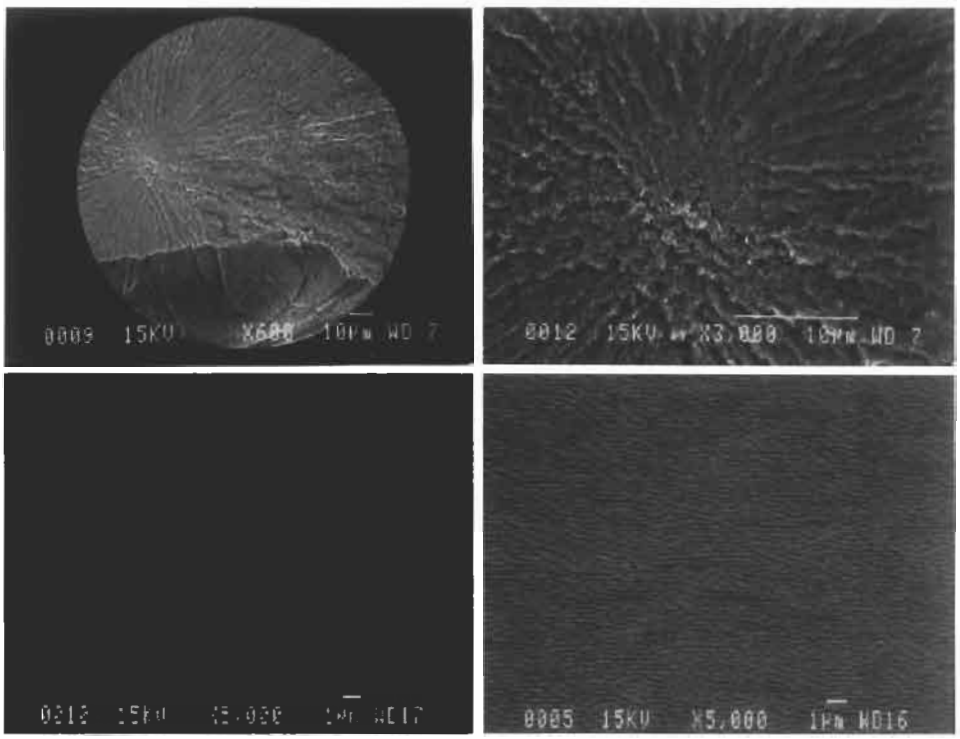

Fig. 6. Low-magnification SEM photo of $Al_2O_3/Y_3Al_5O_{12}$ eutectic fiber showing the overall fracture and its complexity (top left). Higher-magnification photo of the fracture mirror area and failure-initiating flaw; wider bands of $Y_3Al_5O_{12}$ (top right). Different morphologies have been observed along the fiber length. Two examples are shown at the bottom.

was larger than 100, whereas n for ⟨0001⟩ Al_2O_3 at the same conditions was only 12. This clearly indicates that $Al_2O_3/Y_3Al_5O_{12}$ eutectic fibers have superior slow crack growth resistance to ⟨0001⟩ Al_2O_3 fibers at these temperatures for these test durations.

In the second technique, static fatigue, fibers were dead weight loaded. The time to failure for statically loaded $Al_2O_3/Y_3Al_5O_{12}$ eutectic fibers was examined at 1100°C and comparison with ⟨0001⟩ Al_2O_3 fibers is shown in Fig. 7. The $Al_2O_3/Y_3Al_5O_{12}$ eutectic fibers sustained loads of at least 890 MPa without failure at 1100°C in vacuum. Single-crystal ⟨0001⟩ Al_2O_3 fails within 100 h at 620 MPa. Furthermore, residual room temperature tensile strengths of stress rupture survivors were similar to strengths of as-received fibers. Hence, $Al_2O_3/Y_3Al_5O_{12}$ eutectic fibers have superior time to failure under static loading and dynamic loading conditions compared to ⟨0001⟩ Al_2O_3. However, there was an apparent difference in stress levels between dynamic loading (1.39 GPa; Fig. 5) and static loading (0.89 GPa; Fig. 7) conditions. This indicates that, in addition to the slow crack growth parameter, n, the threshold stress intensity factor, K_{I0}, has a profound effect on the life of the material. Thus, the experimental determination of K_{I0} as a function of temperature as well as the intrinsic crack nucleation probability need be assessed.

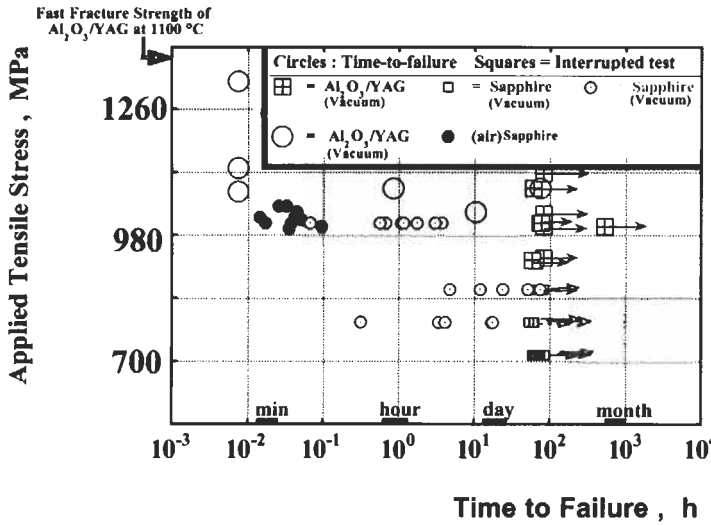

Fig. 7. Time to failure of $Al_2O_3/Y_3Al_5O_{12}$ eutectic fibers as a function of applied stress at 1100°C (vacuum 10^{-6} atm). Circles represent the time to failure at fracture and squares represent experiments typically interrupted at 100 h without fracture.

The directionally solidified $Al_2O_3/Y_3Al_5O_{12}$ eutectic has a very small lamella size of 0.1 to 0.4 μm and hence has a large area of interphase boundaries. The nature of the interface boundaries is very different than grain boundaries of polycrystalline materials. An important characteristic of the $Al_2O_3/Y_3Al_5O_{12}$ eutectic interphase boundary from the fracture point of view is its coherent and strong nature (Matson and Hecht, 1999). The toughness values determined using fracture mechanics analysis (Broek, 1986) assuming entrapped voids as the initial flaw were about 4.6 MPa $m^{-1/2}$. The degree of microstructural anisotropy, although a beneficial condition in promoting improvements in high-temperature mechanical properties, was insufficient to achieve higher toughness and the fine eutectic lamellae have little effect in diverting the path of the fracture crack. The moderate fracture toughness of $Al_2O_3/Y_3Al_5O_{12}$ (4.6 MPa $m^{-1/2}$) is greater than that of either constituent alone (K_{Ic} (Al_2O_3) = 2.4 MPa $m^{-1/2}$) and K_{Ic} ($Y_3Al_5O_{12}$) = 1.7 MPa $m^{-1/2}$). Yang et al. (1996) estimated that $K_{Ic} = 2$ MPa $m^{-1/2}$ using an indentation technique and in regions of exaggerated coarsening. The different estimates of K_{Ic} for $Al_2O_3/Y_3Al_5O_{12}$ are probably due to different estimates of the flaw size. The stress concentration at and around the exaggerated coarsened regions can be greater than the geometric size of the region (Matson and Hecht, 1999).

The strong interface bonding of $Al_2O_3/Y_3Al_5O_{12}$ eutectic is highly beneficial to increased creep resistance by load transfer from one phase to another. For $Al_2O_3/Y_3Al_5O_{12}$ eutectic fibers, typical time-dependent creep strain data measured in vacuum are shown in Fig. 8. The creep rate constantly decreases with time, giving the appearance of a primary or transient creep stage up to 0.4% or more strain. Fiber fracture occurs during this stage at 1100°C. A comparison of creep rate with available literature values for single-crystal ⟨0001⟩ Al_2O_3 and $Y_3Al_5O_{12}$ indicates that the $Al_2O_3/Y_3Al_5O_{12}$

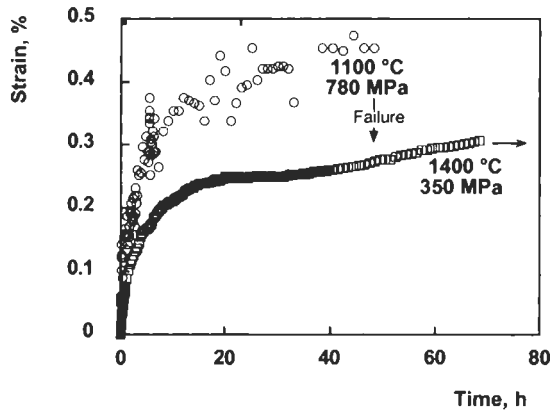

Fig. 8. Creep curves of $Al_2O_3/Y_3Al_5O_{12}$ eutectic fibers at constant stress and temperature (vacuum 10^{-6} atm).

eutectic fiber has comparable creep resistance to ⟨0001⟩ Al_2O_3, is better than off-axis Al_2O_3 but is not as good as single-crystal $Y_3Al_5O_{12}$. Similar conclusions have been suggested for bulk eutectic (Parthasarathy and Mah, 1993) of similar composition. More creep tests on fibers at temperatures of 1400 to 1700°C have been completed by Matson and Hecht (1999). The results showed significant variations in the stress exponent as a function of test temperature. From TEM analysis Matson concluded that the Al_2O_3 phase was deforming by a dislocation mechanism, while the $Y_3Al_5O_{12}$ phase deformed by a diffusional mechanism. This would suggest that producing eutectic fiber with very small lamella size is desirable to increase the creep resistance. The decrease in Al_2O_3 phase thickness would lead to an increase in the backstress due to dislocation pile-up and thereby increase creep resistance. Similar findings have been observed in directionally solidified $Al_2O_3/ZrO_2(Y_2O_3)$ eutectic (Sayir and Farmer, 2000). Any attempt to reduce the lamella size to improve creep resistance requires increasing the pull-rate of the fibers. This may have a limited amount of success due to the facet forming tendency of the phases which are themselves a source of stress concentration.

CONCLUSIONS

To meet the specific requirements for tensile testing of single-crystal fibers, a new technique based on original work by Yamaguchi's speckle shift method was utilized to measure the micro-strain. The Young modulus of ⟨0001⟩ Al_2O_3, ⟨111⟩ $Y_3Al_5O_{12}$ and ⟨111⟩ Y_2O_3 fibers were 453, 290, and 164 GPa, respectively, and agreed well with the literature. Single crystals of ⟨111⟩ Y_2O_3 were the weakest fibers and their strength did not exceed 700 MPa. The fracture characteristics of single-crystal ⟨0001⟩ Al_2O_3, ⟨111⟩ $Y_3Al_5O_{12}$, and ⟨111⟩ Y_2O_3 fibers were anisotropic. All Y_2O_3 fibers fractured by octahedral cleavage, and cleavage was often perpendicular to the fiber axis indicating that this axis coincides with the ⟨111⟩ crystallographic direction as determined from

X-ray characterization. The moderate tensile strength of single-crystal ⟨111⟩ $Y_3Al_5O_{12}$ was controlled by facet forming tendency of the cubic garnet structure and in some cases by the precipitation of cubic perovskite phase $YAlO_3$. The tensile strength of single-crystal ⟨0001⟩ Al_2O_3 fibers was 6.7 GPa and is among the highest tensile strength values reported in the literature for continuous fibers. The strength controlling defects were processing flaws related to facet forming tendency.

High-strength single-crystal ⟨0001⟩ Al_2O_3 fibers did not retain their strength at elevated temperatures. The data suggest that single-crystal ⟨0001⟩ Al_2O_3 failure was dependent on slow crack growth at elevated temperatures. A phenomenological description has been provided to predict the time to failure, but the microscopic mechanism controlling the high-temperature strength of Al_2O_3 remains to be elucidated.

The room temperature tensile strength of $Al_2O_3/Y_3Al_5O_{12}$ eutectic fibers was 2.39 GPa, considerably lower than the tensile strength of single-crystal ⟨0001⟩ Al_2O_3 fibers. The high-temperature tensile strength of $Al_2O_3/Y_3Al_5O_{12}$ eutectic fibers is superior to sapphire (1.3 GPa at 1100°C) and demonstrably less prone to slow crack propagation. The $Al_2O_3/Y_3Al_5O_{12}$ eutectic interphase boundary is of a coherent nature with strong bonding. Fracture occurred in a brittle manner. The $Al_2O_3/Y_3Al_5O_{12}$ eutectic has a high degree of microstructural anisotropy combined with strong bonding between the phases and possesses superior creep resistance.

REFERENCES

Barranger, J.P. (1990) *Two-dimensional surface strain measurement based on a variation of Yamaguchi's laser-speckle strain gauge*. NASA TM-103162.

Broek, D. (1986) *Elementary Engineering Fracture Mechanics*, 4th ed. Martinus Nijhoff, Boston, MA.

Caslavsky, J.L. and Viechnicki, D.J. (1980) Melting behavior and metastability of yttrium aluminum garnet (YAG) and $YAlO_3$ determined by optical differential thermal analysis. *J. Am. Ceram. Soc.*, 15: 1709–1712.

Corman, G.S. (1991) High temperature creep of some single crystal oxides. *Ceram. Eng. Proc.*, 12: 1745–1767.

Evans, A.G. (1974) Slow crack growth in brittle materials under dynamic loading conditions. *Int. J. Fract.*, 10: 251–259.

Farmer, S.C., Sayir, A. and Dickerson, P.O. (1993) Mechanical and microstructural characterization of directionally solidified alumina–zirconia eutectic fibers. In: *Symposium Proceedings of In-Situ Composites, Science and Technology*, pp. 167–182. TMS, Warrendale, PA.

Hsieh, C. and Thomson, R. (1973) Lattice theory of fracture and crack creep. *J. Appl. Phys.*, 44: 2051–2063.

Kitayama, M., Powers, J.D., Kulinsky, L. and Glaesar, A.M. (1999) *J. Eur. Soc.*, 19: 2191–2209.

Lant, C.T. and Barranger, J.P. (1990) *Progress in High Temperature Speckle-Shift Strain Measurement*. NASA TM-103255.

Lawn, B.R. (1975) An atomistic model of kinetic crack growth in brittle solids. *J. Mater. Sci.*, 10: 469–480.

Matson, L.E. and Hecht, N. (1999) Microstructural stability and mechanical properties of directionally solidified alumina/YAG eutectic monofilaments. *J. Eur. Ceram. Soc.*, 19: 2487–2501.

Palko, J.W., Sinogekin, S.V., Kriven, W.M., Bass, J.D. and Sayir, A. (2001) The single crystal elasticity of yttria to high temperature. *J. Appl. Phys.*, 89: 7791–7796.

Parthasarathy, T.A. and Mah, T. (1993) Deformation behavior of an Al_2O_3–$Y_3Al_5O_{12}$ eutectic composite in comparison with sapphire and YAG. *J. Am. Ceram. Soc.*, 76: 29–32.

Roth, R. and Schneider, H. (1960) Stability relations of the polymorphic forms of rare earth sesquioxides. *J. Res. Natl. Bur. Stand.*, 64A: 309–314.

Sayir, A. (1993) Time dependent strength of sapphire fibers at high temperatures. In: *Advances in Ceramic Matrix Composites I*, pp. 691–702, N. Bansal (Ed.). American Ceramic Society, Westerville, OH.

Sayir, A. and Farmer, S.C. (2000) The effect of microstructure on mechanical properties of directionally solidified $Al_2O_3/ZrO_2(Y_2O_3)$ eutectic. *Acta Mater.*, 48: 4691–4697.

Sayir, A. and Matson, L.E. (1991) *Growth and characterization of directionally solidified $Al_2O_3/Y_3Al_5O_{12}$ (YAG) eutectic fibers.* HITEMP Review 1991: Advanced High Temperature Engine Materials Technology Program, NASA CP10082, pp. 83.1–83.13.

Sayir, A., Greer III, L.C., Goldsby, J. and Oberle, L. (1994) Laser speckle micro-strain measurements on small diameter fibers. *Ceram. Eng. Sci. Proc.*, 18: 397–410.

Snow, J.D. and Heuer, A.H. (1973) Slip systems in Al_2O_3. *J. Am. Ceram. Soc.*, 56: 153–157.

Viechnicki, D. and Schmid, F. (1969) Eutectic solidification in the system $Al_2O_3/Y_3Al_5O_{12}$. *J. Mater. Sci.*, 4: 84–88.

Wachtman, J.B. (1960) Elastic constants of synthetic single crystal corundum at room temperature. *J. Res. NBS*, 64A(3).

Wiederhorn, S.M. (1968) Moisture assisted crack growth in ceramics. *Int. J. Fract. Mech.*, 4: 171–177.

Yang, J.-M., Jeng, S.M. and Chang, S. (1996) Fracture behavior of directionally solidified $Y_3Al_5O_{12}/Al_2O_3$ eutectic fiber. *J. Am. Ceram. Soc.*, 79: 1218–1222.

GLASS FIBERS

Fiber Fracture
M. Elices and J. Llorca (Editors)

STRENGTH OF GLASS FIBERS

Prabhat K. Gupta

Department of Materials Science and Engineering, The Ohio State University, 2041 College Road, Columbus, OH 43210, USA

Introduction . . . 129
Basic Concepts . . . 131
Flaws and Cracks . . . 131
Pristine and Non-Pristine Fibers . . . 131
Statistics of Measured Strengths . . . 131
Intrinsic Strength, S^* . . . 132
Extrinsic Strength, S . . . 133
Inert Strength, S_0 . . . 133
Theoretical Strength, S_{th} . . . 133
Diameter and Length Dependence of Inert, Extrinsic Strength, $S_0\,(d, L)$ . . . 134
Fatigue Strength, $S(\varepsilon_t, X, T)$ . . . 134
Delayed Failure (Static Fatigue) . . . 135
Slow Crack Growth Model of Extrinsic Fatigue . . . 135
The Inert Strength . . . 136
The Time to Failure, $t(T, X, s)$ . . . 136
The Strain Rate Dependence of Strength . . . 136
The Temperature Dependence of Strength . . . 136
The Humidity Dependence of Strength . . . 137
Extrinsic Strength of Glass Fibers — Experimental Results . . . 137
Extrinsic Inert Strength . . . 139
Inert Strength Distributions . . . 139
Fractography of Low-Strength Breaks . . . 139
Extrinsic Fatigue Strength . . . 141
Intrinsic Strength of Glass Fibers — Experimental Results . . . 143
Room Temperature Intrinsic Strength, S^*(RT) . . . 143
E-glass Fibers . . . 143
Silica Fibers . . . 144
S-glass Fibers . . . 145
Liquid Nitrogen Temperature Intrinsic Strength, S_0^* . . . 146
E-glass Fibers . . . 146
Silica Fibers . . . 146

Fatigue in Pristine Fibers 146
Concluding Remarks 150
Acknowledgements 151
References 151

Abstract

Present understanding of strength of bare glass fibers is reviewed. Key experimental results on the strengths of E-glass and silica fibers are examined to identify factors which control the strength and fatigue in glass fibers. The strength of pristine fibers can be classified (a) as intrinsic or extrinsic, and (b) as inert or fatigue. For improved fiber reliability and production efficiencies, one is primarily interested in extrinsic fatigue strength. On the other hand, for basic understanding of strength in terms of the structure of glass, one is interested in the intrinsic inert strength and its variation with composition. While much work has been done in the past, fundamental questions remain unanswered about both the extrinsic and the intrinsic strengths. For the extrinsic strengths, the important questions pertain to the identity of the flaws and the role of crack nucleation around inclusions. The difficulty in studying large extrinsic flaws lies in the fact that they occur very infrequently (one flaw in hundreds of kilometers of fiber!). For the intrinsic strengths, the key questions are (a) what determines the intrinsic strength of a fiber? and (b) why do pristine flawless fibers exhibit fatigue which is qualitatively (and to a significant extent quantitatively) similar to that in non-pristine fibers?.

Keywords

Intrinsic strength; Extrinsic strength; Inert strength; Fatigue strength; Flaws; Slow crack growth; Weibull distribution; Fractography; E-glass; Silica glass

INTRODUCTION

Fibers constitute a major component of the glass industry. The traditional fiberglass companies manufacture either reinforcement fibers (E-glass being the principal composition, see Table 1) or fibers for thermal and acoustic insulations (Gupta, 1988; Dwight, 2000). During the last two decades, a new glass fiber industry, namely the fiber optics industry, has seen explosive growth based on the use of silica glass fibers as optical waveguides (Izawa and Sudo, 1987; Hecht, 1999). These applications require high tensile strengths over long periods of time (as much as 20 years in the fiber-optic telecommunication applications). As a consequence, there has been a great interest in the past in studying the strength of glass fibers and much has been learned and reviewed in the literature (Kurkjian, 1985; Kurkjian et al., 1993).

Presently, glass fibers are produced routinely with strengths which are more than adequate for their intended use. For example, silica fibers are manufactured with a proof-tested strength of 700 MPa. With the achievement of such high strengths, the technological interest in furthering the understanding of strength of glass fibers has subsided in recent years and has shifted, instead, towards improving the production efficiencies by elimination of the sources of low strength fibers (Gulati, 1992). Nonetheless, there remains a strong fundamental interest in the strength of glass fibers for two reasons.

(1) The strength of pristine (flaw free) fibers is the 'intrinsic' strength of a glass composition.

Intrinsic strength refers to strength of a glass containing no flaws either in the bulk or on the surface. The intrinsic strength is determined by the composition and structure of a glass. Strength controlled by flaws is called *extrinsic*. Unlike intrinsic strength, extrinsic strength is not a unique function of glass composition. While much has been learned about extrinsic strength, the understanding of intrinsic strength remains poor and unsatisfactory. For example, answers to simple questions such as the ones listed below are not available at present.

(1) How does intrinsic strength vary with composition of a glass?

Table 1. Compositions of technologically important glass fibers

Composition (wt%)	E-glass	S-glass	Silica
SiO_2	52–56	65	100
Al_2O_3	12–16	25	
B_2O_3	5–10		
CaO	16–25		
MgO	0–6	10	
$Na_2O + K_2O$	0–2		
Fiber information			
Diameter (μm)	5–30		125
Composition profile	homogeneous		core/clad
Method of making	melt		preform

(2) How is intrinsic strength related to other intrinsic properties like Young's modulus or surface tension of a glass?
(3) Is intrinsic strength controlled by crack nucleation in a flaw-free glass?
(4) Is there any role of structural or stress relaxation in determining the intrinsic strength of a glass?

(2) Pristine fibers exhibit fatigue much like fibers containing microcracks. However, the mechanisms of fatigue in the absence of cracks are not well understood at present.

Strength of a glass fiber depends on the way it is measured. In other words, the measured strength is a function of testing variables such as the type of test (pure tension or bend test), the strain rate used, and the relative humidity and the temperature of the testing environment. The testing parameters influence the measured value of the strength because of a stress-enhanced environment-induced phenomenon known as *fatigue*. Strength measured in the absence of fatigue is called *inert strength*. Fatigue causes the strength of a glass sample to degrade with time in the presence of stress. Because of fatigue, failure can occur after a sufficiently long time at values of stress much less than the inert strength. The mechanism of fatigue in glasses containing cracks is reasonably well understood. It occurs as a result of a chemical reaction between adsorbed water and the stressed siloxane bond at the crack tip leading to slow growth of the crack length (Wiederhorn et al., 1980):

$$\underset{\text{(adsorbed)}}{H_2O} + \underset{\text{(Siloxane bond)}}{\equiv Si{-}O{-}Si\equiv} \xrightarrow{\text{(tensile stress)}} \underset{\text{(broken bonds)}}{2Si{-}OH}$$

Interestingly, pristine fibers also exhibit fatigue which is qualitatively similar to fatigue in fibers with cracks. However, the mechanism of fatigue in the absence of cracks is not clear at present. Such an understanding is required for the estimation of the life times of fibers under low levels of stress (Gupta et al., 2000).

The purpose of this paper is to provide a review of strength of bare glass fibers. The emphasis is on fundamental aspects. Methods to protect the high strength of fibers, for example by application of coatings (Kurkjian et al., 1993; Dwight, 2000), are not included. Much of the data discussed throughout this paper are for two compositions: silica and E-glass (see Table 1). This is because these two compositions have been studied most extensively and reliable data under a variety of test conditions are available from several independent sources.

The basic concepts of glass fiber strength are summarized first along with an introduction of the relevant terminology. The subject of glass fiber strength naturally partitions into four separate categories: (a) extrinsic, inert strength; (b) extrinsic, fatigue strength; (c) intrinsic, inert strength; and (d) intrinsic, fatigue strength. Extrinsic strength is discussed next as it is better understood than intrinsic strength. This provides a sound basis for subsequent discussion of intrinsic strength which is followed by concluding remarks.

BASIC CONCEPTS

Flaws and Cracks

A flaw is an extrinsic defect in a glass. Common examples of (3-dimensional) flaws are scratches, indents, inclusions, devitrified regions, and bubbles. Sometimes, one speaks of 'intrinsic flaws' when referring to the intrinsic inhomogeneities present in a glass. Examples of intrinsic inhomogeneities are point defects, structural inhomogeneities caused by frozen-in density and composition fluctuations, and nanoscale roughness on glass surface (Gupta et al., 2000). In this paper, the term flaw is used to indicate extrinsic flaws.

A crack is a 2-dimensional flaw; an area across which the bonds are broken. The boundary of this area is called the crack tip. The curvature (normal to the plane of the crack) at the tip is assumed to be infinitely sharp in the continuum models but is of atomistic dimensions in real materials. The detailed atomistic structure of a crack tip is unresolved at present (Lawn, 1993). In silicate glasses, a crack tip has a radius of curvature on the order of 0.3 nm which is approximately the size of a single siloxane bridge [≡Si–O–Si≡].

Under the application of a tensile stress, 3-dimensional flaws (e.g., pores and inclusions) cannot grow. Only cracks can grow under tensile stress. Sometimes one speaks of the 'growth of a flaw' (not a crack), implying the growth of a microcrack nucleated at or near that flaw. It is clear that, when a material does not have a pre-existing crack, a crack must nucleate at some moment of time prior to fracture.

Pristine and Non-Pristine Fibers

Fibers without flaws are called *pristine* or 'flawless'. Fibers with flaws are called *non-pristine*. Routinely manufactured fibers are generally non-pristine. Measuring strength of pristine fibers is tedious. It requires a careful preparation of the starting materials (melt in the case of E-glass and preform in the case of silica fibers) to ensure that they are free of flaws, careful forming of fibers in ultra-clean environments, capturing bare fiber samples before they come in contact with any other surface (such as the coating applicator or the collection drum), and testing of a large number of small fiber lengths immediately after capture with minimum additional handling. Even after all these precautions, it is often not easy to establish whether pristine fiber strengths are being measured in an experiment. This is usually accomplished by accumulating data over many experiments as a function of several experimental parameters and making sure that the measured strengths are amongst the highest ones measured and are reproducible.

Statistics of Measured Strengths

Measured strengths of identically prepared glass fibers always show a distribution. Although without any fundamental basis, it is customary to plot the measured strength distribution on a Weibull plot where the ordinate is $\ln\{\ln[1/(1-P)]\}$ and the abscissa is $\ln S$. Here $P(S)$ is the cumulative probability of failure for strengths less than or equal to

S. When measured strength values fall on a straight line (with slope m), the data imply a (unimodal) Weibull distribution of strengths (Epstein, 1948; Freudenthal, 1968; Hunt and McCartney, 1979; Katz, 1998):

$$P(S) = 1 - \exp\left[-(S/S_R)^m\right] \tag{1}$$

Here S_R is a scaling parameter which is related to the average strength, $\langle S \rangle$, as follows:

$$\langle S \rangle = S_R \Gamma(1 + 1/m) \tag{2}$$

where $\Gamma(x)$ is the Gamma function of x. The coefficient of variation, COV, of strength is related to the Weibull modulus 'm' according to the following relation:

$$\text{COV} = \left\{[\Gamma(1 + 2/m)/\Gamma^2(1 + 1/m)] - 1\right\}^{1/2} \approx 1.28/m \tag{3}$$

According to Eq. 3, the higher the Weibull modulus the lower is the value of COV. For example, a 3% COV corresponds to an m of about 40 and a 12% COV corresponds to an m of about 10.

When the measured strengths do not fall on a straight line in a Weibull plot, one can fit the data to a combination of straight line segments. In this case, the Weibull distribution is referred to as bimodal (if two lines are sufficient to describe the data) or multi-modal (if more than two lines are needed).

Intrinsic Strength, S^*

When there are no flaws present, the measured strengths are called intrinsic. The strength of pristine fibers therefore provides the intrinsic strength of a glass composition. The intrinsic strength is denoted by S^*. Intrinsic strengths are measured when the following three conditions are satisfied:

(1) Measured strength is constant with respect to the fiber diameter and length.

(2) COV (strength) $\approx$ 2 COV (diameter). Diameter variations are always present in fibers. The magnitude of these variations depends on the method of making fibers (Kurkjian and Paek, 1983). However, the primary source of diameter uncertainty in a strength measurement lies in the fact that a high-strength glass fiber upon fracture disintegrates into a large number of small pieces and the fracture surfaces are not available. Therefore, the diameter cannot be measured at the point of fracture and is typically measured at some distance away from the point of fracture. A second source of uncertainty, especially in the case of thin fibers, lies in the measurement precision when using optical microscopy. For example, a 0.1 μm measurement uncertainty in a 10 μm diameter fiber gives rise to a 2% uncertainty in the fiber strength.

(3) Measured strengths are amongst the highest ones measured (typically $> E/20$, E being Young's modulus).

Because the probability of the presence of an extrinsic flaw increases with increase in volume or in total surface of test samples, intrinsic strength measurements require fiber samples of as small a diameter and as small a length as possible. The two-point bend technique (Matthewson et al., 1986) currently provides the simplest way of carrying out such experiments provided the fiber is not too thin (diameter > 50 μm). This technique is routinely used for testing silica fibers (typical diameter of 125 μm). For

smaller-diameter E-glass fibers (5–20 μm), testing in pure tension is the only method available at present for measuring intrinsic strengths.

It should be pointed out that the intrinsic strength of a glass is not a constant. The intrinsic strength values for a given composition vary with testing conditions (environmental humidity, and temperature).

Extrinsic Strength, S

Flaw-controlled strengths are called extrinsic. The strengths of non-pristine fibers are extrinsic by definition. Extrinsic strengths show larger COV than can be accounted for from fiber diameter variations alone. The additional variation in strength arises from the variation in the severity of the most severe flaws in different samples. Gupta (1987) has carried out a detailed analysis of the measured strength distributions by combining the variations in fiber diameter and in the flaw-severity statistics.

Inert Strength, S_0

Strength measured in the absence of fatigue is called the inert strength. Inert strength should not be confused with intrinsic strength. Inert refers to absence of fatigue while intrinsic refers to absence of flaws. In this paper, the inert strength is denoted by S_0.

In principle, inert strength can be measured by using testing conditions which minimize fatigue (such as dry environment or vacuum and sufficiently large strain rates so that the fatigue reaction does not have time to progress). All these approaches have been attempted with varying degrees of success. However, inert strengths are measured most conveniently by testing at the liquid N_2 temperature (77 K) where the rate of the fatigue reaction is sufficiently small to be considered negligible. Several experiments have demonstrated that the measured strength at room temperature under conditions of high vacuum approaches the measured strength at the liquid nitrogen (LN) temperatures (France et al., 1980; Roach, 1986; Smith and Michalske, 1989). In other words, there is no significant temperature dependence of the inert strength. The temperature dependence from other intrinsic properties such as E is negligible. It follows, therefore, that

$$S_0 = S_{LN} \tag{4}$$

where S_{LN} is the strength measured at the liquid N_2 temperature.

Theoretical Strength, S_{th}

The strengths of pristine fibers at the liquid nitrogen temperature, S^*_{LN}, are the highest strength values measured for a given composition. One might expect S^*_{LN} in the absence of flaws to be equal to the theoretical strength, S_{th}, of a glass:

$$S^*_{LN} = S_{th} \tag{5}$$

Unfortunately, at present, theoretical estimates of S_{th} do not exist for multicomponent compositions (such as E-glass) and are not reliable even for simple one-component glasses. For example, estimates of the theoretical strength of silica based on cohesive

bond failure and a perfect crystalline lattice vary by as much as 100% (France et al., 1985). Several models relate the theoretical strength to a product of Young's modulus E and surface tension γ. However, it is not clear whether the intrinsic strength is simply related to E. This is because E is determined by the harmonic part of the pair interaction. The strain to break a bond, on the other hand, is determined by the inflection point (i.e., the anharmonic part) of the interaction. Similarly, the surface tension depends on the depth of the potential well but contains little information about the inflection point. Therefore, a product of E and γ will not have any information about the inflection point of the interaction potential and therefore may not be directly related to the intrinsic strength.

Molecular dynamics (MD) simulations have shed some light on the atomistics of the fracture behavior of silica glass. For example, Soules (1985) has shown that the random structure weakens silica glass, relative to the cristobalite crystalline structure, by about a factor of 3. Simmons (Simmons et al., 1991; Simmons, 1998) has shown that structural relaxation and surface reconstruction play important roles at the crack tip. However, MD simulations do not provide an accurate estimate of intrinsic strength largely because of uncertainty in the anharmonic part of the interaction potentials. It is clear that accurate calculations of theoretical strength will require (1) a detailed knowledge of the long-range behavior of the interatomic interaction potentials (or the nonlinear aspects of the interatomic forces); (2) a knowledge of the covalent bonds which are necessarily three- or multi-body interactions; (3) a knowledge of the intermediate range structure of the glass network; (4) a knowledge of the effect of topological disorder on the stress concentration; and (5) use of finite temperature to allow for structural changes.

Diameter and Length Dependence of Inert, Extrinsic Strength, S_0 (d,L)

Because the probability of finding a flaw of a given severity increases with increase in the volume or surface of a fiber sample, the average strength tends to decrease with increase in length or diameter. Using the weakest link model, the cumulative probability of failure of a fiber can be shown to be (Hunt and McCartney, 1979):

$$P(S_0, L, d) = 1 - \exp\left[-(L/L_R)(d/d_R)^k (S_0/S_R)^m\right] \tag{6}$$

where $k = 1$ for surface flaws and $k = 2$ for volume (or bulk) flaws, and L_R and d_R are reference fiber length and fiber diameter, respectively.

From Eq. 6, it can be shown that the average strength $< S_0 >$ decreases with increase in L or in d according to the following equation:

$$\langle S_0 \rangle (L,d) = S_R \left[(L/L_R)(d/d_R)^k\right]^{(-1/m)} \Gamma(1 + 1/m) \tag{7}$$

It can also be shown that, according to Eq. 6, the coefficient of variation in strength is independent of the fiber length or fiber diameter.

Fatigue Strength, $S(\varepsilon_t, X, T)$

Because of fatigue, strength measured under non-inert conditions increases with increase in strain rate, ε_t. Strength measured at a constant (but moderate) strain rate at

some (not too low) temperature, T, and in an environment of relative humidity, X, is called the fatigue strength. Strength is frequently measured under conditions of constant strain rate, called the 'dynamic fatigue' experiment.

Delayed Failure (Static Fatigue)

Another consequence of fatigue (which is of significant technological importance) is that a sample may fail after a long time under constant stress which is much less than the short-term fracture stress. This phenomenon is known as 'delayed failure' or 'static fatigue'. Experimental results show that the time to failure, $\tau(T, X, \sigma)$, decreases rapidly with increase in applied stress, σ, with increase in relative humidity of the environment, X, and with increase in temperature, T.

Slow Crack Growth Model of Extrinsic Fatigue

Denoting the size of a crack by, C, the rate of growth of this crack (or the crack velocity) due to fatigue increases with relative humidity, X, and temperature, T, of the testing environment and the stress at the crack tip (characterized by the stress intensity factor K) according to the following empirical power law relation (Charles, 1958; Wiederhorn, 1967; Freiman, 1980):

$$V \equiv \mathrm{d}C/\mathrm{d}t = V_0 X^{\alpha} \exp[-Q/\mathrm{RT}][K/K_c]^N \tag{8}$$

Here Q is the activation energy of the reaction, K_c the critical stress intensity factor (also known as the fracture toughness and is considered an intrinsic property of a homogeneous material), N the stress corrosion susceptibility, α the humidity exponent, and V_0 the pre-exponential factor. The stress intensity factor, K, is given by:

$$K = Y\sigma C^{1/2} \tag{9}$$

where σ is the applied stress (far from the crack tip) and Y is a dimensionless coefficient ($\sim \sqrt{\pi}$), the exact value of which depends on crack/sample geometrical configuration (Rooke and Cartwright, 1976; Hertzberg, 1989). It should be clear that a larger N implies less susceptibility to fatigue.

A much discussed alternative to Eq. 8 is the exponential equation (Wiederhorn, 1975; Michalske et al., 1993):

$$V = V_0 X^{\alpha} \exp[-Q/\mathrm{RT}] \exp[b(K - K_c)/\mathrm{RT}] \tag{10}$$

By comparing Eqs. 8 and 10, Gupta (1982) has shown that

$$N \approx bK_c/\mathrm{RT} \tag{11}$$

Experimentally, the values of the stress corrosion susceptibility range from about 15 to 40 and are known to vary with T (Hibino et al., 1984) and the environment (Armstrong et al., 1997). Clearly, N is not a material parameter.

While Eq. 10 has a more sound basis, as follows directly from the phenomenology of chemical kinetics (Wiederhorn et al., 1980), than Eq. 8, both equations appear to fit the data equally well and have the same number of fitting parameters. Since analytical expressions can be readily obtained for Eq. 8, it is more convenient to use.

According to fracture mechanics, catastrophic fracture (fast crack growth) occurs at the Griffith–Irwin criterion (Lawn, 1993) given by

$$K = K_c \tag{12}$$

Eqs. 8, 9, and 12 together are referred to as the slow crack growth model and describe fatigue completely in non-pristine fibers. Important consequences of the slow crack growth model are summarized in the following.

The Inert Strength

The inert strength is given by:

$$S_0 = K_c \Big/ \left[Y C_0^{1/2} \right] \tag{13}$$

where C_0 is the initial size of the most severe crack in a sample.

The Time to Failure, $\tau(T, X, \sigma)$

As a function of the applied stress σ, relative humidity X, and temperature T (Gupta, 1983), it is given by:

$$\tau(T, X, \sigma) \approx \{2/[(N-2)V_0]\} X^{-\alpha} \exp(Q/\mathrm{RT})[K_c/YS_0]^2 [S_0/\sigma]^N \tag{14}$$

The Strain Rate Dependence of Strength

At a constant T and X, strength increases with increase in strain rate, ε_t, according to the following equation (Gupta, 1983):

$$\ln S = [1/(N+1)] \ln \varepsilon_t + \text{constant} \tag{15}$$

This equation for dynamic fatigue provides a convenient way of measuring the stress corrosion susceptibility N.

The Temperature Dependence of Strength

Gupta (1983) has also shown that the temperature dependence of strength caused by fatigue can be expressed as:

$$\ln S(T) = \{Q/[(N+1)\mathrm{RT}]\} + \text{constant} \tag{16}$$

According to Eq. 16, strength decreases with increase in T approximately in an Arrhenius manner with an apparent activation energy equal to $[Q/(N+1)]$. This decrease is caused by the increased slow crack growth rate at higher temperatures. Eq. 16 is valid as long as fatigue is present. It is not valid at sufficiently low temperatures (such as the liquid N_2 temperature where the fatigue reaction is frozen). At sufficiently low temperatures, strength is constant ($= S_{LN}$).

Eq. 16 has been derived assuming constant relative humidity of the testing environment. If the experiment is performed under conditions of constant absolute humidity, a

different equation will be obtained which will show that the strength will increase with increase in temperature (different from the prediction of Eq. 16) due to rapid desorption of water from the crack surface.

The Humidity Dependence of Strength

Using Eq. 8, it can also be shown (Gupta, 1983) that at a fixed temperature and a fixed strain rate, strength will decrease with increase in the relative humidity of the testing environment according to the following equation:

$$\ln S(X) = -[\alpha/(N+1)]\ln X + \text{constant} \tag{17}$$

EXTRINSIC STRENGTH OF GLASS FIBERS — EXPERIMENTAL RESULTS

Potentially, there are many kinds of flaws that may be present in fibers. Fig. 1 shows a fish-bone chart showing parameters in various stages of fiber production (glass melting and fiber drawing) and testing of E-glass fibers which may influence the measured fiber strength. The frequency of occurrence of a given type of flaw decreases with increase in the severity of the flaw. Thus large flaws occur less frequently than small flaws. For

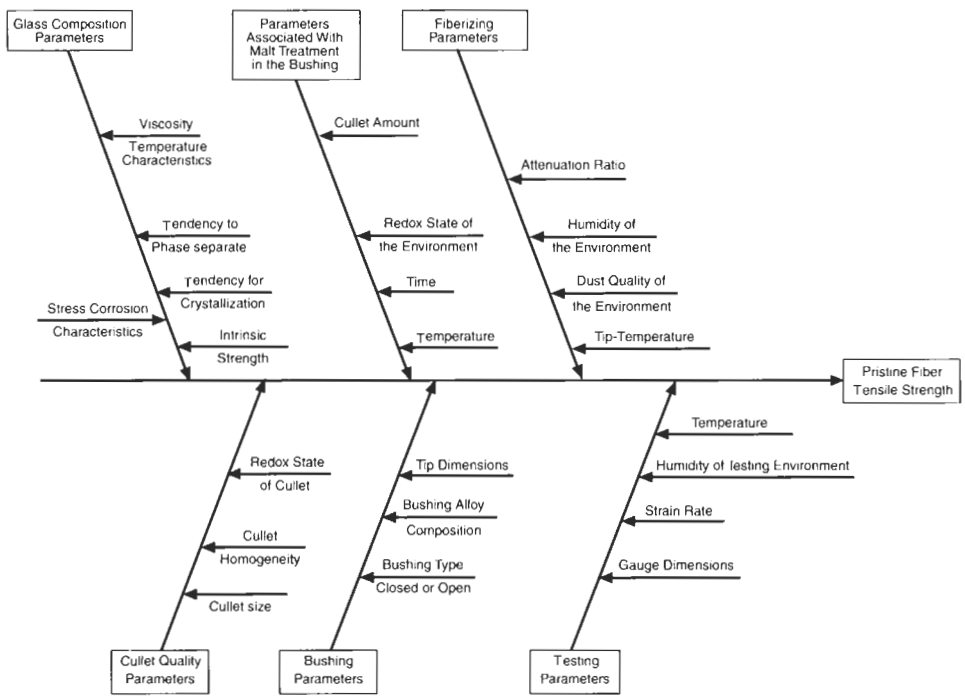

Fig. 1. Fish-bone chart of the experimental parameters which may influence the measured strength of melt-drawn fibers.

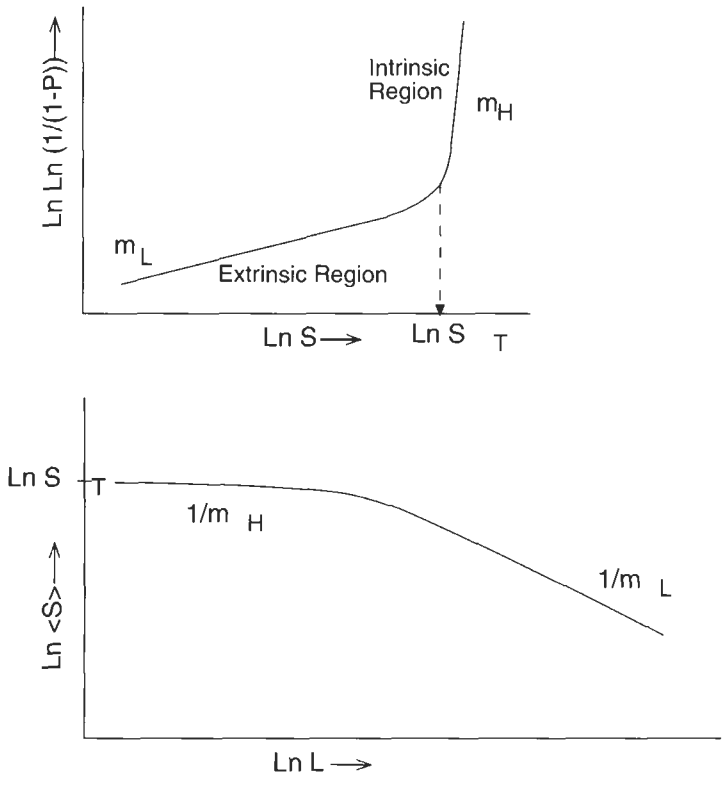

Fig. 2. Length dependence of the extrinsic inert strength of fibers with bimodal distribution.

this reason the fracture initiating flaws in long lengths of fibers are generally different than those in small lengths of fibers. Decrease of strength with increase in length or diameter is generally considered a strong indicator of extrinsic strengths. Intrinsic strengths, on the other hand, are constant with respect to length and diameter. Fig. 2 shows schematically the length dependence of the strength of fibers having a bimodal Weibull distribution of strengths. Eq. 7, which gives the length and diameter dependence of the inert extrinsic strength of fibers, is valid only when a single mode is dominant.

Much of the past work on fiber strengths reported in the literature has two intertwined themes for improvement in the average fiber strength: (1) by adjustments of glass composition, and (2) by adjustments in the fiber manufacture process. The first approach, in principle, requires an understanding of the intrinsic strength as a function of composition. However, frequently, composition changes lead to changes in the nature and density of extrinsic flaws and consequently influence the extrinsic strength. Adjustments in the process are generally designed to eliminate the sources of low strengths which are caused by (relatively large) flaws. In addition, large cracks grow rapidly in fatigue and tend to dominate the fatigue behavior of the long fibers. Thus the strength and fatigue behavior of large cracks is of considerable technological interest in applications requiring long lengths (such as glass fibers for telecommunication).

Extrinsic Inert Strength

Inert Strength Distributions

Inert extrinsic strength is of interest to fiber manufacturers as it is the inert strength which is actually 'sold' by a fiber producer. Inert strength can be measured by testing (a) at liquid nitrogen temperatures, (b) at room temperature in vacuum, (c) at room temperature using very high strain rates, and (d) at room temperature in moisture-free inert environment such as dry nitrogen or in oil. Measurements on small-length samples are convenient but do not sample large flaws. The measurements of inert strengths of long lengths of fibers are difficult but are necessary to sample the low-frequency large flaws. These inert strengths can be estimated from measured room temperature strengths by correcting for the fatigue effects. If the inert strength distribution is single-mode Weibull (as given by Eq. 1) then the measured strength distribution during a constant strain rate, ε_t, experiment at a temperature, T, follows:

$$P(S) = 1 - \exp\left\{-(S/S_R)^m \left[1 + R(S/S_R)^3\right]^{(m/(N-2))}\right\} \tag{18}$$

where

$$R \equiv \left[(N-2)V_0 X^\alpha \exp(-Q/\mathrm{RT}) Y^2 S_R^3\right] / \left[2(N+1)K_c^2 E \varepsilon_t\right] \tag{19}$$

Glaesemann and Helfinstine (1994) have used a similar equation to reconstruct inert strengths of long silica fibers (lengths = 823 km) from measured strength distributions at room temperature.

Fractography of Low-Strength Breaks

Fractography is a powerful method of identifying the nature and location of the fracture initiating flaws (Mecholsky, 1994). It is not possible to use fractography for high-strength fibers because, upon fracture, high-strength fibers disintegrate into powder. When fiber strengths are low (<1 GPa), it generally becomes possible to capture the fracture surfaces and examine them by scanning electron microscopy. This requires examination of several fracture surfaces, since most of the time no flaw is observed. Even when one locates a flaw, there is not a single type that stands out in a population of fracture surfaces. Sometimes, however, unexpected flaws show up. For example, Fig. 3 shows a SEM image of an E-glass fiber fracture surface which failed at room temperature at a strength of 745 MPa (Gupta, 1994). In this case the fiber was drawn using a one-hole platinum bushing in the laboratory. The fracture was clearly initiated by the crystalline platinum inclusion in the bulk of the fiber. The precise mechanism of the melt–platinum interaction which generated such a crystal is unclear. A possible mechanism is oxidation of platinum as oxide vapor, followed by dissolution of some of the oxide vapor in the melt, followed by precipitation of the platinum crystal during cooling. An interesting issue is that the crack size estimated using the Griffith –Irwin relation (Eq. 13) corresponding to the strength of 745 MPa is less than 0.5 μm but the platinum inclusion is much larger (at least 2 μm). Clearly the inclusion itself cannot be treated as a crack. One possible explanation is that during cooling microcracks nucleate

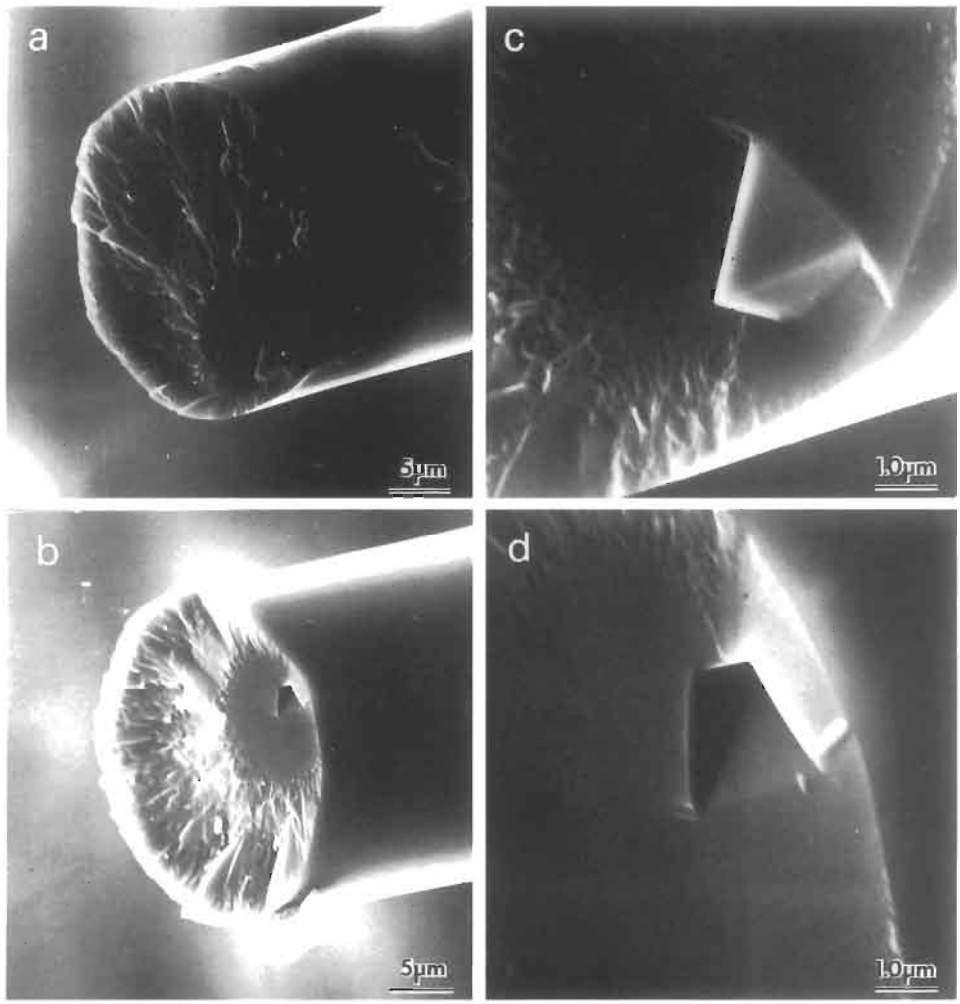

Fig. 3. SEM images of an E-glass fiber fracture surface showing a platinum inclusion in the bulk. The fiber strength was 745 MPa (Gupta, 1994).

from the platinum crystal by thermal stresses. However, this explanation is not entirely satisfactory because the expansion coefficient of platinum is larger than that of the glass which implies that the glass will go in compression. It is possible that the crack forms at about the glass transition temperature when the melt solidifies into glass and therefore structural relaxation around the glass transition has to be taken into account to properly account for the thermal stresses. Similar studies have been reported in the case of optical fibers (Mecholsky et al., 1979; Chandan et al., 1994).

Inclusions are sometimes observed buried in the surface of fibers, indicating a dirty fiber drawing environment as their most likely source. Impact by dust particles at low temperatures (below glass transition temperatures) causes only micro-indents and the

foreign particles do not stick. Foreign particles stick to the fiber surface when the impact occurs above the glass transition temperature. It is clear that fractography — if it can be used — remains a powerful tool to identify the nature of the fracture initiating flaws.

In summary, much of the work in the past has used small-length samples and has been focused on the extrinsic strength controlled by small flaws. Only recently, efforts are being made to study the low strengths of long-length fibers. The following issues about the extrinsic inert strength are not well understood:

(1) the identity and location of the fracture initiating flaws,
(2) the role of residual stresses around these flaws (especially inclusions and indents), and
(3) the role of testing stress, humidity, and temperature in the nucleation of microcracks around these flaws.

Extrinsic Fatigue Strength

In spite of an intuitive feel that flaws such as inclusions should not behave like cracks, the fatigue behavior (dynamic fatigue, delayed failure, dependence on the moisture and temperature of the test environment) of extrinsic flaws is surprisingly well modeled by the assumption of pre-existing cracks and the theory of slow crack growth. One of the major issues that has received a lot of attention (in the past and continues to do so at present) is the precise nature of the equation for crack velocity during slow crack growth, i.e., power function, the exponential function, or some other function (Jakus et al., 1981; Gupta et al., 1994). This is important when the estimates for the times for delayed failure need to be extrapolated to very low levels of stresses; the different laws tend to diverge significantly (Kurkjian and Inniss, 1992). There is, at present, strong experimental evidence (Michalske et al., 1991) and theoretical basis (Wiederhorn et al., 1980) to support the exponential law. However, its consequences are difficult to analyze mathematically. The power law, therefore, remains popular because it is convenient to use. When using the power law, it is found that the stress corrosion susceptibility, N, is not a constant for a composition. N has been found to increase with decrease in temperature (Hibino et al., 1984). This is shown in Fig. 4 for silica fibers. This is expected on the basis of Eq. 11 and supports the validity of the exponential equation. N is also found to increase with increasing strength (Kurkjian and Inniss, 1992). Armstrong et al. (1997) have reported a decrease in N with increase in the humidity of the environment. However, Muraoka et al. (1996) measured crack growth rates directly in silica fibers and did not observe a significant change in N with relative humidity. Experiments can only provide empirical laws whose validities will necessarily be limited. Atomistic simulations of slow crack growth are not mature enough at present to be of use in applications (Fuller et al., 1980; Marder, 1996). This is an area where much work remains to be done.

Artificial cracks generated by other techniques such as indentation or chemically generated pits (Donaghy and Dabbs, 1988; Choi et al., 1990) or by abrasion have been used to model the behavior of real cracks (Sakaguchi and Hibino, 1984; Inniss et al., 1993). While this work is of much interest in itself, it has not yielded any new insights as far as slow crack growth is concerned. This is probably because these artificial cracks

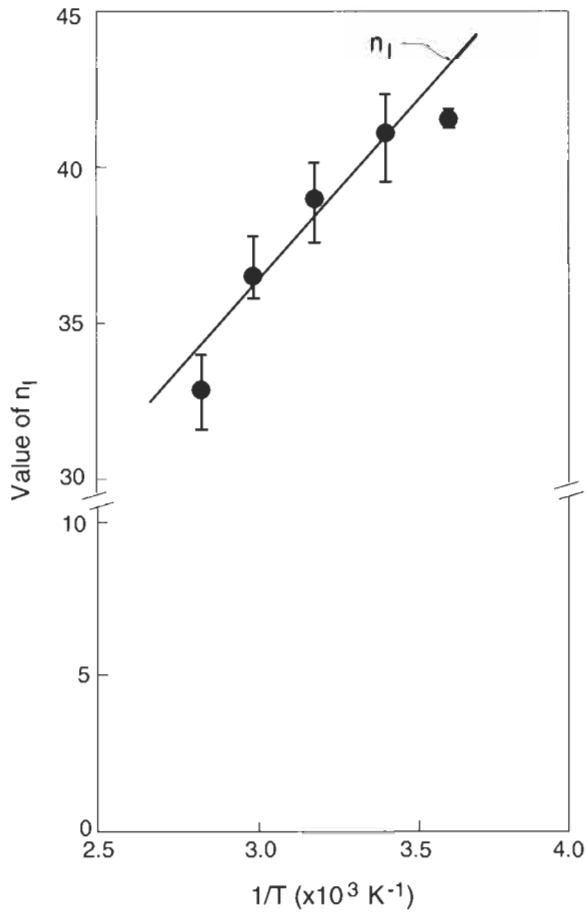

Fig. 4. Variation of the stress corrosion susceptibility, N, with temperature, T, for silica fibers (Hibino et al., 1984).

do not fully model the real cracks in fibers. It is questionable whether the residual stress state around indentation and abrasion-induced cracks is the same as in the case of real cracks in fibers. Similarly, the lack of sharpness of the tip in chemically generated flaws makes them unsuitable to model real cracks (Choi et al., 1990).

In spite of much work on the fatigue strength of fibers, several issues remain not well understood: (a) the difference in the fatigue behavior of surface versus bulk flaws; (b) the difference in the fatigue behaviors of large versus small flaws; (c) the role of residual stresses in modifying the fatigue behavior of flaws.

INTRINSIC STRENGTH OF GLASS FIBERS — EXPERIMENTAL RESULTS

The strengths of pristine fibers have been much studied in the literature. The work on E-glass has been reviewed by Gupta (1983, 1988). Not much new has been reported since about 1990 on E-glass pristine fiber strength and most new results have come from the large amount of work reported on silica fibers. There have been several reviews of the work on silica fibers (Kurkjian et al., 1989, 1993).

Room Temperature Intrinsic Strength, S(RT)*

E-glass Fibers

While high strengths had been reported earlier, Thomas (1960) was the first to measure the intrinsic strengths of E-glass fiber (and probably of any glass). This is best indicated in Fig. 5 which shows the average strength as a function of fiber diameter. It is clear from this figure that all previous efforts measured only extrinsic strengths. In a later work Thomas (1971) showed that the strength was constant up to diameters as large as 50 μm. The COV corresponding to the strength values reported by Thomas (see Fig. 5) is about 1% which, even to this day, is extremely good.

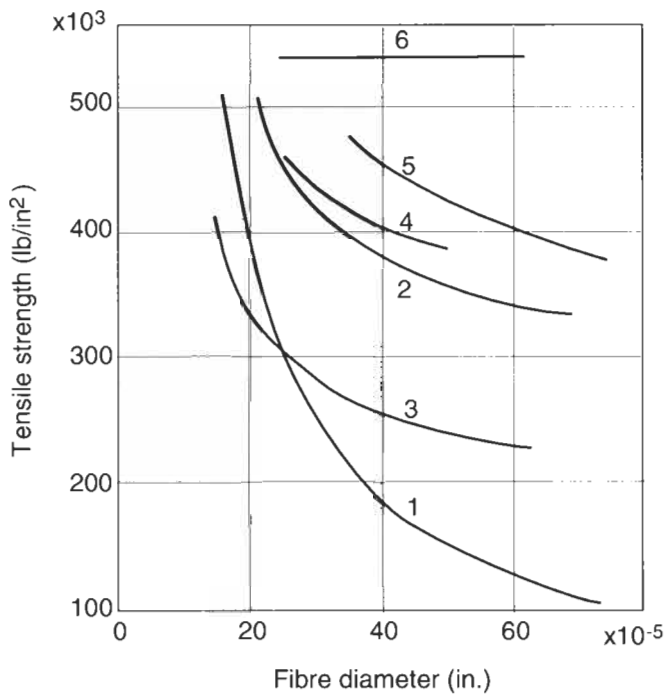

Fig. 5. Strength–diameter relationships for glass fibers: 6, Thomas (1960); 2–5, Otto (1955); 1, Anderegg (1939). (Figure from Thomas, 1960.)

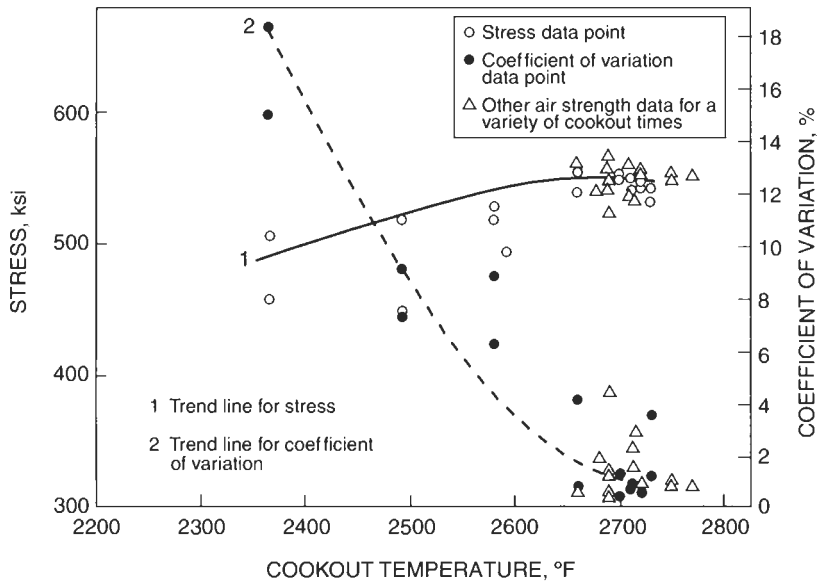

Fig. 6. Effect of melting temperature on mean fiber strength and coefficient of variation (after Cameron, 1966).

Thomas was able to achieve this remarkable breakthrough by building on the work of Otto (1955) who instituted several critical changes in the procedure used for testing fibers: (1) capturing pristine fiber samples on the fly between the bushing and the winder drum before the fibers come in contact with the drum; (2) testing fibers immediately after capturing; and (3) melting the glass in the bushing at sufficiently high temperatures and sufficiently long times. The importance of this last point is shown in Fig. 6, taken from the work of Cameron (1966), which shows the COV as a function of glass melting temperature.

The room temperature intrinsic strengths in terms of the Weibull plot are shown in Fig. 7 (Gupta, 1994). It is clear that the intrinsic strength with an average value of about 3.6 GPa is unimodal with a Weibull modulus of about 40 (COV $\approx$ 3%). This mode is reproducible even when tested samples are not pristine as shown in Fig. 8 which shows the low strength mode due to extrinsic flaws.

Silica Fibers

Kurkjian and Paek (1983) showed that the observed COV in pristine silica fiber strengths could be explained entirely by the measured variations in fiber diameter. This was the first clear demonstration that the measured high strength of silica fibers at room temperature (about 6 GPa) was intrinsic.

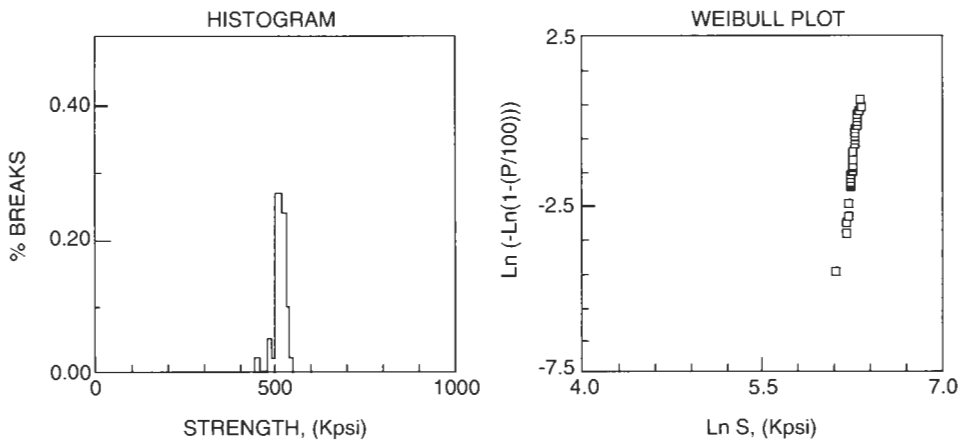

Fig. 7. Weibull plot for the room temperature intrinsic strength of E-glass fibers (Gupta, 1994).

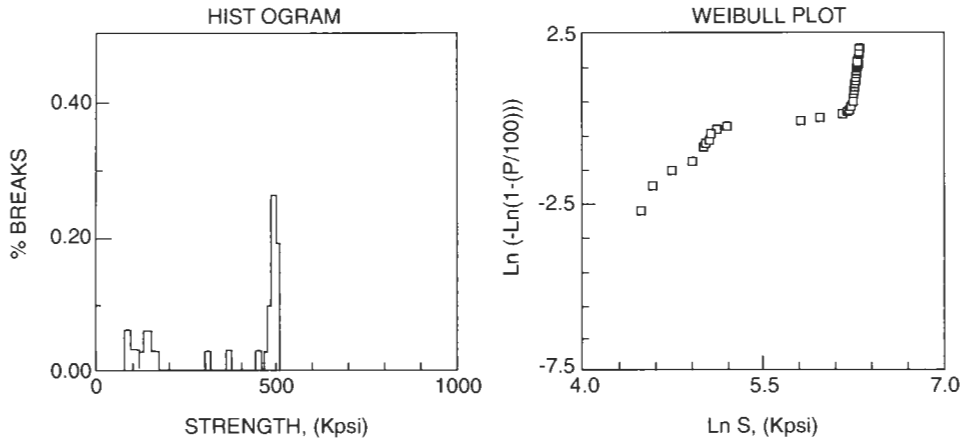

Fig. 8. Weibull plot for the room temperature extrinsic strength of E-glass fibers (Gupta, 1994).

S-glass Fibers

There are not many data available for S-glass fibers. Gupta (1985) has reported an average value of 5.1 GPa at room temperature for S-glass fibers of about 9 μm in diameter and 5 cm gauge length. However, no effort was made to check the diameter dependence of strength. Lowenstein and Dowd (1968) have also reported strength measurements of S-glass fibers in ambient conditions. Their highest reported strength is about 5.8 GPa for a 5 μm diameter fiber. These results also show a decrease of strength with increase in fiber diameter indicating that these strengths are extrinsic. Since Gupta's strength values are smaller, his strength values must be extrinsic as well.

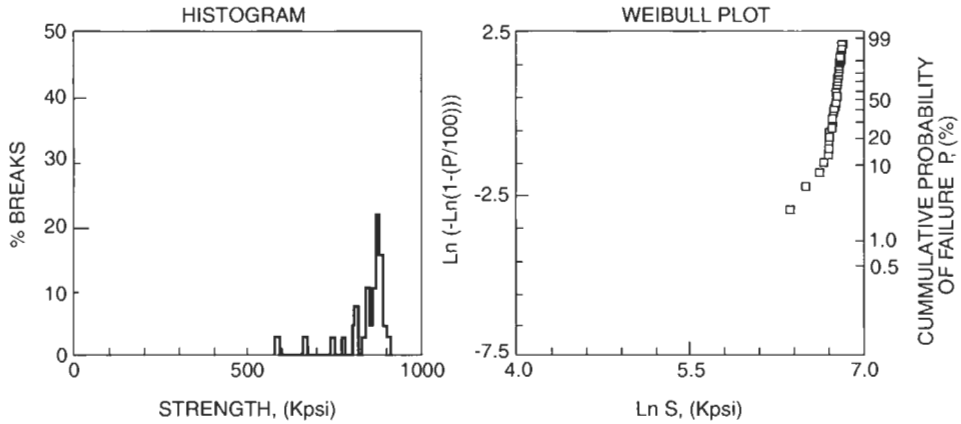

Fig. 9. Weibull plot for the liquid N_2 temperature strengths of pristine E-glass fibers (Gupta, unpublished).

Liquid Nitrogen Temperature Intrinsic Strength, S_0^*

E-glass Fibers

Hollinger and Plant (1964) were the first to report strength measurements for E-glass fibers at liquid N_2 temperature. They reported a median strength of 5.8 GPa for 10 μm diameter fibers. This was soon followed by the work of Cameron (1968) who also reported a median strength of about 5.8 GPa. This work has been reviewed by Gupta (1983, 1988). Fig. 9 shows, on a Weibull plot, the previously unpublished data obtained by the author for the liquid N_2 intrinsic strength measurements of E-glass fibers.

Silica Fibers

The first extensive work on the liquid N_2 temperature strength of bare silica fibers was reported by Proctor et al. (1967). They reported strengths as high as 14.7 GPa. They also measured strength values at the liquid helium temperature (−270°C) which are somewhat greater (~15 GPa) than those at the liquid N_2 temperature. Since this work, many have confirmed these results. Fig. 10 shows results of Duncan et al. (1985) on a Weibull plot. This figure also shows the strength distribution at room temperature. These results show a well defined single mode indicating that these are indeed intrinsic strengths.

Fatigue in Pristine Fibers

There is overwhelming evidence of fatigue in pristine fibers. The room temperature strength shows all the fatigue characteristics which are exhibited by non-pristine fibers, namely (a) an increase with increase in the strain rate, (b) a decrease with increase in relative humidity of the environment (see Fig. 11), and (c) delayed failure.

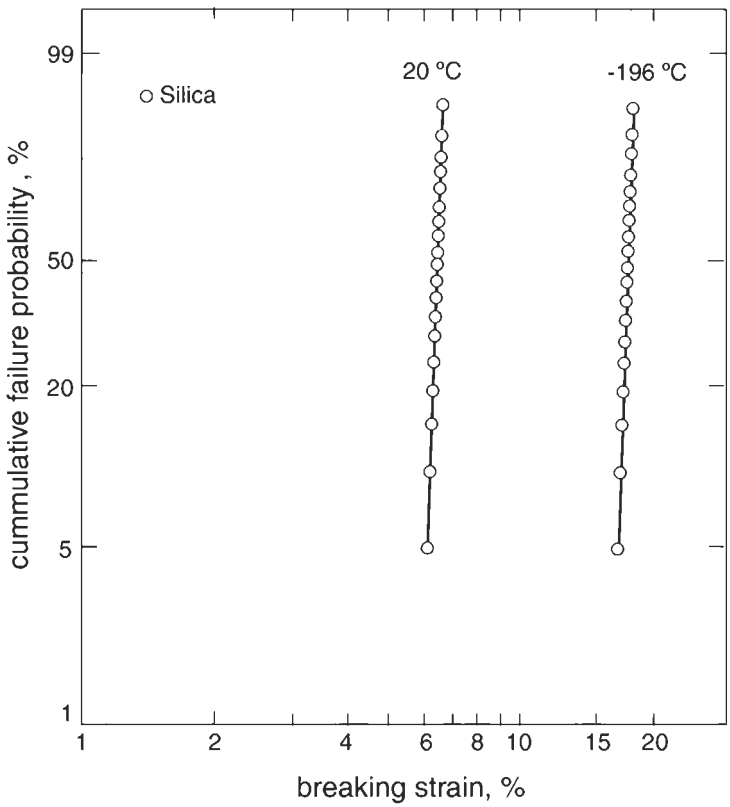

Fig. 10. Weibull plot of the liquid N_2 and room temperature strengths of pristine silica fibers (Duncan et al., 1985).

Gupta (1983) has analyzed these data for E-glass fibers, including the data on the temperature dependence of strength (see Fig. 12) and has shown that the data can be rationalized in terms of the slow crack growth model of fatigue. Duncan et al. (1985) have shown the same for silica fibers. There is clear evidence of fatigue in pristine fibers. What is more intriguing is that the fatigue behavior of pristine fibers is rationalizable to a significant extent in terms of the slow crack growth model. How does one reconcile slow crack growth in these flaw-free fibers? This question remains unresolved at present. One possible explanation is that nucleation of microcracks (Bouten and deWith, 1988; Golubovic and Feng, 1991) — a time/temperature-dependent phenomenon — is the mechanism of fatigue in pristine fibers. Heterogeneous nucleation of a microcrack at the fiber surface will be favored by high stresses and high environmental humidity. After nucleation a crack can grow by slow crack growth. If the crack nucleation time and the size of the critical crack are small, the overall fatigue process will closely resemble that of growth of pre-existing cracks.

Assuming the Griffith–Irwin criterion (Eq. 13), one can calculate crack sizes corresponding to the measured strength values. Values obtained in this fashion are tabulated

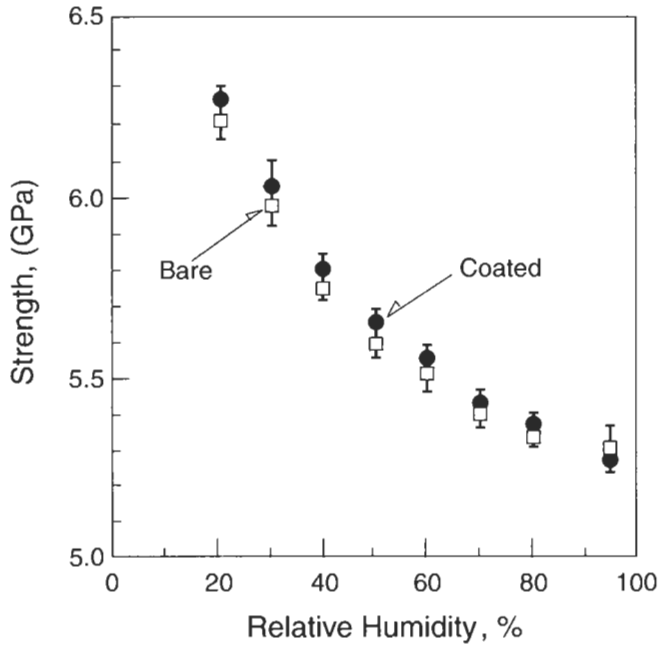

Fig. 11. Room temperature strength vs. environmental humidity for silica fibers (Armstrong et al., 1997).

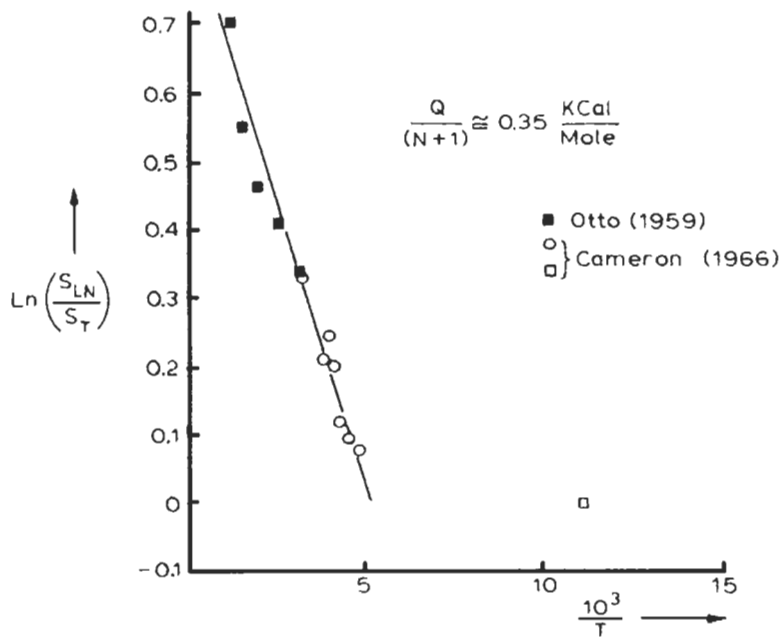

Fig. 12. Temperature dependence of the strength of pristine E-glass fibers; experimental data and prediction of slow crack growth model (Gupta, 1983).

Table 2. Intrinsic strengths and related properties of silica and E-glass fibers

	E-glass	Silica
S_0^* (GPa)	6.0	14
C_0^* (nm)	7.2	1.0
ε_0^* (%)	8.3	20
S^* (RT) (GPa)	3.6	6.0
C^* (RT) (nm)	20	5.6
S_0^*/S^* (RT)	1.7	2.3
E (GPa)	72	70
K_c (MPa $m^{1/2}$)	0.9	0.8

in Table 2 along with the strength values and the values of pertinent fracture mechanical parameters for two glass compositions (E-glass and silica). The crack size corresponding to inert intrinsic strengths are about 1 nm in silica and about 7 nm in the case of E-glass fibers.

Before speculating on the nature of the nm size flaws, we should emphasize that because the strength is known to be affected by the environmental humidity, the strength controlling flaws must be on the fiber surface. Could these flaws be related to the nanoscale intrinsic roughness which has been observed on the surface of pristine fibers (Gupta et al., 2000)? The measured RMS roughness on pristine silica fiber surface is about 0.2 nm and the peak-to-valley roughness is about 1.5 nm. Thus it seems possible that because of its random nature, the roughness may act like a classic Griffith elliptical notch at some locations on the pristine surface, and may lead to stress concentrations which ultimately control the pristine inert strength of fibers. This is also supported by the work of Yuce et al. (1992) who studied the increase in surface roughness upon aging in silica fibers and found that the strength decreases with increase in surface roughness (see Fig. 13 and Kurkjian et al., 1993), approximately linearly on a log–log plot with a slope of approximately −0.22. Clearly, more work is needed to examine in detail the role of intrinsic surface roughness as a source of intrinsic flaw controlling the strength of pristine fibers.

What other nm size features, present in the structure of a glass, can control the intrinsic strength of glass fibers? The structure of E-glass is complex and not well studied. But the structure of silica glass has been very well studied (Grimley et al., 1990). A 1 nm size scale in silica structure corresponds approximately to the size of two planar six-membered rings in the silica structure. If a siloxane bond is broken, the elongated opening created by the two neighboring rings is about 1 nm long. This feature may control the intrinsic strength of silica fibers. There is evidence of broken bonds in silica fibers. For example, it has been shown (Hibino and Hanafusa, 1985) that application of tensile stress leads to generation of point defects (i.e., broken bonds) such as E′ and NBOHC centers in silica fibers. These can be detected using either ESR or photo-luminescence techniques. Kokura et al. (1989) have demonstrated by ESR the generation of point defects in silica glass during mechanical crushing. Thus, it appears that nm size cavities may exist in pristine fibers. Whether they are the strength controlling flaws remains to be studied.

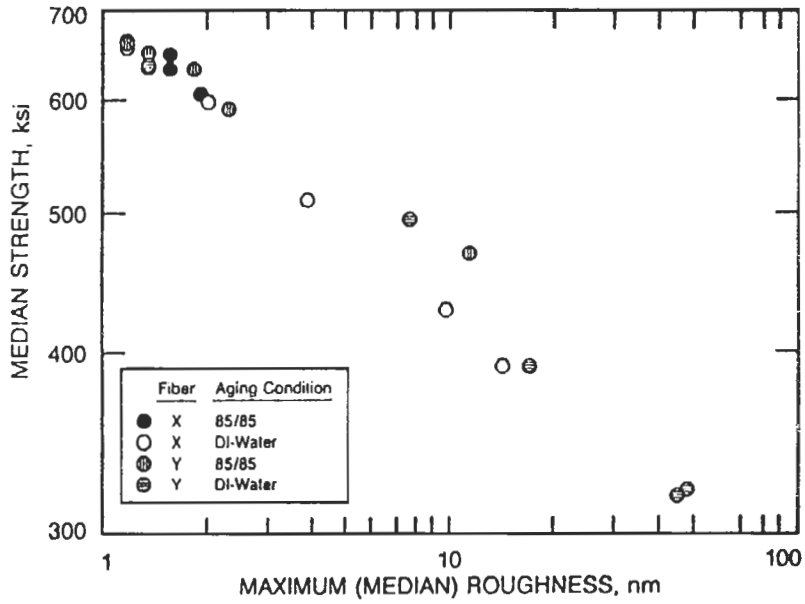

Fig. 13. Strength of silica fibers as a function of the RMS surface roughness (Yuce et al., 1992).

CONCLUDING REMARKS

The strength of pristine fibers can be classified (a) as intrinsic or extrinsic, and (b) as inert or fatigue. For most applications and for improved production efficiencies, one is primarily interested in improving extrinsic fatigue strength. On the other hand, for basic understanding of strength in terms of the structure of glass, one is interested in the intrinsic inert strength.

While the fibers are being produced routinely with strengths adequate for their respective technological applications, fundamental questions about both the extrinsic and the intrinsic strengths remain unanswered. For the extrinsic strengths, the important questions pertain to the identity of the flaws and the role of crack nucleation and residual stresses around inclusions. The difficulty is partly because these large flaws occur very infrequently (one flaw in hundreds of kilometers of fiber!). For the intrinsic strengths, the key questions are: (a) what determines the intrinsic strength of a fiber? and (b) why do pristine fibers exhibit fatigue which is qualitatively (and to a large extent quantitatively) similar to that in non-pristine fibers?

Atomistic modeling of fracture in topologically disordered solids such as silicate glasses remains at a primitive stage primarily because of a lack of knowledge of the anharmonic aspects of the interatomic potentials.

ACKNOWLEDGEMENTS

I thank the conference organizers and especially Prof. Manual Elices for the invitation to this conference, my colleague and 'Strength Guru' Chuck Kurkjian for many enlightening discussions, Scott Glaesemann of Corning Inc., for providing me with reprints and preprints about his recent work on large flaws, Hyungchan Kim for scanning all figures in this manuscript, and NASA grant NAG8-1470 for the support of part of my time spent in writing the manuscript.

REFERENCES

Armstrong, J.L., Matthewson, M.J., Kurkjian, C.R., Chou, C.Y. (1997) Kinetics models for fatigue of high-strength fused silica optical fiber. *Proc. Int. Wire Cable Symp.*, pp. 902–908.

Bouten, P.C.P. and deWith, G. (1988) Crack nucleation at the surface of stressed fibers. *J. Appl. Phys.*, 64: 3890–3900.

Cameron, N.M. (1966) Relation between melt treatment and glass fiber strength. *J. Am. Ceram. Soc.*, 49: 144–148.

Cameron, N.M. (1968) Effect of environment and temperature on the strength of E-glass fibers, Part 1. High vacuum and low temperatures. *Glass Technol.*, 9: 14–21.

Chandan, H.C., Parker, R.D. and Kalish, D. (1994) Fractography of optical fibers. In: *Fractography of Glass*, pp. 143–184, R.C. Bradt and R.E. Tressler (Eds.). Plenum Press, New York.

Charles, R.J. (1958) Static fatigue in glass, I. *J. Appl. Phys.*, 29: 1549–1560.

Choi, S.R., Ritter, J.E. and Jakus, K. (1990) Failure of glass with subthreshold flaws. *J. Am. Ceram. Soc.*, 73: 268–274.

Donaghy, F.A. and Dabbs, T.P. (1988) Subthreshold flaws and their failure prediction in long distance optical fiber cables. *J. Lightwave Technol.*, 6: 226–232.

Duncan, W.J., France, P.W. and Craig, S.P. (1985) The effect of environment on the strength of optical fiber. In: *Strength of Inorganic Glass*, pp. 309–328, C.R. Kurkjian (Ed.). Plenum Press, New York.

Dwight, D.W. (2000) Glass fiber reinforcements. In: *Fiber Reinforcements and General Theory of Composites*, pp. 231–261, T.W. Chou (Ed.). Elsevier, Amsterdam.

Epstein, B. (1948) Statistical aspects of fracture problems. *J. Appl. Phys.*, 19: 140–147.

France, P.W., Paradine, M.J., Reeve, M.H. and Newns, G.R. (1980) Liquid nitrogen strengths of coated optical glass fibers. *J. Mater. Sci.*, 15: 825–830.

Freiman, S.W. (1980) Fracture mechanics of glass. In: *Glass: Science and Technology*, Vol. 5, pp. 21–78, D.R. Uhlmann and N.J. Kreidl (Eds.). Academic Press, New York.

Freudenthal, A.M. (1968) Statistical approach to brittle fracture. In: *Fracture*, Vol. II, pp. 591–619, H. Liebowitz (Ed.). Academic Press, New York.

Fuller, E.R., Lawn, B.R. and Thomson, R.M. (1980) Atomic modelling of chemical interactions at crack tips. *Acta Met.*, 28: 1407–1414.

Glaesemann, G.S. and Helfinstine, J.D. (1994) Measuring the inert strength of large flaws in optical fiber. *Proc. SPIE*, 2074: 95–107.

Golubovic, L. and Feng, S. (1991) Rate of microcrack nucleation. *Phys. Rev. A*, 43: 5223–5227.

Grimley, D.I., Wright, A. and Sinclair, R.N. (1990) Neutron scattering from vitreous silica. *J. Noncryst. Solids*, 119: 49–64.

Gulati, S.T. (1992) Large flaws: The culprit in fiber reliability. *Photonics Spectra*, Dec., pp. 78–82.

Gupta, P.K. (1982) Relation between power and exponential laws of slow crack growth. *J. Am. Ceram. Soc.*, 65: C163–C164.

Gupta, P.K. (1983) Examination of the tensile strength of E-glass fibers in light of slow crack growth. In: *Fracture Mechanics of Ceramics*, Vol. 5, pp. 291–303, R.C. Bradt et al. (Eds.). Plenum Press, New York.

Gupta, P.K. (1985) Effects of testing parameters on the tensile strengths of pristine E and S glass fibers. In: *Strength of Inorganic Glass*, pp. 351–362, C.R. Kurkjian (Ed.). Plenum Press, New York.

Gupta, P.K. (1987) Combined effect of flaw distribution and diameter variation on the statistics of glass fiber strength. *J. Am. Ceram. Soc.*, 70: 486–492.

Gupta, P.K. (1988) Glass fibers for composite materials. In: *Fibre Reinforcements for Composite Materials*, pp. 19–70, A.R. Bunsell (Ed.). Elsevier, Amsterdam.

Gupta, P.K. (1994) Fractography of fiberglass. In: *Fractography of Glass*, pp. 185–206, R.C. Bradt and R.E. Tressler (Eds.). Plenum Press, New York.

Gupta, P.K., Inniss, D., Kurkjian, C.R. and Brownlow, D.L. (1994) Determination of crack velocity as a function of stress intensity from static fatigue data. *J. Am. Ceram. Soc.*, 77: 2445–2449.

Gupta, P.K., Inniss, D., Kurkjian, C.R. and Zhong, Q. (2000) Nanoscale roughness of oxide glass surfaces. *J. Noncryst. Solids*, 262: 200–206.

Hecht, J. (1999) *City of Light — The Story of Fiber Optics*. Oxford University Press, New York.

Hertzberg, R.W. (1989) *Deformation and Fracture Mechanics of Engineering Materials*. Wiley, New York.

Hibino, Y. and Hanafusa, H. (1985) Raman study on silica optical fibers subjected to high tensile stress. *Appl. Phys. Lett.*, 47: 812–814.

Hibino, Y., Sakaguchi, S. and Tajima, Y. (1984) Crack growth in silica glass under dynamic loading. *J. Am. Ceram. Soc.*, 67: 64–68.

Hollinger, D.L. and Plant, H.T. (1964) The role of stress corrosion in glass fibers. *Proc. SPI-19*, 11A, 1–14.

Hunt, R.A. and McCartney, L.N. (1979) A new approach to Weibull's statistical theory of brittle fracture. *Int. J. Fract.*, 15: 365–375.

Inniss, D., Zhong, Q. and Kurkjian, C.R. (1993) Chemically corroded pristine silica fibers: blunt or sharp flaws. *J. Am. Ceram. Soc.*, 76: 3173–3177.

Izawa, T. and Sudo, S. (1987) *Optical Fibers: Materials and Fabrication*. KTK Scientific Publishers, Tokyo.

Jakus, K.E., Ritter, J.E. and Sullivan, J.M. (1981) Dependency of fatigue predictions on the form of the crack velocity equation. *J. Am. Ceram. Soc.*, 64: 372–374.

Katz, J.I. (1998) Statistics and microphysics of the fracture of glass. *J. Appl. Phys.*, 84: 1928–1931.

Kokura, K., Tomozawa, M. and MacCrone, R.K. (1989) Defect formation in SiO_2 glass during fracture. *J. Noncryst. Solids*, 111: 269–276.

Kurkjian, C.R. (1985) *Strength of Inorganic Glass*. Plenum, New York.

Kurkjian, C.R. and Inniss, D. (1992) Strength and fatigue of silica. In: *The Physics of Noncrystalline Solids*, pp. 649–653, L.D. Pye, W.C. LaCourse and H.J. Stevens (Eds.). Taylor and Francis, Philadelphia, PA.

Kurkjian, C.R. and Paek, U.C. (1983) Single-valued strength of perfect silica fibers. *Appl. Phys. Lett.*, 42: 251–253.

Kurkjian, C.R., Krause, J.T. and Matthewson, M.J. (1989) Strength and fatigue of silica optical fibers. *J. Lightwave Technol.*, 7: 1360–1370.

Kurkjian, C.R., Simpkins, P.G. and Inniss, D. (1993) Strength, degradation, and coating of silica lightguides. *J. Am. Ceram. Soc.*, 76: 1106–1112.

Lawn, B. (1993) *Fracture of Brittle Solids*. Cambridge University Press, Cambridge.

Lowenstein, K.L. and Dowd, J. (1968) An investigation of the relationship between glass fiber tensile strength, the temperature of the glass from which the fiber is drawn, and fiber diameter. *Glass Technol.*, 9: 164–171.

Marder, M. (1996) Statistical mechanics of cracks. *Phys. Rev. E*, 54: 3442–3454.

Matthewson, M.J., Kurkjian, C.R. and Gulati, S.T. (1986) Strength measurement of optical fibers by bending. *J. Am. Ceram. Soc.*, 69: 815–821.

Mecholsky, J.J. (1994) Quantitative fractographic analysis of fracture origins in glass. In: *Fractography of Glass*, pp. 37–73, R.C. Bradt and R.E. Tressler (Eds.). Plenum Press, New York.

Mecholsky, J.J., Freiman, S.W. and Morey, S.M. (1979) Fracture surface analysis of optical fibers. In: *Fiber Optics*, pp. 187–207, B. Bendow and S.S. Mitra (Eds.). Plenum Press, New York.

Michalske, T.A., Smith, W.L. and Bunker, B.C. (1991) Fatigue mechanisms in high strength silica-glass fibers. *J. Am. Ceram. Soc.*, 74: 1993–1996.

Muraoka, M. and Abe, H. (1996) Subcritical crack growth in silica optical fibers in a wide range of crack velocities. *J. Am. Ceram. Soc.*, 79: 51–57.

Otto, W.H. (1955) Relationship of tensile strength of glass fibers to diameter. *J. Am. Ceram. Soc.*, 38: 122–124.

Proctor, B.A., Whitney, I. and Johnson, J.W. (1967) The strength of fused silica. *Proc. R. Soc.*, 297A: 534–557.

Roach, D.H. (1986) Comparison of the liquid nitrogen strength and the high stressing rate strength of soda-lime glass. *J. Am. Ceram. Soc.*, 69: C168–C169.

Rooke, D.P. and Cartwright, D.J. (1976) *Compendium of Stress Intensity Factors*. HMSO, London.

Sakaguchi, S. and Hibino, Y. (1984) Fatigue in low strength silica optical fibers. *J. Mater. Sci.*, 19: 3416–3420.

Simmons, J.H. (1998) What is so exciting about non-linear viscous flow in glass, molecular dynamics simulations of brittle fracture and semiconductor-glass quantum composites. *J. Noncryst. Solids*, 239: 1–15.

Simmons, J.H., Swiler, T.P. and Ochoa, R. (1991) Molecular dynamics studies of brittle fracture in silica: bind fracture. *J. Noncryst. Solids*, 134: 179–182.

Smith, W.L. and Michalske, T.A. (1989) Intrinsic strength of pristine silica glass fibers. Department of Energy, report.

Soules, T.F. (1985) Models of glass strength and relaxation phenomena suggested by molecular dynamic simulations. *J. Noncryst. Solids*, 73: 315–330.

Thomas, W.F. (1960) An investigation of the factors likely to affect the strength and properties of glass fibers. *Phys. Chem. Glasses*, 1: 4–18.

Thomas, W.F. (1971) An investigation of the strength of borosilicate glass in the form of fibers and rods. *Glass Technol.*, 12: 42–44.

Wiederhorn, S.M. (1967) Influence of water vapor on crack propagation in soda-lime glass. *J. Am. Ceram. Soc.*, 50: 407–414.

Wiederhorn, S.M. (1975) Crack growth as an interpretation of static fatigue. *J. Noncryst. Solids*, 19: 169–181.

Wiederhorn, S.M., Fuller, E.R. and Thomson, R. (1980) Micromechanisms of crack growth in ceramics and glasses in corrosive environments. *Met. Sci.*, 14: 450–458.

Yuce, H.H., Varachi, J.P., Kilmer, J.P., Kurkjian, C.R. and Matthewson, M.J. (1992) Optical fiber corrosion: coating contribution to zero stress aging. *Proc. Conf. Optical Fiber Communications*, p. 395. Optical Society of America, Washington, DC.

CARBON FIBERS

Fiber Fracture
M. Elices and J. Llorca (Editors)

FRACTURE OF CARBON FIBERS

J.G. Lavin

Carbon Nanotechnologies Inc., 16200 Park Row, Houston, TX 77084, USA

Introduction 158
Physical Properties 159
PAN-Based Carbon Fibers 163
Pitch-Based Carbon Fibers 166
General Purpose Pitch-Based Carbon Fiber 166
High-Performance Pitch-Based Carbon Fibers 167
A Paradox 169
Fiber Formation 169
Vapor-Grown Carbon Fibers 173
Failure Mechanisms 174
Tensile Failure 174
Compressive Failure 175
Concluding Remarks 178
References 178

Abstract

Carbon fibers are made from many different feedstocks. The most important commercial fiber is made from polyacrylonitrile (PAN). It is four times stronger than steel, the same modulus or higher, and does not fail in creep or fatigue. These properties made the fiber attractive for aerospace applications initially, and later for sporting and industrial applications. Another important feedstock is pitch from refinery or steel-making operations, which leads to fibers with very high modulus and thermal and electrical conductivities. Properties of the fibers, and critical steps in their manufacture are described, together with structural characteristics and failure mechanisms.

Keywords

Carbon; PAN; Mesophase pitch; Electrical conductivity; Thermal conductivity; SEM; TEM

INTRODUCTION

Carbon fibers come in many different forms. The most important type commercially is the fiber made from polyacrylonitrile (PAN), which was initially developed for aircraft applications. It was attractive because of its high strength and modulus, and because it is not subject to creep or fatigue failure. Composites made from PAN-based carbon fiber allowed for reduction in aircraft weight, and improvement in range, payload and performance. The composites were first adopted in military aircraft, but rapidly spread to commercial aircraft and then to other applications such as sporting goods. Pitch-based general purpose (isotropic) fibers have been used in Japan for large-volume reinforcement of cementitious matrices, especially exterior building panels. Pitch-based high performance (mesophase) fibers were developed for space applications. They are capable of very high Young's modulus (up to that of in-plane graphite) and have a high negative coefficient of thermal expansion along the fiber axis. This makes possible composites with a zero coefficient of thermal expansion, which is important for space applications. When a panel is facing the sun, it may reach 200°C, and when it is facing away from the sun, it may drop to 200°C below zero.

Carbon fibers are either the strongest or stiffest materials available, when corrected for density, as illustrated in Fig. 1. The mesophase pitch fibers also have high levels of thermal conductivity, as shown in Fig. 2.

The word 'graphite' is much misused in carbon fiber literature. The word refers to a very specific structure, in which adjacent aromatic sheets overlap with one carbon atom at the center of each hexagon as shown in Fig. 3a. This structure appears very rarely in carbon fibers, especially in PAN-based fibers, even though they are conventionally called graphite fibers. While high-performance fibers are made up of large aromatic

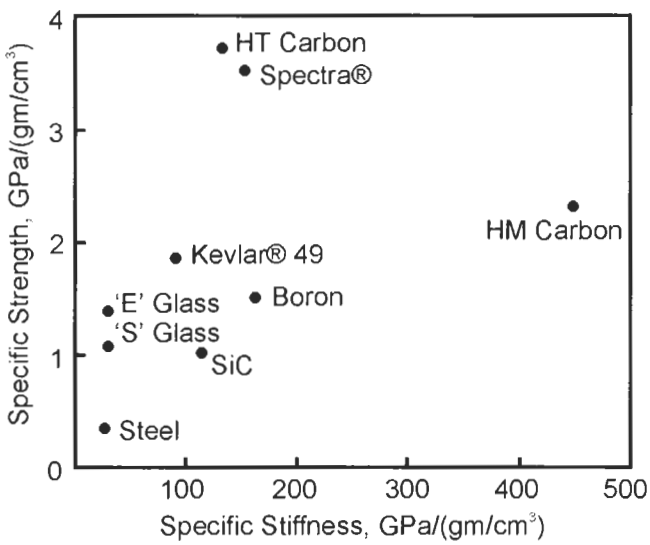

Fig. 1. Specific strength and stiffness of strong fibers.

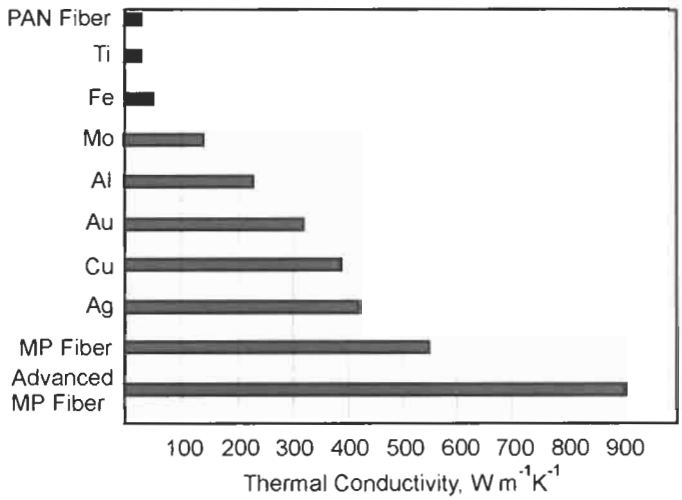

Fig. 2. Thermal conductivity of structural materials.

sheets, these are randomly oriented relative to each other, are described as 'turbostratic' (turbulent and stratified) and are shown in Fig. 3b. Many physical properties depend merely on the large aromatic sheets. The aromatic character of the isotropic carbon is shown in Fig. 3c.

PHYSICAL PROPERTIES

Because of the rich variety of carbon fibers available today, physical properties vary over a broad domain. Fig. 4 shows a plot of strength versus modulus. 'General purpose' fibers made from isotropic pitch have modest levels of strength and modulus. However, they are the least expensive pitch-based fiber, and are useful in enhancing modulus or conductivity in many applications. PAN-based fibers are the strongest available; however, when they are heat treated to increase modulus the strength decreases. Mesophase pitch fibers may be heat treated to very high modulus values, approaching the in-plane modulus of graphite at 1 TPa. The Achilles heel of mesophase pitch-based fibers in composite applications is low compressive strength; this is illustrated in Fig. 5. Electrical and thermal conductivity are important in many applications, and these are illustrated in Figs. 6 and 7 respectively. Mesophase pitch fibers have the highest conductivity and lowest resistivity.

Finally, there is a property of high-performance carbon fibers, both PAN and mesophase pitch-based, which sets them apart from other materials. They are not subject to creep or fatigue failure. These are important characteristics for critical applications. In a comparison of materials for tension members of tension leg platforms for deep-sea oil production described by Salama (1997), carbon fiber strand survived 2,000,000 stress cycles between 296 and 861 MPa. In comparison, steel pipe stressed between 21 and 220 MPa failed after 300,000 cycles. Creep studies on PAN and

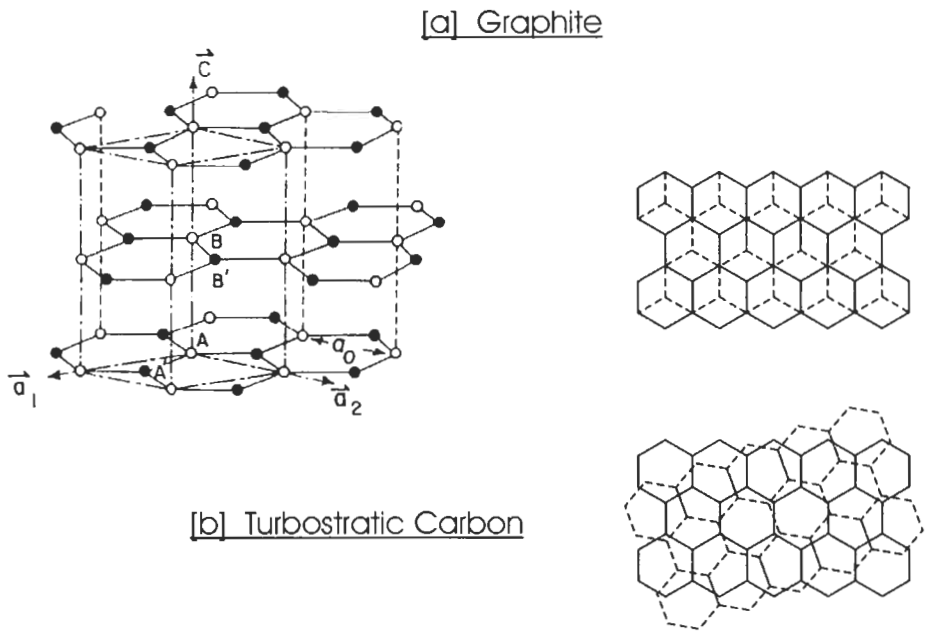

Fig. 3. Forms of carbon.

pitch-based carbon fibers were conducted by Sines et al. (1989) and Kogure et al. (1996) at 2300°C and stresses of the order of 800 MPa. Projections of the data obtained to ambient temperatures indicate that creep deformations will be infinitesimally small.

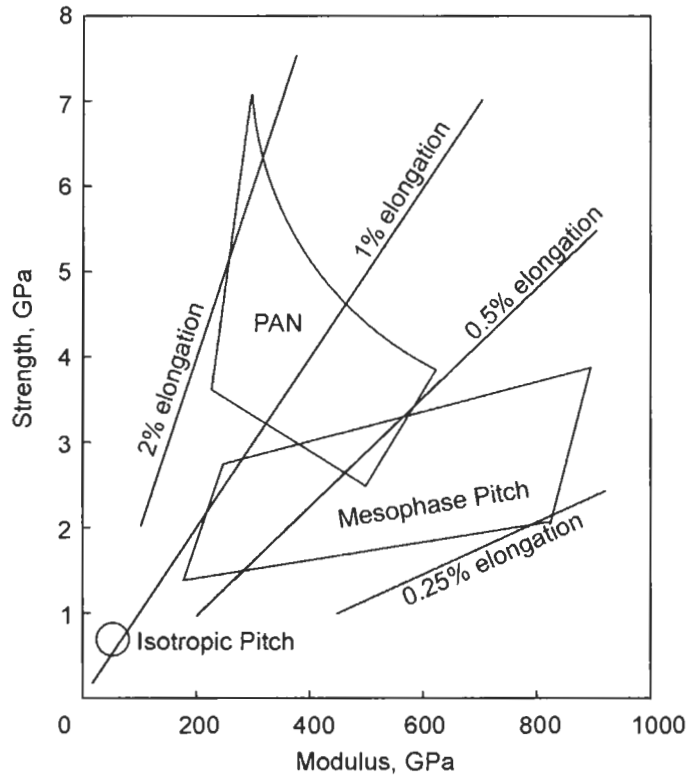

Fig. 4. Strength and stiffness of carbon fibers. From Lavin (2001b).

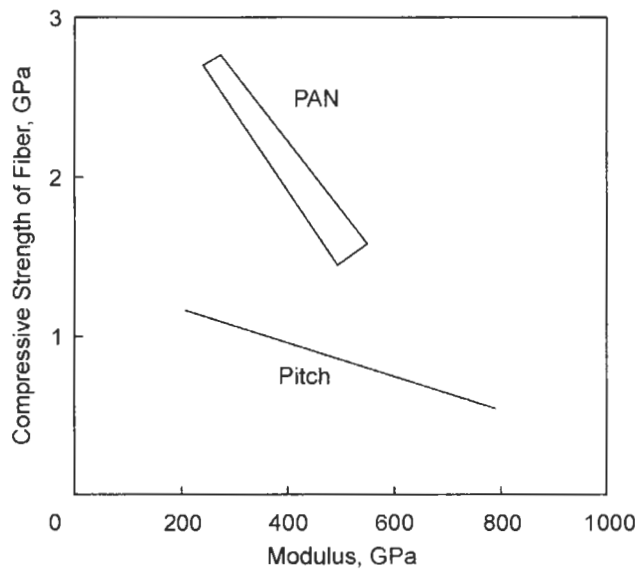

Fig. 5. Compressive strength of carbon fibers. From Lavin (2001b).

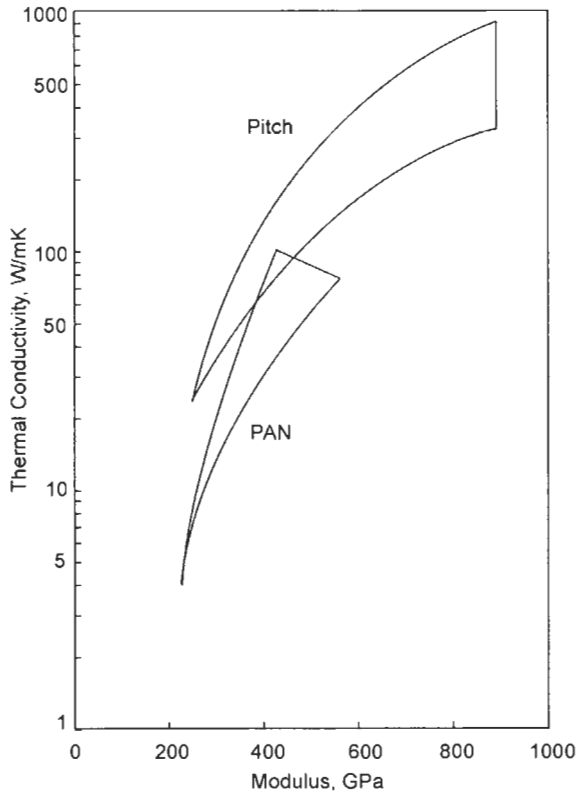

Fig. 6. Thermal conductivity of carbon fibers. From Lavin (2001b).

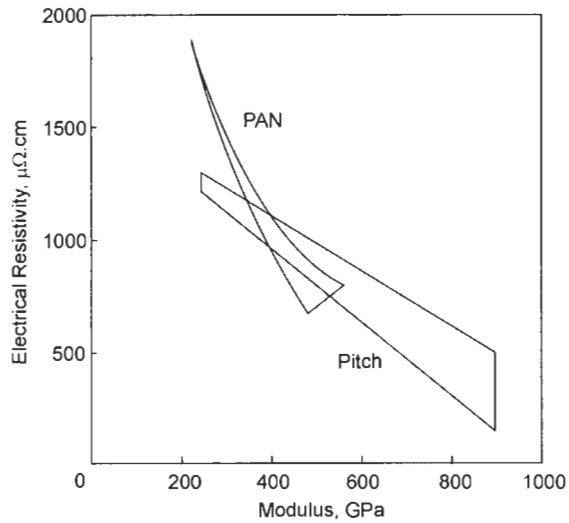

Fig. 7. Electrical resistivity of carbon fibers. From Lavin (2001b).

PAN-BASED CARBON FIBERS

Polyacrylonitrile (PAN) fibers are made by a variety of methods. The polymer is made by free-radical polymerization either in solution or in a solvent–water suspension. The polymer is then dried and re-dissolved in another solvent for spinning, either by wet-spinning or dry-spinning. In the wet-spinning process the spin dope is forced through a spinneret into a coagulating liquid and stretched, while in the dry-spinning process the dope is spun into a hot gas chamber, and stretched. For high-strength carbon fibers, it is important to avoid the formation of voids within the fiber at this step. Dry-spun fibers are characterized by a 'dog-bone' cross-section, formed because the perimeter of the fiber is quenched before much of the solvent is removed. The preferred process for high-strength fiber today is wet-spinning. Processes for melt-spinning PAN plasticized with water or polyethylene glycol have been developed, but are not practiced commercially. A significant improvement in carbon fiber strength was obtained by Moreton and Watt (1974) who spun the PAN precursor under clean room conditions. The strength of fibers spun in this way and subsequently heat treated was found to improve by >80% over conventionally spun fibers. The mechanism is presumed to be removal of small impurities which can act as crack initiators. This technology is believed to be critical for production of high strength fibers such as Toray's T800 and T1000.

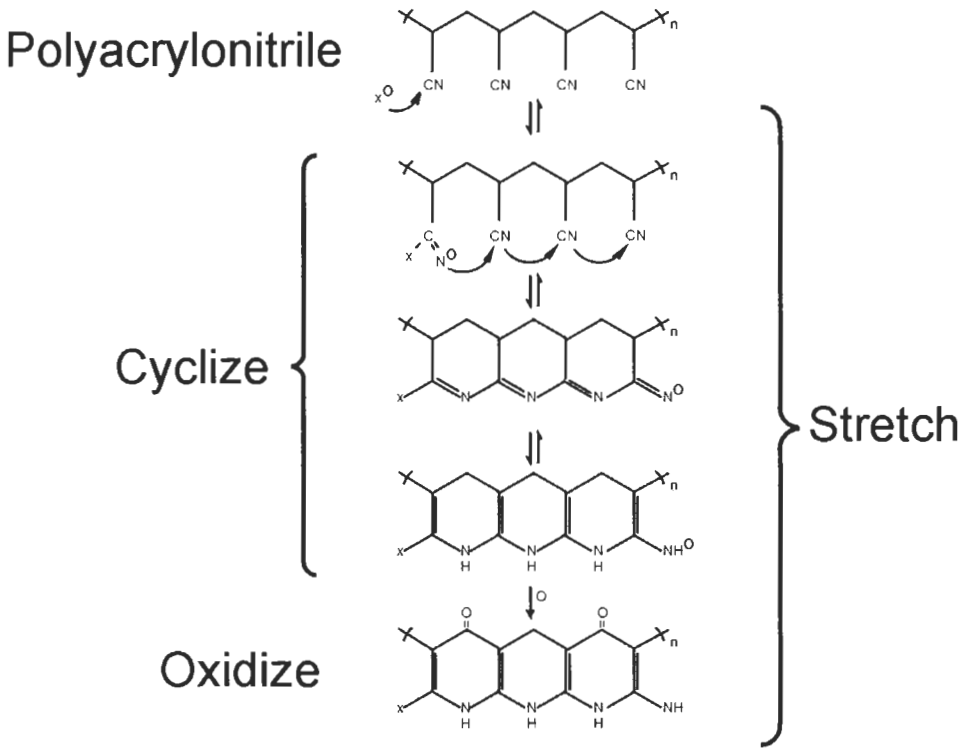

Fig. 8. PAN-based carbon fiber chemistry: cyclization and oxidation.

Initially, commercial PAN-based carbon fibers were made from the polymers developed for textile applications. However, these fibers were neither very stiff nor strong. Development efforts over the 1960s and 1970s focused on increasing molecular weight, introducing co-monomers to assist processing, and eliminating impurities which limited mechanical strength. The chemistry of conversion of PAN to carbon is quite complex, and the interested reader is referred to an excellent treatment in Peebles (1994). The critical steps are outlined below.

The first critical step in making carbon fiber from PAN fiber is causing the pendant nitrile groups to cyclize, as illustrated in Fig. 8. This process is thermally activated and is highly exothermic. The activation temperature is influenced by the type and amount of co-monomer used. It is also important to keep the fiber under tension in this process, and indeed, during the whole conversion process. The next step is to make the fiber infusible: this is accomplished by adding oxygen atoms to the polymer, again by heating in air. The reaction is diffusion limited, requiring exposure times of tens of minutes. When about 8% oxygen by weight has been added, the fiber can be heated above 600°C without melting. When the fiber is heated above this temperature, the processes of decyanization and dehydrogenation take place, and above 1000°C large aromatic sheets start to form, as illustrated in Fig. 9.

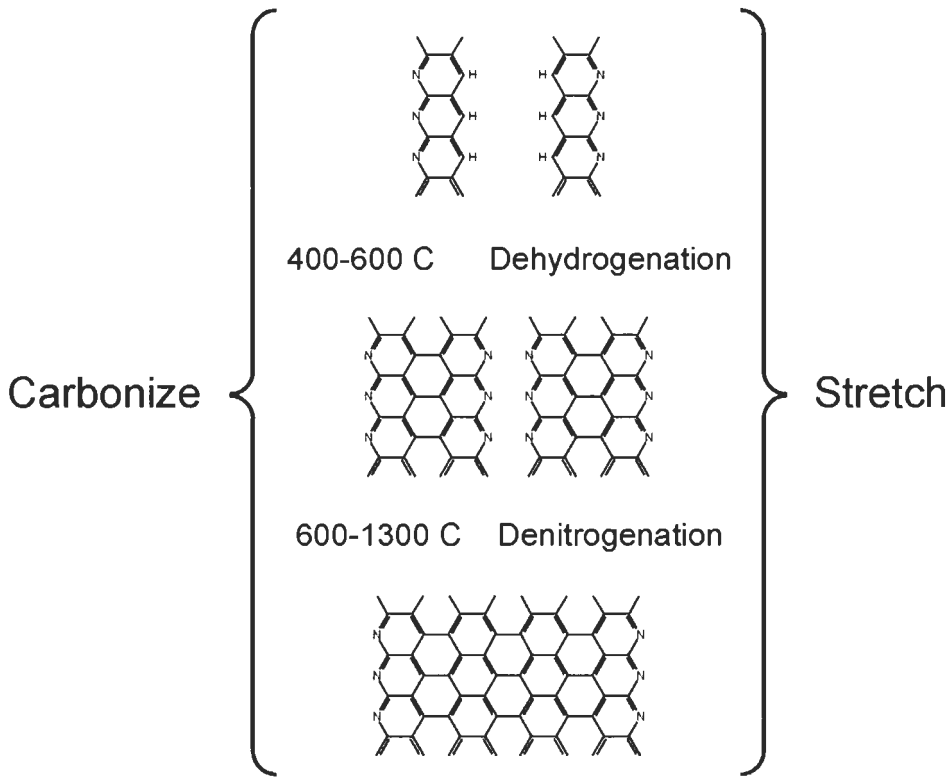

Fig. 9. PAN-based carbon fiber chemistry: carbonization.

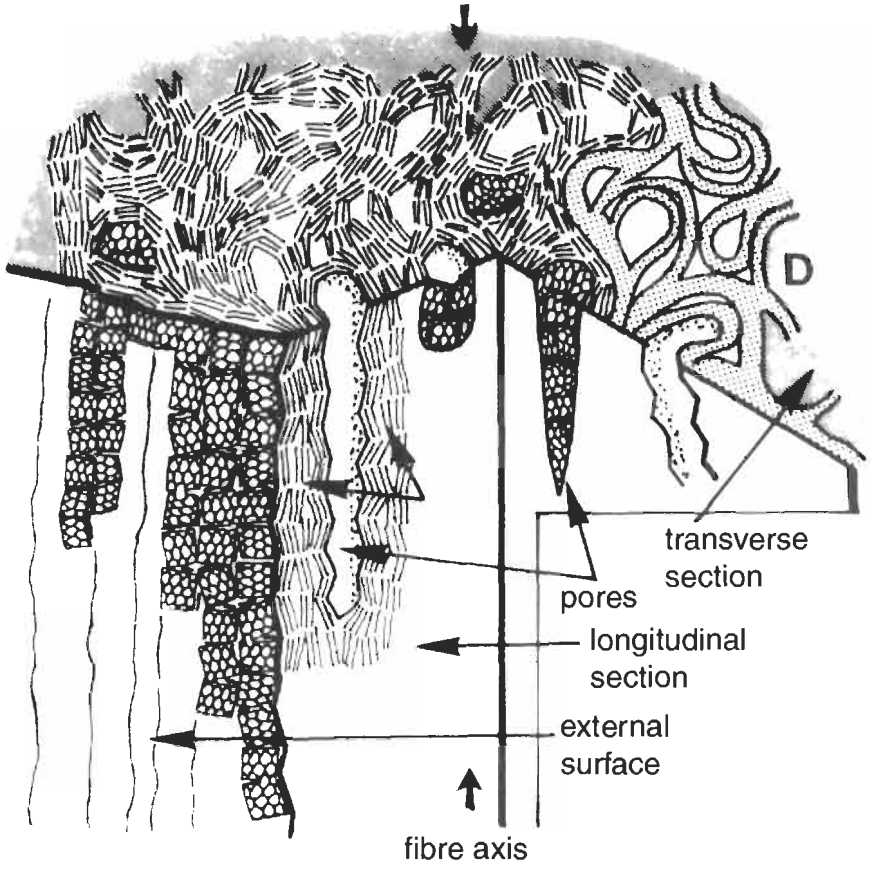

Fig. 10. Model of microtexture of PAN-based carbon fiber. (Copyright 1984, reproduced with permission from Elsevier Science.)

The weight loss experienced in the production of carbon fibers from PAN precursor is approximately 50%. Guigon et al. (1984) showed that this leads to a structure containing many longitudinal voids, as shown in Fig. 10, and a density of $\sim$1.8 g/cm^3, compared with 2.28 g/cm^3 for pure graphite, and 2.1 for pitch-based carbon fibers. Boyes and Lavin (1998) showed evidence for the polymeric nature of the fiber in the fracture surface shown in Fig. 11. The fibrils are evident on the wall of the fiber. An enlargement of the fracture surface in Fig. 12 shows fibrils at the nanometer scale. The results of a remarkable experiment by Kwizera et al. (1982) are shown in Fig. 13. A Celion GY-70 fiber was fractured in vacuum, and exploded into microfibrils roughly 100 nm in diameter, further confirming the fibrillar nature of the PAN-based fiber.

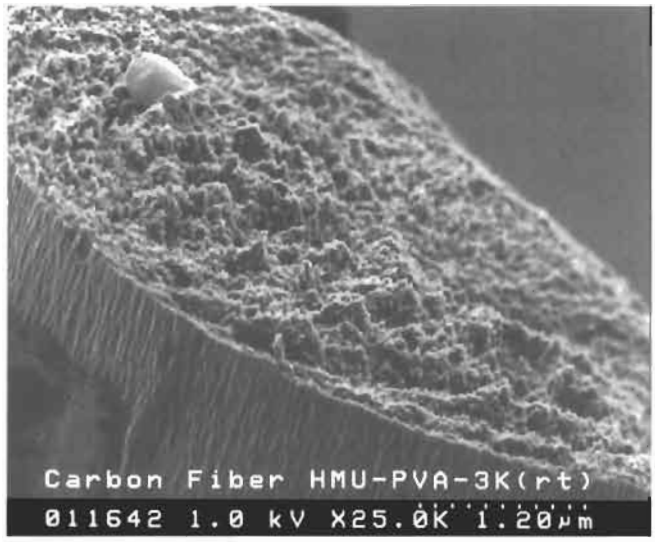

Fig. 11. PAN-based carbon fiber fracture surface.

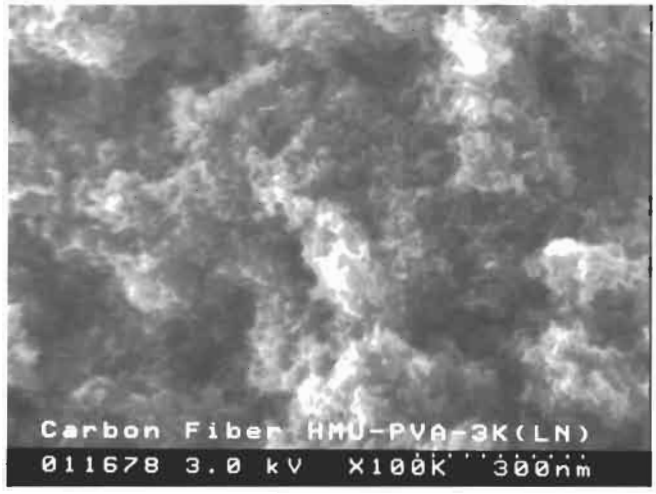

Fig. 12. Enlargement of fibrils in PAN-based carbon fiber fracture surface.

PITCH-BASED CARBON FIBERS

General Purpose Pitch-Based Carbon Fiber

These fibers are sometimes referred to as 'isotropic' carbon fibers, since they are made from isotropic pitch. These pitches are prepared from high boiling fractions of petroleum feedstocks, usually heavy slurry oils produced in catalytic cracking of crude oil.

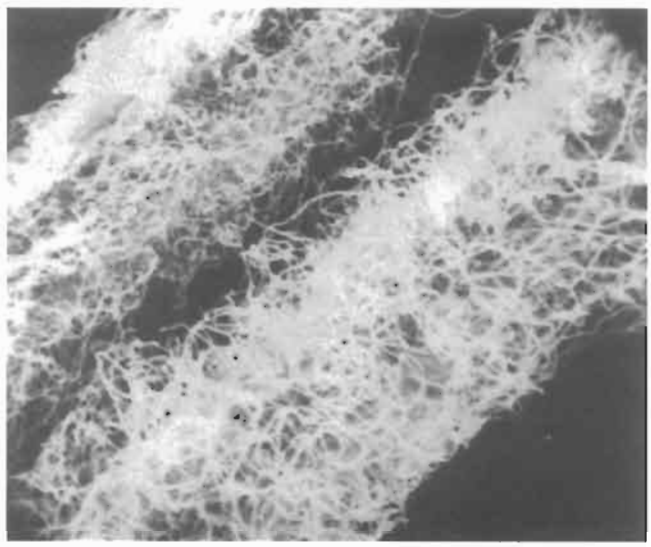

Fig. 13. PAN-based carbon fiber fractured in vacuum. The fibrils are approximately 100 nm in diameter. (Copyright 1982, reproduced with permission from Elsevier Science.)

A typical commercial pitch is Ashland Aerocarb 70, which has a softening temperature of 208°C and a viscosity of 1 Pa s at 278°C. Additional treatments to selectively reduce low molecular weight components are described by Sawran et al. (1985).

General purpose fibers are prepared by two different spinning methods, centrifugal spinning and melt blowing, both of which are high-productivity processes. A more detailed discussion of these processes will be found in Lavin (2001b).

High-Performance Pitch-Based Carbon Fibers

High-performance fibers are made from mesophase pitch, which is a discotic liquid crystalline material. While mesophase pitches can be made from many starting materials, there are only a few which are of commercial interest. These are dealt with in the sections which follow. These fibers are typically melt spun, and spinning technology is the same for all pitch types.

There are three common elements in pitch preparation: first, a highly aromatic feedstock; second, a process for polymerizing the molecules; third, a process for separating out the unreacted feed molecules. The feedstock is typically a decant oil from cat cracker bottoms. When polymerized, the pitch molecule will have characteristics similar to the molecule shown in Fig. 14. When they get sufficiently large, the pitch molecules aggregate to form spheres, as shown in Fig. 15. The spheres are named for their discoverers, Brooks and Taylor (1965). The spheres in turn coagulate to form larger spheres and then, as polymerization continues, there is a phase inversion and a continuous nematic liquid crystalline phase, typically called mesophase (Greek for changing phase), is formed.

Pitches are characterized by their fractional solubility in increasingly powerful sol-

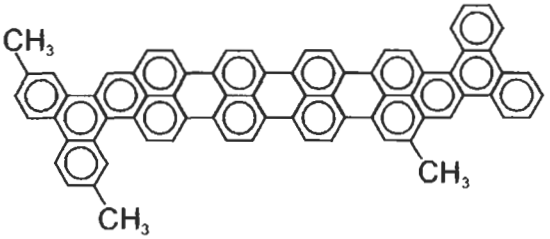

Fig. 14. Typical pitch molecule.

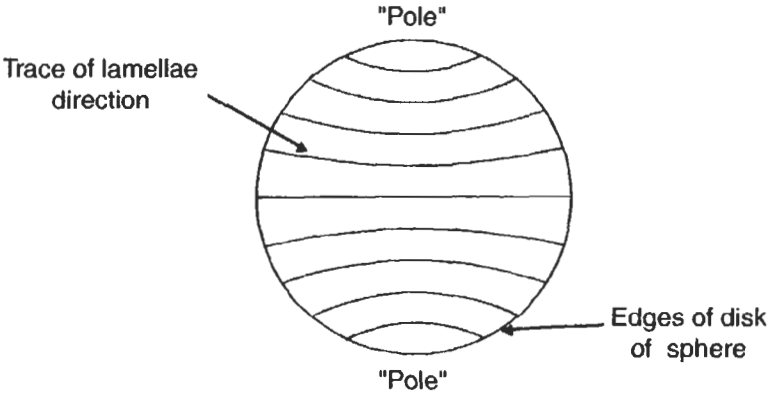

Fig. 15. Brooks and Taylor mesophase sphere.

vents; for example toluene, pyridine, quinoline. The highest molecular weight fractions are not soluble in any known solvent. It is believed that the smaller molecules in the pitch are solvents for the larger ones, and allow the pitch to flow at elevated temperatures.

Petroleum-based pitches are typically made from the same slurry or decant oils used to make isotropic pitches. The earliest processes for making mesophase pitches are similar to that described by McHenry (1977). They used a long heat soak (typically about 30 h at 400°C) under an inert atmosphere, while a gas sparge was used to take away volatile compounds. Such pitches might typically have a molecular weight of about 1000 Dalton, and melt at about 300°C. They would also be characterized by high quinoline insolubles.

Coal tar pitches are a by-product of coke ovens associated with steel-making operations. They differ from petroleum pitches in their rheological properties; for a given molecular weight the flow viscosity is much higher. Coal tar pitches also have fewer aliphatic groups on the molecules, which makes for longer stabilization cycles. A breakthrough in preparation of coal tar pitches came when the Japanese Agency of Industrial Science and Technology (1983) developed a process for hydrogenating them, significantly reducing viscosity and reducing quinoline insolubles to zero. The physical properties of fibers from coal tar pitches are generally competitive with fibers from petroleum pitches, except that, so far, they have not been capable of making the highest modulus products (800 GPa and higher).

Pitch processes have been under continual development for the last two decades, and are now at the stage where high molecular weight, uniform pitches can be produced in continuous processes. A detailed review of this subject will be found in Lavin (2001a).

A Paradox

The requirements for a strong polymer fiber are well known. They start with extremely pure ingredients which are polymerized to very high molecular weights. Once spun, the crystallites are oriented parallel to the fiber axis by stretching. In the case of pitch-based carbon fibers, the situation is very different. The ingredients come from a waste stream of unknown and variable composition. Since the molecular weight of a pitch is positively correlated with its melting point, molecular weight must be kept down, so that fiber can be spun below about 300°C. Above this temperature, seals are unreliable, and equipment becomes very expensive. Finally, the as-spun pitch-based carbon fiber is too weak to stretch. These failings are compensated by the wonderful self-organizing properties of aromatic carbon; particularly its ability to orient crystallites along the fiber axis by heat treatment in the relaxed state.

Fiber Formation

Melt spinning of mesophase pitches, as described by Edie and Dunham (1989), is the preferred method of obtaining high-performance fibers. The controlled drawing process provides the most uniform continuous filament products, while the wound product form necessitates uniform treatment of bundles of fibers in downstream processing. However, processing rates are generally low and greatly depend upon the quality of the pitch feedstock. Pitch rheology and the arrangement of the discotic liquid crystal was found to determine mesophase pitch structure and resultant product responses in a study by Pennock et al. (1993). This structure can be defined on a macroscopic scale by scanning electron microscopy (SEM), whereas microscopic structure on the atomic scale requires use of other techniques, such as transmission electron microscopy (TEM). Bourratt et al. (1990) effectively used these techniques to determine the structure of pitch fibers. Ross and Jennings (1993) and Fathollahi and White (1994) showed that the orientation of discs relative to one another and the fiber axis is an important element to control in the filament formation step.

By utilizing filament formation geometry to establish preferred flow profiles and spin conditions that complement them, structure can be manipulated and controlled. Example geometries, when coupled with appropriate feedstocks and operating conditions, conducive to structure control and resultant product responses, are shown in Fig. 16. Fiber cross-sectional structure, as defined by SEM, are schematically represented while product categorizations of physical and thermal properties are noted. The typical fiber structures illustrated here have been labelled by several researchers as 'pacman' radial, wavy radial and severe 'pacman'. Other structures such as random, onion-skin and 'Pan Am' have also been produced and categorized. An illustration of the most common types is shown in Fig. 17. The fibers with 'pacman' cross-sections have longitudinal splits which may adversely affect physical properties. Downstream processing, within

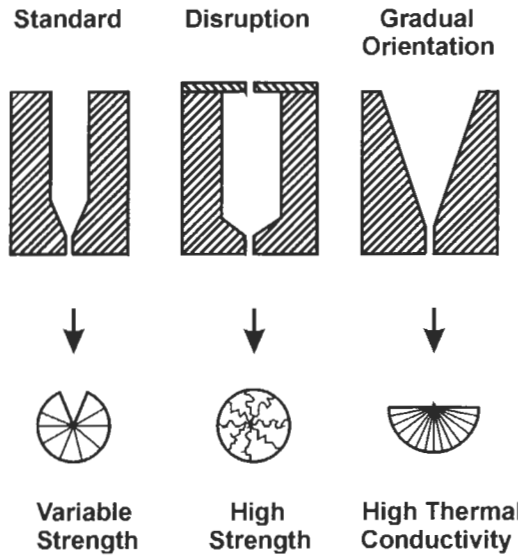

Fig. 16. Influence of spinneret design on fiber morphology.

limits, appears to have minimal influence in changing the general 'structure' established in the filament formation step. Subsequent heat treatment densifies the initial structure, i.e., increases the packing to increase tensile and thermal properties and modulus.

The use of non-round pitch carbon fiber cross-section provides an alternate approach to modify 'structure' with potential enhancement of fiber adhesion to matrices, improved surface characteristics or improved conductivity. This forced filament geometry is routinely practiced with several polymeric systems in melt spinning to control product response. Ribbon and C-shaped carbon fibers have been provided to accomplish this, as

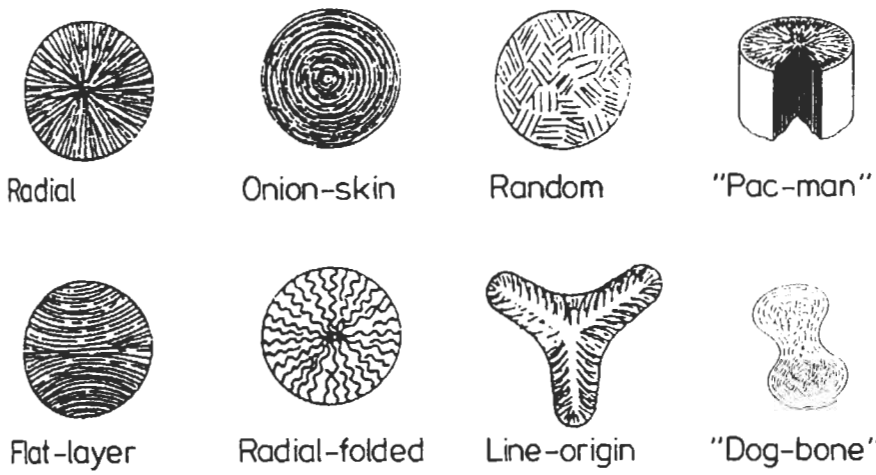

Fig. 17. Summary of possible carbon fiber morphologies.

described by Fain et al. (1988) and Robinson and Edie (1996). However, the stiffness aspects of modified fiber cross-section could be adversely affected while thermal and adhesion responses may be improved. Packing densities of individual fibers in fiber assemblages may also be changed. Processing continuity and part fabrication costs could be critical aspects influencing adoption of this technology to modify product responses. A more detailed discussion of fiber manufacture will be found in Bahl et al. (1998).

Commercially useful fibers are made from mesophase pitch at heat treatment temperatures of 1600°C and above. As heat treatment temperatures are increased, the modulus of mesophase pitch fibers increases, and modulus values close to the theoretical modulus of graphite (1 TPa) are possible. The term 'graphitization' is frequently applied to heat treatment above 2500°C. However, this does not mean that the structure is converted to graphite. Most carbon fibers, even those with a modulus above 700 GPa, are mostly made of turbostratic carbon with small graphitic domains. The inert gases used in carbonizing furnaces are nitrogen and argon. Nitrogen is preferred because of cost. However, above about 2000°C significant quantities of cyanogens are produced by the reaction of nitrogen with the graphite of the furnace, so argon, which is completely inert, is sometimes used instead.

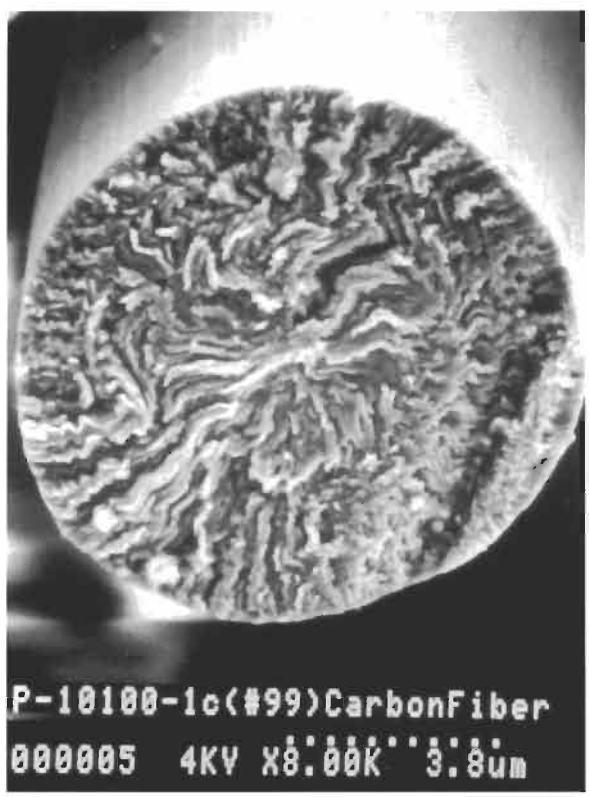

Fig. 18. Pitch-based carbon fiber fracture surface.

An SEM image of the fracture surface of a pitch-based carbon fiber is shown in Fig. 18. It will be noted that there are many zig-zag features, which allow the fiber to sustain a 40% reduction in surface area during heat treatment without introducing damaging hoop stresses. The large, flat crystals which make up the fiber are evident in Figs. 19 and 20, and the nature of the surface is shown in Fig. 21.

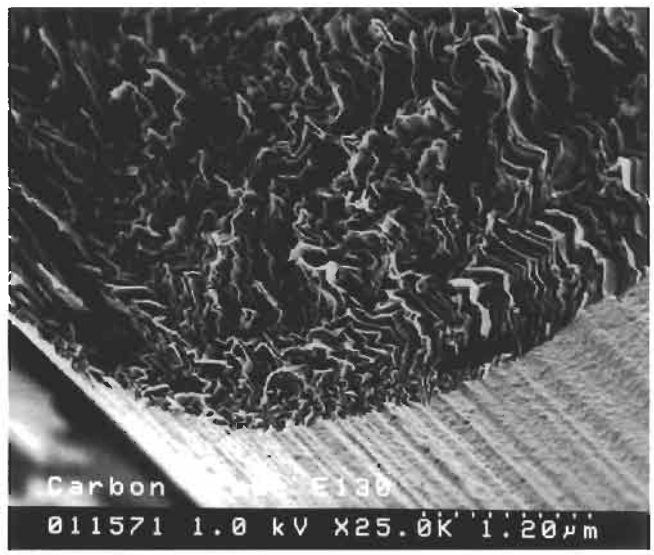

Fig. 19. Pitch-based carbon fiber fracture surface: enlarged view.

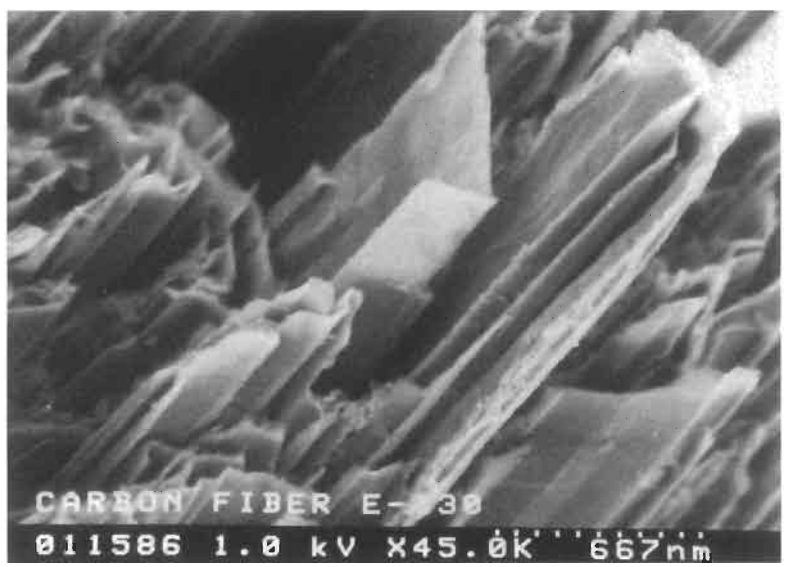

Fig. 20. Pitch-based carbon fiber fracture surface: view of large crystallites.

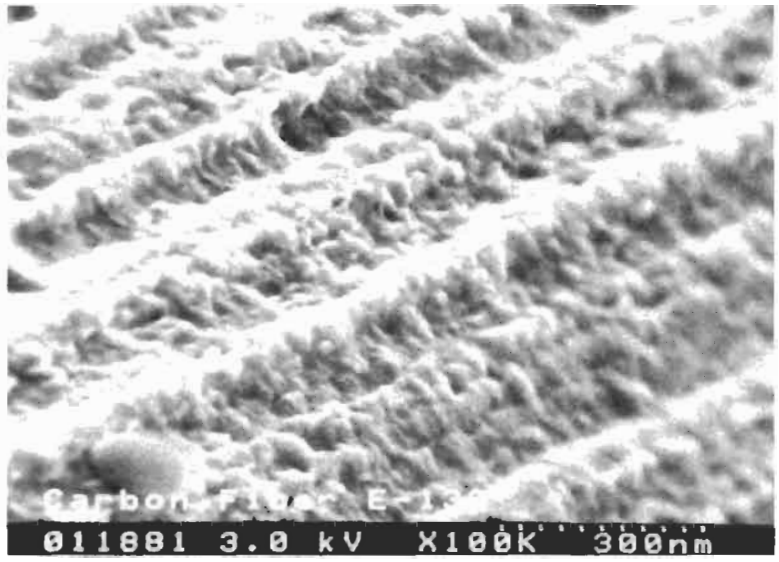

Fig. 21. High-resolution scanning electron micrograph of pitch-based carbon fiber surface.

VAPOR-GROWN CARBON FIBERS

Pure carbon fibers may be grown by a catalytic process from carbon-containing gases. The catalysts are typically transition or noble metals, and the gases are CO or virtually any hydrocarbon. The fibers were first identified by Schutzenberger and Schutzenberger (1890), and they were the subject of study within the oil industry more recently, with the objective of preventing their growth in petrochemical processes. The fibers may take a variety of forms, depending upon the catalyst system and the constituents of the feed gas. The interested reader is referred to an excellent review article by Rodriguez (1993).

A generic process for catalytic formation of carbon fibers is described by Rodriguez (1993). Typically, about 100 mg of powdered catalyst is placed in a ceramic boat which is positioned in a quartz tube, located in a horizontal tube furnace. The catalyst is reduced in a dilute hydrogen/helium stream at 600°C, and quickly brought to the desired reaction temperature. Following this step, a mixture of hydrocarbon, hydrogen and inert gas is introduced into the system, and the reaction is allowed to proceed for about 2 h. This approach will produce about 20 g of carbon fibers from the more active catalyst systems. In this process, the fiber diameter is typically related to the catalyst particle size. The process proposed for fiber formation by Oberlin et al. (1976) involves adsorption and decomposition of a hydrocarbon on a metal surface to produce carbon species which dissolve in the metal, diffuse through the bulk, and ultimately precipitate at the rear of the particle to produce the fiber. This process is described as tip growth. There is an analogous process in which the catalyst particle remains attached to the support.

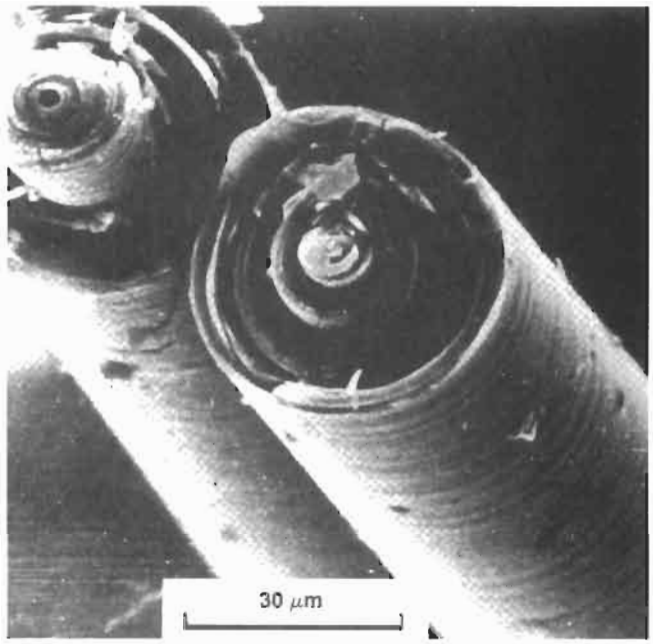

Fig. 22. Vapor-grown carbon fiber fracture surface. From Endo (1988). (Copyright 1988. Reprinted with permission from the American Chemical Society.)

Vapor-grown fibers typically have a hollow center and multiple walls, which are arranged like tree rings, as shown in Fig. 22. However, they may be grown in many other shapes, as shown in Fig. 23.

There are basically two kinds of processes for producing vapor-grown fibers. The most common process is the one described above, in which the catalyst is a metal supported on a ceramic. This process produces long fibers which are tangled together in a ball which is extremely difficult to break up. A variant of this process is one in which the catalyst is an organometallic injected into a chamber containing the gas mixture. These fibers tend to be short and straight. However, they may be aggregated together and bound by amorphous carbon. In either case, the reinforcing capabilities of the fiber are restricted.

FAILURE MECHANISMS

Tensile Failure

The most revealing experiments were conducted by Bennett et al. (1983), who fractured PAN-based carbon fibers in glycol, a medium which absorbed the explosive energy generated at fiber failure. This allowed meaningful examination of the broken ends by SEM and TEM. They observed large misoriented crystals in the internal flaws

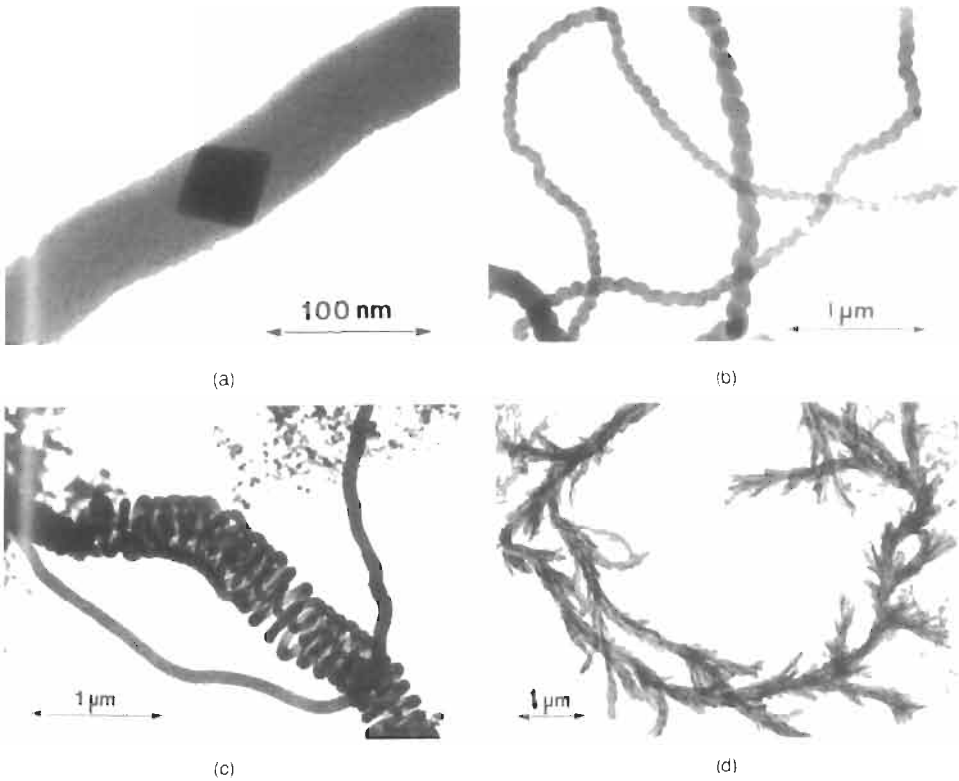

Fig. 23. Transmission electron micrographs of different kinds of vapor-grown fibers: (a) bi-directional; (b) twisted; (c) helical; and (d) branched. (Reprinted from Rodriguez (1993) by permission of the author. Images (a) and (b) originally appeared in the *Journal of Catalysis*. Permission to reproduce them was also granted by Harcourt, Brace and Co.)

which initiated failure. Earlier, a failure model involving misoriented crystals had been proposed by Reynolds and Sharp (1974). The model is illustrated in Fig. 24. The misoriented crystal is shown in (a), crack initiation in (b) and crack propagation leading to crystallite and ultimately fiber fracture in (c). The PAN-based fiber fracture surface shown in Fig. 12 gives evidence of the tremendous amount of new surface which is created, a measure of the high strength of the fiber. A similar mechanism is believed to be responsible for failure of mesophase pitch-based carbon fiber. However, the highly turbostratic nature of the fiber structure will inhibit crack propagation. For example, see the large flat planes which are present in the Fig. 19 fracture surface, also causing generation of large amounts of new surface.

Compressive Failure

Extensive compressive failure studies have been conducted on both individual fibers and composites. Arguably, the individual fiber studies are not meaningful, since carbon

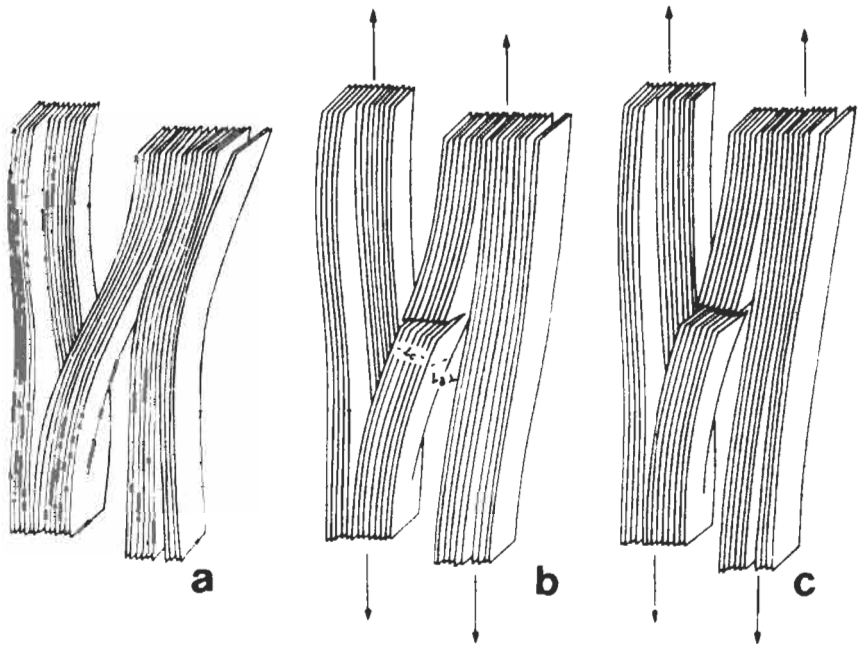

Fig. 24. Mechanism of tensile failure in misoriented crystal. From Bennett et al. (1983). (Copyright 1983, reprinted with permission from Kluwer Academic Press.)

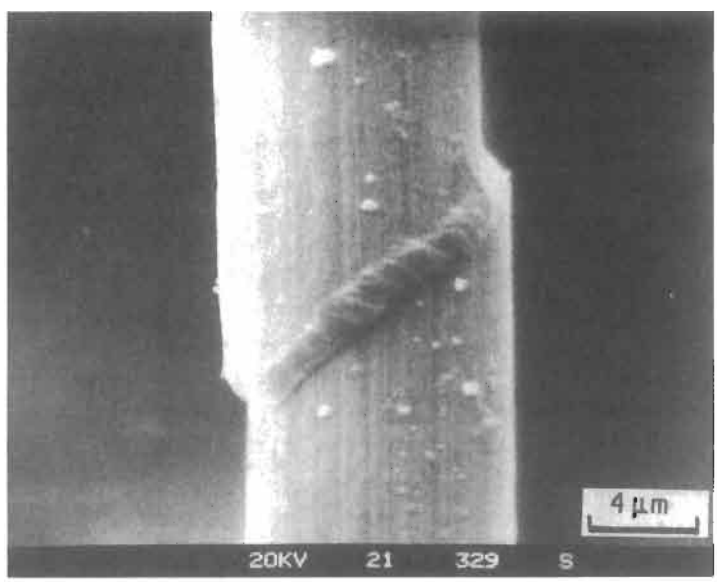

Fig. 25. Shear bands in high modulus mesophase pitch-based carbon fiber after moderate deformation. From Dobb et al. (1990). (Copyright 1990, reprinted with permission from Kluwer Academic Press.)

fibers are seldom subjected to large compressive forces. These tests are typically either knot tests or recoil tests, and PAN-based fibers typically fail in either micro-buckling or shear, while mesophase pitch-based fibers fail in shear at a much lower level. These failure modes are illustrated in Figs. 25 and 26.

In composites, Drzal and Madhukar (1993) observed that the failure mode depended on the level of fiber/matrix adhesion: at low levels, the mechanism was global delamination buckling; at intermediate levels, fiber microbuckling; at high levels fiber compressive (shear) failure. This is illustrated in Fig. 27.

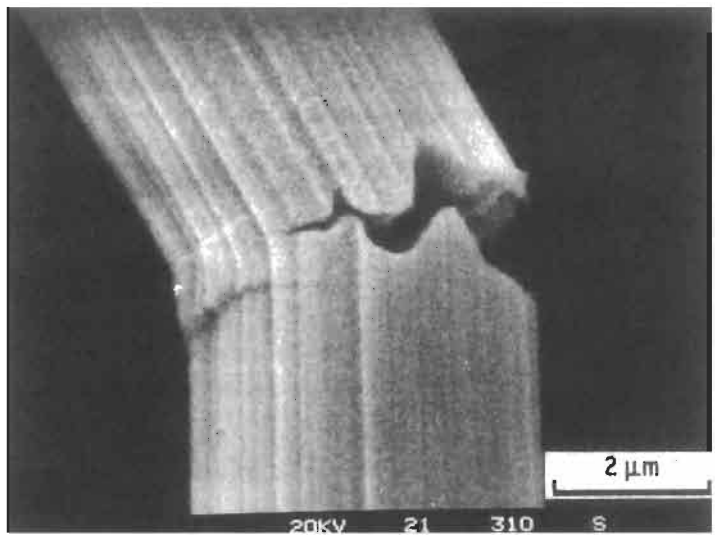

Fig. 26. Kink bands in PAN-based carbon fibers after recoil compression under high deformation. From Dobb et al. (1990). (Copyright 1990, reprinted with permission from Kluwer Academic Press.)

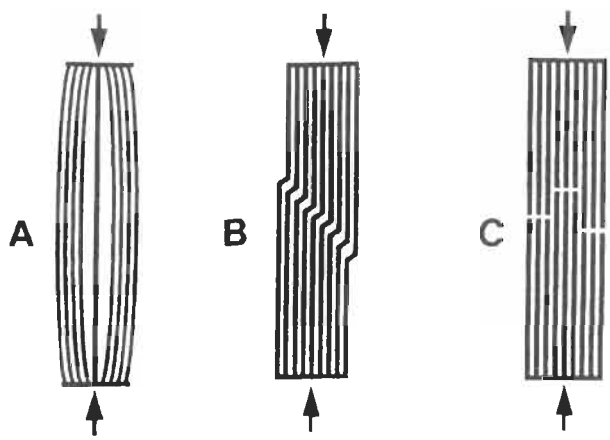

Fig. 27. Major failure modes for carbon fiber/epoxy laminates. From Drzal and Madhukar (1993). (Copyright 1993, reprinted with permission from Kluwer Academic Press.)

CONCLUDING REMARKS

Carbon fiber fracture studies have been extremely valuable in defining the structure of the different kinds of fibers, leading to an understanding of their performance in particular applications. The high contrast obtained with carbon in TEM, and the ability to image directly, without metal coating in SEM, have made these microscopies particularly well suited for carbon fiber fracture studies.

REFERENCES

Bahl, O.P., Shen, Z., Lavin, J.G. and Ross, R.A. (1998) In: *Carbon Fibers*, 3rd ed., pp. 1–85, J.-B. Donnet, T.K. Wang, J.C.M. Peng and S. Rebouillat (Eds.). Marcel Dekker Inc., New York.

Bennett, S.C., Johnson, D.J. and Johnson, W. (1983) Strength–structure relationships in PAN-based carbon fibers. *J. Mater. Sci.*, 18: 3337–3347.

Bourratt, X.M., Roche, E.J. and Lavin, J.G. (1990) Structure of mesophase pitch fibers. *Carbon*, 28: 435–446.

Boyes, E.D. and Lavin, J.G. (1998) In: *Atlas of Fiber Fracture and Damage to Textiles*, 2nd ed., p. 65, J.W.S. Hearle, B. Lomas and W.D. Cooke (Eds.). Woodhead Publishing, Cambridge.

Brooks, J.D. and Taylor, G.H. (1965) The formation of graphitizing carbons from the liquid phase. *Carbon*, 3: 185–193.

Dobb, M.G., Johnson, D.J. and Park, C.R. (1990) Compressional behavior of carbon fibers. *J. Mater. Sci.*, 25: 829–834.

Drzal, M.T. and Madhukar, M. (1993) Fiber–matrix adhesion and its relationship to composite mechanical properties. *J. Mater. Sci.*, 28: 569–610.

Edie, D.D. and Dunham, M.G. (1989) Melt spinning pitch-based carbon fibers. *Carbon*, 27: 647–655.

Endo, M. (1988) Grow carbon fibers in the vapor phase. *Chemtech*, 18: 568–576.

Fain, C.C., Edie, D.D., DuBose, W.A. and Schikner, R.C. (1988) Microstructure formation during the extrusion of pitch fibers. *Carbon '88*, The Institute of Physics, Newcastle upon Tyne, 18–23 September, pp. 540–545.

Fathollahi, B. and White, J.L. (1994) Polarized light observations of flow-induced microstructure in mesophase pitch. *J. Rheol.*, 38: 1591.

Guigon, M., Oberlin, A. and Desarmot, G. (1984) Microtexture and structure of some high tensile strength, PAN-base carbon fibres. *Fibre Sci. Technol.*, 20: 55–72.

Japanese Agency of Industrial Science and Technology (1983) Pat. Appl. No. 2 129 825, UK Patent Office, August 24, 1983.

Kogure, K., Sines, G. and Lavin, J.G. (1996) Creep behaviour of a pitch-based carbon filament. *J. Am. Ceram. Soc.*, 79: 46–50.

Kwizera, P., Dresselhaus, M.S., Uhlmann, D.R., Perkins, J.S. and Desper, C. (1982) The microstructure of intercalated graphite fibers. *Carbon*, 20: 387–394.

Lavin, J.G. (2001a) Mesophase precursors for advanced carbon fibers: pitches, stabilization and carbonization. In: *NATO Science Series E: Applied Sciences - Vol. 374: Design and Control of Structure of Advanced Carbon Materials for Enhanced Performance*, pp. 151–161, Rand, B., Appleyard, S.P. and Yardim, M.F. (Eds.). Kluwer Academic Publishers, Dordrecht.

Lavin, J.G. (2001b) Carbon fibres. In: *High-Performance Fibres*, pp. 156–190, J.W.S. Hearle (Ed.). Woodhead Publishing, Cambridge.

McHenry, E.R. (1977) Process for producing mesophase pitch. US Patent Office, Pat. No. 4 026 788, May 31, 1977.

Moreton, M. and Watt, W. (1974) The spinning of polyacrylonitrile fibres in clean room conditions for the production of carbon fibres. *Carbon*, 12: 543–554.

Oberlin, A., Endo, M. and Koyama, T., (1976) Filamentous growth of carbon through benzene decomposition. *J. Crystal Growth*, 32: 335–349.

Peebles, L.H. (1994) *Carbon Fibers: Formation, Structure and Properties*. CRC Press, Boca Raton, FL.

Pennock, G.M., Taylor, G.H. and FitzGerald, J.D. (1993) Microstructure in a series of mesophase pitch-based carbon fibers from DuPont: zones, folds and disclinations. *Carbon*, 31: 591–610.

Reynolds, W.N. and Sharp, J.V. (1974) Crystal shear limit to carbon fiber strength. *Carbon*, 12: 103–110.

Robinson, K.E. and Edie, D.D. (1996) Microstructure and texture of pitch-based ribbon fibers for thermal management. *Carbon*, 34: 13–36.

Rodriguez, N.M. (1993) A review of catalytically grown carbon fibers. *J. Mater. Res.*, 8: 3233–3250.

Ross, R.A. and Jennings, U.D. (1993) Pitch carbon fiber spinning process. US Patent Office, Pat. No. 5 202 072, Apr. 13, 1993.

Salama, M.M. (1997) Some challenges for deepwater development. *Proceedings of Off-Shore Technology Conference*, OTC, 8455.

Sawran, W.R., Turrill, F.H., Newman, J.W. and Hall, N.W. (1985) Process for the manufacture of carbon fibers. US Patent Office, Pat. No. 4 497 789, Feb. 5, 1985.

Sines, G., Yang, Z. and Vickers, B.D. (1989) Creep of a carbon–carbon composite at high temperatures and high stresses. *Carbon*, 27: 403–415.

Schutzenberger, P. and Schutzenberger, L. (1890) *C. R. Acad. Sci. (Paris)*, 111: 774–778.

METALLIC FIBERS

Fiber Fracture
M. Elices and J. Llorca (Editors)

STRENGTH AND FRACTURE OF METALLIC FILAMENTS

H.U. Künzi

Ecole Polytechnique Fédérale de Lausanne, Département des Matériaux, CH-1015 Lausanne, Switzerland

Introduction 185
Failure Due to Fabrication and Externally Introduced Defects 185
Drawing Defects, Nonhomogeneous Microstructure and Texture 185
Melt-Spinning Defects 194
Intrinsic Strength and Failure Behavior 200
Ideal Behavior of Metallic Whiskers 200
Polycrystalline Micro-Wires 203
Effect of Annealing and Recrystallization on the Mechanical Properties 204
Recrystallization Kinetics of the Mechanical Properties 206
Recrystallization Kinetics of Young's Modulus 210
Size Effect of Polycrystalline Strengthening in Thin Filaments 212
Fatigue of Polycrystalline Wires 215
Fracture and Mechanical Properties of Metallic Glasses 228
Elastic Behavior of Metallic Glasses 229
Anelastic and Viscoplastic Behavior of Metallic Glasses 231
Fracture and Plastic Deformation of Metallic Glasses 231
Fatigue of Metallic Glasses 235
Acknowledgements 238
References 238

Abstract

Fracture of metallic filaments differs in many respects from fracture of bulk samples. Particular fabrication processes that are needed to obtain the small lateral dimensions, may introduce specific defects and textures. Their influence on the fracture behavior is discussed. The intrinsic strength and fracture behavior is mainly dependent on the microstructure. The absence of crystalline defects as in whiskers, as well as the presence

of high defect densities in strain-hardened wires and amorphous ribbons give rise to strong filaments. Polycrystalline strengthening in micro-wires and thin foils becomes size dependent and shows deviations from the Hall–Petch relation. Fatigue of micro-wires and thin foils is difficult to predict. It appears that this property is strongly influenced by microstructural details and the environment. In crystalline wires with only a few grains in their cross-section the fatigue life is strongly size dependent.

Keywords

Fracture of wires; Fracture of metallic glasses; Deformation texture; Drawing defects; Polycrystalline strengthening; Fatigue of micro-wires; Fatigue of metallic glasses; Bonding wires

INTRODUCTION

Fracture of massive brittle and ductile pieces are rather well understood. By taking proper account of the microstructure as well as the micro- and macro-defects, most catastrophic and fatigue failures find a satisfactory explanation within the scope of the linear elastic fracture mechanics or the elasto-plastic fracture mechanics. Metallic filaments are particular and in many respects deserve a treatment of their own. Particular fabrication methods, such as drawing, melt spinning or crystallization from the vapor phase for whiskers are needed to obtain their small lateral dimensions. These processes may give rise to particular textures, intrinsic and extrinsic defects. Thermal treatments may modify or eliminate such defects but in many cases fracture is initiated by defects that stem from the fabrication process. Moreover, the small lateral dimensions, especially in micro-wires, make metallic filaments prone to external influences. Corrosive attacks may rapidly affect an important fraction of their cross-section. Hydrogen, for instance, which usually results in a severe embrittlement, may diffuse up to the core in a rather short time.

Metallic filaments, however, are not always full of such defects. Whiskers with diameters of a few micrometers even approach the picture we have from an ideal crystal. The absence of even intrinsic crystalline defects gives rise to the well-known size effect in the rupture stress. Interestingly, also in the case of a completely disordered crystal structure such as amorphous metals, which apart from a few alloys of complex composition can only be produced in filamentary form, an extremely high resistance to fracture and fatigue is observed.

Similarly, in polycrystalline wires extremely high rupture stresses which by far exceed the values observed in the bulk metals may be obtained through the strain hardening resulting from the drawing process. Recrystallization treatments of polycrystalline wires reduce the intrinsic defect concentrations and increase the grain size, give rise as in bulky samples to soft structures. Interesting size effects in the yield stress and the crack initiation in fatigue become, however, apparent in micro-wires when the number of grains on a cross-section becomes small (oligocrystalline microstructure).

FAILURE DUE TO FABRICATION AND EXTERNALLY INTRODUCED DEFECTS

Drawing Defects, Nonhomogeneous Microstructure and Texture

The majority of wires and metallic filaments are produced by drawing. The extreme cold work to which the metal is subjected modify its microstructure and in most cases introduces a strong fiber texture. Both the microstructure and the texture are known to have a strong influence on the mechanical behavior of the wires and are in many cases exploited to achieve the desired properties. Moreover, the deformation and the material flow are very nonhomogeneous and depend on the form of the die, the friction between wire and die, and the strain hardening capacity of the metal. This gives rise to heterogeneous microstructures and may cause macroscopic structural defects.

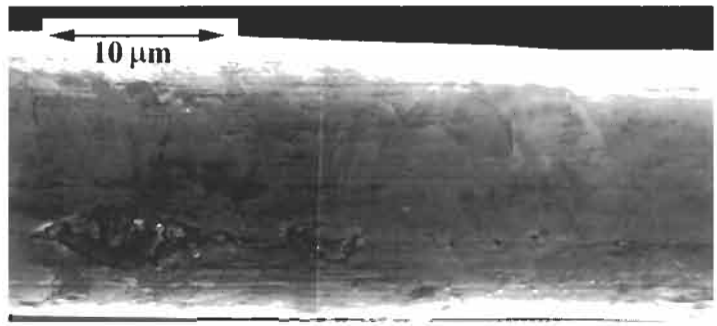

Fig. 1. A brittle inclusion at the beginning of a channel of debris in a 25 μm Au wire.

A great variety of various drawing defects are known to occur (Catalogue of Drawing Defects, 1985). Some defects may already be present in the rod prior to drawing the wire and others appear during the drawing process. The former often produce catastrophic failures during the drawing and fortunately the latter are mostly due to inadequate drawing tools and drawing parameters. These defects are readily detectable and are therefore of little or no concern in commercial products. In some cases, however, hidden defects such as voids along the wire centerline (central bursts) and inclusions may occur even under sound drawing conditions.

Non-metallic inclusions such as oxide particles are often trapped in the metal during remelting. Even though in composite materials hard particles are deliberately added to reinforce ductile metals, the presence of such particles is incompatible with the drawing process. The difference in their yield and flow properties rapidly leads to complete decohesion along the interface and even voids may be formed along the drawing direction. Bigger particles may also break up and produce a channel of debris. Similarly, metallic inclusions with yield properties that are different from the matrix may produce substantial drawing defects. The effect of inclusions is particularly feasible in micro-wires where they may cover an important fraction of the cross-section. Fig. 1 shows a brittle inclusion appearing at the surface in a 25 μm thick Au wire.

Murr et al. (1997) and Murr and Flores (1998) describe an interesting case of contaminated submicron Cu particles in Cu wires. During the fabrication of precursor rods (later used for drawing the wire) bursting vapor bubbles may produce a spray or mist of liquid Cu particles. The vapor in the bubbles results from the reaction of H_2, dissolved in Cu from the reducing furnace atmosphere, with O_2 from the air when molten Cu is cast into open molds. The emanating particles solidify rapidly but remain hot enough to react with air, slagelements or carbon from the graphite blanket covering the liquid Cu. After reintegration in the melt the reaction layer acts as a diffusion barrier and prevents complete dissolution in the Cu melt. During drawing the surface-reacted Cu particles behave somewhat like second-phase particles. The surface layer smears out in the drawing direction and tiny voids form in front and behind the particles.

Cup-shaped voids along the center line of the wire are known to result from a phenomenon called central burst or chevroning. This phenomenon has its primary origin in the flow pattern of the yielding metal. The zone where this occurs is located at the end

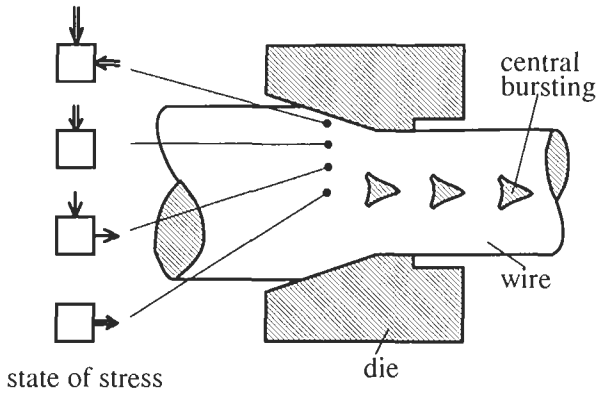

Fig. 2. State of stress during drawing and central bursting defects. They appear along the axis in work-hardened wires when metals become unable to sufficiently yield.

of the conical part of the die (Fig. 2). The flow pattern in this zone depends on the local state of the stress deviator which in turn depends on the die geometry, drawing velocity and friction. The near-surface part of a cylindrical wire below the conical part of the die is under compression. Here all three principal stresses are negative and give rise to a considerable hydrostatic pressure. By far the largest stress component is the radial stress followed by the tangential stress. Even though the wire is pulled through the die, with no pushing force, the axial stress in this part of the wire is compressive. It changes its sign only near 0.6 times the wire radius r and then rapidly increases towards the axis where it becomes the dominant principal (traction) stress. The hydrostatic and tangential stresses vanish at about $0.3r$. The radial stress continuously decreases from the surface towards the center line but remains always compressive. Accordingly, only a part of the cross-section feels the drawing stress and an even smaller section is under a negative hydrostatic pressure. From this it follows that the major plastic elongation takes place in the central part. Atoms from the outer portion are pressed along the radial direction towards the center line but being incompressible, they contribute to the axial flow. Finally, it has to be noted that the axial extension of the plastic zone shrinks towards the axis. We therefore do not only have the largest deformation along the center line but, in addition, this deformation has to be established over a relatively small distance. If for some reason this flow in the central portion cannot be maintained or the axial extent of the plastic zone shrinks too strongly, this ultimately results in internal fractures and the formation of voids whose cup- or chevron-like form reflects the velocity field near the axis.

Such defects have been explained (Avitzur, 1980; Mielnik, 1991) by a reduced strain hardening capacity as occurs in already strongly deformed metal. It resembles closely the necking in a tensile test which also occurs when the strain hardening ability is reduced. Similarly, this happens towards the end of the drawing process when the wire already passed through several dies. For the reasons mentioned above the interior will be more severely deformed (smaller strain hardening exponent) than the outer part. These defects may also be caused by segregation or second-phase particles in the range where a strong negative pressure prevails.

It is also known that too large die opening angles favor the formation of these defects. The drawing force necessary to give a certain cross-section reduction varies strongly with the die opening angle α. At small angles the length (fixed reduction) of the conical part of the die is long. This favors friction and radial compressive stress. In this range of α the drawing force decreases when α increases. At larger angles the excessive plastic work starts to increase and becomes the dominant contribution in the drawing force. The conditions prevailing at the minimum in between these two regimes are usually chosen for drawing wires. Beyond this minimum experimental observations indicate that the state of stress starts to change. Above a critical angle α the wire loses contact with the conical part of the die and the so-called dead zone forms between wire and die. Under these conditions the wire is just kept back by the smallest opening of the die. At a slightly larger angle the wire is even rather shaved than thinned. The increase of the drawing force and the dead zone formation beyond the minimum drawing force indicate that the zone of negative hydrostatic pressure extends with respect to the compressive zone and thus creates the conditions for the central burst phenomenon (voids along the wire axis, see Fig. 3) to become possible.

Since in subsequent traction of the final wire these voids produce stress concentrations, the wire starts to yield prematurely near an internal void until the final rupture separates the two parts in a cup fracture (Murr and Flores, 1998).

Defect-free Cu wires, as most other ductile wires, show usually necking with a rough final fracture surface orthogonal to the wire (Fig. 4a,c). With very ductile wires (recrystallized), necking may go up to the center of the wire before the final failure. In micro-wires recrystallization may give rise to grain sizes that become (comparable or) equal to the wire diameter. In this limiting case of a bamboo structure a single grain having a well-oriented glide system may produce a wedge-shaped neck (Fig. 4b,d).

The nonhomogeneous deformation during drawing not only creates occasional problems with defects but it gives also rise to microstructural differences which influence the mechanical properties and the recrystallization behavior. In heavily drawn wires the grains are usually too small to be observable in an optical microscope (Fig. 5). In fact, TEM observations of as-drawn wires (prior to annealing) reveal a mixture of very small microstructural elements (Busch-Lauper, 1988). Fig. 6 shows a longitudinal TEM image of a 38 μm thick Cu wire (purity 99.99%). Strongly elongated dislocation cells or subgrains appear in the form of micro-bands that are arranged along the drawing direction. Some of them have a thickness of only about 0.01 μm whereas others are clearly thicker (0.1–0.3 μm). The overall dislocation density in these regions is very large. Local diffraction patterns indicate that either their [100] or their [111] crystal axis points in the drawing direction. Sometimes also spontaneously recrystallized regions having extensions of 0.1 to 1 μm or bigger can be observed. They are almost free of dislocations. These regions appear usually in the core of the wire and indicate that the stored deformation energy, which acts as driving force for the recrystallization, is larger here than elsewhere.

Similar observations on as-drawn micro-wires of Cu where made by Murr et al. (1997) and Murr and Flores (1998). In contrast to our results their samples appear to show even bigger microstructural differences between the core and the surface near regions. This may probably be attributed to different drawing conditions and techniques

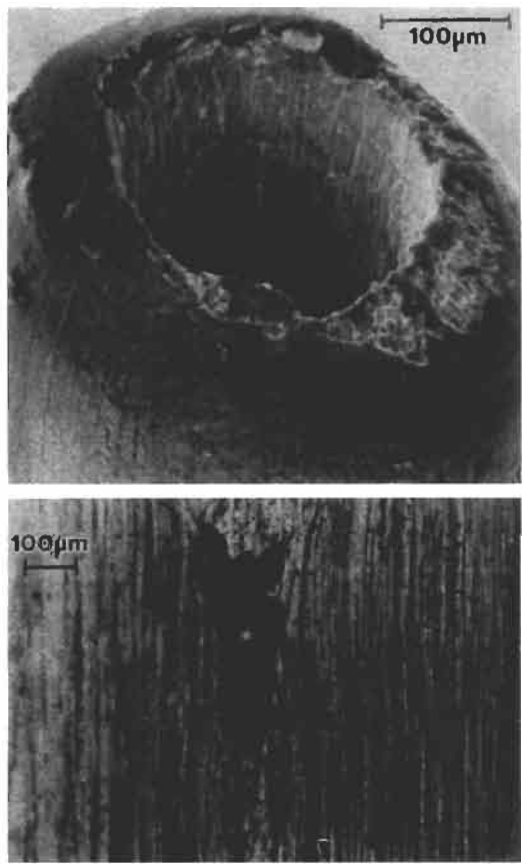

Fig. 3. Deep cup failure in a 0.45 mm diameter drawn Cu wire. The lower half shows a cup formed void (central burst). Reprinted from Murr and Flores (1998), Scripta Materialia, 39, p. 527, with permission from Elsevier Science.

that are usually kept secret by the producers. We observed, in fact more than once, that wires of the same metal and the same diameter but from a different producer have not always the same properties.

The microstructural differences between the inner and the outer regions become also apparent during annealing treatments. Fig. 7 shows the variation of the micro-hardness measured on the cross-section of a Au wire with a diameter of 100 μm (purity 99.98% + 130 ppm Ca). In the as-drawn state the hardness appears to be independent of the radius. This does not allow to conclude that there are no microstructural differences. In the as-drawn state the strain hardening reaches a maximum and consequently the change in hardness may become smaller than the experimental scattering of the measured values. The curve annealed shows the results obtained after a pulsed annealing treatment of 1 s at 300°C. In extremely deformed metals treatments as short as this are enough to initiate recrystallization.

The hardness profile now indicates that the driving force for recrystallization and

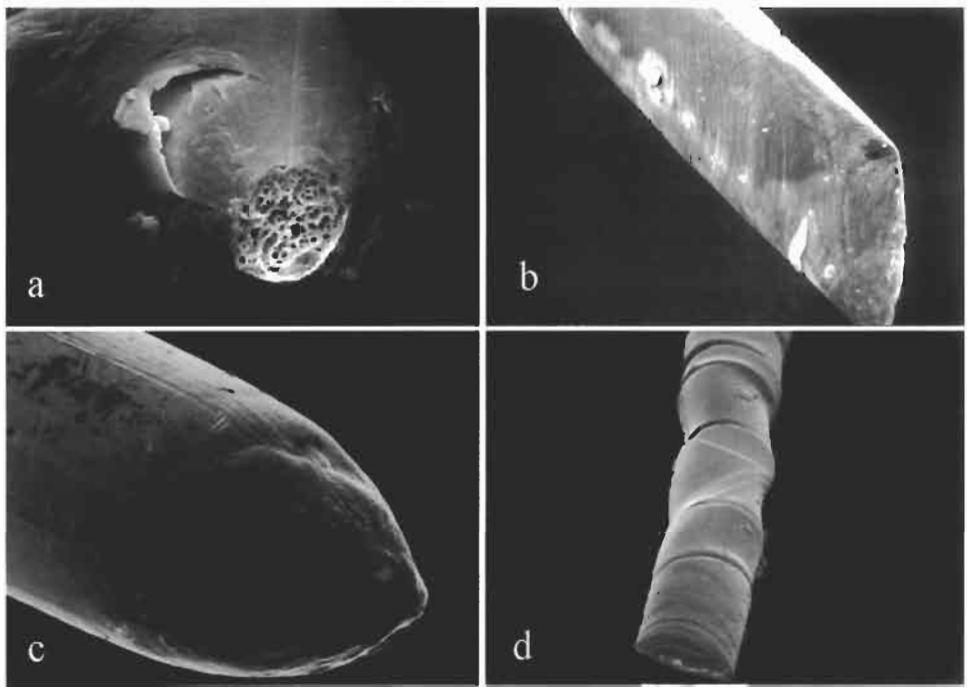

Fig. 4. Typical fracture modes of Au micro-wires: (a) diameter 50 μm, as-drawn, and (b) the same wire strongly annealed (few grains per cross-section); (c) diameter 25 μm, as-drawn, and (d) the same wire annealed to bamboo structure. As-drawn wires show cylindrical necking fracture whereas oligocrystalline wires and wires with bamboo structure show wedge-shaped necking.

hence the deformation was largest at the center of the wire. To complete the recrystallization also in the near-surface regions, annealing times of several minutes are necessary. Occasionally, it was also observed that spontaneous or temperature-initiated recrystallization may also start right at the surface. This is probably due to an extreme deformation resulting from the friction in the die.

The extreme plastic deformation of wires during drawing not only affects the microstructure, but also induces characteristic, material-specific textures (orientation of crystal axis). Since the mechanical properties of drawn wires are equally dependent of strain-hardening, grain size and texture, the knowledge of the degree of crystal orientation is of practical importance.

The plastic deformation during drawing proceeds microscopically by dislocation slip and twinning. Both mechanisms induce also a re-orientation of the crystal lattice which in turn is responsible for the development of textures. Drawing of cylindrical wires results usually in reorientation of the crystal axis, such that particular directions (e.g. [100]) align along the drawing direction. This type of texture is referred to as a fiber texture. In this texture the crystallographic axis perpendicular to the drawing direction ('fiber-direction') may still be randomly oriented. In small-grained wires (grain diameter $<$ wire diameter), however, the fiber texture also develops a cylindrical symmetry, i.e.

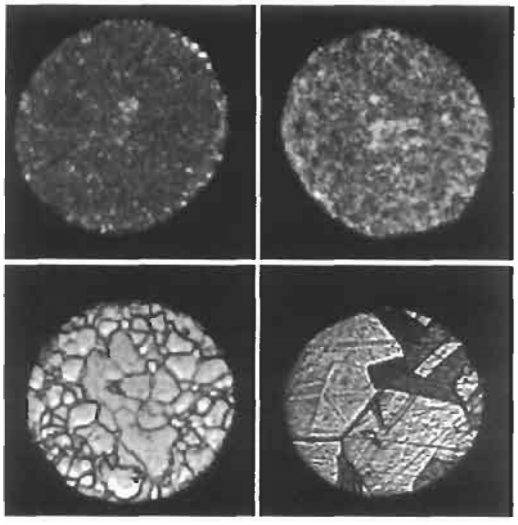

Fig. 5. Microstructure of a 25 μm diameter Au wire in 4 annealing states: as-drawn, 15 min 150°C, 15 min 320°C, and 10 min 700°C.

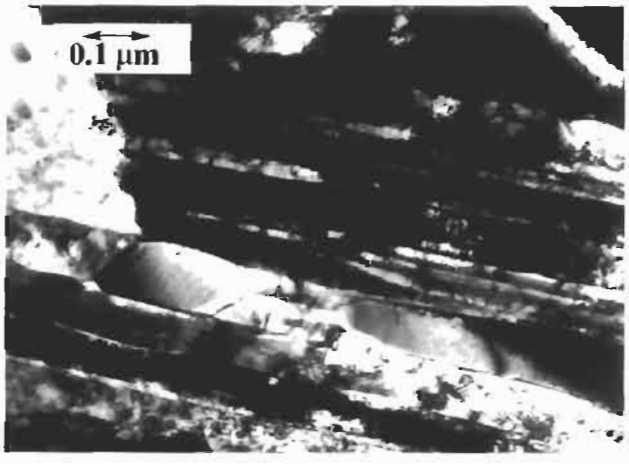

Fig. 6. Longitudinal microstructure of an as-drawn Cu wire (38 μm diameter). TEM observations reveal the heavily deformed and elongated 'grains' of 0.01–0.3 μm thickness that are completely aligned along the drawing direction. (From Busch-Lauper, 1988.)

that a certain crystallographic direction aligns along the radial direction. This, together with the fiber orientation, fixes of course also the tangential orientation. Since the evolution of the texture is driven by the plastic deformation during the drawing process the final textures are not always equally well developed throughout the wire. The radial symmetry sometimes develops only near the surface.

The drawing of bcc metals generally results in a [110] fiber texture, whereas fcc metals develop [100] and [111] textures (Grewen, 1970). The degree of the orientational

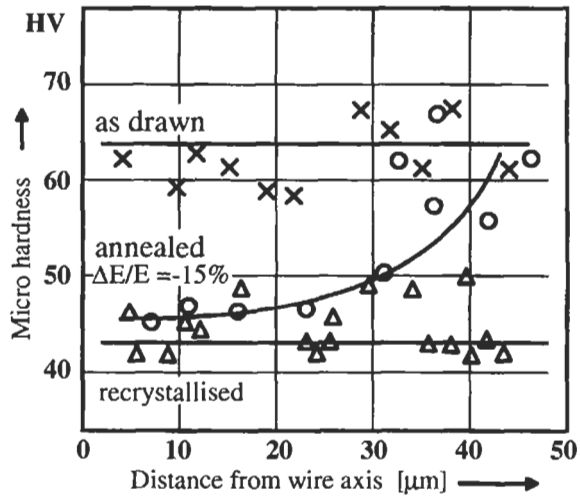

Fig. 7. Micro-hardness measured on the section of a 100 mm thick Au wire in the as-drawn, a partially and the completely recrystallized state.

order increases generally with the total deformation. In fcc metals both textures [100] and [111] may appear simultaneously and their relative occurrence depends strongly on the deformation and the initial orientation. Subsequent restoration or annealing often favor the formation of the (100) texture (Shin et al., 2000). The presence of a second phase strongly perturbs the development of pronounced textures or even prevents its formation when the second-phase particles are undeformable. Such undeformable particles force the matrices to flow around them and therefore modify the flow pattern locally.

Textures are usually determined by X-ray diffraction and the obtained results are conveniently represented by so-called pole figures. These figures give the polar projection of the angular density distribution of a selected crystal axis with respect to a given sample orientation. For wires and sheets the vertical axis of the pole figure is usually chosen as the drawing or rolling direction. Fig. 8 shows the pole figure for the (100) direction of drawn, restored and annealed Cu wires. Fig. 8a,b shows the presence of two dominating grain orientations. The round regions at the top and the bottom belong to grains with one (100) axis almost parallel to the wire axis. The other two (100) directions of these grains make up the intensity in the central strip (going through the center). The remaining two regions (between the central strip and the top and bottom, respectively) belong to grains whose (111) axis is parallel to the drawing direction. Fig. 8b clearly indicates that restoration, which in heavily deformed Cu already sets in at room temperature, gives rise to significant modifications. The (100) texture component becomes much sharper and the number of grains with a (111) direction parallel to the wire is reduced. In view of Fig. 6, the term grain should here probably better be replaced by shear bands. In fact, the orientation remains constant only within a band, whereas it gradually changes in between two neighboring bands. Subsequent heat treatments at higher temperatures and for prolonged times strongly reduce the degree of grain polarization. Similar results have also been observed in Au wires (Busch-Lauper, 1988).

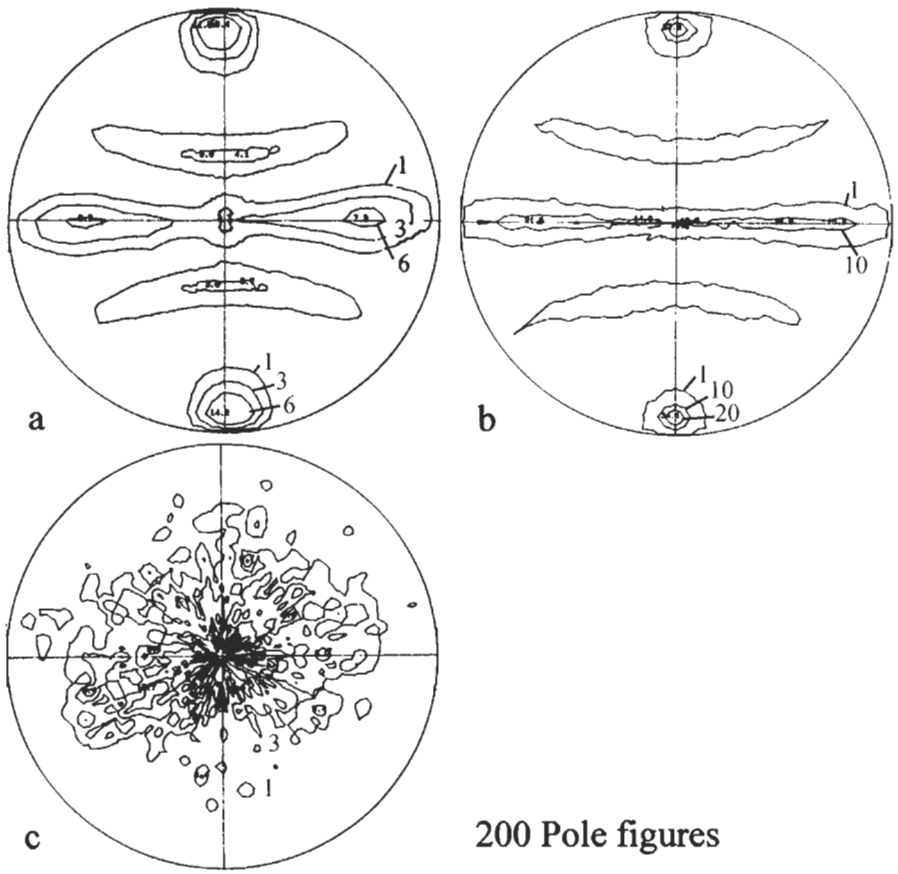

Fig. 8. Pole figure for the (100) axis of drawn, restored and annealed Cu wires. (a) Immediately after drawing. (b) After 4 months restoration at room temperature. (c) Annealed 1 h at 300°C.

The presence of textures may have an important effect on the mechanical properties of drawn wires. In certain metals, Young's modulus is strongly anisotropic with respect to the crystallographic axis. In Cu, for example, the Young modulus varies between 67 GPa in the (100) direction and 191 GPa in the (111) direction. In polycrystalline samples values near 120 GPa are typical. Compared to this we often observed values well below 70 GPa in textured Cu wires. Table 1 shows the evolution of Young's modulus for the wire that was used to measure the pole figures presented in Fig. 8. The Voigt average gives the average for a parallel arrangement of different materials (both subject to the same elongation, and the total stress is the weighted sum of the stresses) and the Reuss average gives the mean value for a sequential arrangement of two materials (both subject to the same stress, and total elongation is the sum of the elongations). These values represent worst-case estimates for the lowest and highest modulus. In many cases, however, we observed that the mean value of these extreme values are rather close to the actually observed value.

Table 1. Texture and Young's modulus E of drawn and restored (4 months at 20°C) 38 μm diameter Cu wires

	As drawn	After 4 months at 20°C
Fraction of (100) texture (%)	66	88
Fraction of (111) texture (%)	34	12
E measured (GPa)	96	72
E Voigt average (GPa)	109	82
E Reuss average (GPa)	86	72
E average of Voigt + Reuss (GPa)	97	77

Small values for Young's modulus may be beneficial in very thin wires to improve the resistance to fracture failure. Machines used to handle thin wires are always much stronger (smaller compliance) than the wires. The small elastic forces produced by the wire in case of a temporary feeding problem will not stop the machine. The machine therefore imposes a given elongation, and the smaller Young's modulus, the smaller the corresponding stress. Well-pronounced textures also have an influence on the yield stress through the Schmid factor. For fcc metals and traction along the (111) direction or along the axis of wire with a (111) texture the yield stress is 3.67 times the critical shear stress. The same is true for a (110) texture. For a traction near the (100) direction this value falls to its minimum that is near 2.4. Textural strengthening may therefore contribute up to 50% with respect to the (100) direction and about 20% with respect to a polycrystalline wire (Grewen, 1970).

Experimental observations made by Rieger (1974) confirm the superior strength of (111) fiber textures. He measured the mechanical properties of Cu and Cu–Zn alloys with variable proportions of (111) and (100) fiber textures and observed that the tensile strength increases by more than 3 times when a (100) texture is replaced by a (111) texture. Kuo and Starke (1985) made a similar study on Al alloys but found much smaller differences.

Unfortunately, the directional dependence is similar to that of Young's modulus. The stress-reducing effect of Young's modulus in textured wires is therefore partially compensated by the corresponding reduction of the yield stress. But the reduction of Young's modulus between its extremal values in the (111) and (100) directions is about twice the reduction of the yield stress between the same directions.

Melt-Spinning Defects

Compared to drawing which is a well established and slow process, melt spinning for metals is more recent, much easier and faster. Clearly, melt-spun products do not have the regular round shape and the surface quality of drawn wires. But for many applications, such as fiber reinforcement, this is not the primary concern. A parameter of much greater importance in this field is the mechanical strength. In fact, melt spinning is particularly useful for the production of continuous- or fixed-length filaments of amorphous metals. Many alloys can be spun to fibers, ribbons and foils that have thickness dimensions of only a few tenths of a micrometer and widths from about 100

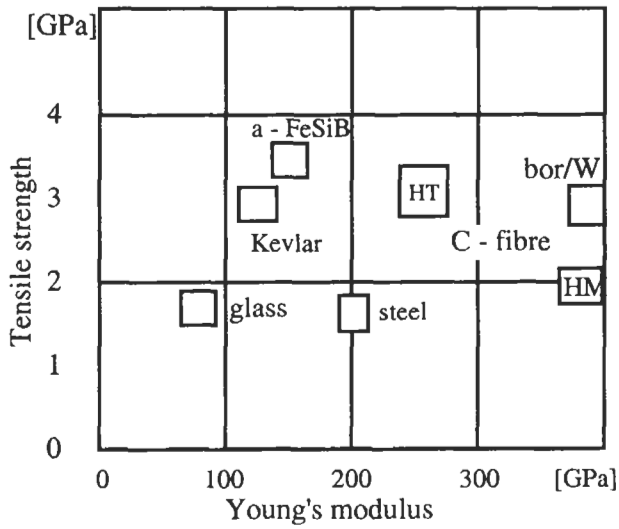

Fig. 9. Tensile strength and Young's modulus of amorphous $Fe_{75}B_{15}Si_{10}$ fibers compared to other reinforcement fibers. HT and HM are high tensile strength and high modulus carbon fibers.

μm up to more than 30 cm (Matthys, 1992). Several of them also have tensile strength of more than 3 GPa. Fig. 9 shows the tensile strength and Young's modulus of glassy $Fe_{75}B_{15}Si_{10}$ fibers in comparison to the classical reinforcement fibers.

Wires and fibers can be produced by quenching a jet of molten metals in water (Fig. 10). The principle behind this technique is quite simple but the practical realization is a challenge. The two major problems encountered in this technique are the stability of the liquid jet and the achievement of a sufficient cooling rate without perturbing the jet. The surface tension which for most liquid metals is particularly high produces an internal pressure in the jet that is inversely proportional to its radius. This pressure is on the order of 0.5 bar for a jet of 50 μm in diameter. Even the smallest diameter variation produces a pressure gradient along the jet axis that rapidly amplifies and disintegrates the jet into small droplets. The only way to prevent this disintegration is to solidify the jet before this happens. The successful production of wires with round sections validates the technical principle, but it is rather difficult to manage. Various process parameters have to be kept within extremely narrow tolerances. Wires produced by this method have very smooth surfaces and circular cross-sections. Small diameter variations along the wire may occur, but they do not affect the mechanical strength as is the case for ribbons (Masumoto et al., 1981a,b; Hagiwara et al., 1982a,b).

Melt-spinning techniques that use a solid quenching medium can only be used to produce filaments of flat cross-sections. Various techniques that differ in small details (single roller, twin roller) are in use. They all have in common that the ribbon forms from a liquid puddle that remains in a fixed position on the moving quench medium which is usually a rotating Cu wheel. The width of the ribbon varies with the width of this puddle and the thickness with the penetration depth of the solidification front that moves into the puddle. Only the solidified metal moves with the wheel and this

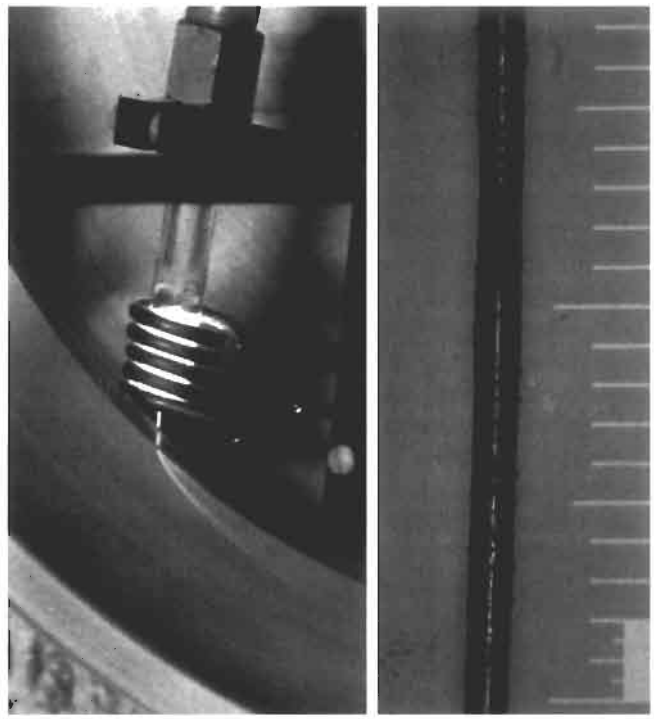

Fig. 10. Production of amorphous wires by quenching a jet of a molten alloy ejected from a nozzle into water that rotates with the turning wheel. On the left side a sample of a 100 μm diameter wire obtained with this method. (From Baltzer and Künzi, 1987.)

determines the ribbon thickness. Foils of up to 30 cm width for the fabrication of transformer cores are now commonly produced by this method. Here we will discuss only filamentary products that are smaller than 1 mm width and have a typical thickness of 20 to 50 μm. In order to get these small dimensions the sessile drop that is usually held between the small orifice of the melting crucible (diameter 50–200 μm) and the rotating wheel has to be kept small. Typically, the velocity of the Cu-wheel surface is about 120 km/h. This high velocity produces vibrations in the liquid droplet, and bubbles are drawn along the liquid metal/Cu interface. Both types of perturbations, vibrations and bubbles, give rise to characteristic surface defects that can affect the tensile strength.

The bubbles moving with the solidifying metal give rise to a porous surface on the ribbon side that was in contact with the wheel. The opposite side is usually quite smooth, but thickness variations due to vibrations may occur. The characteristic serrated edges in these ribbons are produced by rapid vibrations and probably also by air inclusions that may escape from the ribbon edges during solidification. Melt spinning in a vacuum chamber gives much better surface and edge qualities. The tensile strength of ribbons with serrated edges and irregular surfaces due to air inclusions is far inferior to those that are either produced under vacuum or have polished edges and surfaces. Also,

Fig. 11. The surfaces and edges of 600 μm wide $Fe_{75}B_{15}Si_{10}$ ribbon produced on a Cu wheel. The lower half shows the side that was in contact with the wheel and the upper half the side that was in contact with the air. The diameter of the crucible orifice was 0.45 mm and the pressure needed to eject the liquid alloy was 0.4×10^5 Pa. The Cu-wheel of 300 mm diameter turned with 1200 rpm.

water-quenched wires show values that are characteristic for the intrinsic behavior of glassy metals. Rather good surface and edge qualities are also observed for very small and thin ribbons. Such fibrous products can easily be produced on a wheel in air by just using small nozzles. Minimal dimensions of about 100 μm width and a thickness of 20 μm can be reasonably achieved. For smaller dimensions the pressure needed to eject the liquid metal strongly increases.

Figs. 11 and 12 show the surfaces and edges of a 600 μm and a 120 μm wide $Fe_{75}B_{15}Si_{10}$ ribbon melt spun on a Cu wheel and Fig. 13 shows the cross-section for small ribbons. The irregular edges are clearly visible in the upper half of Fig. 11 (air side of ribbon) and the air inclusions in the lower half (wheel side of ribbon). For the smaller ribbons (Fig. 12) the surface tension becomes more important. It rounds and smoothens the surface on the air side (Fig. 13), whereas the smaller width allows the air drawn with the wheel to flow around the liquid droplet. The surface of the small ribbon (lower half of Fig. 12) shows essentially a replica of the Cu-wheel surface. Fig. 14 shows the quantitative surface profiles of the two ribbons shown in Figs. 11 and 12. Here again it becomes evident that the impressions produced by the air inclusions penetrate more than 5 μm into the interior. This amounts to not less than 10 to 20% of the total thickness.

Since also the thin ribbons are not entirely free of edge defects it is important to know whether they act as notches that affect their tensile strength. Fig. 15 shows measurements of the tensile strength as a function of the notch depth on 160 μm wide ribbons. The smallest notches were naturally present, whereas the larger ones were

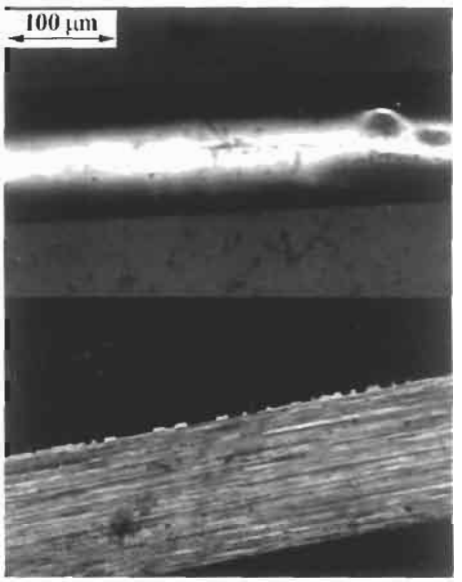

Fig. 12. The surfaces and edges of 120 μm wide $Fe_{75}B_{15}Si_{10}$ ribbon. Upper half: air side. Lower half: wheel side of ribbon. The diameter of the crucible orifice was 0.07 mm and the pressure needed to eject the liquid alloy was 3.5×10^5 Pa. The Cu-wheel of 300 mm diameter turned with 2000 rpm.

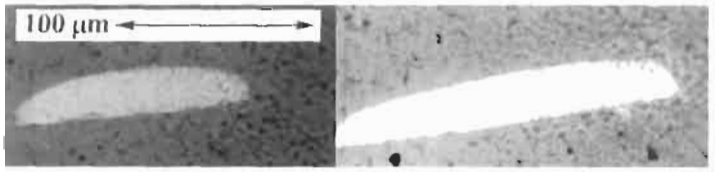

Fig. 13. Cross-section of small ribbons (for parameters see Fig. 12). (From Baltzer and Künzi, 1987.)

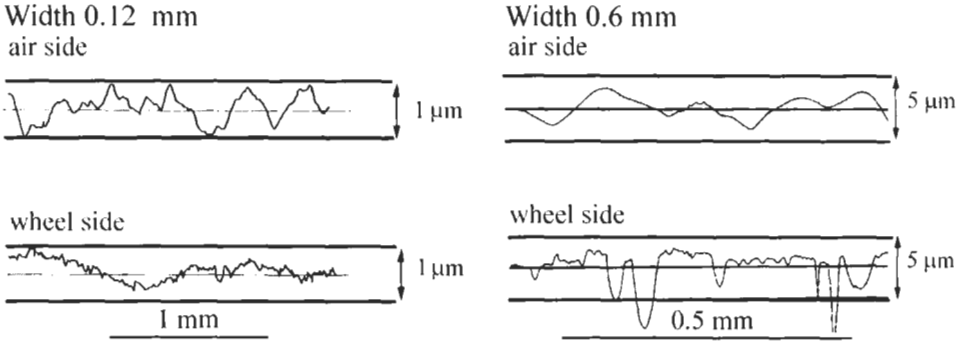

Fig. 14. Surface profiles of the two ribbons shown in Figs. 11 and 12. Note the scale difference between the small and wide ribbons.

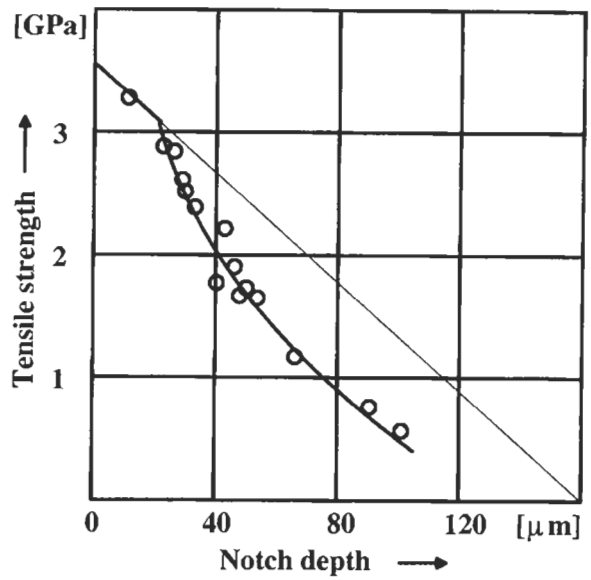

Fig. 15. Notch sensitivity of small $Fe_{75}B_{15}Si_{10}$ ribbons. Naturally occurring edge irregularities in these ribbons are typically lower than 10 μm and do not become critical. (From Baltzer and Künzi, 1987.)

produced by grinding two edges against each other. This gave round notches with a curvature radius of 10 to 20 μm. These are clearly not the ideal dimensions for a notch sensitivity test but with regard to the small sample sizes, it is quite difficult to make it much better. The obtained results cannot be generalized to other sample sizes, but give information on the behavior of these small fibers.

Table 2 clearly shows that only thin fibrous ribbons of glassy metals achieve their high intrinsic tensile strength in the as-produced state. Wider and thicker ribbons often have too many and too large surface defects that cause a substantial reduction of their tensile strength with respect to the intrinsic values.

Table 2. Tensile strength of amorphous filaments [a]

Alloy	Dimensions, wide × thick (mm)	Tensile strength		Produced/polished (%)
		As produced (GPa)	Polished edges (GPa)	
$Fe_{80}B_{20}$	1.0 × 0.04	1.7	3.1–3.7	47–56
$Fe_{40}Ni_{40}B_{20}$	9.4 × 0.035	1.2	2.5	48
$Fe_{40}Ni_{40}B_{20}$	0.6 × 0.02	1.6	2.5	64
$Co_{70}Fe_5Si_{15}B_{10}$	0.9 × 0.04	1.6	3.2	50
$Fe_{75}Si_{10}B_{15}$ [b]	wire 0.120	3.3		
$Fe_{75}Si_{10}B_{15}$	0.15 × 0.016	3.2		

[a] Large ribbons have a tensile strength that is strongly reduced due to the notch effect of edge defects (Baltzer and Künzi, 1987, except [b] from Hagiwara et al., 1982a,b).

Table 3. Whiskers compared to bulk metals (Brenner, 1958a)

Metal	Whisker				Bulk metal	
	Axis	Diameter (μm)	Max. tensile strength (MPa)	Max. shear strength (MPa)	Tensile strength (MPa)	Crit. shear strength (MPa)
Fe	[111]	1.6	13,150	3,570	160–250	44
Cu	[111]	1.25	2,950	804	130–350	1
Ag	[100]	3.8	1,730	706	80–160	0.60

INTRINSIC STRENGTH AND FAILURE BEHAVIOR

In this section we will look at the intrinsic strength of metallic filaments that are free from macroscopic defects. Whiskers show an almost ideal mechanical behavior. Similarly, fibers of amorphous metals show a very high intrinsic tensile strength. Real wires manifest properties that depend on their microstructure. Polycrystalline wires, for instance, in their as-drawn state are for many applications much too hard and brittle. Subsequent annealing allows to modify and stabilize their mechanical behavior and to meet the desired properties.

Ideal Behavior of Metallic Whiskers

Whiskers are filamentary single crystals of high purity with diameters usually well below 10 μm. They are grown under controlled conditions that allow the formation of a highly ordered crystal structure (Brenner, 1956a,b, 1958a). Besides metals, various other materials, including oxides, nitrides and carbides are known to form whiskers. The almost total absence of even the elementary crystal defects, such as voids, dislocations and grain boundaries as well as the atomically smooth surface, gives them tensile strength properties that are far above most other current reinforcement fibers. Table 3 gives a comparison between the high tensile strength and shear strength values observed in Fe, Cu and Ag whiskers and the corresponding values for bulk metals (Brenner, 1958a). Accordingly, the best tensile strength observed for Fe whiskers is about 60 times higher than in the corresponding bulk metal.

Since whiskers have high tensile strengths they are also capable of withstanding exceptionally large elastic strains. Metallic and even some oxide whiskers support strains of 2 to 5% before fracture or yield occurs. Towards the higher strains the stress–strain behavior is often nonlinear and substantial deviations from Hooke's law are observed. The stress–strain curves are similar to the one shown in Fig. 45 for the amorphous iron alloy fiber. At the highest strain some stress relaxation may also occur, giving rise to an irreversible residual deformation.

When whiskers exceed the elastic limit they behave in one of three ways: (1) they fracture by a cleavage; (2) they show an important but strongly localized plastic deformation; (3) they creep. Very thin copper and iron whiskers with high elastic limits fracture in a more or less brittle manner as is the case for materials that are normally brittle. The sudden release of large amounts of elastically stored energy produces high

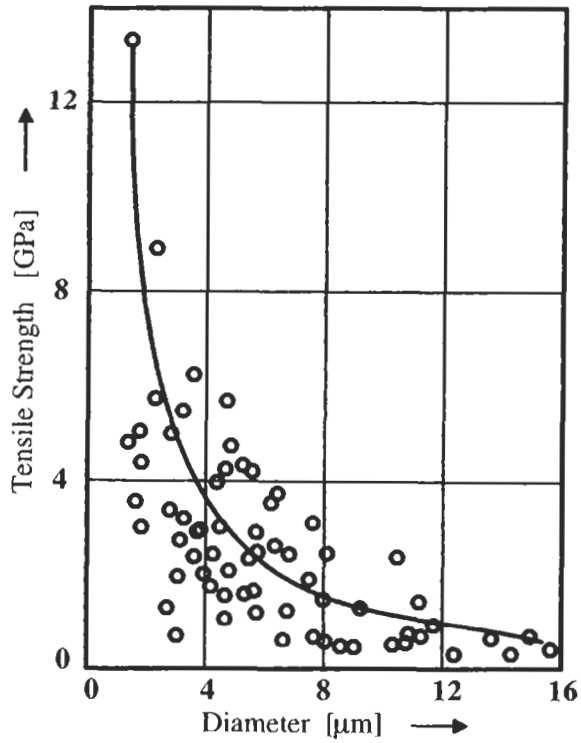

Fig. 16. Effect of the size on the tensile strength of Fe whiskers. (From Brenner, 1958a.)

strain rates that favor brittle fracture. Thicker whiskers often show a localized plastic deformation in a single isolated region. This deformation begins on a line and then expands much in the nature of a Lüders band. The yield stress which is the stress to nucleate plastic deformation is much higher than the stress necessary to maintain the initiated flow. In Cu whiskers the ratio of the yield to flow stress may be as large as 90. The value of the flow stress remains constant during the expansion of the plastic region. Sometimes whiskers also show mechanical properties that deviate from this idealized behavior. Two or more Lüders bands may nucleate at the same time, the difference between yield and flow stress can be much smaller, the flow stress may increase due to obstructed flow and, finally, also the tensile strength varies from sample to sample.

Fig. 16 shows the effect of the size of the diameter on the tensile strength of iron whiskers (Brenner, 1958a). The size dependence and the scatter of this result have been interpreted as indicating that whiskers contain a small number of defects that can cause creep or initiate fracture. In fact, there is no sharp critical size that separates whiskers from ordinary crystals. It is rather a continuous transition from real to more or less ideal crystals and the smaller the size the smaller the probability to contain a defect. When, as appears to be the case for the smaller whiskers, the number of defects capable to produce plastic flow becomes a small integer value also experimental scattering will become important. Moreover, the effectiveness of the defects is not unique. Plastic flow

will start at the weakest defect. When the sample is sufficiently long, so that it can be remounted again without having the first defect in the gauge length, the yield stress is higher (Brenner, 1958b).

A similar size effect of the tensile strength has been reported by Kim and Weil (1989) in foils of Ni. They prepared monocrystalline samples with a thickness from 0.2 to 20 μm by epitaxial electroplating on monocrystalline Cu substrates. The tensile specimens were plated so as to have the desired shape and crystal orientation to be subjected to uniaxial tensile tests on their mini-tensile machine (Kim and Weil, 1987). Their results show that for samples thicker than 3 μm the yield stress of about 130 ± 20 MPa is independent of the thickness and the three tensile directions [110], [120] and [100] studied. Below 3 μm the yield stress drastically increases with decreasing thickness. The highest value, slightly above 400 MPa was observed for a 200 nm thick sample. The same behavior is also reported for the ultimate tensile strength and the critical resolved shear stress. The latter decreases from 155 MPa for the 200 nm thick deposit to 60 MPa when the thickness exceeds 3 μm. These values strongly contrast with the values of 3–7 MPa reported for bulk Ni. Kim and Weil explain this difference by the higher defect density in the electrodeposited Ni. Indeed, their TEM observations revealed a dislocation density of about 10^{10} cm^{-2} which is 3 orders of magnitude higher than in annealed bulk Ni.

Contrary to the tensile strength the elongation at rupture varies with the crystal orientation. The smallest values were observed for samples strained in the [100] direction and the largest for samples oriented in the [110] direction. The elongation at rupture increased for all orientations from almost zero for the thinnest sample to about 5% in the [100] direction and 13% for the [110] orientation. In all samples the plastic deformation was observed to strongly localize.

When [100] was the straining direction, plastic deformation in thin deposits was confined to narrow stripes. These stripes were parallel to the two <110> directions which are the intersections of the four (111) glide planes with the (100) surface. For the given straining direction, all of these four planes have the same Schmid factor. Fracture finally occurred along a staircase-like line that followed the stripes arranged along the two directions. For the thicker [100] samples, however, a strong work hardening and slip lines were observed. Fracture was always preceded by severe necking and followed along cell walls that were built up during deformation. A thickness reduction of 99% was reported for the 20 μm thick sample.

In the very thin deposits that were strained in the [110] and [120] direction TEM analysis revealed the presence of mechanical twins that occurred only near the fracture line. As for the thin [100] specimens there was again no homogeneous plastic deformation in the gauge length. Only thicker samples showed some homogeneous plastic deformation prior to necking and rupture.

With respect to technical application as reinforcement fibers, whiskers suffer from two essential drawbacks that are related to growth rate and the dispersion of the tensile strength. The growth velocity of metallic whiskers is rather small, a few centimeters per hour, and does not allow economic production rates. The as-produced whiskers also show a large dispersion in the values for the tensile strength. Only very few whiskers have a really high tensile strength. The average value is comparatively low.

Table 4. Tensile strength of micro-wires produced by the Taylor process (Nixdorf, 1967)

Metal	Max. tensile strength (MPa)	Bulk tensile strength (MPa)
Fe	2800	180–250
Pt–30% Rh	1500	
Pt	500	140
Ag	650	160
Cu	400	220–350
Zn	150	30

Various attempts have therefore been undertaken to develop alternative methods to produce metallic filaments of μm dimension having the excellent properties of whiskers. Schladitz (1968, 1976) describes the production and the properties of polycrystalline Fe and Fe–C whiskers. These whiskers grow, similarly to the monocrystalline whiskers, from the gas phase but their production rate is several orders of magnitude greater. With diameters in the range of 0.1 to 30 μm their external appearance is similar to monocrystalline whiskers. Their internal structure, however, is completely different. They are made of nanocrystallites (α-Fe with a diameter of 8 nm and carbide particles) and their dislocation density is estimated to be as large as 1.5×10^{12} cm^{-2}. The ultrafine microstructure with the carbide particles gives them excellent mechanical properties. Fe whiskers with less than 1.2% C have tensile strengths between 7 and 8 GPa.

A quite different method to produce wires was invented by Taylor in 1924. Nixdorf (1968), in an effort to produce high-strength filaments, considerably contributed to its perfection. In this method hot glass tubes containing the liquid metal are drawn until the internal diameter of the tube reduces to the desired diameter. After solidification of the metal and removal of the glass, one obtains micro-wires with round cross-sections and a smooth surface. The tensile strength of such wires cannot compete with whiskers but is nevertheless respectable. Table 4 lists some singular values together with values for bulk polycrystalline samples. Similar to monocrystalline whiskers the dispersion in the tensile strength is large. It extends from values characteristic of the corresponding bulk material to the extreme values given in Table 4.

Polycrystalline Micro-Wires

In this section we will discuss the behavior of micro-wires that were produced by the conventional drawing technique. Very thin Cu wires are extensively used for the fabrication of flexible electrical cables. Wires with diameters between 20 and 30 μm made from high-purity Au and Cu or slightly alloyed Al are used as in microelectronics for electrical connections on chips (bonding wires). Probably the oldest application of thin wires was the use of W wires as incandescent filament in light bulbs. These filaments are operated near 2000°C and are likely to recrystallize to a bamboo structure in which state they become extremely fragile. A great number of studies have been and continue to be devoted (Schade, 1998) to this subject. The problem is tackled by adding various grain growth inhibitors to W prior to drawing. Even though we will briefly

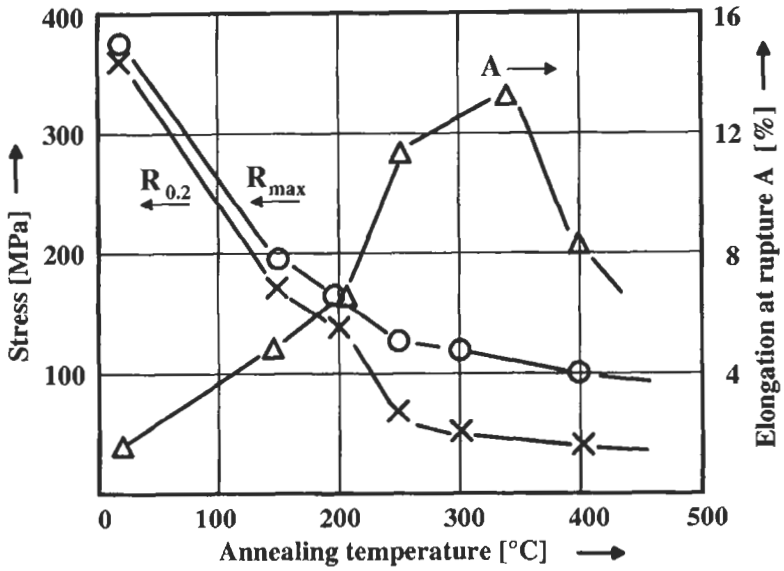

Fig. 17. Effect of annealing on the mechanical properties of as-drawn Au wires with a diameter of 25 μm (purity 4N). The annealing time was 1 h. R_{max} is the ultimate tensile strength, $R_{0.2}$ the 0.2% proof stress and A (right scale) elongation at rupture (Hausmann, 1987).

mention the effect of recrystallization on the strength of thin wires, the problem in W filaments is very specific (it concerns mainly the pinning of grain boundaries) and will not be treated here.

Effect of Annealing and Recrystallization on the Mechanical Properties

Annealing of freshly drawn Au micro-wires for 1 h at increasing temperatures results in a rapid decrease of the tensile strength R_{max} and the yield stress $R_{0.2}$ (Fig. 17). The elongation at rupture starts at the beginning with values that are characteristic for strongly work-hardened metals, increases first with the annealing temperature, passes through a maximum and decreases for the higher annealing temperatures. Annealing at these temperatures does not produce brittle wires but wires with an oligocrystalline microstructure (only few grains cover the cross-section).

In large-grained wires the plastic strain localizes at regions where the grains are large and have glide systems with favorable orientations. The rupture often gives wedge-shaped surfaces as shown in Fig. 18. For annealing times that give large homogeneous deformations, wires fail in a cone-like rupture very similar to as-drawn wires but with a much rougher surface that indicates the onset of strain localization (Fig. 19).

Similar results are obtained as shown in Fig. 20 for high-purity Cu wires (99.999%) of various diameters. The variation of their strength with annealing results from the polycrystalline strengthening which, as Fig. 21 shows, follows the well known $1/\sqrt{d}$ dependence of the Hall–Petch relation (d = grain size).

In order to prevent drawing defects due to over-hardened materials it is often useful

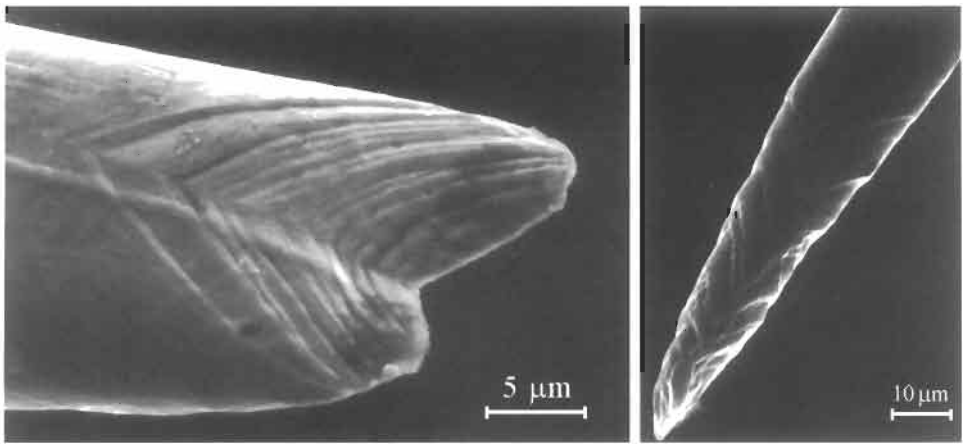

Fig. 18. Wedge-shaped fracture surfaces of well annealed 25 μm diameter Au wires. left 1 h at 800°C, right pulsed annealing 0.5 s at 600°C.

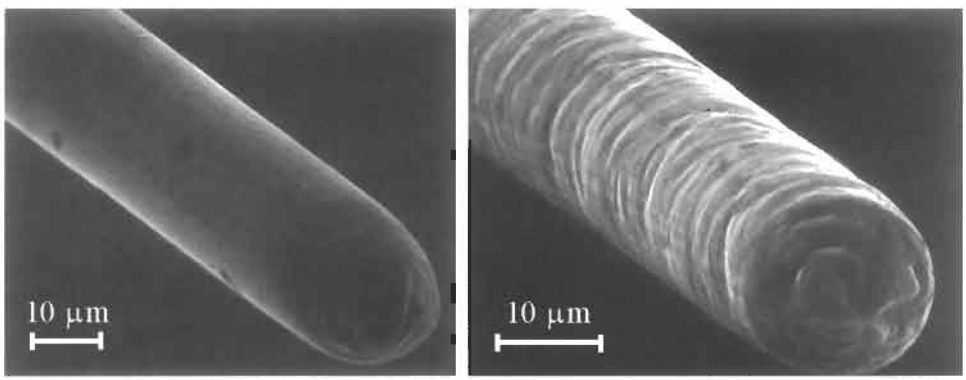

Fig. 19. Wire and fracture surfaces of 25 μm diameter Au wires. Left: as-drawn with smooth surface and almost no elongation at rupture. Right: annealed at 300°C with rough surface indicating begin of strain localization.

to submit wires that have to pass 20 to 40 dies to intermediate annealing treatments. Such treatments are conveniently executed in between two dies in line with the drawing process and may also serve to modify the mechanical properties of the final product. Since wires move at a velocity of a few centimeters per second, annealing times remain necessarily short and the temperature has to be adjusted in order to get the desired result. Such short-pulsed annealing treatments also allow to study the annealing kinetics over several time decades. Fig. 22 shows the tensile stress and Fig. 23 the elongation at rupture for 25 mm diameter Au wires as a function of the annealing time at different temperatures. Wires were heated by direct passage of an electrical current. The temperature was determined from the known temperature dependence of the electrical resistivity. The electrical resistance also served to adjust the current in order to maintain the temperature constant. For details see Hausmann (1987).

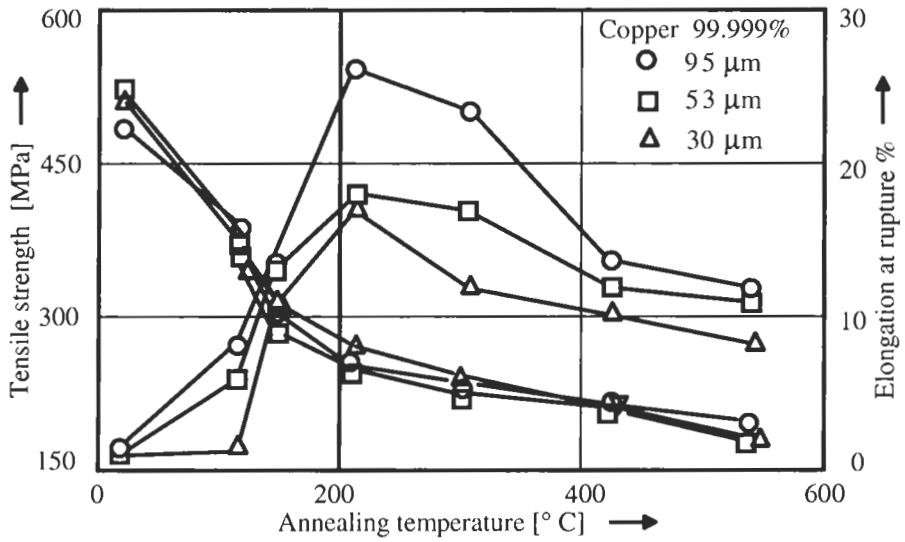

Fig. 20. Tensile strength and elongation at rupture for Cu wires of different diameters as function of the annealing temperature.

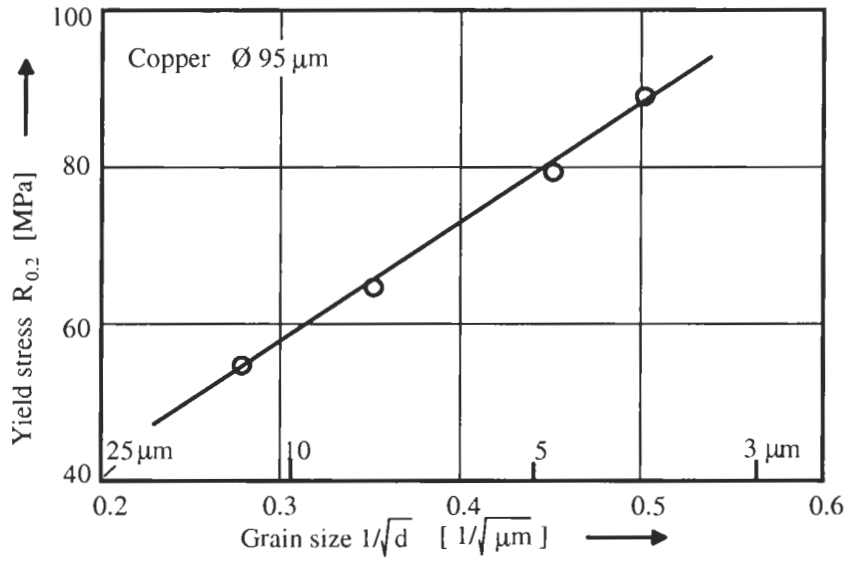

Fig. 21. Yield stress vs. reciprocal square root of the grain size d for 95 µm diameter Cu wires.

Recrystallization Kinetics of the Mechanical Properties

As shown in Fig. 22 the yield stress of polycrystalline wires is mainly dependent on the microstructure. Starting with as-drawn wires the evolution of the microstructure is

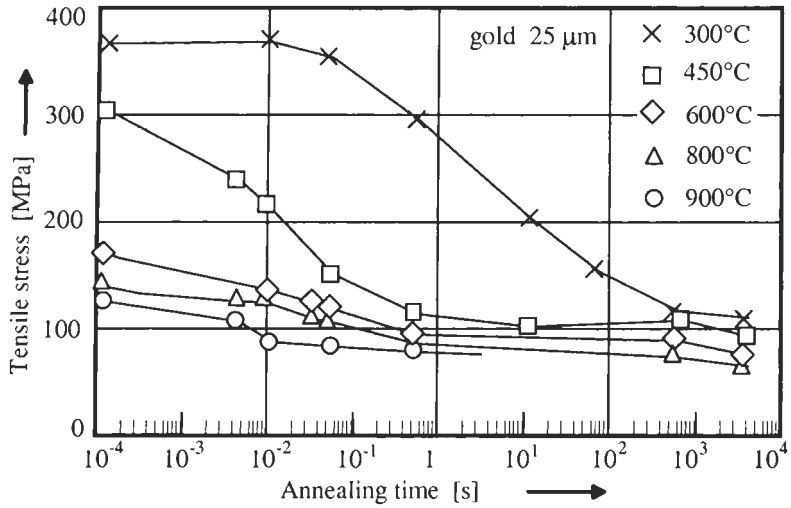

Fig. 22. Tensile strength of 25 μm diameter Au wires after pulsed anneals at different temperatures.

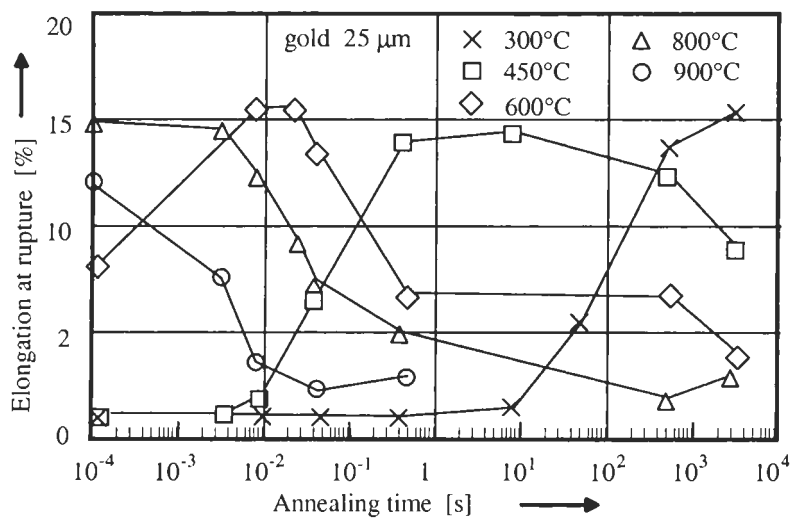

Fig. 23. Elongation at rupture of 25 μm diameter Au wires after pulsed anneals at different temperatures.

determined by the sum of all modifications that occurred through thermal activation. In order to get a unified description of the evolution of the yield stress it appears therefore justified to assume that also the yield stress depends on the thermal activation. For the tensile strength and probably in an even stronger measure for the elongation after rupture we would have to take account also of additional influences that stem from surface defects and sample geometry. The following arguments, therefore, primarily concern the yield stress.

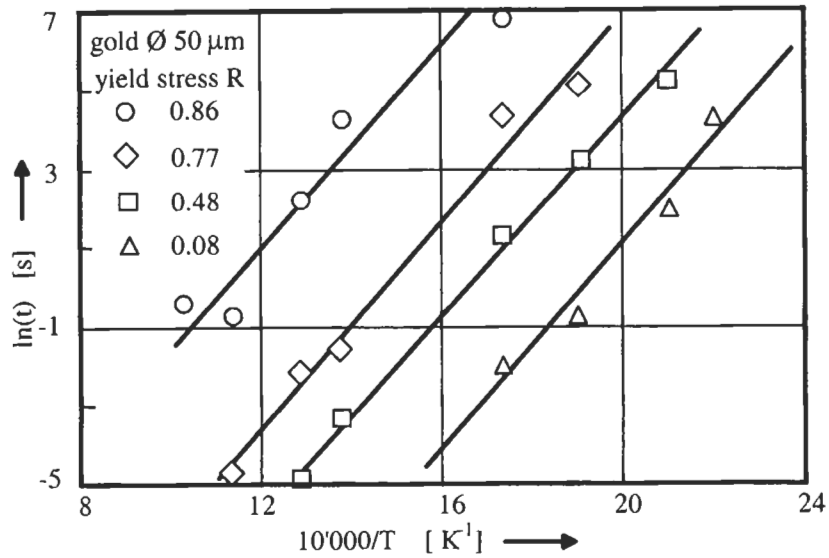

Fig. 24. Arrhenius plot for 50 μm diameter Au wires of 4N purity. The 4 lines correspond to normalized yield stress values R of 0.08, 0.48, 0.77 and 0.86.

In most thermally activated relaxation and diffusion processes, the evolution progresses with time expressed in units of a characteristic temperature-dependent time that elapsed since the beginning of the process. If we apply this argument to the evolution of the yield stress and assume the temperature dependence to follow an Arrhenius law, we can express the actual annealing time t at temperature T by an effective temperature-compensated annealing time Θ

$$\Theta = t \cdot e^{Q/kT}$$

Here Q is an effective activation energy which is to be determined from the slope of the Arrhenius plot

$$\ln(t) \text{ vs } 1/T$$

for a given yield stress. For convenience, the yield stress is given in normalized units

$$R = (R_{0.2} - R_\infty)/(R_0 - R_\infty)$$

where R_0 and R_∞ are the yield stresses at the beginning and after very long annealing times. Fig. 24 shows the Arrhenius plot for 50 μm diameter Au wires of 4N purity. The four lines correspond to normalized yield stress values R of 0.08, 0.48, 0.77 and 0.86. They give an effective activation energy of 1.16 ± 0.10 eV which is roughly in between the activation energies for auto-diffusion (1.8 eV) and for vacancy migration (0.84 eV). A value below the activation energy of auto-diffusion is to be expected, since strong modifications of the yield stress already occur during restoration. Here vacancy migration is important and optical micrographs are thus not visibly changed.

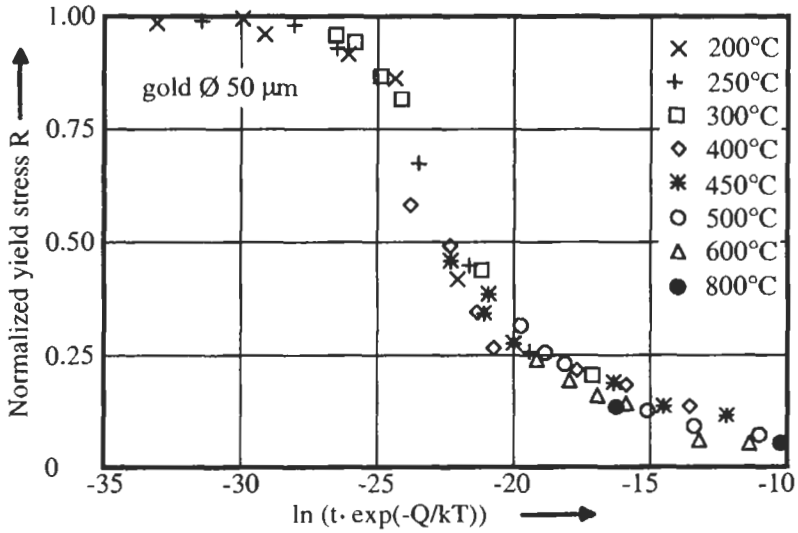

Fig. 25. Evolution of the yield stress during annealing treatments as a function of the temperature compensated time Θ for 50 µm thick Au wire (Hausmann, 1987).

Using the value obtained for Q we can now replot all the curves as given in Fig. 22 to get a single master curve which is the yield stress as a function of temperature-compensated annealing time Θ. Fig. 25 shows this curve for 50 µm thick Au wire. In view of the very different annealing conditions, over five time decades and temperatures from 200 to 800°C the description by a temperature-compensated annealing time is quite satisfactory. Measurement on other Au wires showed master curves of the same form that were slightly shifted to the right or to the left according to the effective activation energy. Another wire of 4N purity gave an activation energy of 0.92 eV and two wires of the same material, but with an addition 85 ppm Be, had activation energies close to 1.5 eV. The effect of Be is to slightly increase the strength and to retard the recrystallization.

Several authors (Leslie et al., 1961; Scheucher, 1969a,b; Murphy and Ball, 1972; Hausmann, 1987) tried to explain this recrystallization behavior by the Avrami and Johnson–Mehl relation. This relation was originally derived by Avrami to explain the kinetics of diffusive phase transitions and later applied by Johnson and Mehl to recrystallization. Accordingly the quantity $1 - R$, where R is normalized yield stress, should behave as a function of annealing time like the growth of the volume of a new phase as a function of time. The experimental curve can in fact be fitted by desired relation

$$R = e^{-k \cdot t^n}$$

with k and n as constants. However, it turns out that the exponent n becomes much too small to find a reasonable interpretation. For 3-dimensional growth of the recrystallized volume n should have a value between 3 and 4 ($n = 4$ for continuous nucleation and $n = 3$ when the nuclei are already present at the beginning). Exponents between 2 and 3

are found by Scheucher (1969a,b) on 0.3 mm thick Cu wires. Murphy and Ball (1972) studied 1.4 mm thick wires and observed n to be between 0.9 and 1.4. Hausmann (1987) used a sum of two Avrami functions to fit the experimental data on Au wires and found that the exponents of both terms are smaller than 1. These findings are clearly not compatible with the original idea of this model. The existence of a master curve therefore just asserts that the evolution of the yield stress is governed by thermal activation during annealing treatments.

The fact that the yield stress may not be described by a theory that just takes into account the evolution of the recrystallized volume may not be astonishing, even though this may work for other properties. The yield stress depends on various microstructural details which during annealing result from different microscopic processes with kinetics of their own. Depending on the annealing temperature, processes with lower activation energies leading to restoration and processes with higher activation energies leading to recrystallization run simultaneously or sequentially.

As opposed to the yield stress the elastic constants measure intrinsic crystalline properties which depend on short-range interatomic forces that remain practically unmodified during recrystallization. The elastic modulus measured along the wire therefore depends only on reorientation of the crystal lattice of grains during recrystallization and might be expected to be more related to the recrystallized volume than the yield stress. Nevertheless, its evolution during recrystallization cannot be described by a single master curve.

Recrystallization Kinetics of Young's Modulus

As mentioned above, the elastic modulus measured along the wire axis depends on the elastic anisotropy of the metal and the texture. Whenever drawing texture and recrystallization texture are not identical Young's modulus may serve as an indicator for the texture evolution. Figs. 26 and 27 show the elastic modulus as determined from the sound velocity at room temperature after cumulative pulsed annealing treatments. For both metals the modulus first decreases, then passes through a minimum and increases again. The Cu wire used for these measurements was taken from the same spool as the sample used for the determination of the pole figures (Fig. 8). Unfortunately, modulus measurements of the decreasing part are missing. Only the initial value of the as-drawn wire is known. When measurements were resumed 4 months later, during which the wire restored at room temperature, the elastic modulus was already at its minimum. The corresponding pole figure (Fig. 8b) indicates that the volume fraction of the (111) fiber texture present in the as-drawn state (Fig. 8a) decreases with a corresponding increase of the (100) texture.

This decrease has been explained by Lee (1995) as being driven by the dominant residual stress. In drawn wires the dominant residual stresses result from the nonhomogeneous plastic deformation and are oriented parallel to the drawing direction. The energy released at constant plastic strain can be maximized when the minimum elastic modulus directions are arranged parallel to the principal directions of the residual stress. Nucleation of grains with this orientation is therefore favored. The (111) fiber texture that results from the deformation is therefore partly replaced by the (100) fiber texture.

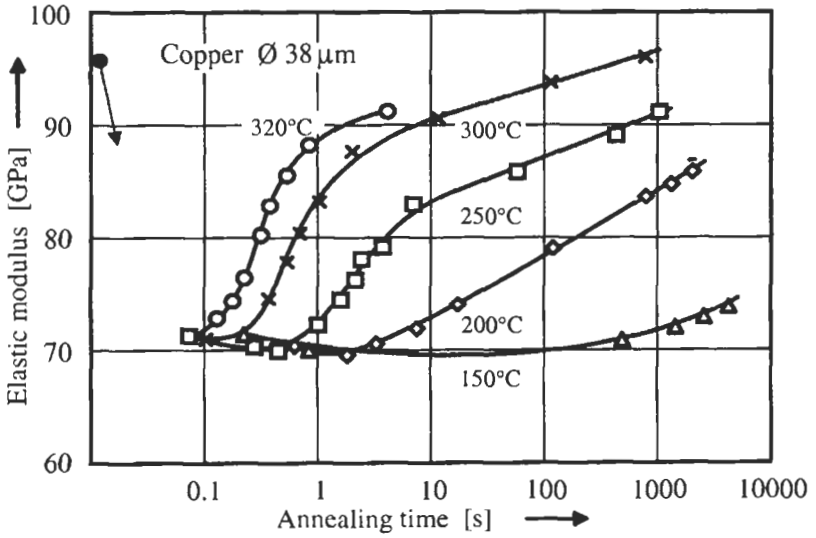

Fig. 26. Evolution of the elastic modulus of an as-drawn 38 μm diameter Cu wire during annealing. The initial decrease occurred while the wire was stored during 4 months at room temperature.

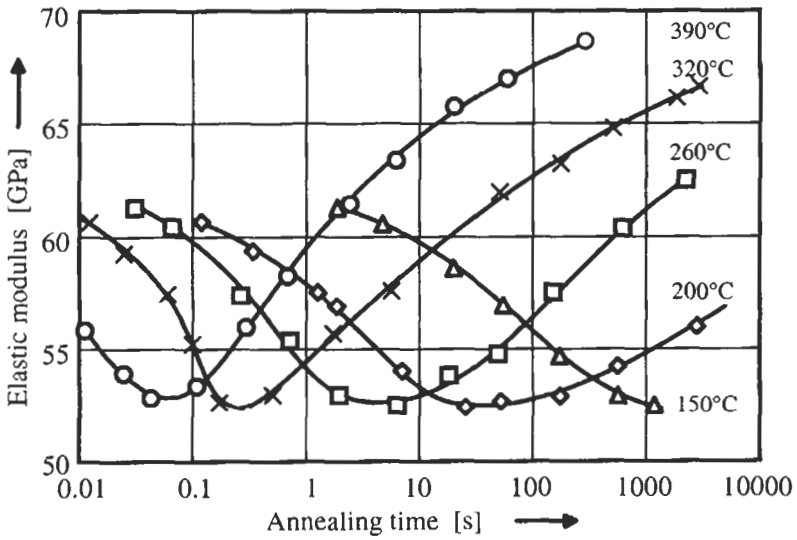

Fig. 27. Evolution of the elastic modulus of an as-drawn 25 μm diameter Au wire during annealing at different temperatures.

With progressing recrystallization the microstructural rearrangements will reduce the non-compatibility of the initial plastic deformation and therefore eliminate the source of residual stresses. Beyond the minimum of Young's modulus, where recrystallization really starts, the residual stresses may have disappeared and leave the field open for other

crystal orientations as stipulated by the pole figure Fig. 8c. A rather strong modulus increase may result from recrystallization twins in grains with a (100) orientation. This turns the $(12\bar{2})$ direction towards the wire axis. Values of young's modulus in this direction, are with 98 GPa for Au and with 158 GPa for Cu, relatively high. The (200) poles of the $(12\bar{2})$ fiber orientation gives two lines on the pole figure which lie close to the (111) orientation. One line forms an angle of 48.2° with the (100) direction and the other 70.5° whereas this angle is 54.7° for the (111) fiber orientation. In fact the pole figure Fig. 8c can roughly be explained by a broadening of the (111) line and a simultaneous reduction of the (100) fiber orientation.

Size Effect of Polycrystalline Strengthening in Thin Filaments

Many measurements in polycrystalline Cu, Au and Al wires have shown that the yield stress σ_y varies as shown in Fig. 21 with the reciprocal square root of the grain size. This relation between yield stress and grain size d, usually referred to as the Hall–Petch relationship, expresses the strengthening effect of the grain boundaries.

$$\sigma_y = \sigma_0 + \frac{k}{\sqrt{d}}$$

The stress increase with respect to the stress σ_0 of a sample with a very large grain size (grain size $\rightarrow \infty$) is generally explained by the mismatch of glide planes at grain boundaries. This holds up dislocations and creates an additional resistance to the plastic flow which has to be overcome before the neighboring grain starts to yield. Hard-drawn wires, in particular, profit from this effect. In thin wires with larger grains, however, dislocations will soon arrive at the free surface where they can leave the grain without this additional resistance. This may be completely negligible in macroscopic samples but in thin wires the surface near volume becomes an important fraction of the total volume. When the generally accepted explanation given above is correct, important deviations from the reciprocal square-root dependence should become manifest in large-grain-sized thin wires. The yield stress should then not only depend on the grain size d but also on the diameter or thickness D of the sample.

Unfortunately, it is not easy to demonstrate this effect experimentally. Many measurements that we have done on thin wires, did not allow confirmation of such deviations. The problem was that the dispersion of the experimental results becomes very large in wires with an oligocrystalline structure. Mean values taken over a few grains show large statistical fluctuations and yielding starts to localize near defects or grains with a low Schmid factor. An other point to consider is that the different grain sizes were obtained by annealing at different temperatures and for different times. This may affect the yield stress also through modifications of σ_0, which has its origin in the critical shear stress of the grains and the texture. In order to get unambiguous results we had to resort to ribbons. There may be few grains in the thickness dimension but with a width of a few mm the statistical fluctuation in the average of the grain orientation distribution is much smaller than in wires. Furthermore, ribbons have the advantage that they can be thinned much easier than micro-wires. Therefore, only relatively thick ribbons had to be annealed to get the desired grain size and thinner samples were then obtained by

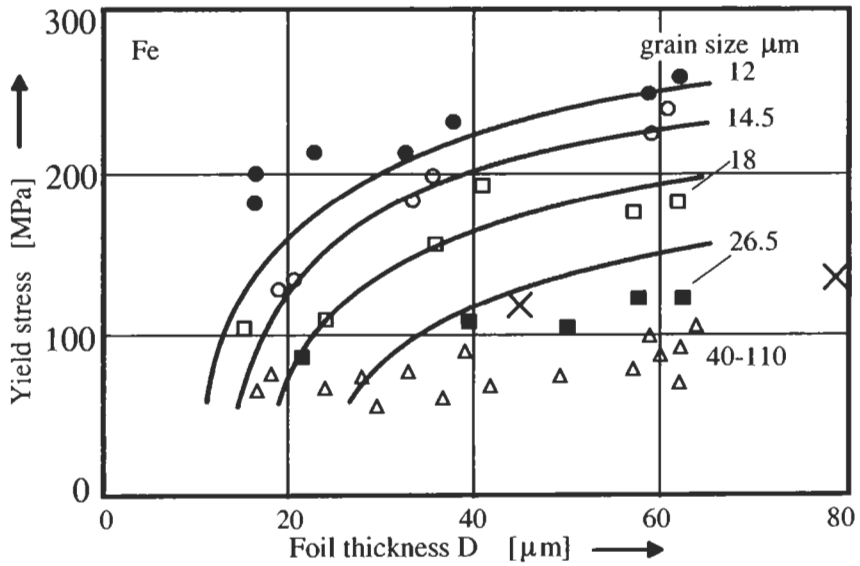

Fig. 28. Dependence of the yield stress on grain size and sample thickness in thin Fe ribbons (Judelewicz, 1993). For an explanation of the fitted curves see text. The 2 measurements marked with × were obtained by Miyazaki et al. (1979) for a grain size of 25 μm.

chemical dissolution in acids. All the samples of a given grain size therefore had exactly the same microstructure and variation of the yield stress with the sample thickness can unambiguously be attributed to a size effect.

Fig. 28 shows measurements of the yield stress $R_{0.2}$ as a function of the ribbon thickness. The ribbons were rolled from Armco iron (purity 99.9%) and from Cu of 4N purity. To get the different grain sizes the Fe ribbons were annealed between 1 and 18 h at temperatures ranging from 600 to 1200°C and between 1 and 3 h at 150 to 800°C for the Cu ribbons. In spite of all the precautions undertaken to get reproducible results, the dispersion still remains very large. But there is clear evidence that the yield stress severely drops in samples with less than 3 to 4 grains across the thickness.

The full lines in Figs. 28 and 29 show theoretical curves which, based on the idea that the grain boundaries forming the free surface, do not contribute to the strengthening effect $k/\sqrt{d}$. In order to get a simple relation, it was assumed that a surface layer of the thickness of half a grain diameter behaves as the non-strengthened material, i.e. has a yield stress σ_0, whereas the remaining part of the cross-section with thickness $(D-d)$ shows the usual grain boundary strengthening of the bulk material. The yield stress then turns out to follow the Hall–Petch relation minus an additional term which vanishes when the sample is much thicker than the grain size ($D \gg d$).

$$\sigma_y = \sigma_0 + \left(1 - \frac{d}{D}\right)\frac{k}{\sqrt{d}}$$

The constants σ_0 and k have been adjusted to get a reasonable description of the experimental data. The values obtained are $\sigma_0 = 10$ MPa, $k = 0.14$ MPa $m^{-1/2}$ for Cu

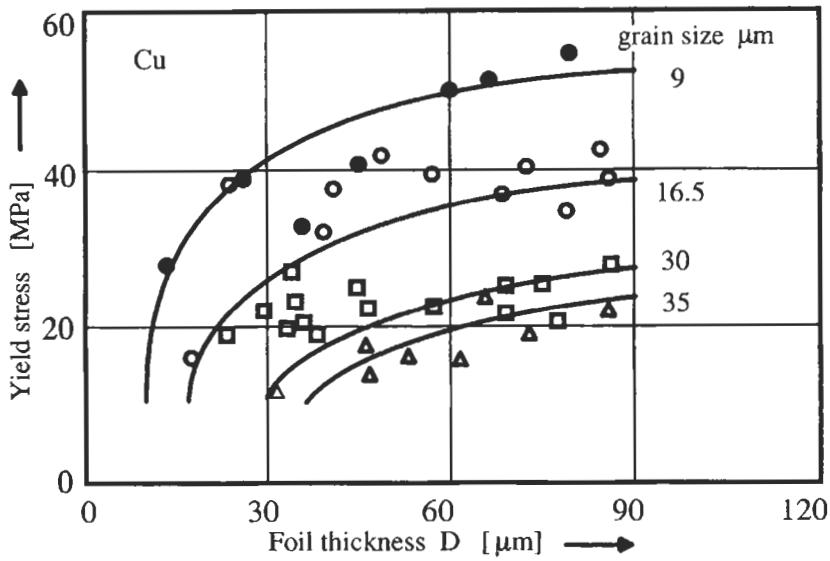

Fig. 29. Dependence of the yield stress on grain size and sample thickness in thin Cu ribbons. For an explanation of the fitted curves see text (Judelewicz, 1993).

and $\sigma_0 = 60$ MPa, $k = 0.83$ MPa $m^{-1/2}$ for Fe. These values are in the range of values given for corresponding bulk materials (Armstrong et al., 1962; Hansen and Ralph, 1982; Courtney, 1990).

Similar measurements as those presented in Figs. 28 and 29 have also be done by Miyazaki et al. (1979). They studied somewhat thicker samples of Al, Cu and Fe with grain sizes of 65 μm for Cu and 25 μm for Fe. Two points at the lower end of their measurements on Fe are given in Fig. 28. For Cu where the sample thickness varied from 140 μm to 1 mm they did not observe any effect in the yield stress, but the effect became manifest below about 3 grains across thickness, when the stress at 10% plastic strain was measured.

Anderson et al. (1968) studied the Hall–Petch relation of Armco iron on macroscopic samples and observed strong deviations from the $d^{-1/2}$ behavior for grain sizes below 10 μm. For larger grain sizes, however, their results are similar to the saturation values we observed for thick samples. Deviations from the Hall–Petch relation are also reported for compacted samples of nanocrystalline Cu and Pd. Chokshi et al. (1989) even found a negative value for the constant k in the range of grain sizes (6 to 16 nm) they studied. In more recent measurements of the Vickers micro-hardness on similar samples of Cu, Sanders et al. (1997) found that this metal follows the coarse-grained Hall–Petch relation down to 16 nm at which point it leveled off. Pell-Walpole (1943) described a size effect in the ultimate tensile strength in very large-grained Sn samples of 2.5–5 mm thickness even before the time Hall and Petch published their papers. He observed a linear increase of the ultimate tensile strength with the number of grains in the cross-section (area) up to 20 to 30 grains (corresponds to about 3 grains in the thickness) at which point the tensile strength continued to increase linearly but with a smaller

slope. His samples, however, had elongations at rupture that varied with the number of grains in the cross-section from 40 to 80%. The observed effect might therefore at least partially stem from strain hardening.

Fatigue of Polycrystalline Wires

Wires are often applied because of their almost unlimited flexibility. Nevertheless repeated bending as well as all other cyclic solicitations fatigue the material. Indeed, fatigue fracture belongs to the most common types of material failure in wires. Many investigators use rod or thick wire-shaped samples to study fundamental aspects of fatigue. Here we will look at micro-wires that are used in electronics for flexible cables or for electrical connections in microelectronics. Almost all modern electronic devices contain several centimeters of interconnections that are made with such bond wires; in vehicles and aircraft these interconnections are subject to fatigue by vibrations. Also from a scientific point of view these micro-wires are interesting objects permitting to study the effect of their high surface to volume ratio on the mechanical properties. Crystalline and amorphous high-strength metallic filaments are promising fibers for reinforcement in composite materials and their fatigue behavior is of technological importance. No attempt is made to review the huge literature on wire ropes where the failure often results from interactions between wires.

Fatigue of micro-wires and thin foils is usually measured in uniaxial tension–tension tests, using load cells with resolutions in the mg range. Clearly tension–compression tests would be more elegant and easier to interpret, but even with gauge lengths of 1 mm, a 25 mm thick wire is 40 times longer than thick and inevitably buckles when compressed. In the tension–tension loading mode wires are subject to a non-vanishing mean stress which even at room temperature induces the sample to creep and results in a complementary stress relaxation. According to whether the sample is tested in strain- or stress-controlled tests this elongation demands a continuous readjustment to keep the strain or stress amplitude constant. In addition, with gauge lengths of few millimeters the strain measurement is not easy. In view of the small forces and sizes it is practically impossible to fix an extensometer directly on the gauge length. Even though it is known to result in a poor precision, strain is therefore often inferred from the grip displacement. Description of experimental setups can be found in Hofbeck et al. (1986), Hausmann (1987), Kim and Weil (1987), Krönert and Raith (1989), Judelewicz (1993), Judelewicz et al. (1994) and Read (1998b). Sometimes much simpler bending tests can be used to establish the fatigue life curves (S–N curves). Geminov and Kopyev (1979) enclose the wire in a curved groove and rotated it around its axis. The total strain is calculated from the curvature of the groove that imposes the bending of the wire but since yielding takes place only at the surface and strain hardening is nonhomogeneous almost nothing can be said about the stress dependence of fatigue. Hagiwara et al. (1985) bend the wire by drawing it over a roll. Similar techniques are used by Doi et al. (1981) and Tanaka et al. (1980). Unfortunately, direct comparisons of these bending tests for micro-wires with tension–tension tests are not available. Since in most of these tests the sample surface is in gliding or rolling contact with another object crack initiation and thus fatigue life might be modified.

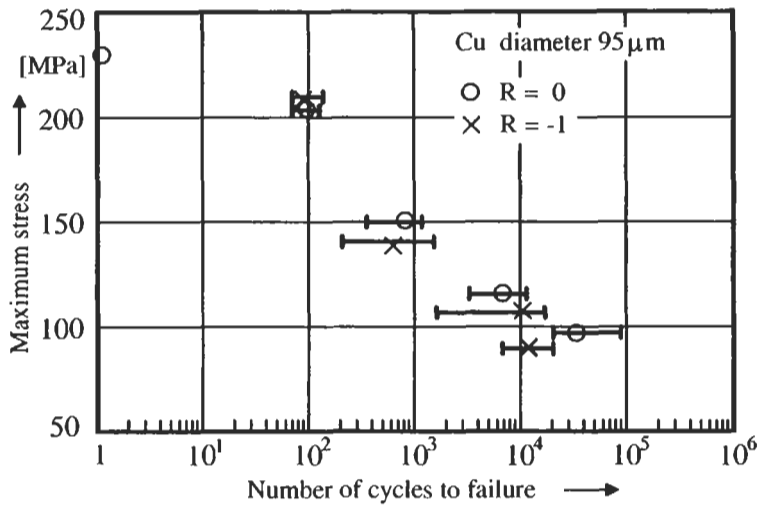

Fig. 30. Low-cycle fatigue curve for a Cu wire measured in the tension–tension ($R = 0$) and in the tension–compression loading mode ($R = -1$).

The mean stress that is present in the tension–tension loading mode with respect to the tension–compression mode, is well known to reduce the fatigue life. The effect is generally more pronounced in brittle materials than in ductile metals. Fig. 30 shows a comparison for a 95 μm Cu wire with a very coarse-grained microstructure. The as-drawn samples were annealed for 2 h at 600°C and had a gauge length of 1 mm for the tension–compression tests. Each point given in Fig. 30 shows the average and the dispersion of the number of cycles to failure for about five measurements. These results indicate that there is almost no difference. All points, except the one for the lowest stress, are within the dispersion limits of the cycle number which are, as usual, large for this kind of samples. The difference at higher cycle number may stem from the mean stress to which samples are subject in tension–tension loading. This favors the crack propagation in the sample that even though very ductile at the beginning becomes brittle at high cycle numbers (brittle fracture see Fig. 35). A more systematic investigation of these two loading modes has been published by Kim et al. (1991). They conclude from their microscopic studies (SEM, TEM) that for a lifetime of 10^5 cycles, cracks initiate on slip bands within the grain (transgranular cracking) in the tension–compression mode, whereas for the tension–tension mode cracks start from preferentially damaged grain boundaries which result from their interaction with the slip bands.

Effect of Grain Size on Fatigue Life

Even though fatigue life considerably depends on the grain size only a few studies have been carried out on the same base material. Figs. 31 and 32 show fatigue curves for Cu wires of 99.97% purity (OFHC) with diameters of 30 and 95 μm in the as-drawn state and two annealed states. Grain size, annealing conditions and tensile strength are given in Table 5.

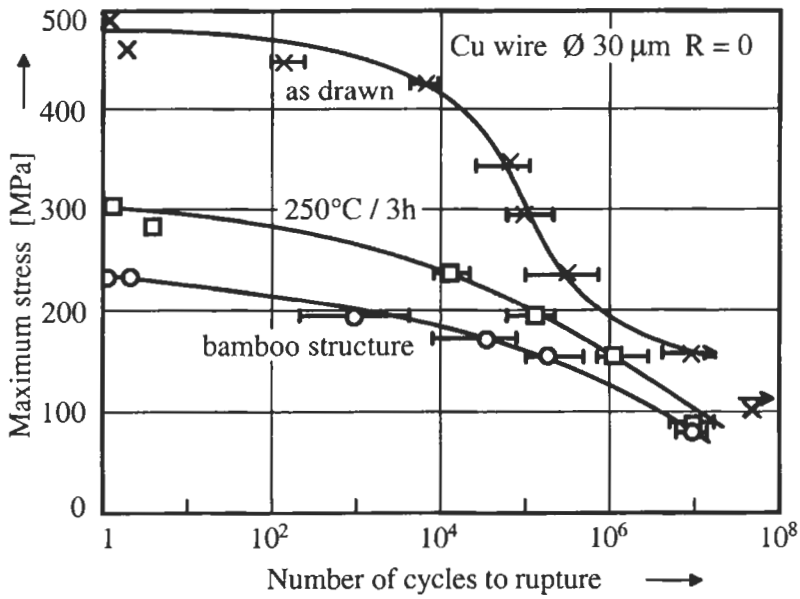

Fig. 31. Fatigue curves of a 30 µm diameter Cu wire in 3 annealing states.

Table 5. Grain size, annealing conditions and tensile strength of Cu wires (99.97% purity) used to measure the *S–N* curves given in Figs. 31 and 32

Diameter (µm)	Annealing conditions	Grain size (µm)	Yield stress, $R_{0.2}$ (MPa)	Tensile strength (MPa)
95	as drawn	<1	437	475
30	as drawn	<1	484	514
95	3 h/250°C	3.1	305	355
30	3 h/250°C	2.5	254	302
95	2 h/600°C	95 (bamboo str.)	70	231
30	2 h/600°C	30 (bamboo str.)	81	222

These results point out that Cu wires in the as-drawn state are superior to the same wires in the annealed states. This result is even more astonishing when we keep in mind that these wires have already been subjected to a severe low cycle 'fatigue treatment' when they were drawn. Strong differences become also apparent when we compare curves for the two diameters in the same state. Thin wires in the as-drawn state and those with a bamboo structure live longer than the thick ones. For the intermediate state the difference is very small but compared to the as-drawn wires they show a good or even better performance in the high-cycle domain. The differences between the two as-drawn states are difficult to comment. These samples have very small grains compared to their diameter, and the proximity of the surface should not affect their fatigue life. Figs. 33 and 34 show the fracture surface of the as-drawn and annealed wires. Thin as-drawn wires (Fig. 33 left) neck down to a cone whereas in the thicker

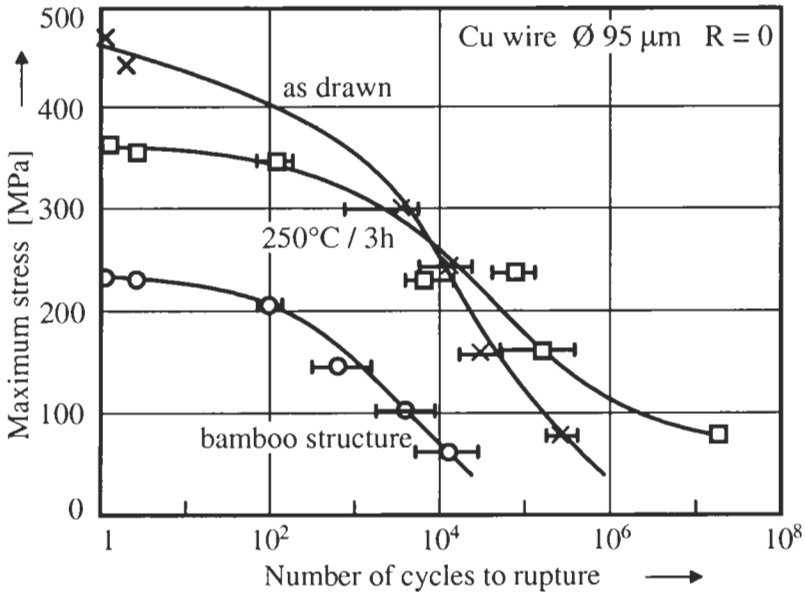

Fig. 32. Fatigue curves of a 95 µm diameter Cu wire in 3 annealing states.

ones fracture occurs through crack propagation and final rupture. In the annealed wires (Fig. 34) the crack appears to initiate at damaged grain boundaries (Fig. 36 right) and continues to follow grain boundaries until final rupture.

Similar results to those presented for Cu wires have been observed in as-drawn polycrystalline Au wires (Hausmann, 1987). This behavior is different in bamboo wires to be discussed next. SEM studies of their fracture surfaces, as shown in Figs. 35 and 36, reveal characteristic differences in their fracture modes. Basically there appear

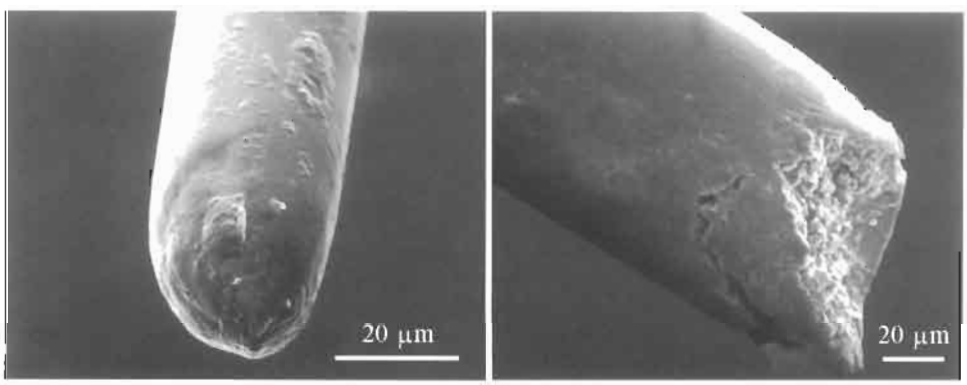

Fig. 33. Fracture surfaces of as-drawn Cu wires. Left: in the low-fatigue domain necking formed a cone-like fracture surface in this 30 µm diameter wire when it failed after 980 cycles with a max. stress of 300 MPa. Right: after some necking a crack moved through the remaining cross-section. Failure occurred after 2.77×10^5 cycles at 160 MPa. Diameter 95 µm.

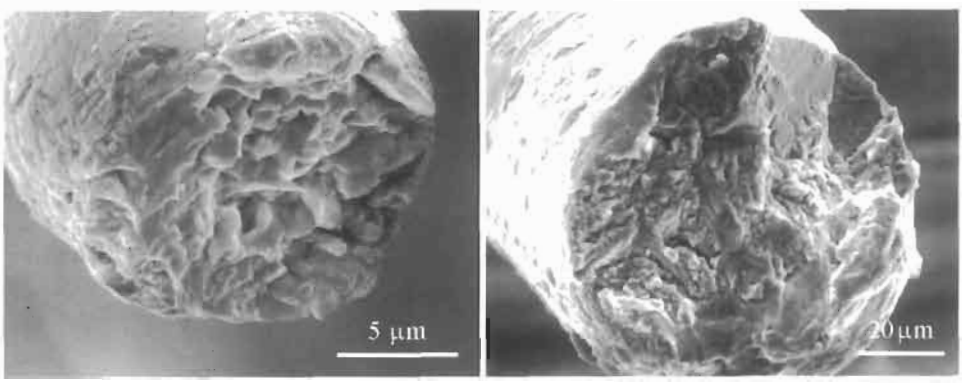

Fig. 34. Fracture surfaces of Cu wires annealed for 3 h at 250°C and fatigued in the high-cycle domain. These surfaces have inter- and transgranular portions. Rupture probably first followed damaged grain boundaries (intergranular) and then sheared of (transgranular). Left: failure after 6.2×10^5 cycles at 160 MPa. Diameter 30 μm, about 10 grains in the thickness. Right: failure after 2.3×10^6 cycles at 80 MPa. Diameter 95 μm.

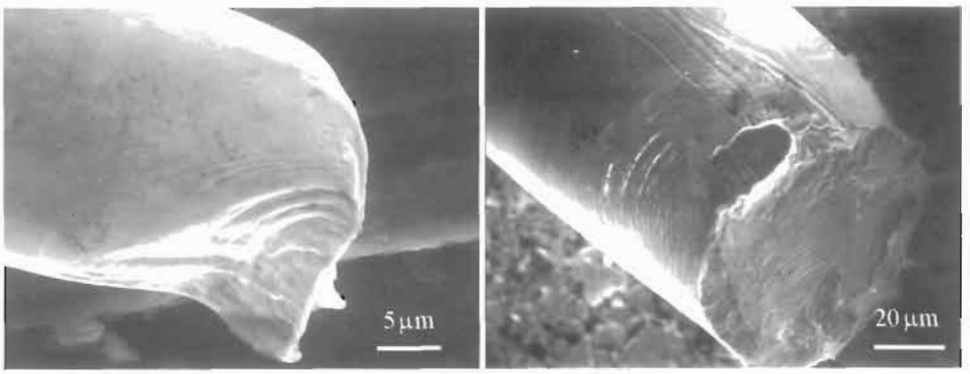

Fig. 35. Fracture surfaces of Cu wires with bamboo structure. The thinner wire on the left (30 μm) necking down to knife edge. Its surface remains smooth. Failure after 2.7×10^4 cycles at 180 MPa. The thicker wire on the right (95 μm) failed in a brittle manner after 1.3×10^4 cycles at 80 MPa.

two fracture modes. In the low-cycle domain samples still have enough ductility to start fracture by necking. For wires with a bamboo structure necking continues until a knife edge forms. Polycrystalline samples show less necking and final transgranular rupture surfaces. Like drawn wires, they often neck down to cone-like fracture surfaces. In the high-cycle domain almost no macroscopic deformation is visible and rupture is brittle. In the intermediate state it appears that the cyclic solicitations considerably damage grain boundaries which then become sites of easy crack nucleation. In fact, damaged grain boundaries were often observed on the wire surface near the fracture. Fig. 36 shows a SEM image taken on a Cu wire with damaged grain boundaries that are characteristic for intermediate grain sizes.

A number of comparable studies, which bear relevance for micro-wires, have been published on thin Cu foils. Judelewicz (1993) and Judelewicz et al. (1994) reported on

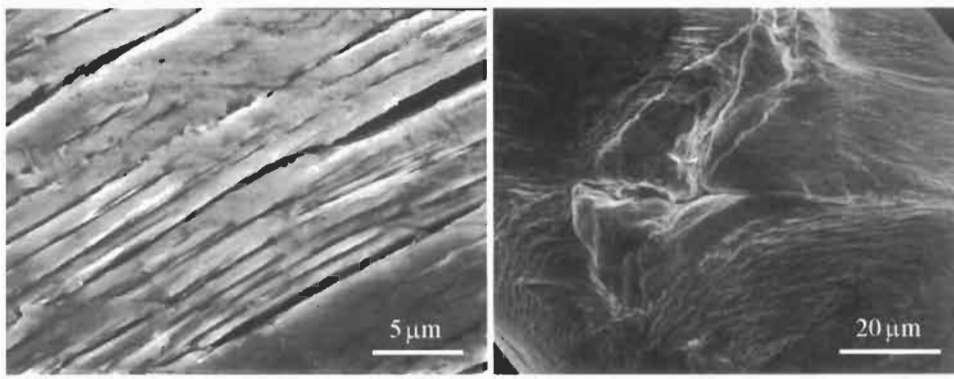

Fig. 36. Left: wire surface of a 95 μm diameter Cu wire with bamboo structure showing extrusions and micro-cracks that result from persistent glide bands (fatigued for 1.2×10^3 cycles). Right: surface of annealed wire after 1.8×10^4 cycles showing damaged grain boundaries that are characteristic for intermediate grain sizes.

rolled foils having a thickness of 20 and 100 μm, Hong and Weil (1996) studied 25 μm thick electrodeposited foils, and Read (1998a) published results on freestanding evaporated foils that were only 1.1 μm thick (see also Read and Dally (1995) for similar Al foils).

In as-rolled foils of 20 and 100 μm thickness that were not annealed prior to the fatigue tests, Judelewicz (1993) and Judelewicz et al. (1994) find a marked difference in fatigue life between samples that were cut parallel and perpendicular to the rolling direction (Figs. 37 and 38). For thin samples the rolling imprints were found to play an important role. Samples that were rolled perpendicular to the stress direction fail at a

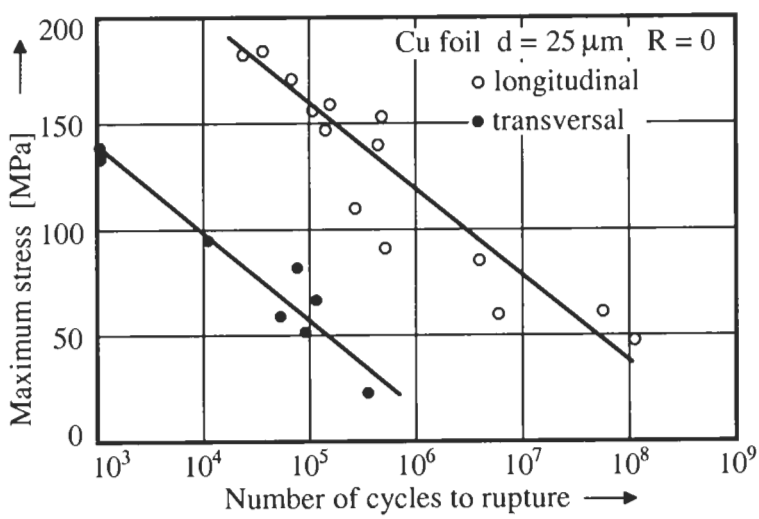

Fig. 37. Fatigue curves for rolled Cu foils (99.99% purity) that were measured in the stress-controlled tension–tension loading mode parallel and perpendicular to the rolling direction. Thickness 25 μm.

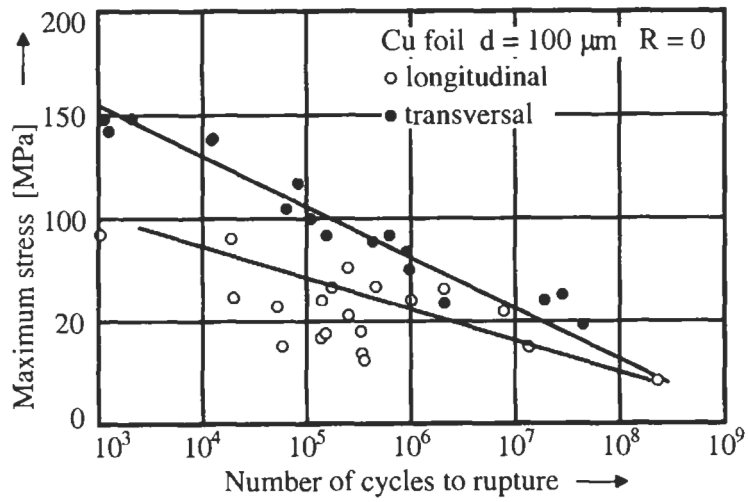

Fig. 38. Fatigue curves for rolled Cu foils (99.99% purity) that were measured in the stress-controlled tension–tension loading mode parallel and perpendicular to the rolling direction. Thickness 100 μm.

cycle number which is about two decades below the cycle number of samples stressed along the rolling direction. A similar observation has also been made by Merchant et al. (1999) on rolled foils of 12–35 μm thickness. For the thick specimens this effect disappears at low stresses and even reverses at high stresses (low cycle number). It should be noted that non-annealed samples have the well-known Cu rolling texture which is markedly different from the cubic texture that is obtained in well annealed samples (see *S–N* curve in Fig. 41). The number of glide systems with a high Schmid factor in the rolling texture is higher when the stress is applied parallel to the rolling direction. The difference in fatigue life observed between the longitudinal and transverse excitation for the 100 μm samples (Fig. 38) where the surface striations were found to be less important than for the 25 μm samples might therefore have its origin in the texture.

Contrary to macroscopic samples where the fracture surface of fatigue specimens is usually normal to the tensile stress direction, thin sheets are similar to micro-wires. They undergo a very large amount of plastic deformation and neck down to zero cross-section, ending in irregular knife edge rupture, very much like a high-temperature creep rupture.

Hong and Weil (1996) prepared one set of 25 μm thick Cu foils with grain sizes of 1 and 10 μm by electrodeposition and another set of 33 μm thick foils by rolling. Samples with a gauge section of 1.5 mm width and 3.75 mm length were obtained by photolytography and electropolishing. This process demanded a temperature rise of 1 min to 90°C that also determined the final state of annealing. Low-cycle fatigue tests were carried out in the stress-controlled tension–tension loading mode at a frequency of 0.2 to 0.5 Hz. Compared to all the other measurements on thin samples that are compiled in Fig. 39, their results show an astonishing small dispersion of about 0.2 decade in the number of cycles to failure whereas for the others one decade is typical (note: dispersions are not shown in Fig. 39). They conclude that both types of samples

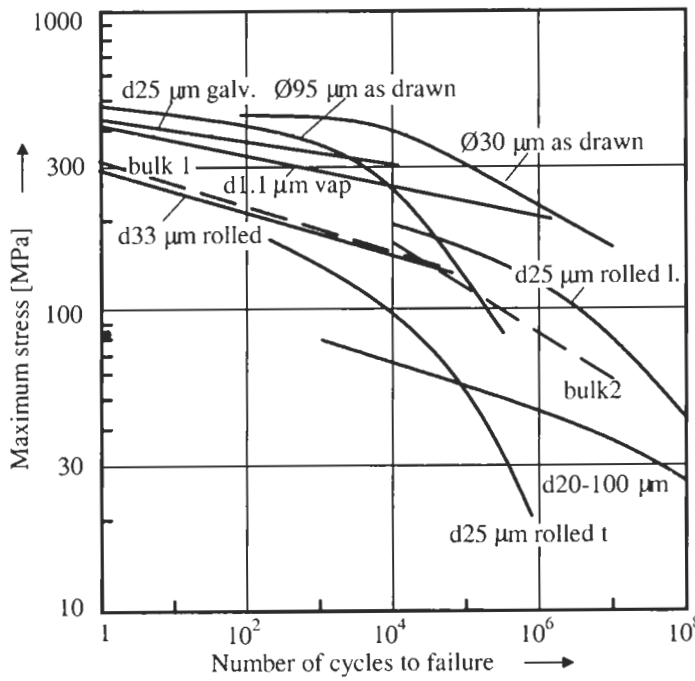

Fig. 39. Fatigue curves of small-grained copper micro-wires and thin foils. Ø, wire diameter; d, foil thickness; l, longitudinal; t, transverse to rolling direction.

obey the Basquin law which states that

$$\Delta\sigma = \sigma_f \cdot N^b$$

Here $\Delta\sigma$ is the applied peak–peak stress amplitude ($R = 0$). The constants σ_f and b are the fatigue strength coefficient and the fatigue exponent, respectively ($\sigma_f \approx$ tensile strength). In a $\log(\sigma)$ vs. $\log(N)$ plot this law gives a straight line whose slope is b. Indeed, their results (d25 μm galv. and d33 μm rolled) as well as others in the low-cycle regime can be described by this law. Nevertheless, in the high-cycle domain this does not always appear to be the case. Curves either change to another slope or remain curved. The fatigue life of their wrought foils does not differ appreciably from those of bulk wrought Cu (bulk 1, cited by Hong and Weil, 1996). The electrodeposited foils, however, have a much higher fatigue life which they explained by the higher dislocation and twin density with respect to their rolled foils. It is well documented that the hardening observed in Cu during cyclic deformation results from the formation of dislocations tangles and the development of cell walls (see e.g. Laird et al., 1986). This is also the hardening mechanism they observed in their large-grained samples. Specimens with grains smaller than 2 μm did not show dislocation cells. In any case all foils exhibited necking prior to fracture.

To get the thinnest samples (probably ever studied in fatigue tests) Read (1998a) evaporated 5-nines Cu on a silicon wafer substrate using an electron beam in vacuum of better than 10^{-6} Torr. Specimens were produced with a thickness of 1.1 μm Cu, but

had on both sides an additional layer of 0.05 μm Ti. Micro-lithography was used to pattern the tensile samples with a gauge section of 200 μm width and 600 μm length. The silicon waver was removed by etching for 4 h at 100°C. This also determined the final annealing state. The average grain size was then found to be 0.98 μm. His tensile specimens have therefore only one or a few grains through the thickness. The extremely delicate fatigue tests were performed with specially designed equipment in the load-controlled tension–tension mode with a frequency of 1/15 Hz Read (1998b). The dispersion on the fatigue life is much larger than for the foils of Hong and Weil, but of the same order (1 decade) as for measurements on wires and the other foils shown in Fig. 39 (see also Table 6). The fatigue resistance for these micro-specimens is quite high and comparable to as-drawn wires and eletrodeposited films. Previous measurements on similar Al foils (Read and Dally, 1995), however, gave fatigue lives that were 2 to 3 decades below those of Al sheets (Forrest, 1966). From his TEM studies Read confirms the observation of Hong and Weil that cyclic deformation does not generate cell walls in small grains and concludes that dislocations move individually and escape through the surface.

By returning once more to Fig. 39 we conclude that most curves have features similar to another, but taken all together there is no clearly visible trend. These curves have been obtained on very different grain sizes, sample thicknesses and grain size to thickness ratios, but do not show a distinct trend whether one of these parameters decisively governs fatigue life in microscopic samples. Of course Cu can be prepared in a broad range of tensile strengths. From over 500 MPa down to values that are difficult to specify, especially when necking, as is usual in fatigue tests on microscopic samples, is not taken into account (i.e. engineering rather than effective stress is used). Obviously the initial tensile strength is a decisive parameter for the duration of the fatigue life, particularly in the low-cycle regime, but in the high-cycle range many crossovers can be observed. It finally appears that many other factors, such as texture, crystalline defect density and surface defects, play an equally important role.

Nevertheless, the question of size effects in fatigue that are related to the proximity of the surface, where dislocations can escape, is of scientific interest. In view of the diversity of the results presented on small-grained Cu, such studies have to be carried out with coarse-grained samples prepared from the same base material. In the following section we will present results that were obtained from studies on thin Cu wires and ribbons.

Size Effect in the Fatigue Behavior of Thin Cu Wires and Foils

Results of fatigue tests on micro-Cu wires with bamboo structures which is the coarsest grain size possible in wires are given in Fig. 40. The *S–N* curves obtained on 30, 50 and 95 μm diameter wires show that the fatigue life at stress amplitudes below half the tensile strength of thin wire is 2 to 3 decades longer than for the thick ones. These wires have been annealed for 2 h at 600°C and are therefore highly ductile (for their mechanical properties see Table 5). Nevertheless, the thick wire that fails first, shows a brittle transgranular fracture above 10^4 cycles (Fig. 35 right), whereas the thin wire always shows severe necking, even at the highest cycles measured

Table 6. Properties, grain sizes and annealing states of samples used for measurements represented in Fig. 39

Cu sample type	Sample size	Grain size (μm)	Anneal. state	Mode and freq. (Hz)	$R_{0.2}$ (MPa)	R_{max} (MPa)	Ref.
Bulk OFHC	Ø 8 mm	3.4	twisted, polished	tc, 30	79	238	Thompson and Backofen (1971)
Wire 99.999	Ø 95 μm	<1	as drawn	tt, 30	437	475	Hausmann (1987)
Wire 99.999	Ø 30 μm	<1	as drawn	tt, 30	487	514	Hausmann (1987)
Foil 99.999 long. + trans.	d 25 μm	<1	as rolled	tt, 700	–	–	Judelewicz (1993)
Foil 99.999	d 20–100 μm	20	annealed	tt, 700	–	–	Judelewicz (1993)
Foil electrodepos.	d 25 μm	1 + 10	1 min 90°C	tt, 0.2–0.5	–	439	Hong and Weil (1996)
Foil rolled	d 33 μm	15	1 min 90°C	tt, 0.2–0.5	–	309	Hong and Weil (1996)
Foil electron beam evap. 99.999	d 1.1 μm	0.98	4 h 100°C	tt, 0.066	330	339	Read (1998a)

Ø, diameter; d, thickness. tc, tension–compression; tt, tension–tension.

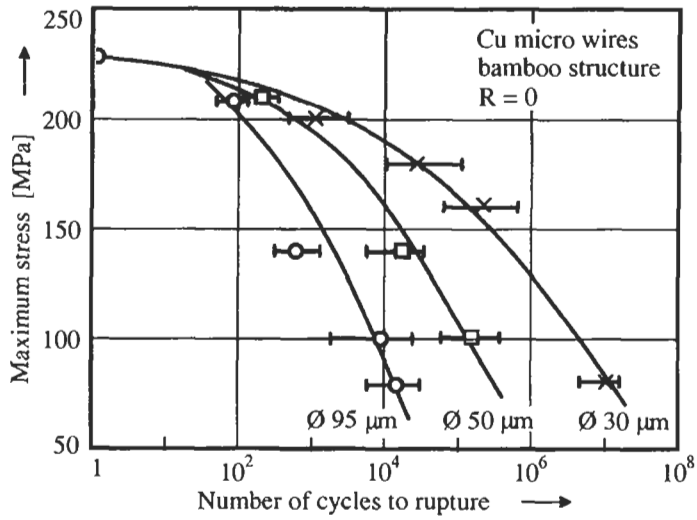

Fig. 40. S–N curves for large-grained (bamboo structure) Cu wires with diameters of 95, 50 and 30 μm.

(Fig. 35 left). A closer observation of the fracture surface of the thick wire also reveals striations that result from the crack propagation. The wire surface after failure was very rough, showing extrusions and open micro-cracks (Fig. 36 left). This contrasts with observations on the thin wire. Here the fracture surface resembles those obtained in tensile tests, where necking goes down to one line and shear offsets cover the surface. There were no extrusions or micro-cracks visible.

Similar tests were made with foils that contained only one grain trough the thickness but about 20 in the width (2 mm). This state was obtained by vacuum annealing for 4 h at 700 to 800°C. This treatment drastically changed the texture. The well known Cu rolling texture observed on our samples prior to recrystallization (fatigue curve d25 rolled in Fig. 39) changed to an almost perfect orientation of the cubic axes along the rolling direction and perpendicular to the sheet ((100) [001] orientation). In order to prevent damaged surfaces, chemical machining was used to prepare the dog-bone-like fatigue specimens with a gauge section of 2 to 4 mm length and 2 mm width. Two sets of samples with different thickness were been prepared. One set with 100 μm thickness was obtained from foils rolled to this thickness. The second set with 20 μm thickness was made from the same foils by chemical machining. This guarantees that both sets have exactly the same microstructure. Results of fatigue tests that were made in the stress-controlled tension–tension loading mode at 70 Hz are shown in Fig. 41. Even though with a factor of ten, the difference in fatigue life between the two sets is not as big as for the wires, the thinner foils have again a better fatigue resistance than the thicker ones. As expected also the dispersion of the individual results is with half a decade somewhat smaller than for the wires.

Obviously, these experimental findings raise the question of what happens on the microscopic level. In fact, considerable progress has been made in recent years in our understanding of the physical origin of fatigue. In particular, a great number of fundamental

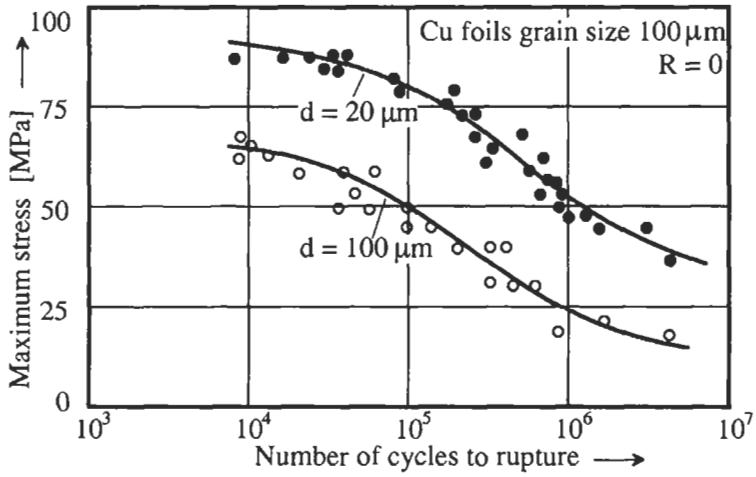

Fig. 41. Fatigue curves for large-grained (100 μm) foils of 20 and 100 μm thickness d.

studies have been done on Cu single crystals. From the large number of publications we mention here but a few overviews: Mughrabi (1985), Laird et al. (1986), and Suresh (1994).

A well annealed metal subject to cyclic deformation initially hardens and finally reaches a state of saturation. For Cu, in fully reversed strain-controlled tests at room temperature, this saturation stress first increases with the imposed strain amplitude and then shows a plateau where it remains fairly constant. Expressed in resolved shear stress and strain, the plateau stress amounts to 28 MPa and extends from 6×10^{-5} to 7.5×10^{-3} in the plastic strain amplitude. At higher strain amplitudes the resolved shear stress increases again with the strain amplitude. Detailed transmission electron microscopy observations of cyclic strain hardening in Cu, oriented for single slip, show that the initial few cycles (10^2–10^4) produce dislocations in the primary glide plane that bundle in a network. These networks consist mainly of edge dislocation dipoles and are also referred to as veins, bundles or loop patches. These veins follow the primary dislocation lines and have a roughly cylindrical cross-section with a diameter of 1–2 μm. They are embedded in the matrix which, when viewed in micrographs perpendicular to the glide plane, appear as channels of about equal width (see schematic drawing Fig. 42). The dislocation density grows up to 10^{15} m^{-2} in the veins and is about 3 orders of magnitude smaller in the channels. Similar to fibers in a soft matrix these veins account for the observed hardening.

For the strain amplitudes in the plateau region, groups of dislocations rearrange in a new order, the persistent slip band (PSB). They develop from veins when a critical dislocation density is achieved near the plateau stress. The PSB are oriented parallel to the primary slip plane and extend from surface to surface. Within this band edge dislocations are arranged in walls, that are perpendicular to the slip plane and have about 1 μm height and 0.1 μm thickness. The walls are regularly spaced by channels with a quadratic cross-section. They contain relatively few screw dislocations that cross over from one wall to the other. When viewed along the edge dislocation lines ([121]

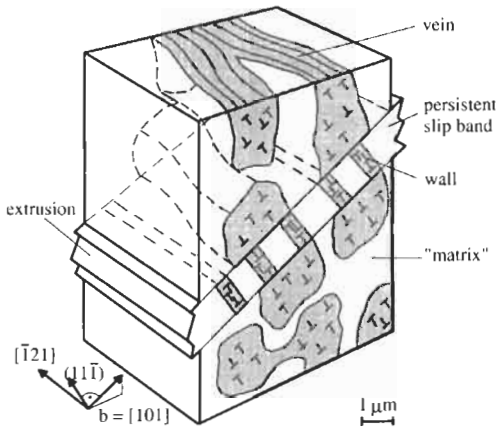

Fig. 42. Persistent slip band in a fcc metal.

direction) in a TEM micrograph, the band forms a ladder that crosses the less regularly spaced spots that result from the veins. The number of PSBs that form in a crystal depend on the strain amplitude. Persistent glide bands are regions of easy glide and sustain deformations up to the upper plateau strain (7.5×10^{-3}). In contrast to this, the vein-covered matrix is comparatively hard. Therefore, when the strain amplitude is increased, the number of PSB also increases, in order to accommodate the strain. The situation as described above develops in the first 10^3 to 10^4 cycles in single crystals and under certain conditions also in polycrystals. Multiple slip, however, appears to perturb or even prevent the establishment of this well ordered dislocation structure. Other structures, such as maze structures or cellular structures, form instead. A cellular structure also forms when a strain amplitude is chosen beyond the upper plateau strain or when PSBs are cycled for a prolonged duration. Nevertheless, the latter case is difficult to achieve, since PSBs, once developed, rapidly form extrusions and intrusions which then become sites of transgranular crack nucleation. These cracks then rapidly propagate in the strain-hardened crystal and produce a fracture of the brittle type.

Inspection of the wire and fracture surfaces of the thick Cu wire (Fig. 35 right, Fig. 36 left) now clearly indicate what happened during fatigue. The wire surface of the fatigued sample is densely packed with extrusions that stem from PSBs; in addition, many open micro-cracks are visible. Since this wire has a bamboo structure (i.e. a chain of single crystals), there are always many grains with orientations where primary slip on a single glide system will occur. Moreover, the formation of PSBs is known to be relatively insensitive to the stress direction; therefore, after fatiguing no obvious cause should prevent the formation of PSBs. The final fracture occurs by crack propagation as is characteristic for strongly strain-hardened metals.

This strongly contrasts with the findings for the thin wire of the same type and subject to exactly the same fatigue test. Its fatigue life is much longer, the final rupture is of the ductile type and the wire surface remains smooth. This ductile fracture suggests that strain hardening did not take place in the usual manner and the smooth surface indicates that PSBs and extrusions did not develop in this wire. Two obvious explanations are that

(1) either the critical dislocation density to form PSBs (of order 10^{14} m^{-2}) has not been achieved, or (2) that multiple slip prevented the formation of PSBs. The latter argument is rather delicate to comment on; on the one hand, it might equally well be applied to the thick wire and, on the other hand, the wedge-shaped fracture surface shown in Fig. 35 is not likely to be the result of slip in a single glide system, but it might have formed in the final state of fatigue. The first argument would find a natural explanation, when in the thinner wire a sufficient number of dislocations escape through the surface to prevent the formation of PSBs. From continuum mechanics it is known that dislocations near the surface are subject to image forces which result from their stress field. These attract dislocations toward the surface and assist them to escape. However, this force, when compared to the resolved shear stress, is only of importance in the immediate proximity of the surface and could not explain a massive loss of dislocations in the more central regions of the wire. In order to profit from this force, dislocations have to migrate first to the surface. The following simple argument shows that under conditions of prolonged cyclic solicitations and in particular when single glide prevails, this may not be completely excluded. We assume that due to the cyclic stress dislocations glide backwards or forwards over a mean distance d. When this back and forward motion occurs in a random sequence, as is the case in chemical diffusion, the mean square displacement x after N cycles amounts to $x = \sqrt{d^2 N}$. The elementary glide distance d is related to the applied plastic shear strain amplitude γ, the dislocation density ρ and the Burgers vector b by $d = \gamma/\rho b$. Taking $\rho = 10^{13}$ m^{-2} which is below the critical density for PSB (10^{14} m^{-2}) formation, $\gamma = 1 \times 10^{-3}$ in the center of the plateau range and $b = 0.25$ nm, one obtains $x = 12$ μm after 10^3 cycles. This is just of the order of magnitude for the radius of the thin wire (15 μm) and consequently predicts an important loss of dislocations during the number of cycles the critical dislocation density and the PSBs usually build up in bulk samples.

For thin sheets the situation is not as clear cut as for the wires. Firstly, the experimentally observed difference in fatigue life between the thin and the thick samples is much smaller. Secondly, the foil samples had an almost perfect cubic annealing texture with the [100] axis in the stress direction. Since for this particular orientation all four primary glide planes have the same Schmid factor, multiple slip will occur. This is known to accelerate strain hardening and precludes the formation of the dislocation structures mentioned before (Jin and Winter, 1984; Laird et al., 1986). Due to the mutual interaction of dislocations on different glide planes their loss through the surface is certainly also much smaller than estimated above. Nevertheless, PSBs and extrusions that give rise to transgranular micro-cracks have occasionally been observed, but all foils failed by severe necking (see Figs. 43 and 44).

Fracture and Mechanical Properties of Metallic Glasses

The mechanical properties of inorganic glasses, such as window glass, are in many respects very different from crystalline metals. The latter have a good ductility that results from their periodic structure and the more or less isotropic electronic bonds. Glasses have disordered structures and strongly oriented covalent bonds. Both these characteristics make them brittle, such that we often associate inorganic glasses with

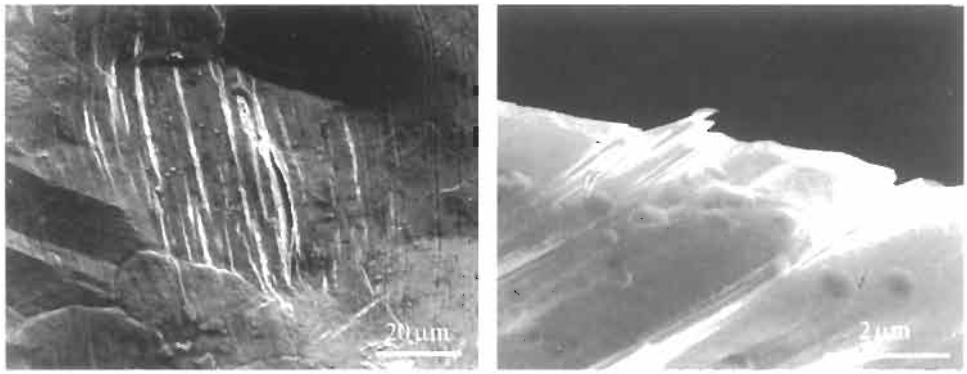

Fig. 43. Left: extrusions and open crack perpendicular to the stress direction in a 20 μm thick Cu foil fatigued for 7×10^6 cycles at 55 MPa. Right: same as left but viewed from the edge of the foil after 1.5×10^4 cycles at 60 MPa. (From Judelewicz, 1993.)

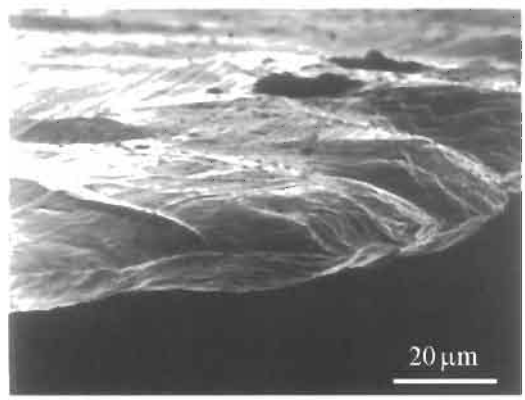

Fig. 44. Typical fatigue fracture in a rolled and annealed Cu foil. This 20 μm thick sample failed after 1.8×10^5 cycles at 77 MPa. (Judelewicz, 1993.)

fragility. Metallic glasses are somewhere in between crystalline metals and inorganic glasses. They have a disordered structure but metallic bonds and this combination asserts then still a certain ductility. In other words, the isotropic bonds allow short-range atomic rearrangements but the lack of periodicity does not allow mobile dislocations, at least not in the sense of crystalline metals. The typical shape of metallic glass ribbons, their production and effects of macroscopic defects on fracture have already been discussed in pp. 195 and following. Here we return to intrinsic mechanical behavior.

Elastic Behavior of Metallic Glasses

In common with all other solids, metallic glasses behave in an essentially elastic manner at low temperatures and low stresses. The elastic constants of amorphous metals are,

however, always somewhat smaller than in crystalline alloys of the same composition. For the bulk modulus B, the difference remains relatively small, on the order of 4 to 6%, and is explained by the lower density which increases by 1 to 2% on crystallization. For the elastic and the shear modulus these differences amount to 25 and 35%, respectively. Using the relations that exist between the elastic constants of isotropic bodies this gives a Poisson ratio that is 3 to 7% larger than in the crystalline state. This elastic softening is explained by small and fast local stress-induced displacement of atoms which result from non-central interatomic forces (Weaire et al., 1971; Lançon et al., 1985). This means that not all atoms displace exactly as we would expect them to do from the macroscopic strain field. Note that an isotropic solid bonded only by central forces (sometimes referred to as a Cauchy solid) would have a single independent elastic constant ($B = \frac{5}{3}G = \frac{2}{3}E$) and Poisson's ratio would have a material-independent value of $\frac{1}{4}$. This does of course not hold in crystalline metals but the effect of non-central forces is stronger in the amorphous state. Due to the extremely high yield stress some metallic glasses sustain elastic deformations of over 2%. As Fig. 45 illustrates the stress–strain relation becomes substantially nonlinear at high stress. This nonlinearity has nothing to do with strain hardening. At room temperature this curve remains fully reversible. For a more detailed review on the elastic and anelastic behavior of metallic glasses see Künzi (1983).

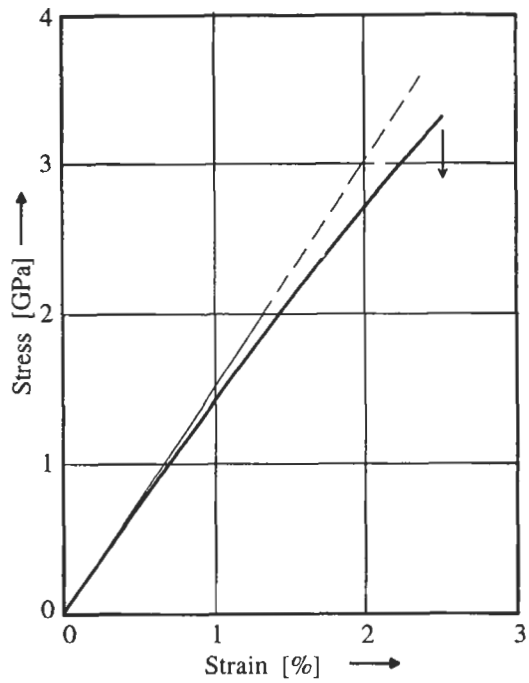

Fig. 45. Stress–strain relation for an amorphous $Fe_{75}Si_{10}B_{15}$ ribbon as shown in Figs. 11 and 13. Nominal cross-section 16 μm × 150 μm. The arrow at 3.2 GPa and 2.5% strain indicates rupture.

Anelastic and Viscoplastic Behavior of Metallic Glasses

Viscous flow sets in only above about 0.6 of the glass transition temperature T_g which for many technical interesting alloys is between 400 and 600°C. Even though amorphous metals have an atomic structure (usually described by the pair correlation function) that is similar to the corresponding alloy in the liquid state, their viscous flow resembles rather the behavior of crystalline metals than those of liquids.

Many investigators have examined homogeneous creep and stress relaxation in metallic glasses (e.g. Kimura et al., 1977; Gibeling and Nix, 1978; Megusar et al., 1978; Patterson and Jones, 1980; Taub, 1980; Perez et al., 1982; Neuhäuser and Stössel, 1985; Russew et al., 1997). However, the experimental findings of the stress–strain rate dependence are often controversial. As is the case in crystalline metals, strain rate curves at higher stresses show primary, secondary and tertiary creep. The creep rate during secondary creep, which sometimes reduces to a minimum as in crystalline metals (i.e. is of short duration), can usually be described by a power law creep $\dot{\varepsilon} = A(T) \cdot \sigma^n$. The observed stress exponent varies between 1 and 12. The exponent 1 indicates Newtonian flow and predominates in studies carried out at lower stress and high temperatures. Some of the higher stress exponents (6–12) have been clarified to stem from simultaneous structural relaxations that occur during the measurement at temperatures close to the glass transition (Patterson and Jones, 1980). Preannealed samples show lower exponents (2–4). The constant $A(T) = A_0 e^{-Q/kT}$ depends on the temperature T and the activation energy for creep Q. In crystalline metals Q agrees usually quite well the activation energy for self-diffusion. In amorphous metals Q is of the same order of magnitude, but it appears that there are several mechanisms that contribute to flow (spectrum of activation energies). In addition to that a proper interpretation of creep data is often complicated due to the simultaneous presence of intrinsic anelastic (time dependent but reversible) creep effects. These result from stress-induced local atomic rearrangements that need assistance from thermal activation and return back to their original configuration when stress is released. Measurements of the mechanical damping (internal friction; Künzi, 1983) indicate that these rearrangements increase in an exponential manner towards the glass transition temperature. At room temperature, however, the intrinsic mechanical damping of metallic glasses is small and therefore again indicative of a good elastic behavior.

Fracture and Plastic Deformation of Metallic Glasses

At room temperature plastic flow of amorphous metals occurs in the form of highly localized shear deformation bands. Multiple irregularly spaced shear bands appear in the deformed region. Fig. 46 gives an example of an almost completely back bent ribbon. Similar observation can be made in uniaxial compression and after rolling (Davies, 1978). Shear bands are less numerous in traction tests even when observed after fracture (Fig. 48a). Since these shear bands are extremely thin, TEM observations indicate a thickness of 5 to 20 nm (Masumoto and Maddin, 1971; Sethi et al., 1978; Donovan and Stobbs, 1981), and the surface step heights are on the order of micrometers, shear strains comparable to superplastic metals occur in this very small volume of the band. Pampillo

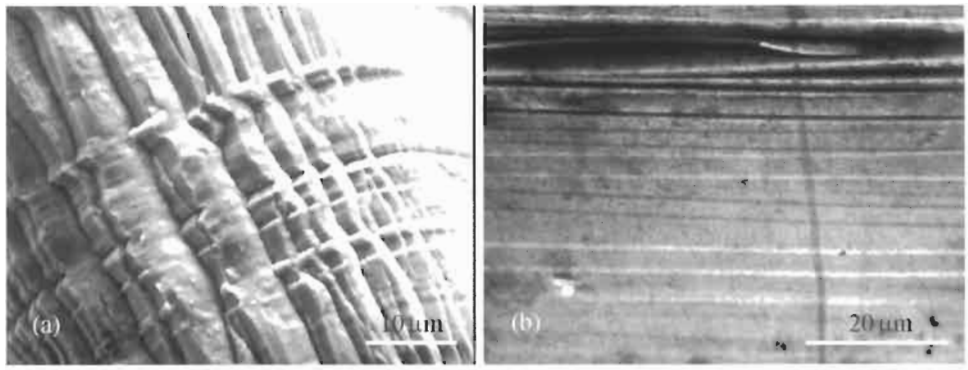

Fig. 46. (a) Shear bands in an almost completely back bent ribbon of $Cu_{50}Zr_{50}$. (b) Same as (a) for a $Co_{70}Fe_5Si_{15}B_{10}$ ribbon about 0.5 mm below the bend.

(1975) demonstrated that some of these bands can reversibly operate when the bending of a previously folded ribbon is reversed. This enormous local shear and the reversibility indicate the total absence of any strain hardening. With the exception of persistent slip bands which appear only in fatigued metals, this simply could not happen in crystalline metals. This point is further confirmed by the absence of necking in uniaxial tension. Here failure occurs simultaneously when yielding starts. Necking can only be observed at higher temperatures when homogeneous flow becomes dominant.

Shear bands once initiated are zones of disturbed structural and chemical short-range order. They are sites of preferred chemical attack (Donovan and Stobbs, 1981) and, as already mentioned, sites of further plastic flow. Annealing at temperatures close to the glass transition restores these zones. The sensibility to preferred etching is eliminated and a new set of shear bands appears when deformation is repeated. Because as-produced metallic glasses are thermodynamically unstable with respect to glassy states of lower free enthalpy, such treatments also give rise to irreversible structural relaxations in the non-deformed regions, and this usually makes metallic glasses very brittle. The procedure of deformation and annealing can thus not be repeated indefinitely as would be the case in crystalline metals.

When the stress is increased above the ultimate tensile strength, which at room temperature can practically not be distinguished from the yield point, fracture typically occurs in the dominant shear band. The fracture surfaces in metallic glasses are unique. They are neither comparable to crystalline metals nor to inorganic glasses. In uniaxial traction the fracture surface is usually plane and occurs at an angle of 45° or slightly more with respect to the wide ribbon surface (oblique to the thickness vector). This plane is well known to be the plane of maximum shear stress and consequently failure is initiated by the shear instability. This type of fracture always occurs without any visible neck. This changes only at higher temperatures when the critical stress for homogeneous flow falls below the critical shear stress. In this case necking prior to fracture sets in and may become even very strong at temperatures near the glass transition. In samples of the usual ribbon form (width >> thickness) the fracture surface remains plane, but takes now an orientation oblique to the width direction and parallel to the thickness vector

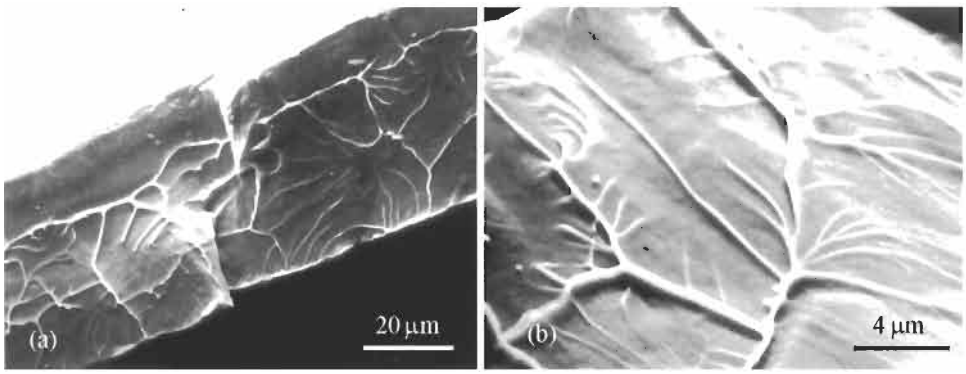

Fig. 47. Tensile fracture surfaces showing the typical vein structure in amorphous metals: (a) $Cu_{50}Zr_{50}$; (b) $Co_{70}Fe_5Si_{15}B_{10}$.

(Pampillo, 1975; Davies, 1978; Megusar et al., 1979). This orientation is explained by the plastic instability in thin sheets. Due to the geometrical constraints, thinning in the width direction is suppressed and necking is expected to follow a direction in which the deviatoric stress resulting from traction does not produce a plastic elongation. This direction is ideally oriented at an angle of 54.7° to the width direction. Strong necking is only visible at the highest temperatures. At lower temperatures the flow rate falls rapidly below the imposed strain rate and the shear instability immediately takes over on the plane defined by necking. Experimentally, fracture surfaces that form angles of 50 to 54° with the width direction and parallel to the thickness vector are observed.

Independent of whether the sample fails in the low- or high-temperature mode fracture surfaces reveal that shearing only starts the fracture by reducing the section. The final rupture then occurs in the tearing mode and usually follows the shear band initially produced. Fig. 47a shows a typical fracture surface that resulted from the shear instability (oblique to the thickness vector). The structureless part indicates the amount of initial shearing (upper part of the fracture surface in Fig. 47a). It should be noted here that in as-produced ribbons with unpolished edges and surface defects, fracture may initiate at these existing defects. In this case the fracture surface is often rather irregular but veins are still formed (Fig. 47b). As mentioned in the section above entitled 'Melt-Spinning Defects', ribbons of metallic glasses have a pronounced notch sensitivity.

Independent of the fracture mode, rupture surfaces are always patched with branching lines which were termed veins (Leamy et al., 1972). Kulawansa et al. (1993) and Watanabe et al. (1994) studied fracture surfaces in a scanning tunneling microscope (STM) and found these veins to have a triangular cross-section of about 100 nm height and width. They resemble closely the lines that one obtains when two plates with a layer of grease in between are separated. From this analogy one might immediately conclude that adiabatic heating due to the intense shearing, which precedes fracture, raises the temperature up to the temperature of the glass transition. At this temperature the viscosity drastically drops to values that might explain these lines. However, subsequent estimates of the adiabatic heating can explain but a temperature rise of a few degrees

(Megusar et al., 1979). More recently, Flores and Dauskardt (1999) measured this temperature rise by infrared imaging techniques in a Zr–Ti–Ni–Cu–Be bulk amorphous alloy and observed a maximum temperature increase relative to ambient of 22.5°C at the crack tip. This is somewhat smaller, but still of the same magnitude as the prediction of about 55°C by their theoretical models. Alternatively, it was suggested (Spaepen, 1975, 1977; Steif et al., 1982) that the intense shearing and the negative hydrostatic pressure produces a dilation of the structure (by production of free volume) which also would decrease the viscosity in the shear bands. Pampillo (1975) and Davies (1978) point out that after the appearance of a strong shear offset, giving rise to the smooth part of the fracture surface, cracks nucleate at different weak spots and propagate. In fact there are many examples where tributary veins, starting from a larger ring-shaped vein, point to spots where cracks probably initiated (see right side of fracture surface Fig. 47a). Veins are then formed by internal necking along lines where two crack fronts meet. The observation of small slip bands along the length of veins in the STM by Kulawansa et al. (1993) provides direct evidence for this deformation.

However, in order to explain the occurrence of veins that point towards a center the crack has to assume rather quickly a star-like form with spikes that move outwards. In fact Li (1978) proposed arguments that can explain the observed vein structures. In his picture, slip in metallic glasses arises from the displacement of generalized dislocations (see also Gilman, 1972; Pampillo, 1975; Davies, 1978). Fig. 48a shows several slip offsets that terminate on the surface. The line pointing to the interior that starts from such a terminal point and separates the slipped from the unslipped area is by definition a dislocation. Such a line is of course not a dislocation in the usual sense. In an amorphous structure there is no constant Burgers vector and also the amount of slip may vary on the slipped area. But these are clearly only points of secondary importance. A dislocation can equally well be characterized by its stress field and, as metallic glasses are perfectly elastic solids, there is no reason why a stress field similar to a dislocation in a crystalline lattice should not exist in an amorphous solid. According to Li this dislocation moves by slip nucleation ahead and behind of it. The shear stress there, which determines

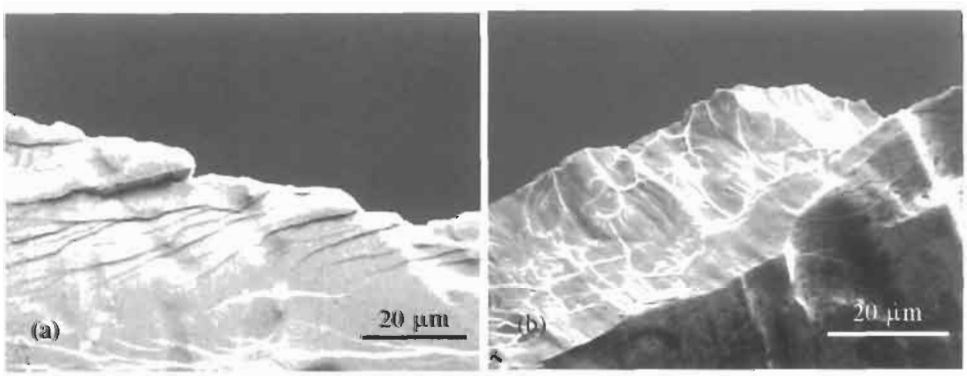

Fig. 48. (a) Shear bands on the wide ribbon surface branching out from the fracture surface. Same ribbon as in Fig. 47a. (b) Irregular fracture surface that started from an edge defect. The initial structure less slip mark along the band width is missing. Same ribbon as in Fig. 47b.

the nucleation rate and therefore the velocity, is the sum of the applied stress and the internal stress from the dislocation. Comparing the total shear stress components ahead of positively and negatively curved dislocations shows that this stress is smaller when the dislocation bows out and larger when it bows in. Consequently, an oscillatory dislocation line will straighten during their displacement. This explains the straight vein that marks the end of the slipped region. The remaining part of the fracture surface occurred in the tensile mode and its structure results from opening of cracks driven by the negative hydrostatic pressure. Tensile crack propagation is faster in the presence of vacancy like defects (free volume). Such defects are supposed to be numerous in the slip band initially produced. In addition to this, the hydrostatic stress gradient ahead of the crack front can transfer free volume towards the crack front and thus further accelerate its propagation. Since the stress gradient is larger for smaller positive curvature of the crack front, the propagation of the front is unstable. Bowing out parts move faster than inward-bowed ones. An alternative model to explain the vein structure has been proposed by Spaepen (1975). He assumes that the viscosity in the shear band drops to values that allow a liquid-like flow.

Fatigue of Metallic Glasses

Only a limited amount of experimental work on fatigue of metallic glasses has been reported in the literature and only few general conclusions can be drawn. Ogura et al. (1975), Davies (1976), Frommeyer and Seifert (1981) and Chaki and Li (1984) studied thin ribbons made of Pd, Fe, Co and Ni based alloys in the tension–tension loading mode. Doi et al. (1981) and Hagiwara et al. (1985) measured wires and ribbons in the bending mode. Gilbert et al. (1998) studied fatigue and crack propagation in a bulk amorphous alloy of the composition $Zr_{41.2}Ti_{13.8}Cu_{12.5}Ni_{10}Be_{22.5}$. Bulk amorphous alloys can only be produced with alloys having an extremely slow crystallization kinetics. Only very few alloys of rather complex composition are known to have this property and remain amorphous with cooling rates as low as 10 K s^{-1}.

Fig. 49 shows some fatigue life curves for amorphous metals. The curves $Fe_{75}Si_{10}B_{15}$ 16×150, $Fe_{80}B_{20}$ and $Pd_{80}Si_{20}$ have been measured in the tension–tension loading mode with $\sigma_{min}/\sigma_{max} \approx 0$. The others have been measured in the bending mode with imposed surface strain. In order to represent these on the same stress scale this strain has been multiplied by their Young modulus. The bulk amorphous alloy has also been measured in the bending mode but with imposed bending stress. Table 7 gives further details of the samples and test procedure used and summarizes other results not shown in Fig. 49. All curves have in common a fatigue endurance limit that is attained between 10^5 and 10^6 cycles. The endurance limit appears to vary more strongly with the form of the sample, or probably also with details of the test procedure and the production method, than with the chemical composition. The three $Fe_{75}Si_{10}B_{15}$ alloys (see Table 7) have very different endurance limits.

When fatigue failure was studied in more detail all authors agree that the critical crack initiates at the surface and rapidly propagates on a plane perpendicular to the stress direction until final fracture occurs. Frommeyer and Seifert (1981) give further details on this critical point in fatigue life. They observed fine shear band offsets at the

Table 7. Fatigue endurance limits for various amorphous and crystalline steel filaments [a]

Composition	Sample size (μm)	UTS (GPa)	Endurance stress (MPa)	Endurance bend. strain (%)	Mode and test frequency (Hz)	Reference
$Fe_{77.5}P_{12.5}C_{10}$	Ø 120	2.87	(262)	0.30	bb, 3.2	Hagiwara et al. (1985)
$Fe_{75}Si_{10}B_{15}$	Ø 120	3.40	(483)	0.32	bb, 3.2	Hagiwara et al. (1985)
$Fe_{75}Si_{10}B_{15}$	~25 × 1500	–	(272)	0.18	br, 1.0	Doi et al. (1981)
$Fe_{75}Si_{10}B_{15}$	16 × 150	3.20	650	–	tt, 30	Baltzer and Künzi (1987)
$Fe_{69}Cr_{11}Si_{10}B_{15}$	40 × 2000	–	(~1950)	1.31	bb, 3.2	Hagiwara et al. (1985)
$Fe_{80}B_{20}$	35 × 900	3.45	150	–	tt, 5	Frommeyer and Seifert (1981)
$Pd_{80}Si_{20}$	~25 × 600	1.34	441	–	tt	Ogura et al. (1975)
ZrTiCuNiBe	bulk 3 × 3 (mm^2)	1.90	~60	–	bb, 25	Gilbert et al. (1998)
Piano wire	Ø 120	3.02	(706)	0.39	bb, 3.2	Hagiwara et al. (1985)
SUS304	Ø 120	0.72	(554)	0.42	bb, 3.2	Hagiwara et al. (1985)
SUS304	30 × 1000	–	(238)	0.18	br, 1.0	Doi et al. (1981)

The test modes are: bb, bending–bending (same direction); br, bending and reversed bending; tt, tension–tension with $\sigma_{min}/\sigma_{max} \approx 0$. Endurance stresses given in parentheses were calculated from the measured endurance bending strain (= max. strain at the surface). Piano wire (cryst.) has the composition Fe–0.8 wt% C and the bulk amorphous metal $Zr_{41.2}Ti_{13.8}Cu_{12.5}Ni_{10}Be_{22.5}$. SUS304 is a standard Cr/Ni stainless steel.

[a] For all materials these limits are attained after 10^5 to 10^6 cycles.

[b] Ultimate tensile strength.

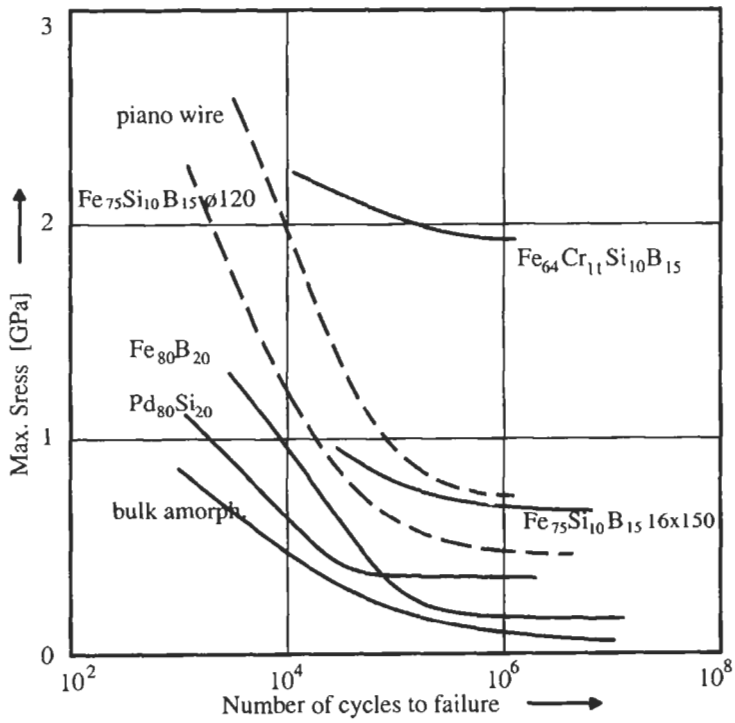

Fig. 49. Fatigue life curves for some filaments of glassy metals. Full curves indicate ribbons and broken curves indicate wires. For further details and references see Table 7. The curves for the wires and the FeCr alloy have been measured in the bending mode with imposed surface strain. In order to represent these on the same stress scale this strain has been multiplied by their Young modulus. The bulk amorphous alloy has also been measured in the bending mode but with imposed bending stress.

surface that were located near production defects (e.g. air inclusions on the wheel side). These fine shear bands always started from the edge of the ribbon and formed an acute angle between 25° and 45° with the edge side of the ribbon. Initiation of the critical crack occurred in this region. The crack then propagates perpendicular to the tensile direction with shear bands growing from the crack tip into the plastic zone of the crack. These shear bands do not appear to cross the entire sample and some of them cross each other. The fracture surface shows a fine-grained, staircase-like structure that probably results from the crossing shear bands. This structure becomes coarser when the crack moves towards the limit where final fracture sets in. The latter produces a vein structure as is characteristic in tensile rupture.

From the observations of Ogura et al. (1975), Frommeyer and Seifert (1981), Chaki and Li (1984) and Gilbert et al. (1998) the crack growth behavior of amorphous metals is similar to crystalline metals. It passes through the threshold, the Paris and the fast fracture regime. Paris exponents between 2 and 6 have been observed.

Further interesting observations, that concern the effect of corrosion during fatigue, have been made by Hagiwara et al. (1985). The fatigue strain endurance limit for

the $Fe_{75}Si_{10}B_{15}$ wire, which is attained near 10^6 cycles, increases from 0.25% to 1% when the relative air humidity decreases from 85% to 35%. This shows once again that fatigue often depends strongly on the chemical composition of the environment. They supposed that the premature failure was caused by hydrogen that was dissociated from the moisture and diffused into the wire. Hydrogen is known to provoke a severe embrittlement also in amorphous metals. Subsequent measurement of wires where, in order to improve the corrosion resistance, Fe was partially substituted with Cr gave a substantial increase in the endurance limit. For the $Fe_{64}Cr_{11}Si_{10}B_{15}$ ribbon the fatigue limit at 65% R.H. is 1.31% bending strain, that is about 4 times higher than for the Cr-free wire and 3.3 higher than the crystalline piano wire. Multiplication of this strain with the known elastic modulus for the Cr-free alloy (150 GPa) gives a stress endurance limit of almost 2 GPa as shown in Fig. 49.

ACKNOWLEDGEMENTS

I would like to thank my colleagues and former collaborators Karin Busch-Lauper, Karlheinz Hausmann, Richard Hofbeck, Nicklaus Baltzer, Moshe Judelewicz and Erwin Török who through their work greatly contributed to this review. I also express my profound gratitude to Prof. Berhard Ilschner who accompanied these studies with enthusiasm and interest as well as to Chris San Marchi whose critical discussions and remarks during the preparation of this review were very helpful. Financial support from Swiss National Science Foundation who supported several projects in this field as well as the grant offered by Degussa (Germany) are gratefully acknowledged.

REFERENCES

Anderson, E., Law, D., King, W. and Spreadborough, J. (1968) *Trans. Metall. Soc. AIME*, 242: 115–119.
Armstrong, R., Codd, I., Douthwaite, R.M. and Petch, N.J. (1962) *Philos. Mag.*, 7: 45.
Avitzur, B. (1980) *Metal Forming*. Dekker, New York.
Baltzer, N. and Künzi, H.U. (1987) (unpublished).
Brenner, S.S. (1956a) *Acta Metall.*, 4: 62–74.
Brenner, S.S. (1956b) *J. Appl. Phys.*, 27: 1484–1491.
Brenner, S.S. (1958a) *Science*, 128: 569–575.
Brenner, S.S. (1958b) In: *Growth and Perfection of Crystals*, pp. 157–190, R.H. Doremus, B.W. Roberts and D. Turnbull (Eds.). Proc. Int. Conf. Crystal Growth, Cooperstone, New York.
Busch-Lauper, K. (1988) Restauration, recristallisation et textures de files minces en Au et Cu, Thèse No. 736, Ecole Polytechnique Fédérale de Lausanne.
Catalogue of Drawing Defects. DGM-Informationsgesellschaft mbH, Oberursel.
Chaki, T.M. and Li, J.C.M. (1984) *Scr. Metall.*, 18: 703–708.
Chokshi, A.H., Rosen, A., Karch, J. and Gleiter, H. (1989) *Scr. Metall.*, 23: 1679–1684.
Courtney, T.H. (1990) *Mechanical Behavior of Materials*. McGraw-Hill, New York.
Davies, L.A. (1976) *J. Mater. Sci.*, 11: 711–717.
Davies, L.A. (1978) Strength, ductility and toughness. In: *Metallic Glasses*, American Society for Metals, Metals Park, OH.
Doi, M., Sugiyama, K., Tono, T. and Imura, T. (1981) *Jpn. J. Appl. Phys.*, 20: 1593–1594.
Donovan, P.E. and Stobbs, W.M. (1981) *Acta Metall.*, 29: 1491–1536.

Flores, K.M. and Dauskardt, R.H. (1999) *J. Mater. Res.*, 14: 638–643.
Forrest, P.G. (1966) *Fatigue of Metals*. Pergamon, Oxford.
Frommeyer, G. and Seifert, K. (1981) *Z. Metallkd.*, 72: 391–396.
Geminov, V. and Kopyev, I. (1979) *Fatigue Eng. Mater. Struct.*, 1: 329–331.
Gibeling, J.C. and Nix, W.D. (1978) *Scr. Metall.*, 12: 919–926.
Gilbert, C.J., Lippmann, J.M. and Ritchie, R.O. (1998) *Scr. Mater.*, 38: 537–542.
Gilman, J.J. (1972) *J. Appl. Phys.*, 44: 675–679.
Grewen, J. (1970) *Z. Metallkd.*, 61: 252–260.
Hagiwara, M., Inoue, A. and Masumoto, T. (1982a) *Metall. Trans. AIME*, 13A: 373–382.
Hagiwara, M., Inoue, A. and Masumoto, T. (1982b) *Mater. Sci. Eng.*, 54: 197–207.
Hagiwara, M., Inoue, A. and Masumoto, T. (1985) In: *Proc. 5th Int. Conf. Rapidly Quenched Metals*, Vol. 2, pp. 1779–1782, S. Steeb and H. Warlimont (Eds.). North-Holland, Amsterdam.
Hansen, N. and Ralph, B. (1982) *Acta Metall.*, 30: 411–417.
Hausmann, K.H. (1987) Kurzzeitrekristallisation und mechanische Eigenschaften von Feinstdrähten aus Gold und Kupfer, Thèse Nr. 702, Ecole Polytechnique Fédérale de Lausanne.
Hausmann, K.H., Ilschner, B. and Künzi, H.U. (1986) In: *Proc. Int. Conf. Interconnection Technology in Electronics*, Fellbach, pp. 69–72, Deutscher Verlag für Schweisstechnik (DVS), Düsseldorf.
Hofbeck, R., Hausmann, K., Ilschner, B. and Künzi, H.U. (1986) *Scr. Metall.*, 20: 1601–1605.
Hong, S. and Weil, R. (1996) *Thin Solid Films*, 283: 175–181.
Jin, N.Y. and Winter, A.T. (1984) *Acta Metall.*, 32: 989–995.
Judelewicz, M.P. (1993) Etude des propriétés des feuilles minces, Thèse 1117, Ecole Polytechnique Fédérale de Lausanne.
Judelewicz, M.P., Künzi, H.U., Merk, N. and Ilschner, B. (1994) *Mater. Sci. Eng.*, A186: 135–142.
Kim, I. and Weil, R. (1987) In: *Testing of Metallic and Inorganic Coatings*, ASTM STP 947, pp. 11–18, W.B. Harding and G.A. Bari (Eds.). ASTM, Philadelphia, PA.
Kim, I. and Weil, R. (1989) *Thin Solid Films*, 169: 35–42.
Kim, G.H., Brown, I.B. and Fine, M.E. (1991) *Mater. Sci. Eng.*, 142: 177.
Kimura, H., Murata, T. and Masumoto, T. (1977) *Sci. Rep. RITU, A*, 26: 270–282.
Krönert, W. and Raith, A. (1989) *Mater.-Wiss. Werkstofftechn.*, 20: 142–148.
Kulawansa, D.M., Dickinson, J.T., Langford, S.C. and Watanabe, Y. (1993) *J. Mater. Res.*, 8: 2543–2553.
Künzi, H.U. (1983) Mechanical properties of metallic glasses. In: *Glassy Metals II*, pp. 167–216, H. Beck and H.-J. Güntherodt (Eds.). Topics in Applied Physics, Vol. 53, Springer, Berlin.
Kuo, V.W.C. and Starke, E.A. (1985) *Metall. Trans.*, A16: 1089–1103.
Laird, C., Charsley, P. and Mughrabi, H. (1986) *Mater. Sci. Eng.*, 81: 433–450.
Lançon, F., L. Billard and A. Chamberod (1985) In: *Proc. 5th Int. Conf. Rapidly Quenched Metals*, Würzburg, pp. 1337–1340. North-Holland, Amsterdam.
Leamy, H.J., Chen, H.S. and Wang, T.T. (1972) *Metall. Trans.*, 3: 669.
Lee, D.N. (1995) *Scr. Metall. Mater.*, 32: 1689.
Leslie, W.C., Plecity, F.J. and Michalak, J.T. (1961) *Trans. Metall. Soc. AIME*, 221: 691–700.
Li, J.C.M. (1978) *Micromechanisms of Deformation and Fracture*. In: *Metallic Glasses*, American Society for Metals, Metals Park, OH.
Masumoto, T. and Maddin, R. (1971) *Acta Metall.*, 19: 725.
Masumoto, T., Inoue, A., Hagiwara, M., Ohnaka, I. and Fukusako, T. (1981a) In: *Proc. 4th Int. Conf. Rapidly Quenched Metals*, Sendai, pp. 47–51.
Masumoto, T., Ohnaka, I., Inoue, A. and Hagiwara, M. (1981b) *Scr. Metall.*, 15: 293–296.
Matthys, E.F. (Ed.) (1992) *Melt-Spinning and Strip Casting: Proceedings of the Melt-Spinning and Strip Casting Symposium*, San Diego, CA. The Minerals, Metals and Materials Society, Warrendale, PA.
Megusar, J., Argon, A.S. and Grant, N.J. (1978) *Proceedings of the 3rd International Conference on Rapidly Quenched Metals*, Metals Society, Brighton.
Megusar, J., Argon, A.S. and Grant, N.J. (1979) *Mater. Sci. Eng.*, 38: 63–72.
Merchant, H.D., Minor, M.G. and Liu, Y.L. (1999) *J. Electron. Mater.*, 28: 998–1006.
Mielnik, E.M. (1991) *Metalworking Science and Engineering*. McGraw-Hill, New York.
Miyazaki, S., Shibata, K. and Fujita, H. (1979) *Acta Metall.*, 27: 855–862.

Mughrabi, H. (1985) In: *Proc. Conf. Dislocations and Properties of Real Materials*, pp. 244–262, Publ. 323, Institute of Metals, London.
Murphy, S. and Ball, C.J. (1972) *J. Inst. Met.*, 100: 225–232.
Murr, L.E. and Flores, R.D. (1998) *Scr. Mater.*, 39: 527–532.
Murr, L.E., Niou, C.-S., Farraro, J.T. and Liu, G. (1997) *Mater. Res. Innovat.*, 1: 26–37.
Neuhäuser, H. and Stössel, R.-P. (1985) In: *Proc. 5th Int. Conf. Rapidly Quenched Metals*, Würzburg 1984, pp. 1349–1352, North-Holland, Amsterdam.
Nixdorf, J. (1967) *Draht-Welt Düsseldorf*, 53: 696–701.
Nixdorf, J. (1968) *Ber. Dtsch. Keram. Ges.*, 45: 141–148.
Nixdorf, J. (1970) *Proc. R. Soc. London*, 319: 17–32.
Ogura, T., Masumoto, T. and Fukushima, K. (1975) *Scr. Metall.*, 9: 109–114.
Pampillo, C.A. (1975) *J. Mater. Sci.*, 10: 1194–1227.
Patterson, J.P. and Jones, D.R.H. (1980) *Acta Metall.*, 28: 675–681.
Pell-Walpole, W.T. (1943) *J. Inst. Met.*, 69: 131–146.
Perez, J., Fouquet, F. and He, Y. (1982) *Phys. Status Solidi*, 72: 289–300.
Read, D.T. (1998a) *Int. J. Fatigue*, 20: 203–209.
Read, D.T. (1998b) *ASTM J. Testing Eval.*, 26: 255–259.
Read, D.T. and Dally, J.W. (1995) *J. Electron. Packag.*, 117: 1–6.
Rieger, S. (1974) *Einfluss von Fasertexturen auf das Verformungsverhalten von Cu und Cu–Zn Legierungen*, Dissertation, Universität Karlsruhe.
Russew, K., de Hey, P., Sietsma, J. and van den Beukel, A. (1997) *Acta Mater.*, 45: 2129–2137.
Sanders, P.G., Eastman, J.A. and Weertman, J.R. (1997) *Acta Mater.*, 45: 4019–4025.
Schade, P. (1998) *Int. J. Refract. Met. Hard Mater.*, 16: 77–87.
Schladitz, H.J. (1968) *Z. Metallkd.*, 59: 18–22.
Schladitz, H.J. (1976) *Forschungsbericht T 76-18*, Bundesministerium für Forschung und Technologie, München.
Scheucher, E. (1969a) *Z. Metallkd.*, 60: 422.
Scheucher, E. (1969b) *Z. Metallkd.*, 60: 808–812.
Sethi, V.K., Gibala, R. and Heuer, A.H. (1978) *Scr. Metall.*, 12: 207.
Shin, H.-J., Jeong, H.-T. and Lee, D.N. (2000) *Mater. Sci. Eng.*, A279: 244–253.
Spaepen, F. (1975) *Acta Metall.*, 23: 615–620.
Spaepen, F. (1977) *Acta Metall.*, 25: 407–415.
Steif, P.S., Spaepen, F. and Hutchison, J.W. (1982) *Acta Metall.*, 30: 447–455.
Suresh, S. (1994) *Fatigue of Materials*. Cambridge Solid State Science Series, pp. 30–56, Cambridge University Press, Reprinted 1994.
Tanaka, S., Ichikawa, M. and Akita, S. (1980) *Int. J. Fatigue*, October, 159–163.
Taub, A.I. (1980) *Acta Metall.*, 28: 633–637.
Thompson, A.W. and Backofen, W.A. (1971) *Acta Metall.*, 19: 597–606.
Watanabe, Y., Nakamura, Y., Dickinson, J.T., Kulawansa, D.M. and Langford, S.C. (1994) *Mater. Sci. Eng.*, A176: 411–415.
Weaire, D., Ashby, M.F., Logan, J. and Weins, M.J. (1971) *Acta Metall.*, 19: 779–788.

Fiber Fracture
M. Elices and J. Llorca (Editors)

FRACTURE OF SUPERFINE METALLIC WIRES

K. Yoshida

Department of Precision Mechanics, School of Engineering, Tokai University, 1117 Kitakaname, Hiratsuka, Kanagawa 259-1292, Japan

Introduction 243
Present Condition of Production of Superfine Wires 244
Minimum Diameter of Wires in Products 244
Product Price and Quality Required for Superfine Wires 245
Background of Research on Wire Breakage and Internal Fracture 245
Dynamic Study on Internal Fracture and Wire Breakage 246
Classification of Wire Breakage 247
FEA of Wire Breakage in Superfine Wiredrawing with Inclusion 248
Analysis Method 248
Deformation Behavior with Inclusions 249
Increase in the Drawing Stress Due to Inclusions 251
Size of Inclusions at the Time of Occurrence of Wire Breaks 252
Simulation in Which Peeling at the Inclusion/Matrix Boundary is Considered 253
Filament Breakage during Composite Wiredrawing 254
AE Detection of Filament Breaks and Internal Fracture 254
Drawing of Cu–NbTi Superconducting Wire 256
Conclusions 260
Acknowledgements 261
References 261

Abstract

The wire breaks and internal defects that occur during the drawing of superfine wires were analyzed. The cause of defects in the wire has been treated from both plastodynamic and metallurgical points of view. Wire breakage during the drawing process of fine wires are often induced by inclusions in the wire material. It was clarified, by finite

element simulation of the drawing of superfine wires with an inclusion, that as a large inclusion passes through a die, drawing stress rapidly increases, inducing wire breakage. It was estimated that inclusions with a D_i/D_o ratio of 0.4 or higher increase the likelihood of wire breakage. In the production technology of a metal superconducting multifilament wire, internal fracture and filament breaks are fatal to the wire quality. The detection of wire defects is extremely difficult, since most of the defects exist inside the wire and cannot be detected by surface observation. These defects were detected during the drawing process through acoustic emission (AE) measurement, and the applicability of this method was also investigated.

Keywords

Fracture; Wiredrawing; Internal fracture; Wire breakage; FEA; Superconducting wire; Acoustic emission; Filament breaks

INTRODUCTION

Wiredrawing has a long history. In the past, wiredrawing, which was a significant processing technique, was kept secret; consequently, there are few reports giving detailed explanations of the technique. At present, the Deutsches Museum in Munich exhibits dies and pictures which illustrate the wiredrawing operation since the 15th century (Fig. 1) as well as Japanese pictures which illustrate the wiredrawing operation (Fig. 2; Nakamura and Wada, 1980), providing us some information on the wiredrawing environment. Wiredrawing has shifted from being powered by man, to oxen or horses, waterwheels and finally electric motors, resulting in great strides in productivity.

Recently, the application of the wiredrawing technique for superfine wires has predominantly been in the fields of precision equipment, semiconductors and printing machines. This is because new products with enhanced functions, including light, thin, short and small wearable equipment, have been developed at the request of wire users, and wire suppliers are reaping the benefits of an expanded market and increased value of their wires. However, various problems, such as the extremely high manufacturing cost of superfine wires, remain unsolved. Until now, the techniques and knowledge in this field have been considered to be corporate know-how. Therefore, few papers or reports on the wiredrawing technique have been published.

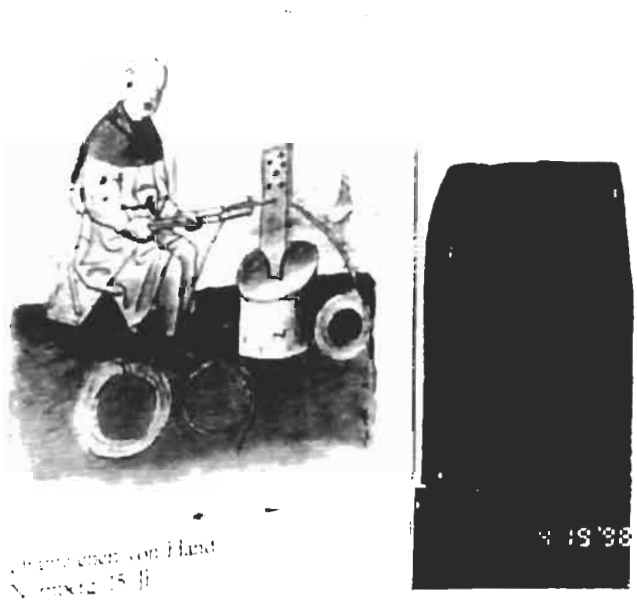

Fig. 1. Wiredrawing operation and an old die in 15th century (Deutsches Museum in Munich).

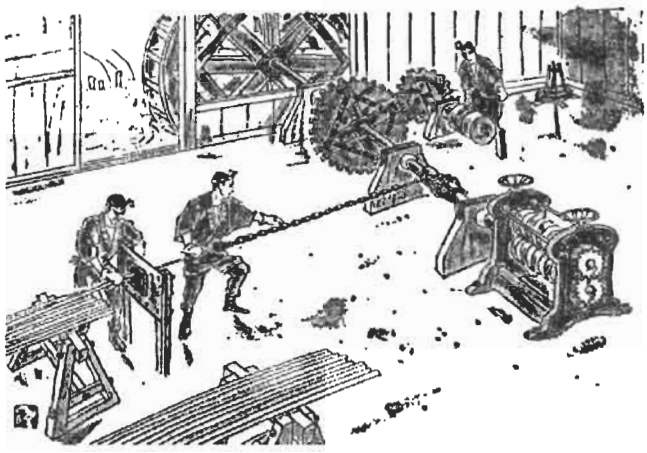

Fig. 2. Wiredrawing operation using a waterwheel in old Japan.

PRESENT CONDITION OF PRODUCTION OF SUPERFINE WIRES

Minimum Diameter of Wires in Products

The author studied the smallest diameter of various wires in commercially available products and wires in the research stage based on questionnaires distributed to approximately 70 major Japanese wiredrawing manufacturers (see Table 1; Yoshida, 2000b). Other than titanium wires, superfine wire products up to around 15 μm in diameter, regardless of whether they are steel or nonferrous wires, are now available on the market. In research, various materials have been thinned into superfine wires of down to 10 μm diameter (Yoshida, 2000a).

Superfine steel wires are used for printing meshes, filters, steel cords, saw wires, wire ropes, precision springs, and precision screws and pins. On the other hand, superfine nonferrous wires are used for semiconductor bonding wires, magnet wires, materials for

Table 1. Minimum diameter and use of superfine wires on the market and in the laboratory in Japan (1998)

Material	Diameter (μm)		Use of the products
	on the market	laboratory	
Special mild steel	−15	−12	Fishing line
Low-carbon steel	−100	–	Screw, pin, bolt
High-carbon steel	150–16	100–10	Steel cord, sawing wire cable, spring
Stainless steel	30–15	20–10	Screen mesh, mesh of filter wire rope
Titanium	100–50	10–5	Mesh of filter, wire rope stiffening wire
Shape-memory alloy	−40	−10	Fishing line, antenna
Amorphous	20–15	30–10	Sensor, stiffening wire
Gold	50–15	−15	Bonding wire
Copper	15–10	15–7	Electronic wire, bonding wire
Aluminum	30–20	−20	Electronic wire, bonding wire

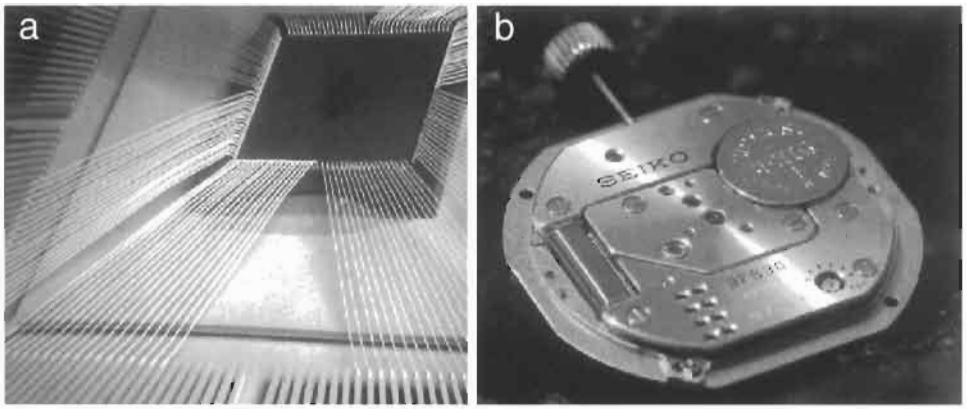

Fig. 3. Use of superfine wire in the fields of precision equipment and semiconductors. Left: bonding wire. Right: magnet wire for wristwatch (courtesy of SEIKO Corp.)

electronic components and electrode wires for electrical-discharge processing (Fig. 3). Recently, the precision of electronic equipment, wearable equipment, micromachines, precision equipment and precision printing machines has been improved significantly, thus the development of superfine wires is greatly anticipated in a wide range of industrial fields.

However, a number of problems exist in the drawing of fine wires, such as the occurrence of wire breaks due to the presence of inclusions during the drawing process, leading to low productivity and high production cost.

Product Price and Quality Required for Superfine Wires

Processing superfine wires requires a large number of passes (drawings) and intermediate softening heat treatments; however, in rare cases, the breakage of wires occurs, resulting in high processing costs. In particular, for wires with diameters of 0.1 mm or less, the product price increases exponentially with the decrease of wire diameter (Yoshida, 2000a).

The quality required for wires may differ depending, to some extent, on their use; however, the following main characteristics are required: (1) high accuracy of dimensions (uniformity of diameter and circularity); (2) good mechanical properties (proof stress, strength, elongation and torsion strength); (3) good electrical properties; (4) lustrous surface of wires without flaws; (5) good rewinding performance (little wire deformation) from a spool.

BACKGROUND OF RESEARCH ON WIRE BREAKAGE AND INTERNAL FRACTURE

There are two methods of manufacturing extrafine wires: one is to use a wire rod as the raw material and repeatedly subject the wire rod to wiredrawing and heat treatment,

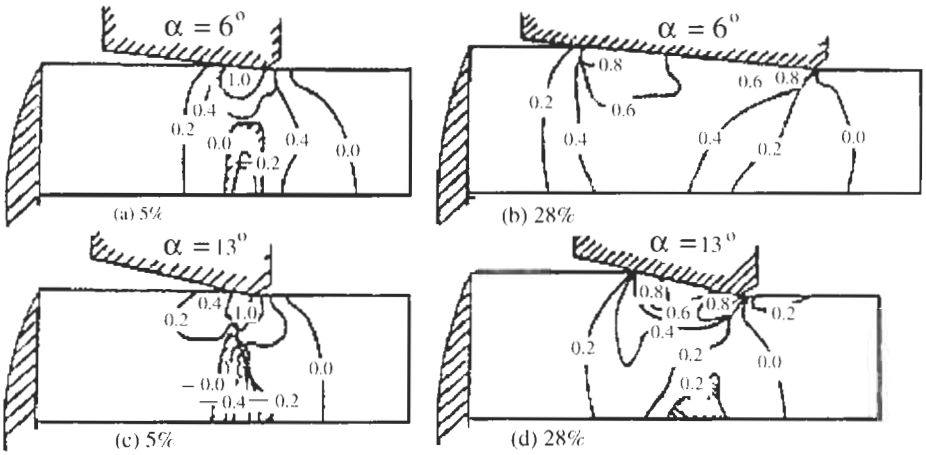

Fig. 4. Distributions of the hydrostatic pressure in wires being drawn. Numerical values refer to the pressure/yield stress.

and the other is to obtain a metallic fiber directly from molten metal. Except for certain materials, most practically used metallic products are manufactured by the former method as it provides favorable wire quality, stability and processing cost.

One of the reasons for the high manufacturing costs of superfine wires is the breakage of wires during processing. The causes of wire breakage have been actively studied for a long time. However, there are few published reports since manufacturers are not willing to take the trouble to make public their know-how or their low technical level.

Dynamic Study on Internal Fracture and Wire Breakage

Many researchers (Jennison, 1930; Remmer, 1930; Tanaka, 1952; Nishioka, 1956; Coffin and Roger, 1967; Avitzur, 1968; Tanaka et al., 1976; Chia and Jackson, 1978; Chen et al., 1979; Tanaka and Yoshida, 1979, 1983; Togashi et al., 1979; Su, 1982; Yoshida, 1982, 2000a,b; Yoshida and Tanaka, 1987; Ikeda et al., 1988; Arashida et al., 1994; Raskin, 1997; Tanimoto, 1998) have investigated optimal wiredrawing conditions with respect to various factors such as die angle, reduction, annealing conditions and selection of lubricants for the defects. Avitzur proposed the conditions under which internal fracture occurs using an energy method (Avitzur, 1968). Coffin and Roger (1967) and Yoshida (1982) studied the occurrence of damage and voids during the drawing using a slip-line field method. Others (Chen et al., 1979; Tanaka and Yoshida, 1979; Yoshida and Tanaka, 1987; Yoshida, 2000a,b) studied the causes of internal cracking and how such cracks grow, using finite-element analysis (FEA) and proposed some processing conditions to prevent defects. Fig. 4 shows the distribution of hydrostatic pressure σ_m/Y for the combinations of die half-angle $\alpha = 6°$, 13° and reduction/pass $R/P = 5\%$, 28%, as determined by FEA. In any of four instances, σ_m/Y is the least at the midpoint of the deforming zone and, except in (b), it is less than zero, i.e., the stress at the midpoint can be tensile, which facilitates the occurrence of internal

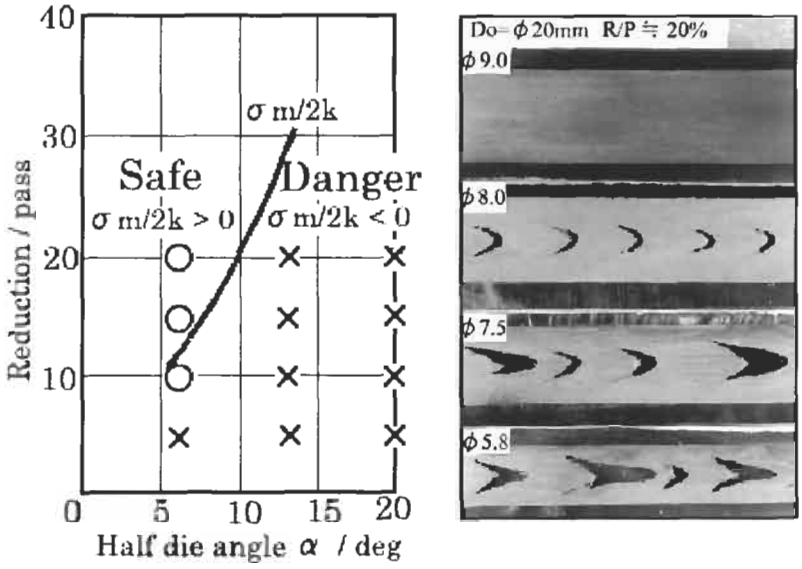

Fig. 5. Safe and danger zones separated by the calculated $\sigma_m/2k = 0$ line and the experimental results plotted in them. Crosses: internal defect. Circles: no defect

fracture to occur. Repeated computations for various α and R/P were carried out and the results have been plotted in Fig. 5. When the combination of and R/P lies in the danger zone, the value of σ_m/Y at the midpoint is negative and internal defects can be expected.

Classification of Wire Breakage

Some researchers (Jennison, 1930; Remmer, 1930; Tanaka, 1952) have reported that the starting points of cracks and wire breaks generated during wiredrawing are at peripheral regions of segregation, the two-phase or inclusions in the castbar. Small cracks grow in size upon repeated passes of the drawing process, finally resulting in wire breakage. Tanaka et al. (1976) and others contributed to the prevention of wire breaks by categorizing the wire-break morphologies during processing. Using these findings and advances in production technologies, the percentage of the occurrence of wire breakage has been substantially reduced by improving the wire quality as much as possible. However, as the diameter of wires decreases, the percentage of wire breaks increases exponentially; accordingly, many problems remain to be solved before safe production of fine wires with diameters of 20 μm or less can be realized.

The most important problem is, reportedly, wire breakage due to inclusions (see Fig. 6). For example, Raskin (1997) reported, based on his survey of 673 wire breaks, that 52% of the breaks are attributable to inclusions, as shown in Fig. 7.

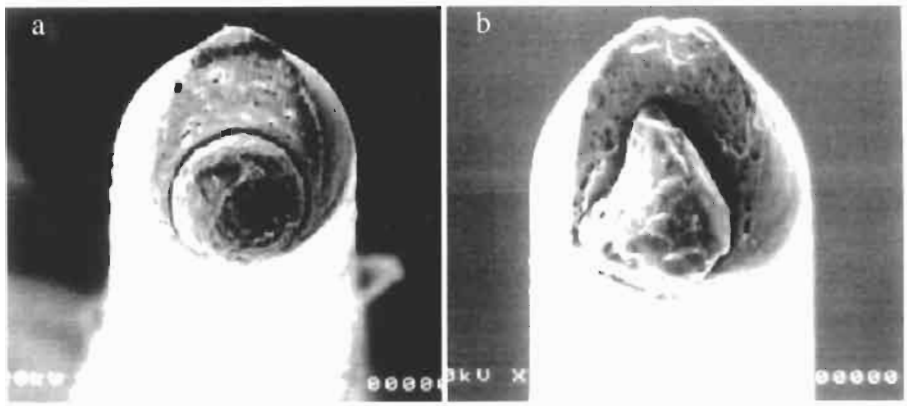

Fig. 6. SEM micrographs of wire breakage due to inclusion. (a) $D_0 = 54$ μm. (b) $D_0 = 60$ μm.

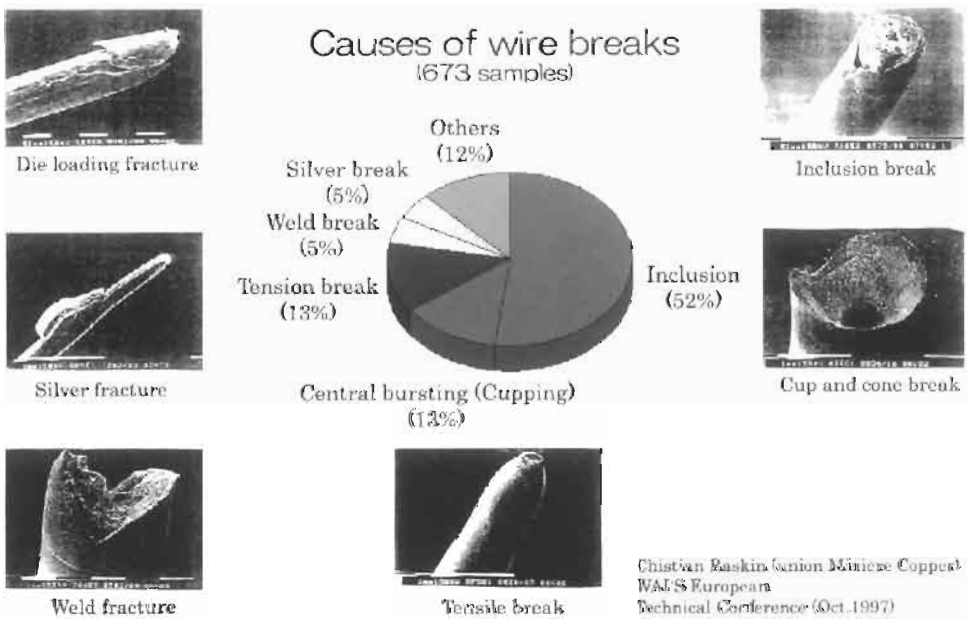

Fig. 7. Causes of wire breakage during copper wiredrawing (Raskin, 1997).

FEA OF WIRE BREAKAGE IN SUPERFINE WIREDRAWING WITH INCLUSION

Analysis Method

A general-purpose finite-element method code (FEM), MARC, was used for the analysis. Fig. 8 shows the analytical model used, where black parts indicate inclusions.

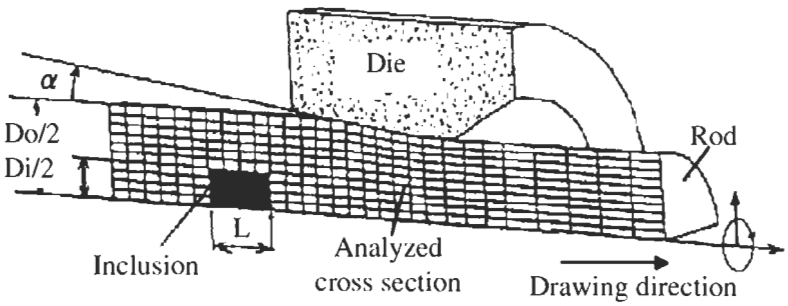

Fig. 8. Model of wiredrawing with an inclusion, in FEM.

Table 2. Material properties and drawing conditions used for FEM

	Copper (wire)	WC (inclusion)
Young's modulus E (MPa)	120,000	1,000,000
Yield stress σ_Y (MPa)	150	1,000
Poisson's ratio ν	0.3	0.22
Die half-angle α (degr.)	6	
Single reduction R_e (%)	20	
Coefficient of friction μ	0.05	

For simple and efficient computation, the inclusion shape was chosen as cylindrical, and the inclusion was positioned at the center of the wire. The author assumed the inclusion to be a sintered hard alloy (WC); Table 2 lists the material properties and drawing conditions used in the analysis. The inclusion length was set to be constant at $L/D_o = 0.25$, and the inclusion size D_i/D_o (where D_i/D_o is the ratio of inclusion diameter to wire diameter) was varied: 0.0, 0.4, 0.6 and 0.8. In the computation, the author assumed that the inclusion and the copper matrix were usually joined at the boundary, and that the materials used were not work-hardened during the process. The die half-angle α, reduction R_e and coefficient of friction μ are in accordance with the operating conditions, which are set within a safe range to guard against the generation of internal cracks.

Deformation Behavior with Inclusions

In a wiredrawing process, a wire is considered to be subjected to steady deformation; however, a copper wire containing hard inclusion matter is subjected to unsteady deformation. Even in the case of small inclusions such as metal powder and dust (coarse particulates), the ratio of inclusion diameter to wire diameter D_i/D_o becomes large for fine wires. Fig. 9 shows the deformation behavior of drawn wires containing inclusions with $D_i/D_o = 0.4$, 0.6 and 0.8, as observed using FEA. Safe conditions which are $\alpha = 6°$, $R/P = 20\%$, and coefficient of friction $\mu = 0.05$ are set. For comparison, a wire devoid of inclusions is also shown. In the figure, it can be seen that the meshes of the

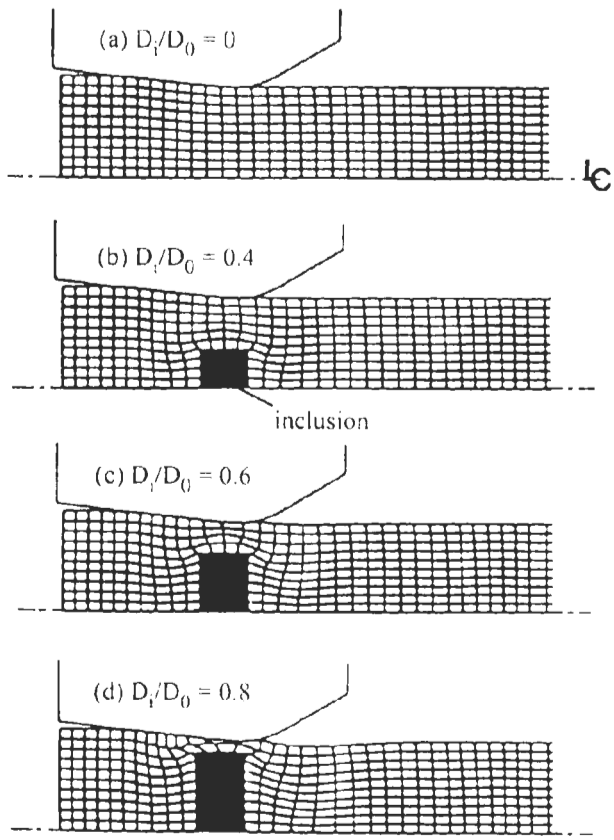

Fig. 9. Deformation of the mesh in drawing wire with no inclusion (a) and with different ratios of inclusion diameter to wire diameter (b–d).

drawn wires containing an inclusion were deformed specifically around the inclusion, and that the inclusion itself was negligibly deformed because of its hardness, resulting in large copper deformation. As the inclusion passes through the die, a large drawing stress acts on the wire; accordingly, necking due to drawing occurs at some parts of the wire.

Fig. 10 shows the hydrostatic pressure distribution for case that inclusions with $D_i/D_0 = 0.4$ and 0.6 pass through the die, under the same drawing conditions as mentioned above. Hydrostatic pressure distribution is frequently used as an index to judge crack generation during plastic working. When the hydrostatic pressure results in high tensile stress, it is believed that a large number of internal fractures are generated. In this study, during the drawing of wires containing inclusions, a tensile stress of 140 MPa or higher was found to act in front of the inclusion. This may lead to the generation of cracks; peeling may also occur at the boundary between the inclusion and the matrix.

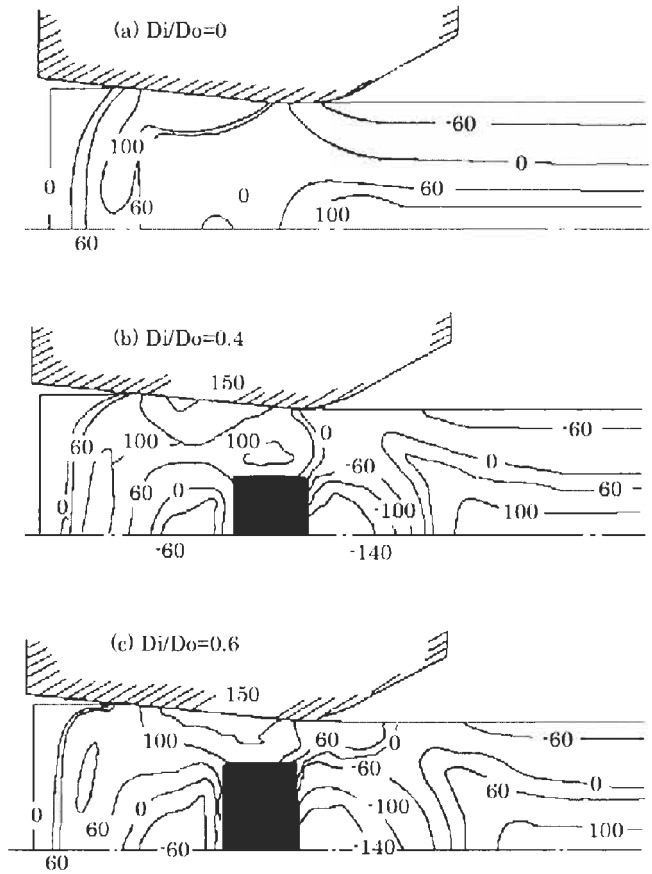

Fig. 10. Distributions of the hydrostatic pressure during wiredrawing with no inclusion (a) and with different ratios of inclusion diameter to wire diameter (b,c).

Increase in the Drawing Stress Due to Inclusions

When the drawing stress during wiredrawing is high, wire breakage occurs easily. Fig. 11 shows drawing stress as an inclusion passes through the die, as determined using FEA. The drawing conditions were identical to those stated above, and the inclusion sizes were assumed to be $D_i/D_o = 0.0$, 0.4, 0.6 and 0.8. When $D_i/D_o = 0.8$, the drawing stress was approximately 2.3 times that in the wire without an inclusion ($D_i/D_o = 0.0$). In addition, in wires which contain inclusions with $D_i/D_o = 0.4$ or 0.6, the drawing stress becomes approximately 1.2 times and 1.6 times larger, respectively, than that in a wire without inclusions. In the drawing of fine wires in particular, the magnitude of this drawing stress greatly affects the occurrence of wire breakage; accordingly, measures to prevent inclusions are required. For example, the use of high-quality elementary wires, operating and processing in a clean room and the use of tools and lubricants which do not generate metal powder should be considered.

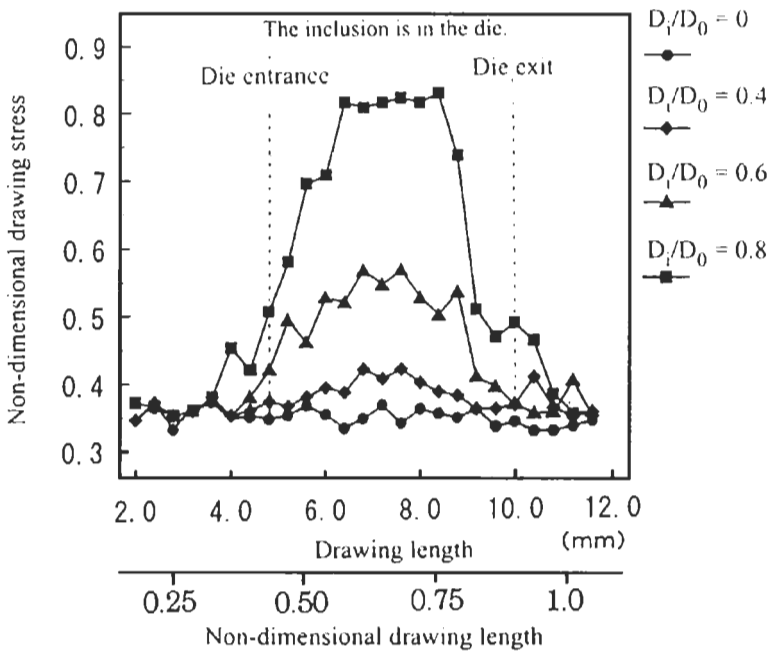

Fig. 11. Drawing stress changes as the inclusion passes through the die.

Size of Inclusions at the Time of Occurrence of Wire Breaks

One report shows the relationship between the occurrence of wire breaks and D_i/D_o (the ratio of mean diameter of inclusion to wire diameter) of samples (see Fig. 12) (Arashida et al., 1994). The results show that in the drawing of wires with a diameter of 50 μm or larger, the frequency of wire breakage increases when inclusions with D_i/D_o of 0.6 or higher are included. However, in the drawing of fine wires with a diameter of 20 μm or less, wire breakage easily occurs even when D_i/D_o is as small as 0.4. In addition, there seems to be no relationship between the inclusion material and the ease with which wire breakage occurs.

During the drawing of wires with inclusions, wire breaks occur as a result of a rapid increase in the drawing stress. The larger the inclusion, the higher the drawing stress, leading to a higher possibility of wire breakage. These FEA results qualitatively agree with operational data. However, it is not sufficient to discuss the effects of the wire diameter on the frequency of occurrence of wire breakage based only on FEA.

Based on the above-mentioned results, the key to preventing wire breaks is the prevention of the incorporation of large inclusions during both the production of wire rods and drawing process. The analytical data and operational data show that in order to reduce the frequency of wire breaks, it is important to prevent inclusions with D_i/D_o of 0.4 or greater.

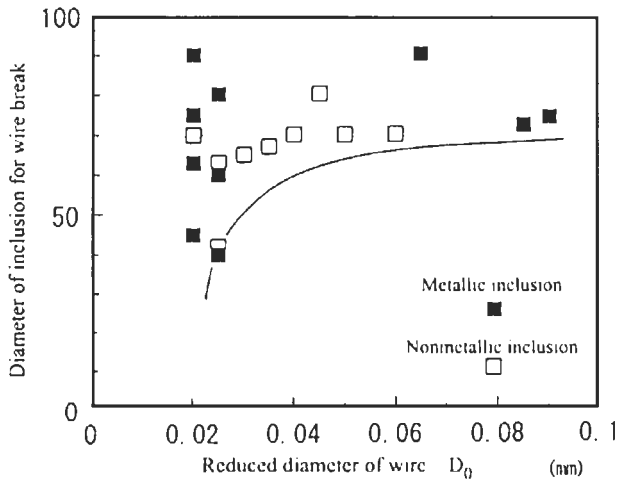

Fig. 12. Relationship between the inclusion diameter for wire breakage and the reduced diameter of a wire.

Simulation in Which Peeling at the Inclusion/Matrix Boundary is Considered

In the above analysis, the inclusion and the base material were completely bonded at their boundary. However, in reality, the inclusion and matrix are often detached at the boundary; therefore, the author performed simulations in consideration of this fact. The inclusion size was set at D_i/D_o of 0.8, and the inclusion length was set to be L/D_o of 0.78.

When an inclusion passes through a die, since tensile stress acts in the drawing direction at the center of the wire, an internal crack occurs at the boundary in front of the inclusion. Fig. 13 shows an example of the formation process of the internal crack, demonstrating the growth of the internal crack with increasing drawing length. Since the

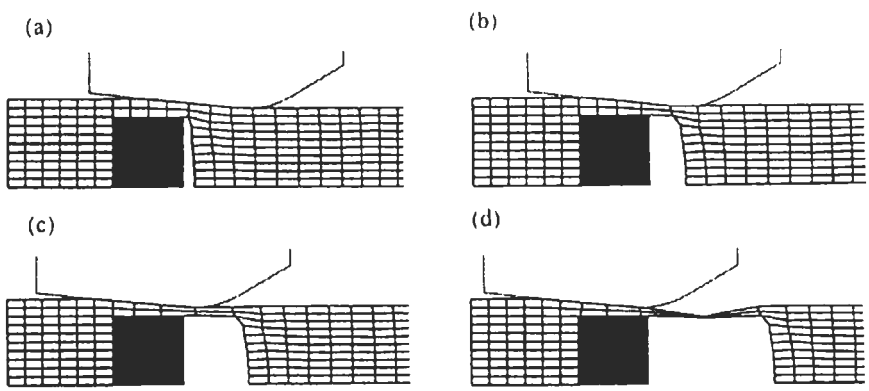

Fig. 13. Internal fracture formation and growth as the drawing length increases during wiredrawing.

drawing stress was high and the wire could not tolerate the stress generated under this condition, the inclusion could not pass through the die and the wire broke.

FILAMENT BREAKAGE DURING COMPOSITE WIREDRAWING

In the fabrication technology of various composite wires, internal fracture and filament breakage of the wire are fatal to the wire quality. The detection of wire defects is extremely difficult, since most of the defects exist inside the wire and cannot be detected by surface observation. In this study, defects of copper-clad nickel wire and composite wires such as Cu–NbTi superconducting wire are detected during the drawing process through acoustic emission (AE) measurement, and also the applicability of these methods is investigated. Table 3 lists the characteristics of the four wires used in this study. Fig. 14 shows the cross-sections of the sample composite wires. Superconducting wires have been used in various fields such as in the medical field for magnetic resonance imaging (MRI), the field of transportation for linear motor cars (Fig. 15) and the electric power field for nuclear fusion. Fig. 16 shows several types of defects in the drawn superconducting wires.

AE Detection of Filament Breaks and Internal Fracture

The block diagram for the detection of internal fracture during wiredrawing in this study is shown in Fig. 17. The key point in the AE method is the elimination of the mechanical and electrical noise signals.

Table 3. Specifications of tested clad and composite wires

No.	Specimens	Diameter (mm)	Filament (core)	Matrix (sleeve)
1	Cu-clad Ni wire	8.0	Nickel	Copper (diam. of core 3.7 mm)
2	Single filament superconducting wire Cu–NbTi	5.1	NbTi	Copper (copper ratio 0.7)
3	Multifilament superconducting wire Cu–NbTi	3.2	NbTi	Copper (copper ratio 3.0)
4	Multifilament superconducting wire Cu–NbTi	3.0	NbTi	Copper (copper ratio 5.0)

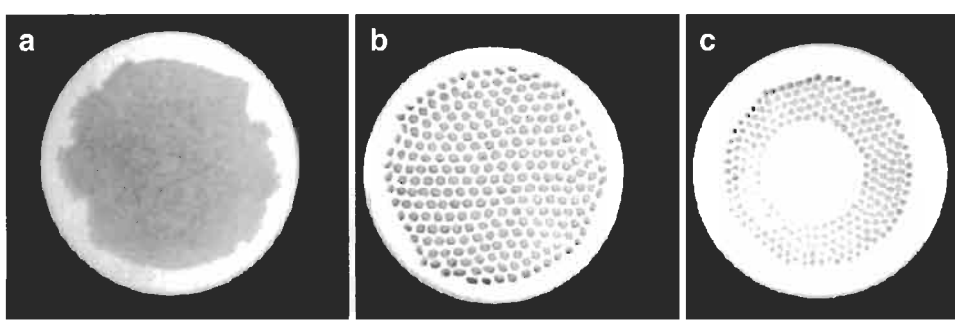

Fig. 14. Photographs of cross-sections of specimens: (a) No. 2, (b) No. 3, (c) No. 4 in Table 3.

Fig. 15. Tested super-express linear motor cars (over 500 km/h). (Courtesy of Japan Railway Technical Research Institute.)

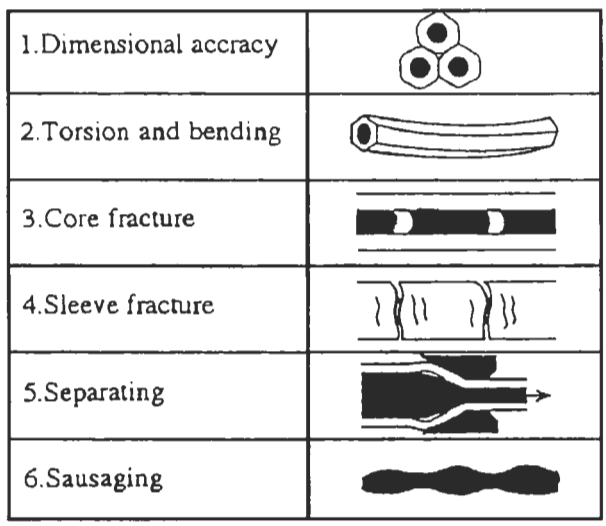

Fig. 16. Types of defects in drawn superconducting wire.

Fig. 18 show AE and drawing stress σ against the drawing length of the wire by three stages of drawing (Yoshida et al., 1994).

(1) After 6 passes (ϕ 5.8 mm $\rightarrow$ ϕ 5.5 mm). Few changes were observable in either AE or σ along the entire length of the wire due to the sound matrix.

(2) After 7 passes (ϕ 5.5 mm $\rightarrow$ ϕ 5.1 mm). Due to many small defects occurring in the core, the responses for both AE and σ become vivid.

(3) After 8 passes (ϕ 5.1 mm $\rightarrow$ ϕ 4.8 mm). Because of the increasing number of defects and fracture growth, a striking cyclic ruggedness in AE and σ appeared, the

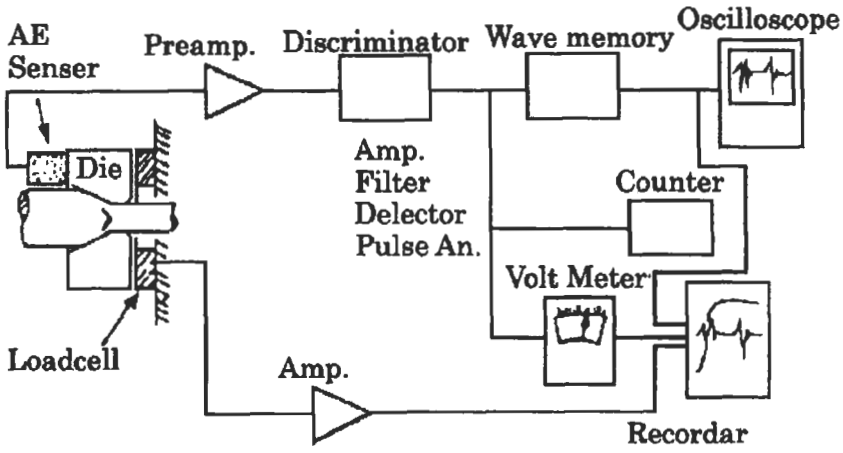

Fig. 17. Block diagram of measurement setup for load and AE.

wavelengths of which were found to be in good accord with the distance between the fractures (see attached schema in Fig. 19).

AE monitoring might be effective and informative for detecting filament breakage and internal fracture in the wires.

Drawing of Cu–NbTi Superconducting Wire

Two kinds of wires (diameters ϕ 3.2 and ϕ 3.0), which are available on the market and which include approximately 300 NbTi filaments were drawn under one pass reduction (R/P) ratios of 5, 10, 15 and 20% to ϕ 1.8 with the die half angles of $\alpha = 6°$ and 13°. The drawn wires were cut into 50-mm-long pieces, and then the copper claddings were completely dissolved with nitric acid. The resulting sample was examined for the absence or presence of filament breakage and the results are summarized in Fig. 20.

Similar to the causes of internal fracturing of the single wire, the tensile stress applied to the multifilament wire during drawing plays an important role; as α increases or R/P decreases, defects are more likely to occur. It was also found that filament breakage was more likely to occur in wire sample No. 3, in which filaments were placed immediately adjacent to the core of the wire, than in the wire sample in which filaments were positioned in a doughnut-shape arrangement.

The filaments of a multifilament wire curled when only part of the copper cladding was dissolved, depending on the drawing condition. It is considered that the residual stress applied to the filament determines the amount of curl (L). L was measured when copper cladding was dissolved to 0 to 25 mm from one edge. Fig. 21 the relationship between the diameter of the drawn wire and L when wires were drawn under an R/P ratio of approximately 20% and α of 6° and 13°. With the smaller α (6°), edges of the filaments did not spread and L was small.

For reference, a tensile test was performed using a sample wire (No. 4, ϕ 2.0) drawn under $R/P = 20\%$ with $\alpha = 6°$, and the fractured surface was observed by SEM

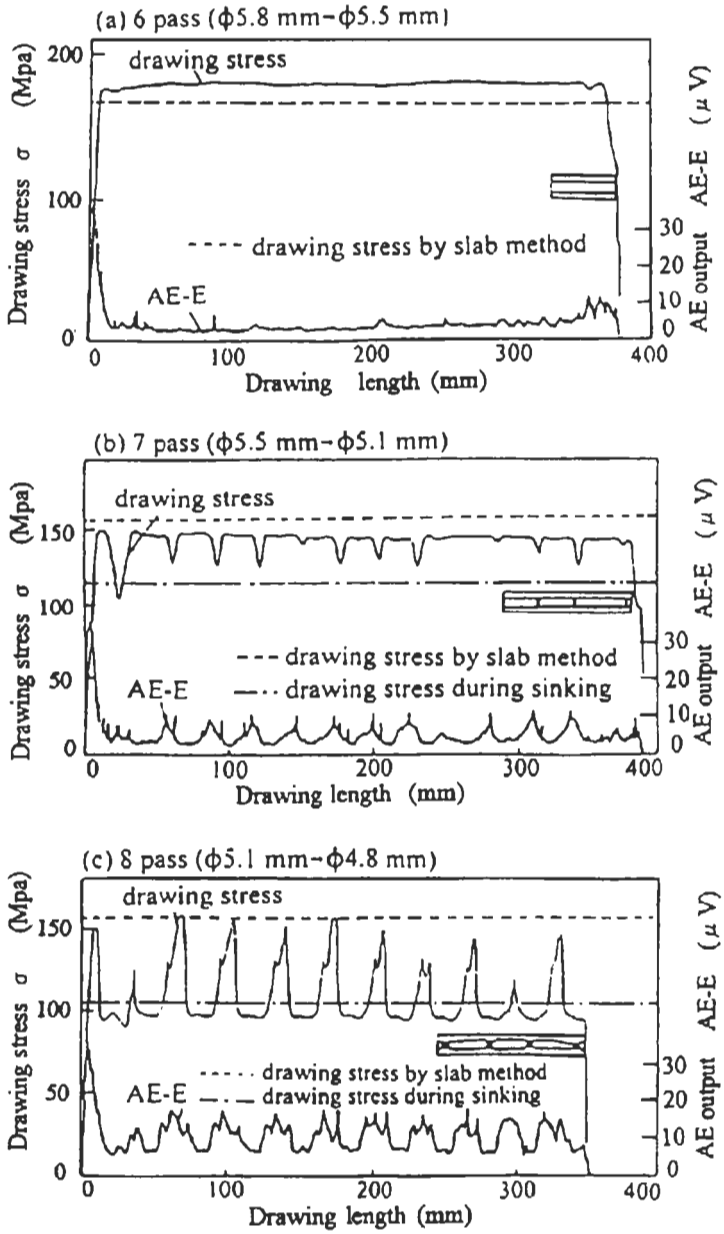

Fig. 18. AE signal and drawing stress during clad wiredrawing ($\alpha = 20°$).

(Fig. 22). The surfaces of both Cu and NbTi contained many dimples. Furthermore, the interfacial adhesive condition between Cu and NbTi was relatively good.

The number of broken filaments among approximately 300 filaments was only 1 to 6 in the Cu–NbTi multifilament superconducting wire during the drawing process,

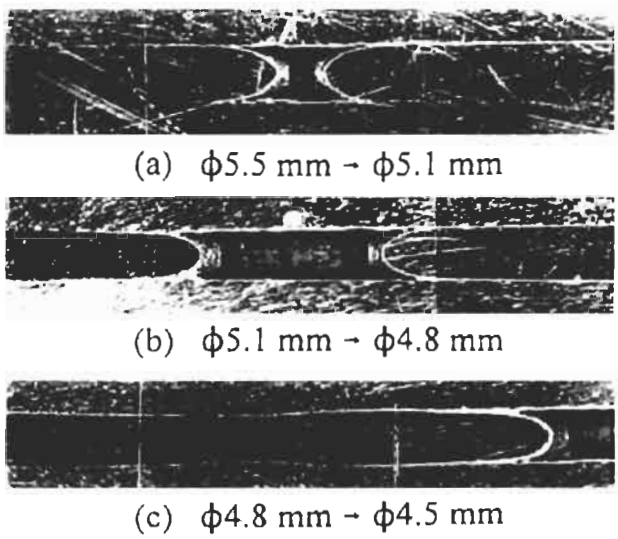

Fig. 19. Internal fracture found during clad wiredrawing ($\alpha = 20°$).

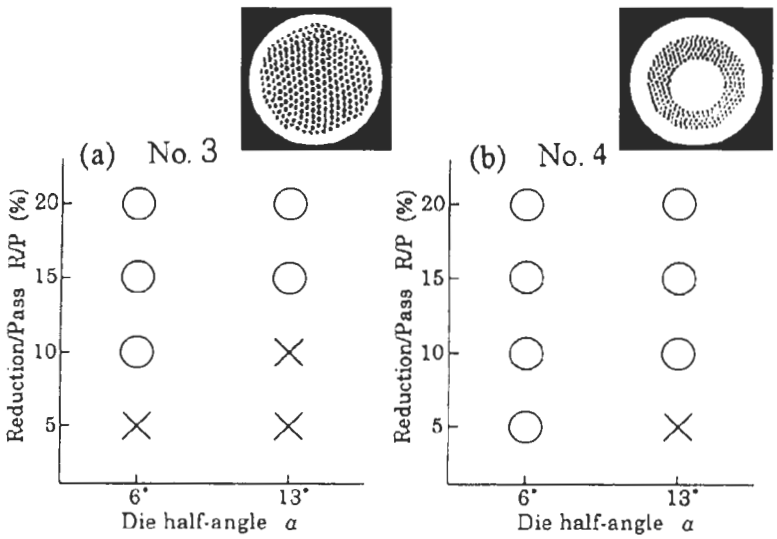

Fig. 20. Absence or presence of filament breakage in drawn wire (→ ϕ 2.1).

indicating that the AE energy was extremely small; therefore, detection of the defects was difficult.

In this study, the diameter of wire sample No. 3 was reduced from ϕ 4.2 to ϕ 1.3 under an R/P ratio of approximately 5% and α of 13°, which are conditions under which defects are likely to occur.

Fig. 23 shows the relationship between drawing length and AE output, and between drawing length and drawing stress. As shown in Fig. 18, there were two drawing lengths

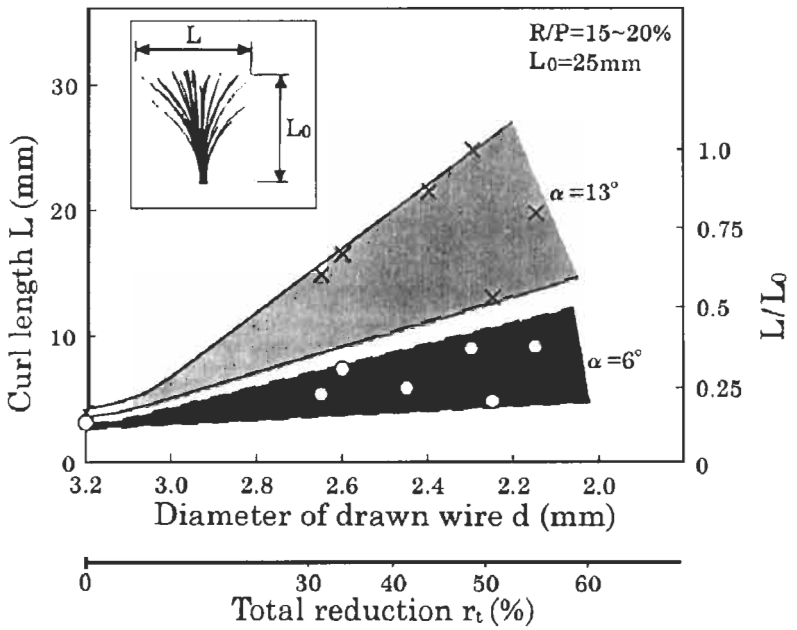

Fig. 21. Relationship between the diameter of drawn wire (No. 3) and amount of curl L.

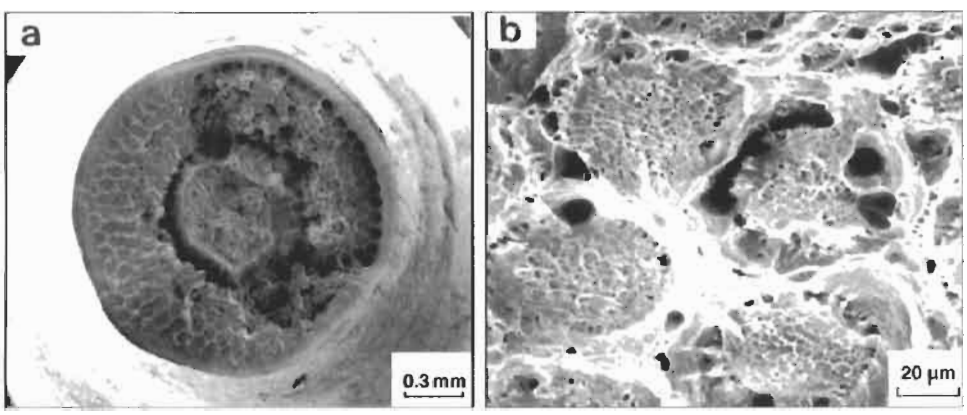

Fig. 22. SEM images of fractured surface in tensile test (No. 4, ϕ 2.0).

at which the emitted AE energy was high. Under this condition, no filament breaks were found; however, the core material was constricted. The drawing lengths at which constriction occurred corresponded to those at which high AE energy was emitted.

The following should be considered in order to detect the generation and development of nonuniform deformation and cracks with high sensitivity. AE output is the accumulation of several signals caused by several factors, including wire defects, as well as plastic deformation, the lubricant condition and electrical noise. To improve the

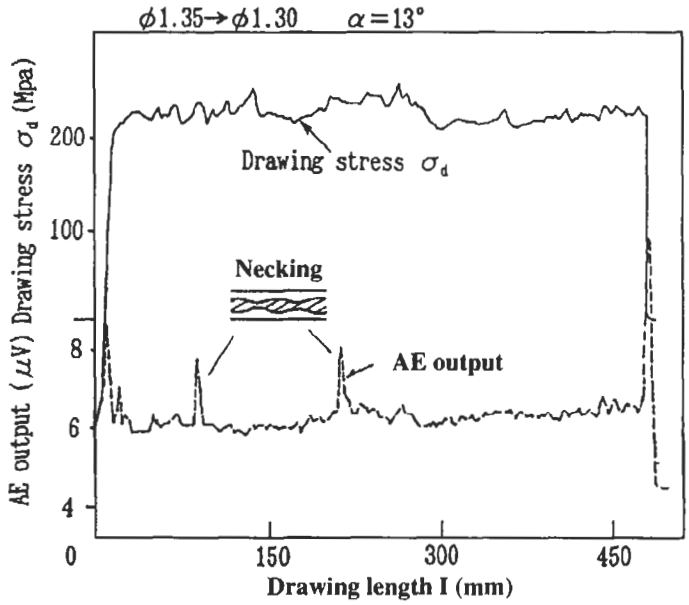

Fig. 23. Relationship between drawing length and AE output and drawing stress in drawing of the superconducting wire (No. 2 in Table 3.).

sensitivity, AE energy that is not related to the type of wire defect should be eliminated using, for example, a frequency filter.

There still remain several problems to be solved using AE; we can detect in-line filament breakage during the drawing process and observe the interfacial adhesive strength using AE. In the future, we expect that more experience and know-how associated with AE will be accumulated.

CONCLUSIONS

Wire breakage during superfine wiredrawing is often induced by inclusions in the wires. In this study, using FEA, the author conducted a simulation of the drawing of wires containing inclusions and investigated the causes of wire breaks in terms of the mechanics of plasticity. Also, the AE detection of internal fracture and filament breaks of a wire occurring during the drawing was discussed. The results obtained are summarized as follows.

(1) The author clarified, based on the FEA, that as a large inclusion passes through a die, drawing stress rapidly increases, inducing a wire break. It was estimated that inclusions with a ratio D_i/D_o of 0.4 or higher increase the likelihood of wire breakage.

(2) When the inclusion and matrix are not completely bonded at their boundary, an internal crack often occurs. The formation process of the crack and the growth of the crack with increasing drawing length was clarified by FEA.

(3) If the die half-angle is too large or the reduction/pass is too small, an internal fracture or core and filament breaks are liable to occur, which has been confirmed by simulation and experiment.

(4) The FEA simulation revealed that high tensile stress is applied to the core of a wire under the conditions under which filament breaks are likely to occur. For this reason, to prevent filament breaks, brittle superconducting filaments should not be placed at the center of a wire.

(5) Filament breaks of a single-filament wire during drawing can be detected by AE. AE motoring is effective and informative for the detection of internal fractures and filament breaks.

ACKNOWLEDGEMENTS

The author would like to thank the many members of the drawing committee in Japan for valuable discussions and is also grateful to Mr. M. Arashida at Daiichidenko K.K and Mr. K. Maeda at NIHON-ESI K.K. for his helpful comments, and to SEIKO Corp., Mr. C. Raskin at Union Miniere Copper, and the Japan Railway Technical Research Institute for giving the precious photographs.

REFERENCES

Arashida, M. et al. (1994) *Optec Rev.* (in Japanese). Daiichi-Denko, Japan, 5, pp. 8–11.
Avitzur, B. (1968). *Trans. ASME, Ser. B*, 90: 79–91.
Chen, C.C., Oh, S.I. and Kobayashi, S. (1979). *Trans. ASME Ser. B*, 101: 23–44.
Chia, E.H. and Jackson, P.M. (1978) *Wire J. Int.*, December, 56–60.
Coffin, L.F. and Roger, H.C. (1967). *Trans. ASM*, 60: 672–686.
Ikeda, T. et al. (1988) *Proceedings of the 27th Japanese Conference for Wire Drawing*. Drawing Committee, Japan Society for Technology of Plasticity, Japan.
Jennison, H.C. (1930). *Trans. AIME*, 89: 121–139.
Nakamura, N. and Wada, T. (1980) *The Cooper Story* (in Japanese). Nihon-doh-senta, Tokyo, pp. 250–258.
Nishioka, T. (1956). *J. Jpn. Inst. Met.*, 20: 181–184.
Raskin, C. (1997) *Proceedings of the WAI International Technical Conference, Italy.*
Raskin, C. and Janssen, J. (1998) *Wire J. Int.*, 31(12): 80–86.
Remmer, W.E. (1930)*Proc. Inst. Met.*, pp. 107–120.
Su, Y.Y. (1982) *Wire J. Int.*, January, 74–79.
Tanaka, H. and Yoshida, K. (1979). *J. Jpn. Inst. Met.*, 43: 618–625.
Tanaka, H. and Yoshida, K. (1983). *J. Jpn. Soc. Technol. Plast.*, 24: 737–743.
Tanaka, H. et al. (1976). *Furukawadenkou-Jihou*, 59: 91–98.
Tanaka, H. (1952). *J. Jpn. Inst. Met.*, 16: 567–571.
Tanimoto, Y. (1998) In: *Proceedings of the 181st Japanese Seminar for the Technology of Plasticity*, pp. 67–75. Japan Society for Technology of Plasticity, Japan.
Togashi, J. et al. (1979). *Furukawadenkou-Jihou*, Furukawa-Denko, Japan, 66, pp. 26–33.
Yoshida, K. (1982) Doctor dissertation at Tokai University. Tokai University, Tokyo.
Yoshida, K. (2000a). *J. Jpn. Soc. Technol. Plast.*, 41: 194–198.
Yoshida, K. (2000b) *Wire J. Int.*, March, 102–107.
Yoshida, K. and Tanaka, H. (1987) *Advanced Technology of Plasticity II*. Springer, Berlin, pp. 857–862.
Yoshida, K., Sato, M. and Sekino, M. (1994) *J. Jpn. Copper Brass Res. Assoc.*, 33: 212–218.

POLYMERIC FIBERS

Fiber Fracture
M. Elices and J. Llorca (Editors)

FRACTURE OF HIGHLY ORIENTED, CHAIN-EXTENDED POLYMER FIBRES

J.W.S. Hearle

The Old Vicarage, Mellor, Stockport SK6 5LX, UK

Introduction 267
Fibre types 267
Structure, Modulus and Strength 269
Experimental Observations 272
Tensile Failures 272
Creep Rupture 273
Tensile Fatigue 275
Surface Abrasion 276
Axial Compression, Bending and Flex Fatigue 276
Theoretical Approaches 277
Failure in Shear 277
Time and Temperature 279
Axial Compression Fatigue 281
References 285

Abstract

Polymeric high-modulus, high-tenacity fibres have a structure consisting of highly oriented, chain-extended, linear macromolecules. Para-aramid, aromatic copolyester, PBO and PIPD fibres are made by liquid-crystal routes, but HMPE is gel-spun. Deviations from an ideal structure reduce stresses below the ideal values. Tensile failure is due to axial splitting. HMPE fails by creep rupture under moderate loads. These fibres suffer from surface abrasion, flex fatigue and axial compression fatigue. Failure in shear is described qualitatively. Time and temperature dependence has been modelled by statistical mechanics. In fibre assemblies, axial compression fatigue is modelled in terms of axial and transverse compressive forces on yarns and axial slip. The same

principles should apply to the formation of kink-bands within fibres, which leads to failure in cyclic flexing.

Keywords

Fracture; Fatigue; Axial compression; Aramids; HMPE; Shear splitting; High modulus; High tenacity

INTRODUCTION

Fibre types

As Black and Preston (1973) point out in their symposium proceedings — a book which concentrates on experimental Monsanto fibres and, like Hamlet without the Prince of Denmark, mentions only in passing the successful para-aramid Kevlar — it was in the earliest days of acceptance of the polymer hypothesis that Mark (1936) made theoretical calculations indicating "that synthetic organic fibres were capable of very high Young's moduli." It was 30 years later, before such fibres were made and, in addition to high-modulus, "tended to be on the order of twice as strong as high-tenacity nylon or polyester." These organic high-performance fibres, as well as others, are described in Hearle (2001).

Three features are needed in high-modulus, high-tenacity (HM-HT) linear polymer fibres: (1) very long chains, i.e. high molecular weight; (2) highly oriented chains; (3) fully extended chains without crystallographic or irregular folds. Fibres with these characteristics can be made by two routes that differ greatly in their molecular type and production method, but give properties that have many similarities, though some significant differences.

The first route to be developed uses rigid polymer molecules with fairly strong interactions that will form liquid crystals in solution (or, for Vectran, in the melt). Dry-jet, wet spinning, through an air-gap into a coagulating bath (or stretching in melt-extrusion of Vectran) orients the liquid crystals. Monsanto concentrated on polyamide-hydrazides and polyoxadiazole-amides. DuPont with Kevlar and later AKZO (now Acordis) with Twaron combined chemical features of nylon and polyester in a para-aramid, polyphenylene-terephthalamide; this polymer links benzene rings with –CO.NH– groups, which form hydrogen bonds between chains in one crystallographic plane. Teijin's Technora and the Russian fibre Terlon are different copolymer variants. There are also Russian heterocyclic aromatic polyamides, SVM and Armos. Vectran is a fully aromatic copolyester, which needs a slow heat treatment of the solid fibre to generate high molecular weight. Subsequently the USAF made polymers containing benzoxazole and benzothiazole groups, having benzene rings between 5-membered rings on either side; commercialisation of PBO occurred in 1999 with Zylon from Toyobo. A more recent development by Sikkema (2001), which it is hoped to commercialise, is PIPD or M5; the important feature of this polymer is hydrogen bonding by –OH in both transverse directions, which increases the shear strength and compressive yield stress.

In view of a comment on fracture to be mentioned later, I will contrast in Fig. 1 two chemical types: the para-aramid of Kevlar and Twaron and one of the experimental polyamide-hydrazide X500 fibres made by Monsanto, whose lack of commercial utility led to the disclosure of extensive technical detail in Black and Preston (1973). A critical difference is the greater number of –CO.NH– groups in the Monsanto polymer, which will give stronger intermolecular bonding.

The second route uses a flexible inert molecule, ultra-high-molecular-weight polyethylene, which can be highly stretched to give highly extended, oriented chains. The

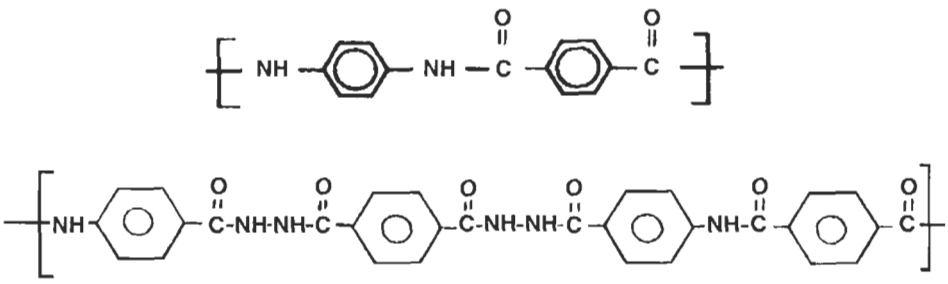

Fig. 1. (a) Para-aramid, polyphenyleneterephthalamide (Kevlar). (b) Polyamide-hydrazide (X500).

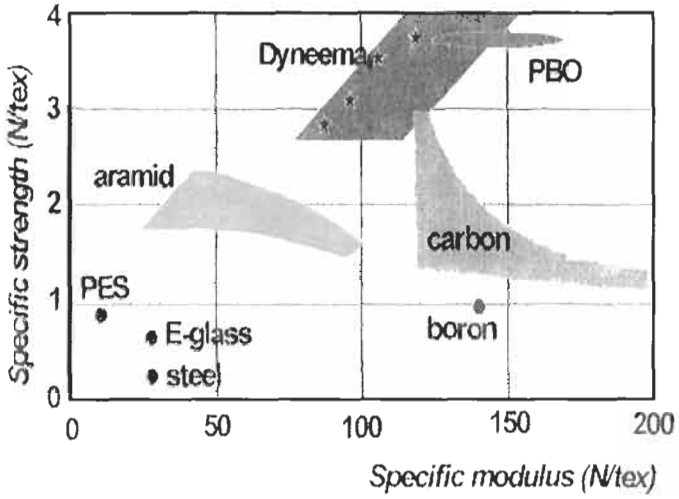

Fig. 2. Fibre strength and modulus from Smit et al. (2000). Specific stress equals 'stress/density', N/tex equals GPa/(g/cm^3). If values in GPa were plotted, aramid with a density of 1.44 g/cm^3 and PBO at 1.57 g/cm^3 would appear about 50% higher in comparison with polyethylene (Dyneema) at 0.97 g/cm^3. PES is high-tenacity polyester as used in tyre cords, etc.

highest strengths are achieved by gel-spinning, in which the coagulant from a concentrated solution can be extended to a high draw ratio. This is the method adopted by Allied Fibers (now Honeywell) for Spectra and by DSM for Dyneema. There are differences in properties among the various grades depending on process conditions. For example, production is helped, but properties are less good, if some lower-molecular-weight polymer is included. A second stage of slow processing under tension close to the melting point increases the modulus and reduces creep. Melt-extrusion followed by super-drawing or solid-state extrusion of compacted powder are two other methods used to make high-modulus polyethylene fibres, but the strengths are not as great as gel-spun fibre.

In order to give a quantitative context, Fig. 2 shows a DSM presentation by Smit et al. (2000) of values on a weight basis for strength and modulus of some HM-HT polymer fibres compared to other materials.

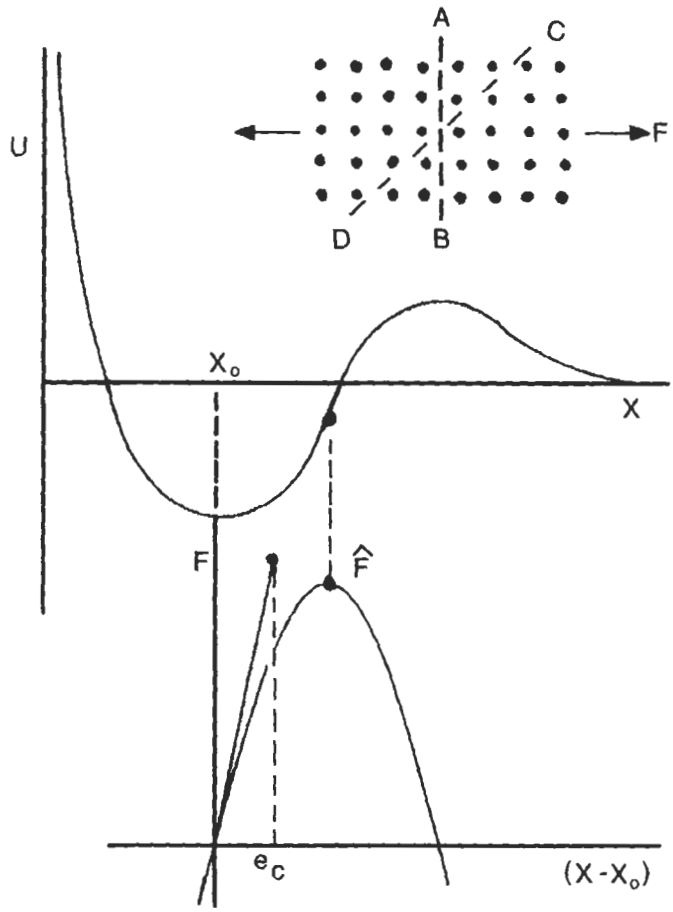

Fig. 3. Simple theory of idealised strength and modulus. Crystal lattice shows planes of failure in tension AB and shear CD. Upper graph shows free energy versus strain. Lower graph shows force versus strain with initial modulus from the equilibrium zero force, minimum-energy position and peak force at point of inflection on energy diagram. From Morton and Hearle (1993).

Structure, Modulus and Strength

The highest polymer fibre strength would presumably come from a perfectly oriented assembly of infinitely long molecules, though in practice some disorder probably helps lateral cohesion and makes the material more robust. The free energy and force–extension relations of such a material would have the form of Fig. 3 and would give estimates of an upper bound for stiffness and strength. The modulus, which depends on the first $A(x-x_o)^2$ term in the free energy equation, can be calculated with confidence. The predicted maximum strength, which depends on the determination of the point of inflection resulting from higher-order terms, is less certain. It is commonly calculated from the modulus as the stress at 2% extension.

Fig. 4. Staudinger's (1933) view of the continuous structure of an oriented polymer.

For finite molecular-weight polymer, a model drawn by Staudinger (1933), remains valid as an ideal structure (Fig. 4). This brings in the first factor to reduce stiffness and strength, slippage at the ends of molecules. This is a feature extensively studied at the larger scale of whole fibres for short-fibre composites and textiles. Strength is reduced by a slip factor, which takes account of the loss of tension from the free ends of the fibres or molecules up to the limiting state in the middle of components, where they are fully gripped. The slip factor has a greater effect when the bonding between components is weak and when the aspect ratio of the components is small. A simple presentation of the theory by Hearle (1982, p. 103) indicated that the stress at a given strain would be reduced by a slip factor S given by:

$$S = (1 - \tfrac{1}{2}K/\beta N) \tag{1}$$

where K is the ratio of shear-bonding stress between molecules to tensile stress in molecules, β is the aspect ratio of a polymer repeat unit and N is the degree of polymerisation. With the high molecular weights used in HM-HT fibres this effect will be small.

Two other factors, which influence stiffness and strength, are the degree of orientation of molecules and disorder in molecular packing. Although mean orientation angles can be determined, the detail of the departures from the ideal structure of Fig. 4 is an area of uncertainty. Diagrams drawn by different researchers (Fig. 5) give different views of structure. The pictures, which are attempts at a two-dimensional representation of what the structure might be despite the lack of adequate experimental evidence, show up contrasting ideas. Fig. 5a–c suggest regions where the crystal lattice is perfect, separated axially and transversely, by zones of disorder. Fig. 5d–f are para-crystalline models with a low level of uniform disorder. Fig. 5g suggests a distribution of local defects in the crystal lattice. My own view is that disorder might be due to defects associated in larger groups than indicated in Fig. 5a. What is needed to solve these problems is a large-scale exercise using all available methods of experimental structural analysis linked to 3-D computer modelling of putative structures. Fig. 5h represents a larger-scale, regular disorientation in Kevlar, which shows up as banding in optical microscopy between crossed polarisers.

As a first approximation, orientation reduces stress by a factor equal to the mean value of $\cos^4\theta$, where θ is the angle between the polymer axis and the fibre axis. There

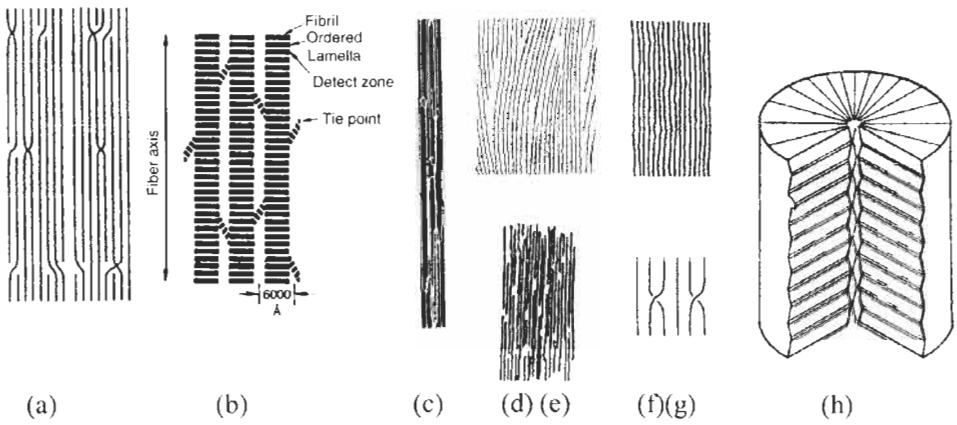

Fig. 5. Views of structure in highly oriented, chain-extended fibres. (a,b) Panar et al. (1983). (c) Jacobs and Mencke (1995). (d) Sikkema (2000). (e) Nakagawa (1994). (f,g) Hongu and Phillips (1997). (h) Aramid pleat structure (Dobb et al., 1977).

are more advanced theories, such as the one of Northolt and van der Hout (1985), which brings in the shear modulus. In many HM-HT fibres the orientation is so high that this effect is small. The pleated structure of Kevlar 29 as first wound up, which is shown in Fig. 5h, does cause an appreciable reduction in modulus and associated creep, but, since the disorientation is pulled out under high stress, has little effect on strength. The post-treatments that increase modulus in other types of Kevlar cause little change in strength.

The above theory and practice show that the modulus, or more generally the tensile stress–strain curve, of HM-HT fibres can be confidently estimated and can come close to the theoretical limit. As mentioned above, the ideal strength of a 'perfect' structure is more difficult to estimate, because it depends on the point of inflection in the free energy diagram. In real fibres, it is also necessary to take account of the fact that break load is not a central statistic but an extreme value. Strength is therefore dependent on the weakest and rarest defects or other forms of variability. Fracture will start where there is a combination of structural weakness and stress concentration, and this will vary with the mode of deformation. However, a hypothetical strength that is related to rupture of molecules across a plane perpendicular to the fibre axis (and the molecular orientation) is not the relevant consideration, though, as suggested below, it may occur as the final stage of rupture over a reduced cross-section. The dominant feature, which influences fracture, is the fact that the axial molecular strength is much greater than the transverse intermolecular strength. This means that axial splitting occurs much more readily than transverse rupture. Axial cracks manifest themselves in different ways in different circumstances with different stress distributions and histories. Complete explanations would require a more certain knowledge of the fine structure than is indicated by Fig. 5 and a comprehensive description of any larger defects in the fibres.

EXPERIMENTAL OBSERVATIONS

Tensile Failures

An early view of fracture of para-aramid fibres was given by Yang (1993, p. 97), who refers to three basic forms. The caption to his fig. 3.28 describes fracture morphology of Kevlar aramid fibre in tensile breaks as: "Type (a), pointed break: type (b) fibrillated break: type (c) kink-band break." The kink-band breaks, which extend over a length approximately equal to a fibre diameter can be attributed to fibres that have been weakened by axial compression and will be discussed in a later section.

The other two types will occur in relatively undamaged fibres. An example of type (a) was shown in fig. 6c,d and of type (b) in fig. 6b (see paper by Hearle, 3rd paper in this volume). The axial splitting, whether single or multiple, commonly extends over about 100 fibre diameters. Type (a) shows a gradual tapering towards the tip. Yang (1993, p. 97) points out that the diameter at the final break point is about 2–4 μm compared to 12 μm for the whole fibre: "Thus the true fibre strength based on the fibre cross-sectional area at break is very high." If the final break is due to axial tensile failure, when the reduction in aspect ratio means that tensile rupture is easier than shear cracking, this implies an ultimate molecular tensile strength of 30 to 100 GPa. There are alternative explanations of why two forms of break, namely the single split of type (a) and the multiple splitting of type (b), are observed.

Yang attributes the difference to differences in fibre type and test conditions: "Pointed fibre breaks are often observed on Kevlar 49 aramid fibres [post-treated to increase initial modulus] at slow strain rate. It reflects a highly ordered lateral fibre structure and is generally associated with high fibre strength."

In contrast to Yang's view, our SEM studies (Hearle et al., 1998, chapter 7) showed that the same fibre break could have one end of type (a) and one of type (b). We attributed this to break starting at a surface flaw and proceeding by a crack which split into multiple cracks, as shown in Fig. 6a. Necessarily, as shown in Fig. 6b, the upper bifurcation in this diagram reaches the opposite side of the fibre first, thus naturally leading to one single-split end of type (a) and one fibrillated end of type (b). The only way of avoiding this geometrical consequence is if, as shown in Fig. 6c, another bifurcation moves faster than the uppermost one. However, the splits on the left end then point in the wrong direction.

If breaks started from internal flaws, both ends would show multiple splitting. It is also possible that the snap-back after break, which, as shown in Fig. 7, causes complicated modes of deformation, might lead to multiple splitting of an initial end of type (a). Breaks of type (a) would occur on both ends if the crack does not bifurcate.

There are probably elements of truth in both explanations. The geometrical explanation for a combination of pointed and fibrillated ends certainly seems valid for the example quoted, but other scenarios could lead to two pointed ends or two fibrillated ends. There may be bias towards different combinations with different forms of Kevlar and Twaron and different test conditions. Examination of a large number of breaks would be needed to clarify the position. Most SEM studies have been limited to the few studies needed to show different, and not necessarily statistically common, forms of break.

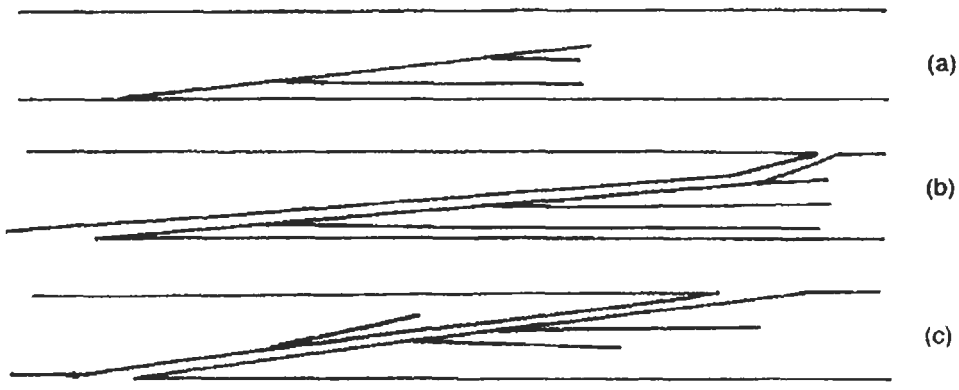

Fig. 6. (a) Crack propagation with bifurcation. (b) Broken fibre showing an end of type (a) on the left and of type (b) on the right. (c) If an inner bifurcation grows faster than an outer one, the multiple splitting on one end would point away from the break and not towards the break.

Fig. 8 shows that long axial splits also occur in the tensile fracture of a high-modulus polyethylene fibre.

Creep Rupture

Time is always a factor in determining the effective strength of polymer fibres. Higher strengths occur in ballistic impact resistance and lower strengths in long-term loading situations. Even when another fatigue mechanism is the main cause of failure, the final stage leading to breakage is creep rupture.

The time-dependent behaviour is different in the two types of highly oriented, chain-extended polymer fibres. Table 1 gives the results of studies in FIBRE TETHERS 2000 (1995), which were made because creep rupture is a concern in deep-water mooring of oil-rigs. The low-load creep in aramid fibres is due to a straightening of the initial structure. It reduces in rate, even on a logarithmic scale, with time and is not a source of creep rupture. In Vectran, the creep is less and is absent after 10 days under load.

HMPE fibres show high creep and in the worst cases break after a few days under moderate loads. Table 1 shows that there are big differences in creep response in

Table 1. Creep properties from Fibre Tethers 2000

	% creep 1 min to 100 days		Days to rupture	
% of break load	15	30	15	30
Kevlar 29	0.13	0.21	>357	>213
Kevlar 49	0.09	0.08	>217	>217
Twaron 1000	0.21	0.25	>357	>214
Vectran	0.06	0.09	>73	>218
Spectra 900	15.8	break	182	4
Spectra 1000	7.96	break	331	28
Dyneema SK60	1.05	6.0	>354	123

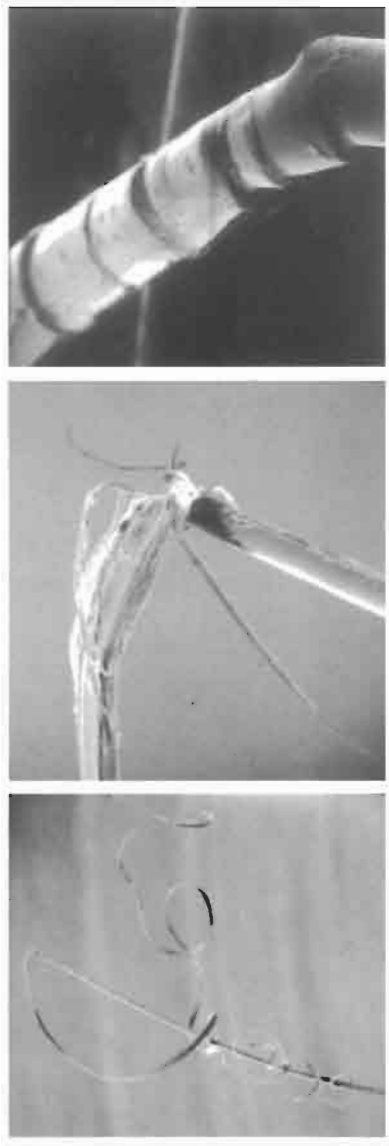

Fig. 7. Complex forms resulting from snap-back after break. (a) General view of splitting with helical buckling. (b) Detail of break zone. (c) Kink-bands due to axial compression on recoil.

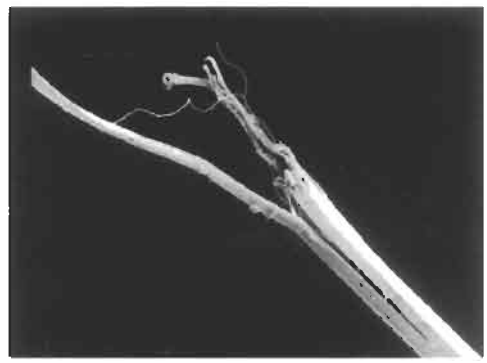

Fig. 8. Tensile break of an HMPE fibre, Spectra 900, from Hearle et al. (1998).

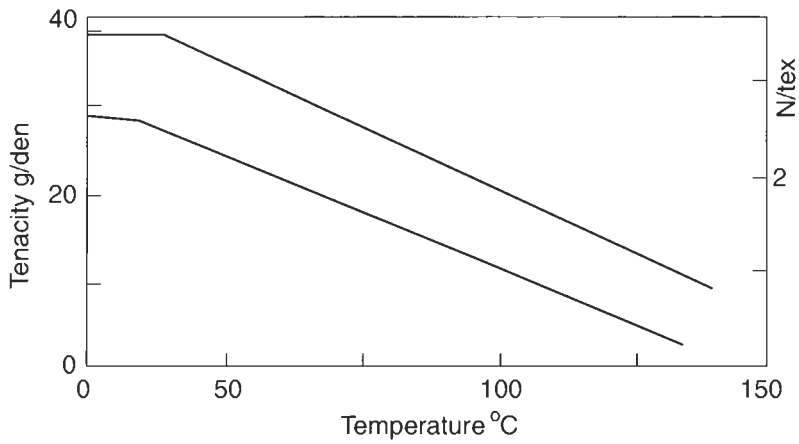

Fig. 9. Effect of temperature on strength of Spectra 900 (lower line) and 1000 (upper line), from Allied Fibers.

different HMPE fibres. Some more recent types of Dyneema and Spectra show further reduced creep. Creep in HMPE fibres increases with increasing temperature. Fig. 9 shows how the strength falls in Spectra fibres with temperature and this corresponds to the increasing rate of creep to rupture and reduction in time-to-break.

Tensile Fatigue

Tension–tension cycling causes little weakening of Kevlar. In a study by Konopasek and Hearle (1977) immediate tensile breaks were mostly scattered over the same range as the peak loads in fibres that failed after many cycles. However, the fatigue breaks had much longer splits than direct tensile breaks. In a fibre cycled to over 90% of break load, which lasted for 285,000 cycles, the fracture extended over a length of 6 mm, which was 485 times the fibre diameter. In order to record the break, it was necessary to make a montage of SEM pictures that was about 3 m long. A variety of forms of splitting

were observed, such as splits that terminated at both ends without breaks and peeling of a layer from the surface.

Surface Abrasion

The shear stresses associated with surface rubbing cause severe abrasion of the surface of aramid fibres. In yarns that have been carelessly handled, fibrillation is clearly apparent. In laboratory tests with rubbing on a pin, the surface becomes worn away until break occurs.

Axial Compression, Bending and Flex Fatigue

At the molecular level, HM-HT polymer fibres can be regarded as lightly bonded assemblies of slender rods, which will buckle under axial compression. It is not easy to put whole fibres into uniform axial compression, because of buckling at the fibre level, and most studies are from compression on the inside of a bend. Compressive yield stresses of an HMPE fibre, estimated from recoil studies, have been reported by Allen (1987) to be only 0.07 GPa, 2.5% of the tensile strength; for Kevlar, he reports 0.37 GPa, 11% of tensile strength. Using estimates from bending tests, van der Zwaag and Kampschoer (1987) report values of 0.5 and 0.9 GPa for aramid (Twaron) fibres. Sikkema (2001) gives compressive strengths of 0.4 GPa for PBO, 0.58 GPa for Twaron, but 1.6 GPa for M5 fibre. This order of values from HMPE to M5 reflects the increase in transverse bonding.

The effects of axial compression are seen internally in fibres viewed in polarised light microscopy and coming out of the surface in SEM pictures (e.g. Fig. 10a). The yielding on the compressive side allows the neutral plane to move outwards and so prevents the tensile strain on the outside reaching its break value. Schoppee and Skelton (1974) found that Kevlar, as well as other lower-modulus fibres, could be bent back on itself without breaking. An interesting exception to this rule for polymer fibres was an experimental X500 Monsanto fibre shown in Fig. 10b. This has broken on the tension side, but with axial splitting as distinct from the classical brittle fracture that would occur in glass and similar fibres. The additional hydrogen bonding shown in Fig. 1 may be the cause of this difference. Weakness in shear is commonly seen as a disadvantage, but it does eliminate brittleness in bending.

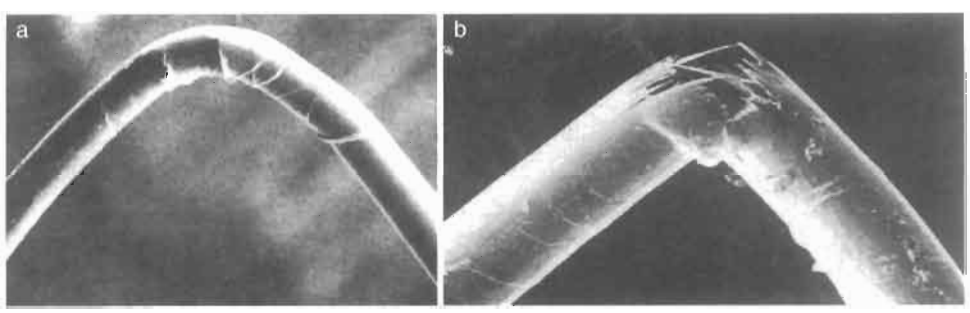

Fig. 10. (a) Bent Kevlar 49 fibre. (b) Bent X-500 fibre. From Schoppee and Skelton (1974).

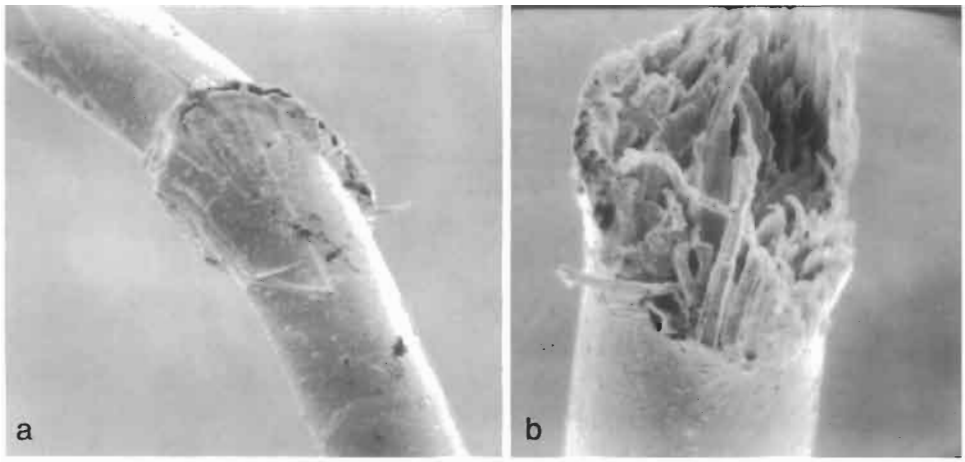

Fig. 11. (a) Kevlar fibre after a week of cyclic buckling. (b) Fibre broken in tension after cyclic buckling.

Although the disruption apparent in kink-bands after bending looks severe, it does not appreciably affect fibre strength. Kink-bands formed in a single bending action are pulled out by tension with little or no loss of break load. However, repeated cycling leads to increasing damage and eventual failure.

Flex fatigue tests over pins proved difficult with Kevlar due to surface abrasion (Hearle and Wong, 1977). An alternative was a single-fibre buckling test, in which a 2.5-mm length of a single Kevlar fibre was cycled between 1.5 and 2.1 mm. After a week at 50 Hz the fibre had not broken, though, as shown in Fig. 11a, it was severely damaged. Fibres broken after cyclic buckling (Fig. 11b) show short multiple splits. These would be the type (c) breaks mentioned by Yang (1993, p. 97).

Probably because of the low coefficient of friction HMPE fibres are less subject to abrasion. Sengonul and Wilding (1994, 1996) found that flexing of Dyneema fibres over a pin gave multiple split breaks. This indicates that shear splitting in zones of variable curvature was the dominant factor.

Yarn buckling tests were carried out in the FIBRE TETHERS 2000 (1994, 1995) joint industry project. Failure due to axial compression fatigue was also studied in fibres from fatigued ropes in the study. As discussed below, the constraints on fibres within the yarns, especially if they were restrained in a shrink-tube in the laboratory test or within ropes, causes very sharp fibre kinks to form. Kevlar, Vectran and Dyneema all showed kink-bands within fibres and breaks over short lengths.

THEORETICAL APPROACHES

Failure in Shear

The dominant factor influencing fracture in highly oriented, chain-extended polymer fibres is the high axial molecular strength, which depends on covalent bonding, and the

Table 2. Sources of shear stresses.

	Source of shear stress	Observed effect
Fibres in tension: defects		
Surface flaws, internal voids, molecular packing defects	Shear stress at tip of discontinuity, which transmits tensile stress to more remote material (Fig. 12)	Tensile breaks showing long axial splits
Direct shear stresses		
Surface abrasion	Direct frictional forces	Surface peeling
Bending	Shear stress due to variable curvature	Axial splitting

low intermolecular strength, which results from weak van der Waals forces between $-CH_2-$ groups in HMPE fibres and somewhat stronger hydrogen bonding and phenyl or related interactions in aramids and other liquid-crystal fibres. Consequently shear splitting is much more likely than transverse fracture. Table 2 lists circumstances in which shear stresses can lead to failure.

At a superficial, qualitative level, the effects are clear. More detailed, quantitative explanations raise more difficulties, and there is little detailed theory available. The direct shear stresses, due to friction or bending, should, at least in principle, be calculable from the overall applied mechanics. The indirect shear stresses depend on the stress distribution around a discontinuity as shown in Fig. 12.

In addition to these calculations in applied mechanics, one is left with the following questions in quantifying fracture.

(a) What flaws are present at a supermolecular scale either on the fibre surface or internally? And are these formed during fibre manufacture or due to subsequent damage? How much variability is there due to the history of a particular fibre before its strength is measured?

(b) What defects are present at the molecular, fine-structure level? To what extent do any of the models shown in Fig. 5 reflect reality?

(c) To what extent do cracks parallel to the fibre axis join up points of axial weakness?

(d) What leads to cracks crossing the fibre at some angle to the fibre axis and hence leading to rupture? Is the transverse component of cracks a result of the detailed stress distribution, or is it due to structural defects? What model of fibre structure should we use to explain the angling?

Fig. 13, which is an early tensile failure model for Kevlar due to Morgan et al. (1982), but also reproduced by Yang (1993), illustrates the problems. Three modes of crack propagation are apparent. In the skin on the left, axial cracks between molecules

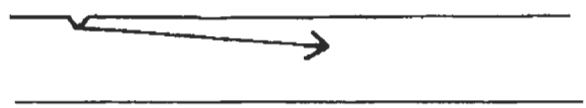

Fig. 12. Shear stress at a discontinuity.

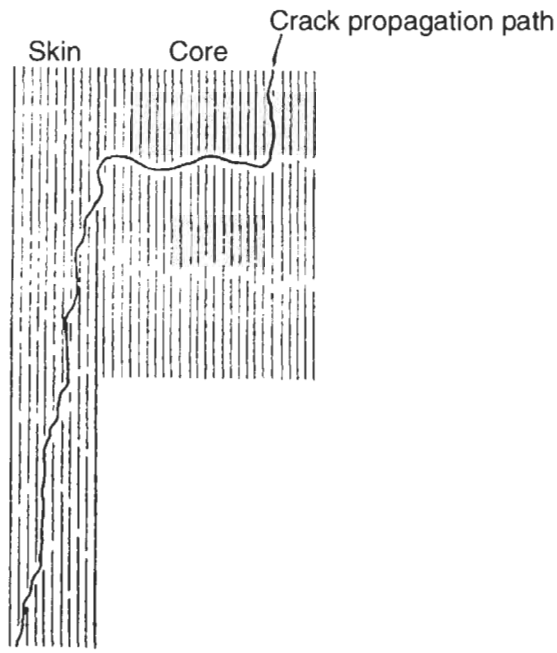

Fig. 13. Tensile failure model due to Morgan et al. (1982).

occasionally jump to the right at what presumably represent the ends of molecules. In the middle of the core, a lining-up of chain ends leads to a longer transverse crack, and on the right the crack becomes purely axial. I am sceptical about attempts at such interpretations at the molecular level. The structure is not well enough known. Long axial breaks, Yang's type (a) and (b), without transverse cracks except perhaps at the tip of a split, are more commonly observed. Where there are transverse cracks as part of a break, they are probably due to kink-band damage. But, although I can raise questions, I cannot provide detailed answers.

Time and Temperature

The strength of highly oriented, chain-extended polymer fibres is time- and temperature-dependent, and, in principle, responses can be predicted by statistical mechanics. Fig. 14 compares experimental results with the theoretical predictions of Termonia and Smith (1986). The agreement is good. The Monte Carlo methods used in this and later studies are described in the paper by Termonia (this volume).

The model in Termonia and Smith (1986) is for "ideal fibres made of a perfectly oriented array of fully extended macromolecules, with no other defects than chain ends resulting from finite molecular weight". Parameters defining the primary covalent bonding and the secondary hydrogen bonding are applied to a system "modelled as a three-dimensional array of bonds which are viewed as coupled oscillators in a state of constant thermal vibration". I have no difficulty in accepting this as a reasonable

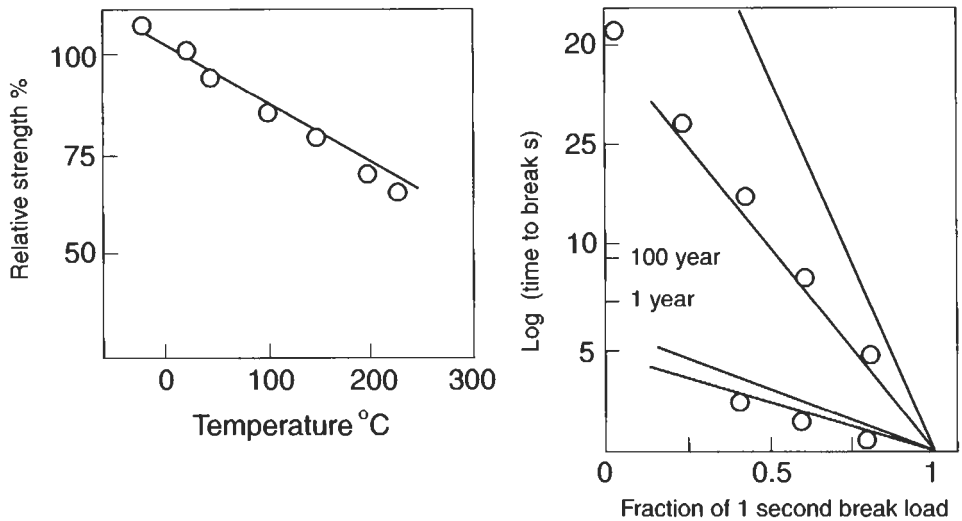

Fig. 14. Comparison of theoretical predictions by Termonia and Smith (1986) with experimental results by Schaefgen et al. (1979). (a) Effect of temperature on strength of Kevlar. (b) Time to break for Kevlar and HMPE.

approximation for the prediction of the elastic properties, the tensile modulus, of a real fibre with a modest degree of disorientation and other defects. However, I have problems with creep and fracture.

It would appear that the only modes for major, inelastic deformation are either breakage of covalent bonds or the movement of whole molecules past one another due to a cooperative breakage of all the intermolecular bonds. The title of the paper refers to "ultimate mechanical properties", and the model may be valid as a prediction of the theoretical maximum values for an ideal fibre, if such a structure could be made. However, both the forms of fracture and theoretical considerations of the stress distributions and the modes of deformation in defective structures suggest that real fibres behave differently. The SEM pictures do not support the view that "fracture ... proceeds through the breaking of a small number of primary bonds". Nor do they support the comments on fracture propagation: namely that, for PPTA, high-stress concentrations build up, so that "catastrophic failure occurs and the specimen breaks in a brittle fashion", and, for polyethylene, that the reduction in chain length due to primary bond breakage increases the stress on the van der Waals bonds and "failure of the specimen is accompanied by a creep-like mode of deformation". In reality, I believe that shear stresses and consequent crack formation and propagation play a much larger role in PPTA, and, as mentioned below, that defect mobility occurs in polyethylene.

As I wrote (Morton and Hearle, 1993, pp. 666–667): "The predictions are, of course, very dependent on the choice of input parameters used in the computational modelling: there is a major effect of activation energies for bond breakage and a less effect for activation volume. The authors' conclusion that fracture in both PPTA [Kevlar] and polyethylene is initiated through primary-bond breakage is not immediately

compatible with explanation of breakage that comes from the morphology." The statistical mechanics, which involves thermally activated jumps over the energy barriers as in Fig. 3, is valid, and can be expected to apply to predictions of modulus, which relates to the central value of structural variability. In the absence of explicit structural detail, it seems questionable to apply the model to failure modes, which depend on extreme structural situations.

The agreement with experiment shown in Fig. 14 is fascinating, and with the vast increase in computer power since 1986, it would be valuable to follow up the approach pioneered by Termonia and Smith for models which included the possible defects in the structure. In HMPE fibres, it seems right to attribute creep to the movement of whole molecules past one another, which eventually leads to separation. However, the most likely mechanism would be the movement of defects such as those described by Reneker and Mazur (1983). A kink in a polyethylene chain due to an extra $-CH_2-$ group could move like a ripple in a carpet.

Axial Compression Fatigue

As listed in Table 3, sharp kinks can develop in oriented systems at many scales. Fibre fracture of Yang's type (c) is the result of breaks after cyclic axial compression acting at the smallest scale, usually on the inside of bends. Studies by Hobbs et al. (2000) at the yarn level provide valuable insights. Although the details will be different, the essentials of the mechanics will be similar inside fibres at the molecular level. It is therefore useful to review the analysis here. These studies were carried out because of the problem of axial compression fatigue in mooring ropes. In 1983, Kevlar ropes, which had been deployed in the Gulf of Mexico in order to moor an oil-rig construction vessel, broke when they were picked up for connection a few weeks later (Riewald, 1986; Riewald et al., 1986). The ropes were tested and found to have lost 80% of their strength. Microscopic examination showed kinks in yarns at intervals along their length. All the fibres in a yarn kinked cooperatively at these locations, and dyeing gave evidence of kink-bands within the fibres. Tension–tension rope fatigue testing in FIBRE TETHERS 2000 confirmed that axial compression fatigue occurred when one component in a rope goes into axial compression even though the rope as a whole remains in tension. Typical examples showed zig-zag sections, or, where damage was more severe, broken pieces a few millimetres long separated by undamaged lengths of a few centimetres. As a result, it has been recommended that aramid ropes in deep-water moorings should not be allowed to go below 10% of rope break load for more than 2000 cycles, HMPE ropes

Table 3. Examples of axial compression kinks

System	Scale
Mountain ranges	kilometres
Cliffs	metres
Yarns in ropes	millimetres
Molecular fine structure in polymers	nanometres

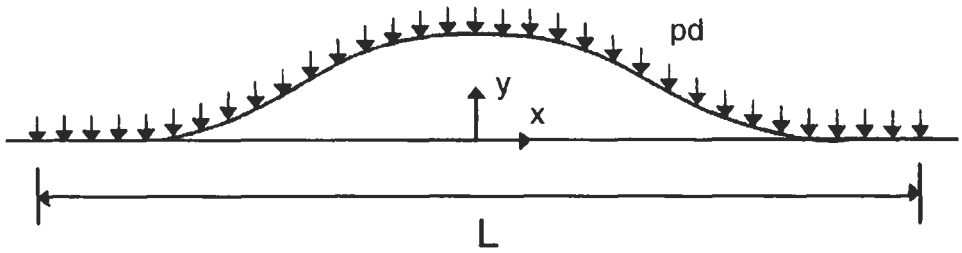

Fig. 15. Lateral elastic buckling, from Hobbs et al. (2000).

under 5% for 40,000 cycles, and polyester ropes under 10% for 100,000 cycles. This reflects the susceptibility of the different fibres to axial compression fatigue.

The theoretical analysis derives from earlier studies (Hobbs, 1984; Hobbs and Liang, 1989) on the buckling of heated pipelines. Thermal expansion causes these to buckle sinusoidally. Different modes are predicted theoretically: mode 1 with single half-waves separated by straight zones; mode 2 with one full wave; mode 3 with three half-waves ... continuous (infinite mode). In the notation of Fig. 15, quoting from Hobbs et al. (2000), the governing differential equation is:

$$y' + n^2 y + (m/8)(4x^2 - L^2) = 0 \tag{2}$$

where a prime denotes differentiation of the displacement y with respect to the longitudinal coordinate x, $m = pd/EI$ and $n^2 = P/EI$. [p is the radial pressure on a beam of diameter d.] E is Young's modulus for the beam, I its effective second moment of area, P the compressive axial load and L the buckle half-wavelength. The solution to this differential equation is presented in Hobbs (1984), but proceeds by considering the boundary conditions for the various modes, whether localised or periodic, and in each case gives a relationship of the form:

$$P = f(L) \tag{3}$$

The other important element in the analysis is to recognise that as the buckle forms the force in it drops to maintain displacement compatibility.This equation gives the solution for the infinite mode, but the localised modes require that the compatibility condition, Eq. 2, should be modified to include the influence of two 'slipping lengths' adjacent to the localised buckle (Fig. 16). The slip lengths form to accommodate the difference between P_0, the force remote from the buckle which is unchanged by the formation of the buckle, and the lower force P, within the buckle itself. The slip length, L_s, is determined by the effective friction between the beam and the surroundings. If the friction coefficient is μ, and the radial pressure p on a beam of diameter d, or perimeter πd, then:

$$L_s = (P_0 - P)/(\mu p \pi d) \tag{4}$$

The analysis shows that the controlling features in the elastic buckling of pipelines are (1) the flexural rigidity of the pipe, (2) the resistance to lateral displacement, (3) the

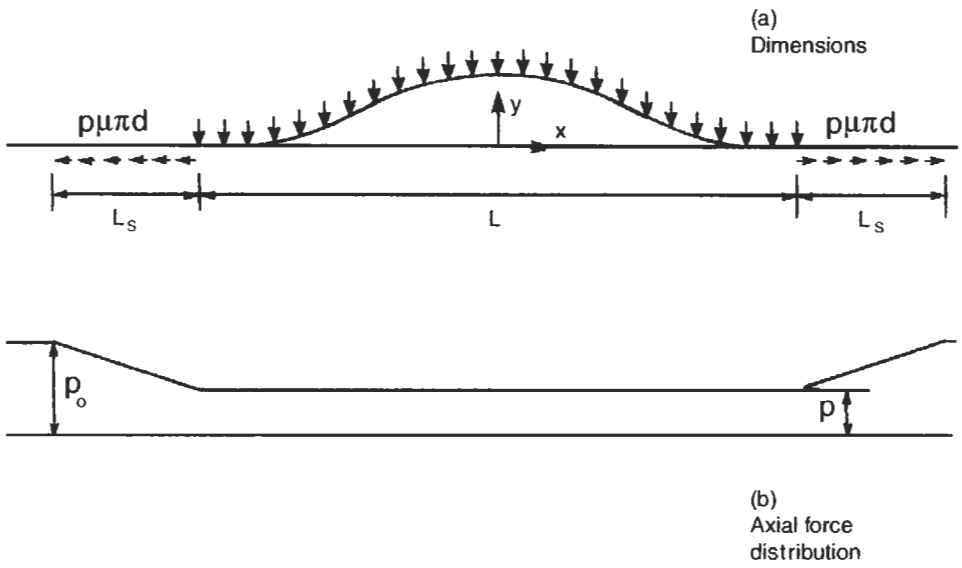

Fig. 16. Slip lengths and force distribution, from Hobbs et al. (2000).

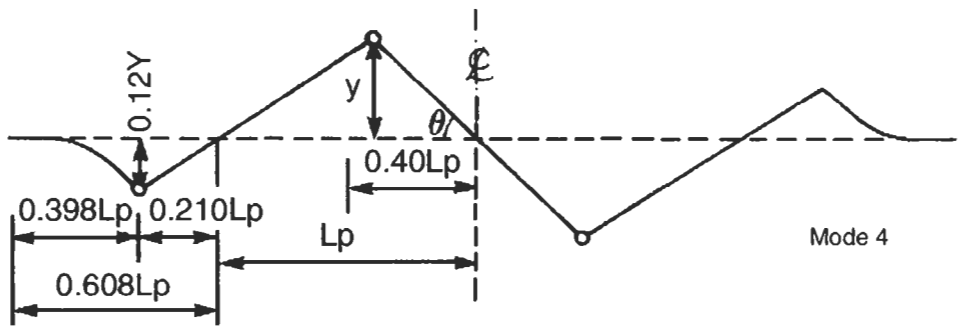

Fig. 17. Form of kinking due to plastic yielding, from Hobbs et al. (2000).

resistance to axial slip. In order to apply this to the kinking of yarns within ropes, it was necessary to introduce appropriate forms for the transverse and axial resistances. The more important difference is the plastic yielding of the fibres, which transforms smooth buckles into sharp kinks. As an approximation, the fibres are assumed to show ideal elastic–plastic behaviour, so that the plastic bending moment has to be introduced as well as the initial flexural rigidity. The predicted form of buckling is shown in Fig. 17. It is assumed that elastic buckling occurs first and determines the form and dimensions of buckles. The plastic solution peels off the elastic solution as shown in Fig. 18.

The ideal solution for perfectly straight rods is the line AC with the plastic solutions coming off at H_1 to H_4. However, there are both theoretical and practical problems with this ideal case. Realistically there will be initial imperfections in the fibre paths. In these

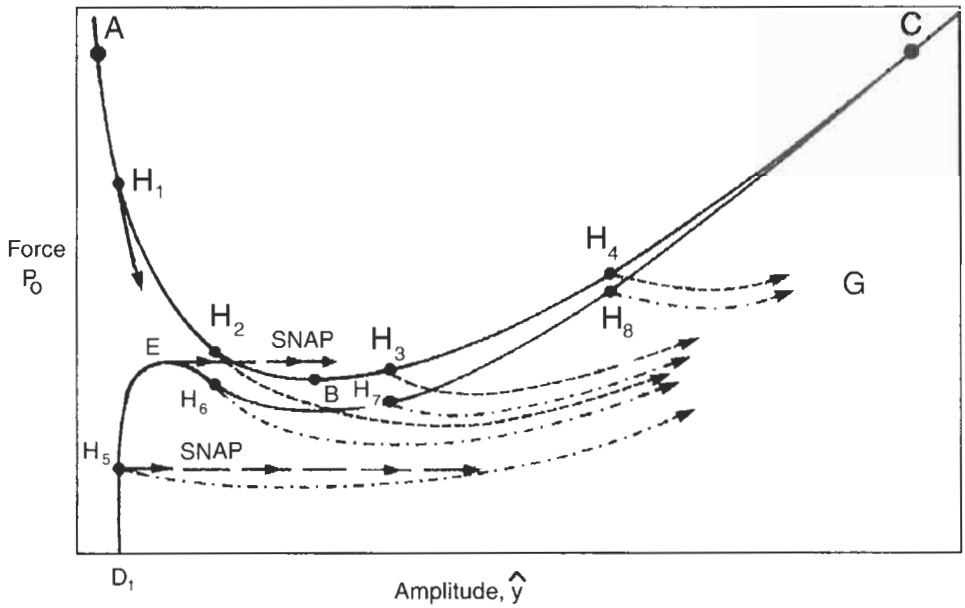

Fig. 18. Force–amplitude plot for elasto-plastic buckling, from Hobbs et al. (2000).

circumstances, the plot follows the line D_1C. If plastic yield occurs at H_5, this will give an unstable plastic solution and there will be snap to the rising part of the curve. However, if point E is reached before plastic buckling occurs, the decreasing portion of the curve will lead to snap in the elastic regime, which will subsequently give the plastic hinge.

A computer program has been written and used to calculate a solution for an aramid rope subject to tension–tension cycling at $38 \pm 24\%$ of break load. Although there is uncertainty in the values chosen for the defining parameters, particularly the bending stiffness and plastic moment of the yarn, the predictions were of the same order of magnitude as the examples of failures in ropes, which are shown in Fig. 19.

The sensitivity analysis in Table 4 shows the effect of the fibre modulus E, the lateral pressure p and the coefficient of friction μ on the buckle dimensions. The solid rod case

Table 4. Sensitivity predictions, from Hobbs et al. (2000)

Input values	Solid rod case			Free sliding case				
E (GPa)	52.3	26.2	52.3	52.3	52.3	26.2	52.3	52.3
p (GPa)	0.1	0.1	0.1	0.1	0.1	0.1	0.05	0.1
μ	0.15	0.15	0.15	0.1	0.15	0.15	0.15	0.1
Calculated								
Half-wave length (mm)	8.75	6.76	10.2	8.98	0.296	0.25	0.346	0.31
Buckle amplitude (mm)	1.85	1.63	1.77	2.18	0.03	0	0.03	0
Slip length (mm)	19.7	9.79	24.1	35.3	1.84	1.48	2.27	3.18

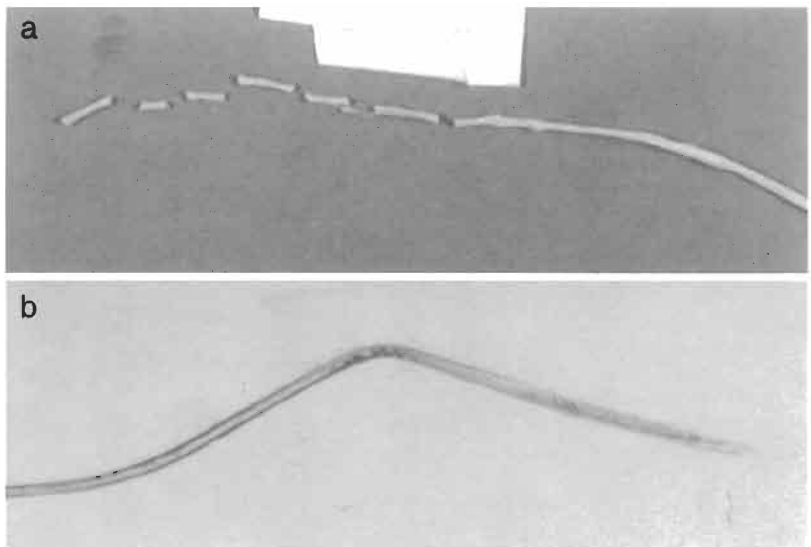

Fig. 19. Axial compression failures, from Hearle et al. (1998, chapter 39). (a) Broken and unbroken yarn segments in a Kevlar rope. (b) Buckling and break of a fibre in a Twaron rope.

will have high bending stiffness and the free sliding case low stiffness. In order to adapt the analysis to the prediction of kinking within a fibre, it would be necessary to have data on the bending properties of molecules, on the resistance to lateral displacement as the kink forms, and the resistance to axial sliding of the molecules. This is an interesting problem for a polymer theoretical physicist.

The conditions for the formation of kink-bands within HM-HT fibres are the first part of the problem. The second part is what happens in repeated cycling. The axial compressive force causes the molecular buckling, and superficially the internal kink appears to be pulled out on retensioning. However, it seems likely that there is some residual structural disturbance, which becomes more severe after repeated cycling and leads to what appears to be crazing. Eventually failure occurs in the characteristic angled form of kink-band breaks, being the Achilles heel of HM-HT fibres.

REFERENCES

Allen, S.R. (1987) Tensile recoil measurements of compressive strength for polymeric high-performance fibres. *J. Mater. Sci.*, 22: 853–859.

Black, W.B. and Preston, F. (Eds.) (1973) *High-Modulus Aromatic Fibres*. Marcel Dekker, New York.

Dobb, M.G., Johnson, D.J. and Saville, B.P. (1977) Supramolecular structure of high-modulus polyaromatic fibre (Kevlar 49). *J. Polym. Sci. Phys.*, 15: 2201–2211.

FIBRE TETHERS 2000 (1994) *Axial Compression Studies for United States Navy*. Joint Industry Study, Phase IIA, Noble Denton, London.

FIBRE TETHERS 2000 (1995) *High Technology Fibres for Deepwater Tethers*. Joint Industry Study, Noble Denton, London.

Hearle, J.W.S. (1982). *Polymers and Their Properties*. Ellis Horwood, Chichester.

Hearle, J.W.S. (Ed.) (2001) *High Performance Fibres*. Woodhead Publishing, Cambridge.

Hearle, J.W.S. and Wong, B.S. (1977) Flexural fatigue and surface abrasion of Kevlar-29 and other high-modulus fibres. *J. Mater. Sci.*, 12: 2447–2455.

Hearle, J.W.S., Lomas, B. and Cooke, W.D. (1998) *Atlas of Fibre Fracture and Damage to Textiles*. Woodhead Publishing, Cambridge.

Hobbs, R.E. (1984) In-service buckling of heated pipelines. *ASCE, J. Transport. Eng.*, 110: 175–189.

Hobbs, R.E., and Liang, F. (1989) Thermal buckling of pipelines close to restraints. *8th Int. Conf. Offshore Mechanics and Arctic Engineering*, The Hague, March 1989, Vol. 5, pp. 121–127.

Hobbs, R.E., Overington, M.S., Hearle, J.W.S. and Banfield, S.J. (2000) Buckling of fibres and yarns within ropes and other fibre assemblies. *J. Text. Inst.*, 91: 335–358.

Hongu, T. and Phillips, G.O. (1997) *New Fibers*, 2nd ed. Woodhead Publishing, Cambridge.

Jacobs, M.J.N. and Mencke, J.J. (1995) New technologies in gel spinning the world's strongest fibre. *Internationales Techtextil Symp.*, Frankfurt, Paper 2.13.

Konopasek, L. and Hearle, J.W.S. (1977) The tensile fatigue behaviour of para-oriented aramid fibres and their fracture morphology. *J. Appl. Polym. Sci.*, 21: 2791–2815.

Mark, H. (1936) In: General Discussion on R. Houwink, High elasticity of three-dimensional polymerised amorphous materials in relation to their internal structure. *Trans. Faraday Soc.*, 32: 144–145.

Morgan, R.J., Pruneda, C.O. and Steele, W.J. (1982) *J. Polym. Sci., Polym. Phys.*, 21: 1757.

Morton, W.E. and Hearle, J.W.S. (1993) *Physical Properties of Textile Fibres*, 3rd ed. Textile Institute, Manchester.

Nakagawa, J. (1994) Spinning of thermotropic liquid-crystal polymers. In: *Advanced Fiber Spinning Technology*, Nakajima (Ed.). Woodhead Publishing, Cambridge.

Northolt, M.G. and van der Hout, R. (1985) Elastic extension of an oriented crystalline fibre. *Polymer*, 26: 310–316.

Panar, M., Avakian, P., Blume, R.C., Gardner, K.H., Gierke, T.D. and Yang, H.H. (1983) *J. Polym. Sci., Polym. Phys.*, 21: 1955.

Reneker, D.H. and Mazur, J. (1983) Dispirations, disclinations, dislocations and chain twist in polyethylene crystals. *Polymer*, 24: 1387–1400.

Riewald, P.G. (1986) Performance analysis of an aramid mooring line. *18th Annual OTC*, Houston, TX, May 1986, Paper OTC 5187.

Riewald, P.G., Walden, R.G., Whitehill, A.S. and Koralek, A.S. (1986) Design and deployment parameters affecting the survivability of stranded aramid fibre ropes in the marine environment. *IEEE OCEANS '86, Conference Proceedings*, Washington, DC, September 1986, p. 284.

Schaefgen, J.R., Bair, T.I., Ballou, J.W., Kwolek, S.L., Morgan, P.W., Panar, M. and Zimmerman, J. (1979) Rigid chain polymers; properties of solutions and fibres. In: *Ultra-High-Modulus Polymers*, Chapter 6, A. Ciferri and I.M. Ward (Eds.). Applied Science Publishers, London.

Schoppee, M.M. and Skelton, J. (1974) Bending limits of some high modulus fibers. *Text. Res. J.*, 44: 968–975.

Sengonul, A. and Wilding, M.A. (1994) Flex fatigue in gel-spun high-performance polyethylene fibres. *J. Text. Inst.*, 87: 13–22.

Sengonul, A. and Wilding, M.A. (1996) Flex fatigue in gel-spun high-performance polyethylene fibres at elevated temperatures. *J. Text. Inst.*, 85: 1–11.

Sikkema, D.J. (2000) New developments in HM/HS fibres. *Polymer Fibres 2000 Conference*, Manchester.

Sikkema, D.J. (2001) In: *High Performance Fibres*, J.W.S. Hearle (Ed.). Woodhead Publishing, Cambridge.

Smit, L., Jacobs, M. and van Dingenen, J. (2000) Dyneema monofilaments, the strongest in the world. *Polymer Fibers 2000 Conference*, Manchester.

Staudinger, H. (1933) *Die hochmolekularen organischen Verbindungen*. Springer, Berlin.

Termonia, Y. and Smith, P. (1986) Theoretical study of the ultimate mechanical properties of poly(*p*-phenylene terephthalamide) fibres. *Polymer*, 27: 1845–1849.

Van der Zwaag, S. and Kampschoer, G. (1987) Paper presented at Rolduc Polymer Conference organized by DSM Central Research, Geleen, Netherlands.

Yang, H.H. (1993) *Kevlar Aramid Fiber*. Wiley, Chichester.

Fiber Fracture
M. Elices and J. Llorca (Editors)

FRACTURE OF SYNTHETIC POLYMER FIBERS

Yves Termonia

Central Research and Development, Building 001, Room 225, Experimental Station, E.I. du Pont de Nemours, Inc., Wilmington, DE 19880-0101, USA

Introduction 289
Model 289
Unoriented Fiber 289
Oriented Fiber 292
Results and Discussion 293
Drawing of Unoriented Fiber 293
Effect of Molecular Weight 293
Effect of Density of Entanglements 294
Effect of Drawing Conditions 295
Effect of Chain–Chain Interactions 296
Ultimate Tensile Strength of Oriented Fiber 297
Effect of Molecular Weight 298
Effect of Molecular Weight Distribution 299
Effect of Chain-End Segregation 300
Conclusions 301
References 302

Abstract

This paper reviews our Monte-Carlo lattice models for the study of the factors controlling the mechanical strength and mode of failure of flexible polymer fibers. We start by focusing on unoriented chain systems and investigate the dependence of their deformation behavior on chain length, density of entanglements and drawing conditions. We then turn to the case of the fully oriented polymer chain and study the importance of molecular weight and segregated chain-end defects in controlling the fiber ultimate

tensile strength. We show that our model predictions are in good agreement with available experimental data.

Keywords

Model; Strength; Drawing; Entanglements; Molecular weight; Segregation; Orientation

INTRODUCTION

The achievement of high mechanical stiffness and strength from flexible and linear commodity polymers has received extensive investigation over the last 20 years (Kinloch and Young, 1983; Ward, 1983). Tensile drawing of polyethylene fibers to very high draw ratios has allowed one to produce fibers with Young moduli above 100 GPa. In view of the obvious commercial interest in these materials, it is of primary importance to have a detailed knowledge of the factors controlling the tensile deformation and failure of solid flexible polymers.

Several models have been proposed for describing the orientation and morphological changes that occur during deformation of polymer fibers (Ward, 1983; Kausch, 1987). All these approaches are, however, essentially phenomenological or semi-empirical descriptions which provide no fundamental understanding of the phenomena occurring at the molecular level. In the present paper, we wish to present a more comprehensive approach which allows a unified description of polymer deformation and fracture encompassing all the effects of molecular weight, molecular weight distribution, defects, entanglement density, etc. . .

Before describing our approach, it is important to briefly describe how fibers are being processed in industry. Immediately after polymerization, polymer chains are in a random coil configuration and they can be compared to an agglomerate of 'cooked spaghetti', see Fig. 1a. The mechanical properties of these systems are extremely poor as any applied load is carried essentially by the weak attractive bonds between chains with little contribution from the strong chain backbone.

For that reason, these agglomerates are further processed by drawing into a fiber form wherein the polymer chains are now perfectly ordered and extended along the fiber axis, see Fig. 1b. In such a configuration, the strong covalent backbone chains play a crucial role and tensile mechanical properties are optimized. Experiments clearly indicate that the higher the draw applied to the macromolecular chains of Fig. 1a, the better their orientation in Fig. 1b and the higher the fiber tensile strength.

The present paper is organized as follows. We start by describing our molecular model for the study of the factors controlling the drawability (Fig. 1) of flexible polymer chains. Effects such as polymer molecular weight, density of entanglements and temperature of drawing are explicitly taken into account. We then present our model for the perfectly oriented fiber (Fig. 1b) and its mode of fracture. Our approach allows for both covalent and non-covalent bonds to break during deformation.

MODEL

Unoriented Fiber

Fig. 2 gives our model representation of the entangled solid polymer network prior to deformation (Termonia and Smith, 1987, 1988). The dots denote the entanglement loci. The dashed lines represent the weak attractive (Van der Waals) intermolecular bonds connecting sections of either the same chain or, of different chains. Since the

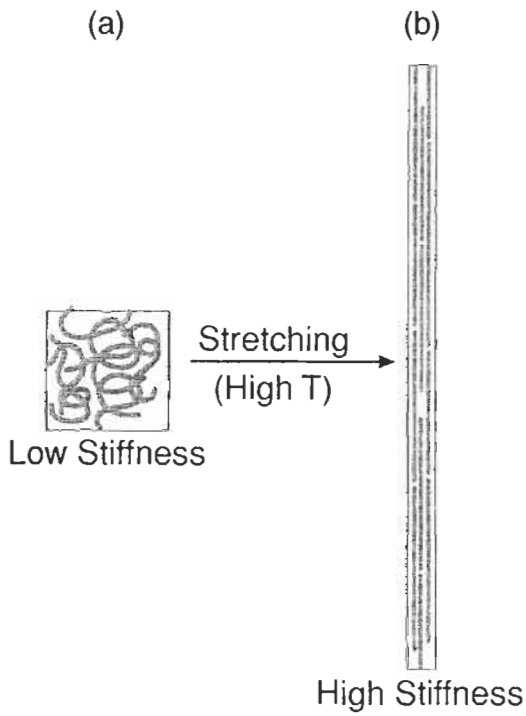

Fig. 1. (a) Network of polymer chains after polymerization. (b) Same network after drawing.

coordination number of an entanglement is assumed to be 4, the actual 3-dimensional network has been for convenience given a planar $x-y$ configuration. The y-axis is chosen as the direction of draw.

The network of Fig. 2 is deformed at a constant temperature T and a rate of elongation $\dot{\varepsilon}$. This leads to straining of the van der Waals (vdW) bonds which are broken according to the Eyring kinetic theory of fracture (Kausch, 1987), at a rate

$$v = \tau \exp\left[-(U - \beta\sigma)/kT\right] \tag{1}$$

In Eq. 1, τ is the thermal vibration frequency, U and β are, respectively, the activation energy and volume whereas

$$\sigma = K\varepsilon \tag{2}$$

is the local stress. In Eq. 2, ε is the local strain and K is the elastic constant for the bond. These vdW bond breakages lead to a release of the chain strands, which are now to support the external load. Once broken, vdW bonds are assumed not to reform.

As the stress of the 'freed' chain strands increases, slippage through entanglements is assumed to set in at a rate that has the same functional form as that for vdW breakings (Eq. 1) but, with different values for the activation energy U and volume β. In Eq. 1, σ now denotes the difference in stress in two consecutive chain strands that are separated by an entanglement. This stress difference is calculated using the classical treatment of

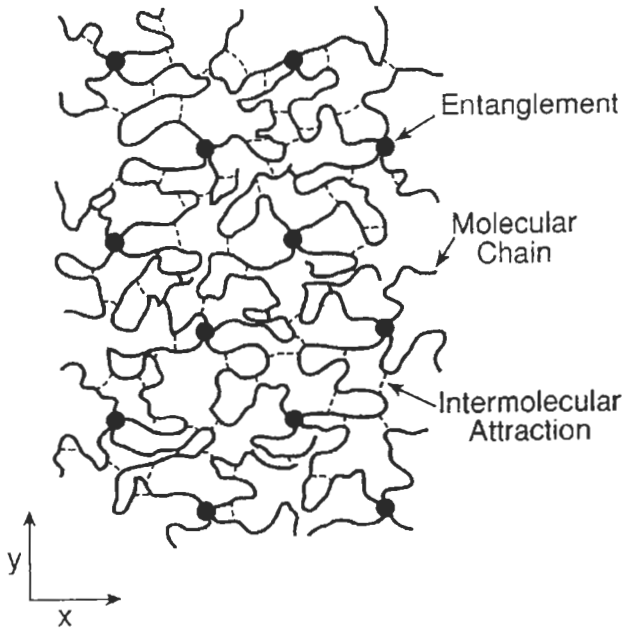

Fig. 2. Model representation of an unoriented polymer network. The dots represent entanglement loci and the dashed lines denote the van der Waals bonds.

rubber elasticity (Treloar, 1958. According to this theory, the stress on a stretched chain strand having a vector length $\boldsymbol{r}$ is given by

$$\sigma = \alpha k T L^{-1}(r/nl) \tag{3}$$

In Eq. 3, n denotes the number of statistical chain segments of length l in the strand. Also, L^{-1} is the inverse Langevin function and α is a proportionality constant.

Eqs. 1–2 for the vdW bond breaking process are implemented on the computer with the help of a Monte-Carlo lottery which breaks a bond i according to a probability

$$P_i = v_i / v_{\max} \tag{4}$$

in which v_i is obtained from Eq. 1, whereas $v_{\max}$ is the rate of breakage of the most strained bond in the array. After each visit of a bond, the time t is incremented by $1/[v_{\max} n(t)]$ where $n(t)$ is the total number of intact bonds at time t. The simulation of chain slippage through entanglements is executed using a similar technique. For that process, $n(t)$ now denotes the total number of entanglements left at time t.

After a very small time interval δt has elapsed, the vdW bond breaking, chain slippage and fracture processes are halted and the network is elongated along the y-axis by a small constant amount that is determined by the rate of elongation $\dot{\varepsilon}$. Subsequently, the network is relaxed to its minimum energy configuration. This relaxation is executed using a series of fast computer algorithms, described in Termonia et al. (1985), which steadily reduce the net residual force acting on each entanglement point. After these

relaxation steps, the Monte-Carlo process of bond breakings and chain slippage is restarted for another time interval δt. And so on and so forth, until the network fails.

Oriented Fiber

Our model representation of the oriented fiber is given in Fig. 3. The nodes in the figure represent the elementary repetition units of the polymer chains, i.e. methyl units for polyethylene. For very long chains, each node is made to correspond to more than one repetition unit (Termonia et al., 1985). The nodes are joined in the x- and z-directions by secondary bonds having an elastic constant K_2. These bonds account for the intermolecular vdW forces in polyethylene or hydrogen bonds in nylon. Only nearest-neighbor interactions are considered. In the y-direction, stronger forces with elastic constant K_1 account for the primary bonds, i.e. C–C bonds in polyethylene.

The network of bonds in Fig. 3 is deformed at a constant temperature T and strain rate $\dot{\varepsilon}$ using a Monte-Carlo process similar to that described for the unoriented case. Both primary and secondary bonds are allowed to break using the Eyring chemical

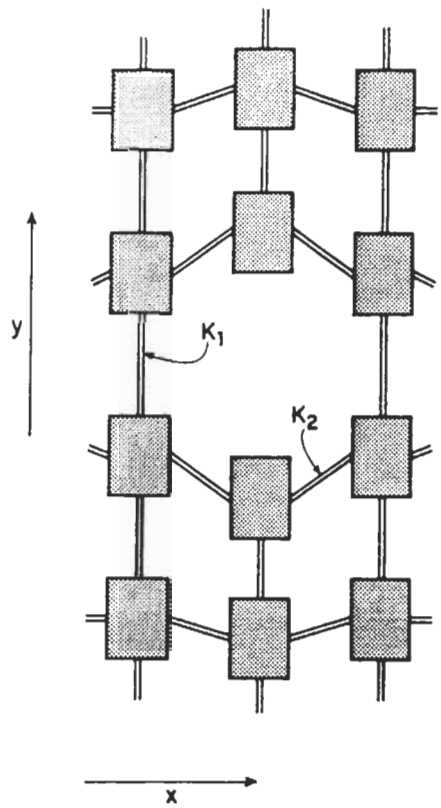

Fig. 3. Model representation of an oriented polymer fiber. K_1 and K_2 are the elastic constants for the primary and secondary bonds, respectively.

activation theory, see Eqs. 1 and 2. At regular time intervals, the network of bonds is relaxed towards mechanical equilibrium using fast convergence algorithms described in Termonia et al. (1985).

RESULTS AND DISCUSSION

Drawing of Unoriented Fiber

Effect of Molecular Weight

Fig. 4 shows a series of stress–strain curves obtained with the help of the model for three monodisperse polyethylene samples having different molecular weights (Termonia and Smith, 1987). The figure reveals that the three samples exhibit an identical behavior for elongations up to 75% (draw ratio = 1.75), which indicates a homogeneous loading of the vdW bonds. At larger elongations, the vdW bonds start breaking and the three samples exhibit a markedly different behavior. This is more clearly exemplified in Fig. 5. The low molecular weight material (Fig. 5a) exhibits brittle failure. At higher $M = 9500$ (Fig. 5b), necking is observed. As M is further increased, so does the number of necks and a micro-necking morphology (Fig. 5c) is obtained. Finally, at large $M = 250{,}000$ (Fig. 5d), the deformation becomes entirely homogeneous. A schematic illustration of the development of these various morphologies can be found in Termonia (2000).

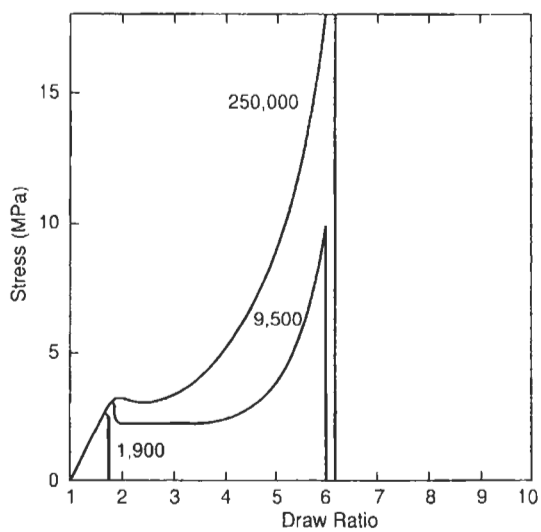

Fig. 4. Calculated stress–strain curves obtained for three monodisperse polyethylene samples having different molecular weights: $M = 1900$; $M = 9500$ and $M = 250{,}000$

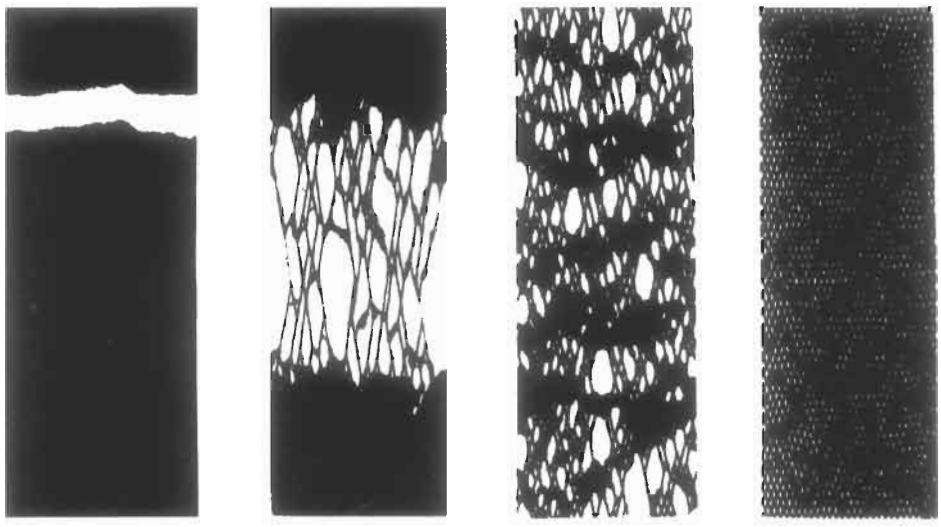

Fig. 5. Typical deformation schemes obtained from the model at different molecular weights. From left to right: $M = 1900$; $M = 8500$; $M = 20{,}000$ and $M = 250{,}000$.

Effect of Density of Entanglements

The results of Figs. 4 and 5 clearly show that the molecular weight has a weak influence on the drawability of flexible polymers. The largest draw ratio value $\lambda = 6$, obtained in Fig. 4, is indeed much too small to attain enough orientation, hence acceptable mechanical properties through tensile drawing. It is now well accepted that the density of entanglements in a polymer network can be easily controlled through a spacing factor ϕ defined as

$$\phi = \left(M_e / M_e^{\text{melt}}\right)^{-1} \tag{5}$$

in which M_e denotes the actual entanglement molecular weight value used in our simulations. Fig. 6 shows a series of nominal stress–strain curves calculated for monodisperse polyethylene of $M = 475{,}000$ at 5 different values of the entanglement spacing factor ϕ (1, 0.1, 0.04, 0.02 and 0.004). The figure shows a dramatic dependence of polymer drawability on the entanglement spacing factor. At $\phi = 0.02$, the draw ratio at break reaches values as high as 45 which are in the range of those required for the attainment of good orientation, hence acceptable mechanical strength. At much lower $\phi = 0.004$, the elongation at break shows a sudden drop and brittle failure is observed. The latter is due to the fact that at $\phi = 0.004$, the molecular weight between entanglements is now comparable to that for the entire chain.

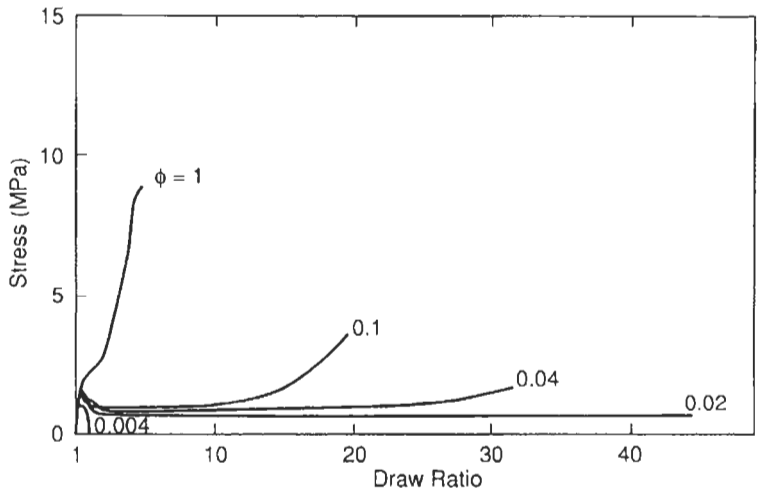

Fig. 6. Calculated stress–strain curves obtained for linear polyethylene ($M = 475{,}000$) at four different values — indicated in graph — of the entanglement spacing factor ϕ (see text).

Effect of Drawing Conditions

Experimental data (Capaccio et al., 1980; Kanamoto et al., 1988) seem to indicate that, for each molecular weight, there exists an optimum drawing temperature and most likely — because of time/temperature superposition principles — an optimum draw rate. Fig. 7 shows the calculated dependence of the maximum draw ratio on drawing temperature and drawing rate for a monodisperse $M = 143{,}000$ (Termonia et al., 1988). These figures reveal the existence of a very narrow temperature (at constant rate) and rate (at constant T) window within which drawability is maximized. Under these optimum conditions, a maximum draw ratio of 23 is obtained. A careful inspection of

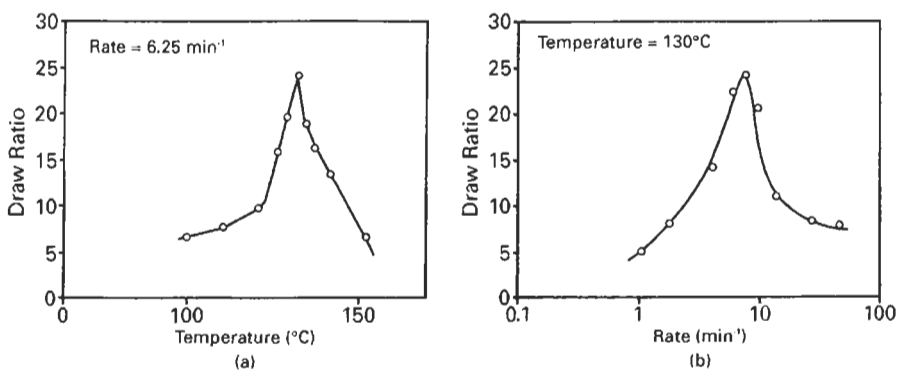

Fig. 7. Calculated dependence of the maximum draw ratio on testing conditions for polyethylene with $M = 143{,}000$. (a) Dependence on temperature at constant elongation rate (6.5/min). (b) Dependence on elongation rate at constant temperature ($T = 130°C$).

our model results of Fig. 7a reveals that, as the temperature of deformation is increased, slippage of chains through entanglements sets in. That process leads to an effective increase in the number n of statistical segments between entanglements and to an increase in the draw ratio at break. However, at much higher temperatures $T > 130°C$, chain slippage becomes substantially faster than the elongation rate. As a result, chains rapidly disentangle and drawability decreases. Further study reveals that, for every molecular weight value, there exists an optimum temperature (or rate) window within which drawability can be optimized. This, in turn, indicates that these effects will not be observed for polydisperse molecular weights as every single chain length will have its own optimum window which will be different from those for the other chains.

Effect of Chain–Chain Interactions

All the results presented so far were for polyethylene for which chain–chain interactions are limited to weak vdW interactions. We now turn to a study of the importance of stronger chain–chain interactions, such as hydrogen bonds, on the chain drawability (Termonia, 1996). The results are presented in Fig. 8 for flexible chains having $n = 50$ statistical segments between entanglements. The latter corresponds to a maximum draw ratio $\lambda_{max} = 10$ (Termonia and Smith, 1988; Termonia, 1996). The figure shows the dependence of drawability on the modulus E_h of the attractive bonds between chains. At small $E_h < 0.1$ GPa, which covers the range of the weak vdW bonds in polyethylene, all the samples can be easily drawn up to their maximum achievable value $\lambda_{max} = 10$. At higher E_h values, the draw ratio shows a dramatic decrease within a very narrow interval $0.1 < E_h < 0.3$ GPa. Examination of our computer results reveals that the decrease in drawability with an increase in E_h is also associated with a change in morphology of deformation from neck formation to brittle fracture.

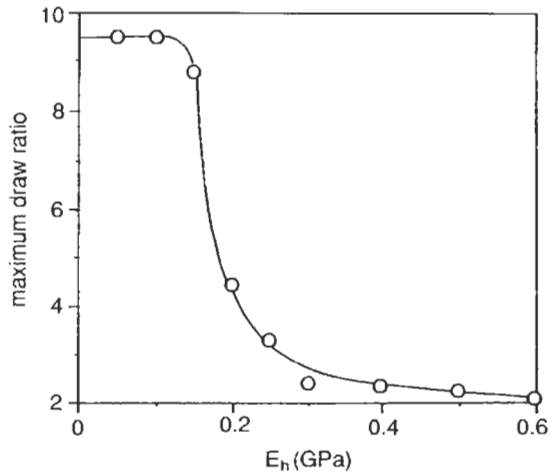

Fig. 8. Calculated dependence of the maximum draw ratio on the modulus E_h of the attractive bonds between chains.

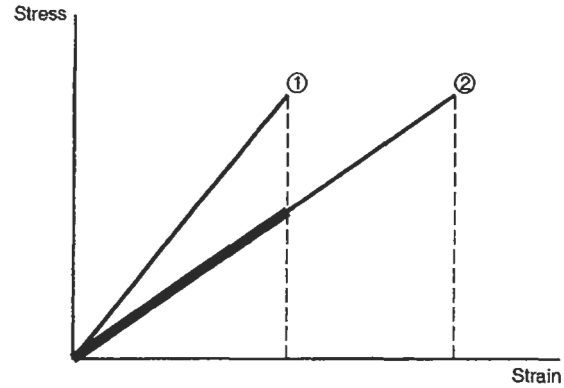

Fig. 9. Two possible routes for improving the tensile strength of a fiber with stress–strain curve indicated by the heavy line.

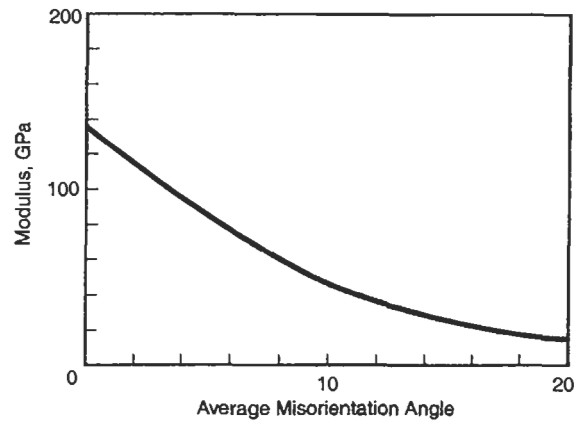

Fig. 10. Calculated dependence of modulus on average misorientation angle of the macromolecules with respect to the fiber axis.

Ultimate Tensile Strength of Oriented Fiber

In the present section, we will assume that the network of polymer chains has been successfully drawn to a large value of the draw ratio, leading to a high degree of orientation of the macromolecules along the fiber axis, see Fig. 1b. We now focus on how to further improve the mechanical properties of that fiber. To this end, let us assume that the latter has a stress–strain curve as represented by the heavy line in Fig. 9. There are two basic routes for improving tenacity. Route (1) consists in increasing the modulus of the fiber, i.e. further improving the molecular orientation of the polymer chains. In Route (2), the modulus stays constant but the elongation at break is increased by removing the defects in the fiber.

Let us start by investigating the usefulness of Route (1). Fig. 10 shows model predictions for the dependence of the fiber modulus on the average misorientation angle

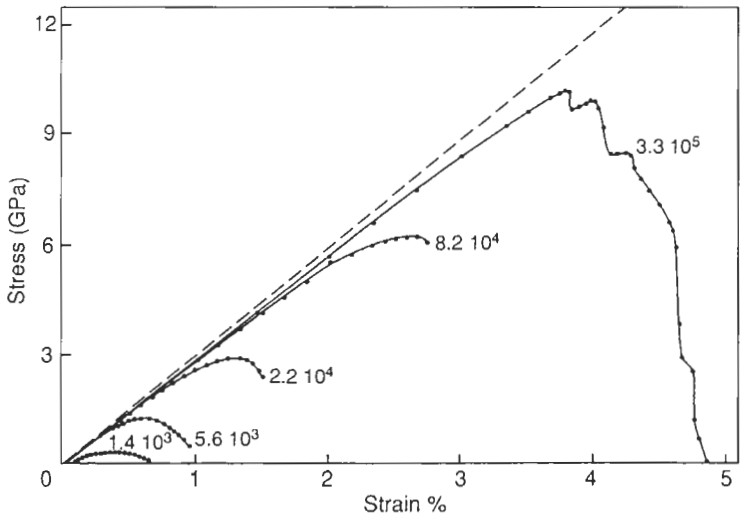

Fig. 11. Calculated stress–strain curves for perfectly ordered and oriented polyethylene fibers. The curves are for different molecular weights. The testing temperature is set equal to room temperature and the rate of elongation equals 100%/min.

ϕ of the polymer chains with respect to the fiber axis. Typical experimental high strength fibers can be easily drawn to ϕ values less than 4–6°. Inspection of Fig. 10 therefore reveals that, assuming that ϕ can be further reduced to values close to 0, we can at best improve the fiber modulus by 20–30%, which does not seem worthwhile.

We now turn to study the usefulness of Route (2) which consists in removing defects. For simplicity, we restrict ourselves to defects of molecular origin such as, molecular weight, molecular weight distribution and chain-end segregation.

Effect of Molecular Weight

Fig. 11 shows a series of calculated stress–strain curves for perfectly oriented polyethylene fibers of various molecular weight values (Termonia et al., 1985). At low molecular weights ($M < 8 \times 10^4$), our results indicate a substantial amount of breaking of vdW bonds with little or no rupture of covalent backbone bonds. Under such circumstances, plastic deformation is observed and the curves are bell-shaped with a very slow decrease in the stress towards the breaking point. At higher molecular weights, we observe rupture of both vdW and covalent backbone bonds and, as a result, the fracture of the sample seems more of a brittle nature. Inspection of the figure reveals a rather weak dependence of the initial modulus on molecular weight. The tensile strength (maximum of the curves), on the other hand, is seen to increase with molecular weight. Our model results for the dependence of tensile strength σ on molecular weight M are summarized in Fig. 12. No well-defined power law for the dependence of σ on M is observed. This is because (1) at low M, the mode of fracture changes from plastic into brittle deformation, and (2) at very large M, the curve reaches a plateau corresponding to

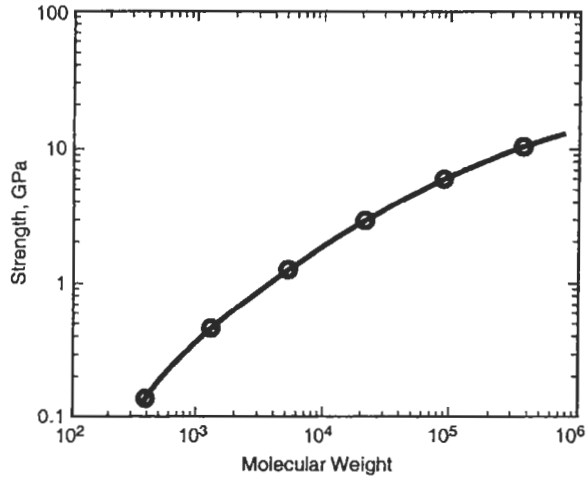

Fig. 12. Calculated dependence of the tensile strength on molecular weight.

the intrinsic strength of the C–C bond. Yet, within the range of commercial interest $2 \times 10^4 < 3 \times 10^5$, the ultimate tensile strength increases as $M^{0.4}$.

Effect of Molecular Weight Distribution

In order to study the importance of the molecular weight distribution, we turn to a bimodal system made of short chains with $M = 5000$ mixed with longer ones with

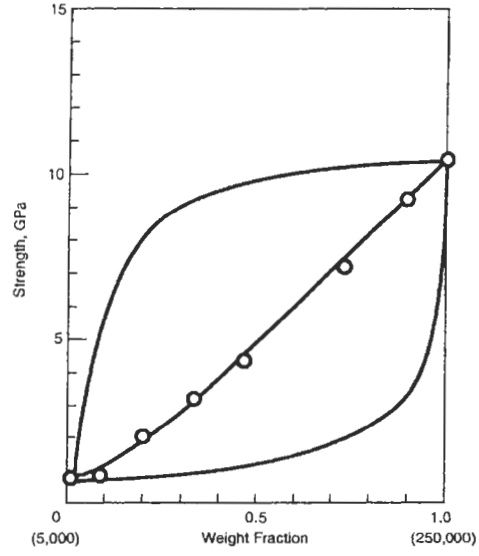

Fig. 13. Calculated dependence of the strength on composition for a blend of $M = 5000$ with $M = 250{,}000$.

$M = 250{,}000$. The dependence of fiber strength on blend composition is studied in Fig. 13 (Termonia et al., 1986). Intuitively, one could have expected that the addition of only a small amount of the high molecular weight component would lead to a tremendous increase in fiber strength (upper curve). Alternatively, one could argue that a minute amount of short chains in a high M fiber would have a deleterious effect on mechanical properties (lower curve). Actual model results (circles) indicate that neither of these two scenarios applies and the tensile strength for the blend follows the weight average summation of the two-component properties.

Effect of Chain-End Segregation

It is well known that chain ends easily segregate during crystallization of polymers and more generally in all polymeric systems under conditions of relatively great

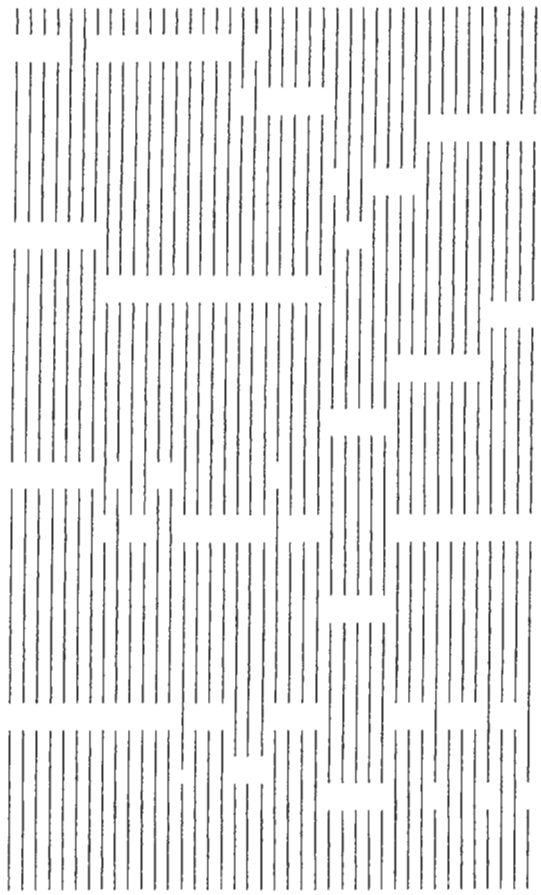

Fig. 14. Segregated structure for a fiber having diameter $d = 40$ lattice units (compare with Fig. 1b).

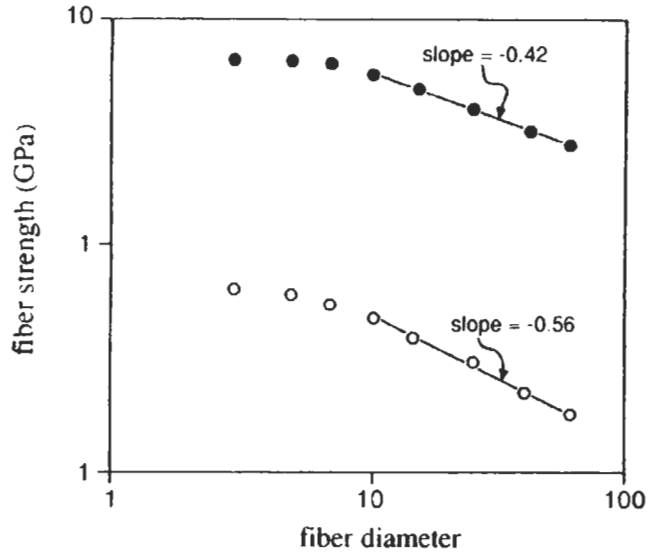

Fig. 15. Calculated dependence of fiber strength on diameter for two close-to-monodisperse polyethylenes with $M_w = 2800$ (circles) and $M_w = 180{,}000$ (dots).

mobility, such as in solution processing. In the present section, we refine the original model of Fig. 1b to take into account the effect of fiber dimensions and molecular weight on segregation extent and ultimate strength. Fig. 14 shows a typical segregated structure using a model for chain diffusion, described previously (Termonia, 1995). The model maximizes the extent of segregation for a given fiber diameter. The mechanical properties of these structures are studied in Fig. 15 for two values of the molecular weight: $M_w = 2800$ and $M_w = 180{,}000$. For large enough fiber diameters, the figure reveals that the strength, σ, decreases as $\sigma \approx d^{-0.42}$ and $\sigma \approx d^{-0.55}$ for the high and low molecular weights, respectively.

CONCLUSIONS

We have reviewed several Monte-Carlo lattice models for the study of the factors controlling the mechanical strength and mode of failure of flexible polymer fibers. We started by focusing on unoriented chain systems and investigated the dependence of their deformation behavior on chain length, density of entanglements and drawing conditions. The models were able to describe the wide variety of deformation morphologies — i.e. brittle fracture and necking — observed experimentally. We found that the attractive forces between chains play a crucial role in controlling the maximum drawability of the chains. Thus, vdW interactions such as those appearing in polyethylene are easily broken during polymer deformation and do not hinder drawability. This is not the case, however, for the hydrogen bonds in nylon which seriously restrict the orientation that can be imparted to the chains during tensile drawing. We then turn to the case of

the fully oriented polymer chain and study the importance of molecular weight and segregated chain-end defects in controlling the fiber ultimate tensile strength. We find a rather weak dependence of the maximum strength on molecular weight, $\sigma \approx M^{0.4}$. Molecular defects, on the other hand, are found to have a profound effect on fiber mechanical properties. We show that our model predictions are in good agreement with available experimental data.

REFERENCES

Capaccio, G., Crompton, T.A. and Ward, I.M. (1980) *J. Polym. Sci.: Polym. Phys. Ed.*, 18: 301.
Kanamoto, T., Tsuruta, A., Tanaka, K., Takeda, M. and Porter, R.S. (1988) *Macromolecules*, 21: 470.
Kausch, H.H. (1987) *Polymer Fracture*. Springer, Berlin, 2nd ed.
Kinloch, A.J. and Young, R.J. (1983) *Fracture Behavior of Polymers*. Applied Science, London.
Termonia, Y. (1995) *Polym. Sci.: Part B: Polym. Phys.*, 33: 147.
Termonia, Y. (1996) *Macromolecules*, 29: 4891.
Termonia, Y. (2000) In: *Structural Biological Materials*, p. 271, M. Elices (Ed.). Pergamon Materials Series, Elsevier, Oxford.
Termonia, Y., Greene, W.R. and Smith, P. (1986) *Polym. Commun.*, 27: 295.
Termonia, Y. and Smith, P. (1987) *Macromolecules*, 20: 835.
Termonia, Y. and Smith, P. (1988) *Macromolecules*, 21: 2184.
Termonia, Y., Meakin, P. and Smith, P. (1985) *Macromolecules*, 18: 2246.
Termonia, Y., Allen, S.R. and Smith, P. (1988) *Macromolecules*, 21: 3485.
Treloar, L.R.G. (1958) *The Physics of Rubber Elasticity*. Clarendon, Oxford, 2nd ed.
Ward, I.M. (1983) *Mechanical Properties of Solid Polymers*. Wiley, New York, 2nd ed.

Fiber Fracture
M. Elices and J. Llorca (Editors)

FRACTURE OF NATURAL POLYMERIC FIBRES

Christopher Viney

Department of Chemistry, Heriot-Watt University, Edinburgh EH14 4AS, Scotland, UK

Introduction 305
A Traditional View of Natural Fibres 305
Nature Revisited 306
Some Thoughts on the Meaning of 'Brittle' 307
Fracture of Natural Self-Assembled Fibres 308
Self-Assembly Favours the Formation of Fibrous, Hierarchical Structures . . 308
Primary and Secondary Bonds Can Have Direct, Distinguishable, Complementary Effects on Fibre Mechanical Properties 309
A Hierarchical Structure Optimises Toughness 310
Water Plays Multiple Roles in the Assembly and Stabilisation of Natural Fibres 311
The Fracture Characteristics of Natural Fibres Can Be Sensitive to Prior Deformation 312
In a Hierarchical Fibre Microstructure, Molecules That Have 'Melted' Can Continue to Carry Loads Usefully 313
The Experimental Methods Used for Characterising the Failure Strength and Other Mechanical Properties of Fibres Must Be Appraised Carefully 315
Conditioning 315
Cross-Sectional Area Characterisation 316
Force Characterisation 317
The Statistical Basis of Fibre Failure Analysis 317
Echinoderm Collagens: Fibre Optimisation in Smart Composites 320
Tensile Property Control 320
Tapered Fibres 320
Acknowledgements 325
References 325

Abstract

Traditional users of natural fibres achieve effective property control at the length scale of yarns, but are able to exercise only limited intervention at the length scale of molecules. Advances in biotechnology, and in understanding nature's processes of self-assembly, offer the possibility of refining structure and properties at all length scales. We consider the factors that are especially important to fibre assembly and therefore to fracture management in this interdisciplinary context. Several desirable consequences of self-assembly and hierarchical structure are catalogued. Hierarchical structures are recognised as providing enhanced toughness compared to just a fine structure. The role of water in ensuring the stability and performance of natural self-assembled fibres is emphasised, along with its implications for biomimetic materials. Loss of structural order is shown to be commensurate with retention — even enhancement — of load-bearing ability in certain cases. The collagen fibres that reinforce composite tissues of echinoderms are highlighted as a source of several stimulating lessons for materials engineering. The lessons include dynamic control of fibre strength and stiffness, and the use of elongated tapered fibres to optimise exploitation of the load carried per unit volume of fibre.

Keywords

Actin; Collagen; Fibre; Fracture; Hydrophobic bond; Myosin; Nature; Self-assembly; Silk; Smart composite; Structural hierarchy; Toughness

INTRODUCTION

A Traditional View of Natural Fibres

Natural polymeric fibres have (literally) supported the development of human civilisation since its prehistoric beginnings. A particularly prominent role has been played by cellulose, a *polysaccharide* which is one of the world's most abundant and versatile fibrous polymers. Cellulose fibres are the reinforcing component of wood, a natural composite that can be fashioned into devices used for shelter, transportation, agriculture, war, communication, ornament and recreation. Cellulose fibres have been woven into clothing, twisted into ropes and bowstrings, and processed into papyrus and paper. Fibrous *proteins*, especially keratin (wool, mohair), collagen (hide, parchment, catgut) and silk also have a rich history and an assured future as useful materials.

There is an extensive literature on the properties — including the fracture characteristics — of fibrous polysaccharides and proteins. Most is written from the perspective of textile science, where traditionally the greatest practical and financial interest in these materials has been concentrated. Analysis of the failure of textile fibres is subject to the following considerations.

(1) Individual natural filaments are too fine and/or too short to be easily used on their own in the weaving of cloth or the reinforcing of composites. Instead, *bundles* of filaments are combined into macroscopic *yarns*.

(2) The bundles are *twisted* to help distribute load among the filaments (Hearle et al., 1980; Warner, 1995). This is necessary because the filaments have polydisperse fracture characteristics: some are weaker than others, so an efficient load transfer mechanism must be in place to compensate for prematurely broken filaments. Increasing the twist leads to enhanced friction and transfer of load within the yarn, and may also increase strength by inactivating defects in the filaments. The effect of twisting on friction and defects can be modelled empirically, phenomenologically, or statistically.

(3) In an axially loaded yarn, the individual twisted filaments are not themselves loaded axially; in other words, the filaments are not loaded along their strongest direction. Therefore, although some consequences of increasing the twist will tend to increase the yarn strength, other consequences will tend to decrease the strength. The net result is that maximum strength is achieved with moderate twist (Warner, 1995).

(4) Failure and other mechanical properties do not only depend on structure at or above the length scales of individual filaments. Structure at smaller length scales is important too.

When native natural fibres are used in conventional textile yarns, the manufacturer has control over the macroscopic degree of twist imparted to the filaments, and (within limits) the length of filaments used. However, (s)he at best has only partial control over structure and properties at length scales smaller than that of the filaments. At these smaller length scales, *nature* controls the structural variables that will dictate fibre strength: the primary structure (monomer sequence) of the polymer chains, the conformation (shape) of the chains, and the supramolecular organisation of the chains. Often the chains adopt hierarchical helical structures, exemplified by those in keratin (Fig. 1). Combined with the macroscopic twist in yarns, the molecular and

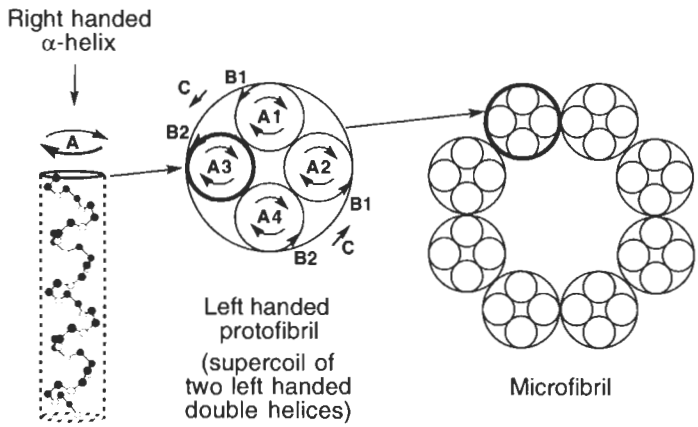

Fig. 1. Hierarchical structure of a keratin microfibril, showing the molecular (A), double-helical (B) and supercoil (C) twists in the constituent protofibrils. The representation of a molecular α-helix shows only the $[-N-C-C-]_n$ backbone for clarity. Note that the twists A occur in the opposite sense to twists B and C. If an attempt is made to stretch the microfibrils, unwinding of twists A is resisted by tightening of twists B and C, and unwinding of twists B and C is resisted by tightening of twists A. The hierarchy of structural order therefore confers stability on the structure. In topological respects, we can regard this hierarchical structure as a well-engineered small-scale version of a rope or yarn. Nature got there first.

supramolecular twists further decouple the net macroscopic mechanical properties of the material from the intrinsic properties of the constituent polymer. Macroscopic properties can therefore be *modified* by subjecting the native fibre to microstructurally invasive processes such as weighting (silk: Chittick, 1913), mercerising (cotton: Nishimura and Sarko, 1987) or 'mothproofing' (wool: Billmeyer, 1984), but the degree of reproducible property *control* in each case is limited.

Nature Revisited

Over the past two decades, we have substantially increased our understanding of how nature produces organic fibres by polymerising available monomers into controlled sequences and then *self-assembling* the product macromolecules into hierarchical microstructures. Progress has been catalysed by a renaissance in interdisciplinary science, drawing on knowledge from the traditionally distinct fields of physiology, engineering, materials characterisation and textile science, and incorporating convergent developments from the emerging disciplines of biotechnology and nanotechnology. Lessons derived from observing nature, along with discoveries about how to manipulate nature at the molecular level, have significantly expanded our expectations for fibrous proteins, polysaccharides and other natural polymers.

(1) The primary structure (amino acid sequence) and the molecular weight of fibre-forming proteins can be controlled *exactly* by genetic engineering. The amino acids need not necessarily be those that are found in nature (Tirrell et al., 1997). In the case of polysaccharides (Linton et al., 1991) and polyesters (Steinbüchel, 1991), the yield and/or composition of the polymer can be controlled.

(2) Polymers synthesised via biotechnological routes can be produced in quantities that enable the economically viable spinning of continuous fibres (Brown and Viney, 1999). Spinning these under controlled conditions offers the promise of cross-sectional uniformity and improved strength reproducibility. The benefits of continuous fibres and artificial spinning have in fact been long established in the context of cellulose fibre (e.g. rayon, Tencel®) regenerated from solution: both strength and strength reliability are improved by eliminating the polydispersity of fibre length, by reducing the variability in fibre cross-section, and by maintaining a reproducible microstructure. In principle it should be possible to spin silk-like, keratin-like and collagen-like proteins into fibres, though it may not always be easy or even possible to mimic the microstructure and properties of the native material.

(3) Much is now known about the processes of supramolecular *self-assembly* by which complex materials are formed in nature. Building on this knowledge, we may look forward to a future in which molecules can be 'preprogrammed' to organise into fibrous structures, by-passing the need for energy-intensive, dangerous and/or environmentally undesirable processes. (We must however bear in mind that nature's thermodynamically attractive routes to high-performance self-assembled materials are a consequence of life operating under near-equilibrium conditions. Kinetically, nature's self-assembly routes are less successful, producing material at rates that are not economically attractive for making large objects at present.)

(4) Self-assembly is a promising route for producing small (fine) fibres in nanocomposites, where a high fibre–matrix interfacial area confers enhanced toughening and ensures efficient load transfer to the fibres.

Some Thoughts on the Meaning of 'Brittle'

For engineering design purposes it is useful to label the fracture behaviour of a material as either brittle or not. There is no single antonym of 'brittle', as 'tough' and 'ductile' are not always interchangeable. The distinction between brittle and non-brittle materials is sometimes intuitive, but materials with borderline characteristics (e.g. limited plasticity) are common. Also, as will be discussed further in the section 'The Fracture Characteristics of Natural Fibres Can Be Sensitive to Prior Deformation', the characteristics of a material can change from non-brittle to brittle during the course of deformation. Researchers who specialise in the different classes of material do not use identical definitions of brittleness (even though their intended meanings are equivalent), and some differences in usage are evident between materials science and materials engineering. Such differences are inevitable when a topic is surveyed across a wide interdisciplinary landscape. In this paper, we will encounter four nuances of the term 'brittle'.

(1) A brittle material can be identified in *microstructural* terms as one that has no effective physical features or mechanisms for hindering the growth of cracks.

(2) Alternatively, a *phenomenological* description is possible by simply noting that cracks propagate rapidly through a brittle material.

(3) The Griffith formula (Cottrell, 1975, and Eq. 1) relates the breaking strength of a material to the length of pre-existing cracks, the tensile stiffness (Young's mod-

ulus) of the material, and γ, the *energy per unit area of new surface* created by the crack. The latter factor embraces both the intrinsic surface energy (i.e. the energy associated with breaking bonds in the interior of the material and replacing these with material–environment contacts) and the energy expended in effecting any associated microstructural rearrangements. A brittle material is characterised by a low value of γ.

(4) A *statistical* definition of brittleness can be formulated in terms of the Weibull distribution of fracture probability for a material (Derby et al., 1992). The Weibull modulus m (see Eq. 2) can range from zero (totally random fracture behaviour, where the failure probability is the same at all stresses, equivalent to an ideally brittle material) to infinity (representing a precisely unique, reproducible fracture stress, equivalent to an ideally non-brittle material).

FRACTURE OF NATURAL SELF-ASSEMBLED FIBRES

Genetic engineering and supramolecular self-assembly offer a wide scope for controlling fibre composition and microstructure. The number and variety of materials that could be engineered with these techniques is extremely large. Much effort will be required to comprehensively characterise and efficiently refine the load-bearing properties of the new fibres. It is therefore opportune to reflect on the factors that determine the characteristics of hierarchical microstructure in natural fibres, and the ability of such microstructures to resist fracture.

Self-Assembly Favours the Formation of Fibrous, Hierarchical Structures

Fibrillar structures are a common consequence of supramolecular self-assembly in nature. The association of polymer molecules that have an anisotropic shape will tend to propagate that anisotropy at higher length scales, and globular polymers that have an uneven distribution of charge at their surface will similarly reflect their molecular-scale anisotropy when they aggregate. If there is a tendency towards anisotropic aggregation, this will promote the formation of liquid crystalline phases, which synergistically reinforces the tendency for anisotropic growth of the aggregates (Renuart and Viney, 2000).

Self-assembly additionally imparts a hierarchical structure to fibres. To maximise fibre growth rates from solution, it is essential that material transport paths should be as short as possible. A given cross-section can be assembled more effectively in a given time if it consists of several fibrils developing in parallel, rather than a monolith. This principle is evident in many collagens (Stryer, 1988; Rawn, 1989; Gorham, 1991), and is advantageous for the construction of hollow tubes as exemplified by microtubules (Hyams and Lloyd, 1994; Lodish et al., 1995). There is mounting evidence that silk fibres, which must solidify quickly under significantly non-equilibrium conditions and therefore can certainly benefit from short transport paths, also contain a hierarchy of fibrils and sub-fibrils (Augsten et al., 2000; Putthanarat et al., 2000; Poza et al., 2002). However, describing the mechanism whereby silk fibre microstructures self-assemble remains a challenging question.

Primary and Secondary Bonds Can Have Direct, Distinguishable, Complementary Effects on Fibre Mechanical Properties

The charge distribution involved in stabilising a bond can be used to compute the bond energy, from which the force needed to break the bond can in turn be derived. Crystallographic information can be used to determine how many such bonds must be broken per unit area of simple fracture surface. The *intrinsic* strength of any material can therefore be calculated from first principles (Kelly and Macmillan, 1986). This fundamental contribution to strength is often modified at higher length scales. For example, we have noted in the section 'A Traditional View of Natural Fibres' that the extrinsic properties of conventional textile yarns are not related in a simple way to the intrinsic properties of the constituent polymers; mechanical interactions between filaments are especially challenging to quantify accurately. In contrast, if we are concerned with individual filaments that have been produced entirely by self-assembly, then the properties of the chemical bonds between subunits (at whatever length scale) will be directly reflected in the properties of the filament.

As an example that will recur throughout this paper, consider the case of actin (Fig. 2). The many roles of this protein include load transmission (muscle fibres), contributions to cell structure and motility (microfilaments) and barrier penetration (sperm acrosomes) (Oster et al., 1982; Tilney and Inoué, 1982; Lodish et al., 1995; Stryer, 1995). Actin has a well defined molecular weight (41.8 kDa: Alberts et al., 1989), and is constructed from a specific sequence of amino acid monomers. Each actin chain naturally folds into a non-spherical globular conformation, that can fit into a space approximately $5.5 \times 5.5 \times 3.5$ nm (Kabsch and Vandekerckhove, 1992). In deference to their shape, these globular molecules are conventionally referred to as *G-actin*. G-actin self-assembles into a right-handed, double-helical, elongated aggregate (Fig. 2) that is called *F-actin* to acknowledge its fibrous structure. From the point of view of these fibrous aggregates, the G-actin molecules act as monomers, so the term 'monomer' always has to be interpreted in context.

- Two distinct domains can be identified in each G-actin molecule; the gap between

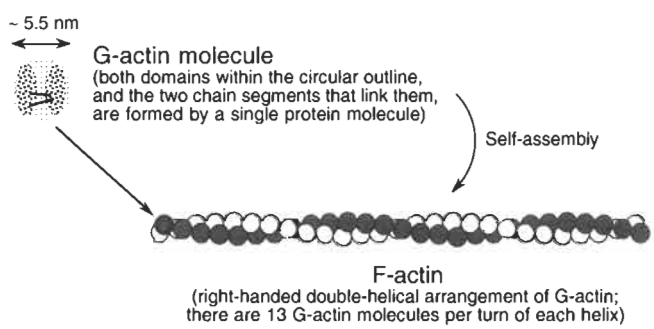

Fig. 2. Molecular and supramolecular features in the hierarchical structure of F-actin. Each circle corresponds to one G-actin molecule. In the depiction of F-actin, the empty and filled circles represent distinguishable helical strands. Self-assembly and stability require the presence of water.

the domains is crossed twice by the protein backbone, forming a hinge that enables actin fibre to exhibit torsional flexibility. Thus, one mechanical property of the fibre is controlled at the *molecular* length scale, by *primary* (covalent) bonds.

- The ability of actin fibre to maintain rigidity and strength under tension (necessary in its load-transmitting roles) depends on the forces that bind G-actin into aggregates. Thus, some mechanical properties of the fibre are controlled at a *supramolecular* length scale, by *secondary* (non-covalent) bonds.
- Because the intermolecular secondary bonds are weaker than the intramolecular primary bonds, the fibre can fail without destroying the integrity of the constituent molecules. The molecules are therefore immediately available for repairing the fibre.

A hierarchical structure can therefore enable different mechanical properties to be selectively and independently tailored by different aspects of that structure. While it is possible in the case of actin to identify specific structural features and bonding types with specific mechanical properties, there are many hierarchical biological fibres for which the corresponding associations are more complex and have yet to be determined fully. As an example, let us consider spider dragline silk (strictly: silk from the major ampullate glands of spiders). The unique combination of mechanical properties exhibited by this fibre can be described qualitatively in terms of a multi-phase microstructure (Viney, 2000). Progress has also been made towards developing quantitative links between microstructure and some individual mechanical properties of this material (Termonia, 2000). However, several microstructure–property relationships for silk — including the nature of the flaws that appear to be ultimately responsible for fracture (Pérez-Rigueiro et al., 1998) — remain to be resolved.

If we know how the hierarchical microstructure of a material is *assembled*, we are in a good position to understand how that microstructure will be *deconstructed* as the material fails. Which bonds are most susceptible to being disrupted will depend on how the sample is loaded (in tension, compression, bending or torsion); we have noted in the case of actin how different microstructural features confer resistance to failure in different loading geometries.

A Hierarchical Structure Optimises Toughness

In courses on materials engineering, we learn almost from day one that toughness requires a *fine* microstructure, with no mention of hierarchy. Here we consider whether a *hierarchical* microstructure confers any toughening benefits additional to those associated with a fine microstructure.

The need for a fine microstructure is usually encountered and justified in the context of the Griffith formula, which quantifies the stress σ needed to propagate a pre-existing crack through a metal or ceramic material (Cottrell, 1975):

$$\sigma \cong \left(\frac{E\gamma}{c}\right)^{1/2} \tag{1}$$

where c is the length of a surface crack (or half the length of an internal crack), E is Young's modulus, and γ is the energy per unit area of new surface created by the crack. According to Eq. 1, the breaking strength remains high if crack lengths can be kept

small. Provided that cracks are *initially* smaller than the grain size, high toughness is ensured: grain boundaries are effective as obstacles to crack growth, and they contribute to the factor γ in Eq. 1. In the case of a fibrous polymer we have to interpret 'grain size' as the linear dimension of a structural subunit in the direction of initial crack growth, and 'grain boundaries' become the interfaces between such subunits. A fine microstructure, which is able to deflect cracks along complex paths, is synonymous with high toughness. A coarse microstructure can accommodate large crack lengths within a grain (or crystal, or other subunit), and so is associated with a low stress to trigger catastrophic failure.

However, sometimes a crack will not initiate within a microstructure but will be *imposed* on the material from outside, for example by impact or cutting. In such circumstances, it is useful if the material contains interfaces that can impede the growth of an *initially large* crack. Such interfaces must (a) be separated by large distances (to accommodate a large crack between them, while not significantly diminishing the load-carrying capacity of the material as a whole), and (b) have geometrical and failure characteristics that interact optimally with the stress field of a large crack.

These requirements can be met by a microstructure that is hierarchical, where different scales of structure can stop different sizes of crack. Although microstructural hierarchy of natural fibres is a fortuitous consequence of fibre self-assembly, it is also a fortunate consequence. It allows independent optimisation of several mechanical properties, and it confers damage tolerance as well as toughness. Fibrous materials that have a hierarchical microstructure are able to fail gracefully.

Water Plays Multiple Roles in the Assembly and Stabilisation of Natural Fibres

Most of the steps involved in the synthesis and assembly of biological fibrous materials take place in the presence of water. The water acts as a solvent and transport medium for reactants. It also can play a significant role in promoting adhesion between biological macromolecules, for example the G-actin monomers in F-actin. The driving force is entropic. G-actin molecules that have become aggregated will immobilise significantly fewer water molecules compared to the same number of independent G-actins, so the entropy of the *water* increases. Although aggregation necessarily decreases the G-actin entropy, the accompanying increase in the disorder of water is more than enough to compensate (Steinmetz et al., 1997; Tuszynski et al., 1997). For every G-actin molecule that is added to an aggregate, several water molecules can be liberated. Thus, the water does not act as a 'glue' linking G-actin molecules, but rather serves to promote association of G-actins by virtue of being *excluded* from the space between them. An analogy is provided by 'non-stick' hydrophobic Teflon® surfaces, which can develop a strong affinity for other hydrophobic materials when immersed in water.

Many natural fibrous materials are stabilised by this type of *hydrophobic bonding* between structural subunits at one or more length scales. Examples (Renuart and Viney, 2000) include keratins, collagen, silk, viral spikes, actin and tubulin. Materials such as the latter three are optimised for continuous use in an aqueous environment, in which case hydrophobic bonds may provide a particularly significant source of stability. Property measurements, including tensile testing to failure, performed in air

are of questionable value for characterising such materials, and there is little point in expecting such materials to retain their optimum functionality in a dry environment. Attempts to spin fibres from genetically engineered analogues of viral spike protein, to produce material of similarly high compressive strength, have yielded disappointing results (Hudson, 1997). The native spikes rely on hydrophobic bonding to maintain their structure. Measured in air, their mechanical properties, and the properties of correctly assembled fibres based on analogous proteins, must therefore be inferior compared to results obtained in water. If a natural material is designed to work in an aqueous medium, attempts to mimic its properties must take this reality into account.

Of course, it is often possible to resort to covalent cross-linking to stabilise a structure that has been self-assembled from an aqueous environment. Indeed, nature does this too in the case of fibrous materials such as hair (keratin) and tendons (collagen) that must exhibit extracellular stability for long periods of time. This approach will be acceptable if we *want* the product properties to reflect the presence of such cross-links, but otherwise it has to be avoided.

Hydrophobically bonded structures will be sensitive to temperature: the entropy penalty that has to be paid for immobilising water at the surface of G-actin increases with increasing temperature, as the driving force for water to disorder increases. The fracture resistance of such structures will therefore also decline with increasing temperature, unless post-assembly cross-linking has been able to occur.

The Fracture Characteristics of Natural Fibres Can Be Sensitive to Prior Deformation

The complexity and hierarchy of natural fibre microstructures can allow a variety of simultaneous microstructural changes to accompany mechanical deformation.

In microstructures where the majority of molecules already have significant extension and alignment, there is little scope for molecular order to be affected by deformation. For this reason, the load-extension curves of cotton and flax (Wagner, 1953) are essentially linear, and the ability of the material to resist flaw propagation does not change with strain. If, in contrast, the microstructure contains a significant volume of material in which the molecules are initially disordered, and/or there are distortable helical structures, the fracture toughness of the material can be altered significantly by strain. So, to understand fracture, we must know about the microstructural changes that occur throughout the deformation process.

As an extreme example, we can profitably consider the case of rubber. Although not itself a fibrous material, rubber is a good model for the disordered microstructural component in many natural fibrous polymers, including silk. Most people would agree that rubber is tough. That is why rubber is used to make tyres and the soles of durable shoes. However, cracks propagate very readily indeed through the skin of an inflated rubber balloon, on the basis of which rubber could be regarded as a brittle material. This apparently dual character can be understood if we note that the microstructure of rubber is changed substantially during the course of deformation. The initial microstructure consists of a random array of tangled molecules, through which there is no easy crack path. On stretching, this microstructure is progressively converted to one in which the

molecules are extended, aligned, and less tangled, and which provides little resistance to cracks propagating parallel to the length of the molecules.

The amorphous matrix phase in spider dragline silk can be likened to rubber (Gosline et al., 1984). Such elastomeric behaviour is promoted if water is available to swell the amorphous regions in the silk microstructure. (Dragline silks undergo a marked shape change when immersed in water (Work, 1981, 1985; Work and Morosoff, 1982; Fornes et al., 1983; Gosline et al., 1984, 1995) or salt solutions (Vollrath et al., 1996.) The radial swelling, to as much as twice the original thickness, is accompanied by an axial shrinkage of up to 40% of the original length; this dramatic effect is therefore known as *supercontraction*.) Many other silks, for example the textile fibre harvested from the cocoons of *Bombyx mori* (domesticated) silkworms, do not exhibit significant supercontraction in water, but they nevertheless can also be regarded as elastomers (Gosline et al., 1994). This description is relevant when we come to address the statistical brittleness of silk (the section 'The Statistical Basis of Fibre Failure Analysis'). It helps us to interpret the observation (Pérez-Rigueiro et al., 2001; Garrido et al., 2002) that the breaking stress of silk (recorded at high strain) is much less reproducible than the yield stress (recorded at low strain).

In a Hierarchical Fibre Microstructure, Molecules That Have 'Melted' Can Continue to Carry Loads Usefully

From everyday experience of conventional materials, we may come to expect that disordering of a microstructure will always lead to a loss of reinforcement and a reduction or even failure of load-bearing ability. In fact, this combination of cause and effect has some notable exceptions, none more significant than the contractile mechanism of muscle (Pollack, 1990, 2001).

We are again dealing with a useful consequence of hierarchical structure in a fibrous material, and of the attendant anisotropic distribution of primary and secondary bonds. There are two fibrous materials in muscle: actin (already described in the section 'Primary and Secondary Bonds Can Have Direct, Distinguishable, Complementary Effects on Fibre Mechanical Properties') and myosin. The myosin-containing filaments consist of bundles of rod-like structures, where each rod is a supramolecular helix (supercoil, or coiled coil) assembled from two α-helical protein strands (Fig. 3). The helical structure is able to locally and reversibly transform to a random one, triggered by one of several environmental signals that can include a change in local packing constraints, a change in pH, or a change in the concentration of various salts. This local conformational change leads to a contraction in rod length (Fig. 3). It does not involve any breaking of primary bonds; it merely requires a local rearrangement in the number and distribution of protein–protein and protein–environment secondary bonds. Because the myosin in muscle is interconnected (by non-covalent associations), and is further supported by actin-containing filaments, the molecular-level contraction leads to a corresponding macroscopic contraction of the muscle, along a structurally predetermined direction. Although the random coil conformation in myosin is similar to the conformation of flexible polymer chains in melts and solutions, its *localisation to particular regions within a hierarchical fibre* means that the controlled contraction

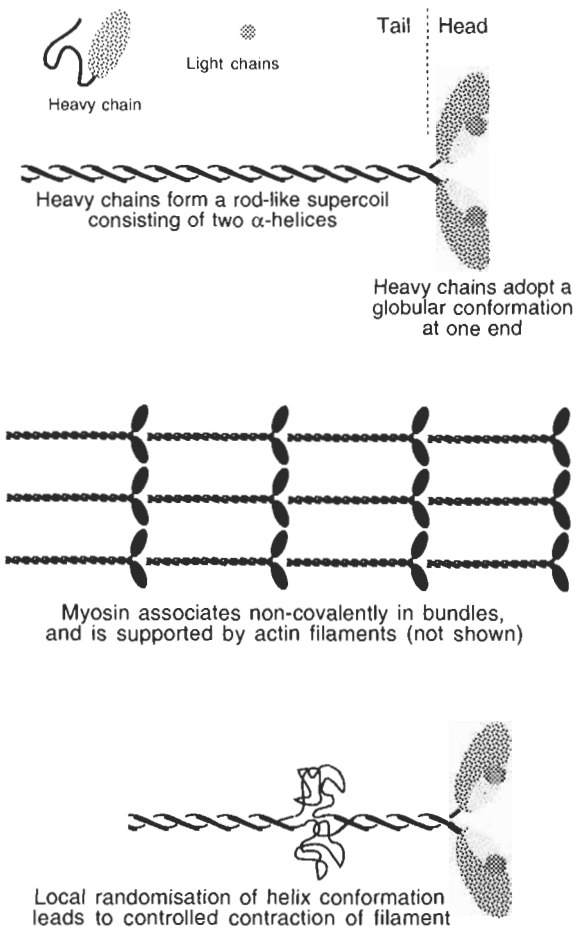

Fig. 3. Molecular and supramolecular features in the hierarchical structure of myosin filaments. Local conformational changes in the rod-like supercoils lead to muscle contraction.

can occur without compromising the overall integrity and load-bearing ability of the filaments.

Thus, the ability of weight-lifters to ply their sport depends on a force generated by molecular *disordering*, and on the capacity for non-covalent bonds to transmit that force. The molecular origin of muscular force generation is illustrated elegantly by the mechanochemical device (Steinberg et al., 1966; Pollack, 1990) shown in Fig. 4. For practical reasons it uses collagen instead of muscle, but, per gram of fibrous biopolymer, the machine can deliver the same maximum power as a frog sartorius (thigh) muscle.

We see, therefore, that microstructural disordering in a fibre can lead to useful force-transducing properties rather than mechanical failure, provided that the disorder can be controlled and localised, and provided that it is reversible. In the final section of this paper, we will consider another material (a fibre-reinforced composite) in

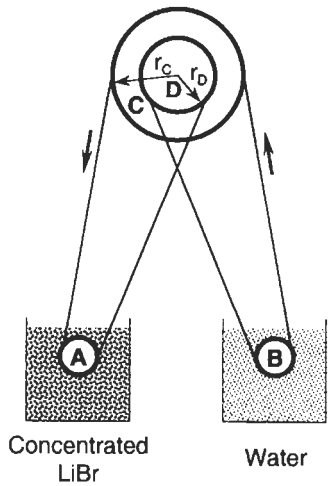

Fig. 4. An example of a mechanochemical engine, based on Steinberg et al., 1966 and Pollack, 1990. A 'belt' of collagen is wound around pulleys A, B, C and D. Pulleys C and D are mounted on a common axis. When concentrated salt solution is added to the left-hand reservoir, the collagen immersed in that solution contracts, exerting equal forces on the rims of pulleys C and D. Because pulley C has a larger radius than pulley D, there is a net anticlockwise torque as shown. Rotation continuously immerses new lengths of collagen in the salt solution, while previously immersed material is able to relax in the right-hand reservoir. Eventual equalisation of the salt concentration in the two reservoirs prevents this engine from being a perpetual-motion device.

which reversible loss of molecular order (in the matrix) equates to an enhancement of mechanical properties.

The Experimental Methods Used for Characterising the Failure Strength and Other Mechanical Properties of Fibres Must Be Appraised Carefully

Methods that are used for characterising the mechanical properties of artificial fibres may not be optimal for characterising natural materials.

Conditioning

Mechanical property characterisation of artificial polymers (fibrous and non-fibrous) is often preceded by a mechanical *conditioning* treatment (Ward and Hadley, 1993) if the material is viscoelastic. This treatment is designed to provide a standard, reproducible microstructural state, so that results from different experiments, materials and laboratories can be compared easily. The conditioning treatment is deemed necessary because the mechanical properties of viscoelastic materials are affected by their entire previous mechanical history, as articulated in the *Boltzmann superposition principle* (Ward and Hadley, 1993). To predict mechanical behaviour accurately, one ought in theory to know the entire loading history of specimens since their manufacture! Under practical conditions, only comparatively recent history is relevant, so specimens can be

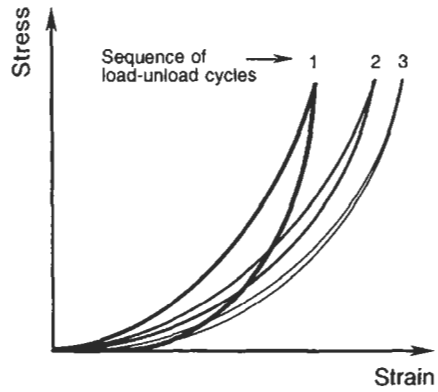

Fig. 5. Response of a viscoelastic biomaterial to mechanical preconditioning. Stress–strain curves are displaced to the right, and hysteresis (the difference between loading and unloading curves in a cycle) decreases.

standardised by a cyclic *conditioning treatment* prior to experimental characterisation. A typical standardisation procedure consists of the following steps: (1) at the temperature of interest, the maximum planned load is applied for the maximum planned loading time; (2) this is followed by a recovery period (after unloading) that lasts ten times as long; (3) this cycle is repeated until reproducible load-extension results are obtained.

A similar (pre)conditioning procedure (Fig. 5) is routinely imposed on natural tissues and materials before biomechanical characterisation (Fung, 1993). While this again can provide a useful basis for comparing results from different experiments, such results may be misleading if we are interested in how the *actual* natural material behaves, i.e. without conditioning. To correctly interpret the in-service mechanical properties of natural fibres in terms of the underlying hierarchical structure, a strong case can be made for leaving both the properties and the structure as *undisturbed* as possible.

Cross-Sectional Area Characterisation

Regardless of whether stress is quoted as nominal values (scaled relative to the initial sample cross-section) or true values (scaled relative to the final cross-section), representative cross-sectional areas are needed for accurate characterisation of fibre strength and stiffness. Depending on the *type* of fibre being tested, the *scale* on which the test has to be performed, and the *environment* in which the fibre strength is being tested, it may or may not be possible to obtain such a measurement.

For example, most of the tensile strength and stiffness data quoted for natural silks are inaccurate. Silks typically have a highly non-uniform cross-section, due to the non-constant linear production rate of the fibre under natural spinning conditions, and the fact that spinneret orifice sizes can be changed continuously by the spider or larva unless the animal is anaesthetised. Here, 'non-uniform' refers both to the cross-sectional shape, which does not have a simple outline, and to the fact that this shape and its enclosed area can vary with position along the fibre (Dunaway, 1994; Dunaway et al., 1995a;

Pérez-Rigueiro et al., 1998). To complicate matters, silks usually have small average cross-sectional dimensions. *B. mori* cocoon silk (bave, consisting of a pair of filaments) has a diameter of around 20 μm, while spider dragline diameters are approximately 1–5 μm and spider cribellate silk (Foelix, 1982) can have a diameter as small as 0.01 μm. Characterisation of failure strength in a tensile test requires knowledge of the cross-sectional area *at the position where failure occurred.* This position is likely to (but not required to) coincide with the smallest initial cross-sectional area of the sample, and is difficult to identify ahead of the tensile test. Therefore, tensile tests will often (but not necessarily) underestimate the stiffness, yield strength and failure strength of silk.

A micro-tensile stage used in conjunction with (environmental) scanning electron microscopy offers a promising route to the necessary area characterisation. The stage will record the load while deforming the sample at a set rate, while the microscope is used to locate the likely region of fracture and to monitor whether the sample draws down uniformly or necks locally. After fracture, the sample cross-section at the point of fracture can be measured, and the results used to obtain the nominal or true fracture stress.

Force Characterisation

To obtain an idea of the intrinsic strength of natural fibres we must be able to acquire tensile data from the smallest constituent fibrils. At these small length scales, characterisation of load-bearing cross-section may be easier than at the overall fibre length scale, since the dimensions of interest can be determined accurately from crystallographic data and/or packing considerations. It is the measurement of *load* (and of extension, if strains and thence elastic modulus are to be measured as well) that becomes challenging at these length scales. Another challenge arises in disrupting the structural hierarchy to the level necessary for specimen preparation. Combinations of optical tweezers and video-assisted fluorescence microscopy (Tsuda et al., 1996), or optical tweezers, a nanometre-resolution piezo-stage and laser interferometry (Luo and An, 1998) have been successful in characterising the stress–strain response of single actin filaments and collagen molecules, respectively. The G-actin/G-actin bond strength under conditions that mimic a physiological environment was determined as 600 pN (Tsuda et al., 1996); this equates to an intrinsic material strength of approximately 50 MPa, similar to the strength of polyurethane (Warner, 1995). Some of the above methodologies might usefully be applied to the cribellate silks referred to in the section 'Cross-Sectional Area Characterisation'.

The Statistical Basis of Fibre Failure Analysis

We turn again to silk as an instructive example. Even if steps are taken to minimise uncertainties in the measurement of sample cross-sectional area, the values of breaking strength obtained for a given type of silk are poorly reproducible (Work, 1976, 1977; Cunniff et al., 1994; Dunaway et al., 1995b; Pérez-Rigueiro et al., 1998, 2000). It is useful to perform a Weibull analysis (Chou, 1992) of the fracture data to quantify this variability in engineering terms. The Weibull modulus of *B. mori* cocoon fibre is 5.8

(sample gauge length 50 mm; strain rate $2{\cdot}10^{-4}$ s^{-1}) (Pérez-Rigueiro et al., 1998), while *Argiope trifasciata* spider dragline has a Weibull modulus of 3.4 (sample gauge length 20 mm; strain rate $2{\cdot}10^{-4}$ s^{-1}) (Pérez-Rigueiro et al., 2001). Thus, the impressively high *average* strength of silk is compromised by a variability similar to that of common, non-engineering ceramics and glasses.

The fact that the silkworm fibre has a higher Weibull modulus, i.e. a more reproducible failure strength, than the spider dragline suggests that silkworm silk has an intrinsically tougher microstructure. This makes sense biologically, in that cocoons require optimised long-term toughness and durability while dragline requires optimised short-term strength and stiffness. Even so, isolated silkworm cocoon fibre is unreliable when compared against the standard of a high-toughness metallic alloy, so it is not surprising that the cocoon is really a high-volume-fraction fibre composite in which the load from fibres that break prematurely can be redistributed onto the higher-strength fibres.

In the above-mentioned experiments, the silkworm fibre samples not only have a longer gauge length, but they are also approximately five times thicker than the spider silk. The silkworm fibre therefore is able to harbour a more polydisperse flaw size distribution, which should increase its variability in fracture strength and decrease its Weibull modulus relative to the results obtained from a set of smaller-volume samples. In this context, the *higher* reliability of silkworm fibre, compared to spider dragline, is further evidence that the silkworm product has an intrinsically tougher microstructure. The microstructural distinction between the two silks is worth emphasising (Thiel et al., 1997) because, erroneously and often, the microstructural description of silkworm silk has been carried over into the literature of spider dragline. As a further demonstration of microstructural variety in silks, the fracture surfaces of fibres from different species of larva (Fig. 6) and from different arthropod classes (Poza et al., 2002) show distinguishable degrees of ductile failure at a constant deformation rate.

Given that silks can show significant ductility, and, as noted in the section 'The Fracture Characteristics of Natural Fibres Can Be Sensitive to Prior Deformation', can be regarded as elastomeric, *is* a Weibull analysis appropriate for characterising the failure strength variability of these materials? One justification can be formulated simply on phenomenological grounds: after significant deformation, silk *develops* the statistical failure *characteristics* of a brittle material, even though it initially deserves classification as an elastomer. While the existence of strength-limiting defects can be inferred from this description, their nature has yet to be determined; it is not clear whether they are present in as-spun material, or whether they begin to develop during the earlier stages of deformation. A possible candidate in silkworm cocoon fibre is the fine-scale voiding that has been detected (Robson, 1999) in silver-sulphide-'stained' samples viewed by transmission electron microscopy.

The appropriateness of the Weibull analysis for a partially ductile material can also be justified fundamentally. Although the Weibull method of reliability analysis is formally developed for classically brittle materials (Kelly and Macmillan, 1986), i.e. materials that fail before they can exhibit a yield point, its use can be generalised for materials that exhibit flaw *sensitivity*. This generalisation can be arrived at simply by examining the equation (Simon and Bunsell, 1984; Chou, 1992) which is plotted to obtain a value

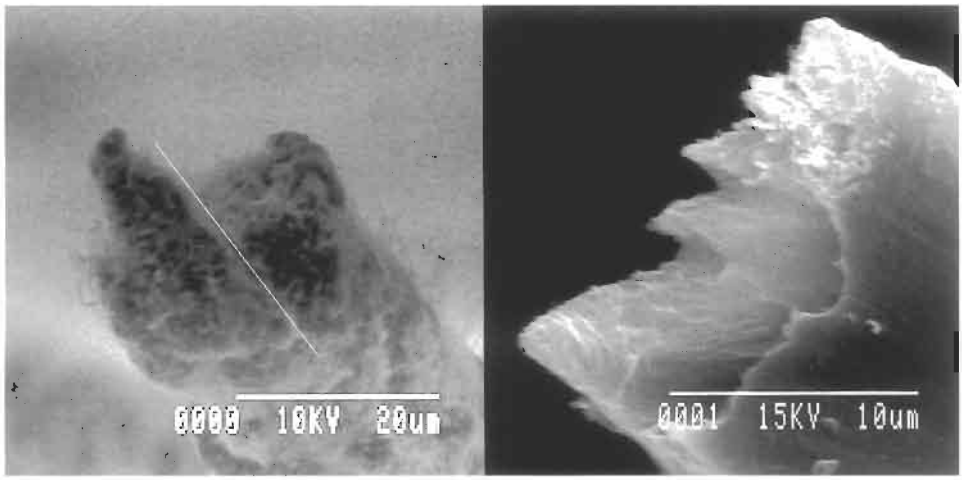

Fig. 6. Fracture surfaces produced in lepidopteran silk by hand-drawing under liquid nitrogen. Different degrees of ductility are evident in the two materials, suggesting that there are significant microstructural differences between them. Left: *Bombyx mori* (domesticated silkworm) cocoon silk. The white line emphasises the fact that the fibre (bave) consists of two filaments (brins). Right: *Rothschildia erycina* cocoon silk. The sample has deformed to an extent that precludes identification of the individual brins.

of the Weibull modulus m:

$$F = 1 - \exp\left(-\frac{\sigma}{\sigma_0}\right)^m \tag{2}$$

where F is the cumulative probability that a sample has a fracture strength of σ, and σ_0 is a constant. If F is to be independent of σ, which is the hallmark of an ideally brittle material (section "Some Thoughts on the Meaning of 'Brittle'"), Eq. 2 requires m to be equal to zero. Since practical Weibull analysis admits to non-zero values of m, it is implicit that ductile contributions to failure can be accommodated too.

The use of Weibull statistics to characterise failure probabilities in batches of natural fibre is therefore appropriate, and can highlight the existence of significant microstructural differences between different materials. Comparison of different materials is most straightforward if similar sample volumes can be used, but this is difficult if the materials have different and irregular fibre cross-sections. A further complication is introduced by *viscoelasticity*, which will make strength depend on the detailed stress–strain profile of the material and the rate at which samples are loaded. Comparisons should therefore be conducted at defined and reproducible strain rates. It must be recognised, however, that comparison of different polymers under exactly equivalent conditions can never be achieved in practice, because it is most unlikely that different polymers will have identical viscoelastic characteristics. Silks are especially 'unusual': while increased deformation rates are associated with higher strength, higher stiffness and lower elongation to failure in most viscoelastic materials, silk exhibits an increased elongation to failure (Kaplan et al., 1997). This observation supports the idea that the propagation characteristics of defects, rather than bulk viscoelastic behaviour, governs the fracture of natural silk fibres.

ECHINODERM COLLAGENS: FIBRE OPTIMISATION IN SMART COMPOSITES

We have reflected on several issues that are important to fracture characterisation and control in the context of natural self-assembled fibrous materials. To conclude this discussion, it is appropriate to consider some of nature's best examples of optimisation and versatility in fibre-reinforced composites: sea cucumber body and the 'catch' ligament associated with the ball-and-socket joint at the base of the sea urchin spine (Fig. 7). These materials are among the living world's oldest fibrous composites, which is testimony to their successful design. They offer several time-tested and thought-provoking lessons for the materials engineer.

(1) Their mechanical properties are not permanent; they change on a physiological timescale typically measured in seconds (Trotter et al., 2000b).

(2) They demonstrate how controlled, reversible 'melting' of one phase in a microstructure need not cause an overall loss of cohesion, and can enable useful mechanical functions.

(3) They demonstrate how the failure of *inter*fibrillar bonds in a composite can be controlled to tailor the net load-bearing properties of the composite.

(4) They demonstrate how water plays a central role in controlling the load-bearing ability and failure resistance of natural materials.

(5) They make use of *tapered* rather than cylindrical fibres, to provide reinforcement with the minimum amount of 'expensive' material.

Tensile Property Control

Sea cucumbers and sea urchins control the tensile properties of some connective tissues by regulating stress transfer between collagen fibrils (Trotter et al., 2000b). Strength and stiffness can vary by more than an order of magnitude between the stiff and pliant states. Interactions between the fibrils are regulated by water-soluble macromolecules. Based on these observations, progress is being made towards developing a synthetic material that exhibits dynamically controlled tensile properties. The artificial route involves identifying reagents that bind covalently to fibril surfaces and reversibly form cross-links with other (synthetic) reagents. At present, that work is focussed on a chemically controlled stress-transfer capacity. However, molecular processes which can be effected by chemical control can often be achieved by thermodynamically equivalent triggers (e.g. electric fields, light, pressure, temperature, pH: Urry, 1992). In principle, the artificial analogue could contain self-assembled fibres made from a genetically engineered polymer. In this way, detailed tailoring of structure and properties across several length scales could be coupled with dynamic property control of the bulk material.

Tapered Fibres

The collagen fibres in sea cucumber dermis and sea urchin ligament are tapered rather than cylindrical. The shape is ensured by the nucleation and growth mechanism (Trotter et al., 1998; Trotter et al., 2000a) by which the fibres are formed (Fig. 8). We will see

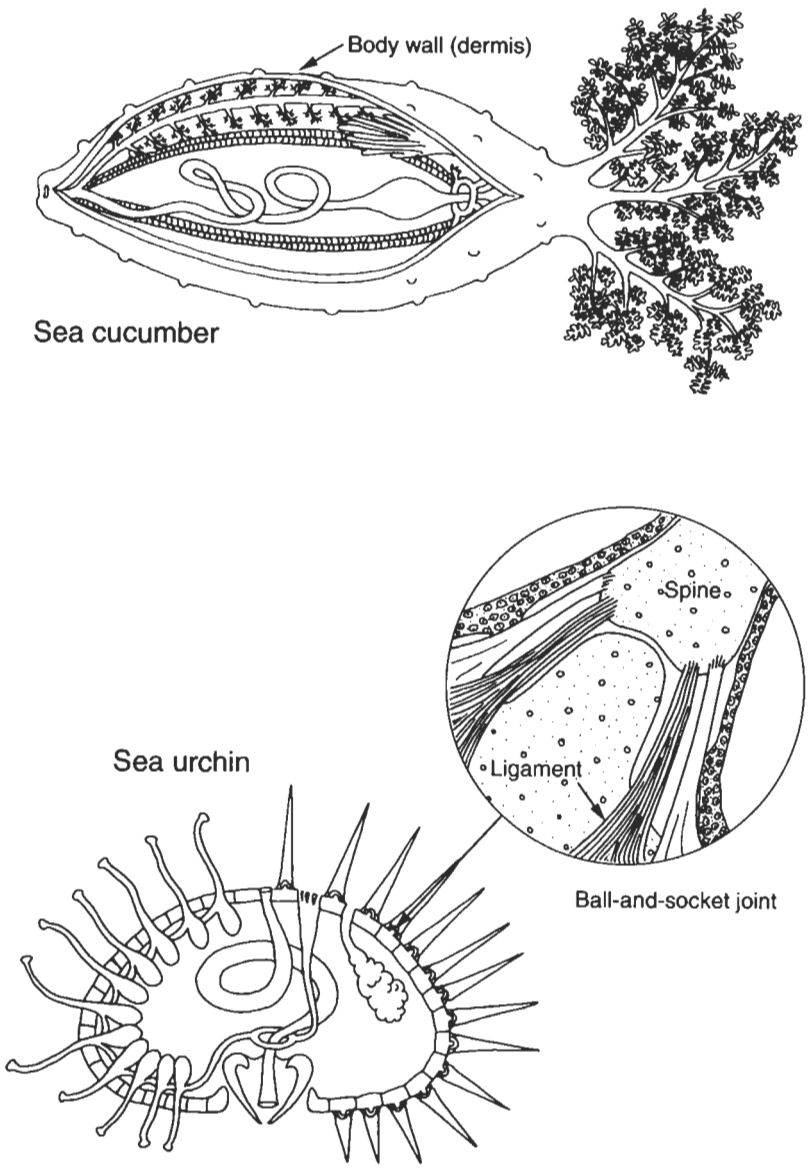

Fig. 7. Sections of sea cucumber and sea urchin, respectively showing the location of the body wall and the 'catch' ligament in these animals. For clarity, the sea urchin is drawn with spines on the right and tube feet on the left; in reality, these structures are intermixed over the whole surface. (After Hyman, 1955; Banister and Campbell, 1985; Pearse et al., 1987; Lambert, 1997.)

that this shape reduces the volume of fibre that is not exploited at close-to-maximum load-bearing capacity. Therefore, supramolecular self-assembly in this instance has the further advantage of ensuring that the tensile strength of the fibre is exploited efficiently.

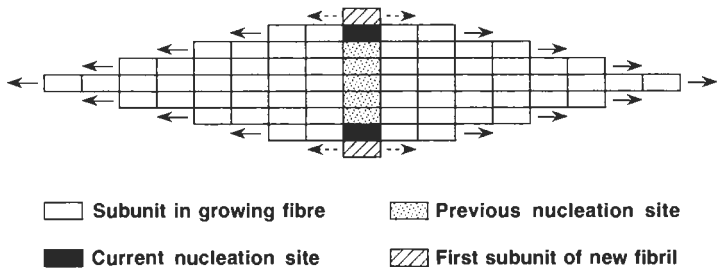

Fig. 8. Mechanism of collagen fibril growth in sea cucumber dermis and sea urchin ligament, based on literature descriptions (Trotter et al., 1998, 2000a). The mechanism ensures a tapered shape and a consistent axial ratio.

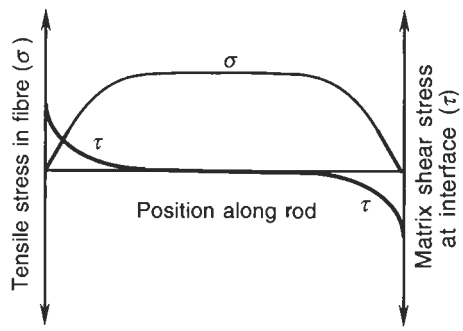

Fig. 9. Stress distributions associated with a reinforcing fibre in a more ductile matrix (according to equations 6.40 (tensile stress) and 6.49 (shear stress) in Kelly and Macmillan, 1986).

In the case of conventional, cylindrical reinforcing fibres, the diameter is the same at all points along the fibre length. If, as is expected, the fibres deform less readily than the matrix, the shear stress in the matrix at the fibre–matrix interface is largest at the fibre ends (see Kelly and Macmillan, 1986, equation 6.49), while the tensile stress in the fibre is greatest at the middle of the fibre (see Kelly and Macmillan, 1986, equation 6.40). These results are summarised in Fig. 9. Ideally, discontinuous fibres will be long enough for the stress at their midpoint to approach the fibre failure strength. The necessary length depends on the fibre radius, in a manner that is easily and commonly (Kelly and Macmillan, 1986) quantified as follows. With reference to Fig. 10, consider a small length dx of a fibre, near one end. The tensile stress in the fibre increases by $d\sigma$ over this distance. This increase in tensile stress is achieved by the interfacial shear stress τ acting on the interface area accommodated within the distance dx. A simple force balance

$$\tau(2\pi r\,dx) = d\sigma(\pi r^2) \tag{3}$$

can be rearranged to give

$$d\sigma = \frac{2\tau}{r}dx \tag{4}$$

If the failure stress σ_{uf} of the fibres is reached over a transfer distance x_{uf}, Eq. 4 can be integrated between the corresponding limits to obtain an expression that incorporates

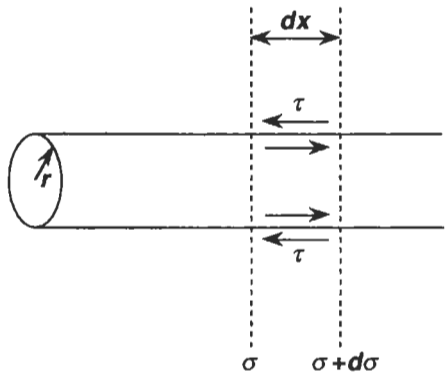

Fig. 10. The geometry referred to in the derivation of Eq. 6, pertaining to cylindrical fibres.

this distance:

$$\int_0^{\sigma_{uf}} d\sigma = \frac{2\tau}{r} \int_0^{x_{uf}} dx \tag{5}$$

Explicit integration of Eq. 5, followed by rearrangement, leads to:

$$x_{uf} = \frac{r\sigma_{uf}}{2\tau} \tag{6}$$

So x_{uf} is an increasing function of r: an increased fibre thickness will increase the capacity of the interfacial surface area to *transfer* load to the fibre (in proportion to r), but will also (and even more effectively) increase the capacity of the fibre cross-section to *carry* that load (in proportion to r^2).

It follows that much of the material in the fibre is wasted, in that the tensile strength is not being properly exploited along almost the whole length of the fibre! This problem is exacerbated in thicker fibres. The load near the ends of the fibres could be carried adequately by a thinner fibre cross-section, compared to the load near the middle of fibres. A less wasteful use of material, and a more efficient exploitation of the fibre properties, would therefore be achieved if the fibres were to *taper* from the middle towards the ends. Also, regions of the fibre having a smaller cross-section would then be able to undergo a larger elastic deformation, thus matching more closely the deformation of the matrix; therefore, the shear stress concentration in the matrix near the fibre ends would be reduced. These gains have been recognised and discussed qualitatively in the context of sea cucumber and sea urchin collagen fibres, which are appropriately tapered (Trotter and Koob, 1989; Trotter et al., 1994, 2000b).

It is instructive to consider how the force balance in Eq. 3 and the critical half-length (transfer distance) of the fibres in Eq. 6 are affected by allowing the fibres to taper towards their ends. Reference should be made to Fig. 11, which again considers the shear stress acting on a small length dx near the end of a fibre. The tensile stress in the fibre again increases by $d\sigma$ over this distance, and the fibre radius increases by dr. From the geometry of Fig. 11,

$$\frac{dr}{}dx = \tan\theta; \qquad \text{i.e. } r = x\tan\theta \tag{7}$$

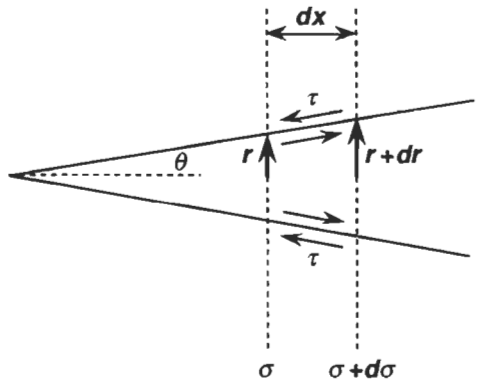

Fig. 11. The geometry referred to in the derivation of Eq. 14, pertaining to tapered fibres.

and the interface area accommodated in the distance dx is

$$\text{Area} = 2\pi r\,dx + 2\tfrac{1}{2}\pi\,dr\,dx = 2\pi r\,dx + \pi\,dr\,dx \approx 2\pi r\,dx \tag{8}$$

provided that θ is small so that the second-order term containing the product of two differentials can be ignored. θ is indeed found to be small for the collagen fibres under consideration here: their length-to-width ratio is of the order of 2000 (Trotter et al., 2000b).

A simple force balance now gives

$$\tau(2\pi r\,dx)\cos\theta \approx \tau(2\pi r\,dx) = d\sigma(\pi r^2) \tag{9}$$

Substitution of Eq. 7 into Eq. 9, followed by simplification, leads to

$$d\sigma = \frac{2\tau}{\tan\theta}\frac{dx}{x} \tag{10}$$

If the stress in a fibre increases from a very small value σ_{if} (at a point x_{if} that is arbitrarily close to the end of the fibre) to the failure stress σ_{uf} (at a point x_{uf} that ideally is at the midpoint of the fibre), Eq. 10 can be integrated between the corresponding limits to obtain an expression in which x_{uf} again represents the transfer distance

$$\int_{\sigma_{if}}^{\sigma_{uf}} d\sigma = \frac{2\tau}{\tan\theta}\int_{x_{if}}^{x_{uf}} \frac{dx}{x} \tag{11}$$

Explicit integration of Eq. 11, followed by rearrangement, then leads to:

$$\sigma_{uf} - \sigma_{if} = \frac{2\tau}{\tan\theta}\ln\frac{x_{uf}}{x_{if}} \tag{12}$$

Therefore

$$\sigma_{uf} \approx \frac{2\tau}{\tan\theta}\ln x_{uf} - C \tag{13}$$

where C is a constant that subsumes events at the end of the fibre. The adoption of a small, non-zero lower limit when performing the integration is a device that circumvents the need to consider the logarithm of zero in the calculation. A similar approach is conventionally

used when considering the strain energy associated with a screw dislocation in a crystal (Cottrell, 1953): a small volume around the dislocation line is assigned a 'core energy' that is not calculated explicitly.

Eq. 13 can be rearranged to give

$$x_{\mathrm{uf}} = \exp\left[\frac{\tan\theta}{2\tau}(\sigma_{\mathrm{uf}} + C)\right] \tag{14}$$

So x_{uf} is an increasing function of $\tan\theta$: the fibre is shortest, promoting the most effective use of reinforcing material, if the taper is gradual. This is precisely what sea cucumbers and sea urchins do.

ACKNOWLEDGEMENTS

Fruitful collaborations with Professors M. Elices and J. Pérez-Rigueiro (Departamento de Ciencia de Materiales, Universidad Politécnica de Madrid) are acknowledged gratefully, as is the British Council for supporting that collaboration through an Acción Integrada. Professor J. Trotter (University of New Mexico School of Medicine) provided the stimulus for the section 'Echinoderm Collagens: Fibre Optimisation in Smart Composites', and kindly faxed reprints of his publications at short notice. Fraser Bell (Department of Chemistry, Heriot-Watt University, Edinburgh) provided the images used in Fig. 6. The sea cucumber and sea urchin illustrations used in Fig. 7 were provided by Dr. Lisa Gilliland.

REFERENCES

Alberts, B., Bray, D., Lewis, J., Raff, M., Roberts, K. and Watson, J.D. (1989) *Molecular Biology of the Cell*. Garland, New York, NY.

Augsten, K., Muhlig, P. and Herrmann, C. (2000) Glycoproteins and skin-core structure in *Nephila clavipes* spider silk observed by light and electron microscopy. *Scanning*, 22(1): 12–15.

Banister, K.E. and Campbell, A.C. (Eds.) (1985) *The Encyclopedia of Aquatic Life*. Equinox, Oxford.

Billmeyer, F.W. (1984) *Textbook of Polymer Science*. Wiley, New York, NY.

Brown, D. and Viney, C. (1999) New materials. In: *Biotechnology: The Science and the Business (2nd ed.)*, pp. 351–366, D.G. Springham, V. Moses and R.E. Cape (Eds.). Harwood Academic Publishers, Amsterdam.

Chittick, J. (1913) *Silk Manufacturing and its Problems*. James Chittick, New York, NY.

Chou, T.-W. (1992) *Microstructural Design of Fiber Composites*. Cambridge University Press, Cambridge.

Cottrell, A.H. (1953) *Dislocations and Plastic Flow in Crystals*. Oxford University Press, Oxford.

Cottrell, A.H. (1975) *An Introduction to Metallurgy*. Edward Arnold, London.

Cunniff, P.M., Fossey, S.A., Auerbach, M.A. and Song, J.W. (1994) Mechanical properties of major ampullate gland silk fibers extracted from *Nephila clavipes* spiders. In: *Silk Polymers: Materials Science and Biotechnology*, pp. 234–251, D. Kaplan, W.W. Adams, B. Farmer and C. Viney (Eds.). American Chemical Society, Washington, DC.

Derby, B., Hills, D.A. and Ruiz, C. (1992) *Materials for Engineering: A Fundamental Design Approach*. Longman Scientific and Technical, Harlow.

Dunaway, D.L. (1994) *Mechanical Property and Diameter Evaluation of Epoxide-Treated Silk Fibers*. MSE Thesis, University of Washington, Seattle, WA. (Copies available from University Microfilms, 1490 Eisenhower Place, P.O. Box 975, Ann Arbor, MI 48106.)

Dunaway, D.L., Thiel, B.L., Srinivasan, S.G. and Viney, C. (1995a) Characterizing the cross-sectional geometry of thin, non-cylindrical, twisted fibers (spider silk). *J. Mater. Sci.*, 30: 4161–4170.

Dunaway, D.L., Thiel, B.L. and Viney, C. (1995b) Tensile mechanical property evaluation of natural and epoxide-treated silk fibers. *J. Appl. Polym. Sci.*, 58: 675–683.

Foelix, R.F. (1982) *Biology of Spiders*. Harvard University Press, Cambridge, MA.

Fornes, R.E., Work, R.W. and Morosoff, N. (1983) Molecular orientation of spider silks in the natural and supercontracted states. *J. Polym. Sci. Polym. Phys. Ed.*, 21: 1163–1172.

Fung, Y.C. (1993) *Biomechanics: Mechanical Properties of Living Tissues*. Springer, New York, NY.

Garrido, M.A., Elices, M., Viney, C. and Pérez-Rigueiro, J. (2002) Active control of spider silk strength: comparison of drag line spun on vertical and horizontal surfaces. *Polymer*, 43: 1537–1540.

Gorham, S.D. (1991) Collagen. In: *Biomaterials: Novel Materials from Biological Sources*, pp. 55–122, D. Byrom (Ed.). Stockton Press, New York, NY.

Gosline, J.M., Denny, M.W. and DeMont, M.E. (1984) Spider silk as rubber. *Nature*, 309: 551–552.

Gosline, J.M., Pollak, C.C., Guerette, P.A., Cheng, A., DeMont, M.E. and Denny, M.W. (1994) Elastomeric network models for the frame and viscid silks from the orb web of the spider *Araneus diadematus*. In: *Silk Polymers: Materials Science and Biotechnology*, pp. 328–341, D.L. Kaplan, W.W. Adams, B.L. Farmer and C. Viney (Eds.). American Chemical Society, Washington, DC.

Gosline, J., Nichols, C., Guerette, P., Cheng, A. and Katz, S. (1995) The macromolecular design of spiders' silks. In: *Biomimetics: Design and Processing of Materials*, pp. 237–261, M. Sarikaya and I.A. Aksay (Eds.). American Institute of Physics, Woodbury, NY.

Hearle, J.W.S., Thwaites, J.J. and Amirbayat, J. (Eds.) (1980) *Mechanics of Flexible Fibre Assemblies*. Sijthoff and Noordhoff, Alphen aan de Rijn.

Hudson, S.P. (1997) The spinning of silk-like proteins into fibers. In: *Protein-Based Materials*, pp. 313–337, K. McGrath and D. Kaplan (Eds.). Birkhäuser, Boston, MA.

Hyams, J.S. and Lloyd, C.W. (Eds.) (1994) *Microtubules*. Wiley-Liss, New York, NY.

Hyman, L.H. (1955) *The Invertebrates, Volume IV (Echinodermata)*. McGraw-Hill, New York, NY.

Kabsch, W. and Vandekerckhove, J. (1992) Structure and Function of Actin. *Annu. Rev. Biophys. Biomol. Struct.*, 21: 49–76.

Kaplan, D.L., Mello, C.M., Arcidiacono, S., Fossey, S., Senecal, K. and Muller, W. (1997) Silk. In: *Protein-Based Materials*, pp. 103–131, K. McGrath and D. Kaplan (Eds.). Birkhäuser, Boston, MA.

Kelly, A. and Macmillan, N.H. (1986) *Strong Solids (3rd ed.)*. Oxford University Press, Oxford.

Lambert, P. (1997) *Sea Cucumbers of British Columbia, Southeast Alaska and Puget Sound*. UBC Press, Vancouver, BC.

Linton, J.D., Ash, S.G. and Huybrechts, L. (1991) Microbial polysaccharides. In: *Biomaterials: Novel Materials from Biological Sources*, pp. 215–261, D. Byrom (Ed.). Stockton Press, New York, NY.

Lodish, H., Baltimore, D., Berk, A., Zipursky, S.L., Matsudaira, P. and Darnell, J. (1995) *Molecular Cell Biology*. W.H. Freeman and Company, New York, NY.

Luo, Z.-P. and An, K.-N. (1998) Development and validation of a nanometer manipulation and measurement system for biomechanical testing of single macro-molecules. *J. Biomech.*, 31: 1075–1079.

Nishimura, H. and Sarko, A. (1987) Mercerization of cellulose, IV. Mechanism of mercerization and crystallite sizes. *J. Appl. Polym. Sci.*, 33: 867–874.

Oster, G., Perelson, A.S. and Tilney, L.G. (1982) A mechanical model for elongation of the acrosomal process in thyone sperm. *J. Math. Biol.*, 15(2): 259–265.

Pearse, V., Pearse, J., Buchsbaum, M. and Buchsbaum, R. (1987) *Living Invertebrates*. Blackwell, Oxford.

Pérez-Rigueiro, J., Viney, C., Llorca, J. and Elices, M. (1998) Silkworm silk as an engineering material. *J. Appl. Polym. Sci.*, 70(12): 2439–2447.

Pérez-Rigueiro, J., Viney, C., Llorca, J. and Elices, M. (2000) Mechanical properties of single-brin silkworm silk. *J. Appl. Polym. Sci.*, 75: 1270–1277.

Pérez-Rigueiro, J., Elices, M., Llorca, J. and Viney, C. (2001) Tensile properties of *Argiope trifasciata* drag line silk obtained from the spider's web. *J. Appl. Polym. Sci.*, 82: 2245–2251.

Pollack, G.H. (1990) *Muscles and Molecules*. Ebner and Sons, Seattle, WA.

Pollack, G.H. (2001) *Cells, Gels and the Engines of Life*. Ebner and Sons, Seattle, WA.

Poza, P., Pérez-Rigueiro, J., Elices, M. and Llorca, J. (2002) Fractographic analysis of silkworm and spider silk. *Engineering Fracture Mechanics*, 69: 1035–1048.

Putthanarat, S., Stribeck, N., Fossey, S.A., Eby, R.K. and Adams, W.W. (2000) Investigation of the nanofibrils of silk fibers. *Polymer*, 41(21): 7735–7747.

Rawn, J.D. (1989) *Proteins, Energy, and Metabolism*. Neil Patterson Publishers, Burlington, NC.

Renuart, E. and Viney, C. (2000) Biological fibrous materials: self-assembled structures and optimised properties. In: *Structural Biological Materials*, pp. 221–267, M. Elices, (Ed.). Pergamon/Elsevier Science, Oxford.

Robson, R.M. (1999) Microvoids in *Bombyx mori* silk. An electron microscopy study. *Int. J. Biol. Macromol.*, 24: 145–150.

Simon, G. and Bunsell, A.R. (1984) Mechanical and structural characterization of the nicalon silicon-carbide fiber. *J. Mater. Sci.*, 19: 3649–3657.

Steinberg, I.Z., Oplatka, A. and Katchalsky, A. (1966) Mechanochemical engines. *Nature*, 210: 568–571.

Steinbüchel, A. (1991) Polyhydroxyalkanoic acids. In: *Biomaterials: Novel Materials from Biological Sources*, pp. 123–213, D. Byrom (Ed.). Stockton Press, New York, NY.

Steinmetz, M.O., Stoffler, D., Hoenger, A., Bremer, A. and Aebi, U. (1997) Actin: from cell biology to atomic detail. *J. Struct. Biol.*, 119: 295–320.

Stryer, L. (1988) *Biochemistry*. W.H. Freeman and Company, New York, NY.

Stryer, L. (1995) *Biochemistry*. W.H. Freeman and Company, New York, NY.

Termonia, Y. (2000) Molecular modeling of the stress/strain behavior of spider dragline. In: *Structural Biological Materials*, pp. 335–349, M. Elices (Ed.). Pergamon/Elsevier Science, Oxford.

Thiel, B.L., Guess, K.B. and Viney, C. (1997) Non-periodic lattice crystals in the hierarchical microstructure of spider (major ampullate) silk. *Biopolymers*, 41: 703–719.

Tilney, L.G. and Inoué, S. (1982) Acrosomal reaction of thyone sperm, II. The kinetics and possible mechanism of acrosomal process elongation. *J. Cell Biol.*, 93: 820–827.

Tirrell, J.G., Tirrell, D.A., Fournier, M.J. and Mason, T.L. (1997) Artificial proteins: *De novo* design, synthesis and solid state properties. In: *Protein-Based Materials*, pp. 61–99, K. McGrath and D. Kaplan (Eds.). Birkhäuser, Boston, MA.

Trotter, J.A. and Koob, T.J. (1989) Collagen and proteoglycan in a sea urchin ligament with mutable mechanical properties. *Cell Tissue Res.*, 258: 527–539.

Trotter, J.A., Thurmond, F.A. and Koob, T.J. (1994) Molecular structure and functional morphology of echinoderm collagen fibrils. *Cell Tissue Res.*, 275(3): 451–458.

Trotter, J.A., Chapman, J.A., Kadler, K.E. and Holmes, D.F. (1998) Growth of sea cucumber collagen fibrils occurs at the tips and centers in a coordinated manner. *J. Mol. Biol.*, 284: 1417–1424.

Trotter, J.A., Kadler, K.E. and Holmes, D.F. (2000a) Echinoderm collagen fibrils grow by surface-nucleation-and-propagation from both centers and ends. *J. Mol. Biol.*, 300: 531–540.

Trotter, J.A. et al. (2000b) Towards a fibrous composite with dynamically controlled stiffness: lessons from echinoderms. *Biochem. Soc. Trans.*, 28(4): 357–362.

Tsuda, Y., Yasutake, H., Ishijima, A. and Yanagida, T. (1996) Torsional rigidity of single actin filaments and actin–actin bond breaking force under torsion measured directly by *in vitro* micromanipulation. *Proc. Natl. Acad. Sci., USA*, 93: 12937–12942.

Tuszynski, J.A., Trpisova, B., Sept, D. and Brown, J.A. (1997) Selected physical issues in the structure and function of microtubules. *J. Struct. Biol.*, 118: 94–106.

Urry, D.W. (1992) Free energy transduction in polypeptides and proteins based on inverse temperature transitions. *Prog. Biophys. Mol. Biol.*, 57(1): 23–57.

Viney, C. (2000) Silk fibres: origins, nature and consequences of structure. In: *Structural Biological Materials*, pp. 293–333, M. Elices (Ed.). Pergamon/Elsevier Science, Oxford.

Vollrath, F., Holtet, T., Thøgersen, H.C. and Frische, S. (1996) Structural organization of spider silk. *Proc. R. Soc. London B*, 263: 147–151.

Wagner, E. (1953) *Mechanisch–technologische Textilprüfungen*. Fr. Staats, Lüdenscheid-Wuppertal.

Ward, I.M. and Hadley, D.W. (1993) *An Introduction to the Mechanical Properties of Solid Polymers*. Wiley, Chichester.

Warner, S.B. (1995) *Fiber Science*. Prentice Hall, Englewood Cliffs, NJ.

Work, R.W. (1976) The force–elongation behavior of web fibers and silks forcibly obtained from orb-web-spinning spiders. *Textile Res. J.*, 46(July): 485–492.

Work, R.W. (1977) Dimensions, birefringences, and force–elongation behavior of major and minor ampul-

late silk fibers from orb-web-spinning spiders — the effects of wetting on these properties. *Textile Res. J.*, 47(October): 650–662.

Work, R.W. (1981) A comparative study of the supercontraction of major ampullate silk fibers of orb-web-building spiders (araneae). *J. Arachnol.*, 9: 299–308.

Work, R.W. (1985) Viscoelastic behaviour and wet supercontraction of major ampullate silk fibers of certain orb-web-building spiders (araneae). *J. Exp. Biol.*, 118: 379–404.

Work, R.W. and Morosoff, N. (1982) A physico-chemical study of the supercontraction of spider major ampullate silk fibers. *Textile Res. J.*, 52(May): 349–356.

Fiber Fracture
M. Elices and J. Llorca (Editors)

FRACTURE OF COMMON TEXTILE FIBRES

J.W.S. Hearle

The Old Vicarage, Mellor, Stockport SK6 5LX, UK

Introduction 331
Cotton and Related Fibres 333
Structure and Stress–Strain Curves 333
Fracture 335
Wool and Hair 337
Structure and Stress–Strain Curve 337
Fracture 339
Melt-Spun Synthetic Fibres 341
Structure and Stress–Strain Curves 341
Fracture 344
Solution-Spun Fibres 346
Structure and Stress–Strain Curves 346
Fracture 348
Other Modes of Failure 350
References 352

Abstract

Cotton, polyester, nylon, acrylic, rayon, wool and some other fibres are used in large quantities by the textile industry for a great variety of uses. Their tensile fracture results from the total deformation up to the break point. In cotton, a helical assembly of fibrils, with reversals and convolutions, determines the stress–strain curve. Three forms of break are found as transverse bonding becomes weaker with moisture absorption. In wool, extension is controlled by a special microfibril–matrix structure, with fracture occurring when the rubbery matrix reaches its limiting extension. In melt-spun synthetics, the structure is uncertain, but deformation combines plastic yielding associated with crystalline regions and rubber elasticity in amorphous tie-molecules. Failure is due to ductile crack propagation. Solution-spun fibres have a coarse structure that gives granular fractures. Weakness in the transverse direction leads to axial cracks under shear

stresses and kink-band failures in axial compression. These are the commonest modes of failure in cyclic fatigue testing and in use.

Keywords

Fracture; Fatigue; Defects; Cracks; Cotton; Wool; Melt-spun synthetics; Solution-spun fibres

INTRODUCTION

Most of the presentations at the Fibre Fracture conference, which appear as papers in this book, were primarily concerned with fracture in high-performance fibres. Among polymeric fibres these include the synthetic HM-HT fibres in the papers by Hearle (paper 11) and by Termonia and natural fibres in the context of living organisms in the paper by Viney. However, there is another group of fibres that are by far the most important economically, namely the fibres that are used by most of the textile industry. About half are used in clothing, a quarter in various household uses, and a quarter in technical and engineering uses. Cotton (cellulose) and polyester (polyethylene terephthalate) each account for 30 to 40% of total usage, with smaller amounts of polyamides (nylon), acrylics (polyacrylonitrile), other synthetics, including copolymers, rayon (regenerated cellulose), cellulose acetate, other natural cellulose fibres, wool, other hair fibres, and silk. In order to put this in context, it can be noted that global polyester production is in the tens of millions of tonnes per year, whereas the various high-performance fibres are in hundreds or thousands of tonnes.

For most of these uses, fracture in the narrow sense of failure under a peak load is not directly relevant. Durability under the sequence of complex loading experienced in use is of greater importance, although some products are discarded when they are no longer fashionable or for other reasons, rather than when they are worn out. However, the tensile break load is commonly used as a scaling factor for the intensity of applied loads, whether in use or in fatigue testing.

After thousands of years of practical experience, the textile industry generally takes an empirical approach to the choice of fibres and the design of fabrics. Even for the manufactured fibres, which were introduced in the 20th century, the mechanics of the internal structure is at a much weaker theoretical level than the chemistry. Perhaps the first case where a full engineering approach has involved fibre producers, manufacturers and users, is in the use of fibre ropes for deep-water moorings (Tension Technology International and Noble Denton Europe, 1999). There are now about 15 oil-rigs deployed by Petrobras off the coast of Brazil, and, for 20 years, the US Navy has been interested in the possibility of deep-water mooring of mobile bases. When these problems were first examined in a Joint Industry Study (Noble Denton Europe and National Engineering Laboratory, 1995), the general view was that high-performance fibres, such as aramids, Vectran, and HMPE or carbon fibres in pultruded rods, would be the materials to use. In reality, although the strength of high-tenacity polyester of the type used in tyres and ropes is only 1.1 GPa, which is 1/3 of aramid strength, this has proved to be the fibre to use. A typical rig would have 16 lines of 700 tonnes break load ropes, each about 1.4 km long, which will use 400,000 kg of polyester yarn.

The principal criteria for deep-water moorings, which engineering design has to satisfy, are that the peak loads should be safely below the break load, that the offset of the rig, which depends on fibre rope modulus, should be limited, and that the fatigue life should typically be at least 20 years. Marine engineers have mooring analysis programs, which input data on sea and weather states and are used to compute the response of the rig. The mechanics is partly strain-driven by wave heights and partly stress-driven by wind and current forces. The problem for fibre moorings is different

to that for steel cable moorings, which depend on catenary forces determined by the weight of the cable to hold the rig in place, whereas taut fibre moorings depend on rope tensions determined by their extension. An incidental advantage is that the footprint of the moorings on the sea-bed is much smaller with taut moorings. In order to input rope tensions, engineers have to come to terms with the complex visco-elastic properties of polymer fibres, with moduli that vary with the current state and previous history, in contrast to the elastic–plastic response of steel. Rope length is a determinant of strain for given displacements. For the strains in mooring lines resulting from wave motion at 1000 to 2000 m depths, polyester has the best combination of properties: intermediate modulus with good, strength and durability. At lesser depths, where strains would be larger, nylon, with a lower modulus, would be better than polyester, but, at these depths, catenary steel moorings, which are too heavy in longer lines, have a good record of use. At greater depths, higher-modulus fibres may be preferred.

For the common textile uses, fibres are characterised by flexibility, fineness and a high ratio of length to width (McIntyre and Daniels, 1995), but, they must also have an intermediate extensibility. Most have at least partially recoverable extensions up to typical break extensions of 7 to 50%, much higher than for brittle solids or the yield extension of elastic–plastic materials and much lower than for elastomers. Such properties are achieved by partially oriented, partially crystalline polymers, and are almost completely satisfied by six chemical types: cellulose, protein, polyamide, polyester, polyacrylonitrile and polypropylene.

The diverse forms of fibre failure were described in the paper by Hearle (3rd paper), with some qualitative comments on the mechanics of failure. More details of failures of textile fibres in both scientific studies and after use are given in Hearle et al. (1998). However, as Christopher Viney comments (see paper 13), "the entire stress–strain curve of a fibre is relevant to fracture". The aim of this paper is to outline 'the microstructural changes that occur throughout....deformation', and lead to ultimate failure. More information on relevant physical properties of textile fibres is given by Morton and Hearle (1993). The behaviour differs according to the type of fibre, and there has only been limited quantitative modelling of the deformation mechanics.

One general comment is that defects are not as strong a controlling feature of breakage in these extensible textile fibres as in many other materials. Rupture forces cannot be calculated from modulus and crack depth as in Griffiths brittle fracture, or even from the later theories of fracture mechanics. As described below, Moseley (1963) showed that severe damage could be imposed on nylon and polyester fibres with no effect on strength at room temperature.

By far the greatest share of both experimental studies of mechanical properties of fibres and theoretical studies of structural mechanics has been on tensile properties. This paper therefore concentrates on explanations of tensile stress–strain curves and the way in which they lead to fracture. Some comments on other forces, particularly in cyclic loading, will be included in a concluding section.

COTTON AND RELATED FIBRES

Structure and Stress–Strain Curves

Essential features of the structure of cotton and the influence on the stress–strain curve are shown schematically in Fig. 1. Experimental and theoretical studies of deformation and fracture have been reported by Hearle and Sparrow (1979a,b).

After a thin primary wall has grown to the external dimensions of the final cotton fibre, microfibrils are laid down in a helical array as a secondary wall until growth is completed with a small cylindrical lumen left in the centre of the fibre. Each microfibril is generated by an enzyme complex as a set of 30 parallel cellulose molecules, which crystallise in the cellulose I lattice. In this sense, cotton is close to 100% crystalline. The apparent disorder, which shows up in density measurements and techniques such as X-ray diffraction, is due to imperfections in the packing of the microfibrils. The helix angle θ in the secondary wall varies slightly from outside to inside, but is typically 21°. At intervals along the fibre, the helix alternates from right-handed to

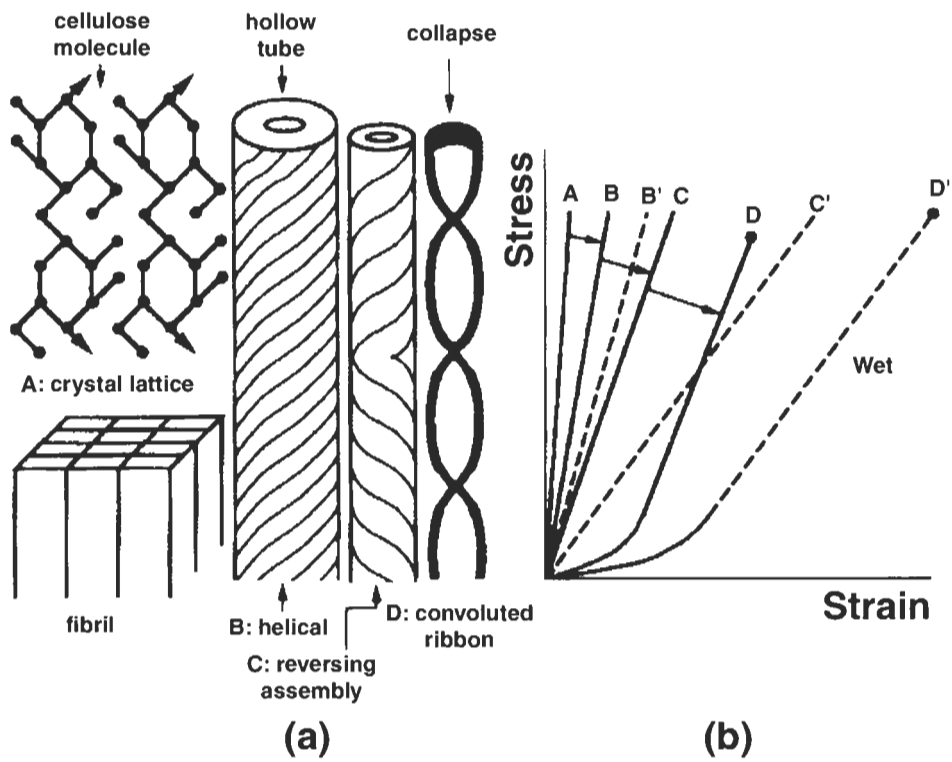

Fig. 1. Cotton fibre structure–property relations: (a) structure; (b) mechanics. The modulus of the crystal lattice A is reduced in the helical assembly B to a greater extent with free rotation at reversals C. Straightening of the convoluted ribbon D allows additional extension at low stress to give the stress–strain curve of a dry fibre. Lower shear resistance in the wet state shifts lines to B′, C′, D′. From Hearle (1991).

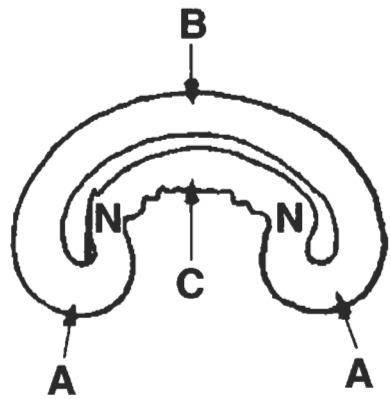

Fig. 2. Cross-section of cotton fibre. Collapse leads to tightening of the structure at A, little change at B, and disturbance at C and N, which are zones most susceptible to chemical attack. From Kassenbeck (1970).

left-handed. The fibre is formed in the wet state within the cotton boll, with more than 30% of water absorbed between the fibrils. When the fibre is dried, it collapses into a flattened tube with the cross-section shown in Fig. 2. The helical structure with reversals causes the tube to take up a twisted form. A similar effect can be seen if a twisted rubber tube is evacuated, but in cotton fibres there are convolutions related to the helix reversals.

The analysis of the stress–strain curve starts with A, the linear stress–strain curve of the cellulose crystal, which has a modulus E_f calculated by Treloar (1960) to be 57 GPa. The theory of twisted continuous-filament yarns, as described for example by Hearle (1989), is then applied. With a Poisson ratio of 0.5, this would predict a reduction of the modulus by a factor of $(\cos^2\theta - 1/2\sin^2\theta)^2$ to give line B. In yarn theory, it is assumed that there is free slippage between fibres in the yarn, whereas in the dry fibre there is hydrogen bonding between microfibrils. Strictly, the theory should be modified to take account of shear stress, but, with a shear modulus S_f calculated by Jawson et al. (1968) to be between 0.36 and 6.72 GPa, the correction is small. The shear modulus plays a part in another way. Line B is based on the assumption that yarn extension occurs without rotation. If the ends are free to rotate, then untwisting under tension increases the extension. In the cotton fibre there is freedom for rotation at each reversal, against the resistance of the shear stress. This gives line C, with a modulus E derived by Hearle and Sparrow (1979b) as:

$$E = \left(E_f S_f \cos^2\theta\right) / \left(E_f \sin^2\theta + S_f \cos^2\theta\right) \tag{1}$$

Experiment has shown that convolutions have a major effect on the initial extension. Fig. 3 compares the load–extension curves of cotton fibres, (a) in the normal state and (b) after stretching wet and drying. This was modelled by a stress analysis based on an inverse application of the treatment of Timoshenko (1957) (p. 259) of the contraction of a flat ribbon on twisting. The additional extension gives line D, similar to the experimental curve (a) in Fig. 3. There is reasonable quantitative agreement when appropriate values of the tensile and shear moduli are used.

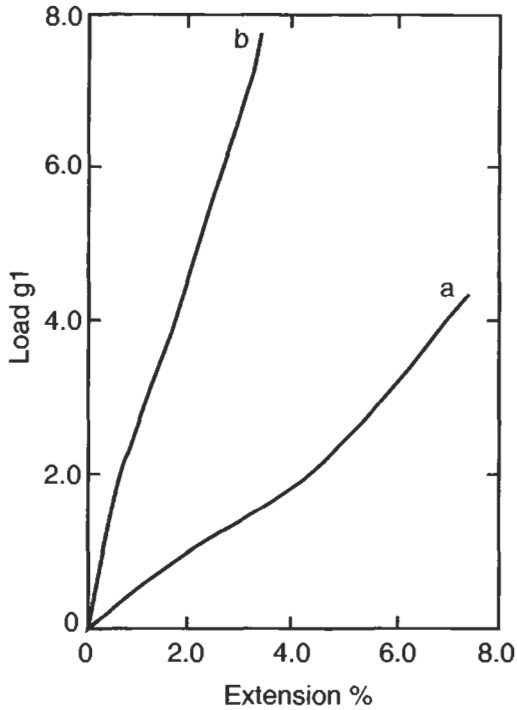

Fig. 3. Load–extension curves for Acala cotton fibres: (a) normal; (b) after stretching wet under tension of 2 g and drying at stretched length. From Hearle and Sparrow (1979a).

The above description applies to dry fibres. In wet fibres, the hydrogen bonding between microfibrils is replaced by mobile absorbed water, which effectively gives zero shear modulus. In the schematic diagram of Fig. 1, this is shown as reducing the modulus from line B to B′, although, as noted above, the effect of the shear modulus is small. The effect on rotation at reversals and removal of convolutions is much greater and moves C to C′ and D to D′. Measurements show that the initial modulus of wet cotton is 1/3 of that at 65% rh, and the strength and break extension are 10% higher wet that at 65% rh. The changes are greater at lower relative humidities: the values of strength and break extensions at 25% rh are half those at 100% rh.

Fracture

What eventually leads to rupture? The form of break of cotton depends on the state of the fibre.

In the dry state, with no absorbed water, the limit is the extension of the cellulose crystals. This is more difficult to calculate theoretically, because it depends on the position of the point of inflection in the plot of free energy versus extension, but would be expected to be at about 2% extension. Due to the helical structure, the extension in the cotton fibre will be greater and the other resulting stresses may influence the fracture.

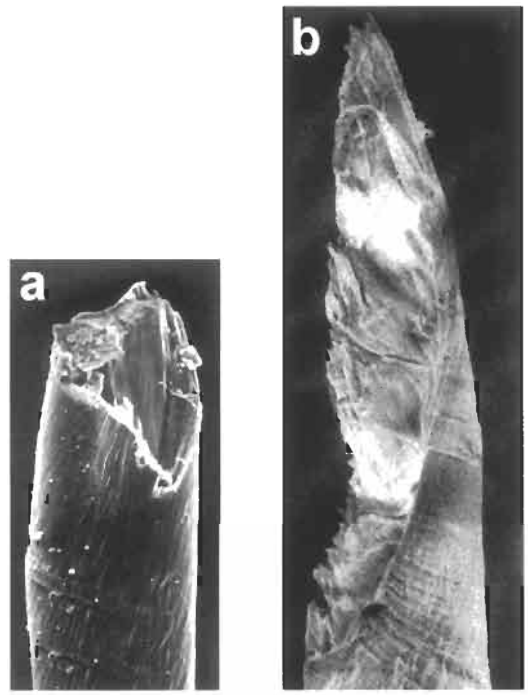

Fig. 4. Fracture of resin-treated cotton: (a) at 65% rh, showing a granular form cutting across the fibre; (b) in wet state, showing a crack following the helical line between fibrils. From Hearle et al. (1998).

As with the effect of the matrix in fibre-reinforced composites, the bonding between the fibrils is not strong enough to cause direct crack propagation across the fibre from a break in a fibril, but is strong enough to transfer some stress and trigger the next break in a neighbouring fibril. The result is a granular break as described in the 3rd paper in this volume. Fig. 4 shows that a granular fracture occurs at 65% rh in cotton that has been treated with a resin cross-linking agent, which increases the bonding between fibrils.

At an intermediate humidity (65% rh), absorbed water weakens the bonding of fibrils. In untreated cotton, the shear stress associated with untwisting then becomes the source of failure. Starting at the stress concentration adjacent to a reversal and a weakness at point N in Fig. 2, a shear crack follows the helical line around the fibre, as shown in fig. 8 of the 3rd paper in this volume. Eventually the crack reaches the position N further along the fibre, which leads to rupture by tearing back along the NN line. A similar form is shown by a resin-treated cotton in the wet state.

In the wet state, the inter-fibrillar bonding is weaker still, and an untreated fibre acts as a bundle of separate fibrils, which break independently. This is the fibrillar form of fracture shown in fig. 6 of the 3rd paper in this volume. The progressive increase of water absorption leads to a continuous increase of tenacity from dry to wet cotton. This is an interesting example of where a reduction of intermolecular cohesion leads to greater strength, as a result of relieving stress concentrations and allowing other modes of deformation.

WOOL AND HAIR

Structure and Stress–Strain Curve

Wool and hair have the most complex structures of any textile fibres. In the paper by Viney, fig. 1 shows how keratin proteins, of which there are more than one type, all having a complicated sequence of amino acids, assemble into intermediate filaments (IFs or microfibrils). But, as shown in Fig. 5a, this is only one part of the story. The microfibrils are embedded in a matrix, as shown in Fig. 5b. The keratin-associated proteins of the matrix contain substantial amounts of cystine, which cross-links molecules by $-CH_2-S-S-CH_2-$ groups. Furthermore, terminal domains (tails) of the IFs, which also contain cystine, project into the matrix and join the cross-linked network. At a coarser scale, as indicated in Fig. 5c, wool is composed of cells, which are bonded together by the cell membrane complex (CMC), which is rich in lipids. As a whole, wool has a multi-component form, which consists of para-cortex, ortho-cortex, meso-cortex (not shown in Fig. 5a), and a multi-layer cuticle. In the para- and meso-cortex the fibril–matrix is a parallel assembly and the macrofibrils, if they are present, run into one another, but in the ortho-cortex the fibrils are assembled as helically twisted macrofibrils, which are clearly apparent in cross-sections.

A review by Hearle (2000) of three current theories concludes that the stress–strain curve can be essentially explained in terms of a fibril–matrix composite, which is referred to as the Chapman/Hearle (C/H) model. In a total model, account should be taken of secondary influences of other structural features. The stress–strain curve of wet wool, Fig. 6a, shows initial stiffness up to 2% extension, a yield region (2% to 30%), subsequent stiffening in the post-yield region (30 to 50%) and breakage at 50% extension. This is not unusual for polymers, but typically the yield extension would not be recovered on reducing the stress. In wool and hair, there is complete recovery up to the end of the yield region, and almost complete recovery from the post-yield region, but along lines that are different to the extension curve.

The model of the mechanics by Chapman (1969) is based on the two-phase model of microfibrils in a matrix, originally proposed by Feughelman (1959) and illustrated by the internal structure of the macrofibril in Fig. 5. In the unstrained state the IFs have a crystal lattice with the molecules following a modified form of Pauling's α-helix, with *intra*-molecular hydrogen bonding, but under tension this transforms to the extended chain β-lattice with *inter*-molecular bonding. The elongation in the ideal structures is 120%, but in the more complicated IFs of wool is probably 80%. The stress–strain curve assumed for the microfibrils is shown by the α–β line in Fig. 6b, where Chapman assumes that the transition is governed by a critical stress, c, and an equilibrium stress, eq. The matrix of the composite structure is treated as a fairly highly cross-linked rubber. Experiments reported by Chapman (1970) on chemically treated wool, which disrupts the structure and leads to supercontraction, indicate that the matrix has the stress–strain curve shown as M in Fig. 6b. This curve follows the theoretical rubber elasticity curve, using the inverse Langevin function form with two free links between network junctions, up to 30% extension. The rubber elasticity curve would be asymptotic to infinite stress at 40% extension, but beyond 30% there is rupture of cystine cross-links, which leads to a turnover in the curve.

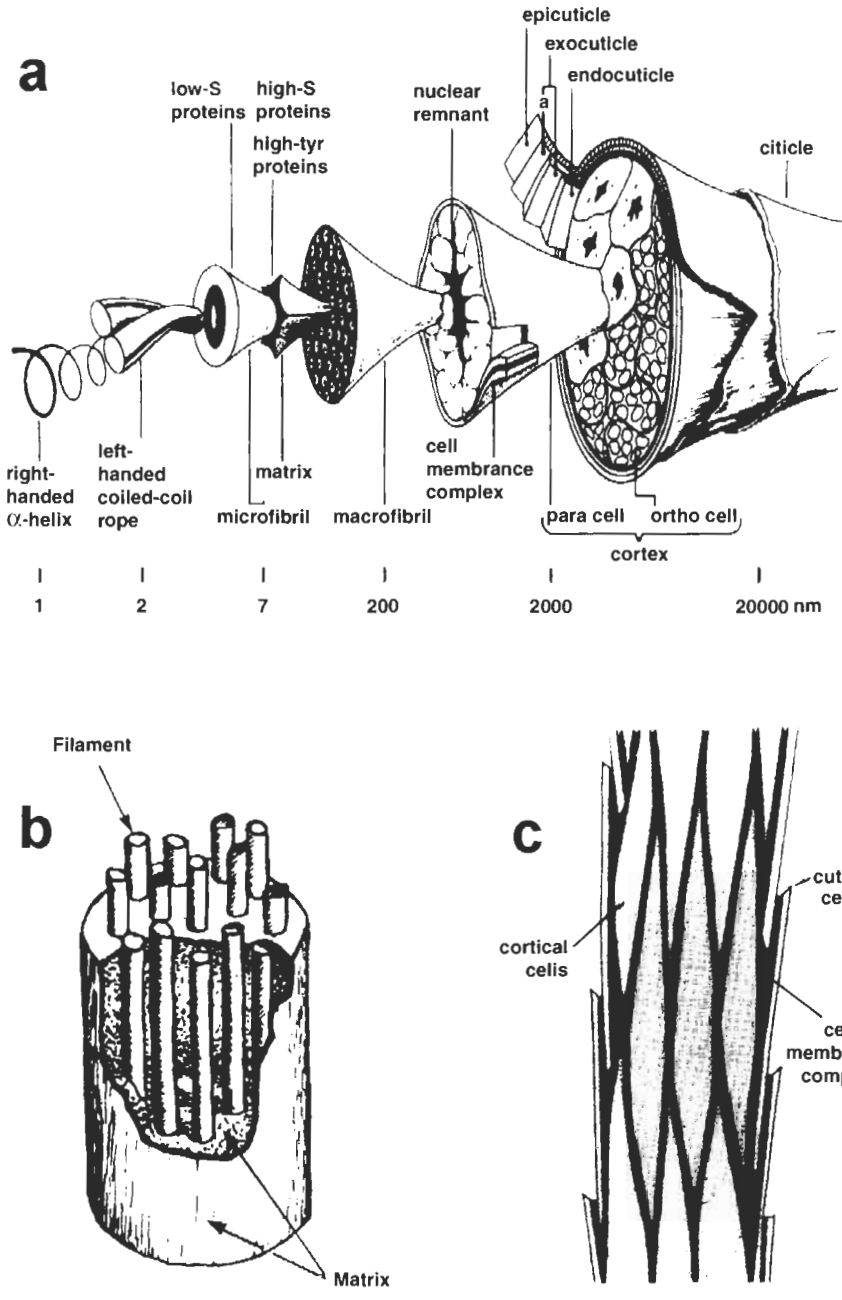

Fig. 5. (a) The structure of wool, reproduced by permission of Robert C. Marshall of CSIRO. (b) The two-phase composite model (Postle et al., 1988). (c) A schematic model of the cell structure of wool (Anon., 1986).

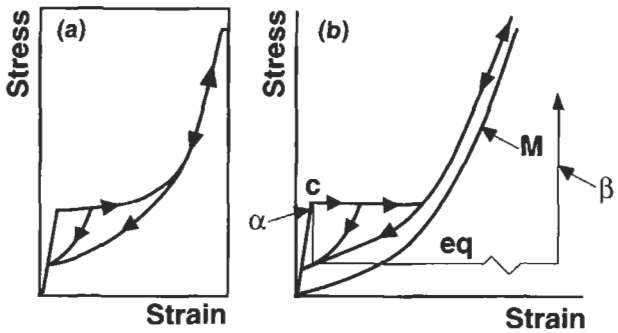

Fig. 6. (a) The observed stress–strain curve of wet wool. The stress in the middle of the yield region is 0.35 GPa and the maximum extension is 50%. (b) Predicted stress–strain curve, thick line marked with arrows, based on the composite analysis of Fig. 7. The independent stress–strain properties of the components are shown as α–c–eq–β for the microfibrils (IFs) and M for the matrix.

Fig. 7 illustrates Chapman's treatment of the mechanics of this composite system. The system is treated as a set of zones consisting of fibril and matrix elements. Originally, this was introduced as a way of simplifying the analysis, but, the later identification of the links through IF protein tails makes it a more realistic model than continuous coupling of fibrils and matrix. Up to 2% extension, most of the tension is taken by the fibrils, but, when the critical stress is reached, the IF in one zone, which will be selected due to statistical variability or random thermal vibration, opens from α to β form. Stress, which reduces to the equilibrium value in the IF, is transferred to the associated matrix. Between 2% and 30% extension, zones continue to open. Above 30%, all zones have opened and further extension increases the stress on the matrix. In recovery, there is no critical phenomenon, so that all zones contract uniformly until the initial extension curve is joined. The predicted stress–strain curve is shown by the thick line marked with arrows in Fig. 6b. With an appropriate set of input parameters, for most of which there is independent support, the predicted response agrees well with the experimental curves in Fig. 6a. The main difference is that there is a finite slope in the yield region, but this is explained by variability along the fibre. The C/H model can be extended to cover other aspects of the tensile properties of wool, such as the influence of humidity, time dependence and setting.

Fracture

On the C/H model, the limiting factor is the break extension of the matrix, which is less than that of the fibrils. Once the matrix has failed, the fibrils will come under higher tensions and will rupture to give a granular break. Cells may also break semi-independently, reflecting the composite of cells bonded by the CMC.

The tensile strength of wool fibres is important because the fibres are subject to severe forces during the initial stages of processing, when the fleeces are cleaned and the fibres are separated into forms that can be spun into yarn. The strength of wool is commonly tested as the 'staple strength', which involves all the complications of load

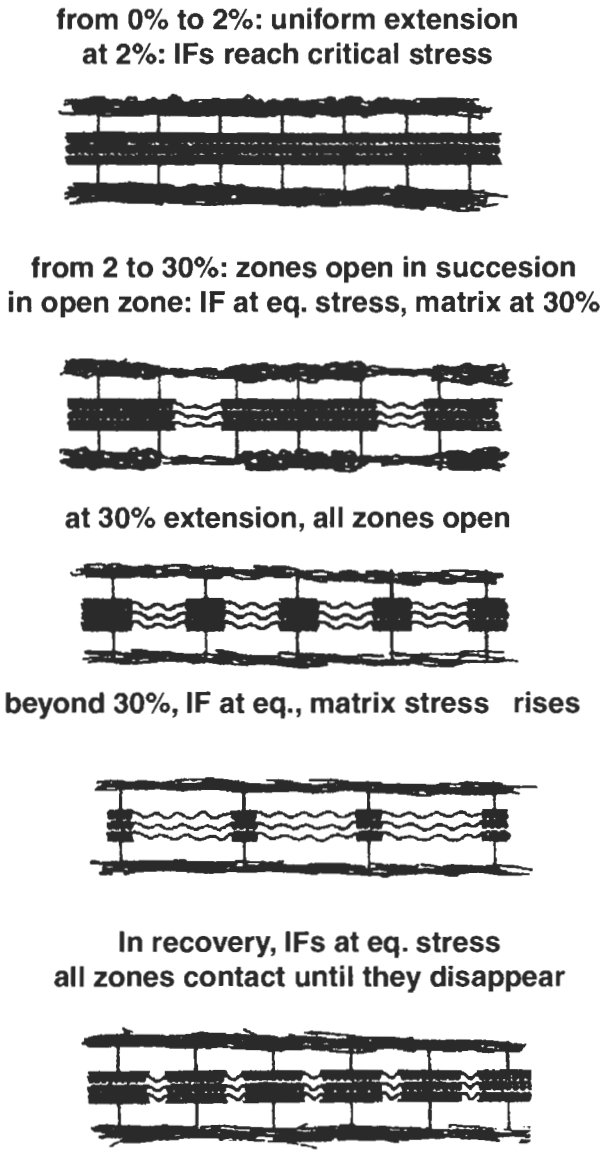

Fig. 7. Schematic representation of the sequence of changes during extension of the C/H model, based on Chapman (1969).

sharing in bundles of fibres. The strength of individual wool fibres is sensitive to fibre variability. For example in Western Australia, there is a dry period in the summer when feed is short. This leads to 'tender wools', which break at thin places in the fibres, which gives a low tenacity if expressed on the basis of the average linear density (tex, denier) or area of the fibre.

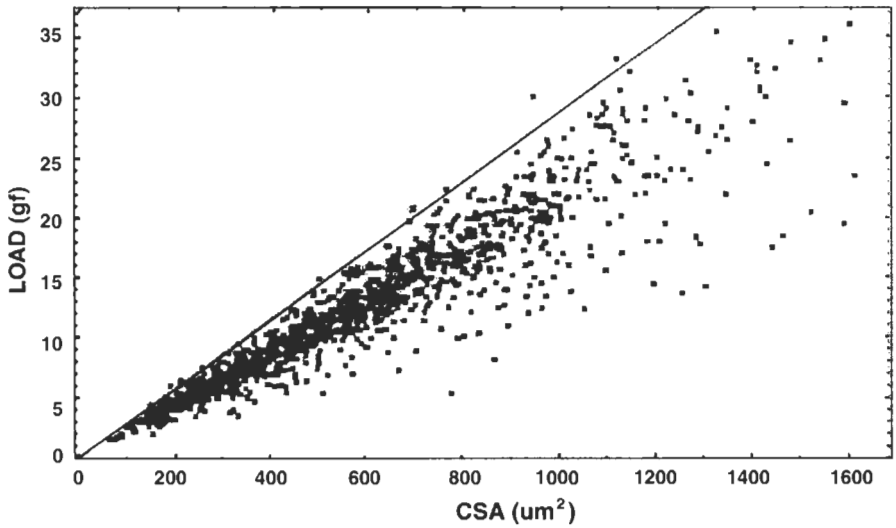

Fig. 8. Break load of wool fibres plotted against area of cross-section at point of break. From Woods et al. (1990).

Fig. 8 is a plot of break load of wool fibres against the area of cross-section at the point of break. The slope of the upper bound line, which is 100 MPa, is a measure of the 'intrinsic strength' of wool at a break extension of 50 to 60%. The points below the line are due to defects of one sort or another. Some of these will be associated with localised damage, but others may have physiological causes associated with the growth of the fibres. One suggestion is that weakness in the CMC may cause cells to pull out from one another, particularly if they are shorter or thicker with a low aspect ratio.

MELT-SPUN SYNTHETIC FIBRES

Structure and Stress–Strain Curves

In contrast to the detailed information on the structure of natural fibres, there is great uncertainty about the structure of the melt-spun synthetic fibres, of which the most important are polyester (polyethylene terephthalate), polyamides (nylon 6 and 66) and polypropylene. They are known to be about 50% crystalline, in the sense that the density is mid-way between the densities of crystalline and amorphous material. This is confirmed by other analytical studies. It is also known that they are moderately highly oriented, with the high-tenacity types, used in technical textiles, being more highly oriented than those used for apparel. However, this leaves open a great variety of possible structures: different sizes and shapes of crystallites, different interconnections between crystallites, and a range of possibilities from well-defined crystallites in an amorphous matrix to a uniform structure of intermediate order. Fig. 9 shows some of the pictures drawn to give impressions of the likely fine structure, which has a scale of the

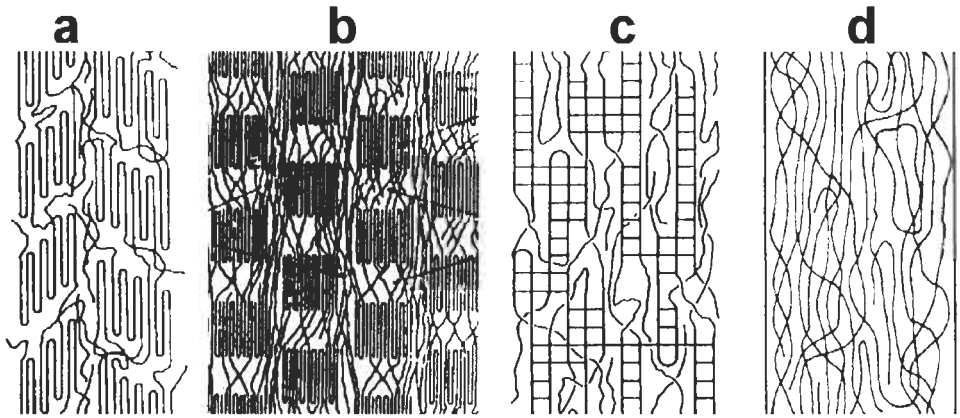

Fig. 9. Four views suggesting the fine structure of nylon or polyester fibres: (a) from Hearle and Greer (1970); (b) from Prevorsek et al. (1973); (c) from Hearle (1977); (d) from Heuvel and Huisman (1985). Note that these diagrams, which were drawn to indicate the authors' views of particular features of the structure, are grossly inadequate representations of reality. They are pseudo-two-dimensional views of three-dimensional structures, and nylon and polyester molecules are inadequately represented by lines.

Table 1. Alternating sequences in nylon and polyester

	flexible inert sequences	interactive sequences
Nylon 6	$(-CH_2-)_5$	–CO–NH–
Nylon 66	$(-CH_2-)_4$ and $(-CH_2-)_6$	–CO–NH–
Polyethylene terephthalate	$-O-CO-CH_2-CH_2-CO-O-$	benzene ring

order of 10 nm. Another contrast is that the natural fibres are laid down under genetic control from solution and thus have well-defined structures, which vary only in specific details and are far from a liquid state, whereas melt-spun fibres are processed close to their molten form, and the structure varies with the crystallisation conditions and subsequent thermo-mechanical treatments. There is no single type of structure. These problems are discussed in a recent book, Salem (2001).

A feature of nylon and polyester, which makes them good textile fibres, is that their molecules have long repeats (7 to 14 units) with the different chemical groups shown in Table 1. Above about −100°C, the flexible inert sequences are free to rotate in a rubbery state between each unit, but up to about +100°C the interactive groups stiffen the amorphous regions by hydrogen bonding in nylon or phenyl interaction in polyester. This combination gives the required limited extensibility to the fibres. In polypropylene, there is a single transition around 20°C, and the tendency of the molecules to take up a helical form is an important factor. Much more could be written on structure and thermo-mechanical responses, including the influence of water absorption on nylon and the stiffening effect of the benzene rings in polyester, but this brief account is sufficient as a basis for a discussion of mechanical properties (see Morton and Hearle, 1993).

Fibres that are extruded and cooled slowly solidify in an unoriented state. When tension is applied, there is a small amount of elastic extension but then the fibre yields

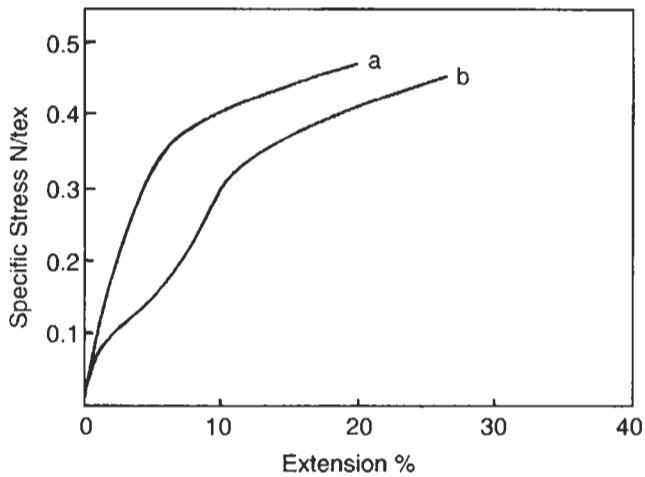

Fig. 10. Stress–strain curves of polyester fibres at 65% rh, 20°C. (a) As received, after drawing which partly orients and tightens non-crystalline regions. (b) After treatment in water at 95°C under zero tension, which allows non-crystalline regions to contract and form intermolecular bonds on cooling. The rupture of these bonds gives the sigmoidal start to the stress–strain curve.

plastically and can be drawn typically to 4× (i.e. to four times their initial length) in order to produce fibres with the right properties for use. There are variants on this description. Modern high-speed spinning produces partially oriented yarns, or, at the highest speeds, high-extension yarns directly suitable for some uses. Subsequent thermal processing changes properties. By shifting the origin, plots of true stress against strain can be superimposed. Breaking extensions of drawn fibres range from 10 to 50% in fibres for different uses. If a 'natural draw ratio' is exceeded, the fibres will break. Consequently, processing must stay below this limit. A typical stress–strain curve, such as shown in Fig. 10, is almost linear up to near-peak load and then terminates with a small yield region. Bonding in amorphous regions can lead to some curvature in the low-stress part of the curves.

No detailed quantitative analysis of the stress–strain curve has been published. Hearle (1991) refers to an unpublished network analysis that models the structure as a system of crystallites linked by tie-molecules. Two contributions to deformation energy are taken into account. The energy of elastic extension of tie-molecules is given by rubber elasticity theory, using the inverse Langevin function form. The energy of volume change depends on the bulk modulus of the material. Starting with an assumed reference state, minimisation of energy determines first the state under zero stress and then at increasing extension. Differentiation gives the stress–strain curve. The results are qualitatively reasonable, but there are uncertainties about some of the assumptions and the values of some of the 20 input parameters, listed in Table 2. This model would apply to nylon at around 150°C, when the hydrogen bonds are mobile or to a similar situation in polyester. Bonding in the amorphous regions at lower temperatures would stiffen the amorphous regions. One interesting feature of the model is that, even when there is zero stress on the fibre, the tie-molecules are extended and under relatively high

Table 2. Parameters for analysis of mechanics of a simplified model

Features of the polymer
Molar mass of the repeat unit [a]
Length of repeat unit in crystal [a]
Crystal density [a]
Amorphous density, stress-free [a]
Number of equivalent free links per repeat [b]
Degree of polymerisation [c]
Features of fine structure
Fractional mass crystallinity [a]
Number of repeats in crystallite length [a]
Number of repeats across crystallite [a]
Series fraction of amorphite [a]
Fraction of sites with crystallographic folds [c]
Fraction of sites with loose folds [c]
Length factor for free ends [c]
Length factor for loose folds [c]
Relative probability of connector types [c]
Other parameters
Bulk modulus of amorphous material [b]
Stress at which chains break [b]
Temperature [b]
Mass of proton [b]
Boltzmann's constant [b]

[a] Is required to characterise two-phase structure.
[b] Is required to characterise connectivity.
[c] Is required to analyse mechanics.

tension, which acts against the resistance to volume reduction. A large-scale analogue would be a collection of rigid blocks linked together by rubber bands under tension.

The general picture of the stress–strain response in the melt-spun synthetics is thus one of elastomeric extension of a rubbery network, which is constrained by being tied to the crystallites, as well as by internal bonding, up to stresses that cause a plastic disruption of the structure by further yielding of crystalline regions.

Fracture

A consequence of the above account of the deformation behaviour is that, for what is in practice a fully drawn fibre but is strictly an *almost* fully drawn fibre, the fibre strength is given by the yield stress. The break load, which corresponds to the true stress at break, is almost independent of the initial state. An unoriented fibre will fail at the same tension as an oriented fibre, but at a much higher extension. The critical question is what prevents a continuation of drawing to higher extensions. At some point, the structure locks. Yielding is prevented and rupture occurs instead. Alternatively, one can say that continued yielding would require a greater stress than is required to break molecules. The likely explanation for this is that there is an underlying entangled network of molecules, and when this reaches a critical strain it cannot be further extended.

In the theoretical model described above, the drawing and locking conditions are not directly taken into account, but are implicit in that the fibre is regarded as fully drawn. The tie-molecules are locked into rigid crystallites. At low stress, there is no cause for crystal yielding to occur. At high stress, the tensions in the tie-molecules reach a level at which they break. There is a sequence of chain breakage, which starts with those that are most strained and continues to the least strained.

So far no account has been taken of stress distributions. The experimental evidence, described in the 3rd paper in this volume (fig. 3), is that there is ductile fracture with a crack which progressively opens into a V-notch until catastrophic failure occurs when the notch covers about half the fibre cross-section. If there is a defect, usually on the surface but sometimes internally (when the V-notch becomes a double cone), the stress concentration will lead to the start of the rupture, although it has a negligible effect on the mean fibre stress at which this occurs. If there is no defect, the evidence is that an initial crack will form by a coalescence of voids that form under high stress. Variation in the degree of orientation across a fibre may well play a part. If the skin of the fibre is more highly oriented, it will reach its limiting extension before the core.

In contrast to brittle fracture, the crack does not grow catastrophically, but increases steadily in size as extension continues. Material on the other side from the crack extends by further yielding, which appears to be spread over lengths of several fibre diameters in opposite directions along the fibre. The link between the low stress material in line with the crack and the extended material on the other side is by a band of plastic shear deformation.

A quantitative explanation of the effect requires an advance in fracture mechanics. Griffiths' theory explains fracture in a perfectly elastic material as dependent on crack depth. This has been extended to cover the situation where there is a small zone of plastic deformation ahead of the crack. The problem is more difficult when the plastic deformation is large compared to the crack size, and, as far as I know, there has been no treatment of the situation when plastic deformation covers the whole thickness of the specimen over an appreciable length. Any analysis would also require an understanding of the transition in material from crystalline yielding to locking and chain breakage and the form of the local stress–strain curve beyond that which is measured.

The above discussion relates to tests at or near room temperature. There is an interesting paper by Moseley (1963) on the effect of internal structure and local defects on fibre strength, which reports experiments at different temperatures on nylon and polyester. When a 1 mil (25 μm) nick was made in an 8 mil (200 μm) nylon monofil, the strength of 4 g/den at 21°C was unchanged, but the strength at −196°C dropped from 6 g/den to 3 g/den. With a 5 mil (125 μm) nick, which is more than half the fibre thickness, the strength at both 21°C and −196°C fell to 1.5 g/den. In another experiment a single polyester filament was repeatedly hit by an electric typewriter key. The strength at −196°C decreased with the number of hits, but that at 21°C was unchanged. Moseley concluded that at relatively high temperatures, strength depended on the whole internal fibre structure and local defects were of negligible importance, whereas below −100°C local defects were the dominant factor. This conclusion was supported by the different effects of test length on the break statistics at low and higher temperatures.

SOLUTION-SPUN FIBRES

Structure and Stress–Strain Curves

Regenerated cellulose, cellulose acetate, acrylic and some other fibres are spun from solution, either by dry spinning, with evaporation of solvent, or by wet spinning into a coagulation bath. In viscose rayon, the solute is sodium cellulose xanthate, which is a chemical derivative of cellulose soluble in caustic soda, so that a chemical reaction is involved in fibre formation.

There is structural uncertainty similar to that for the melt-spun synthetics. The fibres are partially crystalline and partially oriented. The density and other analyses of regenerated cellulose fibres indicate an effective crystallinity of about 33%. The method of regeneration affects the structure. In ordinary viscose rayon, there is a micellar structure, which could be represented somewhat as in Fig. 9b. Due to the differential mobility of sodium and hydrogen ions, the regeneration produces a skin, which has a fine texture and is stronger than the core, which has a coarser texture. Modification of the chemistry gives higher-strength rayons, which are 'all-skin'. Other variations give high-wet-modulus rayons, which have a fibrillar texture. The newer lyocell fibres, which are spun from a solution of cellulose in an organic solvent, also have a fibrillar texture. Secondary cellulose acetate, with one –OH group to five acetate groups, is poorly crystalline due to the irregularity of the molecules. More information on regenerated cellulose fibres is given in Woodings (2000). Acrylic fibres are atactic copolymers, with a small percentage of a monomer other than acrylonitrile, and the structure is assumed to be quasicrystalline, with regions of locally aligned molecules that are not in 3D crystallographic register.

In both cellulose and acrylic fibres, there are strong intermolecular forces in the disordered as well as the more ordered regions, though these are weaker than the covalent bonds in the main chains. In cellulose, the cross-links are hydrogen bonds, and in acrylic fibres they are polar interactions of the –CN groups. The stress–strain curves of an acrylic fibre, shown in Fig. 11, are typical of these materials. The curves, S, S_T and W_{20}, at 20°C all show a marked yielding at about 2% extension, when the intermolecular bonds in the disordered regions start to break. The upper graph shows that the elastic recovery falls off sharply at the same strain. There is a second-order transition at around 80°C, when the polar interactions become mobile, and this leads to the low modulus and high break extension at 95°C in curve W_{95}. As shown below, viscose rayon shows a similar behaviour, except that it is absorption of water, not increase of temperature, that results in the low modulus due to the mobility of hydrogen bonds.

There has been little analytical modelling of the mechanical properties of this group of fibres. Hearle (1967) treated the wet and dry properties of rayon fibres in terms of the composite models shown in Fig. 12 by following the well-known mixture laws. The series structure, Fig. 12a, which is dominated by the soft component, averages the strains at the same stress, and the parallel structure, Fig. 12c, which is dominated by the stiff component, averages stresses at the same strain. The stress for the micellar, Fig. 12b, form is somewhat arbitrarily placed in a mid-way position. In the wet state, Fig. 12d, the component stress–strain curves are assumed to be linear, with a high

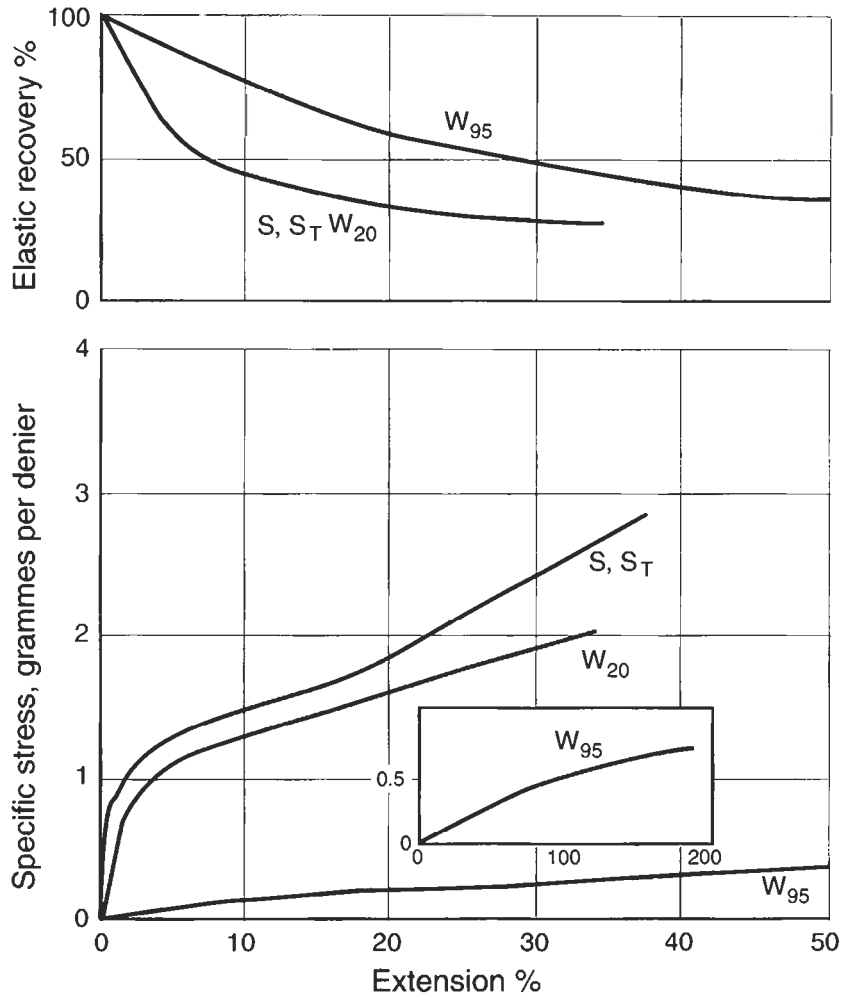

Fig. 11. Stress–strain and recovery behaviour of Courtelle acrylic fibre. S, as received, tested at 65% rh and 20°C; S_T, treated in water at 95°C, tested at 65% rh and 20°C; W_{20}, as received, tested in water at 20°C; W_{95}, as received, tested in water at 95°C. From Ford (1966).

modulus for the crystalline material C and a low modulus for the amorphous material D. The composite curves, at 2/3 crystalline to 1/3 disordered, are shown as F for a fibrillar (series) structure, L for a lamellar (parallel) structure, and M for a micellar structure. The dry state, Fig. 12e, has the same linear plot for the crystalline material C, but the disordered material D shows the influence of the hydrogen bonding by an initially higher modulus followed by a yield point. Fig. 12f shows a comparison of the theoretical predictions for a standard rayon, S,D and S,W, which is assumed to have a micellar structure, and a high-wet-modulus rayon, H,D and H,W, which is assumed to have a fibrillar structure. The numerical values of the slopes of the stress–strain plots

in Fig. 12d,e are found by fitting stress–strain curves for one type of fibre and are then used to predict the response for the other type. Although this model provides some insights into the structural mechanics, it neglects many features, notably the influence of orientation.

Fracture

Fracture in these solution-spun fibres is probably triggered by the amorphous material reaching its limiting extension and polymer molecules breaking. Fig. 13a shows how two crystalline regions in viscose rayon will be linked together by tie-molecules, which break when they reach a critical load. In the wet state, the free chain ends will not contribute to the tension. Consequently, as shown in Fig. 13b, the degree of polymerisation (DP) has a major effect on the fibre strength. At low DP, there will be a large number of free chain ends, but as chain length increases there will be fewer and the strength approaches an asymptotic maximum. Fig. 13b also shows the considerable influence on strength of degree of orientation, as given by the birefringence.

Although one can identify the cause of fracture with chain breakage, its manifestation is determined by larger-scale structural discontinuities in solution-spun fibres. The fibres coagulate in a sponge-like form with solid material separated by voids of residual solvent. On drying, the solvent is removed and stretching elongates the voids. What remains is a coarse structure with regions of integral material separated by weaknesses in the structure corresponding to the original void surfaces. The rupture of one integral zone does not lead to continuous crack propagation, because of the region of weakness, but does transfer sufficient stress to neighbouring zones to cause them to break in contiguous positions. This leads to granular breaks as shown in fig. 5 of the 3rd paper (this volume). These SEM pictures are similar to low-magnification views of the

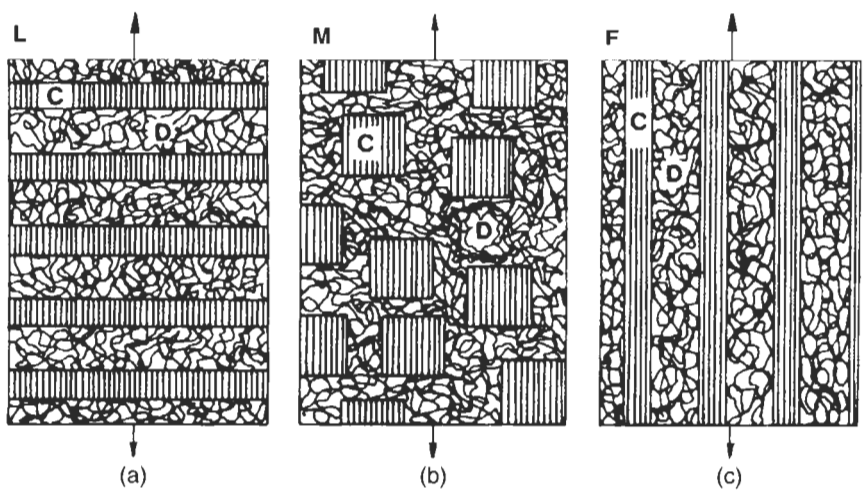

Fig. 12. A model for the stress–strain properties of viscose rayon, Hearle (1967). (a–c) Composite models of crystalline C and disordered D material in (a) lamellar L, (b) micellar M, and (c) fibrillar F forms.

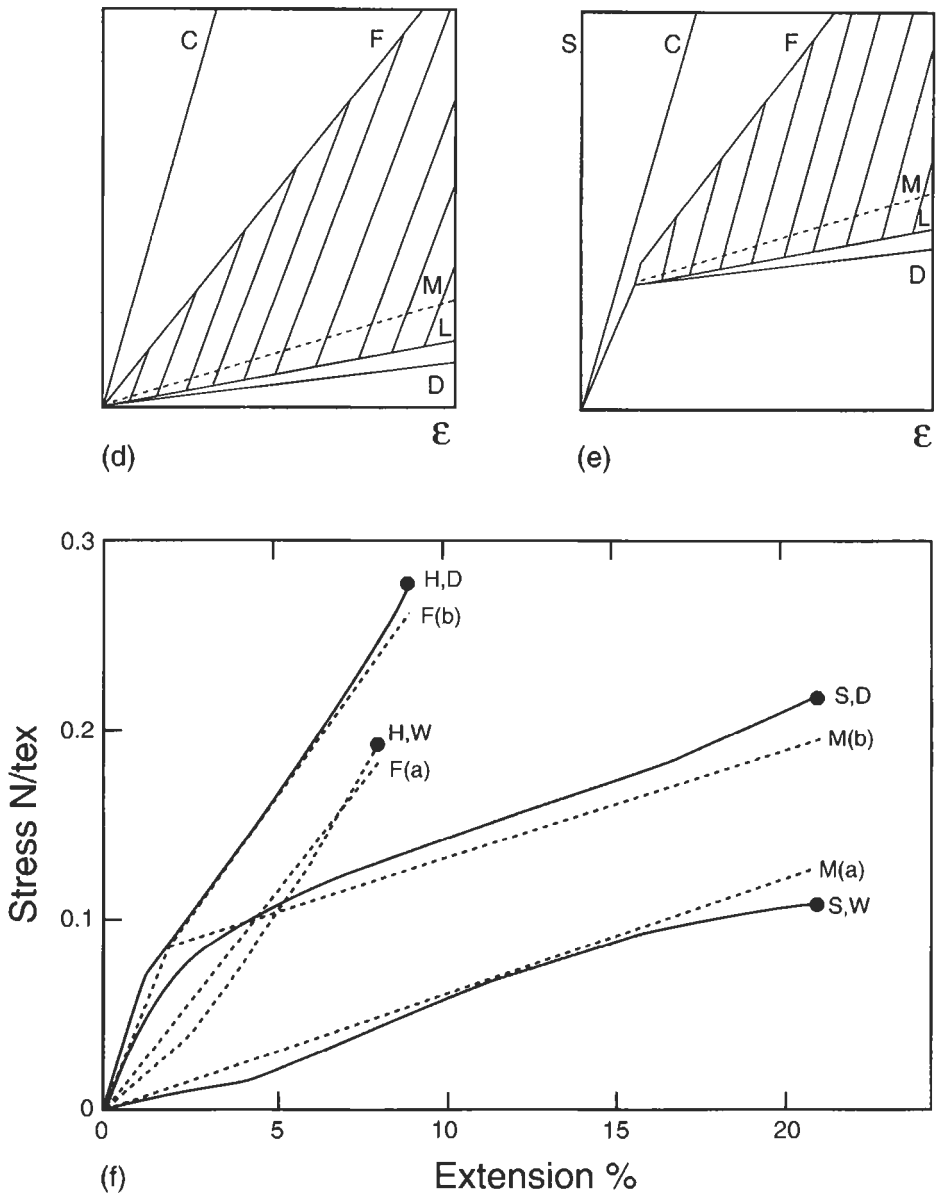

Fig. 12 (continued). (d,e) Theoretical stress–strain plots for composite forms based on plots for crystalline C and disordered D material in (d) wet and (e) dry state. (f) Comparison of theoretical plots with experimental curves for standard rayon S and high-wet-modulus rayon H, dry D and wet W.

fracture of reinforced composites. The mechanisms are analogous, with separate rupture of neighbouring units, though in the composites the scale is larger and the breakage of individual fibres can be seen in SEM pictures.

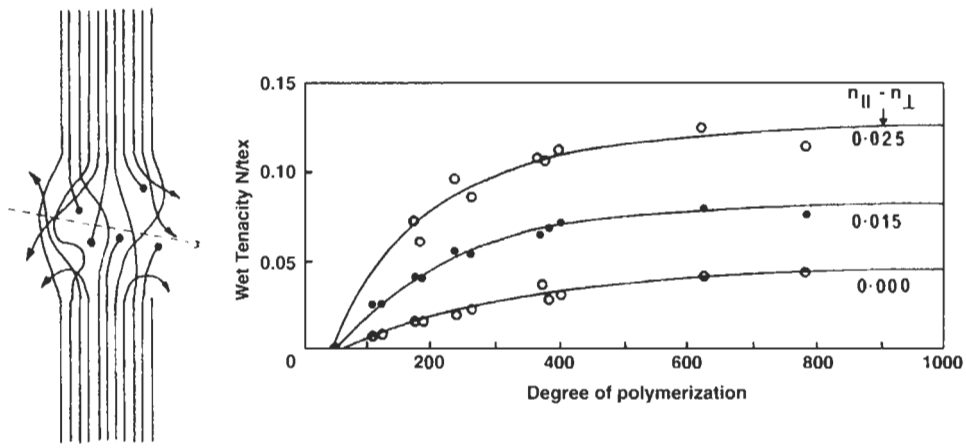

Fig. 13. (a) Tie-molecules and free ends between a crystalline micelle. (b) Change of strength (tenacity) with degree of polymerisation and with orientation as given by the difference between parallel and perpendicular refractive indices. From Cumberbirch and Mack (1961).

OTHER MODES OF FAILURE

As mentioned in the introduction to this paper, scientific study has concentrated on the tensile mode. Except for two forms of break in cotton, all the tensile failures discussed in this paper consist of breaks that run transversely across the fibre. However, the fibres are fairly highly oriented, so that the bonding across the fibre is much weaker than along the fibre. Transversely, there are weak intermolecular bonds plus a small component of the covalent bonding. In use, failure is rarely due to a direct tensile overload, unless this is on fibres weakened by chemical degradation. The common forms of wear in use are due to weakness in the transverse direction, related either to shear stresses or to axial compression. There is no detailed structural prediction of the response to shear stresses or axial compression at a molecular or fine-structure level. All that one can say is that at a certain level of shear stress cracks will form and that at a certain level of axial compressive stress the structure will buckle internally. What can be described is how these stresses occur.

Every known example of failure due to these causes comes from repetitive loading. Even twist breaks, where there is a direct shear stress, fail at such high twists that the extension in the outer zones becomes the controlling factor (Hearle et al., 1998, chapter 17), though there is some axial cracking. Cyclic loading in shear, which leads to single or multiple cracking or peeling, can arise in various ways. Twist cycling directly involves shear. This is difficult to study in the laboratory, but it may occur in fibres contained in fibre assemblies in use. Beam bending theory shows that the changes in bending moment in variable curvature are balanced by shear stresses which are a maximum on the central plane of the fibre. This leads to the shear splitting in nylon and polyester shown in fig. 10f,g of the 3rd paper (this volume). More information on the stresses involved in flexing a fibre over a pin and in the biaxial rotation test (3rd paper,

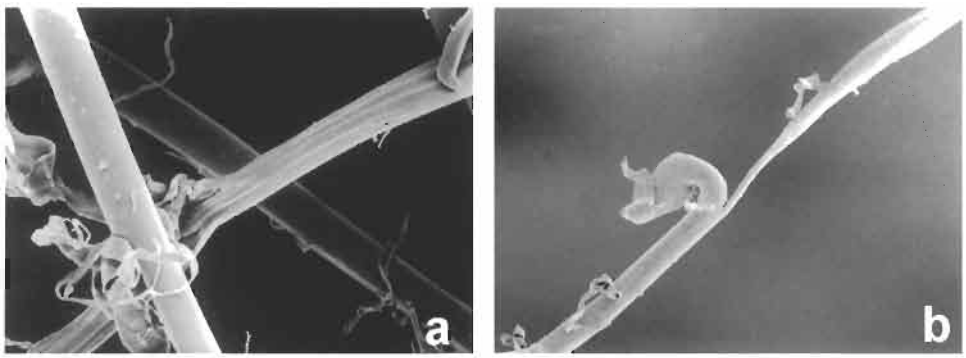

Fig. 14. Shear splitting due to internal abrasion in a wet nylon rope under tension–tension cycling, eventually leading to complete fibre rupture. From Hearle et al. (1998).

fig. 11), which is more complicated, is given by Morton and Hearle (1993), chapter 26). By far the commonest form of damage in worn textiles is multiple splitting, which can be attributed to bending and/or twisting.

In surface abrasion, the external friction forces are balanced by internal shear stresses, which lead to peeling damage (3rd paper, fig. 12). Internal abrasion is a major problem in wet nylon ropes. In one test, where a wet nylon rope was cycled up to 50% of its break load, it broke after 970 cycles. The shear stresses caused by the rubbing of fibres against another had caused cracks to run across the fibres converting the continuous filaments into fibres about 1 cm long, with a consequent reduction of strength, Fig. 14. In tensile fatigue down to zero or low loads, which gives the breaks shown in fig. 9 of the 3rd paper (this volume), shear stresses result from an initial transverse crack on the surface of the fibre. This mechanism was believed to be a source of failure in nylon brake parachutes for aircraft (Hearle et al., 1998, pl. 40G). An unexplained difference is that in both abrasion and tensile fatigue, shear stresses cause cracks to run across the fibre at an angle of about 10° in nylon, which rapidly leads to complete breaks; whereas in polyester the cracks are parallel to the fibre axis, which is far less damaging.

Axial compression fatigue was discussed in the final section of the 11th paper in this volume, because of its importance in failure of high-performance fibres. However, similar breaks occur in the textile fibres covered in this paper. Axial compression occurs on the inside of bent fibres, and, as shown in fig. 10a–e (3rd paper, this volume) is one cause of failure in flex fatigue tests. A single bend, which leads to the formation of visible kink bands, is not damaging, but cyclic bending eventually leads to structural rupture. An example of where this is found to occur in use is in the wear of wool carpets. Severe damage is found where there is turning walk. This leads to repeated compression of the pile and the fibres buckle into sharp kinks. Cracks develop on the inside of the bends and eventually the fibres break, so that the carpet pile is progressively lost.

Some interesting results for nylon and polyester fibres have received no more than vague explanations. Kurokawa et al. (1973) found that kink-bands were formed in a single bend in PET fibres up to 80°C, then rose to needing a maximum of 2000 bends at 190°C, before falling to a single bend at 200°C and rising again to 3000 at 240°C. Our

own studies have shown that kink-bands in polyester result from a single bend at 20°C but not around 100°C, whereas nylon forms visible kink-bands around 100°C but not at 0°C. The conditions requiring large numbers of bends correspond roughly to peaks in the loss modulus, which indicates a thermal transition. Studies of flex fatigue of nylon and polyester fibres at different temperatures and humidities were found by Hearle and Miraftab (1991) to show peaks in fatigue life in conditions which correlated with peaks in the loss modulus.

REFERENCES

Anon. (1986) The cell membrane complex and its influence on the properties of the wool fibre. *Wool Sci. Rev.*, 63, 3–35.

Chapman, B.M. (1969) A mechanical model for wool and other keratin fibres. *Textile Res. J.*, 39: 1102–1109.

Chapman, B.M. (1970) Observations on the mechanical behaviour of Lincoln-wool fibres supercontracted in lithium bromide solution. *J. Textile Inst.*, 61: 448–457.

Cumberbirch, R.J.E. and Mack, C. (1961) A quantitative theory of the loss of strength of regenerated cellulose filaments on hydrolysis by acids. *J. Textile Inst.*, 52: T382–T389.

Feughelman, M. (1959) Two-phase structure for keratin fibres. *Textile Res. J.*, 29: 223–228.

Ford, J.E. (Ed.) (1966) *Fibre Data Summaries*. Shirley Institute, Manchester.

Hearle, J.W.S. (1967) The structural mechanics of fibres. *J. Polym. Sci.: Part C, Polym. Symp.*, 20: 215–249.

Hearle, J.W.S. (1977) On structure and thermomechanical responses of fibres and the concept of a dynamic crystalline gel as a separate thermodynamic state. *J. Appl. Polym. Sci.: Appl. Polym. Symp.*, 31: 137–161.

Hearle, J.W.S. (1989) Mechanics of yarns and nonwoven fabrics. In: *Textile Structural Composites*. pp. 27–65, Chou, T.-W. and Ko, F.K. (Eds.). Elsevier, Amsterdam.

Hearle, J.W.S. (1991) Understanding and control of textile fibre structure. *J. Appl. Polym. Sci.: Appl. Polym. Symp.*, 47: 1–31.

Hearle, J.W.S. (2000) A critical review of the structural mechanics of wool and hair fibres. *Int. J. Biol. Macromol.*, 27: 123–138.

Hearle, J.W.S. and Greer, R. (1970) On the form of lamellar crystals in nylon fibres. *J. Textile Inst.*, 61: 240–244.

Hearle, J.W.S. and Miraftab, M. (1991) The flex fatigue of polyamide and polyester fibres, Part I. The influence of temperature and humidity. *J. Mater. Sci.*, 26: 2861.

Hearle, J.W.S. and Morton, W.E. (1993) *Physical Properties of Textile Fibres*. Textile Institute, Manchester.

Hearle, J.W.S. and Sparrow, J.T. (1979a) Mechanics of the extension of cotton fibres, I. Experimental studies of the effect of convolutions. *J. Appl. Polym. Sci.*, 24: 1465–1477.

Hearle, J.W.S. and Sparrow, J.T. (1979b) Mechanics of the extension of cotton fibres, II. Theoretical modelling. *J. Appl. Polym. Sci.*, 24: 1857.

Hearle, J.W.S., Lomas, B. and Cooke, W.D. (1998) *Atlas of Fibre Fracture and Damage to Textiles*. Woodhead Publishing, Cambridge.

Heuvel, H.M. and Huisman, R. (1985) In: *High-Speed Fiber Spinning*, p. 310, A. Ziabucki and H. Kawai (Eds.). Wiley-Interscience, New York.

Jawson, M.A., Giles, P.P. and Mark, R.E. (1968) *Proc. R. Soc. London, Ser. A*, 306: 389.

Kassenbeck, P. (1970) *Textile Res. J.*, 40: 330.

Kurokawa, M., Konishi, T., Taki, F. and Ikeda, T. (1973) *Sen-I Gakkashi*, 29: T173.

McIntyre, J.E. and Daniels, P.N. (1995) *Textile Terms and Definitions*. The Textile Institute, Manchester.

Morton, W.E. and Hearle, J.W.S. (1993) *Physical Properties of Textile Fibres*. The Textile Institute, Manchester, 3rd ed.

Moseley, W.W. (1963) Effect of structure and local defects on fibre strength. *J. Appl. Polym. Sci.*, 7: 187–201.

Noble Denton Europe and National Engineering Laboratory (1995) *Fibre Tethers 2000* — Final Report. Noble Denton Europe, London.

Postle, R., Carnaby, G.A. and de Jong, S. (1988) *The Mechanics of Wool Structures*. Ellis Horwood, Chichester.

Prevorsek, D.C., Harget, P.J., Sharma, R.K. and Reimschussel, A.C. (1973) *J. Macromol. Sci. B.*, 8: 127.

Salem, D.R. (Ed.) (2001) *Structure Formation in Polymeric Fibres*. Hanser Publishers, Munich.

Tension Technology International and Noble Denton Europe (1999) *Deepwater Fibre Moorings: an Engineers' Design Guide*. Oilfield Publications, Ledbury.

Timoshenko, S. (1957) *Strength of Materials*. Van Nostrand, New York.

Treloar, L.R.G. (1960) *Polymer*, 1: 290.

Woodings, C. (Ed.) (2000) *Regenerated Cellulose Fibres*. Woodhead Publishing, Cambridge.

Woods, J., Orwin, D.F.G. and Nelson, W.G. (1990) Variation in the breaking stress of Romney wool fibres. *Proc. 8th Int. Wool Textile Res. Conf.*, pp. 557–568.

NANOFIBERS

Fiber Fracture
M. Elices and J. Llorca (Editors)

ATOMIC TRANSFORMATIONS, STRENGTH, PLASTICITY, AND ELECTRON TRANSPORT IN STRAINED CARBON NANOTUBES

J. Bernholc, M. Buongiorno Nardelli, D. Orlikowski, C. Roland and Q. Zhao

Department of Physics, North Carolina State University, Raleigh, NC 27695, USA

Introduction 359
Mechanical Properties 360
Adatoms-Induced Transformations and Plasticity 368
Electron Transport Properties of Strained Nanotubes 371
Summary 375
Acknowledgements 375
References 375

Abstract

Nanotubes are hollow cylinders consisting of 'rolled-up' graphitic sheets. They form spontaneously in the same apparatus as the famed C_{60} molecule, and have been predicted and/or observed to have even more spectacular properties than C_{60}, including extremely high strength and flexibility, ability to form nanoscale electronic devices consisting entirely of carbon, strong capillary effects, cold cathode field emission, etc. Carbon nanotubes have also been theoretically predicted to be among the strongest materials known. Their strength, which has already been verified experimentally, may enable unique applications in many critical areas of technology. While very high strain rates must lead to tube breakage, nanotubes with (n,m) indices, where $n,m < 14$, can display plastic flow under suitable conditions. This occurs through the conversion of four hexagons to a 5–7–7–5 defect, which then splits into two 5–7 pairs. The index of the tube changes between the 5–7 pairs, potentially leading to metal–semiconductor junctions. Furthermore, carbon adatoms-induced transformations in strained nanotubes can lead to the formation of quantum dots. The high-strain conditions can be imposed

on the tube via, e.g., AFM tip manipulations, and we show that such procedures can lead to intratube device formation. The defects and the index changes occurring during the mechanical transformations also affect the electrical properties of nanotubes. The computed quantum conductances of strained defective and deformed tubes show that the defect density and the contacts play key roles in reducing the conductance at the Fermi energy. The role of bending in changing the electrical properties was also explored. It was found that mechanical deformations do not significantly affect the conductance of bent armchair nanotubes up to substantial bending angles, while a conductivity gap is induced by the bending of chiral nanotubes. These results are in good agreement with recent experimental data.

Keywords

Carbon nanotube; Molecular dynamics; Tensile strength; Plasticity; Adatoms; Defects; Electron transport

INTRODUCTION

Carbon is unique among the elements in its ability to assume a wide variety of different structures and forms. It is now a little more than ten years ago since a new family of carbon cage structures, all based on a three-fold coordinated sp^2 network, was discovered, thereby inaugurating the science of fullerenes. Of these, C_{60} is the best known member. However, perhaps the most exciting among the recent additions to the fullerene family are carbon nanotubes, discovered soon after the C_{60} was made in quantity. Carbon nanotubes are hollow cylinders consisting of single or multiple sheets of graphite (graphene) wrapped into a cylinder, as illustrated in Fig. 1. They are believed to have extraordinary structural, mechanical and electrical properties, which derive from the special properties of carbon bonds, their unique quasi-one-dimensional nature, and their cylindrical symmetry. For instance, the graphitic network upon which the nanotube structure is based is well known for its strength and elasticity, thereby providing for unmatched mechanical strength. Nanotubes can also be metallic or semiconducting, depending on their indices (see Fig. 1). This opens up the very interesting prospects of junctions and devices made entirely out of carbon. Because of these very unusual characteristics and the potential compatibility of nanotubes with organic matter, their discovery has been greeted with a considerable amount of excitement within the scientific community. However, since they were originally synthesized in minute quantities only, relatively few experimental techniques were initially available for their study. Indeed, the original experimental work was only able to address nanotube structure through high-resolution transmission electron microscopy (HRTEM). Their discovery, however, has stimulated much theoretical work. In turn, these investigations have benefited significantly from the substantial progress achieved in the past 2–3 decades in the development of theoretical methods, some of which now have a truly predictive power. Astonishing properties have been predicted, which has stimulated further experiments, so that the progress has been very rapid, with hundreds

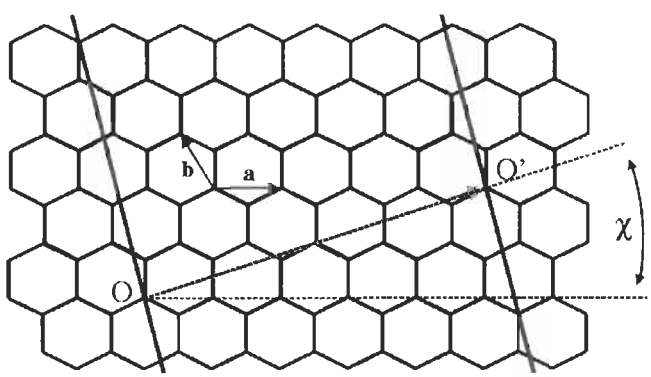

Fig. 1. Nanotube structures are obtained by rolling a graphene sheet into a cylinder, so that the lattice points O and O′ fold onto each other. Mathematically, their structures are uniquely defined by specifying the coordinates of the smallest folding vector (n,m) in the basis of graphene lattice vectors $\boldsymbol{a}$ and $\boldsymbol{b}$. The $(n,0)$ zigzag and (n,n) armchair tubes are mirror-symmetric; all other tubes are chiral.

of nanotube-related papers being published every year. Several recent books and articles provide a comprehensive description of the early progress in the field of nanotubes and an extensive bibliography (Dresselhaus et al., 1996; Bernholc et al., 1997; Ebbesen, 1997; Saito et al., 1998).

This paper focuses mainly on the mechanical properties of carbon nanotubes and discusses their elastic properties and strain-induced transformations. Only single-walled nanotubes are discussed, since they can be grown with many fewer defects and are thus much stronger. It is shown that under suitable conditions some nanotubes can deform *plastically*, while others must break in a brittle fashion. A map of brittle vs. ductile behavior of carbon nanotubes with indices up to (100,100) is presented. The electrical properties of nanotubes are also affected by strain. We will focus here on quantum (ballistic) conductance, which is very sensitive to the atomic and electronic structure. It turns out that some nanotubes can tolerate fairly large deformations without much change to their ballistic conductance, while others are quite sensitive. Both properties can be used in applications, provided that nanotubes of the appropriate symmetry can be reliably prepared or selected.

MECHANICAL PROPERTIES

It is by now well established that carbon nanotubes can be reversibly bent to very high bending angles with very little damage, if any. Nearly atomic resolution images show highly bent nanotubes (see Fig. 2a), while molecular dynamics simulations that used realistic many-body potentials have predicted highly reversible bending (Iijima et al., 1996) (see Fig. 2b). Indeed, reversible bending has subsequently been observed by manipulation using an AFM tip (Falvo et al., 1997). Furthermore, it has been shown that even highly distorted configurations (axial compression, twisting) can be due to elastic deformations with no atomic defects involved (Chopra et al., 1995; Ruoff and Lorents, 1995; Yakobson et al., 1996). In analyzing these deformations, one can use macroscopic continuum mechanics, despite the fact that nanotubes are only ~1 nm wide. For example, the elastic shell model describes very well the various buckling and twisting modes (Yakobson et al., 1996).

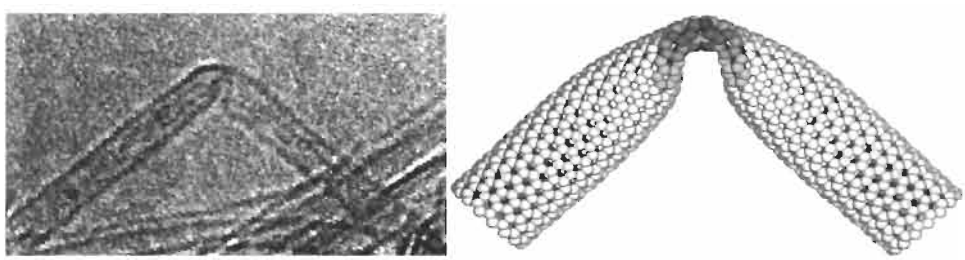

Fig. 2. (a) HREM image of kink structures formed under mechanical duress in nanotubes with diameters of 0.8 nm and 1.2 nm. (b) Atomic structure of a single kink obtained in the computer simulation of bending of the single-walled tube with a diameter of ~1.2 nm. The shading indicates the local strain energy at the various atoms. From Iijima et al. (1996).

However, when very large strains are involved, the continuum description is no longer adequate and one needs a fully atomistic picture. In order to identify the first stages of the mechanical yield of carbon nanotubes, ab initio and classical molecular dynamics simulations were performed at high temperatures, so that defect formation could be observed during the simulation times, which are of the order of several picoseconds for quantum molecular dynamics and several nanoseconds for classical dynamics. These simulations uncovered the dominant strain release mechanisms as well as their energetics (Buongiorno Nardelli et al., 1998a,b). Beyond a critical value of the tension, the system releases its excess strain via a spontaneous formation of topological defects. The first defect to form corresponds to a 90° rotation of a C–C bond about its center, the so-called Stone–Wales transformation (Stone and Wales, 1986), which produces two pentagons and two heptagons coupled in pairs (5–7–7–5), see Fig. 3. Static calculations under fixed dilation show a crossover in the stability of this defect configuration with respect to the ideal hexagonal network. The crossover is observed at about 5% tensile strain in (5,5) and (10,10) armchair tubes. This implies that the (5–7–7–5) defect is effective in releasing the excess strain energy in a tube under tensile strain. Moreover, through its dynamical evolution, this defect acts as a nucleation center for the formation of dislocations in the ideal graphite network and can lead to plastic behavior.

After the dominant defect process was identified, the energetics of the defect formation was determined through static calculations, in order to obtain reliable estimates of defect processes at low temperatures. Fig. 4 plots the formation energies of a (5–7–7–5) defect in an armchair (5,5) tube, as obtained in ab initio calculations. Calculations for other armchair tubes show that the crossover value is only weakly dependent on their diameters and always falls in the range of 5–6%.

Subsequent experiments (Walters et al., 1999; Yu et al., 2000) indeed find that nanotubes fail at strains of up to a little over 5%. Since the most recent measurements of the Young modulus of nanotubes give about an exceptionally large value of 1.25 TPa (Krishnan et al., 1998), nanotubes are among the strongest materials known. Indeed, a direct measurement of breaking strengths of nanotube 'ropes' gave values ranging up to 52 GPa (Yu et al., 2000). Furthermore, the computed activation energies for the bond rotation transformation are very high (cf. Fig. 5), indicating that perfect, defect-free nanotubes could be kinetically stable at even greater strain values. However, due to the high temperature at which the growth of nanotubes occurs, defects will form for thermodynamic reasons and then remain frozen in. For a material at thermal equilibrium, the number of defects of a particular type is given by $N_{\text{sites}}e^{(-G_F/kT)}$, where N_{sites} is the number of potential sites and G_F is the Gibbs free energy of formation of the defect. The entropic contributions are usually a small part of G_F; one can thus use the energy of formation to obtain a lower bound. For single-walled tubes, which are grown at ~1500 K, the above formula suggests that even at zero strain there might be point defects every few tenths of a mm. The presence of the frozen-in defects certainly limits the ultimate strength of nanotubes and thus some of their proposed uses.

The appearance of a (5–7–7–5) defect can be interpreted as the nucleation of a degenerate dislocation loop in the planar hexagonal network of the graphite sheet. The configuration of this primary dipole is a (5–7) core attached to an inverted (7–5) core. The (5–7) defect behaves thus as a single edge dislocation in the graphitic plane. Once

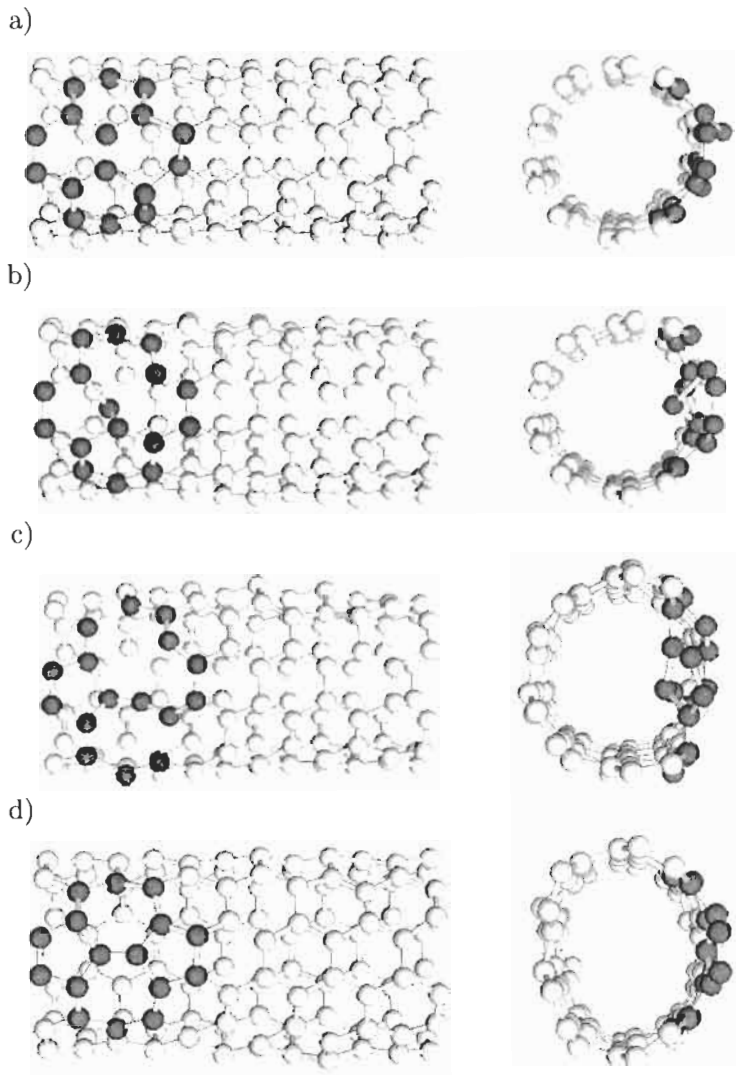

Fig. 3. The mechanism of (5–7–7–5) defect formation from an ab initio quantum mechanical molecular dynamics simulation for the (5,5) tube at 1800 K. The atoms that are involved in the creation of the defect are highlighted in black. The four snapshots show the various stages of the defect formation: (a) the system in the ideal configuration; (b) the breakage of the first bond; (c) the breakage of the second bond; (d) the defect is formed.

formed, the (5–7–7–5) dislocation loop can ease further relaxation by separating the two dislocation cores, which glide through successive bond rotations. This corresponds to a plastic flow of dislocations and gives rise to ductile behavior, as shown in Fig. 6b. Alternatively, larger defects may be nucleated from the 5–7–7–5) defect, leading to crack extension (Fig. 6c).

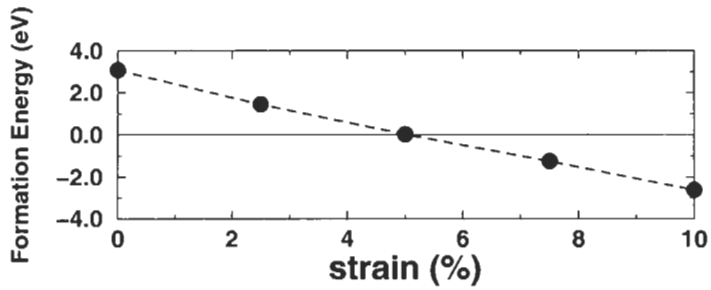

Fig. 4. Formation energy of the (5–7–7–5) defect in the (5,5) tube at different strains.

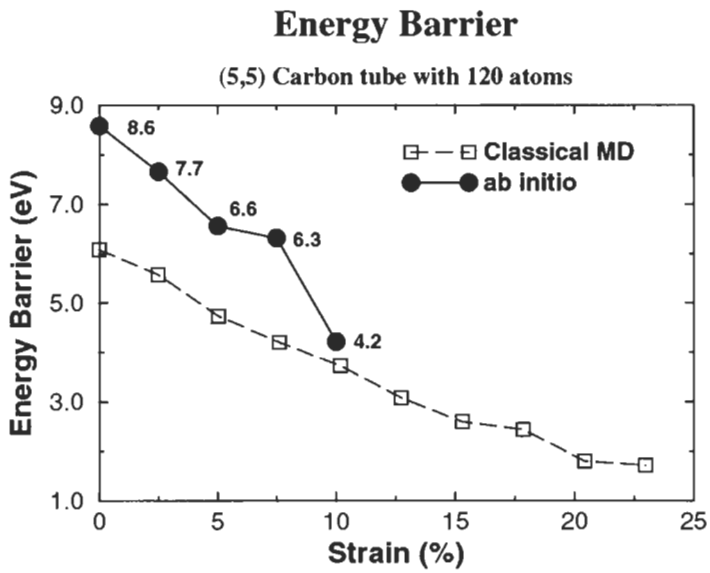

Fig. 5. The activation energy for bond rotation for the (5,5) tube computed by the ab initio multigrid method. The corresponding values obtained by molecular statics using the classical Tersoff–Brenner potential are also shown. Note that while the qualitative trends are similar between the two approaches, there are substantial quantitative differences.

We have investigated the energetics of further bond rotations in the presence of a pre-existing (5–7–7–5) defect at various strains, mostly in the (10,10) tube. The choice of this particular tube structure is due to the fact that (10,10) tubes are the most abundant product in the laser ablation apparatus (Thess et al., 1997). However, the results are qualitatively valid for all armchair tubes. Fig. 7 shows the formation energies of: (1) an octagonal defect at the preexisting (5–7–7–5) defect as produced by a further rotation of a strictly azimuthal bond; (2) the initial stage of separation of the two dislocation cores (5–7) and (7–5), as produced by the rotation of the 'shoulder' bond in the (5–7) core. These results show that the separation of the dislocation cores is energetically favored over the formation of a larger open ring structure for strains up to ~6%. The

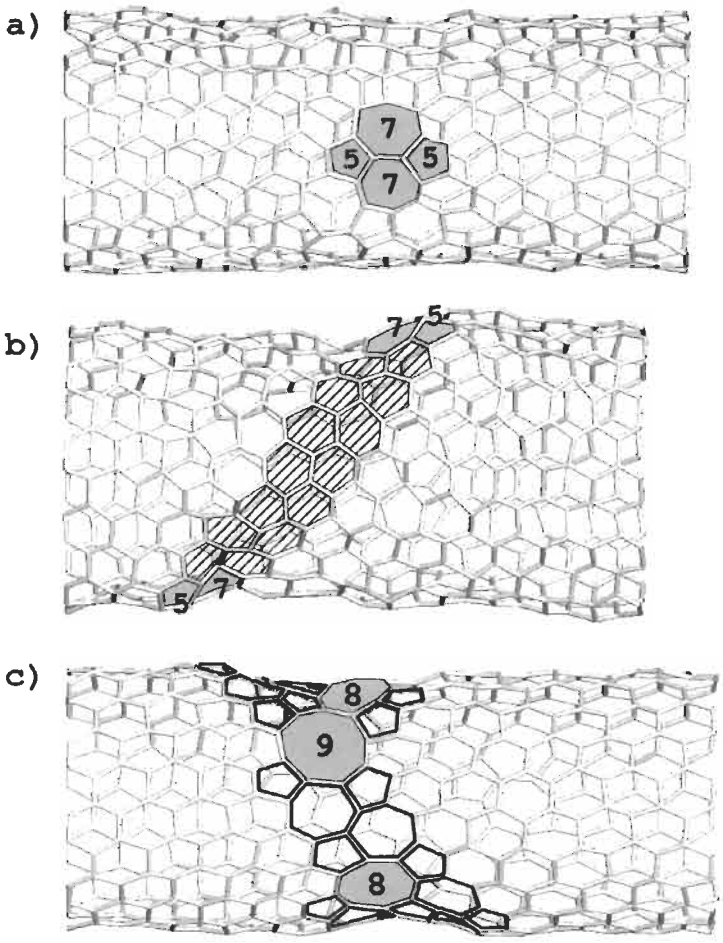

Fig. 6. Three snapshots of molecular dynamics simulations of a (10,10) nanotube under axial tension. (a) Formation of a bond rotation defect at $T = 2000$ K and 10% strain. (b) Plastic flow behavior after ~2.5 ns at $T = 3000$ K and 3% strain. The shaded area indicates the migration path of the (5–7) edge dislocation. (c) Nucleation of large open rings and initiation of the brittle relaxation after ~1.0 ns at $T = 1300$ K and 15% strain. See text.

calculated activation barriers are also lower for dislocation glide at strains lower than ~6%, and show a decrease with the decreasing formation energy (the activation barriers at 0% strain are 5.14 and 4.7 eV for the formation energy of the octagonal defect and the initial separation of the (5–7) cores, respectively. These values are lowered to 3.1 and 3.4 eV at 10% strain). One can then expect that for strains lower than 6% and at sufficiently high temperatures, the most commonly observed behavior will correspond to the separation and glide of the individual dislocation cores. For large strains and relatively low temperatures, on the other hand, one should expect the formation of larger ring structures.

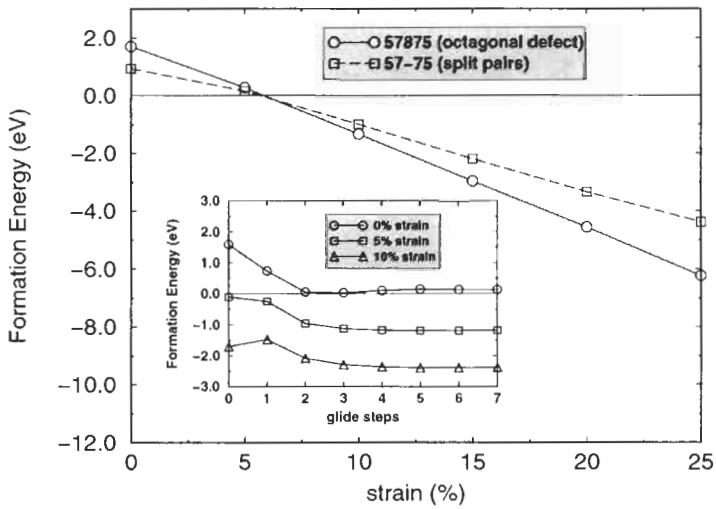

Fig. 7. Formation energy of an octagonal defect and of the initial step in the glide of the dislocation cores in a (10,10) tube as a function of uniaxial strain. Inset: formation energy for the glide of the dislocation core as a function of the glide step under three different strain conditions (each glide step corresponds to a bond rotation at the 'shoulder' bond that separates the two cores of one lattice parameter). Note that the values of the dashed curve in the main panel correspond to the values for glide step = 1 of the three curves in the inset.

The motion of dislocation edges in a strained structure is a well known phenomenon in the theory of dislocations. Under uniform stress conditions in the limit of linear elasticity theory, the dislocation line is not fixed and the energy of the system can change if the dislocation moves. In particular, a glide of an edge dislocation via the successive rotation of the 'shoulder' bond in the (5–7) core can reduce the total energy. Our results for the energetics of such a glide are summarized in the inset of Fig. 7. For all the strains considered, the initial energy gain is always smaller (more positive) in the first few gliding steps than in the large separation limit. This is the signature of a relatively long range attractive interaction between the two dislocation cores, which extends up to four gliding steps (four lattice parameters). For the glide of non-interacting dislocations, the activation barriers are significantly lower (the activations barrier for the initial separation of the two dislocation cores is 4.7 eV in unstrained (10,10) nanotubes, but it decreases to 3.0 eV when the cores are separated by four lattice parameters). It is important to note that large strains are not needed in order to have plastic flow of dislocations. In fact, it is clear from the inset in Fig. 6 that once the 5–7–7–5 dislocation cores are spatially separated, their motion is always energetically favored and the tube will show a ductile behavior even for strains smaller than 5%. Even though strain-induced dislocation loops are energetically favored to form at strain values >5%, one can expect that a certain number of such defects will be present in the as-grown tube (Ebbesen and Takada, 1995; Buongiorno Nardelli et al., 1998a,b) thus making a ductile behavior possible.

The rotation of the C–C bond is particularly advantageous in armchair tubes, where this bond is perpendicular to the applied tension. In contrast, in the case of a zigzag

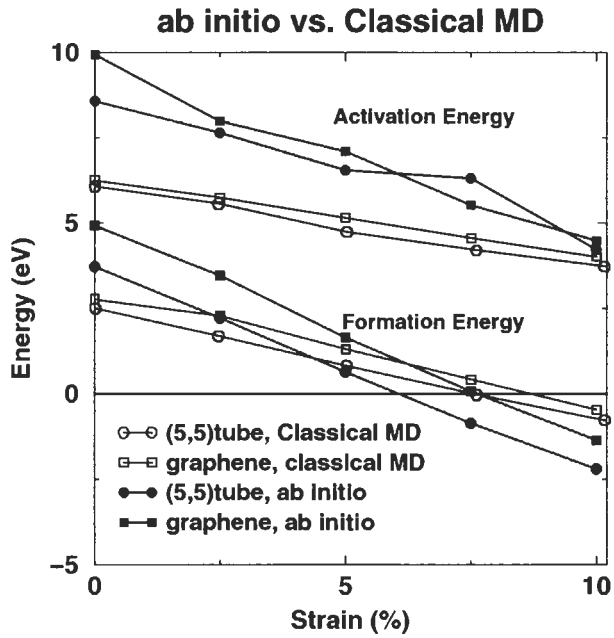

Fig. 8. Formation energy of the off-axis (5–7–7–5) defect in $(n,0)$ tubes of various diameters. In $(n,0)$ tubes, $D = 0.078n$ nm. Inset: formation energy of the off-axis (5–7–7–5) defect in $(10,m)$ tubes of different chiralities. Note that in (n,m) tubes the chiral angle $\chi = \arctan[\sqrt{3}m/(2n+m)]$ is zero in zigzag tubes and 30° in armchair tubes. All data refer to 10% strain.

nanotube, the same C–C bond will be parallel to the applied tension, which is already the minimum energy configuration for the strained bond. The formation of the Stone–Wales defect is then limited to rotation of the bonds oriented 120° with respect to the tube axis. Our analysis shows that the formation energy of these defects is strongly dependent on curvature and thereby on the diameter of the tube. In fact, a number of different behaviors have been observed when constructing the brittle vs. ductile map of stress response of carbon nanotubes. The results of static energetics calculations and molecular dynamics simulations for $(n,0)$ tubes of various diameters D at 10% strain are summarized in Fig. 8. Remarkably, the formation energy of the off-axis (5–7–7–5) defect (obtained via the rotation of the C–C bond oriented 120° wrt. tube axis) shows a crossover with respect to the diameter, and it is negative for $(n,0)$ tubes with $n < 14$ ($D < 1.1$ nm). Similarly, the formation energy of this defect in chiral tubes of the $(10,m)$ family (chosen as a particular example) is always negative, although it changes with the chiral angle χ. This result implies that the bond-rotation transformation is still efficient in releasing the strain energy of the tube. This effect is clearly due to the variation in curvature, which in the small-diameter tubes makes the process energetically advantageous. Therefore, above a critical value of the curvature a plastic behavior is always possible and the tubes can be ductile.

From these calculations one can identify the full range of elastic responses in strained carbon nanotubes. In particular, under high-strain and low-temperature conditions, all

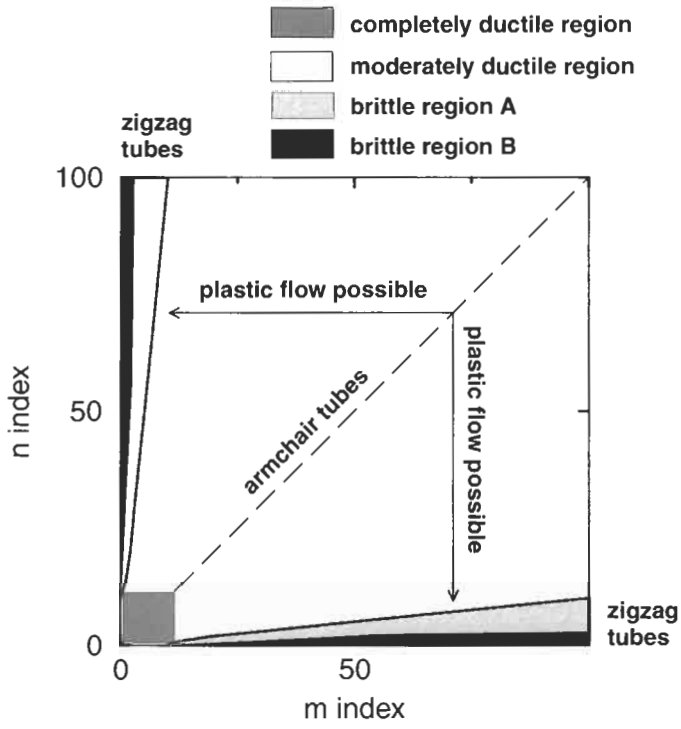

Fig. 9. Ductile–brittle domain map for carbon nanotubes with diameters up to 13 nm. Different shaded areas correspond to different possible behaviors (see text).

tubes are brittle. If, on the contrary, external conditions favor plastic flow, such as a low strain and a high temperature, (n,m) tubes with $n,m < 14$ can be completely ductile, while larger tubes are moderately or completely brittle depending on their symmetry. These results are summarized in Fig. 9 where a map of the ductile vs. brittle behavior of a general (n,m) carbon nanotube under an axial tensile load is presented. There are four regions indicated by the different shadings. The small hatched area near the origin is the region of complete ductile behavior, where the formation of (5–7–7–5) defects is always favored under sufficiently large strain. In particular, plastic flow will transform the tube section between the dislocation cores along paths parallel to the axes of Fig. 9. During the transformations, the symmetry will change between the armchair and the zigzag type. The same transformations will occur in the larger (white) moderately ductile region. Tubes with indices in this area are ductile, but the plastic behavior is limited by the brittle regions near the axes. Tubes that belong to the last two regions will always follow a brittle fracture path with formation of disordered cracks and large open rings under high tensile strain conditions.

ADATOMS-INDUCED TRANSFORMATIONS AND PLASTICITY

Nanotubes are obviously produced at carbon-rich conditions and additional carbon atoms are likely to be present on nanotube walls. These 'adatoms', introduced either during growth or processing, can facilitate structural transformations in nanotubes, as described below.

The energetically preferred position for single carbon adatoms is to form *handles* between pairs of nearest-neighbor carbon atoms (Maiti et al., 1997). The adsorption energy for the adatoms varies weakly as a function of the nanotube diameter, ranging from 5.5 eV on a (5,5) tube with a 0.78 nm diameter to 4.9 eV for a graphene sheet. The most important effect of adatoms on strained nanotubes is to reduce the activation energy for the Stone–Wales transformation. Essentially, the activation energies for the bond rotation are all uniformly reduced by 1.0–1.2 eV for all strains (Orlikowski et al., unpublished). This effect may be understood in terms of an increased flexibility for rotation of bonds that are next to the adatom handle, and implies that the presence of adatoms on strained nanotubes significantly enhances the rate of (5–7–7–5) defect formation.

The adatoms diffuse relatively fast and will eventually condense into 'addimers'. When a nanotube is strained, an addimer can induce additional bond rotations. Fig. 10 shows a typical dynamical evolution of a 3 nm long (480 atoms) (10,10) armchair tube with a carbon addimer at 2500 K and under a 3% strain. This addimer initially sits on the surface of the nanotube. Within 4 ps, it is incorporated into the nanotube, forming a novel defect consisting of back-to-back pentagons plus two heptagons, i.e., a (7–5–5–7) defect (Fig. 10a). This defect then undergoes substantial further evolution. After 356 ps, the bond emanating from the vertex of one of the pentagons and pointing away from the defect rotates to form a defect structure consisting of a single, rotated hexagon that is separated from the rest of the nanotube through a 'layer' of (5–7) pairs (Fig. 10b). Moreover, the creation of rotated hexagons continues; after 421 ps, a defect with two hexagons forms (Fig. 10c), while a third hexagon is incorporated after 2.35 ns (Fig. 10d). If this process of adding hexagons were to continue, the defect structure would eventually wrap itself completely about the circumference of the tube, forming a short segment of a nanotube with a different helicity.

In the absence of strain, the formation energy of the (7–5–5–7) defect is lowest for both the armchair (10,10) and the zigzag (17,0) tubes, indicating that structures with rotated hexagons are not to be expected. However, the formation energy is strongly strain-dependent. For the (10,10) tube under a 5% strain, the defect with *two* rotated hexagons has the lowest energy, indicating that structures containing more hexagons represent transient, metastable configurations. Under a 10% strain, the formation energy decreases as the number of hexagons in the defect increases, showing that larger strains lead to the wrapping of the defect about the tube. Furthermore, the formation energy of the (10,10) tube oscillates with the number of hexagons it contains. This is simply a reflection of the geometry of the armchair tubes. For a defect containing an *even* number of hexagons, the bonds that need to be rotated in order to incorporate the next hexagon are all at an angle with respect to the ones already present (Fig. 10d), so that the hexagon must necessarily be formed *next to* rather than *directly above* the existing hexagons.

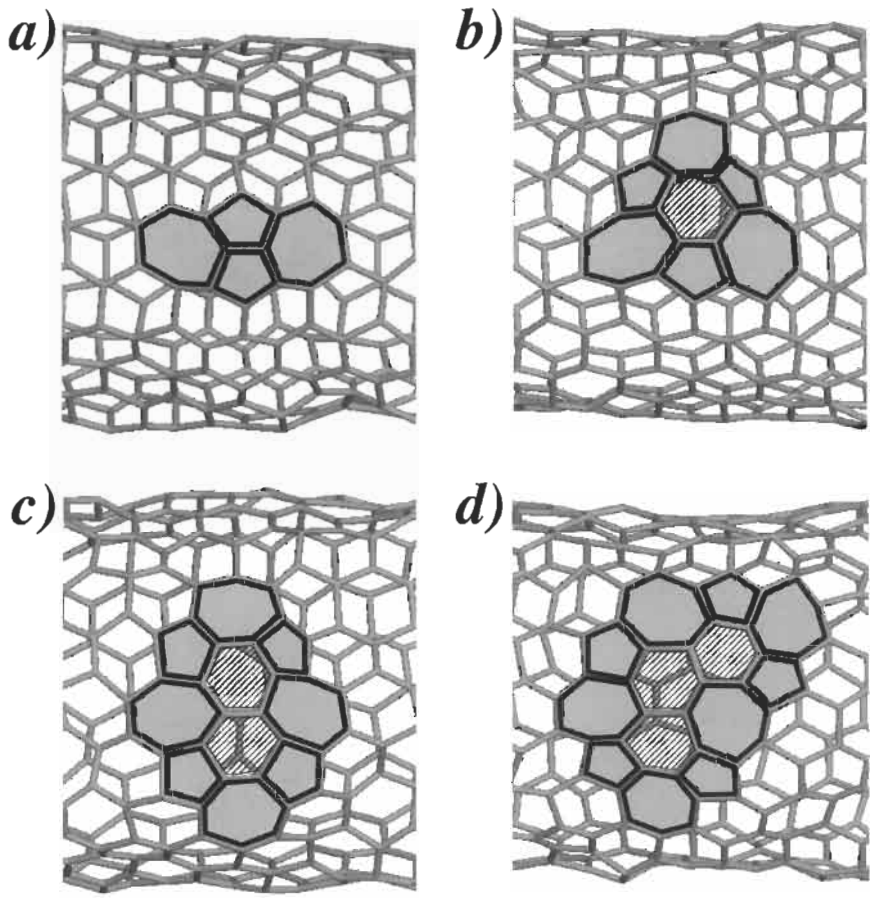

Fig. 10. Sample configurations showing the time evolution of a carbon addimer on (10,10) tube under 3% strain: (a) (7–5–5–7) defect forms after 4 ps; (b) bond rotation leads to defect with one rotated hexagon, 346 ps; (c) two hexagons, 421 ps; and (d) three hexagons at 2.35 ns. The bonds that need to be rotated in order to incorporate more hexagons are the ones emanating from the vertex of the pentagons, pointing away from the defect.

This behavior is to be contrasted with that of the strained (17,0) zigzag tube. Here, there are no oscillations in the variation of energy, indicating that hexagons are all added to the structure in a similar manner. Under 5% strain, the defect with *three* hexagons has the lowest energy. However, the energy differences between adjacent configurations are quite small, so that energetically the structures are nearly degenerate. Structures with a larger number of hexagons may therefore readily be formed at finite temperatures. Under the larger 10% strain, the formation energy now decreases continuously so that the wrapping of the defect about the circumference of the nanotube is favored. The above results have been obtained with the many-body Tersoff–Brenner potential, but qualitatively similar results have also been obtained with a more accurate tight binding model (Orlikowski et al., 1999).

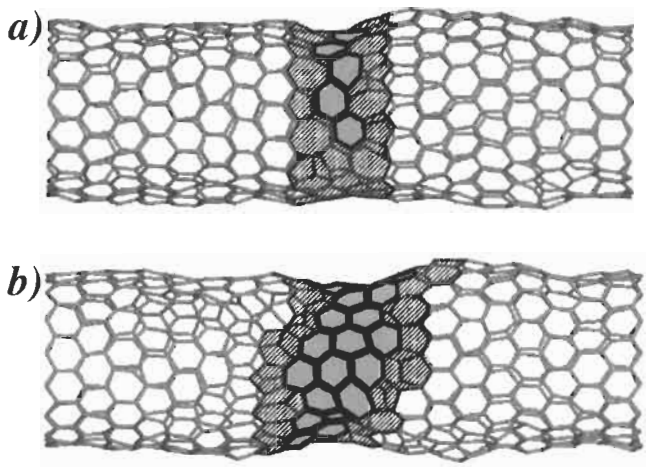

Fig. 11. Time evolution of the (17,0) tube with an addimer under 7.5% strain at 3000 K, illustrating the spontaneous winding of the defect about the tube: (a) initial configuration consisting of a single turn; (b) final configuration corresponding to about 3 turns after 1 ns.

The winding of the defect about the nanotube suggests that the combination of addimers plus strain in the 5–10% range may be a natural way to produce different electronic heterojunctions, thereby leading to the formation of different carbon nanotube-based quantum dots. To test this idea, we constructed various addimer-based defect structures at different strains and annealed at temperatures in the 2500–3000 K range, with the following results. Structures on the (10,10) armchair tubes were not observed to be stable. Competing bond rotations (e.g., bond rotations away from the defect, or bonds on the heptagons) lead to the degradation of the structure within a few nanoseconds. It therefore seems quite unlikely that good quantum dots can be made with the help of addimers from the (10,10) and/or other armchair tubes. Much more promising results were obtained for the (17,0) zigzag tube. Fig. 11 shows sample configurations of such a tube consisting of 682 atoms, annealed at 3000 K and 7.5% strain. As is evident, there is no sign of any competing ductile behavior that would lead to the degradation of the structure. Rather, hexagons are added in a uniform fashion about the circumference of the tube, ultimately leading to the formation of two to three different windings of an (8,8) tube over the period of a nanosecond. This suggests that with the addition of addimers to strained zigzag tubes one can selectively induce ductile behavior on tubes that are otherwise brittle, and thus form clean interfaces between tubes of different helicities.

To characterize the electronic properties of the induced (17,0)/(8,8)/(17,0) structure we have calculated the local density of states (LDOS) using a recursion method (Haydock et al., 1975) within a tight-binding description of the carbon π bonds. Only nearest-neighbor interactions were considered. Depending on the length of the (8,8) segment, a clear emergence of a quantum dot structure was observed, with orbitals becoming localized in the (8,8) segment and falling inside the fundamental energy gap of the (17,0) tube (Chico et al., 1998; Orlikowski et al., 1999).

ELECTRON TRANSPORT PROPERTIES OF STRAINED NANOTUBES

Graphite is a semi-metal and the electronic structure of carbon nanotubes can be derived from that of graphene, a single sheet of graphite. It turns out that single-walled carbon nanotubes can be either metallic or semiconducting, depending on their helicity. In particular, nanotubes with indices (n,m) are predicted to be metallic if $n - m = 3q$ with q = integer (we do not discuss the many-body effects that may lead to insulating behavior at temperatures near 0 K). While armchair NTs are always metallic, diameter plays an important role in modifying the electronic properties of chiral and zigzag NTs. In particular, in small-diameter NTs, the hybridization of s and p orbitals of carbon can give rise to splitting of the π and π^* bands responsible for metallic behavior (Blase et al., 1994). For example, $(3q,0)$ zigzag nanotubes of diameters up to 1.5 nm are always small-gap semiconductors.

The unique electronic and conducting properties nanotubes have attracted the attention of a number of experimental and theoretical groups (Song et al., 1994; Langer et al., 1994, 1996; Tian and Datta, 1994; Chico et al., 1996; Collins et al., 1996; Saito et al., 1996; Tamura and Tsukada, 1997, 1998; Tans et al., 1997; Anantran and Govindan, 1998; Bezryadin et al., 1998; Bachtold et al., 1999; Buongiorno Nardelli, 1999; Buongiorno Nardelli and Bernholc, 1999; Choi and Ihm, 1999; Farajian et al., 1999; Paulson et al., 1999; Rochefort et al., 1999). Below, we discuss the quantum conductance properties of nanotubes under strain or in the presence of strain-generated defects.

We begin with the analysis of the electrical behavior of bent nanotubes. It has recently been observed (Bezryadin et al., 1998) that in individual carbon nanotubes deposited on a series of electrodes three classes of behavior can be distinguished: (1) non-conducting at room temperature and below, (2) conducting at all temperatures, and (3) partially conducting. The last class represents NTs that are conducting at a high temperature but at a low temperature behave as a chain of quantum wires connected in series. It has been argued that the local barriers in the wire arise from bending of the tube near the edge of the electrodes.

In Fig. 12 we show the conductance of a (5,5) armchair nanotube ($d = 0.7$ nm) that has been symmetrically bent at angles $\theta = 6°$, 18°, 24°, 36°. θ measures the inclination of the two ends of the tubes with respect to the unbent axis. No topological defects are present in the tubes. For θ larger than 18° the formation of a kink is observed, which is a typical signature of large-angle bending in carbon nanotubes (Iijima et al., 1996). Although armchair tubes are always metallic because of their particular band structure, the kink is expected to break the degeneracy of the π and π^* orbitals, thus opening a pseudo-gap in the conductance spectrum (Ihm and Louie, 1999). However, if the bending is symmetric with respect to the center of the tube, the presence of the kink does not alter drastically the conductance of the system (Rochefort et al., 1999), since the accidental mirror symmetry imposed on the system allows the bands to cross. When this accidental symmetry is lifted, a small pseudo-gap (~6 meV) occurs for large bending angles ($\theta \geq 24°$), see the inset of Fig. 12. The same calculations have been repeated for a (10,10) tube ($d = 1.4$ nm), and no pseudo-gap in the conductance spectrum was observed in calculations with energy resolution of 35 meV, even upon large-angle asymmetric bending. Our calculations thus indicate that even moderate-diameter armchair

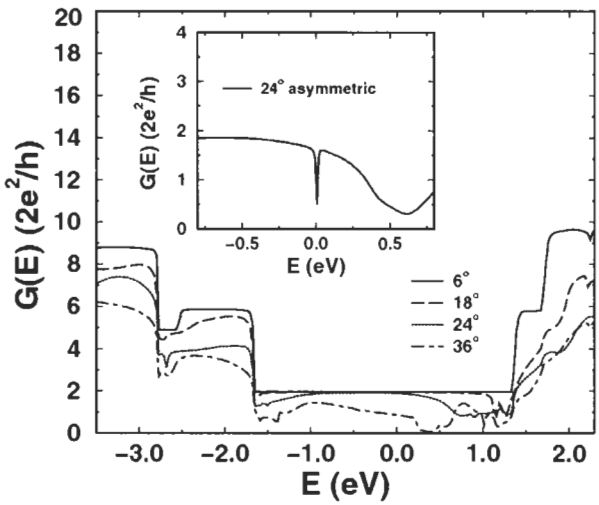

Fig. 12. Conductance of a symmetrically bent (5,5) armchair nanotube. Different curves correspond to different bending angles: 6°, 18°, 24° and 36°, as shown in the legend. Inset: conductance of a (5,5) tube with an asymmetric bend of 24°. A pseudo-gap at the Fermi energy (always taken as reference) is clearly present, see text.

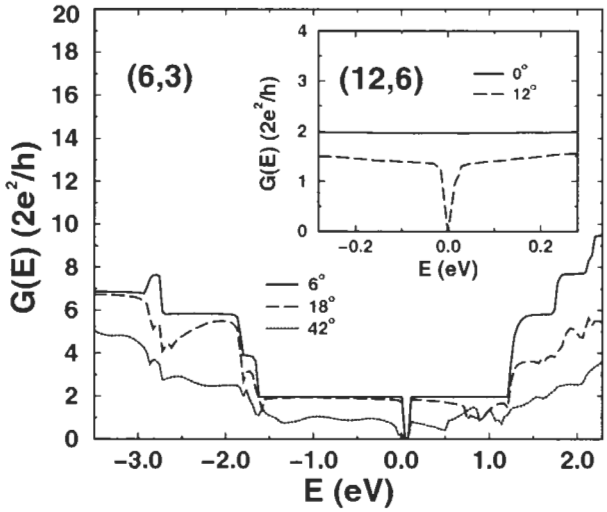

Fig. 13. Conductance of a bent (6,3) chiral nanotube. Different curves correspond to different bending angles: 6°, 24°, and 42°, as shown in the legend. Inset: conductance of a bent (12,6) chiral nanotube for $\theta = 0°$, 12°. The Fermi energy is taken as reference.

tubes essentially retain their metallic character even after large-angle bending and can therefore be assigned to the (2) class of behavior in Bezryadin et al. (1998).

In Fig. 13 we present the conductance of a bent (6,3) chiral nanotube, for $\theta = 6°$, 18° and 42°. Because of the relatively small diameter ($d = 0.6$ nm), the curvature-induced

Table 1. Conductances of armchair nanotubes with point defects

	Pristine	(5–7–7–5)	(5–7)–(7–5)	(5–7–8–7–5)
(5,5)	2.00	1.70	1.11	1.26
(10,10)	2.00	1.85	1.33	1.72

(5–7–7–5) is the bond rotation defect; (5–7)–(7–5) corresponds to the onset of plastic behavior with the two (5–7) pairs separated by one row of hexagons; (5–7–8–7–5) corresponds to the onset of brittle behavior, with the opening of a higher-order carbon ring, see text. In units of $2e^2/h$.

breaking of the degeneracy in the band structure opens a gap ($E_g \approx 0.1$ eV), clearly present in Fig. 13. For large deformations ($\theta = 42°$), this gap is widened ($E_g \approx 0.2$ eV), increasing the semiconducting character of the nanotube. One can then expect that bending in a large-diameter, metallic chiral nanotube will drive it towards a semiconducting behavior. This behavior is actually computed for a (12,6) chiral tube ($d = 1.2$ nm), as shown in the inset of Fig. 13. A bending-induced gap of ~60 meV is opened at a relatively small angle (12°), whereas the NT was perfectly conducting prior to bending. This result demonstrates that local barriers for electric transport in metallic chiral NTs can occur with no defect involved and just be due to a deformation in the tube wall. Given the relatively small values of the energy gaps, the conductance will be affected only at low temperatures, leading to the assignment of these tubes to the (3) class of behavior in Bezryadin et al. (1998).

Although bending by itself can already cause a significant change in the electrical properties, defects are likely to form in a bent or a deformed nanotube, because of the strain occurring during the bending process. It is now well established that a carbon nanotube under tension releases its strain via the formation of topological defects (Buongiorno Nardelli et al., 1998a,b). We have investigated how these defects affect the conductance of metallic armchair nanotubes of different diameters. Table 1 summarizes our results for (5,5) and (10,10) NTs under 5% strain, both pristine and in the presence of different topological defects: (1) a (5–7–7–5) defect, obtained via the rotation of the C–C bond perpendicular to the axis of the tube; (2) a (5–7) pair separated from a second (7–5) pair by a single hexagon row, as in the onset of the plastic deformation of the nanotube; and (3) a (5–7–8–7–5) defect, where another bond rotation is added to the original (5–7–7–5) defect, producing a higher-order carbon ring (onset of the brittle fracture). While strain alone does not affect the electronic conduction in both tubes, the effect of defects on conductance is more evident in the small-diameter (5,5) NT, while it is less pronounced in the larger (10,10) NT. Our results for the (10,10) tube with a single (5–7–7–5) defect compare very well with a recent ab initio calculation (Choi and Ihm, 1999). If more than one (5–7–7–5) defect is present on the circumference of the NT, the conductance at the Fermi level is lowered: for the (10,10) NT it decreases from 2 ($2e^2/h$) to 1.95, 1.70 and 1.46 ($2e^2/h$) for one, two or three defects, respectively.

The decrease in conductance is accompanied by a small increase in the DOS at the Fermi energy. This is due to the appearance of defect states associated with the pentagons and heptagons within the metallic plateau near the Fermi level. These localized states behave as point scatterers in the electronic transmission process and are responsible for the decrease in conductance (Crespi et al., 1997). This result confirms that in

large-diameter nanotubes the key quantity in determining the electrical response is the density of defects per unit length. This is also in agreement with recent measurements of Paulson et al. (1999) of the electrical properties of carbon nanotubes under strain applied with an AFM probe. As the AFM tip pushes the tube, the strain increases without any change in the measured resistance until the onset of a structural transition is reached. This corresponds to the beginning of a plastic/brittle transformation that releases the tension in the NT and coincides with a sharp yet finite increase in resistance. Since the onset of the plastic/brittle transformation that precedes the breakage is associated with the formation of a region of high defect density (Buongiorno Nardelli et al., 1998a,b), the conductance at the Fermi energy is drastically reduced.

In the experiments of Paulson et al. (1999), a clamped multi-walled nanotube was stretched until breakage with an AFM tip, but after the breakage the ends were manipulated back into contact and a finite resistance was established. As a partial simulation of this process, we have considered the tube–tube junction depicted in Fig. 14a. Two open-ended (5,5) tubes have been put in contact with a small overlap region. The system was then annealed via a molecular dynamics simulation at a high temperature (3000 K) for ~30 ps, after which the atoms were quenched to their ground state configuration. In

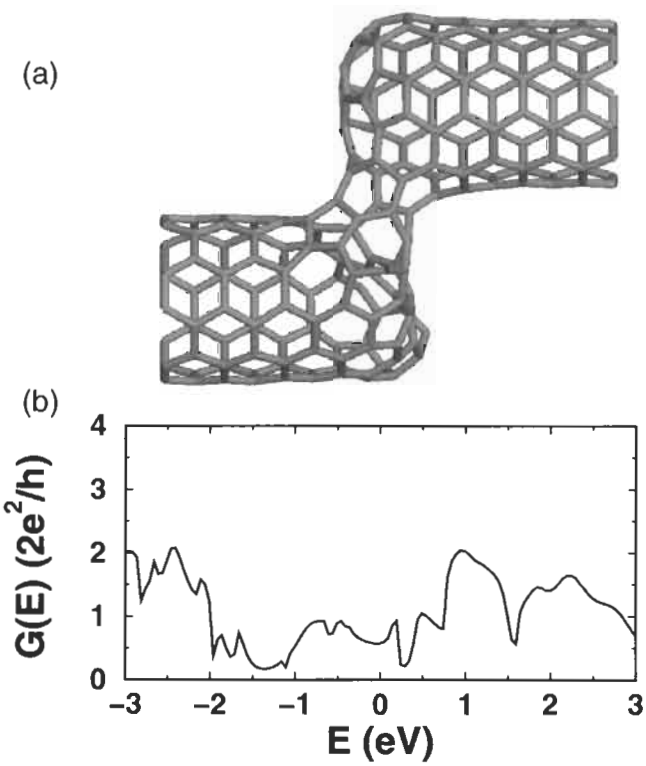

Fig. 14. The geometry (a) and the conductance (b) of an annealed contact between two open-ended (5,5) nanotubes. See text. The Fermi energy is taken as reference.

the resulting geometry the two ends bind together to form a small channel between the tubes, while the tips close in a partial hemisphere (Buongiorno Nardelli et al., 1998c). The conductance of the final structure is shown in Fig. 14b. The small contact channel between the nanotubes enables electron transmission, although at a low level of conductance ($G(E_F) \approx 0.6(2e^2/h)$). This result does not change significantly if a larger overlap region is considered, provided that a transmission channel is formed in the process. This observation is consistent with the experimental findings of Paulson et al. (1999).

SUMMARY

In summary, we have shown that in carbon nanotubes high-strain conditions can lead to a variety of atomic transformations, often occurring via successive bond rotations. The barrier for the rotation is dramatically lowered by strain, and ab initio results for its strain dependence were presented. While very high strain rates must lead to breakage, (n,m) nanotubes with $n,m < 14$ can display plastic flow under suitable conditions. This occurs through the formation of a 5–7–7–5 defect, which then splits into two 5–7 pairs. The index of the nanotube changes between the 5–7 pairs, potentially leading to metal–semiconductor junctions. Such transformations can be realized via manipulations of the nanotube using an AFM tip. Carbon addimers can also induce structural transformations in strained tubes, potentially leading to the formation of quantum dots in otherwise brittle tubes.

Defects and strain can obviously affect the electrical properties of nanotubes. We have computed quantum conductances of strained, defective and deformed nanotubes. The results show that bent armchair nanotubes keep their metallic character for most practical purposes, even though an opening of a small symmetry-related pseudo-gap is predicted in small diameter ($d < 0.7$ nm) nanotubes. Metallic chiral nanotubes undergo a bending-induced metal–semiconductor transition that manifests itself in the occurrence of effective barriers for transmission, while bent zigzag nanotubes are always semiconducting for the diameters considered in this study (up to 1.5 nm). Topological defects increase the resistance of metallic nanotubes to an extent that is strongly dependent on their density per unit length.

ACKNOWLEDGEMENTS

This work was supported in part by grants from ONR and NASA. The computations were carried out at DoD, NSF and NC Supercomputing Centers.

REFERENCES

Anantram, M.P. and Govindan, T.R. (1998) *Phys. Rev. B*, 58: 4882.

Bachtold, A., Strunk, C., Salvetat, J.P., Bonnard, J.M., Forró, L., Nussbaumer, T. and Schönenberger, C. (1999) *Nature*, 397: 673.

Bernholc, J., Roland, C. and Yakobson, B.I. (1997) *Curr. Opin. Solid State Mater. Sci.*, 2: 706.

Bezryadin, A., Verschueren, A.R.M., Tans, S.J. and Dekker, C. (1998) *Phys. Rev. Lett.*, 80: 4036.
Blase, X., Benedict, L.X., Shirley, E.L. and Louie, S.G. (1994) *Phys. Rev. Lett.*, 72: 1878.
Buongiorno Nardelli, M. (1999) *Phys. Rev. B*, 60: 7828.
Buongiorno Nardelli, M. and Bernholc, J. (1999) *Phys. Rev. B*, 60: R16338.
Buongiorno Nardelli, M., Yakobson, B.I. and Bernholc, J. (1998a) *Phys. Rev. B*, 57: R4277.
Buongiorno Nardelli, M., Yakobson, B.I. and Bernholc, J. (1998b) *Phys. Rev. Lett.*, 81: 4656.
Buongiorno Nardelli, M., Brabec, C.J., Maiti, A., Roland, C. and Bernholc, J. (1998c) *Phys. Rev. Lett.*, 80: 313.
Collins, P.G., Zettl, A., Bando, H., Thess, A. and Smalley, R. (1996) *Science*, 278: 100.
Crespi, V.H., Cohen, M.L. and Rubio, A. (1997) *Phys. Rev. Lett.*, 79: 2093.
Chico, L., Benedict, L.X., Louie, S.G. and Cohen, M.L. (1996) *Phys. Rev. B*, 54: 2600.
Chico, L., Sancho, M.P. and Munoz, M.C. (1998) *Phys. Rev. Lett.*, 81: 1278.
Choi, H.J. and Ihm, J. (1999) *Phys. Rev. B*, 59: 2267.
Chopra, N., Benedict, L., Crespi, V., Cohen, M.L., Louie, S.G. and Zettl, A. (1995) *Nature*, 377: 135.
Dresselhaus, M.S., Dresselhaus, G. and Eklund, P.C. (1996) *Science of Fullerenes and Carbon Nanotubes*. Academic Press, San Diego, CA.
Ebbesen, T.W. (Ed.) (1997) *Carbon Nanotubes: Preparation and Properties*. CRC Press, Boca Raton, FL.
Ebbesen, T.W. and Takada, T. (1995) *Carbon*, 33: 973.
Falvo, M.R., Clary, G.J., Taylor II, R.M., Chi, V., Brooks Jr., F.P., Washburn, S. and Superfine, R. (1997) *Nature*, 389: 582.
Farajian, A.A., Esfarjani, K. and Kawazoe, Y. (1999) *Phys. Rev. Lett.*, 82: 5084.
Haydock, R., Heine, V. and Kelly, M.J. (1975) *J. Phys. C*, 8: 2591.
Ihm, J. and Louie, S.G. (1999) private communication.
Iijima, S., Brabec, C., Maiti, A. and Bernholc, J. (1996) *J. Chem. Phys.*, 104: 2089.
Krishnan, A., Dujardin, E., Ebbesen, T.W., Yianilos, P.N. and Treacy, M.M.J. (1998) *Phys. Rev. B*, 58: 14013.
Langer, L., Stockman, L., Heremans, J.P., Bayot, V., Olk, C.H., Haesendonck, C., van Bruynseraede, Y. and Issi, J.P. (1994) *J. Mater. Res.*, 9: 927.
Langer, L., Bayot, V., Grivei, E., Issi, J.P., Heremans, J.P., Olk, C.H., Stockman, L., van Haesendonck, C. and Bruynseraede, Y. (1996) *Phys. Rev. Lett.*, 76: 479.
Maiti, A., Brabec, C.J. and Bernholc, J. (1997) *Phys. Rev. B*, 55: 6097.
Orlikowski, D., Buongiorno Nardelli, M., Bernholc, J. and Roland, C. (1999) *Phys. Rev. Lett.*, 83: 4132.
Paulson, S., Falvo, M.R., Snider, N., Helser, A., Hudson, T., Seeger, A., Taylor II, R.M., Superfine, R. and Washburn, S. (1999) *Appl. Phys. Lett.*, 75: 2936.
Rochefort, A., Lesage, F., Salahub, D.R. and Avouris, P. (1999) *Phys. Rev. B*, 60: 13824.
Ruoff, R. and Lorents, D. (1995) *Bull. Am. Phys. Soc.*, 40: 173.
Saito, R., Dresselhaus, G. and Dresselhaus, M.S. (1996) *Phys. Rev. B*, 53: 2044.
Saito, R., Dresselhaus, G. and Dresselhaus, M.S. (1998) *Physical Properties of Carbon Nanotubes*. Imperial College Press, London.
Song, S.N., Wang, X.K., Chang, R.P.H. and Ketterson, J.B. (1994) *Phys. Rev. Lett.*, 72: 697.
Stone, A.J. and Wales, D.J. (1986) *Chem. Phys. Lett.*, 128: 501.
Tamura, R. and Tsukada, M. (1997) *Phys. Rev. B*, 55: 4991.
Tamura, R. and Tsukada, M. (1998) *Phys. Rev. B*, 58: 8120.
Tans, S.J., Devoret, M.H., Dai, H., Thess, A., Smalley, R.E., Georliga, L.J. and Dekker, C. (1997) *Nature*, 386: 474.
Thess, A., Lee, R., Nikolaev, P., Dai, H., Petit, P., Robert, J., Xu, C., Lee, Y.H., Kim, S.G., Rinzler, A.G., Colbert, D.T., Scuseria, G., Tomanek, D., Fisher, J.B. and Smalley, R.E. (1997) *Science*, 273: 483.
Tian, W. and Datta, S. (1994) *Phys. Rev. B*, 49: 5097.
Walters, D.A., Ericson, L.M., Casavant, M.J., Liu, J., Colbert, D.T., Smith, K.A. and Smalley, R.E. (1999) *Appl. Phys. Lett.*, 74: 3803.
Yakobson, B.I., Brabec, C.J. and Bernholc, J. (1996) *Phys. Rev. Lett.*, 76: 2511.
Yu, M.F., Files, B.S., Arepalli, S. and Ruoff, R.S. (2000) *Phys. Rev. Lett.*, 84: 5552.

AUTHOR INDEX

(Page numbers in italics correspond to the reference list at the end of each chapter)

Abe, H., *152*
Abe, Y., 92, *104*
Abhiraman, A.S., 9, *25*
Adams, W.W., *327*
Aebi, U., *327*
Akita, S., *240*
Al-Dawery, I., *105*
Alberts, B., 309, *325*
Alexander, I.C., *105*
Allen, S.R., 276, *285*, *302*
Amirbayat, J., *326*
An, K.-N., 317, *326*
Anantran, M.P., 371, *375*
Anastassakis, E., *55*
Anderson, E., 214, *238*
Anderson, T.L., 41, *54*
Anon., 338, *352*
Ansell, M.P., 63, *71*
Arashida, M., 246, 252, *261*
Arcidiacono, S., *326*
Arepalli, S., *56*, *376*
Argon, A.S., 7, *25*, 41, *54*, *239*
Armstrong, J.L., *151*
Armstrong, R., 214, *238*
Ash, S.G., *326*
Ashby, M.F., *240*
Auerbach, M.A., *325*
Augsten, K., 308, *325*
Auvray, S., *54*
Avakian, P., *55*, *286*
Avitzur, B., 187, *238*, 246, *261*
Avouris, P., *376*

Bachtold, A., 371, *375*
Backofen, W.A., 224, *240*
Bacon, R., 34, *54*
Bae, C.M., 42, *55*
Bahl, O.P., 171, *178*
Bair, T.I., *286*
Ball, C.J., 209, 210, *240*
Ballou, J.W., *286*
Baltimore, D., *326*
Baltussen, J.J.M., 45, *54*
Baltzer, N., 196, 198, 199, 236, *238*
Bando, H., *376*
Banfield, S.J., *286*
Banister, K.E., 321, *325*
Barranger, J.P., 109, *122*
Bass, J.D., *122*
Bayot, V., *376*
Benedict, L.X., *376*
Bennett, S.C., 174, 176, *178*
Beremin, F.M., 41, *54*
Berger, M.H., 78, 80, 84, *87*, 91, *104*, *105*
Berk, A., *326*
Bernholc, J., 34, *54*, 360, 371, *375*, *376*
Berta, Y., *105*
Besson, J., *105*
Bezryadin, A., 371–373, *376*
Billard, L., *239*
Billmeyer, F.W., 306, *325*
Birchall, J.D., 92, *105*
Black, W.B., 267, *285*
Blase, X., 371, *376*
Blume, R.C., *55*, *286*
Blumenthal, W.R., *25*
Boakye, E.E., *105*
Boelen, A., *25*
Bogoyavlenskii, P.S., *56*
Bonnard, J.M., *375*
Bourratt, X.M., 169, *178*
Bouten, P.C.P., *151*
Boyes, E.D., 165, *178*
Brabec, C.J., *376*
Bray, D., *325*
Bremer, A., *327*

Brenner, S.S., 30, 36, *54*, 200–202, *238*
Briant, C.L., 15, *25*
Brikowski, D., *25*
Broberg, K.B., 41, *54*
Broek, D., 120, *122*
Brooks Jr., *376*
Brooks, J.D., 167, *178*
Brower, A.L., *54*
Brown, D., 307, *325*
Brown, I.B., *239*
Brown, J.A., *327*
Brownlow, D.L., *152*
Brownrigg, A., 13, *25*
Bruynseraede, Y., *376*
Buchsbaum, M., *326*
Buchsbaum, R., *326*
Bunker, B.C., *152*
Bunn, C.W., 31, *54*
Bunsell, A.R., 66, *71*, 77, 78, *87*, *104*, *105*, 318, *327*
Buongiorno Nardelli, M., 361, 365, 371, 373–375, *376*
Busbey, R.F., 37, *56*
Busch-Lauper, K., 188, 191, 192, *238*
Butler, E.G., *105*
Butt, D.P., *25*

Cameron, N.M., 144, 146, *151*
Campbell, A.C., 321, *325*
Capaccio, G., 295, *302*
Cardona, M., *55*
Carlsson, A.E., *54*
Carlsson, J.O., *56*
Carnaby, G.A., *353*
Cartwright, D.J., 135, *153*
Casavant, M.J., *376*
Caslavsky, J.L., 114, *122*
Chaki, T.M., *238*
Chamberod, A., *239*
Chandan, H.C., 18, 19, 22, *25*, 140, *151*
Chang, R.P.H., *376*
Chang, S., *25*, *123*
Chapman, B.M., 52, *54*, 337, 340, *352*
Chapman, J.A., *327*
Charles, R.J., 135, *151*
Charsley, P., *239*
Chawla, K.K., 5, 12, 19, 22, 24, *24*, *25*, 32, 47, 50, *54*
Chen, C.C., 246, *261*
Chen, H.S., *239*
Chen, K.C., 103, *105*
Chen, R.T., *25*
Cheng, A., *326*
Cheng, T.T., 47, *54*
Chi, V., *376*
Chia, E.H., 246, *261*
Chico, L., 370, 371, *376*
Chittick, J., 306, *325*
Choi, H.J., 371, 373, *376*
Choi, S.R., 141, 142, *151*
Chokshi, A.H., 214, *238*
Chopra, N., 34, *54*, 360, *376*
Chou, C.Y., *151*
Chou, T.-W., 45, *55*, 317, 318, *325*
Chung, D.D.L., *54*
Clary, G.J., *376*
Codd, I., *238*
Coffin, L.F., 246, *261*
Cohen, M.L., *376*
Colbert, D.T., *376*
Coleman, B.D., 39, 50, *54*
Collins, P.G., 371, *376*
Collins, W.D., 38, *54*
Cooke, W.D., *71*, *286*, *352*
Corman, G.S., 103, *105*, 110, 111, *122*
Cottrell, A.H., 307, 310, 325, *325*
Courtney, T.H., 214, *238*
Craig, S.P., *151*
Crespi, V.H., 373, *376*
Crist, B., 31, *54*
Crompton, T.A., *302*
Cumberbirch, R.J.E., 350, *352*
Cunniff, P.M., 317, *325*
Curtin, W.A., 48, 51, *54*

Dabbs, T.P., 141, *151*
Dai, H., *376*
Dally, J.W., 220, 223, *240*
Daniels, P.N., 332, *352*
Darnell, J., *326*
Datta, S., 371, *376*
Dauskardt, R.H., 234, *239*
Davies, L.A., 231, 233–235, *238*
de Hey, P., *240*
de Jong, S., *353*
de Mont, M.E., *326*

de With, G., *151*
Dekker, C., *376*
Deléglise, F., *105*
Denny, M.W., *326*
Derby, B., 308, *325*
Desarmot, G., *178*
Desper, C., *178*
Deurbergue, A., 9, *25*
Devoret, M.H., *376*
Dhingra, A.K., *25*, 94, *105*
DiCarlo, J.A., 103, *105*
Dickerson, P.O., *122*
Dickinson, J.T., *239, 240*
Dobb, M.G., 176, 177, *178*, 271, *285*
Doege, E., 42, *54*
Doi, M., 215, 235, 236, *238*
Doleman, P.A., *105*
Donaghy, F.A., 141, *151*
Donovan, P.E., 231, 232, *238*
Doorbar, P., *54*
Douthwaite, R.M., *238*
Dowd, J., 145, *152*
Dresselhaus, G., *376*
Dresselhaus, M.S., *178*, 360, *376*
Dronyuk, M.I., *56*
Drzal, L.T., 35, *56*
Drzal, M.T., 177, *178*
DuBose, W.A., *178*
Duckett, K.E., *71*
Dujardin, E., *55*, *376*
Dunaway, D.L., 316, 317, *325, 326*
Duncan, W.J., 146, 147, *151*
Dunham, M.G., 169, *178*
Dwight, D.W., 129, 130, *151*
Dyos, K., *54*

Eastman, J.A., *240*
Ebbesen, T.W., *55*, 360, 365, *376*
Eby, R.K., *327*
Edie, D.D., 169, 171, *178, 179*
Ehrenreich, H., *54*
Eklund, P.C., *376*
Elices, M., 40, *54–56*, *326*
Endo, M., 174, *178*
Engin, A.E., *56*
Epstein, B., 132, *151*
Ericson, L.M., *376*
Esfarjani, K., *376*
Esposito, E., 36, *54*
Evans, A.G., 118, *122*

Fain, C.C., 171, *178*
Falvo, M.R., 360, *376*
Farajian, A.A., 371, *376*
Farber, B., 36, *55*
Farmer, S.C., 103, *105*, 109, 121, *122, 123*
Farraro, J.T., *240*
Fathollahi, B., 169, *178*
Faucon, A., 48–50, *54*
Feng, S., 147, *151*
Feughelman, M., 52, *54*, 337, *352*
Files, B.S., *56*, *376*
Fine, M.E., *239*
Fisher, J.B., *376*
Fitzer, E., 34, 35, *54, 55*, 77, *87*
FitzGerald, J.D., *179*
Flores, K.M., 234, *239*
Flores, R.D., 186, 188, 189, *240*
Foelix, R.F., 317, *326*
Ford, J.E., 347, *352*
Fornes, R.E., 313, *326*
Forró, L., *375*
Forrest, P.G., 223, *239*
Fossey, S.A., *325–327*
Fouquet, F., *240*
Fournier, M.J., *327*
France, P.W., 133, 134, *151*
Freeman, C., *105*
Freiman, S.W., *25*, 135, *151, 152*
Freudenthal, A.M., 132, *151*
Frische, S., *327*
Frohs, W., 34, *54*
Frommeyer, G., 235–237, *239*
Fujimura, K., *104*
Fujita, H., *239*
Fukuda, H., 45, *55*
Fukumoto, T., *105*
Fukusako, T., *239*
Fukushima, K., *240*
Fuller, E.R., 141, *151, 153*
Fung, Y.C., 316, *326*

Gardner, K.H., *55*, *286*
Garner, E.V., 31, *54*
Garrido, M.A., 313, *326*
Gasdaska, C.G., *105*

Gelatt, C.D., *54*
Geminov, V., 215, *239*
Georliga, L.J., *376*
Gibala, R., *240*
Gibeling, J.C., 231, *239*
Gierke, T.D., *55*, *286*
Gieske, J.H., 36, *55*
Gilbert, C.J., 235–237, *239*
Giles, P.P., *352*
Gilman, J.J., 234, *239*
Glaesar, A.M., *122*
Glaesemann, G.S., *25*, 139, *151*
Gleiter, H., *238*
Goldsby, J., *123*
Golubovic, L., 147, *151*
González, C., *55*
Gooch, D.J., 91, *105*
Gorham, S.D., 308, *326*
Gosline, J.M., 313, *326*
Goswami, B.C., 69, *71*
Govindan, T.R., 371, *375*
Grant, N.J., *239*
Greene, W.R., *302*
Greer III, L.C., *123*
Greer, R., 342, *352*
Grether, M.F., *105*
Grewen, J., 191, 194, *239*
Grimley, D.I., 149, *151*
Grimsditch, M.H., 35, *55*
Grivei, E., *376*
Groves, G.W., 91, *105*
Guerette, P.A., *326*
Guess, K.B., *327*
Guigon, M., 165, *178*
Guinea, G.V., 38, *55*
Gulati, S.T., 129, *151*, *152*
Gupta, P.K., 19, *25*, 129–131, 133, 135–137, 139–141, 143–149, *151*, *152*
Gurson, A.L., 41, *55*

Hüttinger, K.J., 10, 11, *25*
Ha, J.-S., *25*
Hadley, D.W., 315, *327*
Haesendonck, C., *376*
Hagiwara, M., 195, 199, 215, 235–237, *239*
Haider, M.I., *25*
Hall, N.W., *179*
Hamersma, W., *56*
Hanafusa, H., 149, *152*
Hansen, N., 214, *239*
Harget, P.J., *353*
Hasegawa, Y., *87*
Hausmann, K., *239*
Hausmann, K.H., 204, 205, 209, 210, 215, 218, 224, *239*
Hay, R.S., 102, *105*
Hayashi, J., *87*
Haydock, R., 370, *376*
He, T., 32, *55*
He, Y., *240*
Hearle, J.W.S., 52, 53, *55*, 59, 60, 66, 71, *71*, 267, 269, 272, 275, 277, 280, 285, *285*, *286*, 305, *326*, 332–337, 342, 343, 346, 348, 350–352, *352*
Hecht, J., 129, *152*
Hecht, N., 120, 121, *122*
Heine, M., 77, *87*
Heine, V., *376*
Helfinstine, J.D., 139, *151*
Helser, A., *376*
Heremans, J.P., *376*
Herrmann, C., *325*
Hertzberg, R.W., 135, *152*
Heuer, A.H., 110, *123*, *240*
Heuvel, H.M., 342, *352*
Hibino, Y., 135, 141, 142, 149, *152*, *153*
Hiki, Y., 36, *55*
Hills, D.A., *325*
Hobbs, R.E., 281–284, *286*
Hochet, N., *87*
Hoenger, A., *327*
Hofbeck, R., 215, *239*
Hollinger, D.L., 146, *152*
Holmes, D.F., *327*
Holmes, S.A., 63, *71*
Holtet, T., *327*
Holtz, A.R., *105*
Hong, S., 220–222, 224, *239*
Hongu, T., 271, *286*
Horascek, O., 17, *25*
Horikiri, S., *104*
Hsieh, C., 117, *122*
Hudson, S.P., 312, *326*
Hudson, T., *376*
Huisman, R., 342, *352*
Hunt, R.A., 132, 134, *152*

Hutchison, J.W., *240*
Huybrechts, L., *326*
Hyams, J.S., 308, *326*
Hyman, L.H., 321, *326*

Ichikawa, H., *87*
Ichikawa, M., *240*
Ichiki, E., *104*
Ihm, J., 371, 373, *376*
Iijima, S., 360, 371, *376*
Iimura, M., *87*
Ikeda, T., 246, *261*, *352*
Ilschner, B., *239*
Im, J., *54*
Imai, Y., *87*
Imura, T., *238*
Inniss, D., 141, *152*
Inoué, S., *327*
Inoue, A., *239*
Irwin, G.R., *56*
Ishijima, A., *327*
Ishikawa, T., *87*
Issi, J.P., *376*
Itou, S., *105*
Iwai, T., *87*
Iwanaga, K., *105*
Izawa, T., 129, *152*

Jackson, P.M., 246, *261*
Jacob, K.I., *25*
Jacobs, M., *286*
Jacobs, M.J.N., 271, *286*
Jain, M.K., 9, *25*
Jakus, K.E., 141, *151*, *152*
Jamieson, M., *25*
Jawson, M.A., 334, *352*
Jeng, S.M., *25*, *123*
Jenkins, S., 8, *25*
Jennings, U.D., 169, *179*
Jennison, H.C., 246, 247, *261*
Jeong, H.-T., *240*
Jeulin, D., *105*
Jin, N.Y., 228, *239*
Johnson, D.D., 92, *105*
Johnson, D.J., 9, 12, *25*, *178*, *285*
Johnson, J.W., *56*, *153*
Johnson, R.A., 36, *55*
Johnson, W., *178*

Jones, D.R.H., 231, *240*
Jones, I.P., *54*
Judelewicz, M.P., 213–215, 219, 220, 224, 229, *239*

Künkele, F., 35, *55*
Künzi, H.U., *196*, 198, 199, 230, 231, 236, *238*, *239*
Kabsch, W., 309, *326*
Kadler, K.E., *327*
Kalish, D., *151*
Kalish, K., *25*
Kampschoer, G., *286*
Kanamoto, T., 43, *55*, 295, *302*
Kaplan, D.L., 319, *326*
Kar, G., *25*
Karch, J., *238*
Kassenbeck, P., 334, *352*
Katchalsky, A., *327*
Katz, J.I., 132, *152*
Katz, S., *326*
Kausch, H.H., *55*, 289, 290, *302*
Kawazoe, Y., *376*
Kelly, A., 30, 31, 36, *55*, 102, *105*, 309, 318, 322, *326*
Kelly, M.J., *376*
Ketterson, J.B., *376*
Kilmer, J.P., *153*
Kim, G.H., 216, *239*
Kim, I., 202, 215, *239*
Kim, S.G., *376*
Kimura, H., 231, *239*
King, W., *238*
Kinloch, A.J., 289, *302*
Kitayama, M., *122*
Kobayashi, H., 36, *55*
Kobayashi, S., *261*
Kogure, K., *178*
Kokura, K., 149, *152*
Konishi, T., *352*
Konopasek, L., 275, *286*
Koob, T.J., *327*
Kopyev, I., 215, *239*
Koralek, A.S., *286*
Koyama, T., *178*
Kozey, V.V., 5, 8, *25*
Krause, J.T., *152*
Krishnan, A., 34, *55*, 361, *376*

Kriven, W.M., *122*
Kröff, A., *54*
Krönert, W., 215, *239*
Kulawansa, D.M., 233, 234, *239, 240*
Kulinsky, L., *122*
Kumar, S., 5, 8, 12, *25*
Kuo, V.W.C., 194, *239*
Kurkjian, C.R., 129, 130, 132, 141, 143, 144, 149, *151–153*
Kurokawa, M., 351, *352*
Kwizera, P., 165, *178*
Kwolek, S.L., *286*

Ladik, J., *55*
Laird, C., 222, 226, 228, *239*
Lambert, P., 321, *326*
Lançon, F., *239*
Langer, L., 371, *376*
Langford, S.C., *239, 240*
Lant, C.T., 109, *122*
Lara-Curzio, E., 47, *55*
Lavaste, V., 95, 97, 99, *104, 105*
Lavin, J.G., 161, 162, 165, 167, 169, *178*
Law, D., *238*
Lawn, B.R., 117, *122*, 131, 136, *151, 152*
Le Coustumer, P., 80, *87*
Leamy, H.J., *239*
Lee, D.N., 210, *239, 240*
Lee, R., *376*
Lee, Y.H., *376*
Lepetitcorps, Y., *54*
Lesage, F., *376*
Leslie, W.C., 209, *239*
Levan, A., 38, *55*
Lewis, J., *325*
Lewis, M.H., 103, *105*
Li, J.C.M., 234, *238, 239*
Liang, F., 282, *286*
Lieder, S.L., *105*
Limberger, H.G., *25*
Ling, D.D., *54*
Linton, J.D., 306, *326*
Lippmann, J.M., *239*
Liu, G., *240*
Liu, J., *376*
Liu, Y.L., *239*
Llorca, J., *55, 56, 326*
Lloyd, C.W., 308, *326*
Lodish, H., 308, 309, *326*
Logan, J., *240*
Lomas, B., *71, 286, 352*
Lorents, D., 360, *376*
Lorriot, T., *54*
Louie, S.G., 371, *376*
Lowe, T.C., *25*
Lowenstein, K.L., 145, *152*
Lu, K.E., 22, *25*
Lueneburg, D.C., *105*
Luo, Z.-P., 317, *326*

MacCrone, R.K., *152*
Mack, C., 350, *352*
Macmillan, N.H., 30, 31, 36, *55*, 309, 318, 322, *326*
Maddin, R., 231, *239*
Madhukar, M., 177, *178*
Mah, T., 121, *122*
Maiti, A., 368, *376*
Marder, M., 141, *152*
Mark, H., 267, *286*
Mark, R.E., *352*
Marsh, S.P., 36, *55*
Martin, E., *54*
Maschio, R.D., *25*
Mason, T.L., *327*
Masumoto, T., 195, 231, *239, 240*
Matson, L.E., 109, 111, 117, 120, 121, *122*, *123*
Matsudaira, P., *326*
Matthewson, M.J., 132, *151–153*
Matthys, E.F., 195, *239*
Mazur, J., 281, *286*
McCartney, L.N., 132, 134, *152*
McHenry, E.R., 168, *178*
McIntyre, J.E., 332, *352*
McQueen, R.G., 36, *55*
Meakin, P., *56, 302*
Mecholsky, J.J., 18, 19, 24, *25*, 139, 140, *152*
Megusar, J., 231, 233, 234, *239*
Mello, C.M., *326*
Mencke, J.J., 271, *286*
Mercadini, M., *25*
Merchant, H.D., 221, *239*
Merk, N., *239*
Meyers, M.A., 12, 24, *25*

Michalak, J.T., *239*
Michalske, T.A., 133, 141, *152*, *153*
Mielnik, E.M., 187, *239*
Milstein, F., 36, *55*
Minor, M.G., *239*
Miraftab, M., 352, *352*
Miyazaki, S., 213, 214, *239*
Monthioux, M., *87*
Moreton, M., 163, *178*
Moreton, R., *56*
Morey, S.M., *25*, *152*
Morgan, P.W., *286*
Morgan, R.J., 43, *55*, 278, 279, *286*
Morosoff, N., 313, *326*, *328*
Morris, R.C., *105*
Morscher, G.N., 103, *105*
Morton, W.E., 71, *71*, 269, 280, *286*, 332, 342, 351, *352*
Moseley, W.W., 332, 345, *352*
Mughrabi, H., 226, *239*, *240*
Muhlig, P., *325*
Muller, W., *326*
Munoz, M.C., *376*
Muraoka, M., 141, *152*
Murata, T., *239*
Murphy, S., 209, 210, *240*
Murr, L.E., 186, 188, 189, *240*

Náray-Szabó, I., *55*
Nakagawa, J., 271, *286*
Nakamura, N., 243, *261*
Nakamura, Y., *240*
Nam, W.J., 42, *55*
Narasimhan, D., *105*
Needleman, A., 41, *56*
Nelson, W.G., *353*
Neuhäuser, H., *240*
Newman, J.W., *179*
Newns, G.R., *151*
Nichols, C., *326*
Nieh, T.G., *25*
Nikolaev, P., *376*
Niou, C.-S., *240*
Nishida, S., *25*
Nishimura, H., 306, *326*
Nishioka, T., 246, *261*
Nix, W.D., 231, *239*
Nixdorf, J., 203, *240*
Northolt, M.G., 8, *25*, 45, *54*, *55*, 271, *286*
Nussbaumer, T., *375*

O'Dell, E.W., *105*
Oberle, L., *123*
Oberlin, A., 9, *25*, *87*, 173, *178*
Ochiai, I., *25*
Ochoa, R., *153*
Ogura, T., 235–237, *240*
Oh, S.I., *261*
Ohnaka, I., *239*
Okamura, K., *87*
Olk, C.H., *376*
Omori, M., *87*
Oplatka, A., *327*
Orlikowski, D., 369, 370, *376*
Orowan, E., 30, *55*
Orwin, D.F.G., *353*
Oster, G., 309, *326*
Otto, W.H., 143, 144, *152*
Oudet, Ch., 66, *71*
Overington, M.S., *286*

Pérez-Rigueiro, J., *56*, 231, *240*, *326*
Paek, U.C., 132, 144, *152*
Palko, J.W., 111, *122*
Pampillo, C.A., 231, 233, 234, *240*
Panar, M., 45, *55*, 271, *286*
Paradine, M.J., *151*
Paris, H., 13, *25*
Paris, P., *56*
Park, C.R., *178*
Parker, R.D., *25*, *151*
Parnianpour, M., *56*
Parthasarathy, T.A., 121, *122*
Patterson, J.P., 231, *240*
Paulson, S., 371, 374, 375, *376*
Pearse, J., *326*
Pearse, V., 321, *326*
Peebles, L.H., *179*
Pell-Walpole, W.T., 214, *240*
Pennings, A.J., *56*
Pennock, G.M., 169, *179*
Perelson, A.S., *326*
Perepelkin, K.E., *55*
Perkins, J.S., *178*
Petch, N.J., *238*
Peterlin, A., 43, *55*

Petit, P., *376*
Petry, M.D., *105*
Phillips, G.O., 271, *286*
Picken, S.J., 45, *55*
Pigliacampi, J.J., *25*
Plant, H.T., 146, *152*
Plecity, F.J., *239*
Polanyi, M., 30, *55*
Pollack, G.H., 313–315, *326*
Pollak, C.C., *326*
Porter, R.S., *55*, *302*
Postle, R., *353*
Poulon-Quintin, A., 101, *105*
Powers, J.D., *122*
Poza, P., 50, *56*, 308, 318, *326*
Preston, F., 267, *285*
Prevorsek, D.C., 342, *353*
Proctor, B.A., *56*, 146, *153*
Pruneda, C.O., *55*, *286*
Putthanarat, S., *327*
Pysher, D.J., 97, 99, *105*

Raff, M., *325*
Raith, A., 215, *239*
Ralph, B., 214, *239*
Raskin, C., 246–248, *261*
Ratner, M.A., *54*
Rawn, J.D., 308, *327*
Read, D.T., 215, 220, 222–224, *240*
Reeve, M.H., *151*
Reimschussel, A.C., *353*
Remmer, W.E., 246, 247, *261*
Reneker, D.H., 281, *286*
Renuart, E., 51, *56*, 308, 311, *327*
Reynolds, W.N., 10, *25*, *56*, 175, *179*
Rice, J.R., 41, *56*
Rieger, S., 194, *240*
Riewald, P.G., 281, *286*
Rinzler, A.G., *376*
Ritchie, R.O., *239*
Ritter, J.E., *151*, *152*
Roach, D.H., 133, *153*
Robert, J., *376*
Roberts, K., *325*
Robinson, K.E., 171, *179*
Robson, R.M., 318, *327*
Roche, E.J., *178*
Rochefort, A., 371, *376*
Rodriguez, N.M., 173, 175, *179*
Roger, H.C., 246, *261*
Rojo, F.J., *55*
Roland, C., *375*, *376*
Romine, J.C., 99, *105*
Rooke, D.P., 135, *153*
Rosen, A., *238*
Ross, R.A., 169, *178*, *179*
Rosselló, C., *55*
Rotarescu, M.I., *54*
Roth, R., 112, *122*
Royer, J., 38, *55*
Rubio, A., *376*
Ruiz, C., *325*
Ruoff, A.L., 35, *56*
Ruoff, R.S., *56*, 360, *376*
Russew, K., 231, *240*

Sabin, J.R., *54*
Safoglu, R., *54*
Saito, R., 360, 371, *376*
Saitow, Y., 95, *105*
Sakaguchi, S., 141, *152*, *153*
Salahub, D.R., *376*
Salama, M.M., 159, *179*
Salathe, R.P., *25*
Salem, D.R., 342, *353*
Salvetat, J.P., *375*
Sancho, M.P., *376*
Sanders, P.G., 214, *240*
Sandulova, A.V., 35, *56*
Sarko, A., 306, *326*
Sato, M., *261*
Satoh, H., *25*
Saville, B.P., *285*
Sawran, W.R., 167, *179*
Sawyer, L.C., 19, *25*
Sayir, A., 103, *105*, 109–111, 115–117, 121, *122*, *123*
Schönenberger, C., *375*
Schade, P., 203, *240*
Schaefgen, J.R., *286*
Scheucher, E., 209, 210, *240*
Schikner, R.C., *178*
Schladitz, H.J., 203, *240*
Schmücker, M., *25*
Schmid, F., 109, *123*
Schneider, H., *25*, 112, *122*

Schoppee, M.M., 65, *71*, 276, *286*
Schutzenberger, L., 173, *179*
Schutzenberger, P., 173, *179*
Scuseria, G., *376*
Seeger, A., *376*
Seifert, K., 235–237, *239*
Sekino, M., *261*
Senecal, K., *326*
Sengonul, A., 277, *286*
Sept, D., *327*
Sethi, V.K., 231, *240*
Sharma, R.K., *353*
Sharp, J.V., 175, *179*
Shatwell, R.A., *54*
Shen, Z., *178*
Shibata, K., *239*
Shibuya, M., 78, *87*
Shin, H.-J., 192, *240*
Shirazi-Ade, A., *56*
Shirley, E.L., *376*
Sietsma, J., *240*
Sikkema, D.J., 267, 271, 276, *286*
Simmons, J.H., 134, *153*
Simon, G., 77, *87*, 318, *327*
Simpkins, P.G., *152*
Sinclair, R.N., *151*
Sines, G., 160, *178, 179*
Sinogekin, S.V., *122*
Skelton, J., 65, *71*, 276, *286*
Smalley, R., *376*
Smit, L., 268, *286*
Smith, K.A., *376*
Smith, P., *56*, 279, 280, *286*, 289, 293, 296, *302*
Smith, W.L., 133, *152, 153*
Smook, J., 32, *56*
Sneddon, I.N., 38, *56*
Snider, N., *376*
Snow, J.D., 110, *123*
Soltis, P.J., 36, *56*
Song, J.W., *325*
Song, S.N., 371, *376*
Soraru, G.D., 19, *25*
Soules, T.F., 37, *56*, 134, *153*
Spaepen, F., 234, 235, *240*
Sparrow, J.T., 52, *55*, 333–335, *352*
Spreadborough, J., *238*
Srinivasan, S.G., *326*
Stössel, R.-P., *240*
Starke, E.A., 194, *239*
Staudinger, H., 270, *286*
Steele, W.J., *55*, *286*
Steif, P.S., 234, *240*
Steinbüchel, A., 306, *327*
Steinberg, I.Z., 314, 315, *327*
Steinmetz, M.O., 311, *327*
Sternstein, S., 47, *55*
Stobbs, W.M., 231, 232, *238*
Stockman, L., *376*
Stoffler, D., *327*
Stone, A.J., 361, *376*
Stout, M.G., *25*
Stribeck, N., *327*
Strunk, C., *375*
Stryer, L., 308, 309, *327*
Su, Y.Y., 246, *261*
Sudo, S., 129, *152*
Sugiyama, K., *238*
Sullivan, J.M., *152*
Sung, I.-M., 19, *25*
Sung, Y.-M., 19, *25*
Superfine, R., *376*
Suresh, S., 226, *240*
Swiler, T.P., *153*

Tada, H., 38, *56*
Tait, R.J., 38, *56*
Tajima, Y., *152*
Takada, T., 365, *376*
Takahashi, T., 13–15, *25*
Takeda, M., *55*, 77, *87*, *302*
Taki, F., *352*
Tamura, R., 371, *376*
Tanaka, H., 246, 247, *261*
Tanaka, K., *55*, *302*
Tanaka, S., 215, *240*
Tanimoto, Y., 246, *261*
Tanner, D., 8, *25*
Tans, S.J., 371, *376*
Tarui, T., 13, *25*
Tashiro, H., *25*
Taub, A.I., 231, *240*
Taylor II, R.M., *376*
Taylor, G.H., 167, *178, 179*
Taylor, M.D., 91, *105*
Taylor, S.T., 19, *25*

Termonia, Y., 45, *56*, 279, 280, *286*, 289, 291–293, 295, 296, 298, 300, 301, *302*, 310, *327*
Thess, A., 363, *376*
Thiel, B.L., 318, *326, 327*
Thomas, W.F., 143, *153*
Thomason, P.F., 41, *56*
Thompson, A.W., 224, *240*
Thomson, R., 117, *122*, *151*, *153*
Thurmond, F.A., *327*
Thwaites, J.J., *326*
Thøgersen, H.C., *327*
Tian, W., 371, *376*
Tilney, L.G., *326, 327*
Timoshenko, S., *353*
Tirrell, D.A., *327*
Tirrell, J.G., 306, *327*
Togashi, J., 246, *261*
Tomanek, D., *376*
Tomozawa, M., *152*
Tono, T., *238*
Toyama, M., *25*
Tracey, D.M., 41, *56*
Treacy, M.M.J., *55*, *376*
Treloar, L.R.G., 291, *302*, 334, *353*
Tressler, R.E., 97, 99, *105*
Trotter, J.A., 320, 322–324, *327*
Trpisova, B., *327*
Tsuda, Y., 317, *327*
Tsukada, M., 371, *376*
Tsuruta, A., *55*, *302*
Turrill, F.H., *179*
Tuszynski, J.A., 311, *327*
Tvergaard, V., 41, *56*

Uhlmann, D.R., *178*
Urry, D.W., 320, *327*
Utsunomiya, T., *105*

van Bruynseraede, Y., *376*
van den Beukel, A., *240*
van der Hout, R., 45, *55*, 271, *286*
van der Zwaag, S., *286*
van Dingenen, J., *286*
van Haesendonck, C., *376*
Vandekerckhove, J., 309, *326*
Varachi, J.P., *153*
Varelas, D., 22, 24, *25*
Vega-Boggio, J., 47, *56*
Verschueren, A.R.M., *376*
Vickers, B.D., *179*
Viechnicki, D.J., 109, 114, *122*, *123*
Vigo, T.L., *71*
Viney, C., 51, *56*, 307, 308, 310, 311, *325–327*
Vingsbo, O., 47, *56*
Visser, L.R., 101, *105*
Vollrath, F., 313, *327*
Von Lehmden, K., *105*
Vukcevich, M.R., 15, *25*

Wachtman, J.B., 110, *123*
Wada, T., 243, *261*
Wadsworth, J., *25*
Wagner, E., 312, *327*
Walden, R.G., *286*
Wales, D.J., 361, *376*
Walters, D.A., 361, *376*
Wang, J.L., 53, *56*
Wang, T.T., *239*
Wang, X.K., *376*
Ward, I.M., 289, *302*, 315, *327*
Warner, S.B., 305, 317, *327*
Washburn, S., *376*
Watanabe, Y., 233, *239, 240*
Waterbury, M.C., 35, *56*
Watson, J.D., *325*
Watt, W., 163, *178*
Wawner, F.E., 47, *56*
Weaire, D., 230, *240*
Weertman, J.R., *240*
Weil, R., 202, 215, 220–222, 224, *239*
Weins, M.J., *240*
Welch, J., *105*
Whalen, P.J., 103, *105*
White, J.L., 169, *178*
Whitehill, A.S., *286*
Whitlock, J., 35, *56*
Whitney, I., *56*, *153*
Wiederhorn, S.M., 116, 118, *123*, 130, 135, 141, *153*
Wilding, M.A., 277, *286*
Wilks, E., 35, *56*
Wilks, J., 35, *56*
Wilson, D.M., 95, 101, *105*
Wilson, W.D., 36, *55*

Winter, A.T., 228, *239*
Wittenauer, J.P., 15, *25*
Wong, B.S., 277, *286*
Woodings, C., 346, *353*
Woods, J., 341, *353*
Work, R.W., 313, 317, *326–328*
Wortmann, F.J., 52, *56*
Wright, A., *151*

Xu, C., *376*
Xu, Z.R., *25*

Yajima, S., 76, 77, *87*
Yakobson, B.I., 360, *375, 376*
Yamamura, T., 77, 78, *87*
Yanagida, T., *327*
Yang, H.H., *55*, 272, 277, 278, *286*
Yang, J.-M., 19, *25*, 120, *123*
Yang, Z., *179*
Yasutake, H., *327*
Yianilos, P.N., *55, 376*
Yoon, H.N., 45, *56*
York, S., *105*
Yoshida, K., 244–246, 255, *261*
Young, R.J., 289, *302*
Yu, M.F., 30, 34, *56*, 361, *376*
Yuce, H.H., 149, 150, *153*

Zahn, H., 52, *56*
Zettl, A., 34, *54, 376*
Zhong, Q., *152*
Zhu, Y.T., *25*
Zimmerman, J., *286*
Zipursky, S.L., *326*

SUBJECT INDEX

(Page numbers in italics refer to figures)

Abrasion, 47, 69, *70*, 141, 142, 276, 277, 351
Acoustic emission (AE), 254–256, *257*, 258–261
Acrylic, 62, 63, 331, 346, 347
Actin, 309–313, 317, 322
Adatoms in nanotubes, 368, *369*, *370*
Addimer in nanotubes, 368, 370, 375
Aluminum (Al), 13, 15, 78, 91, 99, 103, 109, 194, 203, 212, 214, 220, 223
Alumina
  α-alumina (single phase), *20*, 38, 94–99
  α-alumina-zirconia, 99–101
  α-alumina-mullite, 101, 102
  inclusions, 13
  fibre, 19, 21, 63, 91–95, 104
Amorphous metal, 185, 194, *198*, 199, 200, 229, 231, 233, 235–238
Aramid, 5, 6, 8, 9, 45, 63, 267, 272, 273, 276, 278, 281, 284, 331
Atomistic approach, 29–37, 117, 134, 141, 150, 361–367
Axial compression, (see fibre fracture)

Bending, 13, 38, 65–67, 69, 70, 215, 232, 235, 238, 276–278, 283–285, 310, 350, 351, 360, 371–373, 375
Bond
  covalent, 5, 29–33, 35, 64, 134, 228, 277, 279, 280, 289, 298, 310, 314, 346, 350
  hydrogen, 8, 46, 64, 267, 276, 278, 279, 292, 296, 301, 334, 335, 337, 342, 343, 346, 347
  van der Waals, 31, 46, 278, 280, 289, 290
Boron (B), 19, 34, 46, 47, 78, 83, 92, 158
Boron Nitride (BN), 19, 34, 47, 83
Buckling, 6, 7, 67, 177, 178, 276, 277, 282–285, 360
Bundle, 13, 29, 34, 46, 50, 51, 169, 226, 305, 313, 336, 340

Cable, 13, 14, 17, 18, 21, 203, 215, 332
Carbon (C)
  forms, *160*
  isotropic, 159, 160
  nanotube, 30, *33*, 33f, 359–361, 365–375
Carbon fibre
  failure mechanisms, 171f
  morphology, 78, 80–83, 104, 170
  PAN-based carbon fibres, 8, 12, 158, 159, *161*, 162, 163, *166–168*, 175, 177
  pitch-based carbon fibres, 9, *11*, 13, 158–161, *161*, 169, 171, *172*, *173*, 175, 177
  vapour grown, 171f
Cellulose, 8, 37, 51, 305, 307, 331–335, 346
Ceramic fibre, 5, 8, 9, 17f, 38, 59, 77, 78, 91, 116, 118, 171, 174, 310, 318
Collagen, 53, 305, 307, 308, 311, 312, 314, 317, 320, 323–325
Composite fibre, 46, *47–50*, 51, 158, 159, 177, 245f
Continuum approach, 37f
Copper (Cu), 13, 30, 36, 50, 186, 188, 192–197, 200–204, 210, 212–214, 216–219, 221–223, 225–227, 234, 249, 250, 254, 256, 257
Copper wire (see wires)
Cotton, 5, 51, 52, *53*, 63, 64, *65*, 306, 312, 331, 333–336, 350
Crack
  growth, 38, 41, 102, 109, 115–119, 122, 136, 141, 142, 147, 237, 311, 362
  nucleation, 12, 43, 119, 130, 141, 147, 150, 219, 227, 320
  velocity, 115, 116, 135, 141

Creep resistance, 17, 85, 86, 92, 94, 100–103, 109, 110, 120–122
Cross-link, 8, 30, 63, 64, 77, 78, 80, 81, 312, 320, 336, 337, 346
Cup failure, *189*
Chain slippage, 291, 292, 296

Defect
  Gibbs free energy, 361
  internal, 19, 62, 114, 175, 247, 272
  melt spinning, 76, 161, 169, 171, 184, 194–196, 233
  Stone-Wales transformation, 7, 361, 366, 368
  surface, 5, 12, 19, 21, 36, 38, 47, 63, 86, 93, *94*, 96, 113, 134, 196, 199, 207, 223, 233, 272
Diamond, 35f
Diffraction, 45, 110, 188, 192, 333
Directional solidification, 109, 117, 120, 121
Dislocation, 34–36, 97, 102, 117, 121, 188, 190, 200, 202, 203, 212, 222, 223, 226–229, 234, 235, 325, 361–365, 367
Drawing, *8*, *246*, *249–253*, 293, 295
  defects, 40, 185, 186, 204
Ductility, 15, 29, 219, 228, 229, 318

E-glass, (see glass)
Elastic (Young's) modulus, *11*, 12, 43, 83–85, 87, *93*, 99, 110–112, 114, 121, 130, 132, 134, 158, 193–195, 210–212, 235, 238, 267, 282, 289, 307, 310, 317, 361
Elasto Plastic Fracture Mechanics (EPFM), 37, 41, 185
Elastomer, 52, 59, 313, 318, 332, 344
Electrical conductivity, 159
Electron transport, 373
Entanglements, 46, 289–291, 294, 296, 301
Eutectic fibre, 18, 109f
Extrinsic strength, (see strength)

F-actin, 309, 311
Fatigue strength, (see strength)
Fibre
  coating, 47
  composite, 51f
  heterogeneous, 46f
  hierarchical, 29, 37, 51–53, 305, 306, 308, 310, 311, 313, 316
  melt-spun, 59, 194, 341, 342, 344, 346
  morphology, *170*
  oriented, 6, 37, 42–46, 50, 59, 63, 159, 169, 190, 289, 292, 298, 344
  self-assembled, 307, 312, 320
  solution-spun, 58, 63, 346, 348
  tapered, 320, 323
  unoriented, 59, 289, 293–296, 344
Fibre fracture
  axial compression, 5, 67, 272, 276, 277, 281, 282, *285*, 350, 351, 360
  axial splitting, 42, *68*, 70, 271, 272, *276*
  bending, 65, 66, 68, 235, 276
  brittle, 19, 29, 34, 39, *40*, 42, 46, 49, 59, *61*, 65, 91, 92, 122, 185, 200, 201, 216, 223, 227, 276, 280, 298, 307, 308, 312, 313, 318, 319, 332, 360, 366, 367, 370, 374, 375
  creep, 14, 15, 85, 86, 98, 99, 101, 102, 158, 159, 201, 273
  drawing (during), 13, 15, 23, 42, 63, 137, 140, 169, 185–188, 190, 191, 203, 215, 245–247, 250–254, 256, 257, 260, 261
  ductile, 37, 39–42, 59, *61*, 66, 185, 188, 227, 318, 345, 360, 362, 365–367, 370
  fatigue, 18, 38, 130, 133, 134–136, 138, 139, 142, 158, 159, 185, 215, 217, 221, 223, 227, 237
  fibrilar, *64*
  flex fatigue, 66, *68*, 69, 277
  granular, *63*
  internal, 187, 245, 250, 254, 256, 260, 261, 345
  kink band, 7, 8, 12, 13, 67, 70, 272, 277, 279, 281, 285, 351, 352
  lateral pressure, 66, 284
  shear splitting, 277, 278, 350, *351*
  tensile, 34, 38–40, 42, 65, 69, 117, 131, 149, 272, 278, 350
  tensile fatigue, 66, *67*, 69, 351
  torsional fatigue, 69
  twisting, 38, 65
  wear, 69
Fibril, 8, 32, 37, 42, 43, 45, 46, 50–53, 63, 64, 69, 163, 308, 317, 320, 333–337,

339, 346, 347
Filament break, 254, 256, 259–261
Finite element analysis, 42, 49, 53, 246, 248, 249, 251, 252, 260, 261
Flaw, 5, 12, 18, 19, 21, 22, 24, 30, 38, 40, 47, 59, 62, 63, 66, *94*, 96, 112–114, 116, 117, 120, 122, 129–134, 137–139, 141, 142, 144, 147, 149–151, 175, 245, 272, 278, 310, 312, 318
Fractography, 5, 29, 39, 139, 141
Fracture
  brittle, 29, 34, 39, 40, 42, 46, 49, 59, 65, 201, 216, 276, 296, 301, 332, 345, 367, 373
  change, 121
  cleavage, 19, 35, 112, 121, 200
  ductile, 37, 39–42, 227, 345
  fibrillar, 6, 8, 45, *64*
  granular, *63*, 87, 223, 336
  kinetic theory, 32, 46, 290
  modes, 43, 47, 59f, 218, 219, 233
  morphology, 24, 78, 80–83, 87, 104, 272
  shear, 177, 178, 231–233
  toughness, 18, 24, 29, 38, 48, 114, 120, 135, 312
Fullerene, 33, 359

Garnet, 103, 109, 122
Glass fibre
  basic concepts, 17f, 131f, 228f
  E-glass, 19, 22, 37, 129–131, 133, 137, 139, *140*, 143, 145–147, 149
  extrinsic strength, 133, 137f
  intrinsic strength, 132, 143f
  S-glass, 37, 145
  silica, 37, 129, 134, 144, 146, 149
Gold wire (see wire)
Graphite, 9, 34, 46, 47, 158, 159, 162, 171, 186, 359, 361, 371
Gurson model, 41

Hierarchical structures, 29, 51, 53, 305, 308, 310, 313, 316
High modulus fibre, 12, 13, 45, 65, 159, 267, 268, 273
High-modulus polyethylene (HMPE), 268, 273, *275*
High temperature, 12, 14, 15, 17, 47, 77, 78, 83, 85–87, 92, 93, 96, 99, 102, 104, 114, 115, 117, 120, 122, 144, 221, 231, 233, 345, 361, 364, 367, 371, 374
High tenacity fibre, 267, 331, 341

Inclusion, 10, 12–14, 22, 40, 42, 99, 103, 131, 139–141, 150, 186, 196, 197, 237, 242, 245, 247, *248*, 249–254, 260.
Inert strength, (see strength)
Interface, 29, 37, 42, 48, 311, 370.
Intrinsic strength, (see strength)
Iron (Fe), 30, 36, 101, 200, 201, 203, 213, 214

Keratin, 37, 52, 53, 305–307, 311, 312, 337.
Kink bands, *7*, 8, 12, 13, 67, *177*, 277, 281, 285, 351, 352

Laser heated floated zone (LHFZ), 109
Linear Elastic Fracture Mechanics (LEFM), 29, 37–39, 47, 185

Melt spinning, 76, 161, 169, 171
Melt-spun synthetic, 59, 341, 344, 346
Mesophase pitch, 8–10, 13, 159, 165, 166, 169, 171, 175, 177
Mesophase pitch fibre, 158, 159
Metallic fibre
  basic concepts, 5, 13f, 36, 39, 185f, 243f
  fabrication, 185f, 244f
  fracture modes, 190
  intrinsic strength, 200f
Metallic glasses, 228–235
  fatigue, 235, 237
  fracture, 228, 230, 232
Microbuckling, 6, *7*, 178.
Micro-wires, 185, 186, 188, 203, 204, 212, 215, 219, 221
Mirror radius, *19*
Molecular dynamics, 29, 34, 37, 134, 360, 361, 366, 374
Molecular weight, 43, 45, 46, 76, 77, 162, 165–169, 267, 268, 270, 279, 289, 293, 294, 296, 298–302, 306, 309
Monte-Carlo, 46, 291, 292, 301
Mullite, 13, 19, 92, 93, 101–104.

Myosin, 313, 314.

Nanofibres, 29
Nanotubes, 30, 33, 34, 359f
  electron transport, 371–375
  mechanical properties, 33, 359–367
  structures, 359, 368, 371, 375
Nylon, 43, 46, 59, 61, *62*, 66–69, *70*, 71, 267, 292, 301, 331, 332, 341–343, 345, 350–352

Oxidation curing, 77
Oxide ceramic fibres, 38, 102–104

PAN (Polyacrylonitrile), 8, 10, 12, 34, 77, 158, 159, 161–163, 175, 177, 331, 332
PBO (Polyphenylene bisoxazole), 8, 46, 267, 276
PBT (Poly(butylene terephthalate)), 46
PCS (Polycarbosilane), 76–78
PEEK (Poly(etherether ketone)),
Peeling, 60, 69, 250, 253, 276, 278, 350, 351.
Perovskite, 114, 122
PET (Poly(ethylene terephthalae)), 351
PIPD, 8, 267
Plastic deformation, 30, 42, 62, 190–191, 200, 202, 210–211, 221, 231, 259, 298, 345, 373
Plasticity, 41, 91, 97, 99, 260, 307, 368
Polyamide, 31, 45, 267, 331, 332, 341
Polyester, 31, 45, 59, 62, 63, 66, 67, 69, 267, 282, 306, 331, 332, 341–343, 345, 350, 352
Polyethylene (PE), 8, *31*, *32*, 43, 46, 161, 267, 268, 273, 280, 281, 289, 292–294, 296, 301, 331, 341, 342
Polymer fibre
  basic concepts, 5f, 31f, 42f, 67, 76, 77, 80, 161f, 267f, 305f, 333f, 337f, 341f, 346f
  creep rupture, 66, 273
  experimental observation, 272f
  highly oriented, 42f, *46*
  structure, 8, 9, 42, 269–271, 273, 301
  surface abrasion, 276
  tensile failure, 30, 272
  tensile fatigue, 275
  theoretical approach, *44*, 277f, 289f
  types, 5, 18, 24, 42, 267
Polyolefin, 31
Porosity, 78–80, 91, 95, 97
PPTA (Poly(para-phenylene terephthalamide)), 43, 45, 46, 280
PTC (Polytitanocarbosilane), 76–78, 81
Pyrolysis, 76–78, 80, 92, 103

Radiation curing, 77
Rayon 307, 331, 346–348
Residual stress, 13, 47, 48, 141, 142, 150, 210, 211, 256

Scanning electron microscopy, 67, 71, 80, 110, 113, 114, 117, *119*, 139, 169–171, 175, 178, 216, 218, 219, 256, 272, 275, 276, 280, 317, 348, 349
Segregation, *14*, 24, 101, 187, 247, 298, 300, 301
Self-assembly 306–309, 311, 312, 320, 321
S-glass, (see glass)
Shear band, *176*, 192, 231, 232, *234*, 237
Shear modulus, 6, 111, 230, 271, 334, 335
Shear splitting, 277, 278, 350
Silica glass, (see glass)
Silica (SiO_2), 17–19, 37, 38, 86, 91, 92, 94, 95, 101, 129–132, 139, 141, 143–145, 147–149
Silicon carbide (SiC) fibre
  fabrication, 76f
  fracture, 78f, *79*, *81–83*
  high temperature, 83f
  mechanical properties, 83f
Silk, 6, 8, 50, 305–308, 310–313, 316–319, 331
Silkworm, 313, 318
Single crystal fibre, 19, 109–112, 114–119, 121, 122, 200, 226, 227
Smart composite, 320, 325
Solution-spun fibres, (see fibre)
Speckle-shift technique, 109–111
Spinneret design, 170
Spinning, 5, 10, 76, 91, 95, 161, 165, 169, 171, 185, 194–196, 233, 267, 268, 307, 316, 343, 346
Steel, 13, 14, 40, 42, 159, 167, 236, 244, 332

Stiffness, 5, 36, 92, 95, 99, 111, 171, 269, 270, 284, 285, 289, 307, 316–320, 337
Stone-Wales transformation, (see defect)
Strain rate, 99, 109, 115, 117, 118, 130, 133–137, 139, 146, 201, 231, 233, 272, 292, 318, 319, 375
Strength
  basic concepts, 29f, 37f, 131f, *158*, *268*, 277f, 289f
  compressive, 5, 8, 12, 35, 267, 276, 312
  extrinsic, 96, 129, 130, 132–134, 137–139, 141, 143, 145, 150
  fatigue, 18, 69, 130, 134, 135, 142, 150, 158, 115, 222, 223
  inert,14, 130, 133, 134, 136, 138, 139, 141, 149, 150
  intrinsic, 95, 112, 129, 130, 132–134, 138, 143, 144, 146, 149, 150, 199, 200, 299, 309, 317, 341
  shear, 63, 200, 232, 267, 272, 277, 351
  tensile, 5, 8, 12, 13, 29–32, 35–37, 45, 51, 69, 78, 102, 112–114, 117–119, 122, 129, 175, 194–197, 199–204, 207, 214, 216, 222, 223, 232, 236, 271, 272, 275, 276, 289, 297–300, 302, 316–319, 321, 323, 339, 351
  theoretical, 10, 12, 29–36, 109, 113, 133, 134, 271, 277, 332
  yield, 32, 48, 49, 201, 204, 207, 267, 317, 344,
Stress intensity factor, 18, 38, 115, 116, 119, 135
Structural hierarchy, 311, 317
Superconducting wire, 254, 256, 257

Tenacity, 267, 297, 331, 336, 340, 341
Textile, 9, 53, 63, 65, 70, 162, 270, 305, 306, 309, 313, 331, 332, 337, 341, 342, 351
Texture, 19, 40, 185, 190–194, 210, 212, 221, 223, 225, 228, 346
Thermal conductivity, 114, 158, 159
Toughness, (see fracture)
Transmission electron microscopy, *16*, 30, 78, 82, *92*, *93*, *95*, *96*, 114, 121, 169, 175, 178, 188, 202, 216, 223, 227, 231
Tungsten (W), 5, 13–17, 46–50, 203, 204, 346
Tungsten filament, *16*, *17*
Turbostratic carbon, *10*, 159, 160, 171

Twisting, 38, 52, 64, 69, 70, 305, 334, 336, 351, 360

Void, 10, 12, 13, 19, 33, 40–42, 45, 47, 59, 62–64, 77, 113, 120, 161, 162, 186–188, 200, 246, 345, 348

Wear, 9, 67, 69, 70, *71*, 350, 351
Weibull, 5, 10, 19, 23, 24, 39, 50, 51, *52*, 117, *118*, 131, 132, 138, 139, 144, 146, 308, 317–319
Whisker, 30, 34–36, 185
  metallic, 200–203
Wire
  amorphous, 184, 195–200
  breakage, 40, 42, 245–248, 251, 252, 260
  copper
    elastic modulus, *194*, 210
    fatigue, 217, 218, 200–225, *216*
    fracture surface, *218*, *219*, 220, 227, *248*
    microstructure, 191, 200, 204, 206, 216
    pole figure, 192, 193, 210
    tensile strength, 13, *36*, 203, 206
    texture, 194, 210
  drawing, 15, 42, 188, 243–252, 254, 260
  gold
    annealing, 188, 204, 205, 209
    elastic modulus, 210, 211
    fracture surfaces, *190*, *205*, 218–220, 227, 248
    micro-hardness, 189, *192*
    microstructure, *191*, 200, 204, 206, 216
    tensile strength, 13, 203, 206, 207
    yield stress, 194, 206, 209, 212
  polycrystalline, 185, 194, 200, 206, 212, 215, 218
Wool, 8, 52, 63, 66, 69, *70*, 305, 306, 331, 337, *338*, 339–341, 351

YAG ($Y_3Al_5O_{12}$), 103, 109–112, *113*, 114, 117–122
Yarn, 9, 52, 69, 276, 277, 281, 283, 284, 305, 309, 331, 334, 339, 343
Yttria (Y_2O_3), 109–112, *113*, 114, 121

Zirconia (ZrO_2), 99, 100, 103, 104, 121

FIBER FRACTURE

Fiber Fracture describes and discusses the current ideas concerning the mechanisms and models of fiber fracture and is aimed at graduate students and researchers interested in fiber composite materials and mechanical properties of fibers.

Sections include:

Introduction
Ceramic Fibers
Glass Fibers
Carbon Fibers
Metallic Fibers
Polymeric Fibers
Nanofibers

ISBN 0 08 044104 1
9 780080 441047